The University Of Sheffield.

Fatigue Characterization of Ex-service Pipeline Metals in the Hydrogen Environment

By:

Elvis Ngaifoingwe Kufoin

A thesis submitted in the partial fulfilment of the requirements for the degree of Doctor of Philosophy

The University of Sheffield

Faculty of Engineering

Department of Civil and Structural Engineering

Supervisors:

Prof. Luca Susmel

Prof. Iman Hajirasouliha

Submission Date

December 2024

To my family …

Abstract

Reducing greenhouse gas emissions, particularly carbon dioxide, has become a key objective in global environmental policies, especially within the European Union. Achieving this goal relies on adopting renewable energy sources and eco-friendly technologies, with one promising approach being the blending of hydrogen with natural gas. This emerging trend in the energy sector represents a significant step toward decarbonisation. Blending hydrogen into the existing natural gas pipeline network is seen as a way to enhance renewable energy output, reduce domestic carbon emissions, and address the global carbon footprint. Many developed economies, including the UK, have devised strategies to support this transition. For example, the UK's HyDeploy project aims to blend 20% hydrogen by volume with natural gas. However, introducing hydrogen into natural gas networks can affect the behaviour of pipeline materials through a phenomenon known as hydrogen embrittlement. This a process whereby hydrogen atoms diffuse into metals and alter their mechanical properties, by weakening the metal and making it more susceptible to cracking under stress, even at relatively low loads. Therefore, it is crucial to assess the durability of materials in hydrogen-rich environments to safely execute this project.

This research therefore aims to assess the impact of hydrogen exposure on the mechanical properties of ex-service pipeline materials in the UK's natural gas network. To achieve this, the fatigue properties under controlled temperature and pressure conditions of these materials were investigated. The specimens were exposed to a hydrogen-rich environment using specialized equipment, where they were soaked or charged with hydrogen for varying durations of up to nine months, allowing hydrogen to diffuse into the material.

The results indicated that the mechanical properties of the tested metals were altered due to hydrogen embrittlement. However, statistical parametric analysis revealed that these changes were insignificant enough to compromise the safety of deploying the existing pipeline network for distributing natural gas blended with 20% hydrogen by volume. Nonetheless, the extent of impact varied across different pipeline materials, influenced by material composition, exposure duration, and operating conditions.

Acknowledgement

Foremost, I extend my deepest gratitude to my PhD supervisors, Prof. Luca Susmel and Prof. Iman, whose invaluable guidance made my doctoral journey possible. Their inspiration, wealth of knowledge, and unwavering patience during challenging times have been instrumental in shaping my academic experience. Through their mentorship, they have not only sharpened my intellect but also fostered my curiosity, resulting in a heightened sense of critical thinking and independence. I am immensely grateful for their remarkable support throughout this journey.

To my dad, from the very moment of my birth until now, you have been my constant teacher, guiding me not only through the classroom but through life itself. I have gleaned numerous skills from you, especially in navigating challenges to make ends meet. This milestone we have reached is a testament to your dedication and hard work. To my mum, who resides in blessed memory, the mere thought of your absence brings tears to my eyes. The radiance and vitality that accompany me every day are a reflection of you. The pain of your premature departure still lingers, yet I find solace in the belief that you are watching over us from your peaceful abode, proud of your son. Words cannot express how much I miss you. This line will forever be a conduit for tears streaming down my cheeks. Phyllis, you have played an instrumental role in shaping my life and guiding me to where I am today. Your absence is deeply felt, and I am reminded of your presence in every step I take. My dear sister, the void left by your absence is incomprehensible. The pain is profound and agonizing. Yet, I find solace in the miraculous manner in which I have coped without you. The mantle of our family legacy that you passed onto me remains afloat, and I vow to protect it from sinking. Yvonne, the challenges we have faced have tested us, but I hold onto hope that one day we will reunite as a family. Auntie Rose, only the divine knows why you were taken from us. Your unwavering support for me was immeasurable, and I deeply lament your absence, especially on this momentous occasion. Alongside your sister and my siblings, may you continue to watch over and guide us.

To my dearest wife my hero behind the scenes, you have not only provided financial support but also served as the stepping stone for both our son and myself as we embarked on this educational journey. Your resilience in the face of adversity, the sacrifices you've made, and the hardships you've endured are truly commendable. You willingly embraced frugality, sacrificing our holidays and trips, all to ensure the success of your husband. I cannot help but swell with pride. Your unwavering dedication fills me with renewed and everlasting love.

Table of Content

List of Figures

List of Tables

Acronyms

AIDE	Adsorption Induced Dislocation Emission
ASTM	American Society for Testing and Materials
ASME	American Society of Mechanical Engineers
HE	Hydrogen Embrittlement
HSE	Health and Safety Environment
EHE	External Hydrogen Environment
FCG	Fatigue Crack Growth
GCI	Grey Cast Iron
HAFCG	Hydrogen-Assisted Fatigue Crack Growth
HAZ	Heat Affected Zone
HCF	High Cycle Fatigue
HEDE	Hydrogen-Enhanced Decohesion
HELP	Hydrogen-Enhanced Localized Plasticity
HESIV	Hydrogen-Enhanced Strain-Induced Vacancies
HIPT	Hydrogen-Induced Phase Transformation
IIW	International Institute of Welding
IHE	Internal Hydrogen Environment
LCF	Low Cycle Fatigue
LRM	Linear Regression Method
MCF	Medium Cycle Fatigue
NPT	National Pipe Thread
VHCF	Very High Cycle Fatigue

Nomenclature:

C_0	Intercept of mean S-N curve (constant)
C_1	Coefficient of independent variable (constant)
$C_{1,i}$	Coefficient of the independent variable of i[th] data set, $i = 1,2..$
f	Degrees of freedom
F_{cal}	F-test statistic for variance calculated
F_{crit}	F-test statistic for variance from tables
k	Negative inverse slope
$K_{D(Owen)}$	Scatter factor from Owen tolerance limit approach
$K_{D(LM)}$	Scatter factor from the linear regression approach
$K_{D(ASTM)}$	Scatter factor from the ASTM approach
K_D	Scatter factor
$logN_{f,ij}$	Log of life at the replication level
$\overline{logN_{fij}}$	Mean log of life at the replication level
$\overline{log\sigma_i}$	Mean log of stress level, $\overline{log\sigma_i} = \sum_{i=1}^{n} \frac{log\sigma_i}{n}$
$\overline{logN_{f,i}}$	Mean log of fatigue life, $\overline{logN_{f,i}} = \sum_{i=1}^{n} \frac{logN_{f,i}}{n}$
$logN_{f,D}$	Log of estimated life for design life
m_i	Replication level at the i[th] stress level
N_f	Number of cycles to failure
$N_{f,i}$	Number of cycles to failure at the i[th] stress level
n	Number of experimental results (sample set)
n_σ	Number of stress levels
N_A	Reference number of cycles to failure
N_{kp}	Number of cycles to failure at the knee point
P_s	Probability of survival
q	Index depending on the probability of survival
R	Stress ratio (R=$\sigma_{min}/\sigma_{max}$)
s	The standard deviation of log cycles to failure
${s_{x_1}}^2$	Variance of measured quantity x
${s_e}^2$	Equivalent variance of two homogenous data sets
${s_{C_1}}^2$	Variance of the common line when slopes of parallel lines are insignificant
x_i	Arbitrary measured quantities
t	Test statistic
t_β	Critical value corresponding to a significance level β
t_μ	Test statistic calculated for means
t'_μ	Test statistic calculated for means that are significant
t_{C_1}	The test statistic for slopes
σ	Generic stress level (stress amplitude, maximum stress or stress range)
σ_i	i[th] stress level ($i = 1, 2 \ldots, n$)
$\sigma_{min}, \sigma_{max}$	Minimum and maximum stress in the cycle
σ_0	Endurance limit
$\sigma_{0,P\%}$	Endurance limit at a probability of survival P
$\sigma_{0,(1-P)\%}$	Endurance limit in error at a probability of survival P

T_σ	Scatter ratio of reference stress for (1-P) % and P% probabilities of survival
β	Level of significance
δ	Random variable for collinear lines
$\mu_{Y/X}$	Expected value of $logN$ given $log\sigma$

Chapter 1

General Introduction

1.1 Introduction to Background

To address the escalating global climate crisis, countries worldwide signed the Paris Agreement in April 2016 [1], committing to limit the rise in global warming. To meet this goal, nations must identify low-carbon, sustainable, and clean energy sources to replace fossil fuels. These efforts to cultivate environmental consciousness in today's society have resulted in the adoption of a notable strategy, which involves the use of hydrogen, especially when combined with natural gas. The key attractive feature is that hydrogen does not contain carbon atoms and therefore does not produce harmful carbon compound gases [2,3]. Therefore, hydrogen in the energy sector holds the potential for reducing emissions and therefore advancing sustainability objectives. According to ref [4] the energy sector was responsible for 77.01% of greenhouse gas emissions in 2019, and blending natural gas with hydrogen will contribute to a green society. The process involves mixing hydrogen typically derived from renewable sources, with natural gas to create a cleaner fuel mixture

that can be used across various sectors, including transportation and domestic heating. The incorporation of hydrogen into natural gas offers several advantages. Firstly, it enables the reduction of carbon emissions associated with natural gas consumption, contributing to efforts to combat climate change [2,5,6]. By substituting a portion of natural gas with hydrogen, emissions from combustion processes can be significantly lowered, thereby mitigating environmental impacts. Secondly, hydrogen blending with natural gas presents opportunities for enhancing energy efficiency and promoting renewable energy integration. By using surplus renewable energy to produce hydrogen through processes like electrolysis, excess energy can be effectively stored and used in the form of blended natural gas. This facilitates the integration of renewable energy sources into the existing natural gas infrastructure, thereby bolstering grid stability and reliability.

Nevertheless, due to its small size, materials easily absorb hydrogen, leading to an uneven and unstable distribution within them. [2,7]. In particular, when a metal is placed in a hydrogen-rich environment, it absorbs hydrogen, a process known as uptake. The hydrogen atoms tend to concentrate in specific areas of the metal's crystal lattice [8]. As these hydrogen atoms accumulate, they weaken the chemical bonds within the lattice. This weakening makes the metal more brittle and susceptible to fractures [9]. The combination of hydrogen uptake and bond weakening leads to a phenomenon called hydrogen embrittlement, where the metal becomes more prone to cracking and failure, even under low-stress conditions. This effect on the metal's mechanical properties is crucial to consider in various industrial applications.

The National Transmission System in the UK comprises nearly 5,000 miles of high-pressure steel pipelines and over 500 above-ground installations [10]. These are welded pipes and must withstand internal fluid pressure as well as harsh external conditions. Welding high-strength pipeline materials presents a significant challenge for engineers, particularly in the construction of pipelines and oil and gas transportation lines [11]Developing and implementing effective welding techniques for these materials is essential to enhancing reliability and profitability within the industry.

Despite the aforementioned significance of incorporating hydrogen into the energy system, a significant obstacle persists known as hydrogen embrittlement (HE). HE is a phenomenon whereby metals become brittle and susceptible to fracture when exposed to hydrogen atoms [12,13]. This phenomenon was first observed by Johnson when he noticed a change in some

of the physical properties of iron as a result of its temporary immersion in hydrochloric and sulfuric acids [7,14]. It arises when hydrogen atoms penetrate solid metals, and inducing failure is often known as hydrogen-induced cracking. This emerges when significant amounts of hydrogen infiltrate the material and the excess hydrogen can recombine as molecular hydrogen at matrix interfaces, leading to microstructure defects such as inclusions and carbides. Consequently, a substantial internal pressure builds up, facilitating the initiation and propagation of cracks. This phenomenon impacts various materials with its effects being particularly notable around ambient temperature [15,16]. For crack growth to occur, both atomic hydrogen and mechanical stress are necessary. The propensity to experience embrittlement when exposed to hydrogen is known as the susceptibility of the material to hydrogen embrittlement [8]. It involves the material's vulnerability to hydrogen-induced cracking, which can lead to reduced ductility, increased brittleness, and potential structural failure. Factors affecting susceptibility include the type of metal, hydrogen concentration, stress levels, and exposure conditions. As such, HE has become one of the biggest obstacles to the deployment of hydrogen energy infrastructure, including the repurposing of natural gas pipelines for the transport of gaseous hydrogen [17], whose failures could lead to catastrophic accidents.

Hydrogen embrittlement can be classified into two categories [18]: (i) Subcritical crack growth occurring above a threshold stress that is below the yield stress, and (ii) Fracture initiation at a stress level between the yield stress and the ultimate tensile strength (UTS). In the second category, the fracture can start either through micro-void coalescence, similar to fractures occurring in air, or through a more brittle fracture mode starting at the surface. The source of this hydrogen originates from sources such as the environment, electrochemical processes, and manufacturing activities e.g. welding. This problem is relatively accurate for pipes transporting hydrogen pure or blended with natural gas. However, if the diffusible hydrogen content is below the critical level of hydrogen which is known as critical hydrogen concentration, then the chances of HE can be neglected. The main degradation mechanisms are fatigue crack growth due to cyclic loading and slow crack growth under constant loads, particularly around welds and heat-affected zones in pipes [5]. Therefore, design considerations must be accurately constructed to accommodate hydrogen embrittlement when designing structures intended for exposure to hydrogen-rich environments.

1.2 HE in pipeline material and network

The hydrogen embrittlement of steels has been extensively researched. Hydrogen can accelerate the degradation of pipeline steel, primarily through embrittlement, which leads to cracks and can ultimately cause pipeline failure [19]. While hydrogen concentration and pressure contribute to embrittlement [5], the grade of steel and the mechanical properties of both the steel and welds [20] also significantly affect the embrittlement process [5]. Consider for example some common metals used in the energy network like X52 (steel with a minimum yield strength of 52 kilo pounds per square inch) low carbon steel, grey cast iron and brass. Refs [19,21] suggest that lower-grade, more ductile steel (grades below X52) could be less affected by hydrogen embrittlement than less ductile steel (grades above X52). However, the susceptibility of X52 pipeline steel to HE increases with both hydrogen charging time and hydrogen pressure. At a charging time of 96 hours, the HE susceptibility index reaches 45.86%, approximately 3.6 times that at a charging time of 0 hours [22,23]. Similarly, a charging pressure of 4 MPa results in a HE susceptibility index of 31.61%, approximately 2.5 times higher than that at a charging pressure of 0.3 MPa. The key question arising is how the susceptibility of degraded pipeline X52 low-carbon steel changes when it is exposed to a higher-pressure hydrogen gas environment for extended periods of up to nine months. In the case of welds in the pipeline, the heat-affected zones are especially susceptible to hydrogen embrittlement because they can experience residual stresses that are much higher than those in the main pipe body [5]. Special strategies like inner coating, intelligent pigging, operational pressure management, admixing degradation inhibitors, etc. [19], have been adopted in the industry to prevent hydrogen embrittlement in steel pipelines yet these strategies only minimise the rate of hydrogen ingress to the metal.

Unlike high-strength steels, cast irons present graphite that can accommodate diffused hydrogen, delaying the embrittlement effect [24]. The graphite diameter has a significant effect on the hydrogen embrittlement, due to its microstructural design [25]. Hydrogen causes multiple small cracks to form and link at the graphite/ferrite interfaces, increasing the elongation of cast iron during constant load testing [26]. The ferrite matrix then cracks through a brittle cleavage fracture mechanism. However, graphite content in cast irons can accommodate diffused hydrogen, delaying the embrittlement effect [24]. Other strategies include selecting materials with added alloy elements such as nickel, chromium, or molybdenum can improve resistance [7,27]. Surface treatments, including the application

of protective coatings also create a barrier against hydrogen. Heat treatments such as tempering and annealing reduce internal stresses and enhance ductility [28,29]. Additionally, cathodic protection using impressed current systems and sacrificial anodes like zinc or magnesium can prevent hydrogen uptake.

Presently, the materials used in hydrogen equipment are limited to austenitic stainless steel and aluminium alloy due to their reduced susceptibility to hydrogen embrittlement [25,30]. Other equipment includes compressor stations and regulator stations [5]. Compressor stations serve to both pressurize and purify the gas to maintain flow and quality, while regulator stations typically reduce pressure between transmission and distribution systems. The selection of materials is therefore crucial and based on a combination of factors, including available strength, durability, and cost requirements. To realize the vision of a hydrogen-based society, it becomes imperative to broaden the selection of materials for hydrogen equipment to include more common and cost-effective options. This expansion would necessitate establishing safety guidelines for materials that may exhibit susceptibility to hydrogen embrittlement. Therefore, from both safety and economic perspectives, there is a crucial need to investigate the behaviour of common and affordable materials used in hydrogen environments concerning hydrogen embrittlement.

Having summarised the effects of hydrogen blending on the potential impacts on the distribution network, the safety concern poses a significant challenge to the safety of existing distribution networks. While the rate of embrittlement is dependent on numerous factors, including the type of materials used in the network, the extent of material degradation overuse, and the operating conditions, this further justifies the scope of continuous research in this domain. For example, when conducting tensile tests on API L X52 pipe steel, specimens were loaded in air, and then subjected to hydrogen introduction through an electrolytic process at a potential of −1volts, it was observed that the elongation at failure decreased by 38%, while the yield stress decreased by 3.8%, and the ultimate strength decreased by 7.4% [31]. This further buttresses the fact that slight changes in a variety of parameters will lead to changes in the mechanical properties of the network. Therefore, to ensure the safe blending of natural gas with hydrogen, it is imperative to evaluate the mechanical properties of network materials for compliance with design considerations post-hydrogen embrittlement. Therefore, by overcoming the technical, economic, and regulatory barriers through collaborative efforts and innovative solutions,

the potential of hydrogen blending of natural gas to pave the way towards a cleaner, more sustainable energy future can be achieved.

1.2.1 Global advances in natural gas blending and the situation in the UK

Many countries have ambitious targets for hydrogen production and many projects to blend natural gas exist globally. In 2020, the U.S. Department of Energy released the "Hydrogen Program Plan," outlining strategies for research, development, and validation of hydrogen technologies, while addressing market and institutional barriers to facilitate multiple application pathways [32]. A Hydrogen Strategy for a Climate-Neutral Europe to use green hydrogen energy as the development target was set in 2020 [6]. Similarly, Japan developed a fundamental strategy for hydrogen energy aimed at expanding its use in households, industry, and transportation [3]. Australia's "National Hydrogen Strategy" aimed to establish a cluster of hydrogen hubs with large demand, improve efficiency through economies of scale, and promote synergistic effect through sector coupling [33]. China's National Development and Reform Commission (NDRC) and National Energy Administration (NEA) jointly issued the "Energy Technology Revolution and Innovation Action Plan (2016–2030)" (cited in ref [3]) to incorporate the hydrogen energy industry into the national energy strategy. Although the reasons, methods, and approaches for developing the hydrogen energy industry differ from country to country, the global climate change response has made the development of clean energy the prevailing trend. It is the essential pathway to achieving a green, low-carbon, and sustainable global economy.

In actioning the policies described above, Europe has an advanced natural gas network and repurposing of existing pipelines in blended natural gas is expected to result in significant savings compared to the building of new pipelines [2,3]. Some European countries allow the blending of hydrogen and the blending limits vary significantly within countries as shown in Figure 1-1 with many countries aiming to increase these limits.

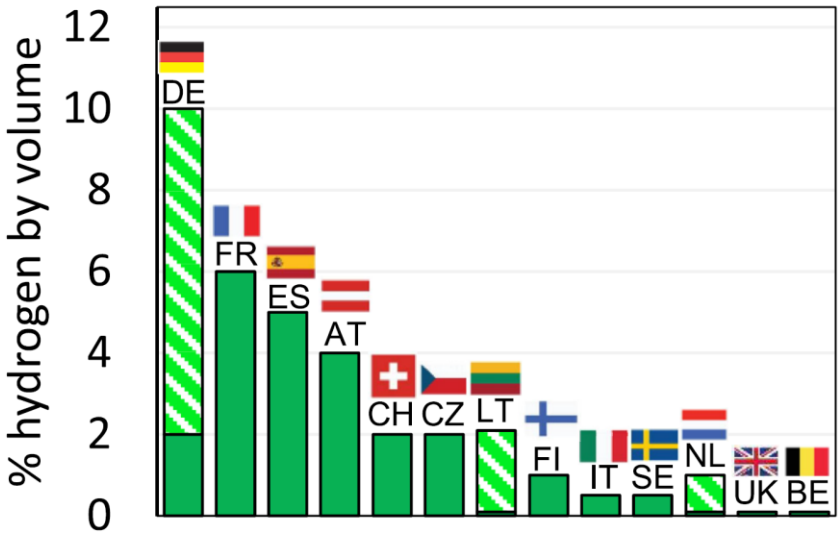

Figure 1-1 Current National Limitations on Hydrogen Blending in Gas Networks in Europe

The percentage blend of natural gas across Europe is down to legislation and because these networks are connected, there is a growing importance to have uniform rules in this light. Most of the implemented or ongoing projects inject only a small amount of hydrogen into the natural gas grid (less than 2 %), but some projects have reached high blending rates (up to 20% [2], the projects only used non-steel pipeline materials. Table 1-1 summarises some of the hydrogen blending projects that are ongoing or have been conducted as in the literature.

Table 1-1 Summary of some hydrogen blending projects [2]

Project	Country	% blend	Operating pressure	Pipeline material or use	Repurposing
IRES [34]	Italy	<20	Variable	Heat plant	Safe
The Wind Gas Falkenhagen (E.ON) [35,36]	Germany		Variable	Network	
Energinet's project [2]	Denmark	12	Variable	Network	
HyNTS Hydrogen Flow Loop	UK	30	Variable	Network	Unsafe
Jupiter 1000	France				Unspecified
Gasunie [37,38]	Netherlands	100	40 bar	Adjusted network	Safe
Denmark [39]	Denmark	100	Variable	Network	Safe
H21[2]	UK	100	Variable		
Ameland [2]	Netherlands	<20	Variable	Non-steel	Safe
GRHYD [2,40]	France	<20	Variable	Non-steel	Safe
HyDeploy [41,42]	UK	20	Variable	Non-steel	Safe
Gasnetz Hamburg	Hamburg	< 30	Variable	heat plant	Unsafe
H2BER			Variable	filling station	Useable
Wind to Gas Energy	Brunsbu¨ttel		Variable	filling station	Useable
The Wind Gas	Hassfurt		Variable	Powerplant with NG	Useable
Hybrid Power Plant	Enertrag		Variable	Powerplant with NG	Useable
P2G Ibbenbüren demonstration plant (RWE) [36,43]	Germany	100	Variable	Network	Useable
[44]	USA	20	Variable	Network	Safe

The UK is also taking advantage of the emergent hydrogen technologies and the use of blended natural gas. For instance, it is committed to achieving a zero target for emissions by 2050 and part of this will be achieved by the use of blended natural gas [45]. At the moment, the economy heavily relies on fossil fuels and natural gas to meet the high demands for energy supply, although there has been significant progress in utilizing renewable energy sources such as wind and solar farms for electricity [45–48]. The UK government has tasked the HyDeploy project with effectively realizing its plan to meet NetZero targets by 2050 by replacing some of the fossils with hydrogen. Thus, to reduce

overdependence on fossil fuels and natural gas, it is expected that approximately 20% volume of hydrogen will be blended with natural gas for the economy. This blending aims to reduce the amount of excess hydrogen in the atmosphere, decrease the exploitation of natural gas, and promote a cleaner environment. For this initiative to be successful, it is crucial to determine if the existing network can transport and store the blended natural gas. It is against this backdrop that this research has set out to investigate the fatigue properties of steel, welded steel, cast iron, and brass when exposed to hydrogen gas. If there is no noticeable change in the fatigue properties of these materials used in the present network, it could significantly impact cost savings by avoiding the need to change existing boilers and pipe networks. However, if there are changes in the fatigue properties of these materials, engineers will need to design according to these new fatigue properties. With this in mind, this research aims to contribute to addressing the challenges of hydrogen embrittlement, which presents a potential hindrance to the application of the government's NetZero target in the HyDeploy project [42,49] and globally.

This problem statement underscores the challenges impeding the adoption of blending hydrogen with natural gas, particularly in light of the UK government's pursuit of its net zero targets. These challenges span technical compatibility, safety concerns, economic barriers, and regulatory obstacles. Addressing these issues is crucial to fully realizing the benefits of hydrogen-natural gas blends in reducing emissions and advancing sustainability goals. To overcome these barriers and facilitate the effective integration of hydrogen blending into the energy sector, comprehensive research and collaborative efforts are necessary. This PhD aims to provide some of the technical knowledge needed to contribute to the reformulation of regulatory standards in the UK energy industry, thereby assisting in overcoming these challenges.

1.2.2 Pipeline material behaviour in the vicinity of hydrogen

Fatigue crack growth rates in a hydrogen environment can be influenced by a multitude of factors including temperature [50–52], presence of coatings on the metal surface, pressure of the hydrogen environment, hydrogen concentration, frequency of loading, microstructure of the material, and the presence of molecular defects such as voids, traps, and grain boundary defects [18,53,54]. Other factors such as material hardness, tensile and yield strength, residual stresses, crystal structure, stress rate during service and application, and heat treatment during manufacturing also play crucial roles. However, this section will review the existing literature only on studies in the mechanical properties of metals used in

a hydrogen environment. Specifically, it will focus on the materials employed in natural gas transmission pipelines that have undergone degradation over time due to usage. This review will encompass the current state of research and findings in this area.

The feasibility of using existing pipelines despite defects in their material for transporting hydrogen through natural gas pipelines was investigated and subsequently confirmed [55,56]. By analysing surface defects, a reduction of the safety factor remains within the conventional value, indicating that the existing European natural gas pipeline can be used for transporting a mixture of natural gas and hydrogen. The impact of hydrogen embrittlement on the pipeline defects and material fracture toughness was established [57,58].

The nodal pressure of the pipeline increases with increased hydrogen doping rate in natural gas, thereby accelerating the expansion of pipeline cracks and ultimately leading to pipeline failure [59]. When the operating pressure of the pipeline network does not exceed 7 MPa and the hydrogen doping ratio remains below 5%, the pipelines carrying hydrogen-enriched natural gas do not pose a threat to the safe operation of the system. For carbon steel pipeline material, the fatigue life curve in 0.7 MPa hydrogen gas was equivalent to the fatigue life curve in the air. However, in 115 MPa hydrogen gas environment, the fatigue life was significantly degraded within a relatively short fatigue life regime [60]. Also, the associated risk of pipelines when transporting hydrogen-enriched natural gas through natural gas pipelines, along with the transfer risk of energy between natural gas and electricity has been assessed [61].

The influence of hydrogen gas on the fatigue crack growth (FCG) and fracture toughness of X80 welded metal show that when used in pipeline material in China, hydrogen increased the FCG rate of both the X80 base metal and weld metal [62–64]. Interestingly, the rate of hydrogen-induced FCG of the weld metal was smaller compared to that of the base metal [57]. Hydrogen significantly accelerated intermediate-rate (Stage II) crack growth, particularly at low-stress ratios, but this effect diminished as the stress ratio approached 0.5. Conversely, hydrogen prompted the premature initiation of accelerated (Stage III) crack growth [65]. Using this material to transport blended natural gas and analysing fatigue life, fracture strength, and material deterioration under varying hydrogen blending ratios (0%, 5%, 10%, 20%, and 50%) at an internal pressure of 12 MPa, assessments of the service capacity of high steel-grade pipes in hydrogen blending

environments was deemed crucial for determining optimal hydrogen blending ratios and their compatibility was inconclusive [66]. This then underscored the need for further exploration into the hydrogen damage mechanism through theoretical analysis, experimental research, and numerical simulation. Similarly, blending ratios impacted average flow velocities at leak points [67]. While assessing the potential barriers associated with hydrogen transport like material challenges in using parallel or unused pipelines, the prospects for utilizing the existing gas network for hydrogen in Finland were less favourable due to factors such as limited network coverage, network location, and gas usage profiles [2].

While many studies suggested that blending up to 20% of hydrogen into the existing natural gas grid may not necessitate major modifications, the analysis highlighted the need to consider factors such as pressure range, maximum operation pressure, pipeline structure, and material variability [2]. It emphasized that careful evaluation of each pipeline is essential before repurposing, given variations in structure and materials. Conflicting findings in earlier studies regarding the limitations of hydrogen pipeline transport underscored the need for further research and experimentation to confirm hydrogen compatibility with pipelines and related assets in other parts of Europe.

The recommendations summarised above inspire investigations into aspects specific to hydrogen blending in the UK, pipeline material compatibility, and safety considerations. The emphasis on the need for further research and experimentation underscores the importance of advancing knowledge in these areas to support the practical implementation of hydrogen transport solutions in the other parts of Europe and the UK inclusive. This PhD research's outcome will provide some of the solutions to the challenges summarised above, which in particular are necessary for the safe design and execution of HyDeploy initiatives, by guiding decision-making processes and addressing challenges related to pipeline compatibility, material integrity, and safety.

1.2.3 Gaps in the formalisation of hydrogen embrittlement in degraded metals in the gas network

There is extensive research on hydrogen embrittlement of pipeline materials. However, there is limited data in the literature that accesses the varying parameters of pipeline material in the course of use over time. For instance, X52 pipeline steel has been extensively studied and is commonly recommended for hydrogen pipelines as it is a lower-strength steel considered more resistant to hydrogen embrittlement. However, limited

research exists on the hydrogen embrittlement behaviour of X52 steel specifically in a pure hydrogen environment under varying hydrogen charging times and pressures [22]. Therefore, there is currently a notable absence of research data in the literature focusing on the fatigue properties of ex-service X52 steel due to measured amounts of hydrogen exposure in a hydrogen environment. Most existing studies primarily address the hydrogen embrittlement of X52 pipeline materials and the degradation of X52 over time, but they neglect the examination of ex-service X52 steel materials exposed to hydrogen environments for specific durations. Moreover, available research in the UK has mainly focused on testing materials for fatigue properties in natural gas blended with 15% hydrogen [31], while Ref [5] confirms that 10%–12% hydrogen blend is safe to use. Similarly, ref [68] confirms that blends of approximately 17% should not pose any challenges. Therefore, conducting research on the fatigue properties of ex-service X52 steel subjected to hydrogen embrittlement from 20% hydrogen-blended natural gas for various durations in months will significantly contribute to expanding the existing literature in a further recommendation from ref [2]. This research will fill the gap in knowledge by providing valuable insights into the behaviour of ex-service materials under a 20% hydrogen blended natural gas environment.

1.3 PhD research aims and objectives

The novelty of this PhD research lies in the recognition that the mechanical properties of materials used in natural gas transmission degrade over time. This degradation coupled with exposure to a hydrogen environment leads to further deterioration due to hydrogen embrittlement. The primary aim of this research is to determine if the existing pipeline materials in the distribution network would safely contain hydrogen gas operating at 8bars. In particular, to quantify the changes in the fatigue properties of ex-service X52 steel, ex-service X52 welded steel, ex-service grey cast iron, and ex-service brass resulting from both their degradation over time and exposure to a hydrogen environment. Investigating the fatigue properties will provide technical insights to stakeholders involved in the safe implementation of the HyDeploy project [42]. To comprehend these changes in fatigue properties, specimens are retrieved from ex-service pipeline materials exposed to a hydrogen environment and then tested for fatigue. To achieve this aim, the following objectives are required:

1) Characterise the mechanical properties of uncharged pipeline materials. Ex-service pipeline materials (X52, grey cast iron, and brass) will be obtained from the existing gas network. Subsequently, conduct tensile tests to characterize these specimens.
2) Establish the endurance limit of extracted pipeline materials after 2 million cycles to determine the baseline or reference point.
3) Expose these materials to a hydrogen environment for varying durations, ranging from several months to allow for significant amounts of hydrogen diffusion into the materials and then investigate their mechanical properties. The hydrogen environment will be created using hydrogen-pressurized tubes maintained at room temperature.
4) Characterise the fatigue properties of hydrogen-charged materials based on their length of exposure times to a hydrogen environment. This is necessary to compare with the baseline results obtained from uncharged materials after 2 million cycles.
5) Use parametric statistical approaches to assess statistical significance. This statistical test will be used to determine if the observed changes in the fatigue properties of these materials are statistically significant, using a predetermined significance level of 95%.

Meeting the above objectives will assist in formulating an answer to the research question, which seeks to find out if it is safe to use the existing pipeline network to distribute blended natural gas.

Therefore, in conclusion, the fatigue properties of these ex-service pipeline materials, when charged with hydrogen, and compared with uncharged data using statistical methods to detect any changes in endurance limits based on a predefined level of confidence. If the analysis reveals significant differences in the fatigue properties, these will be compared against the current design procedures used in the network. If the differences fall within the conservative limits of the network's design code, it would be concluded that, although there is a noticeable change in the fatigue properties of these materials when exposed to a hydrogen environment, the change is not significant enough to compromise safety in the current network. However, if the differences exceed these conservative limits, it would be deemed unsafe to blend natural gas with 20% hydrogen and use the existing network for distribution.

1.4 Thesis Outline

The research work presented in this thesis is structured as follows:

Chapter 2 provides a detailed review of available information on the static and fatigue behaviour of metals. This chapter offers a quick overview of theories used in fatigue assessments and delves into the theoretical formulation of bodies under dynamic loading. Additionally, the chapter outlines the fundamental aspects of stress-based approaches, which constitute the core of this research. It is demonstrated in this chapter that fatigue assessment can be approached in various ways, with the stress-based approach being the most straightforward and widely used method for measuring fatigue or endurance limits.

Chapter 3 reviews the literature to gain an understanding of the hydrogen embrittlement phenomenon. It must be emphasized that this research did not study hydrogen embrittlement mechanisms; rather, it is reviewed solely for completeness purposes. This review is limited to factors affecting hydrogen embrittlement rates and its transmission mechanisms in metals.

Chapter 4 elaborates on the methodology employed to determine the fatigue properties from the generated fatigue data. This involves a detailed comparison of standard approaches such as the methods suggested by the ASTM, IIW, and LRM for determining fatigue curves. Additionally, practical approaches found in the literature are explained, along with reasons for their exclusion from this PhD research are summarised. The chapter highlights that the approach recommended by ASTM is highly conservative and suitable for critical design considerations. Conversely, the IIW method is deemed the least conservative and is recommended for less critical design considerations. The LRM is identified as the simplest method to use, requiring the least number of fatigue sample sets. This helps in deciding the experimental protocols as well as the desired quantities needed to complete the fatigue analysis.

In addition, focuses on the statistical significance methods applied to fatigue datasets to discern whether differences observed in these datasets are meaningful. The chapter specifically examines whether discrepancies are attributable to error or chance, or if they are linked to alterations in the mechanical properties of the materials or loading configurations. By employing notches of varying sizes, the study demonstrates the possibility of detecting changes in fatigue properties solely through statistical analysis, without requiring an in-depth understanding of the geometry. This approach enables the

determination of whether observed changes in fatigue properties of the materials under investigation are significant, occurring by chance or due to alterations in mechanical properties resulting from degradation and hydrogen embrittlement.

Chapter 5 provides a comprehensive summary of the experimental protocols employed throughout the research. It outlines the methods used for sourcing materials, details the hydrogen soaking process for different durations in months from the soaking lab to the testing lab and also measures the recommended quantities that will be used to generate the fatigue data. The results generated are reported in this chapter. Additionally, this chapter also includes a thorough description of the experimental procedure and reports the fatigue results obtained from notched specimens. These data sets from notches were used to illustrate and validate the statistical tests used for assessing the significance of fatigue curves due to any observed differences.

Chapter 6 delves into the analysis of results obtained from hydrogen-charged specimens. The fatigue outcomes derived from each metal are compared with existing data from the literature. Moreover, statistical significance tests are conducted on the datasets for each metal. The chapter also compares the fatigue properties obtained for various charging durations with those of uncharged specimens. The findings reveal that statistical insignificance is observed up to a certain level of significance.

Chapter 7 encompasses the discussion and analysis of the observed changes in the fatigue datasets and their implications for the industry. It explores practical approaches and considers the effects of making certain considerations about specimens based on observed testing outcomes. Additionally, the chapter provides an overall conclusion on the significance of the differences observed in the fatigue datasets from hydrogen specimens.

Chapter 8 summarizes the conclusions drawn from this research and suggests. This chapter also aims to continue contributing significantly to the ongoing discourse surrounding pipeline integrity management and structural resilience in the face of hydrogen embrittlement in green energy projects.

1.5 Journal Publications

From the research presented in this thesis, the following papers have been published or submitted for publication:

1.4 Thesis Outline

1) E. Kufoin, L. Susmel, Quantitative review of probabilistic approaches to fatigue design in the medium cycle fatigue regime, Probabilistic Eng. Mech. (2024) 103589. https://doi.org/10.1016/j.probengmech.2024.103589.
2) E.N. Kufoin, L. Susmel, On the parametric assessment of fatigue disparities, Probabilistic Eng. Mech. 77 (2024) 103651. https://doi.org/10.1016/j.probengmech.2024.103651.

1.6 References

[1] United Nations, The Paris Agreement - Climate Action, (2015). https://www.un.org/en/climatechange/paris-agreement (accessed July 26, 2024).

[2] S. Lipiäinen, K. Lipiäinen, A. Ahola, E. Vakkilainen, Use of existing gas infrastructure in European hydrogen economy, Int. J. Hydrogen Energy. 48 (2023) 31317–31329. https://doi.org/10.1016/j.ijhydene.2023.04.283.

[3] Q. Zhang, W. Chen, W. Ling, Policy optimization of hydrogen energy industry considering government policy preference in China, Sustain. Prod. Consum. 33 (2022) 890–902. https://doi.org/10.1016/j.spc.2022.08.017.

[4] European Parliament, Greenhouse gas emissions by country and sector, (2023). https://www.europarl.europa.eu/news/en/headlines/society/20180301STO98928/greenhouse-gas-emissions-by-country-andsector-infographic. (accessed July 20, 2024).

[5] M.D. Kass, J.R. Keiser, Y. Liu, A. Moore, Y. Polsky, Assessing Compatibility of Natural Gas Pipeline Materials with Hydrogen, CO2, and Ammonia, J. Pipeline Syst. Eng. Pract. 14 (2023). https://doi.org/10.1061/JPSEA2.PSENG-1431.

[6] European Commission, A hydrogen strategy for a climate-neutral Europe, Brussels, Belgium, 2020. https://www.eu2018.at/calendar-events/political-events/BMNT-.

[7] J. Liu, M. Zhao, L. Rong, Overview of hydrogen-resistant alloys for high-pressure hydrogen environment: on the hydrogen energy structural materials, Clean Energy. 7 (2023) 99–115. https://doi.org/10.1093/ce/zkad009.

[8] W.J. Qi, R.G. Song, X. Qi, H. Li, Z.X. Wang, C. Wang, J.R. Jin, Hydrogen Embrittlement Susceptibility and Hydrogen-Induced Additive Stress of 7050 Aluminum Alloy Under Various Aging States, J. Mater. Eng. Perform. 24 (2015) 3343–3355. https://doi.org/10.1007/s11665-015-1616-9.

[9] D. Sobola, R. Dallaev, Exploring Hydrogen Embrittlement: Mechanisms, Consequences, and Advances in Metal Science, Energies. 17 (2024) 2972. https://doi.org/10.3390/en17122972.

[10] National Gas, National Gas Transmission: Our network and assets, (2024). https://www.nationalgas.com/our-businesses/our-network-and-assets#:~:text=The National Transmission System consists,than 500 above-ground installations. (accessed September 13, 2024).

[11] S.K. Sharma, S. Maheshwari, A review on welding of high strength oil and gas pipeline steels, J. Nat. Gas Sci. Eng. 38 (2017) 203–217. https://doi.org/10.1016/j.jngse.2016.12.039.

[12] ASTM F2078, Standard Terminology Relating to Hydrogen Embrittlement Testing, ASTM Int. (2022). https://doi.org/10.1520/F2078-22.

[13] B.N. Popov, J.-W. Lee, M.B. Djukic, Hydrogen Permeation and Hydrogen-Induced Cracking, in Handb. Environ. Degrad. Mater., Elsevier, 2018: pp. 133–162. https://doi.org/10.1016/B978-0-323-52472-8.00007-1.

[14] W.. Johnson, On some remarkable changes produced in iron and steel by the action

of hydrogen and acids, Proc. R. Soc. London. 23 (1875) 168–179. https://doi.org/10.1098/rspl.1874.0024.

[15] K. Xu, Gaseous Hydrogen Embrittlement of Materials in Energy Technologies, , Woodhead, 2012.

[16] A. Atrens, J. Venezuela, Q. Liu, Q. Zhou, K. Verbeken, C. Tapia-Bastidas, E. Gray, F. Christien, K. Wolski, Electrochemical and Mechanical Aspects of Hydrogen Embrittlement Evaluation of Martensitic Steels, in: Encycl. Interfacial Chem., Elsevier, 2018: pp. 201–225. https://doi.org/10.1016/B978-0-12-409547-2.13770-9.

[17] Y.S. Chen, C. Huang, P.Y. Liu, H.W. Yen, R. Niu, P. Burr, K.L. Moore, E. Martínez-Pañeda, A. Atrens, J.M. Cairney, Hydrogen trapping and embrittlement in metals – A review, Int. J. Hydrogen Energy. (2024). https://doi.org/10.1016/j.ijhydene.2024.04.076.

[18] S.K. Dwivedi, M. Vishwakarma, Hydrogen embrittlement in different materials: A review, Int. J. Hydrogen Energy. 43 (2018) 21603–21616. https://doi.org/10.1016/j.ijhydene.2018.09.201.

[19] European Union Agency for the Cooperation of Energy Regulators, Transporting Pure Hydrogen by Repurposing Existing Gas Infrastructure: Overview of existing studies and reflections on the conditions for repurposing, 2021.

[20] J.A. Ronevich, E.J. Song, B.P. Somerday, C.W. San Marchi, Hydrogen-assisted fracture resistance of pipeline welds in gaseous hydrogen, Int. J. Hydrogen Energy. 46 (2021) 7601–7614. https://doi.org/10.1016/j.ijhydene.2020.11.239.

[21] and P. 1 P.R. European Hydrogen Backbone, Delivery of an offshore hydrogen supply programme via industrial trials at the Flotta Terminal HOP Project-HS413, The Oil & Gas Technology Centre, 2020. https://assets.publishing.service.gov.uk/media/5e4ab9bf40f0b677ca249fed/Phase_1_-_OGTC_-_Hydrogen_Offshore_Production.pdf (accessed July 31, 2024).

[22] H.J. Wan, X.Q. Wu, H.L. Ming, J.Q. Wang, E.H. Han, Effects of Hydrogen Charging Time and Pressure on the Hydrogen Embrittlement Susceptibility of X52 Pipeline Steel Material, Acta Metall. Sin. (English Lett. 37 (2024) 293–307. https://doi.org/10.1007/s40195-023-01625-5.

[23] J. Keller, B. Somerday, C.S. Marchi, D. Manager, S. Weil, Annual Progress Report DOE Hydrogen and Fuel Cells Program Fiscal Year (FY) 2011, 2011.

[24] J. Turola, R.B. Obara, A. Ferrarese, A.F. Albaneze, C. de Souza Cabezas, Microstructure of cast iron resistant to hydrogen embrittlement, in: 2024. https://doi.org/10.4271/2023-36-0063.

[25] T. Yoshimoto, T. Matsuo, T. Ikeda, The effect of graphite size on hydrogen absorption and tensile properties of ferritic ductile cast iron, Procedia Struct. Integr. 14 (2019) 18–25. https://doi.org/10.1016/j.prostr.2019.05.004.

[26] P. Sahiluoma, Y. Yagodzinskyy, A. Forsström, H. Hänninen, S. Bossuyt, Hydrogen embrittlement of nodular cast iron, Mater. Corros. 72 (2021) 245–254. https://doi.org/10.1002/maco.202011682.

[27] H.K.D.H. Bhadeshia, Prevention of hydrogen embrittlement in steels, ISIJ Int. 56

(2016) 24–36. https://doi.org/10.2355/isijinternational.ISIJINT-2015-430.

[28] Q. Xu, J. Zhang, Novel Methods for Prevention of Hydrogen Embrittlement in Iron, Sci. Rep. 7 (2017) 16927. https://doi.org/10.1038/s41598-017-17263-8.

[29] X. Li, X. Ma, J. Zhang, E. Akiyama, Y. Wang, X. Song, Review of Hydrogen Embrittlement in Metals: Hydrogen Diffusion, Hydrogen Characterization, Hydrogen Embrittlement Mechanism and Prevention, Acta Metall. Sin. (English Lett. 33 (2020) 759–773. https://doi.org/10.1007/s40195-020-01039-7.

[30] T. Matsuo, The effect of pearlite on the hydrogen-induced ductility loss in ductile cast irons, J. Phys. Conf. Ser. 843 (2017) 012012. https://doi.org/10.1088/1742-6596/843/1/012012.

[31] G. Pluvinage, J. Capelle, M.H. Meliani, Pipe networks transporting hydrogen pure or blended with natural gas, design and maintenance, Eng. Fail. Anal. 106 (2019). https://doi.org/10.1016/j.engfailanal.2019.104164.

[32] Department of Energy, Department of Energy Hydrogen Program Plan, 2020. (n.d.). https://www.hydrogen.energy.gov/docs/hydrogen-programlibraries/pdfs/hydrogen-program-plan-2020.pdf?Status=Master (accessed July 26, 2024).

[33] C. Energy Council Hydrogen Working Group, AUSTRALIA'S NATIONAL HYDROGEN STRATEGY, n.d. https://www.dcceew.gov.au/energy/publications/australias-national-hydrogen-strategy (accessed July 26, 2024).

[34] S. Bellocchi, M. De Falco, M. Facchino, M. Manno, Hydrogen blending in Italian natural gas grid: Scenario analysis and LCA, J. Clean. Prod. 416 (2023) 137809. https://doi.org/10.1016/j.jclepro.2023.137809.

[35] Bioenergy IEA, Renewable gas hydrogen in the grid40, Darmstadt. (2021).

[36] RWE, RWE starts up P2G plant with ITM electrolyser, Fuel Cells Bull. 2015 (2015) 1. https://doi.org/10.1016/S1464-2859(15)30205-4.

[37] Gasunie, Gasunie Hydrogen pipeline from Dow to Yara brought into operation, (2018). https://www.gasunie.nl/en/news/gasunie-hydrogen-pipeline-from-dow-to-yara-brought-into-operation (accessed July 31, 2024).

[38] HyWay 27, T. Gülbahar, Hydrogen Transmission Using the Existing Natural Gas Grid? Final report for the Ministry of Economic Affairs and Climate Policy, 2021. www.pwc.nl.

[39] C.J. Quarton, S. Samsatli, Power-to-gas for injection into the gas grid: What can we learn from real-life projects, economic assessments and systems modelling?, Renew. Sustain. Energy Rev. 98 (2018) 302–316. https://doi.org/10.1016/j.rser.2018.09.007.

[40] ENGIE, The GRHYD demonstration project, (2022). https://www.engie.com/en/businesses/gas/hydrogen/power-to-gas/the-grhyd-demonstration-project (accessed July 31, 2024).

[41] HyDeploy, Pioneering the safe use of blended hydrogen in gas networks to reduce carbon emissions, (2022). https://hydeploy.co.uk/ (accessed July 31, 2024).

[42] HyDeploy 2024, Pioneering the safe use of blended hydrogen in gas networks to reduce carbon emissions, (2017). https://hydeploy.co.uk (accessed April 5, 2023).

[43] A.J. Gaul, Power-to-Gas demonstration plant Ibbenbüren, (2015). https://doi.org/10.13140/RG.2.1.3069.1288.

[44] P.W. Parfomak, Specialist in Energy and Infrastructure Policy, 2021. https://www.catf.us/wp-content/.

[45] HyDeploy, Demonstrating non-disruptive carbon savings through hydrogen blending // August 2021, (2021) 52.

[46] GOV.UK, Hydrogen blending into GB gas distribution networks: a strategic policy decision for Energy Security, 2023. https://www.gov.uk/government/consultations/hydrogen-blending-into-gb-gas-distribution-networks.

[47] D. Engelberg, F. Scenini, Y. Zhou, J. Duff, HyDeploy2 –Materials Analysis & Testing, 2023.

[48] HyDeploy, HyDeploy Project, Project Close Down Report, Revision 03 (Final), 2021.

[49] GOV.UK, Net Zero Government Initiative: UK roadmap to net zero government emissions, London, 2023.

[50] U. De Francisco, N.O. Larrosa, M.J. Peel, The influence of temperature on hydrogen environmentally assisted cracking of AA7449-T7651 in moist air, Corros. Sci. 180 (2021) 109199. https://doi.org/10.1016/j.corsci.2020.109199.

[51] U. De Francisco, N.O. Larrosa, M.J. Peel, Hydrogen environmentally assisted cracking during static loading of AA7075 and AA7449, Mater. Sci. Eng. A. 772 (2020) 138662. https://doi.org/10.1016/j.msea.2019.138662.

[52] U. De Francisco, F. Beckmann, J. Moosmann, N.O. Larrosa, M.J. Peel, 3D characterisation of hydrogen environmentally assisted cracking during static loading of AA7449-T7651, Int. J. Fract. 232 (2021) 93–116. https://doi.org/10.1007/s10704-021-00595-y.

[53] U.M. Gadade, P.D. Maskar, Study of Different Factors Affecting T Bolt Failure of Band Clamp, 10 (2021) 77–84.

[54] A. Khare, M. Vishwakarma, S. Ahmed, Experimental Investigation of Failure of High Strength Steel on Account of External Hydrogen Embrittlement, Int. J. Mech. Prod. Eng. Res. Dev. 10 (2020) 369–384. http://www.tjprc.org/view-archives.php?page=131&keyword=&from_date=&to_date=&id=67&jtype=2&journal=67.

[55] H. Boukortt, M. Amara, M. Hadj Meliani, O. Bouledroua, B.G.N. Muthanna, R.K. Suleiman, A.A. Sorour, G. Pluvinage, Hydrogen embrittlement effect on the structural integrity of API 5L X52 steel pipeline, Int. J. Hydrogen Energy. 43 (2018) 19615–19624. https://doi.org/10.1016/j.ijhydene.2018.08.149.

[56] I.M. Dmytrakh, J. Capelle, J. Gilgert, I. Dmytrakh, G. Pluvinage, Defect assessment on pipe used for transport of mixture of hydrogen and natural gas, (2009) 12–14. https://doi.org/10.9.2009.

[57] R.M. Andrews, N. Gallon, O.J.C. Huising, Assessing damaged pipelines transporting hydrogen, J. Pipeline Sci. Eng. 2 (2022) 100066. https://doi.org/10.1016/j.jpse.2022.100066.

[58] I.M. Dmytrakh, J. Capelle, J. Gilgert, I. Dmytrakh, G. Pluvinage, Hydrogen Effect on Fatigue and Fracture Resistance of a Pipe Steel, 2008. https://www.researchgate.net/publication/277105934.

[59] J. Zhang, Y.F. Cheng, Modeling of hydrogen atom distribution at corrosion defect on existing pipelines repurposed for hydrogen transport under pressure fluctuations, Int. J. Hydrogen Energy. 58 (2024) 1075–1087. https://doi.org/10.1016/j.ijhydene.2024.01.213.

[60] Y. Ogawa, H. Matsunaga, J. Yamabe, M. Yoshikawa, S. Matsuoka, Unified evaluation of hydrogen-induced crack growth in fatigue tests and fracture toughness tests of a carbon steel, Int. J. Fatigue. 103 (2017) 223–233. https://doi.org/10.1016/j.ijfatigue.2017.06.006.

[61] K. Yang, Z. Zhao, A. Zhang, W. Yang, Q. Li, S. Zeng, G. Peng, Risk modelling of hydrogen-enriched natural gas on pipelines and gas-electric coupled systems, IET Energy Syst. Integr. (2023). https://doi.org/10.1049/esi2.12124.

[62] L. Briottet, R. Batisse, G. de Dinechin, P. Langlois, L. Thiers, Recommendations on X80 steel for the design of hydrogen gas transmission pipelines, Int. J. Hydrogen Energy. 37 (2012) 9423–9430. https://doi.org/10.1016/j.ijhydene.2012.02.009.

[63] H. Wei, B. Duan, X. Shi, R. Gao, Z. Hua, S. Qiu, Y. Zhao, Influence of hydrogen in natural gas mixed hydrogen environment on mechanical properties of X80 pipeline steel, Int. J. Hydrogen Energy. 54 (2024) 908–921. https://doi.org/10.1016/j.ijhydene.2023.09.138.

[64] T. An, S. Zhang, M. Feng, B. Luo, S. Zheng, L. Chen, L. Zhang, Synergistic action of hydrogen gas and weld defects on fracture toughness of X80 pipeline steel, Int. J. Fatigue. 120 (2019) 23–32. https://doi.org/10.1016/j.ijfatigue.2018.10.021.

[65] H.J. Cialone, J.H. Holbrook, Effects of gaseous hydrogen on fatigue crack growth in pipeline steel, Metall. Trans. A. 16 (1985) 115–122. https://doi.org/10.1007/BF02656719.

[66] X. Tian, J. Pei, Study progress on the pipeline transportation safety of hydrogen-blended natural gas, Heliyon. 9 (2023). https://doi.org/10.1016/j.heliyon.2023.e21454.

[67] J. Zhu, S. Wang, J. Pan, H. Lv, Y. Zhang, H. Han, C. Liu, Z. Duo, Y. Li, Experimental study on leakage temperature field of hydrogen blending into natural gas buried pipeline, Appl. Energy. 359 (2024). https://doi.org/10.1016/j.apenergy.2024.122656.

[68] D. HAESELDONCKX, W. DHAESELEER, The use of the natural-gas pipeline infrastructure for hydrogen transport in a changing market structure, Int. J. Hydrogen Energy. 32 (2007) 1381–1386. https://doi.org/10.1016/j.ijhydene.2006.10.018.

1.5 References

Chapter 2

Fatigue Assessment of Engineering Materials

2.1 Introduction

The purpose of this chapter is to review the technical literature on the fundamental concepts essential for exploring the mechanical properties of metals. This includes continuum mechanics which is the foundational discipline in engineering that underpins many aspects of materials science. Continuum mechanics governs the behaviour of materials under various loading conditions, involving topics such as stress, strain, and deformation, providing a solid framework for comprehending subsequent discussions on linear and fracture mechanics. Building upon the concepts established in continuum mechanics, linear mechanics forms the basis for analysing the response of materials to external forces within the elastic regime. This progresses into fracture mechanics, which concerns understanding the behaviour of materials when subjected to mechanical loading beyond the elastic limit, leading to crack propagation and ultimately failure. Parameters such as stress intensity factor and fracture toughness are explored, which are pivotal for predicting the behaviour of materials in relation to fracture under varying load conditions. This is followed by an

exploration of the realm of fatigue, a persistent mode of material failure characterized by the propagation of cracks under cyclic loading. Through an in-depth exploration of the fatigue mechanisms, the factors influencing fatigue life and the methodologies employed in fatigue analysis are examined.

2.2 Introduction to Continuum Mechanics.

Before delving into the central focus of this research, it is imperative to establish a solid foundation by exploring the fundamental aspects essential for evaluating mechanical components against fatigue. This entails a comprehensive understanding of stress quantities and their application conditions, as well as an examination of the diverse effects exerted by these stress factors. Additionally, it involves familiarizing oneself with the analytical tools required to conduct thorough stress analyses, laying the groundwork for subsequent investigations into fatigue behaviour.

Assessing mechanical components for fatigue resistance is a critical aspect of the design process to prevent catastrophic failures. When materials are subjected to varying loads over time, fatigue failure can occur even without significant plastic deformation, especially in medium to high-cycle fatigue scenarios. The complex geometries of mechanical assemblies often lead to stress concentration and fatigue crack initiation. Designing components with larger notch root radii is ideal to mitigate stress concentration effects, although this is not always feasible. Safe engineering methods are necessary to address the impact of geometric features on fatigue resistance. Regardless of the approach used for fatigue assessment, identifying the weakest points in components is crucial. This involves determining stress and strain states using classical continuum mechanics. These states are then recalculated in terms of amplitudes, mean stresses, and ranges to accurately estimate fatigue damage. This chapter aims to review common procedures for determining these quantities.

2.2.1 Stress state under external loading

Consider a state where a body is subjected to loading from an external system of forces as shown in Figure 2-1. Within this context, the body is subjected to specific boundary conditions that define its interaction with its surroundings. These boundary conditions allow for the identification of singular points within the body, which serve as focal points for analysing the stress state at those locations. By precisely defining a reference frame, the stress state experienced by these points can be accurately described. To illustrate this

concept, examine a practical example of a body subjected to a system of external forces as shown below:

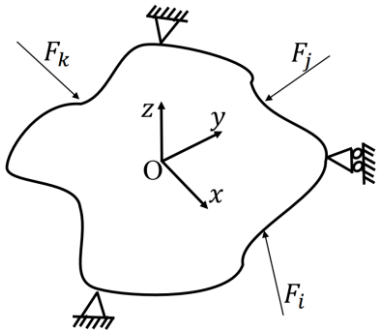

Figure 2-1 Body subjected to an external system of forces and frame of reference at point O.

To have a 3-dimensional state of stress, consider an internal point O, which serves as the origin for convenience, the stress state can then be comprehensively defined by the stress tensor:

$$[\sigma] = \begin{bmatrix} \sigma_x & \tau_{xy} & \tau_{xz} \\ \tau_{xy} & \sigma_y & \tau_{yz} \\ \tau_{xz} & \tau_{yz} & \sigma_z \end{bmatrix} \tag{2-1}$$

where σ_x, σ_y and $\sigma_z$are the normal stress components, while τ_{xy}, τ_{xz} and τ_{yz} are the shear stress components. The stress state varies from point to point within the material, meaning that at any given location, the numerical values of the normal and shear stress components fluctuate with alterations in the orientation of the frame of reference. Under this schematisation, there exists a frame of reference with principal axes such that the shear stress components are always equal to zero. The stress tensor above reduces to:

$$[\sigma] = \begin{bmatrix} \sigma_1 & 0 & 0 \\ 0 & \sigma_2 & 0 \\ 0 & 0 & \sigma_3 \end{bmatrix} \tag{2-2}$$

In which σ_1, σ_2 and σ_3 become the principal stresses such that $\sigma_1 \geq \sigma_2 \geq \sigma_3$. These stress components can be determined by calculated by using Eigen values. By assuming a unit vector $\vec{n}(n_1, n_2, n_3)$ defining the orientation of a principal direction such that:

$$([\sigma] - \sigma_n)[\vec{n}] = 0 \tag{2-3}$$

Where σ_n is the eigenvalues and becomes the principal stress parallel to $\vec{n}(n_1, n_2, n_3)$ and the Eigen vectors determine the orientation of the principal directions. These principal stress can then be calculated by imposing the condition that the determinant of the stress matrix is equal to zero as:

$$\begin{bmatrix} (\sigma_1 - \sigma_n) & \tau_{12} & \tau_{13} \\ \tau_{12} & (\sigma_2 - \sigma_n) & \tau_{23} \\ \tau_{13} & \tau_{23} & (\sigma_3 - \sigma_n) \end{bmatrix} \begin{bmatrix} n_1 \\ n_2 \\ n_3 \end{bmatrix} = \begin{bmatrix} 0 \\ 0 \\ 0 \end{bmatrix} \quad (2\text{-}4)$$

$$\sigma_n{}^3 - (\sigma_1 + \sigma_2 + \sigma_3) - [(\sigma_1{}^2 + \sigma_2{}^2 + \sigma_3{}^2) - (\sigma_1\sigma_2 + \sigma_1\sigma_3 + \sigma_2\sigma_3]\sigma_n - det[\sigma] = 0 \quad (2\text{-}5)$$

The solution to the above equation produces the Eigen values σ_n and their corresponding Eigen vectors σ_1, σ_2 and σ_3.

2.2.2 Introduction to Mohr's Circle

Mohr's circle illustrates the transformation equations for plane stress problems in a graphical format. It serves as a valuable tool for visually showing the interrelations between normal and shear stresses exerted on a stress element at any given orientation. Consider that the body in Figure 2-1 was acting upon by both normal and shear stresses. Mohr's Circle can be used to determine the maximum normal and shear stress on this body. Suppose that point O is subjected to plane stress. Consider also that the z-axis is the principal axes because it is experiencing no shear stress. it is possible to fully describe the stress state relative to any material plane perpendicular to plane x-y. By drawing the points $A(\sigma_x, \tau_{xy})$ and $B(\sigma_y, -\tau_{xy})$ on an $\sigma - \tau$ coordinate axes, the stress state in terms of normal and shear stresses for the body passing through point O is then described to be the cycle having a diameter equal to the line segment A-B. The centre of such a circumference has coordinates defined as [1,2];

$$C = \left(\frac{\sigma_x + \sigma_y}{2}, 0\right) \quad (2\text{-}6)$$

Such a circle is illustrated in Figure 2-2 and has a radius also defined as

$$R_C = \sqrt{\left(\frac{\sigma_x - \sigma_y}{2}\right)^2 + \tau_{xy}{}^2} \quad (2\text{-}7)$$

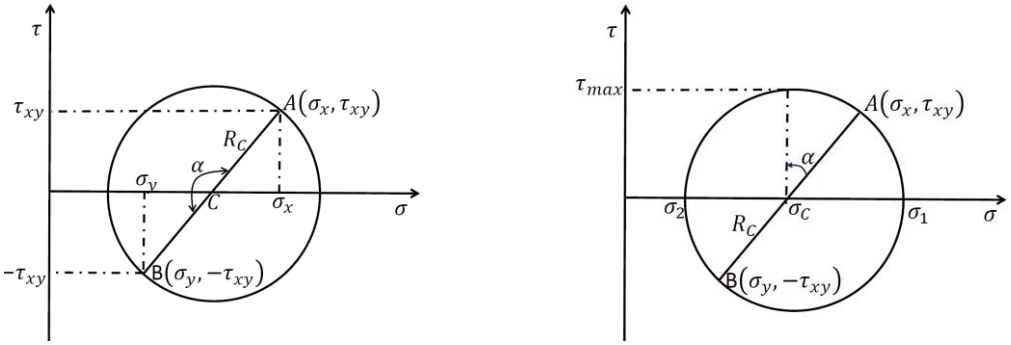

a) b)

Figure 2-2 a) Resulting Mohr's circle from an elementary loaded body b) Orientation of the plane experiencing the maximum shear stress τ_{max},

The correlation between angles in Mohr's representation and those in the conventional representation is $\theta = {}^{\alpha}/_{2}$. Mohr's circle facilitates the determination of the stress state concerning any plane parallel to axis z and passing through point O, providing a straightforward means to identify the maximum shear stress τ_{max}, as equal to R_C (see Figure 2-2b) and the stress perpendicular to such a plane is equal to $\sigma_C = \frac{\sigma_x+\sigma_y}{2}$. Therefore, the principal stresses σ_1 and σ_2 can be calculated as follows:

$$\sigma_1 = \sigma_C + \sqrt{\left(\frac{\sigma_x - \sigma_y}{2}\right)^2 + {\tau_{xy}}^2}$$
$$\sigma_2 = \sigma_C - \sqrt{\left(\frac{\sigma_x - \sigma_y}{2}\right)^2 + {\tau_{xy}}^2} \quad (2\text{-}8)$$

In general, the normal stress $\sigma_n(\phi)$, and the shear stress $\tau_n(\phi)$, pertaining to a generic material plane perpendicular to the component's surface, with a normal unit vector $\vec{n}$ positioned at an angle ϕ to axis x, can be computed as follows [1]

$$\sigma_n(\phi) = \frac{\sigma_x + \sigma_y}{2} + \frac{\sigma_x - \sigma_y}{2}\cos(2\phi) + \tau_{xy}\sin(2\phi)$$
$$\tau_n(\phi) = \frac{\sigma_x - \sigma_y}{2}\sin(2\phi) - \tau_{xy}\cos(2\phi) \quad (2\text{-}9)$$

2.2.3 Uniaxial Loading Paths

Suppose the system of forces acting on the body is unidirectional over time. A uniaxial stress distribution tensor is defined in this case as:

$$[\sigma] = \begin{bmatrix} \sigma_x & 0 & 0 \\ 0 & 0 & 0 \\ 0 & 0 & 0 \end{bmatrix} \tag{2-10}$$

In this scenario, the stress function exhibits a time-dependent profile. The unidirectional stress σ_x can thus be approximated in the following form:

$$\sigma_x = \sigma_{x,m} + \sigma_{x,a} \sin(\omega - t) \tag{2-11}$$

Where ω is the angular velocity, t is the time, $\sigma_{x,m}$ is the mean value of the stress and $\sigma_{x,a}$ the mean amplitude of the stress. It turns out that σ_x attends a maximum value at some point and a minimum value at another point since by this definition the applied stress is cyclic. In this case $\sigma_{x,max}$ and $\sigma_{x,min}$ are defined as:

$$\begin{aligned} \sigma_{x,max} &= \sigma_{x,m} + \sigma_{x,a} \\ \sigma_{x,max} &= \sigma_{x,m} - \sigma_{x,a} \end{aligned} \tag{2-12}$$

Consequently, it becomes feasible to define a stress range that characterizes the applied stress acting on the body. This stress range $\Delta\sigma_x$and stress amplitude $\sigma_{x,a}$ are therefore defined as:

$$\begin{aligned} \Delta\sigma_x &= \sigma_{x,max} - \sigma_{x,min} = 2\sigma_{x,a} \\ \sigma_{x,a} &= {}^{\Delta\sigma_x}/_{2} \end{aligned} \tag{2-13}$$

The stress profile representing the unidirectional loading in the x-direction for example is represented as:

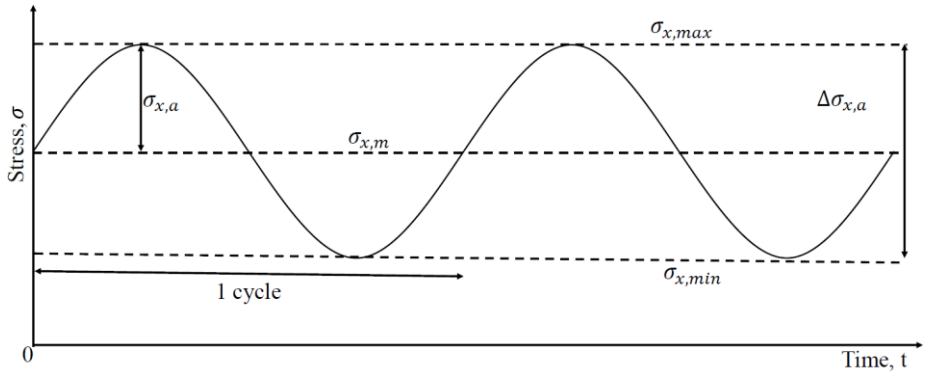

Figure 2-3 Fluctuating stress profile over time in the x-direction (unidirectional)

It is the stress range $\Delta\sigma_{x,a}$ rather than the maximum stress $\sigma_{x,max}$ that drives fatigue damage. The stress amplitude $\sigma_{x,a}$ and the mean stress $\sigma_{x,m}$ are the important parameters in fatigue life analyses and $\sigma_{x,m}$ is estimated by the equation:

$$\sigma_{x,m} = \frac{\sigma_{x,max} + \sigma_{x,min}}{2} \tag{2-14}$$

The diagram provided above outlines a uniaxial loading sequence in the x-direction. However, real-world structural components typically endure a combination of loading stresses from multiple directions, known as multiaxial loading. Each stress loading direction has its distinct profile, and analysing the cumulative effect of these loadings is important.

2.2.4 Stress ratio (R)

The load ratio R, quantifies the relationship between the alternating stress and the mean stress on a body. It is calculated as the ratio of the minimum stress to the maximum stress in the load sequence.

$$R = \frac{\sigma_{x,min}}{\sigma_{x,max}} \tag{2-15}$$

It helps in determining the severity of the cyclic loading and can significantly affect the fatigue life and behaviour of materials. Typically, the load ratio R can take on many values as illustrated in the figure below.

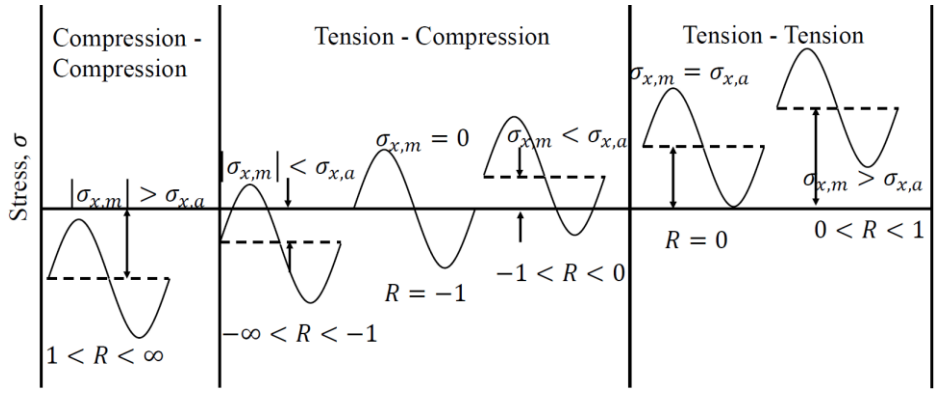

Figure 2-4 Definition of stress quantities used to predict fatigue damage under uniaxial loading

2.2.5 Stress concentration factor, K_f

Mechanical components exhibit a range of geometric features that lead to stress concentration. These occurrences demand constant consideration during the design phase because of their adverse impact on material fatigue strength. The challenge of incorporating stress raiser influences is extensive and will be explored further in subsequent research

endeavours. This PhD study offers only a concise overview of the stress concentration factor as explained in Ref [1,3].

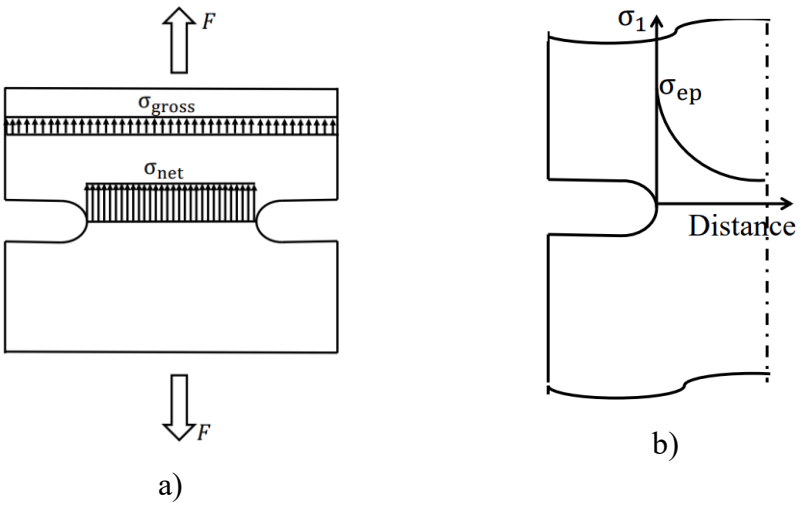

Figure 2-5 Definition of net and gross nominal stress, and linear-elastic peak stress at the tip of a notch

To accurately define the stress concentration factor K_f, consider a U-notched plate under tension. Due to the plate's geometric feature, the maximum linear-elastic principal stress σ_1 gradually decreases along the bisector from the notch's apex to the mid-section of the specimen itself (see Figure 2-5b) [1,4,5]. If the width of the sample is sufficiently large, the stress field tends towards its nominal net value. However, at the notch's tip, the maximum principal stress reaches its peak value, denoted as σ_{ep}. These stress quantities allow the stress concentration factor K_f to be defined as follows [1,6]:

$$K_{t,net} = \frac{\sigma_{ep}}{\sigma_{net}} \tag{2-16}$$

$$K_{t,gross} = \frac{\sigma_{ep}}{\sigma_{gross}} \tag{2-17}$$

The stress parameter K_f is commonly employed in notch fatigue problems. Its values, for a specific loading configuration, depend solely on the shape of the component being evaluated and are independent of its absolute dimensions [3].

When linear-elastic materials are weakened by sharp geometrical discontinuities (such as cracks), the stress analysis problem becomes much more complex, because the linear-elastic stress fields in the vicinity of the stress raiser apices become singular, resulting in

values of the peak stress tending to infinity. Before addressing this, it is good to briefly explain how these discontinuities can be loaded into a material.

2.2.6 Introduction to Notches

In mechanical engineering and materials science, a notch refers to a deliberate defect introduced into a flat material. When a notch is present, it creates a stress concentration in the material. This means that the stress distribution is amplified at the location of the notch, potentially resulting in the initiation and propagation of cracks [2,5,7]. In fracture mechanics, notches play a crucial role in determining properties related to fracture toughness and fatigue crack growth rates [8]. Notch geometries can vary and come in different shapes, such as V-shaped, U-shaped, or semi-circular [9], as illustrated below. Unlike notches, cracks are treated as sharp notches with zero root radius.

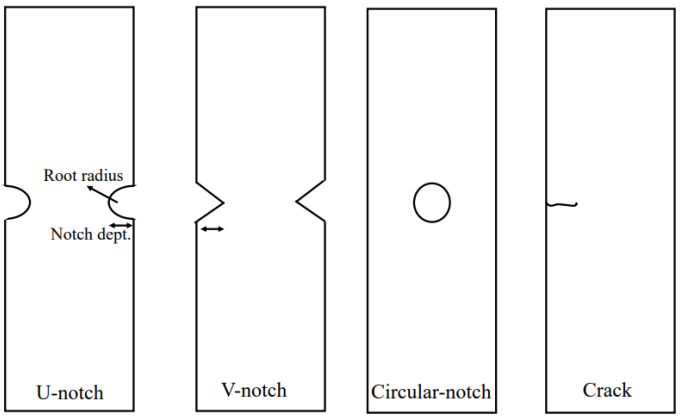

Figure 2-6 Notch geometries and crack

Defects such as notches or cracks are unavoidable in engineering components due to design specifications and damage incurred during service. For a component with a surface notch, the maximum elastic notch stress σ_{eff} can be determined by the product of a nominal stress (σ) and the elastic stress concentration factor K_t as [7,10,11]:

$$\sigma_{eff} = K_t \sigma \tag{2-18}$$

The elastic stress concentration factor depends on both the notch geometry and the type of loading [12]. In situations where the component geometry and loading conditions are straightforward, and the nominal stress can be readily determined, elastic stress concentration factors are established using methods like Peterson's stress concentrators [6,13]. However, for more complex geometries and loading scenarios, numerical models such as finite element analyses are employed. Nonetheless, the stresses and strains at the

notch are governed by the material behaviour of the net section [8], which means that the nominal stress used to determine K_t is derived from an engineering stress formula based on basic elasticity theory and the net section properties, without accounting for the presence of the notch. How a material behaves near these stress raisers is also governed by the nature of the external loads.

2.2.7 Loading modes of stress raisers in engineering materials

In the field of engineering materials, understanding loading modes is essential for analysing how structures and materials respond to external forces in the presence of cracks or stress raisers. There are three different kinds of loading profiles: Mode I (opening mode), Mode II (shearing mode) and Mode III (tearing mode) [1,5,14]. Mode I occurs when a tensile force is applied perpendicular to a crack. It's the most common and leads to significant damage. Imagine pulling a piece of paper apart along a straight line. The shear component is negligible. In Mode II loading, shearing of the crack faces happens due to in-plane shear stresses. It influences crack growth direction, minimizing further Mode II loading while maximizing Mode I. The shear component is significant in the plane. Mode III results from out-of-plane shear stresses. It's less frequent than Modes I and II. The dominant shear component is out-of-plane. These various modes are illustrated in the figure below.

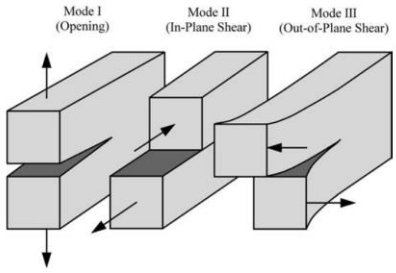

Figure 2-7 Definition of the three fundamental loading modes [5]

2.2.8 Stress analysis at a crack tip

Returning to the linear-elastic stress distributions near the stress concentrator, let's now examine a plate subjected to tensile loading and featuring a central through crack. The width, w, of the plate is initially assumed to be much larger than the crack length, 2a as shown in Figure 2-8.

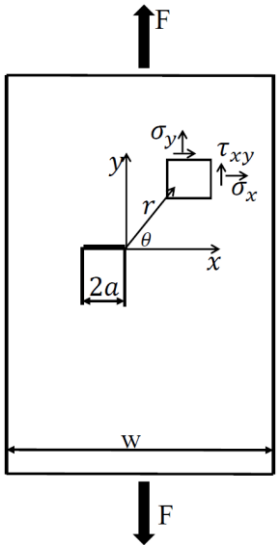

Figure 2-8 Central through crack in a plate loaded in tension

According to Irwin, the linear-elastic stress field damaging the material in the vicinity of the above crack tip in Mode I loading can be described by using the following well-known relationships [1,5]:

$$\sigma_x = \frac{K_I}{\sqrt{2\pi r}} \cos\frac{\theta}{2}\left[1 - \sin\frac{\theta}{2}\sin\frac{3\theta}{2}\right] \tag{2-19}$$

$$\sigma_y = \frac{K_I}{\sqrt{2\pi r}} \cos\frac{\theta}{2}\left[1 + \sin\frac{\theta}{2}\sin\frac{3\theta}{2}\right] \tag{2-20}$$

$$\tau_{xy} = \frac{K_I}{\sqrt{2\pi r}} \sin\frac{\theta}{2}\cos\frac{\theta}{2}\cos\frac{3\theta}{2} \tag{2-21}$$

The stress components σ_x, σ_y and τ_{xy} in Equations (2-19) to (2-21) are calculated with respect to the frame of reference as defined in Figure 2-8, with K_I being the stress intensity factor (SIF). These equations can always be used to determine the linear elastic fields in any cracked body provided that the body is subjected to Mode I loading. The distance r from the crack tip is lower than $a/10$.

Stress intensity factors K_I play a pivotal role in evaluating real cracked components under both static and fatigue loading conditions [9,15]. The magnitude of these factors varies based on the particular geometry and load configuration of the problem at hand. For example, consider the stress intensity factor for a flat cracked specimen in Figure 2-8 is estimated as:

$$K_I = \sigma_{gross}\sqrt{\pi a} \tag{2-22}$$

If the length of the crack cannot be considered small compared to the width of the plate, the actual geometry's influence must be directly incorporated using a shape factor denoted as F [1]. Taking this shape factor into account, the aforementioned equation can be expressed as:

$$K_I = F\sigma_{gross}\sqrt{\pi a} \tag{2-23}$$

$$F = \sqrt{\frac{w}{\pi a}\tan\left(\frac{\pi a}{w}\right)} \tag{2-24}$$

Apart for the case of a central through-crack in an infinitely sized plate under tension, typically the shape factor F exceeds unity. Its value is specific to a given geometrical configuration and is influenced not only by the shape of the component in question, but also by the applied loading type and other relevant factors. Both K_I and F factors can be determined using numerical or analytical methods. Alternatively, values for these factors can be obtained from various handbooks, which compile data for commonly encountered scenarios in practical engineering applications.

2.3 Brief review of linear and fracture mechanics in engineering materials

Metals are the backbone of many industrial applications and they derive their mechanical properties from the intricate arrangement of atoms within their crystalline structure. Each metal is composed of countless grains or crystals, wherein atoms are meticulously packed to minimize potential energy. However, these crystalline structures are not flawless as they contain various defects otherwise known as dislocations being the most prominent. Dislocations can be visualized as extra half-planes of atoms that disrupt the uniformity of atomic distribution within a crystal lattice. When subjected to stress or strain, dislocations within grains can move along designated paths known as easy glide planes, driven by shearing forces acting along the easy glide directions. This movement of dislocations enables metals to deform plastically, a crucial characteristic for their practical utility. Moreover, there exist two distinct types of dislocations: edge and screw dislocations, each exhibiting unique motion patterns under applied stress. Understanding the behaviour of dislocations is pivotal in understanding stress concentrators and crack initiation in metallic materials.

2.3.1 Fracture toughness

It is also important to mention fracture toughness and its significance in fracture mechanics, especially regarding fatigue. Fracture toughness characterizes the resistance to crack propagation under applied stress, and it quantifies a material's ability to withstand the growth of existing flaws or cracks without catastrophic failure [16,17]. It is a function of the loading mode, the chemical environment, the material microstructure, the test temperature, the strain rate, and the state of the stress [2]. Essentially, it measures the energy required to propagate a crack through the material, typically represented by the critical stress intensity factor. The fracture toughness value indicates the material's ability to resist brittle fracture and is crucial for evaluating the structural integrity and safety of engineering components, particularly in applications where the presence of flaws or cracks is possible. For example, consider a linear elastic isotropic body subjected to Mode I uniaxial loading, with a sharp crack through its thickness, as depicted in Figure 2-8 above. In this case, $\sigma_x = \tau_{xy} = \tau_{yz} = 0$ and the fracture toughness in Mode I loading K_{Ic} becomes the critical value of the stress intensity factor wherein a crack extends rapidly without an increase in the applied loading. That is,

$$K_{Ic} = \sigma_c \sqrt{\pi a_c} f\left(\frac{a_c}{w}\right) \tag{2-25}$$

in which a_c is the critical length of the crack and σ_c is the applied nominal stress at this critical point. $f\left(\frac{a_c}{w}\right)$ is a function of the material, strain rate, thickness and to a lesser extent the crack length of the crack for which the fracture toughness is dependent upon [1,18]. The corresponding fracture toughness in Mode II and Mode III are K_{IIc} and K_{IIIc} respectively.

2.3.2 Crack initiation

Consider now a single crystal subjected to an external uniaxial cyclic loading shown in Figure 2-9. By assuming that only one specific glide plane is active within the crystal, dislocations can move under the cyclic shearing forces applied to that plane [1,5,17,19]. This movement leads to the formation of thin layers known as Persistent Slip Bands (PSBs), causing the grain's profile to become irregular with alternating extrusions and deep intrusions. The presence of PSBs creates areas of localised stress concentration, triggering the initiation of micro-cracks within the fatigued crystal [2,19]. These cracks typically originate at the deepest intrusions or the interface between the matrix and PSBs. Once

initiated, the micro-cracks propagate within the grain due to plastic deformation occurring within the slip bands. This deformation is a result of the cyclic shearing forces acting on the active glide planes and aligning with the corresponding directions. These forces can be quantified in terms of either microscopic shear strains or microscopic shear stresses.

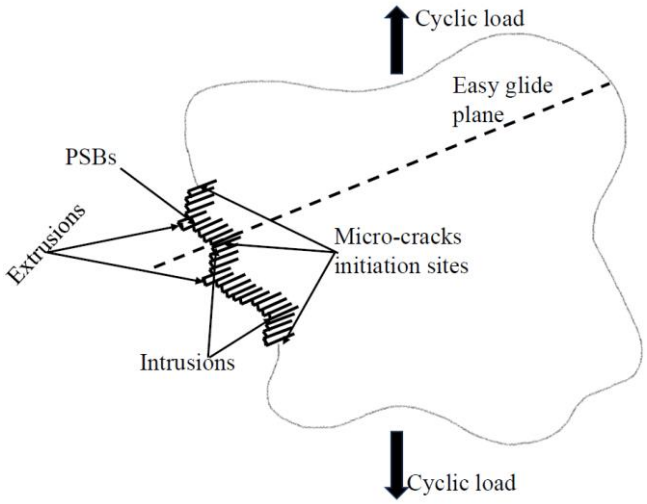

Figure 2-9 PSB in a single crystal subjected to an external cyclic load and a potential micro-crack initiation site

The scenario shown above simplifies the structure of a single grain by assuming that it has only one glide plane. However, in reality, grains exhibit multiple easy glide planes and directions with various orientations. When subjected to microscopic shearing loadings, both edge and screw dislocations can cross intersecting glide planes, impeding each other's movement. Considering the multitude of these processes simultaneously occurring within a real grain under external cyclic loading, modelling the formation of PSBs and subsequent micro-crack initiation becomes significantly more complex. Nonetheless, the process of micro-crack formation follows the simple pattern as described above.

Crack initiation in structural and equipment components typically arises in areas of stress concentrations, such as notches, due to fluctuations in stress levels. At the tip of a notch in a component subjected to cyclic loading, the material experiences the highest stress range. Consequently, this region is highly prone to fatigue damage and commonly serves as the point of origin for crack initiation. More on this type will be reviewed under the fatigue crack initiation section.

2.3.3 Crack propagation

Single crystals form only under specific conditions while the typical solid form of a material is polycrystalline and composed of numerous crystals. The properties of a polycrystal differ notably from those of a single crystal [20,21]. The individual crystallites making up the polycrystal are often termed grains, and the interfaces between these grains are referred to as grain boundaries. Real metallic materials consist of numerous grains that are interconnected at grain boundaries, distorting the crystal structure [22]. These grains within polycrystals possess diverse orientations [1,23]. While conventional metallic materials may appear homogenous and isotropic at a macroscopic level, their behaviour at a microscopic scale is significantly influenced by factors such as material morphology and the presence of hard inclusions like grain boundaries, non-metallic particles, [17], precipitates, and defects.

By analysing a polycrystal subjected to external forces, determining the macroscopic stress tensor at any material point and instant of the load history is straightforward according to continuum mechanics principles if homogeneity and isotropy are assumed at a macroscopic scale. However, calculating the microscopic stress and strain states responsible for the formation of PSBs is considerably more complex. This complexity arises from the dependency of normal and shear stress and strain components on various factors, including the mechanical properties of individual crystals, grain orientations, and the presence of grain boundaries and hard inclusions. In the calculation of microscopic stress and strain, the mesoscopic approach, pioneered by Dang Van and formalized by Papadopoulos, is valuable. This approach asserts that under macroscopic elastic deformations and when only one easy glide plane is active within a grain, normal micro-stresses ($\mu\sigma$) are equivalent to their macroscopic counterparts, while microscopic shear stresses ($\mu\tau$) are proportional to those calculated using continuum mechanics concepts. This is illustrated in Figure 2-10 below.

Now, consider a polycrystal experiencing external uniaxial fatigue loading, as the cyclic force is applied, a micro-crack initiates within the material after a certain number of loading cycles, marking the initiation phase. Following this, the crack gradually extends in length under the ongoing fatigue loading, constituting the propagation phase. Eventually, when the maximum force exerted during the loading cycle surpasses the material's ultimate tensile strength at a localized point, the polycrystal undergoes quasi-static fast fracture, resulting in its final breakage.

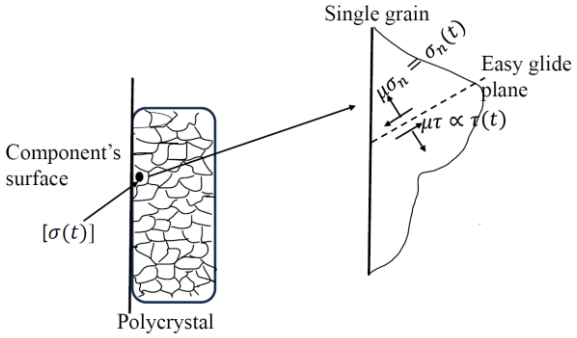

Figure 2-10 Polycrystal subjected to an external system of forces and the existing relationship between macro- and micro-stress components according to the mesoscopic approach.

It has been observed through investigations found in the literature that a general pattern in micro/meso-crack propagation exists, which can be divided into two distinct stages Stage I and Stage II [18,24]. In Stage I, cracks develop along crystallographic planes of maximum shear, primarily influenced by Mode II. In Stage II, these cracks transition from Stage I and tend to align themselves to experience maximum Mode I loading (see Figure 2-11). Specifically, Stage I growth is dictated by microscopic shear stress/strain on planes of maximum shear, as well as by the material's morphology and the magnitude of applied loading. Typically, Stage I micro/meso-cracks extend only a few grains in length [25]. According to Ref. [26], Stage II propagation occurs due to plastic de-cohesion on the planes of maximum shear strain gradient at the crack tip. Additionally, it is noted that the same mechanism is operative also in Stage I growth, but de-cohesion occurs on only one of the available shear planes.

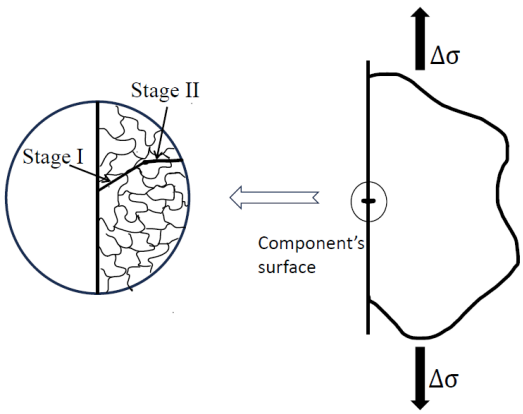

Figure 2-11 Stage I and Stage II crack in a polycrystal subjected to uniaxial loading

Typically, fatigue cracks initiate at the surface of fatigued components, unless localized stress concentration phenomena exist within the material due to defects or hard inclusions

[2,14,25]. Fatigue is primarily understood as a propagation phenomenon [26,27]. The majority of a conventional metallic specimen's fatigue life is spent propagating cracks rather than initiating them. At room temperature, crack propagation in metals mainly occurs in a trans-crystalline mode, as highlighted in Ref. [25], with microstructural barriers like grain boundaries playing a crucial role, especially in the initial growth phase. The presence of high stresses or stress concentration phenomena due to macroscopic geometrical features reduces the length of Stage I cracks, which are nonetheless always present. In Ref [28], experiments were conducted on specimens with stress concentration factors ranging from 3.8 to 25 and found that Stage I cracks are consistently present, even in sharply notched specimens. However, their orientation primarily depends on the crystallographic features of the grains near the stress concentrator tips.

2.4 Overview of weld technology in the pipeline

A weld is a joint created by fusing two or more pieces of metal using heat, pressure, or both. This process can involve melting the base materials and adding a filler material to form a strong bond upon cooling. The mechanical properties of a weld are therefore influenced by several factors, including the welding process and parameters such as the type of welding method used, heat input, welding speed, and the type and purity of shielding gases. The first challenge in designing welded connections for fatigue resistance is selecting the most appropriate stress analysis method to calculate a stress value that can efficiently estimate fatigue strength [1]. The simplest method for performing this fatigue assessment is to use nominal stresses, where fatigue strength is directly estimated from the specific S–N curve provided in standard codes for the type of welded detail being considered.

The welding method used in natural gas pipelines is crucial in determining the performance of the welds. The formation of weld appearance, potential cracks, and defects during the welding process can greatly impact how hydrogen atoms diffuse and redistribute within the microstructure [29,30]. This results in a deterioration of the weld's mechanical properties and changes in its microstructure. Consequently, it is essential to study both the welding methods and weld morphology in natural gas pipelines to understand how these methods influence weld structure and performance. Pipeline welding is typically carried out using one of several arc welding processes [31], and the American Petroleum Institute (API) 1104 Standard also outlines suitable welding techniques for carbon and low-alloy steel pipes used in natural gas distributions. These include arc welding methods for butt, fillet, or

socket welds, utilizing manual, automated, semi-automated, or combined processes [31,32]. The welding is usually circumferential between the connecting pipes [30]. Failures are uncommon in longitudinal and spiral welds formed during manufacturing, with most issues arising in the circumferential welds, especially in large-diameter, high-grade gas pipelines. Current long-distance, high-pressure natural gas pipelines are primarily welded using semi-automatic techniques [29]. However, with the construction of new large pipelines like the China-Russia Eastern Gas Pipeline, which has higher flow rates, pressures, and larger sizes, there is a shift toward fully automated welding to enhance weld quality and safety. Automated welding achieves over 97% in non-destructive examination rates, while semi-automatic welding achieves up to 95%.

Natural gas pipelines are susceptible to erosion-corrosion on welds due to gas flow and the presence of small particles, leading to eventual wear regardless of welding technique. When welding on pipelines containing hydrogen, two key factors must be considered: the risk of burn-through from localized heating and the thermal effects on the heat-affected zone (HAZ), which can alter microstructure and performance [29]. Changes such as grain growth, phase transformations, and hardening can impact the strength, toughness, and corrosion resistance of the pipeline.

2.4.1 Welding technology in natural gas pipeline

The welding process can significantly affect the metallurgical and mechanical properties of a material, often leading to a degradation of its overall properties. In pipeline transmission, several welding processes are commonly utilized to ensure quality and efficiency. Gas Tungsten Arc Welding (GTAW), or TIG welding, is prized for its high-quality welds and precise control, making it ideal for root passes and smaller-diameter pipelines despite being slower. This is a welding process that produces a more ferritic microstructure in both the fusion zone (FZ) and the HAZ [33,34], due to the high cooling rate that occurs during welding. During the cooling process, the formation of delta (δ)-ferrite and the ferrite-austenite transformation occur due to the diffusion of atomic nitrogen within the microstructure. This welding process is a widely used welding technique in the oil and gas industry because of its precision and versatility [35,36]. The Gas Metal Arc Welding (GMAW), also known as MIG welding, is either a semi-automated, automatic or machine welding process which joins metals by heating them to their melting point with an electric arc [37,38], and it is frequently used for larger-diameter pipes due to its faster application. Shielded Metal Arc Welding (SMAW), or stick welding, is widely favoured in

field conditions for its portability and versatility [36,39]. However, the weld strength and ductility achieved with GMAW welding are superior to those obtained with the SMAW process and it generates less spatter and better weld geometry. Flux-Cored Arc Welding (FCAW) is a manual arc welding process that uses a consumable electrode covered with flux to lay the weld and is chosen for its high welding speed and portability, making it well-suited for outdoor pipeline projects [39]. Lastly in Submerged Arc Welding (SAW), the acicular ferrite phase forms due to the interaction of various oxides in the weld pool at high temperatures [40]. This specific phase plays a key role in improving the impact strength of SAW weldments, enabling this technique to be primarily employed in manufacturing plants for creating longitudinal and spiral seams on large-diameter pipes, offering high-quality welds. It is for this reason that it is widely used in the design of liquified natural gas-fuelled vessels [39].

2.5 Fatigue and fracture of engineering components

Fatigue, as defined, is the progressive localized structural change occurring in a material subjected to fluctuating stresses and strains, leading to cracks or complete fractures over time [41,42]. Fatigue failure is therefore a phenomenon that commonly occurs in mechanical structures, particularly in components subjected to repeated or cyclic loading, at stress levels far below their yield stress. While fatigue failure may seem sudden, it develops gradually through repeated stress cycles [2,14]. It initiates at specific points within the component or structure, where stress concentrations are typically higher due to various factors such as temperature, external loads, geometry, residual stresses, environment, microstructure state, corrosion, and crack initiation or material deformity [7]. Fatigue represents a permanent process resulting from cyclic stresses and strains, often occurring at stress levels significantly lower than the material's ultimate tensile stress. According to Refs [2,43,44], the total fatigue life of a component can be segmented into three distinct phases, the initial phase known as crack initiation, constitutes the longest duration making up approximately 40–90% of the overall fatigue life. During this phase, cracks begin to form, and their progression may be impeded by various barriers such as grain boundaries. In some instances, cracks may stall completely at these barriers, preventing them from reaching a critical size that would lead to stable growth [2,5,43]. Following crack initiation, the component enters a phase of stable crack growth, where cracks propagate steadily at a relatively constant rate. Finally, the last phase is the unstable crack growth, which is marked by the rapid propagation of cracks until the component ultimately fails by breakage.

2.5 Fatigue and fracture of engineering components

Although unstable crack growth represents a smaller portion of the total fatigue life compared to crack initiation, it signifies the culmination of the fatigue process, leading to failure. In this case, failure is considered to be the final breakage. In other circumstances, failure modes encompass a range of configurations, including excess deformation (elastic, yielding, or plasticity), brittle fracture, ductile fracture, creep, thermal shocks, wear, buckling, corrosion, and fatigue, among others. Among these, fatigue failure is predominant in engineering, approximately 50 to 90% of all mechanical failures, and is responsible for a significant portion of mechanical failures. This type of failure is prevalent in everyday objects like door springs, chairs, paper clips, hinges, and bicycles, as well as in more complex systems such as ground vehicles, aircraft, ships, and human body implants. These failures often carry significant costs and potential risks of fatalities. But what instigates these mechanical failures? Understanding fatigue life therefore is crucial in structural engineering to ensure components' long-term reliability and safety under cyclic stresses.

Mechanical failures stem from a myriad of factors, including various loading scenarios, environmental conditions, temperature fluctuations, and corrosion, among others. To address these challenges, design principles have been established, leading to significant successes in the engineering field. These principles aim to mitigate risks and ensure the reliability and safety of engineering structures, contributing to overall advancements in engineering practices.

2.5.1 Factors influencing fatigue failure in engineering materials

Fatigue in engineering is influenced by a multitude of factors ranging from material properties to loading conditions and environmental factors. However, the propagation of fatigue cracks is not instantaneous but takes some time, which allows for preventing accidental situations in certain cases by timely component diagnostics. The understanding of the cases, when fatigue cracks may form, and the knowledge of the basic causes of their generation would help significantly cut the material and time costs of both, examining the components and eliminating damage effects. Some of these factors are discussed below.

2.5.1.1 Material properties

Non-metallic inclusions in metals are compounds composed of both metals and non-metals, such as oxides, sulphides, or nitrides, and may include more complex species like oxysulphides or carbonitrides [45–47]. These inclusions can be classified as either

endogenous, formed within the metal through reactions of the liquid melt with deoxidizers like silicon, manganese, or aluminium particles during processes like desulfurization, or exogenous, originating from external sources such as refractory fragments, slag covering the molten metal or sand in cast alloys, and then mechanically incorporated into the metal. Typically, exogenous inclusions are larger in size compared to their endogenous counterparts. The presence of these non-metallic inclusions, grain size and orientation [48,49] along with other internal flaws, significantly reduces the reliability of components as they act as stress raisers within the material [2,50].

2.5.1.2 Surface finish and defects

Surface defects resulting from mechanical treatment or thermal and thermochemical processes can significantly increase the likelihood of fatigue crack occurrence and propagation, even under smaller loads compared to the base metal [47,50,51]. Manual polishing, for instance, reduces surface pores and enhances compressive residual stresses, thereby improving fatigue resistance by a factor of about 1.5 – 3.5 for austenitic stainless steels [49,52]. A smoother surface with lower roughness tends to enhance fatigue performance, while fewer local defects and inclusions also contribute positively to fatigue resistance. Surface treatments that induce large compressive residual stresses are particularly beneficial for fatigue resistance, as these stresses counteract applied loads and reduce crack initiation and propagation. Additionally, work hardening increases the material's yield strength thereby delaying crack nucleation, although excessive work hardening may lead to brittleness and accelerate crack growth [53]. Various changes induced by machining, such as the formation of a white layer, grain refinement, dislocation, or martensitic transformation, also influence fatigue behaviour. Chromium plating is a widely utilized procedure in the industry, known for its ability to enhance the surface condition of critical industrial components [54]. This process provides a high level of hardness, resistance to wear and corrosion, and a low coefficient of friction, making it invaluable for various industrial applications in the aerospace, automotive and petrochemical fields.

2.5.1.3 Heat treatments

Premature fatigue failures of machine components often stem from various factors, including intense heat generated during the friction of mating components. Heat treatment plays a significant role in influencing mechanical and low cycle fatigue behaviours [55] and at room temperature, the strength of a material improves due to dislocation theory (the

abrupt change in the arrangement of atoms within a crystal). In Ref [56], heat treatment, the bonding between matrix and filler increases, enhancing the stability of resulting composites by improving the interaction between filler and matrix phases. However, the impact of heat treatment on thermomechanical fatigue responses is less significant with the difference in fatigue lifetime between heat-treated alloys (such as A356.0-T6) and as-cast alloys (such as A356.0) decreasing as the temperature range increases [55]. Notably, plastic strain increases significantly during fatigue cycles in heat-treated alloys due to over-aging.

2.5.1.4 Thermochemical treatment surface treatment

Fatigue often originates at the surface of a component. To enhance fatigue performance, various methods are frequently employed alongside surface finish improvements. These methods are designed to introduce compressive residual stress to the high-stress surface of the component, aiming to increase its fatigue life. Common techniques for enhancing component fatigue life include surface shot peening [57,58], cold extrusion of parts, and the introduction of residual compressive stress on the surface. Shot peening, particularly effective in areas with stress gradients or notch stress concentrations, stands out among these methods. Surface nitriding or carburizing treatments can strengthen the material surface and induce compressive residual stress, both contributing to improved fatigue performance [59]. Nitriding or carburizing treatments can double the fatigue limit of steel, with a more pronounced effect observed in specimens with notches [60]. The material's strength directly influences its fatigue performance, as higher material strength results in a lower cyclic stress level, thus extending service life and enhancing life extension effects.

2.5.1.5 Environmental

The presence of a liquid or gaseous environment typically results in a reduction in fatigue life, with chemical interactions and diffusion playing significant roles [61,62]. This is because fatigue initiation commonly occurs at surface imperfections, such as cracks, flaws, or inclusions, and the surfaces' interaction with the environment enhances the diffusion of gases like hydrogen or corrosion reactions, ultimately diminishing fatigue life. Additionally, factors like pressure, temperature, and solution chemistry further influence this phenomenon [47,63]. Corrosive fatigue in environments such as seawater, acids, and alkalis has a detrimental effect on fatigue. It is thought to cause rupture of the protective passive film on materials increasing crack growth rates. However, corrosion-resistant steels with good corrosion fatigue resistance perform better than ordinary carbon steels, which

see a significant decrease in their fatigue limit, or even their complete disappearance, in corrosive environments.

2.5.1.6 Applied loads or operational conditions

The likelihood of fatigue failure depends primarily on both the magnitude of the applied stress, an external factor, and the material's resistance to fatigue failure, an internal factor. Typically, failure occurs in regions experiencing high stress or material defects [2,14]. The operational durability of components and their susceptibility to fatigue failure largely hinge on the quality of the metal used and the fabrication precision of the part itself. In situations where the maximum cyclic stress is equivalent, the larger volume of material in high-stress areas during tension and compression cycles heightens the likelihood of defects and crack initiation [47]. Consequently, under identical stress levels, the lifespan of a specimen subjected to tension-compression cyclic loads is shorter than that under bending [64,65]. This indicates that the fatigue strength under tension-compression cycles is lower compared to bending for the same service life. Furthermore, fatigue life further diminishes during torsion, although the volume of material has minimal impact in this scenario.

2.5.2 Mean stress effect on fatigue

The mean stress effect is significant in determining the overall fatigue strength of engineering materials. Specifically, under uniaxial fatigue loading, fatigue damage increases with higher applied tensile static stress [66]. Similarly, reducing the load ratio (R) causes fatigue curves to shift upwards in Wöhler's diagrams, indicating a decrease in material fatigue limit [1]. For materials with a fatigue limit, the number of cycles to failure at the knee point of the fatigue curve can vary with changes in mean stress or load ratio. The effects of mean stress as the load ratio changes are depicted in the figure below.

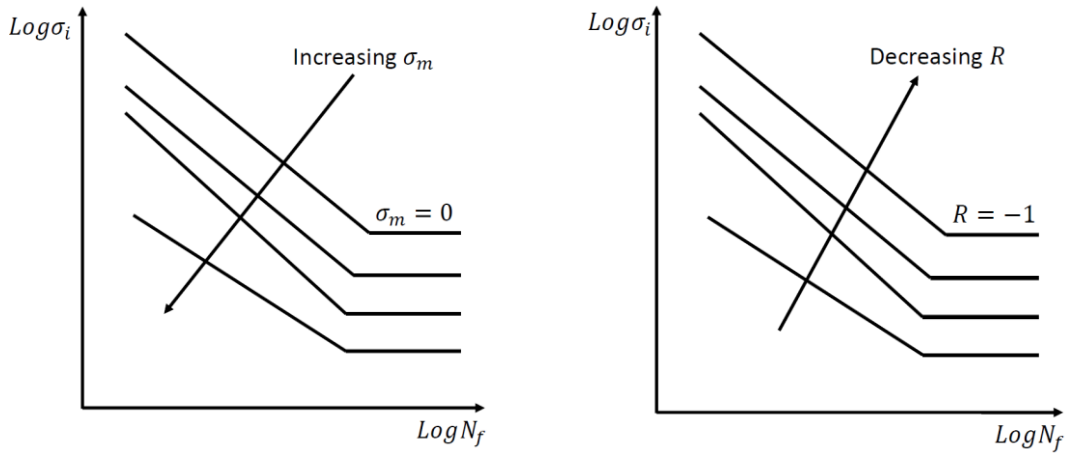

a) b)

Figure 2-12 effect of uniaxial loading on the a) mean stress and b) load ratio R on fatigue curves.

many attempts have been made to propose sound engineering rules suitable for predicting the mean stress effect in fatigue. Almost all the proposed criteria can concisely be summarised by using Marin's general equation [1,67]

$$\left(\frac{\sigma_0}{\sigma_{0,R=-1}}\right)^n + \left(f\frac{\sigma_m}{\sigma_{UTS}}\right)^m = 1 \tag{2-26}$$

In this equation, $\sigma_{0,R=-1}$ is the fatigue limit generated under fully reverse load conditions. σ_{UTS} is the ultimate tensile strength, while f, m and n are constants which take on different values according to the considered fatigue damage model. The most adopted criteria is derived as follows:

Soderberg's relation.

Bu considering m, n = 1, and $f = {}^{\sigma_{UTS}}/_{\sigma_Y}$ in which σ_Y is the material's yield stress, Marin's general equation becomes:

$$\frac{\sigma_0}{\sigma_{0,R=-1}} + \frac{\sigma_m}{\sigma_Y} = 1$$
$$\sigma_0 = \sigma_{0,R=-1}\left(1 - \frac{\sigma_m}{\sigma_Y}\right) \tag{2-27}$$

Goodma's relationship

By setting m, n, and f = 1, this becomes

$$\frac{\sigma_0}{\sigma_{0,R=-1}} + \frac{\sigma_m}{\sigma_{UTS}} = 1$$
$$\sigma_0 = \sigma_{0,R=-1}\left(1 - \frac{\sigma_m}{\sigma_{UTS}}\right) \tag{2-28}$$

Gerber's parabola

This is obtained by imposing $n = 1$, $m = 2$ and $f = 1$ in the Marin's equation.

$$\frac{\sigma_0}{\sigma_{0,R=-1}} + \left(\frac{\sigma_m}{\sigma_{UTS}}\right)^2 = 1$$
$$\sigma_0 = \sigma_{0,R=-1}\left(1 - \frac{\sigma_m}{\sigma_{UTS}}\right)^2 \tag{2-29}$$

Dietman's parabola

Similarly, by setting $n = 2$, $m = 1$ and $f = 1$, Marin's equation turns to:

$$\left(\frac{\sigma_0}{\sigma_{0,R=-1}}\right)^2 + \frac{\sigma_m}{\sigma_{UTS}} = 1$$
$$\sigma_0 = \sigma_{0,R=-1}\sqrt{1 - \frac{\sigma_m}{\sigma_{UTS}}} \tag{2-30}$$

Elliptical relationship

This is achieved by imposing $n = 2$, $m = 2$ and $f = 1$ in the Marin's equation. This becomes:

$$\left(\frac{\sigma_0}{\sigma_{0,R=-1}}\right)^2 + \left(\frac{\sigma_m}{\sigma_{UTS}}\right)^2 = 1$$
$$\sigma_0 = \sigma_{0,R=-1}\sqrt{1 - \left(\frac{\sigma_m}{\sigma_{UTS}}\right)^2} \tag{2-31}$$

Experimental evidence shows that most data points fall within the area defined by an elliptical relationship (equation (2-31)) and Goodman's straight line (equation(2-28). This suggests that when examining how a specific metal material responds to non-zero mean stresses, Goodman's criterion is recommended if appropriate tests cannot be conducted [1,67]. This criterion provides a margin of safety for accounting for the mean stress effect under uniaxial fatigue loading. Additionally, Soderberg's straight line, which uses the yield stress as a calibration reference instead of the ultimate tensile strength, is often preferred for practical applications. This preference arises because it offers a higher level of safety. These criteria can also be applied when using endurance limits.

In the finite life regime, Marin's general relationship can be utilized to assess how superimposed static stresses impact the number of cycles until failure. This method involves substituting the fully reversed fatigue limit with the plain fatigue curve produced under a load ratio, R = -1. In this case, the Marin's equation becomes:

$$\left(\frac{\sigma_a}{\sigma_0}\left(\frac{N_f}{N_0}\right)^{\frac{1}{k}}\right)^n + \left(f\frac{\sigma_m}{\sigma_{UTS}}\right)^m = 1 \tag{2-32}$$

$$\sigma_a = \sigma_0 \left(\frac{N_f}{N_0}\right)^{\frac{1}{k}} \sqrt[n]{1 - \left(f\frac{\sigma_m}{\sigma_{UTS}}\right)^m}$$

Clearly, the S-N curve of a plain material can be expressed also in terms of endurance limit, σ_0 extrapolated at N_A cycles to failure. It has been shown by examples in the literature that the use of Goodman's equation results in the highest level of conservatism (See Ref [1]).

It is important to note that while the impact of superimposed tensile stresses on fatigue strength has been extensively studied, the effect of compressive mean stresses has received less attention. However, compressive mean stresses either have no effect or can even be beneficial for overall material fatigue strength. As a result, negative mean stresses are typically disregarded, and fatigue assessment under these conditions relies on material fatigue properties obtained under fully reversed loading.

2.5.3 Notch fatigue

While notches are intentionally created for studying properties like fracture toughness and fatigue crack growth, they also have a well-known detrimental effect on the overall fatigue strength of real mechanical components, known as the notch fatigue problem. Consider for example the V-notched cylindrical bar as shown in Figure 2-13a, subjected to a dynamic load force with amplitude F_a. The stress experienced by the cylindrical bar can be calculated using either the net stress or the gross nominal stress. Since the bar is loaded with a cyclic force, it's clear that the nominal stress amplitudes can be calculated concerning either the net or the gross cross-sectional area. In fatigue assessment, continuum mechanics typically employ nominal net stresses, whereas linear elastic and fracture mechanics use gross nominal stress.

In particular, consider the Wohler curve shown in Figure 2-13b with three different sets of fatigue curves. The upper curve is supposedly generated by testing plain specimens of a given material, while the other two curves are determined by testing specimens of the same material but with a known geometrical feature, such as a notch. The difference between the two notch curves lies in their representation: the higher one is plotted in terms of the amplitude of the nominal net stress, whereas the dashed one is plotted in terms of the amplitude of the nominal gross stress. The dashed curve is simply scaled with respect to the other one by a factor proportional to the ratio between the net and the gross cross-sectional area. This is the fatigue strength reduction factor K_f [1,2,68]

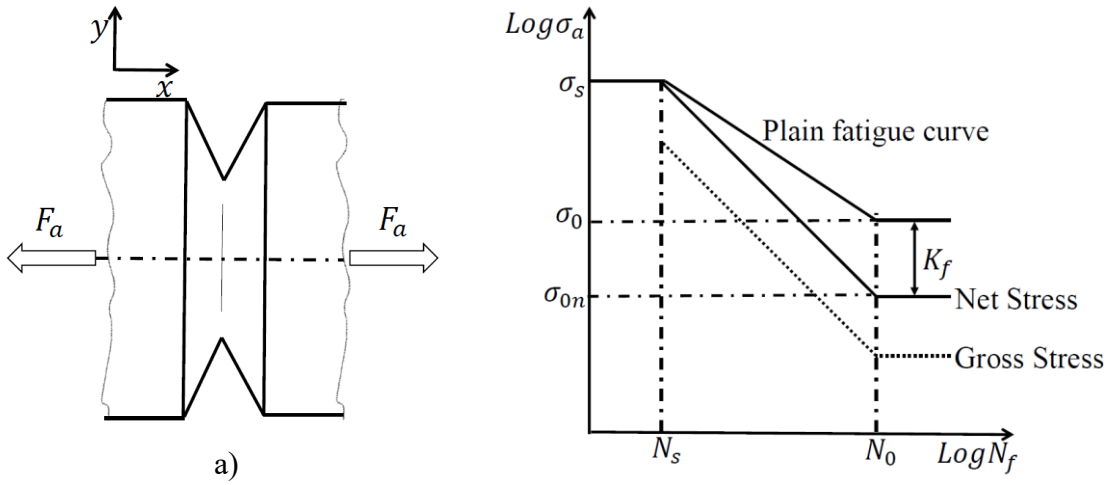

Figure 2-13 Wohler fatigue curve for plain and notched specimens and definition of the fatigue strength reduction factor K_f [2]

$$K_f = \frac{\sigma_0}{\sigma_{0,n}} \tag{2-33}$$

Where σ_0 is the endurance limit of the plain fatigue curve and $\sigma_{0,n}$ is the endurance limit of the notched fatigue curve. To coherently determine K_f, these two fatigue curves must always be determined under the same experimental conditions.

K_f is determined experimentally. However, there exist formulae to estimate K_f that have been validated in the literature. This involves another parameter known as the notch sensitivity factor q, defined as:

$$q = \frac{K_f - 1}{K_t - 1} \tag{2-34}$$

K_t is a function of the component geometry and the loading conditions, as is also available in handbooks [2,5,68]. For any given geometrical feature, the strength reduction factor is expressed as a function of both q and the corresponding linear elastic stress concentration factor K_t, in which K_t has been calculated using the net nominal stress. i.e:

$$K_f = 1 + q(K_t - 1) \tag{2-35}$$

where q ranges between 0 and 1. $q = 0$ when the presence of the considered stress raiser does not result in any reduction of the plain fatigue limit as is the case with non-damaging notches. When $q = 1$ in full-notch sensitivity, then $K_f$is equal to K_t so that the fatigue

damage can estimated by using the linear elastic stress calculated at the tip of the stress concentrator being assessed.

One of the popular approaches to estimate K_f is suggested by Neuber, which is defined as [1,2]:

$$K_f = 1 + \frac{K_t - 1}{1 + \sqrt{\frac{a_N}{r_n}}} \tag{2-36}$$

In which a_N is a constant whose value depends on the strength and ductility of the material and $r_n$is the notch-root radius. Accordingly, K_f depends on the notch root radius, which is assumed to be the most important parameter controlling the linear-elastic stress field distribution along the notch bisector, as well as on a critical distance parameter. This concept arises from the observation that the elastic stresses near stress raisers do not reach the levels predicted by continuum mechanics. Consequently, Neuber proposed averaging the stress near the notch apex over material units, such as crystals or structural particles. This approach calculates an engineering quantity that represents the actual stress causing fatigue damage in the process zone.

Furthermore, it's widely recognized that in conventional notches, the opening angle plays a crucial role in accurately calculating the resulting linear-elastic stress fields. To address this significant geometric variable, Ref [69] proposed the following formula, designed to estimate the reduction factor in fatigue strength when open notches are present.

$$K_f = 1 + \frac{K_t - 1}{1 + \frac{\pi}{\pi - 2\alpha}\sqrt{\frac{A}{r_n}}} \tag{2-37}$$

In the above relationship, 2a represents the notch opening angle, whereas A denotes a material constant that depends on the ultimate tensile strength. This constant typically ranges from 0.025 mm up to 0.51 mm [1,2,5].

Peterson proposed a reference strength method for estimating K_f along the notch bisector, formalizing the point method. This approach assumes that the notch root radius is the key geometrical parameter defining the stress field profile along the notch bisector. Peterson suggested using the following formula [3,70]:

$$K_f = 1 + \frac{K_t - 1}{1 + \frac{a_P}{r_n}} \tag{2-38}$$

Where $a_P$is a constant which is a property of the material. However, this formulation by Peterson is not recommended to be used to perform the fatigue assessment of mechanical components containing very sharp notches.

Another empirical relationship that certainly deserves to be mentioned is the one reported by Heywood in Refs [1,71] which is suitable for estimating the detrimental effect of notches in cylindrical bars of steel. In particular, the formula below in which a_H is a constant, a function of the material static properties as well as of the geometrical feature to be assessed, is used.

$$K_f = \frac{K_t - 1}{1 + 2\sqrt{\frac{a_H}{r_n}}} \tag{2-39}$$

Thus, Numerous engineering tools are available for estimating the fatigue strength reduction factor K_f. This implies that the calculated notch fatigue limits or endurance limits adjusted with an appropriate safety factor, can be directly applied to conduct high-cycle fatigue assessments of actual mechanical components.

The challenge of addressing the negative impact of notches was approached by focusing solely on stress concentrators with a tip radius greater than zero. When notch radii approach zero, the formulas outlined above become ineffective for estimating K_f because linear elastic peak stresses tend towards infinity, leading to stress concentration factors also trending toward infinity. Therefore, alternative strategies must be pursued in the presence of singular stress fields to estimate fatigue damage while still retaining the clear advantages of linear-elastic methods. This will be the primary focus of the following section.

2.5.4 Fatigue characterisation of welds

Fatigue failure of metals is a widespread challenge encountered across many industries. In structural integrity assessments of intermittently loaded components, welded joints are often the critical areas of concern. The fatigue strength of welded joints is typically lower than that of the base metal due to several factors. One such factor is the abrupt change in geometry at the weld toe, which creates a stress concentration unless mitigated through machining [1,5]. Additionally, thermal contraction during cooling induces tensile residual stresses of a magnitude comparable to the yield strength of the base metal, which

significantly weakens the fatigue strength of the welded joint. Moreover, the inhomogeneous microstructures and potential defects present in welded joints further increase their susceptibility to fatigue failure during service. In such cases, material strength primarily influences crack initiation [77]. Additionally, the presence of welding residual stresses often affects fatigue life, frequently leading to its reduction. Therefore, developing effective design methods for estimating fatigue life must also rely on localized approaches. According to the IIW Fatigue Design Recommendations, the four main methods used are [78]: Nominal stress approach, Structural/Geometrical "hot-spot" stress approach, Effective notch stress approach and the Linear elastic fracture mechanical crack growth approach.

Similarly, to classify the fatigue of a welded joint in the high cycle regime for example, which is characterised by stresses less than the yield strength and where purely elastic deformation in each loading cycle takes place, many approaches have been used to quantify the fatigue properties of the weld [72–74]. In particular, ref [73] suggests that fatigue data generated from a weld is compared with a target S-N curve of a known slope and this curve depends on the material and application. In this case, the target curve has predefined curve parameters and is always a factor above the standard design curve. A detailed explanation of the approach used to access the fatigue property of a welded joint in this research is presented in the methodology chapter of this research.

2.6 Estimation of the fatigue properties of a material quantitative analysis

Fatigue life prediction methods can be categorized into two primary groups based on their approach [44]. The first group consists of models focused on predicting crack nucleation. These models use a combination of damage evolution rules and stress/strain criteria for components. The distinguishing feature of this approach is its independence from loading and specimen geometry, with fatigue life determined solely by a stress/strain criterion [75].

On the other hand, the second group employs continuum damage mechanics (CDM). In this approach, fatigue life is predicted by computing a damage parameter cycle by cycle [76].

A review of current methodologies reveals a range of stress- and strain-based approaches for designing components against fatigue. A common challenge faced by structural engineers is the unavailability of all required material properties. While conducting experiments is the most accurate method, it's often constrained by resource limitations in

terms of time and budget. In such cases, empirical relationships come in handy, allowing for the estimation of fatigue constants directly. While these relationships may not be suitable for designing critical components, they can aid in preliminary design stages or assess components where failure wouldn't pose significant risks. Classical relationships for estimating fatigue properties are readily available in scientific literature. Despite their reliability in practice, it's important to note that relying solely on estimated material properties for fatigue assessment may lead to non-conservative designs under specific circumstances.

2.6.1 Estimation of uniaxial Wöhler curves

Consider for example the Wöhler shown in the figure below which is believed to come from a nonferrous material without a defined fatigue limit, like aluminium alloys for example. In this case, an endurance limit is defined at a referenced number of cycles to failure N_A, and also a change in the fatigue properties at the knee point N_{kp}.

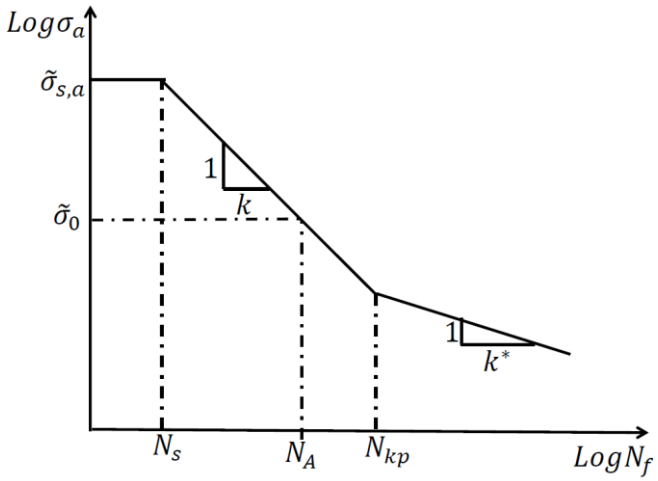

Figure 2-14 Uniaxial fatigue curve of non-ferrous material

This figure summarises constants like the inverse slope k before and k^*after the knee point and the referenced points which ought to be known to properly define uniaxial fatigue curves. The practical rules required to estimate the mentioned constants are then outlined, starting with the estimation of plain material fatigue properties and then addressing the detrimental effect of notches.

2.6.1.1 Fully reversed plain endurance limit

According to Ref [7] the plain endurance limits for $R = -1$ under bending is estimated as:

Steel.

$N_A = 10^6$ cycles to failure

$\sigma_A = 0.5\sigma_{UTS}$ for $\sigma_{UTS} < 1400$MPa

$\sigma_A = 700$MPa for $\sigma_{UTS} \geq 1400$MPa

Aluminium.

$N_A = 5 \times 10^8$ cycles to failure

$\sigma_A = 0.4\sigma_{UTS}$ for $\sigma_{UTS} < 336$MPa

$\sigma_A = 130$MPa for $\sigma_{UTS} \geq 336$MPa

Cast iron.

$N_A = 5 \times 10^7$ cycles to failure

$\sigma_A = 0.4\sigma_{UTS}$ for $\sigma_{UTS} < 336$MPa

There are other classical rules suitable for estimating the endurance limits of different engineering materials subjected to in-service bending loading. This is summarised in the Table 2-1below.

2.6.1.2 Correcting the endurance limit through the estimated values of the modifying factors

The response of engineering materials to fatigue is significantly influenced by various parameters, including the type of applied loading (C_L), surface treatments and roughness (C_S), size effect (C_D), and the statistical dispersion of fatigue failures (C_R). These factors must always be considered during the design process, as they can sometimes reduce the overall fatigue strength of the material used in the component being evaluated [1,2,7,14]. The influence of these factors is typically accounted for using specific indices, which are usually determined through experimental testing. However, if experimental values are unavailable, they can be estimated using practical rules. The corrected fully reversed plain endurance/fatigue limit $\bar{\sigma}_A$ is estimated using the corrected equation:

$$\bar{\sigma}_A = C_L . C_S . C_D . C_R . \sigma_A \quad (2\text{-}40)$$

Table 2-1 : Estimated fully reversed endurance limits under bending for different engineering materials [7]

Material	σ_A[MPa]	N_A [Cycles]	Observation
Steel – Ferrite	$0.58\sigma_{UTS}$	10^6	
Steel – Ferrite + Pearlite	$0.38\sigma_{UTS}$	10^6	
Steel – Pearlite	$0.38\sigma_{UTS}$	10^6	
Steel – Untempered martensite	$0.26\sigma_{UTS}$	10^6	
Steel – Highly tempered Martensite	$0.55\sigma_{UTS}$	10^6	
Steel – Highly Tempered Martensite + Tempered Bainite	$0.50\sigma_{UTS}$	10^6	
Steel – Tempered Bainite	$0.50\sigma_{UTS}$	10^6	
Steel – Austenite	$0.37\sigma_{UTS}$	10^6	
Wrought Steels	$0.50\sigma_{UTS}$	10^6	$\sigma_{UTS} <$ 1400MPa
Wrought Steels	700	10^6	$\sigma_{UTS} \geq$ 1400MPa
Cast iron	$0.40\sigma_{UTS}$	5×10^7	
Aluminium alloys	$0.40\sigma_{UTS}$	5×10^8	$\sigma_{UTS} <$ 336MPa
Aluminium alloys	130	5×10^8	$\sigma_{UTS} \geq$ 336MPa
PM cast aluminium	80	5×10^8	
Sand cast aluminium	55	5×10^8	

1) Load factor C_L

The load factor is used to consider how engineering materials respond to the applied time-dependent loading. For example, the endurance limit of a cylindrical bar under tension-compression loading is typically lower than that of the same shaft subjected to bending. This difference arises because in bending, a stress gradient exists due to the type of loading, resulting in a smaller portion of the material experiencing the highest stress level. In contrast, under axial loading, the entire section of the bar undergoes uniform cyclic stress significantly increasing the likelihood of fatigue crack initiation. In practical situations, the load factor is employed to adjust either the endurance or the fatigue limit and in the absence of experimental data, the following load factors are used.

Table 2-2 : Recommended values for load factor

Type of loading	C_L		
	From Bending	From Rotating bending	From Axial loading
Bending	1	1.25	1.4
Rotating bending	0.8	1	1.1
Axial Loading	0.7	0.9	1

2) Surface finishing factor (C_S)

2.6 Estimation of the fatigue properties of materials

In general, fatigue curves are established through testing laboratory samples that are polished to minimize the adverse impact of superficial scratches and roughness. These geometric irregularities lead to local stress concentration phenomena, which must be considered when designing real components for fatigue resistance. If the effect of surface finishing cannot be experimentally investigated, it is common practice to adjust the fatigue (or endurance) limit determined from polished samples using the surface finishing factor [79]. The most widely used formula in practical situations utilizes the material's ultimate tensile strength and is defined as:

$$C_S = a.\sigma^b{}_{UTS} \tag{2-41}$$

The constants a and b are summarised as:

Table 2-3 : Values of the constants in Noll and Lipson's relationship [80]

Surface finishing	a	b
Ground	1.58	-0.085
Machined	4.51	-0.265
Hot Rolled	57.5	-0.718
Forged	272	-0.995

3) Size factor C_D

a cylindrical bar subjected to cyclic bending has its fatigue damage diminished as the diameter of the bar decreases. This trend can be attributed to the larger portion of material experiencing the critical stress range as the diameter increases. When designing components to withstand fatigue, this phenomenon is typically considered by incorporating a size factor CD. If this factor cannot be determined through experimentation, empirical relationships using d as the diameter of the component being assessed can be employed as [7].

$$C_D = 1 \text{ for } d <\leq 8\text{mm}$$

$$C_D = 1.189d^{-0.097} \text{ for } 8mm < d < 250\text{mm} \tag{2-42}$$

Experimental studies indicate that when engineering materials undergo axial loading, the influence of size on fatigue damage is minimal. Therefore, in such scenarios, it is recommended to consider the size factor as consistently equal to unity [2,7].

Another crucial consideration involves assessing the size effect when the critical section of the component under evaluation is not circular. In these cases, an equivalent diameter can be approximated using the portion of the cross-sectional area where 95% of the maximum stress is experienced. Denoting this reference critical area as $A_{95\%}$, the equivalent diameter can be estimated as follows.

$$d_{eq} = \sqrt{\frac{A_{95\%}}{0.077}} \tag{2-43}$$

4) Reliability factor (C_R)

When the inherent scattering of physical data points in fatigue results cannot be addressed using suitable statistical methods the endurance or fatigue limits can be directly adjusted based on the values listed in Table 2-4.

Table 2-4 Reliability factor [2,7]

Reliability	C_R
0.5	1.000
0.9	0.897
0.95	0.868
0.99	0.814
0.999	0.753
0.9999	0.702
0.99999	0.659
0.999999	0.620

2.6.1.3 Estimating the endurance limit in the presence of superimposed static stresses

The presence of non-zero mean stresses has been observed to negatively impact the fatigue strength of engineering materials. Therefore, it is crucial to always consider the influence of superimposed static stresses. For fully reversed loading Marin's equation becomes,

$$\left(\frac{\tilde{\sigma}_A}{\bar{\sigma}_A}\right)^n + \left(f\frac{\sigma_m}{\sigma_{UTS}}\right)^m = 1 \tag{2-44}$$

Where $\bar{\sigma}_A$is the endurance limit or the fatigue limit for fully reversed loading and obtained by using the appropriate modifying factors shown in equation (2-40). Meanwhile, $\tilde{\sigma}_A$ is the endurance or fatigue limit in the presence of superimposed static stresses. The other variables f, m and n are as defined in section 2.5.2. if σ_m is the non-zero mean stress, the following approximations are made.

Soderberg n=1, m=1, $f = {\sigma_{UTS}}/{\sigma_Y}$

$$\frac{\tilde{\sigma}_A}{\bar{\sigma}_A} + \frac{\sigma_m}{\sigma_Y} = 1 \Longrightarrow \tilde{\sigma}_A = \bar{\sigma}_A\left(1 - \frac{\sigma_m}{\sigma_Y}\right) \quad (2\text{-}45)$$

Goodman's relationship, $n = 1, m = 1, f = 1$

$$\frac{\tilde{\sigma}_A}{\bar{\sigma}_A} + \frac{\sigma_m}{\sigma_{UTS}} = 1 \Longrightarrow \tilde{\sigma}_A = \bar{\sigma}_A\left(1 - \frac{\sigma_m}{\sigma_{UTS}}\right) \quad (2\text{-}46)$$

Gerber' parabola is obtained by setting $n = 1, m = 2, f = 1$

$$\frac{\tilde{\sigma}_A}{\bar{\sigma}_A} + \left(\frac{\sigma_m}{\sigma_{UTS}}\right)^2 = 1 \Longrightarrow \tilde{\sigma}_A = \bar{\sigma}_A\left[1 - \left(\frac{\sigma_m}{\sigma_{UTS}}\right)^2\right] \quad (2\text{-}47)$$

Dietman's parabola is obtained by setting $n = 2, m = 1, f = 1$

$$\left(\frac{\tilde{\sigma}_A}{\bar{\sigma}_A}\right)^2 + \frac{\sigma_m}{\sigma_{UTS}} = 1 \Longrightarrow \tilde{\sigma}_A = \bar{\sigma}_A\sqrt{1 - \frac{\sigma_m}{\sigma_{UTS}}} \quad (2\text{-}48)$$

Elliptical relation is obtained by setting $n = 2, m = 2, f = 1$

$$\left(\frac{\tilde{\sigma}_A}{\bar{\sigma}_A}\right)^2 + \left(\frac{\sigma_m}{\sigma_{UTS}}\right)^2 = 1 \Longrightarrow \tilde{\sigma}_A = \bar{\sigma}_A\sqrt{1 - \left(\frac{\sigma_m}{\sigma_{UTS}}\right)^2} \quad (2\text{-}49)$$

As seen previously, Goodman's criterion is widely favoured in practical applications because among the corrections using the ultimate tensile strength, it provides the highest safety margin. The safest adjustment is the Soderberg method, which incorporates the material yield stress as the second calibration parameter.

2.6.1.4 Estimation of plain uniaxial fatigue curve in the presence of superimposed static stresses

To estimate the plain uniaxial fatigue curve of engineering materials, two calibration points are typically required. Firstly, the endurance limit $\tilde{\sigma}_A$ after N_A cycles to failure, is always the initial calibration point. This limit is adjusted to account for modifying factors as well as non-zero mean stresses. Secondly, in the low-cycle fatigue regime, the second calibration point is set after N_S cycles to failure as in Figure 2-14. Typically, N_S is chosen to be equal to 10^3 cycles to failure [2,5,81]. The stress amplitude at N_S cycles to failure is estimated based on the material's ultimate tensile strength. However, this estimate needs to be adjusted to consider factors such as the load ratio (or mean stress value), the type of applied loading, and the desired reliability level. Specifically, for fully reversed loading conditions, the stress amplitude at this fatigue life can be approximated as [7],

$$\bar{\sigma}_{s,a} = C_R.0.9\sigma_{UTS} \text{ under fully reversed loading}$$
$$\bar{\sigma}_{s,a} = C_R.0.75\sigma_{UTS} \text{ under bending} \quad (2\text{-}50)$$

For a load ratio R larger than -1 in axial loading, this is accounted for by computing the corrected stress at N_S defined as

$$\tilde{\sigma}_{s,a} = \frac{1-R}{2}\bar{\sigma}_{s,a} \tag{2-51}$$

Meanwhile, if the mean stress is kept constant and equal to σ_m, the corrected stress level at N_S is estimated as:

$$\tilde{\sigma}_{s,a} = \bar{\sigma}_{s,a} - \sigma_m \tag{2-52}$$

The equations summarised in this section can be used independently from the material type [7]. Once the stresses at N_S and at N_A are established, the remaining factor is the value of the inverse slope (k) for the respective curve. This value of k can be derived from the two points $N_S \cong 10^3$ and N_A chosen at the referenced points according to the material and summarised in Table 2-1, is defined as:

$$k = \frac{log\left({}^{N_A}/_{N_S}\right)}{log\left({}^{\tilde{\sigma}_{s,a}}/_{\tilde{\sigma}_A}\right)} \tag{2-53}$$

Table 2-5 summarises some knee-point as well as the value of the inverse slope beyond the knee point of the Wohler curve for non-ferrous materials. In order to estimate these values, the simplest approach is to maintain the negative inverse slope constant and equal to k. This method offers the advantage of designing components with a higher level of conservatism, especially in cases of low-stress amplitude cycles. Alternatively, if this level of safety is deemed excessive, recommended values for both N_{kp} and k^* under constant amplitude, loading can be referenced as provided in Table 2-5.

Table 2-5 Recommended values for N_{kp} and k^* [82]

Material	N_{kp} [Cycles to Failure]	k^*
High strength steel	5×10^5	45
Structural steel	2×10^6	45
High strength cast steel	5×10^5	45
Medium strength cast steel	2×10^6	45
High strength sintered steel	5×10^5	45
Medium strength sintered steel	2×10^6	45
High strength cast nodular iron	5×10^5	45
Medium strength cast nodular iron	2×10^6	45
Wrought aluminium alloys	$1 \times 10^6 \div 5 \times 10^6$	22
Cast aluminium	$1 \times 10^6 \div 5 \times 10^6$	22
Sintered aluminium	1×10^6	22
Wrought magnesium alloys	$5 \times 10^4 \div 1 \times 10^5$	45
Cast magnesium	$1 \times 10^5 \div 5 \times 10^5$	22

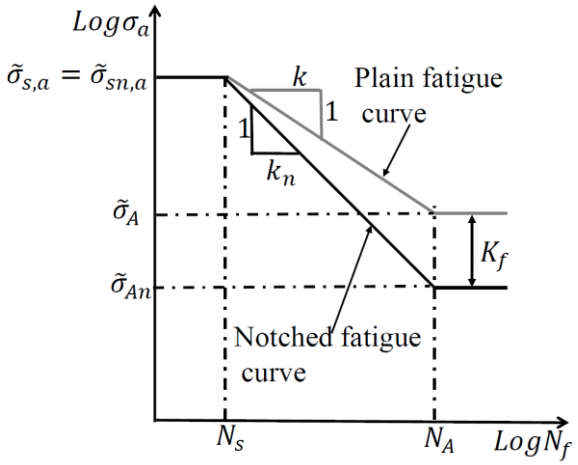

Figure 2-15 Fatigue strength reduction factor K_f

2.6.1.5 Estimation of Notch endurance limit in the presence of superimposed static stresses

The schematic Wöhler diagram in Figure 2-15 represents both a fatigue curve generated by testing unnotched samples (Plain Fatigue Curve) and another curve generated by testing specimens containing a known geometrical feature (Notch Fatigue Curve). The latter curve is plotted in terms of amplitudes of the nominal net stress. According to this diagram, the detrimental effect of a stress concentrator is quantified through the fatigue strength reduction factor K_f [68]. In this case the value of the notched endurance limit $\tilde{\sigma}_{An}$ is estimated as:

$$\tilde{\sigma}_{An} = \frac{\tilde{\sigma}_A}{K_f} \tag{2-54}$$

Where $\tilde{\sigma}_{An}$ is the corrected endurance limit of the notched curve. In practical situations, K_f is typically estimated using formulations in section 2.5.3.

2.6.1.6 Estimation of Notch uniaxial fatigue curve in the presence of superimposed static stresses

Once the notch endurance limit is determined, the corresponding notch uniaxial fatigue curve can be directly estimated, provided that both $\tilde{\sigma}_{sn,a}$ (the amplitude of the net stress at N_S to failure) and N_S are defined coherently. By assuming that $\tilde{\sigma}_{sn,a}$ and $\tilde{\sigma}_{s,a}$ are equal at N_S equal to a thousand cycles as shown in Figure 2-15, the inverse slope of the notch curve is estimated in the same way as in equation (2-52) as:

$$k_n = \frac{log\left({N_A}/{N_S}\right)}{log\left({\tilde{\sigma}_{s,a}}/{\tilde{\sigma}_{An}}\right)} \tag{2-55}$$

Another widely adopted approach in practical situations to estimate the negative inverse slope of the notch uniaxial fatigue curve is assuming $N_S = 1$ in the above equation [83]. In both situations, the reference cycles to failure N_A are chosen as recommended in Table 2-1. There are no universally accepted relationships for quantifying K_f at $N_S = 10^3$ cycles to failure in the literature, it is recommended to use the schematisation proposed by both approaches ($N_S = 10^3$ and $N_S = 1$) to design notched components against uniaxial fatigue. K_f at N_S has not been quantified [7,71].

2.7 Chapter summary and feedforward

Having reviewed the various ways in which continuum mechanics and linear elastic fracture mechanics approach fatigue failures due to different loading formats, these concepts can then be applied to study the fatigue properties of metals when exposed to quantified hydrogen. Hydrogen embrittlement is a well-known phenomenon that affects the mechanical properties of metals. This concept is the driving motive and the core of this PhD research. For completeness, the next chapter will review hydrogen embrittlement mechanisms in metals. It's important to emphasize that this project is not focused on researching hydrogen embrittlement mechanisms in metals, but rather intends to utilize the

impacts of hydrogen embrittlement to quantify the fatigue properties of the metals involved in this research.

2.8 References

[1] L. Susmel, Multiaxial Notch Fatigue, From nominal to local stress/strain quantities, Woodhead Publishing Limited and CRC Press LLC, Cambridge, 2009.

[2] Suresh S., Fatigue of Materials, Second, Cambridge University Press, New York, 2004.

[3] W.D. Pilkey, Peterson's Stress Concentration Factors, Second, John Wiley & Sons, Inc., New York, 1974.

[4] T. Dobson, N. Larrosa, H. Coules, The role of corrosion pit topography on stress concentration, Eng. Fail. Anal. 157 (2024) 107900. https://doi.org/10.1016/j.engfailanal.2023.107900.

[5] T.. Anderson, Fracture Mechanics, Fundamentals and Applications, Third, Taylor & Francis Group, CRC Press, New York, 2005.

[6] W.D. Pilkey, D.F. Pilkey, Frontmatter, in: Peterson's Stress Conc. Factors, Wiley, 2007. https://doi.org/10.1002/9780470211106.fmatter.

[7] Y.-L. Lee, J. Pan, R.B. Hathaway, M.E. Barkey, Fatigue testing and analysis : theory and practice, Elsevier Butterworth-Heinemann., Amsterdam ; Boston: , 2005.

[8] A.I. Gorunov, O.V. Kudimov, A.K. Gilmutdinov, Effect of stress concentrators on fracture resistance of specimens fabricated by direct metal laser sintering, Eng. Fail. Anal. 131 (2022) 105900. https://doi.org/10.1016/j.engfailanal.2021.105900.

[9] N.O. Larrosa, A dislocation based method using generative algorithms to model notch geometries: Determination of Mode I SIFs, Eng. Fract. Mech. 127 (2014) 327–335. https://doi.org/10.1016/j.engfracmech.2014.06.001.

[10] J. SCHIJVE, STRESS GRADIENTS AROUND NOTCHES, Fatigue Fract. Eng. Mater. Struct. 3 (1980) 325–338. https://doi.org/10.1111/j.1460-2695.1980.tb01382.x.

[11] J. Schijve, Fatigue of Structures and Materials, , second, Springer, Netherlands, 2009.

[12] J. Schijve, Stress Concentration at Notches, in: Fatigue Struct. Mater., Kluwer Academic Publishers, Dordrecht, 2001: pp. 45–70. https://doi.org/10.1007/0-306-48396-3_3.

[13] Metals Society, Metals Science Committee and Institute of Physics (1986); Fracture at stress concentrators : proceedings of the 1984 International Conference Mechanics and Physics of Fracture III, Institute of Metals, London, 1986.

[14] F. Campbell, Fatigue and Fracture, Understanding The Basics, ASM International, Materials Park, Ohio, 2012.

[15] N.O. Larrosa, M. Treifi, R.A. Ainsworth, Rapid parametric analysis of SEN(T) specimens using algorithmic modelling: Evaluation of strain energy density and notch stress intensity factors, Mater. Des. 85 (2015) 771–777. https://doi.org/10.1016/j.matdes.2015.06.151.

[16] J.S. Kim, N.O. Larrosa, A.J. Horn, Y.J. Kim, R.A. Ainsworth, Notch bluntness effects on fracture toughness of a modified S690 steel at 150 °C, Eng. Fract. Mech. 188 (2018) 250–267. https://doi.org/10.1016/j.engfracmech.2017.05.047.

[17] H. Ghadbeigi, C. Pinna, S. Celotto, Failure mechanisms in DP600 steel: Initiation, evolution and fracture, Mater. Sci. Eng. A. 588 (2013) 420–431. https://doi.org/10.1016/j.msea.2013.09.048.

[18] R.I. Stephens, A. Fatemi, R.R. Stephens, H.O. Fuchs, Metal Fatigue In Engineering, Second, John Wiley & Sons, INC, New York, 2001.

[19] P. Efthymiadis, R. Dashwood, B. Shollock, L. Curry, H. Ghadbeigi, A. Barrow, D. Robertson, Multiscale characterisation of the mechanical properties of austenitic stainless steel joints, Mater. Sci. Eng. A. 676 (2016) 324–335. https://doi.org/10.1016/j.msea.2016.08.020.

[20] E.P. Busso, From Single Crystal to Polycrystal Plasticity: Overview of Main Approaches, in: Handb. Damage Mech., Springer International Publishing, Cham, 2022: pp. 1251–1276. https://doi.org/10.1007/978-3-030-60242-0_7.

[21] TLP Library, Polycrystals: Dissemination of IT for the Promotion of Materials Science (DoITPoMS), Department of Materials Science & Metallurgy, Univ. Cambridge. (2024).

[22] F. Weinberg, Grain boundaries in metals, Prog. Met. Phys. 8 (1959) 105–146. https://doi.org/10.1016/0502-8205(59)90014-0.

[23] H. Zheng, X.-G. Li, R. Tran, C. Chen, M. Horton, D. Winston, K.A. Persson, S.P. Ong, Grain boundary properties of elemental metals, Acta Mater. 186 (2020) 40–49. https://doi.org/10.1016/j.actamat.2019.12.030.

[24] P.J.. Forsyth, A two-stage fracture mechanism, in: Proc. Crack Propag. Symp., Royal Aircraft Establishment, Cranfield, UK, 1961: pp. 76–94.

[25] F. Ellyin, Fatigue Damage, Crack Growth and Life Prediction, First Edition, Springer Netherlands, Dordrecht, 1997. https://doi.org/10.1007/978-94-009-1509-1.

[26] B. Tomkins, Fatigue crack propagation—an analysis, Philos. Mag. 18 (1968) 1041–1066. https://doi.org/10.1080/14786436808227524.

[27] K.J. Miller, THE TWO THRESHOLDS OF FATIGUE BEHAVIOUR, Fatigue Fract. Eng. Mater. Struct. 16 (1993) 931–939. https://doi.org/10.1111/j.1460-2695.1993.tb00129.x.

[28] G. Meneghetti, L. Susmel, R. Tovo, High-cycle fatigue crack paths in specimens having different stress concentration features, Eng. Fail. Anal. 14 (2007) 656–672. https://doi.org/10.1016/j.engfailanal.2006.02.004.

[29] J. Ban, X. Yan, B. Song, S. Deng, H. Wu, Y. Tang, W. Yin, Research Progress and Prospects on Hydrogen Damage in Welds of Hydrogen-Blended Natural Gas

Pipelines, Processes. 11 (2023). https://doi.org/10.3390/pr11113180.

[30] G. Huang, J. Zheng, B. Meng, Z. Hua, Q. Lu, X. Li, P. Xu, Mechanical Properties of X70 Welded Joint in High-Pressure Natural Gas/Hydrogen Mixtures, J. Mater. Eng. Perform. 29 (2020) 1589–1599. https://doi.org/10.1007/s11665-020-04680-6.

[31] TWI, What is Pipe Welding? (Everything You Need To Know), Tech. Knowl. (2024). https://www.twi-global.com/technical-knowledge/faqs/what-is-pipe-welding#TypesOfWeldingUsed (accessed October 8, 2024).

[32] AMI, Natural Gas Pipeline Welding Procedures for Orbital Systems, Eng. Dep. Arc Mach. Inc. (2023).

[33] J. Ya'u Muhammad, H.A. Usman, Mechanical Characterization of Duplex Stainless Steel Joined by Gas Tungsten-arc Welding (GTAW) and Shielded Metal-arc Welding (SMAW): A Comparative Study, 2023. https://www.researchgate.net/publication/371120954.

[34] W. Dan, C. Tang, H. Shi, X. Wang, Study on Mechanical Behaviours and Microstructure Features of Q690 Steel Weldments with Various Electrochemical Hydrogen Charging Conditions, (2024) 1–21.

[35] A. Mason, TIG Welding (GTAW) In Oil And Gas Industry, WeLDingpros.Net. (2023). https://weldingpros.net/tig-welding-gtaw-in-oil-and-gas-industry/#:~:text=Tungsten Inert Gas welding%2C also known as Gas,to shield the weld pool from atmospheric contamination. (accessed November 14, 2024).

[36] S. Das, J. Vora, V. Patel, S. Bogum, Experience with advanced welding techniques (RMD & P-GMAW) with seamless metal cored wire for Oil & Gas pipeline industries, J. Phys. Conf. Ser. 1950 (2021). https://doi.org/10.1088/1742-6596/1950/1/012043.

[37] A. Moarrefzadeh, Study of heat affected zone (HAZ) in Gas Metal Arc Welding (GMAW/MIG) process, Appl. Mech. Mater. 110–116 (2012) 3448–3452. https://doi.org/10.4028/www.scientific.net/AMM.110-116.3448.

[38] S. Liu, S. Zhao, Z. Wu, Z. Wei, G. Hu, Study of microstructure and mechanical properties of SA553/SA537 steels joints using multi-pass welding for pressure vessels application, Int. J. Press. Vessel. Pip. 209 (2024) 105186. https://doi.org/10.1016/j.ijpvp.2024.105186.

[39] B.E. Kim, J.Y. Park, J.S. Lee, J.I. Lee, M.H. Kim, Effects of the Welding Process and Consumables on the Fracture Behavior of 9 Wt.% Nickel Steel, Exp. Tech. 44 (2020) 175–186. https://doi.org/10.1007/s40799-019-00321-3.

[40] L. Sharma, R. Chhibber, Effect of Physico-Chemical Properties of Submerged Arc Welding Fluxes on Pipeline Steel - a Brief Review, Arch. Metall. Mater. 68 (2023) 409–421. https://doi.org/10.24425/amm.2023.142417.

[41] ASTM E08, Standard Terminology Relating to Fatigue and Fracture Testing, ASTM. (2023).

[42] A. Fajri, A.R. Prabowo, N. Muhayat, D.F. Smaradhana, A. Bahatmaka, Fatigue analysis of engineering structures: State of development and achievement, Procedia Struct. Integr. 33 (2021) 19–26. https://doi.org/10.1016/j.prostr.2021.10.004.

[43] M. Makkonen, Predicting the total fatigue life in metals, Int. J. Fatigue. 31 (2009) 1163–1175. https://doi.org/10.1016/j.ijfatigue.2008.12.008.

[44] E. Santecchia, A.M.S. Hamouda, F. Musharavati, E. Zalnezhad, M. Cabibbo, M. El Mehtedi, S. Spigarelli, A Review on Fatigue Life Prediction Methods for Metals, Adv. Mater. Sci. Eng. 2016 (2016). https://doi.org/10.1155/2016/9573524.

[45] U. Zerbst, M. Madia, C. Klinger, D. Bettge, Y. Murakami, Defects as a root cause of fatigue failure of metallic components. II: Non-metallic inclusions, Eng. Fail. Anal. 98 (2019) 228–239. https://doi.org/10.1016/j.engfailanal.2019.01.054.

[46] D. Krewerth, T. Lippmann, A. Weidner, H. Biermann, Influence of non-metallic inclusions on fatigue life in the very high cycle fatigue regime, Int. J. Fatigue. 84 (2016) 40–52. https://doi.org/10.1016/j.ijfatigue.2015.11.001.

[47] L. Zhang, B. Jiang, P. Zhang, H. Yan, X. Xu, R. Liu, J. Tang, C. Ren, Methods for fatigue-life estimation: A review of the current status and future trends, Nanotechnol. Precis. Eng. 6 (2023) 025001. https://doi.org/10.1063/10.0017255.

[48] H. Ye, F. Le, C. Wei, K. Ye, S. Liu, G. Wang, Fatigue crack growth behavior of Ti-6Al-4V alloy fabricated via laser metal deposition: Effects of building orientation and heat treatment, J. Alloys Compd. 868 (2021). https://doi.org/10.1016/j.jallcom.2021.159023.

[49] J. Diller, J. Blankenhagen, D. Siebert, C. Radlbeck, M. Mensinger, Combined effect of surface treatment and heat treatment on the fatigue properties of AISI 316L, manufactured by powder bed fusion of metals using a laser (PBF-LB/M), Int. J. Fatigue. 178 (2024) 108025. https://doi.org/10.1016/j.ijfatigue.2023.108025.

[50] M. V. Maisuradze, E. V. Antakov, Analysis of Fatigue Failure Causes of Machine Components, Steel Transl. 51 (2021) 745–751. https://doi.org/10.3103/S0967091221100089.

[51] H.M. Rafsanjani, J.D. Sørensen, Effect of defects distribution on fatigue life of wind turbine components, in: Procedia IUTAM, Elsevier B.V., 2015: pp. 144–150. https://doi.org/10.1016/j.piutam.2015.01.014.

[52] M. Vankeerberghen, M. De Smet, C. Malekian, Gauge-strain-controlled air and pwr fatigue life data for 304 stainless steel—some effects of surface finish and hold time, Metals (Basel). 10 (2020) 1–15. https://doi.org/10.3390/met10091248.

[53] G. Liu, C. Huang, B. Zhao, W. Wang, S. Sun, Effect of Machined Surface Integrity on Fatigue Performance of Metal Workpiece: A Review, Chinese J. Mech. Eng. 34 (2021) 118. https://doi.org/10.1186/s10033-021-00631-x.

[54] M.. Nascimento, R.. Souza, W.L. Pigatin, Voorwald H.C, Effects of surface treatments on the fatigue strength of AISI 4340 aeronautical steel, Int. J. Fatigue. 23 (2001) 607–618.

[55] M. Azadi, M.M. Shirazabad, Heat treatment effect on thermo-mechanical fatigue and low cycle fatigue behaviors of A356.0 aluminum alloy, Mater. Des. 45 (2013) 279–285. https://doi.org/10.1016/j.matdes.2012.08.066.

[56] H.M. Mahendra, G.S. Prakash, K.S. Keerthi Prasad, S. Rajanna, Fatigue and Facture Behaviour of Al6061-Al $_2$ O $_3$ Metal Matrix Composite: Effect of Heat Treatment, IOP Conf. Ser. Mater. Sci. Eng. 925 (2020) 012042.

https://doi.org/10.1088/1757-899X/925/1/012042.

[57] J. Walker, D.J. Thomas, Y. Gao, Effects of shot peening and pre-strain on the fatigue life of dual phase Martensitic and Bainitic steels, J. Manuf. Process. 26 (2017) 419–424. https://doi.org/10.1016/j.jmapro.2017.03.010.

[58] T. Gurova';, J.R. Teodhio', ; Jo20, M.A. Rebello';, V. Monin, STUDY OF THE RESIDUAL STRESS STATE DURING PLASTIC DEFORMATION UNDER UNIAXIAL TENSION IN A 5.OCr AND OSMo STEEL, 1997.

[59] A. Veiga, C. Luno-Bilbao, S. Sainz, F. Castro, Effect of low-pressure carburizing and plasma nitriding on mechanical properties and fatigue endurance limits of low alloy sintered steels, Powder Metall. 63 (2020) 75–79. https://doi.org/10.1080/00325899.2020.1758883.

[60] T. Morita, K. Inoue, X. Ding, Y. Usui, M. Ikenaga, Effect of hybrid surface treatment composed of nitriding and DLC coating on friction-wear properties and fatigue strength of alloy steel, Mater. Sci. Eng. A. 661 (2016) 105–114. https://doi.org/10.1016/j.msea.2016.03.015.

[61] S. Cicero, M. Bruchhausen, Environmental Fatigue Assessment of Metallic Materials and Components, Metals (Basel). 11 (2021) 1565. https://doi.org/10.3390/met11101565.

[62] S. Cicero, T. Metais, Y. Voloshyna, S. Cuvillez, S. Arrieta, R. Cicero, Environmental Fatigue Analysis of Nuclear Structural Components: Assessment Procedures, Loads, and a Case Study, Metals (Basel). 10 (2020) 609. https://doi.org/10.3390/met10050609.

[63] J. Pelleg, The Effect of Environment, in: Cycl. Deform. Oxides, Carbides Nitrides, Struct. Integr. , Springer, Cham, 2022: pp. 387–429. https://doi.org/10.1007/978-3-030-86118-6_12.

[64] T. Asayama, K. Aoto, Y. Wada, Effect of nonproportional loading on creep-fatigue properties of 304 stainless steel at low strain ranges near the elastic region, 1993.

[65] W. Li, T. Sakai, Q. Li, L.T. Lu, P. Wang, Effect of loading type on fatigue properties of high strength bearing steel in very high cycle regime, Mater. Sci. Eng. A. 528 (2011) 5044–5052. https://doi.org/10.1016/j.msea.2011.03.020.

[66] L. Pallarés-Santasmartas, J. Albizuri, A. Avilés, R. Avilés, Mean Stress Effect on the Axial Fatigue Strength of DIN 34CrNiMo6 Quenched and Tempered Steel, Metals (Basel). 8 (2018) 213. https://doi.org/10.3390/met8040213.

[67] L. Susmel, On the estimation of the material fatigue properties required to perform the multiaxial fatigue assessment, Fatigue Fract. Eng. Mater. Struct. 36 (2013) 565–585. https://doi.org/10.1111/ffe.12035.

[68] R.. Peterson, Notch Sensitivity In Metal Fatigue, McGraw Hill, Ney York, 1959.

[69] P. Kuhn, H.F.H. Langley, A. Laboratwy, L. Field, V. Washington, P.F. Hardrath, National Advisory Committee For Aeronautics Technical Note 2805, 1952.

[70] M.D. Chapetti, A.O. Guerrero, Estimation of notch sensitivity and size effect on fatigue resistance, in: Procedia Eng., Elsevier Ltd, 2013: pp. 323–333. https://doi.org/10.1016/j.proeng.2013.12.087.

[71] R.. Heywood, Designing Against Fatigue, Chapman and Hall, London, 1962.

[72] E. Kufoin, L. Susmel, Quantitative review of probabilistic approaches to fatigue design in the medium cycle fatigue regime, Probabilistic Eng. Mech. 75 (2024) 103–589. https://doi.org/10.1016/j.probengmech.2024.103589.

[73] C. Johnston, STATISTICAL ANALYSIS OF FATIGUE TEST DATA, Trondheim, Norway, 2017.

[74] R.C. Rice, B.C. Laboratories, Fatigue Data Analysis, ASM Handb. Comm. (2015).

[75] M.A. Miner, Cumulative Damage in Fatigue, J. Appl. Mech. 12 (1945) A159–A164. https://doi.org/10.1115/1.4009458.

[76] G. Ayoub, M. Naït-abdelaziz, F. Zaïri, J.M. Gloaguen, Multiaxial fatigue life prediction of rubber-like materials using the continuum damage mechanics approach, Procedia Eng. 2 (2010) 985–993. https://doi.org/10.1016/j.proeng.2010.03.107.

[77] Z. Barsoum, Guideline For Fatigue and Static Analysis of Welded and Un-welded Steel Structures, 2020.

[78] A. Hobbacher, Recommendations For Fatigue Design of Welded Joints and Components, France, 2008.

[79] F. Curà, R. Sesana, Surface factor assessment in HCF for steels by means of empirical and non destructive techniques, in: Procedia Struct. Integr., Elsevier B.V., 2017: pp. 500–507. https://doi.org/10.1016/j.prostr.2017.07.151.

[80] C.. Noll, C. Lipson, Allowable Working Stresses. Society for Experimental Stress Analysis, 3 (1946) 29.

[81] R.C. Juvinall, K.M. Marshek, Fundamentals of Machine Component Design, Fifth, JOHN WILEY & SONS, INC., 2006. http://www.wiley.com/college/juvinall.

[82] C.M. Sonsino, Course of SN-curves especially in the high-cycle fatigue regime with regard to component design and safety, Int. J. Fatigue. 29 (2007) 2246–2258. https://doi.org/10.1016/j.ijfatigue.2006.11.015.

[83] J.A. Collins, Failure of Materials in Mechanical Design. Analysis, Predistion, Prevention, Second, John Wiley & Sons, Inc, Canada, 1993.

2.8 References

Chapter 3

Introduction to Hydrogen Embrittlement

3.1 Chapter Introduction

This chapter concisely reviews the hydrogen embrittlement (HE) phenomenon, forming the foundation for subsequent discussions. Although HE is not the primary focus of this study, understanding it is crucial, as it serves as the motivation for the research conducted in this PhD project. The review explores existing literature, examines the mechanisms by which hydrogen permeates metals, and explains its destructive effects on the mechanical properties of materials. Particular attention is given to the HE effects on X52 carbon welded and unwelded steel, grey cast iron and brass pipeline materials used in this research. A detailed analysis of the mechanics behind HE, in general, is provided, including mechanisms such as hydride formation, hydrogen-induced phase transformation (HIPT), hydrogen-enhanced decohesion (HEDE), hydrogen-enhanced localised plasticity (HELP), hydrogen-enhanced strain-induced vacancy mechanism (HESIV), adsorption-induced dislocation emission (AIDE), and the hydrogen pressure theory. Additionally, the impacts of the various hydrogen-related factors on HE, such as temperature, pressure, charging time, and the microstructural characteristics of these materials, are discussed. Specifically,

the analysis determines whether a hydrogen pressure of 8 bars is capable of causing significant degradation in the mechanical properties of these pipeline materials.

Thus, this comprehensive overview sets the stage for the exploration of the mechanical properties of metals subjected to HE, thereby providing robust answers to the research question and meeting the overall objective of this PhD study.

3.2 Introduction to Hydrogen Embrittlement

Hydrogen is the lightest element and can dissolve in most metals and alloys [1,2] and its interactions with the crystal lattice are a significant concern for most engineering metals. These interactions lead to metal degradation observed in reduced fracture toughness, fatigue resistance and ductility [3]. The mechanical degradation of structural materials due to hydrogen is a significant issue and has led to numerous accidents during production, storage, transportation, and use. These problems manifest in various ways, such as stress corrosion cracking, hydrogen-induced cracking, hydride cracking, and other harmful effects, often resulting in catastrophic fractures [4,5]. Hydrogen-induced degradation and the range of phenomena associated with its harmful effects are collectively known as hydrogen embrittlement (HE), which involves a hydrogen-induced transition from ductile to brittle behaviour. HE is therefore a complex phenomenon that occurs across various length and time scales, affecting a wide range of metals. It can greatly reduce ductility and load-bearing capacity [6], leading to cracking and catastrophic brittle failures at stress levels below the yield stress of susceptible materials [4]. Therefore, HE is one of the major challenges in developing hydrogen energy infrastructure, particularly in the repurposing of natural gas pipelines [7].

HE is a phenomenon whereby hydrogen atoms penetrate the lattice structure of metals, leading to a reduction in their mechanical properties (brittle) and increased susceptibility to fracture [5,8]. The degree of embrittlement is influenced both by the amount of hydrogen absorbed and the microstructure of the material as well as the environment (hydrogen pressure and temperature). Microstructures which present high strength with a distribution of grain boundary particles or inclusions can result in increased susceptibility to embrittlement [9].

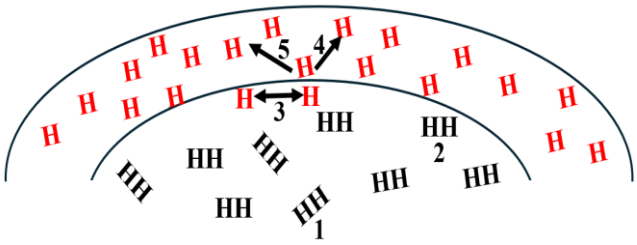

1 Diatomic hydrogen gas HH
2 Diatomic hydrogen undergoes adsorption at the metal surface
3 Diatomic hydrogen dissociates to monatomic hydrogen (H)
4 Monatomic hydrogen (H) absorbs into the metal
5 Monatomic hydrogen (H) diffuses through interstitial spacings in the metal

Figure 3-1 Interaction of hydrogen with metal surface

Due to the complexity of HE, it is essential to understand the interactions of hydrogen on the metal surface, how it enters the metal, its transport through the crystal lattice, and its interactions with crystal defects [10]. Most importantly, understanding its effect on the modification of material properties is crucial. Figure 3-2 shows a schematic view of the ingress of hydrogen as it comes in contact with a metal. When hydrogen comes in contact with a metal surface, Hydrogen molecules (H_2) initially adsorb onto the metal surface. For many metals, this involves the hydrogen molecules dissociating into individual hydrogen atoms facilitated by the metal's catalytic properties [11] as shown in Figure 3-1. At certain elevated temperatures and pressures, atomic hydrogen can easily penetrate metal surfaces and react internally with specific elements, compounds, or the metal matrix, leading to the formation of metallic compounds like metal hydrides, even at relatively low temperatures [12]. A typical reaction involves hydrogen and iron carbides, resulting in the production of methane, as shown in the following equation:

$$4H + Fe_3C = CH_4 + 3Fe \quad (3\text{-}1)$$

Once dissociated, hydrogen atoms can diffuse into the metal's crystal lattice due to its small size and this diffusion by tunnelling [13,14], a situation where hydrogen atoms penetrate a potential barrier (grain boundary) higher than the kinetic energy itself and are influenced by the metal's structure and temperature [15]. This is followed by interactions with the crystal lattice which are dominant in determining the properties of the metal.

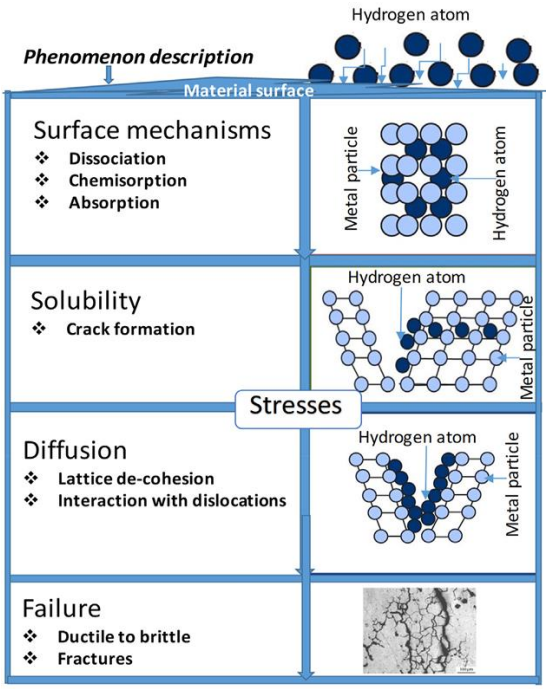

Figure 3-2 Schematic diagram of hydrogen embrittlement mechanism

Hydrogen atoms that move around in the crystal lattice are referred to as diffusible hydrogen, and trapped hydrogen is non-diffusible and resides around various crystal imperfections. In steel pipelines in particular, hydrogen atoms diffuse through interstitial sites, with octahedral sites being preferentially occupied at high temperatures and tetrahedral sites at low temperatures [16]. These imperfections serve as traps for hydrogen atoms, which include vacancies, dislocations, grain boundaries, solutes, precipitates, inclusions, and interfaces as shown in Figure 3-3 [17–19]. At these imperfections, these atoms can either be strongly trapped and irreversible which will not be released during service or weakly trapped hydrogen residing in reversible or shallow traps which can be released during service [4]. As hydrogen diffuses into voids and microcracks pressure is built up on these points. Also, the influence of a stress gradient occurs as more hydrogen diffuses where the hydrogen interacts with the metal lattice to reduce its cohesive strength. The hydrogen decreases the surface energy at the tip of any crack subjected to tensile stresses thereby reducing its fracture strength.

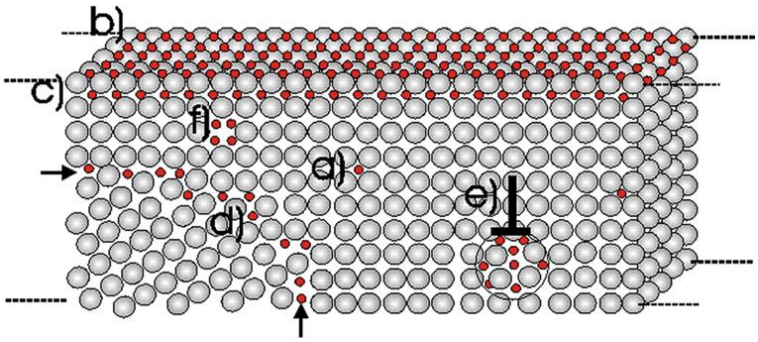

Figure 3-3 Diagram illustrating hydrogen trapping at different sites within pipeline steel: a) interstitial sites, b) surface traps c)subsurface traps d)grain boundary traps, e)dislocation traps, f) vacancy traps [7,18].

Hydrogen environment embrittlement occurs when materials are exposed to a hydrogen atmosphere, particularly affecting those with low hydrogen solubility like metals with body-centred cubic (bcc) and hexagonal close-packed lattice structures [12,20]. It is most severe at 20°C, low strain rates, and under high hydrogen purity and pressure [21]. Hydrogen stress cracking or internal embrittlement which occurs as a result of the unintentional introduction of hydrogen into susceptible metals during forming or finishing operations, affects ductile steels containing mobile hydrogen under sustained loads between a specific threshold and yield strength, leading to brittle fractures [12]. As material strength increases, the threshold stress decreases, resulting in reduced elongation and area in tensile tests for steels [5,20,22].

HE manifests in two distinct forms. Firstly, subcritical crack growth occurs when stress exceeds a threshold level below the material's yield stress [5,6]. At this critical stress juncture, hydrogen becomes highly concentrated at the crack tip, leading to the absorption of hydrogen atoms and initiating embrittlement within the material. Secondly, fracture initiation arises at stress levels lying between the yield stress and the UTS [23]. Fracture initiation mechanisms may involve micro-void coalescence, akin to fractures occurring in air, or a more brittle fracture mode originating from the surface. Upon reaching a critical crack length, as determined by Griffith's equation, fracture develops. Understanding these categorizations is vital for comprehending the complexities of hydrogen embrittlement and its implications for material integrity and safety.

In general, the factors affecting embrittlement are the local stress and plastic strain, the strength of the microstructural interfaces such as the grain boundaries [24,25] and the environment [6]. High-strength steels are generally more susceptible to hydrogen

embrittlement due to their increased strength when they are exposed to hydrogen-containing environments, such as during electroplating, corrosion, or exposure to hydrogen gas [26,27]. This occurs because the γ-austenite phase undergoes a transformation to BCC α'-martensite under deformation, a process known as strain-induced martensite. The α'-martensite phase has higher diffusivity than the γ-austenite phase [28], creating a rapid pathway for hydrogen to reach grain boundaries and localized stress areas, such as microcracks, where it can facilitate embrittlement [4,29–31]. Because of the small size of hydrogen atoms, they permeate steels in atomic form, and this can significantly compromise the structural integrity of the metal, leading to catastrophic failures, particularly in critical applications such as aerospace, automotive, and oil and gas industries. Moreover, the concentration of hydrogen within the metal lattice or at grain boundaries affects susceptibility, as higher concentrations lead to increased pressure and a higher likelihood of embrittlement cracking.

Hydrogen migration in metals can be categorized into reversible and irreversible forms [25]. In reversible HE, hydrogen atoms migrate and gather at potential crack initiation sites, resulting in delayed fracture of the alloys. Conversely, irreversible HE involves hydrogen atoms combining to form molecules at defect sites, creating high-pressure hydrogen gas and inducing cracking. While reversible HE can be mitigated through hydrogen removal treatments, irreversible HE persists even after such treatments.

3.2.1 Recall of experimental methods and hydrogen kinetic models used to measure the entry and exit of hydrogen in metals

Absorption of hydrogen in pure iron exceeds the solubility limit due to trapping at defects. To evaluate the quantity of hydrogen within a metal, and the effects of trapping sites, several methods have been developed such as linearly increasing stress test techniques (LIST), constant extension rate test (CERT), slow strain rate testing (SSRT) [5], Electrochemical impedance spectroscopy (EIS). The most commonly used methods include the thermal desorption analysis (TDA) where the hydrogen desorption rate is measured as a function of temperature [4]. The binding energies of traps and their corresponding specific hydrogen capacities are quantified from measured results. These results can be analysed using several methods like the reaction kinetics model, McNabb–Foster trapping–de-trapping model and hydrogen local equilibrium model [4]. These TDA approaches will not be used in this research and hence will not be discussed beyond this section.

Another technique used to experimentally determine the trap behaviour of hydrogen is the measurement of permeability rate through a metallic membrane [4,5]. To achieve this, a Devanathan–Stachurski (DS) cell is used [32]. The DS cell is a system consisting of two separate electrolytic cells, divided by the sample under investigation. In the cathodic compartment, hydrogen is produced electrochemically and absorbed at the surface of the sample before diffusing through its bulk. Once the hydrogen diffuses through the sample, it is oxidized at a constant potential in the anodic compartment, where the anodic current is continuously measured. The amount of hydrogen that diffuses through the sample is directly proportional to the measured oxidation current. Because currents can be measured with high accuracy, the DS method is a highly sensitive and precise technique for determining hydrogen flux over time. To ensure the reliability of this method, the conditions at each membrane surface within each compartment must be well defined, with impurities and surface effects minimized to focus on bulk diffusion. This can be quite a challenge when comparing with various metals as is the case in this research.

Scanning Electron Microscopy (SEM) and Transmission Electron Microscopy (TEM) are widely used analytical techniques for examining the internal microstructure of materials, as well as assessing the impact of hydrogen on microstructure and material characterization. SEM is particularly user-friendly, and versatile, and is often the preferred method [5]. The electron beam is concentrated, shaped, and narrowed into a fine spot on the specimen. Real-time observation and image capturing of the specimen surface are facilitated by the specimen stage, electron beam scanning coils, and signal detection and processing equipment. Meanwhile, TEM is also an approach that has been used to detect hydrogen atoms in metals only in very specific situations [33], such as at the macroscopic level for hydrides [34] and also at the atomic scale for hydrides [35].

3.2.2 Advances in experimental techniques used to detect hydrogen atoms in metals

Xray and electron diffraction are the two common techniques which are arguably the standard materials analysis methods, but they do not interact appreciably with hydrogen [4]. This lack of interaction is due to the combination of the hydrogen's low electron and x-ray cross-section, which originates due to the small electron cloud [33]. In steels, in particular, this is further complicated by the low solubility of hydrogen, which under normal conditions may be on the order of ppm. An alternative approach to this is the use of neutron scattering [4]. A hydrogen nucleus will scatter more strongly in steel than in

iron[36,37]. However, this technique requires access to costly neutron sources, which are generally not available. Additionally, as a diffraction method, it involves a beam that is challenging to control due to its inherently lower interaction compared to x-rays or electron sources. As a result, this method will not be utilized in this research; however, it provides valuable insights into alternative approaches that could be considered.

As described above, TEM is not the most effective method for detecting low hydrogen concentrations in bulk materials or hydrogen isolated to complex features like dislocations. However, evidence of hydrogen interaction with dislocations has been observed using TEM when samples are exposed to hydrogen in a specialized environmental cell. This exposure causes otherwise stationary dislocations to move, and they stop moving when the hydrogen is removed. This effect demonstrates that even at low hydrogen concentrations, the energy barriers to dislocation motion can be lowered [4,38].

Another microscopic imaging method is an indirect technique called microprinting [4]. In this approach, hydrogen is diffused through the material and made to interact with a chemical species like silver, forming silver crystals in areas where hydrogen is present. These images often reveal silver formation at grain boundaries or around inclusions, suggesting that hydrogen preferentially diffuses at or near these microstructural features. This observation indicates that hydrogen may enter the material at higher rates than bulk diffusion analyses would suggest.

3.3 Sources of hydrogen involved in hydrogen embrittlement

Sources of hydrogen contributing to embrittlement are encountered throughout various stages, including production, part processing, welding, hydrogen gas storage or containment, and environmental contamination. Hydrogen can also be generated through corrosion reactions such as rusting, cathodic protection, and electroplating. Additionally, hydrogen may be intentionally introduced into systems like blending natural gas with hydrogen and introduced into reactor coolant systems to eliminate oxygen. The entry of hydrogen, a necessary condition for embrittlement, can occur through several pathways, as outlined below. There are three typical sources of hydrogen embrittlement and hydrogen damage [39,40]: i) internal (residual) hydrogen from the manufacturing process, (ii) hydrogen from internal/external reactions and (iii) external hydrogen which enters into metal from the environment. Therefore, hydrogen embrittlement phenomena can be divided

into two categories depending on the source of the offending hydrogen supplied: internal HE (IHE) and external-environmental HE (EHE)

3.3.1 Internal hydrogenation through the manufacturing process

Hydrogen entering metals often occurs during various manufacturing, processing, and thermal procedures, such as welding, casting, surface chemical cleaning, electroplating, electrochemical machining, and heat treatment (HT). When hydrogen enters metal during manufacturing and processing, it is referred to as "internal" hydrogen [40,41]. To mitigate this risk, a final baking heat treatment is often employed to expel any hydrogen absorbed during these processes [42].

3.3.2 Hydrogen from internal/external reactions

Internal hydrogen can be generated and readily enter metal in atomic form due to various external electrochemical corrosion reactions on the metal surface during its manufacturing and processing, which produce hydrogen as a byproduct. This atomic hydrogen is referred to as internal/external "cathodic" hydrogen. Conversely, hydrogen in molecular form in contact with the metal surface cannot penetrate the metal [40,43]. Also, in circumstances where corrosion reactions occur, hydrogen can be produced as a by-product. For instance, when the hydrogen production reaction acts as the cathodic reaction, some of the hydrogen generated may enter the metal in atomic form rather than being completely evolved as a gas into the surrounding environment [41–43]. In such situations, cracking failures are often similar to stress corrosion cracking. If hydrogen sulphide is present and causes the entry of hydrogen into the component, the cracking phenomenon is often referred to as "sulphide stress cracking (SSC)".

3.3.3 Diffusible hydrogen from the environment

Metals can experience hydrogen uptake and permeation when exposed to different environments (external hydrogen sources), leading to phenomena like hydrogen environment-assisted cracking, external-environmental HE and hydrogen-induced crack initiation [40]. These processes usually happen when metals are exposed to aqueous environments like water, water solutions, and humid air, or during corrosion processes where hydrogen is a byproduct on the metal surface. Other common external sources of hydrogen include hydrogen-rich atmospheres or gaseous hydrogen. These external hydrogen sources can originate from exposure to gaseous hydrogen at high pressure and

temperature (external "gaseous" hydrogen) or from cathodic electrochemical reactions during corrosion processes on the metal surface (external "cathodic" hydrogen) [41].

3.4 Overview of Advances in HE

The literature review on hydrogen embrittlement will predominantly centre on metallic materials, with a primary focus on understanding the S-N behaviour within the hydrogen environment.

There exist complex mechanisms underlying the HAFCG behaviour of commercially pure iron under hydrogen gas pressure and varying stress conditions. Under specific hydrogen gas pressure, loading frequency, and stress intensity factor range ΔK conditions, Hydrogen-Affected Fatigue Crack Growth (HAFCG) has three distinct HAFCG rate regimes [44,45]: a non-accelerated regime at low ΔK values, a transition regime, and an accelerated regime at high ΔK values, where the fatigue crack growth rate enhancement in hydrogen can reach up to 50 times higher than in air. For instance, in the X80 pipeline both base metal and weld metal, the fracture toughness of the base metal was decreased by 7.92% and the weld metal by 39.36% [46]. Similarly, the fatigue life curve under 0.7 MPa hydrogen gas closely resembled that in air, while under 115 MPa hydrogen gas, fatigue life was significantly diminished within a relatively short fatigue life regime. While fatigue-fractured specimens tested in air and 0.7 MPa hydrogen gas displayed typical ductile characteristics, those tested in 115 MPa hydrogen gas exhibited a distinct fracture surface devoid of shear-lip, appearing entirely flat in the final fracture region[47–49]. Thus, hydrogen gas significantly influences fatigue crack growth and fracture toughness in metallic materials [50]. This underscores the importance of understanding the effects of hydrogen on material behaviour, particularly in industries where hydrogen exposure is common, such as hydrogen-blended natural gas or coal gas transportation.

Nickel contents of austenitic stainless steel also have an impact on the S-N curve [48]. Varying nickel contents (12.6–13.7 wt%) under high pressure gaseous helium and hydrogen at -50°C, due to the temperature-dependent nature of hydrogen effects, with maximum effects anticipated at this temperature, a notable decrease in low cycle fatigue life due to hydrogen was observed in the steel with 12.6 wt% Ni. The S-N curve in hydrogen shifted to lower stress values compared to the reference curve in helium, although the slopes of the two curves were similar [51]. The influence of hydrogen diminished with increasing nickel content.

Additionally, test frequency and hydrogen pressure test conditions also impact the S-N behaviour of the materials [48,51]. Fatigue crack growth rate of specimens charged in high-pressure hydrogen gas and tested under specific conditions of R and frequency was notably higher when the testing frequency was reduced [52]. In a higher stress amplitude regime, the presence of hydrogen gas led to a significant degradation in fatigue life. Conversely, in a lower stress amplitude regime, the fatigue life appeared to be unaffected by the presence of hydrogen gas when compared to tests conducted in air [53]. However, no discernible difference in fatigue limits was observed between the uncharged specimens and those subjected to high-pressure hydrogen gas, tested under varying conditions of R and frequency at 20 and 500 Hz. More so, high-cycle fatigue tests were conducted at a frequency of 20 Hz in 0.1 MPa revealing that the fatigue limit of the smooth specimen increased in hydrogen gas compared to that in air. However, the fatigue limit of the deep-notched specimen remained unchanged from that observed in the air. Additionally, hydrogen was found to assist in the development of persistent slip bands [54].

To examine the impact of hydrogen gas on the fretting fatigue strength of austenitic stainless steel, the fretting fatigue strength in hydrogen gas was notably lower than that in air, with variations in tangential force among environments identified as a contributing factor [55,56]. Analysis of fretted samples indicated hydrogen absorption during fretting in a hydrogen gas environment [57]. It was observed that the major crack leading to specimen failure originated from one of the small cracks emanating at the adhered spots. Notably, preventing adhesion resulted in no reduction in fretting fatigue strength in hydrogen gas, as it prevented the formation of small cracks. In contrast, the small cracks, which had the potential to propagate in hydrogen gas, became non-propagating cracks when tested in air. This suggests that the stress conditions around the local adhesion were more severe compared to those in the air.

The temperature impact on the fatigue properties in a hydrogen environment was also investigated. Tension-compression tests were carried out on smooth specimens of two types of steels, a tempered martensitic microstructure and carbon steel, with a ferrite/pearlite microstructure in both nitrogen and hydrogen gas environments under a pressure of 115 MPa at three different temperatures: 233 K, room temperature, and 393 K [58]. At room temperature, these steels exhibited no noticeable degradation in fatigue strengths when tested in hydrogen gas, particularly in the relatively long-life regime.

In the work done by Refs [45,59], fatigue initiation resistance was assessed for API 5L X52 gas pipe steel using Roman Tile specimens, with fatigue initiation detected via acoustic emission. A comparison was made between specimens electrolytically charged with hydrogen and those without hydrogen absorption. It was observed that when hydrogen embrittlement occurred, the fatigue initiation time was reduced by approximately threefold.

Considering fatigue properties in the LCF, the detrimental effect of hydrogen on fatigue life becomes apparent although no significant influence on the fatigue limit was observed. Interestingly, no significant influence of hydrogen was observed on the elastic component or the cyclic hardening/softening behaviour of the material [60]. The strain ranges of the cyclic hysteresis loops for hydrogen-charged specimens were smaller compared to uncharged specimens under a constant stress amplitude test. However, no significant difference was observed in either the fatigue life or the crack growth curve between uncharged specimens and those charged with hydrogen, with a hydrogen content of approximately 0.5 ppm [61].

Additionally, Ref [62] conducted fatigue tests on cold-drawn eutectoid steels with varying activation energies for irreversible hydrogen trap sites and sensitivities to hydrogen embrittlement. The aim was to explore the mechanism of fatigue strength degradation caused by irreversible hydrogen. Results indicated that the fatigue strength decreased in samples with low activation energy due to irreversible hydrogen, while those with high activation energy remained unaffected. Interestingly, annealing a sample with high activation energy at 473 K led to a decrease in fatigue strength caused by irreversible hydrogen. It was concluded that high sensitivity to hydrogen embrittlement contributes to the degradation of fatigue strength by irreversible hydrogen, despite similar ease of irreversible desorption through cyclic loading before and after annealing.

In summary, the examination of the state of the art suggests that while the yield stress, ultimate strength, and fatigue endurance limit remain relatively unchanged, crucial properties such as elongation at failure, fracture toughness, and resistance to fatigue crack propagation are significantly diminished in the presence of hydrogen. In particular, it has been observed that the crack growth rate increases when hydrogen is present, with the extent of its detrimental effect depending on various factors including microstructural features, temperature, pressure, and loading frequency. Generally, the presence of hydrogen leads to an approximately tenfold increase in crack growth rate. Regarding crack

initiation behaviour, hydrogen seems to have a slight impact on medium-cycle fatigue, although proper statistical investigations are lacking in this area. However, in the high-cycle fatigue regime, the effect of hydrogen on crack initiation appears to be minimal, with some suggesting it may even be negligible. These observations hold for metallic materials containing stress concentrators. Moreover, fretting fatigue strength is notably reduced by the presence of hydrogen, which can pose challenges, particularly in mechanical joint applications.

3.5 Hydrogen Embrittlement Mechanism

Extensive research has focused on understanding how hydrogen causes failure in metals, with various hydrogen embrittlement mechanisms proposed in the literature. However, no single mechanism is considered solely responsible for hydrogen embrittlement. In some cases, multiple mechanisms may act simultaneously [4,40,63]. Some of the very popular mechanisms include: the hydrogen pressure theory, the hydrogen-induced phase transformation (HIPT) theory, the hydrogen-enhanced decohesion mechanism (HEDE), the hydrogen-enhanced localized plasticity mechanism (HELP) and the hydrogen-enhanced strain-induced vacancies (HESIV) have been proposed to explain HE phenomena [4,39,40,42,43].

3.5.1 Hydride formation mechanism

This embrittlement mechanism primarily affects alloy systems with a high propensity for hydride formation [3,17,64]. Hydrogen, acting as an interstitial solute in the metal lattice, rapidly diffuses and accumulates at areas of high hydrostatic stress, such as the crack tip as in Figure 3-4A. When hydrogen concentration surpasses solubility limits, hydrides form as in Figure 3-4b, and brittle hydride cleavage occurs along the crystallographic direction where the hydride forms. The crack is halted when it encounters the ductile matrix, initiating another cycle of this process. Crack propagation can be further accelerated by the presence of pre-existing hydrides along the crack path within the microstructure.

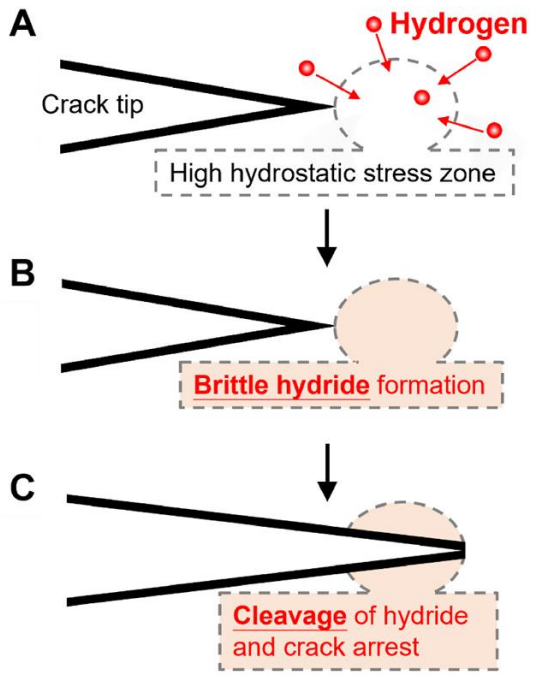

Figure 3-4 The mechanism of hydride-induced hydrogen cracking in sub-critical crack propagation [3]

3.5.2 The hydrogen-induced phase transformation (HIPT) theory

Face-centred cubic alloys like austenitic stainless steels can undergo significant structural changes in the surface layer when subjected to hydrogen charging due to a large supersaturation of hydrogen. This phenomenon is known as hydrogen-induced phase transformation (HIPT). This involves two types of transformations hydride formation and hydrogen-induced martensitic transformation [4]. In hydride-forming systems, embrittlement happens when hydrides form at stress concentrations and are subsequent cleavage of the hydride. This process and associated cleavage fracture are observed in systems where hydrides are stable or can be stabilized by stress [65]. Since the hydride phase is generally brittle, the crack propagates in a cleavage-like fashion through the hydride phase or along the hydride-matrix interface as seen in Ti.

Hydrogen-induced martensitic transformations consist of the FCC $\gamma_{Hydride}$ phase which is larger because of a higher hydrogen concentration transforming into (1) an HCP phase (∈-martensite) and (2) a BCC phase (α-martensite). According to ref [66], steels tested in aggressive environments exhibited a transformation from γ to BCC α near the crack, with fractures occurring predominantly through the α phase. Conversely, steels tested in less aggressive environments showed little to no α phase formation near the fracture surface. Therefore, the γ to BCC α transition is crucial in HE of stainless steels and enhancing the

stability of the γ phase improves resistance to HE. Austenitic stainless steels are more vulnerable to HE due to the above explained reason [4,30]. In addition, the harmful impact of hydrogen in α'-martensite is also linked to its reduced solubility in this phase.

In summary, the HIPT mechanism revolves around the creation and breaking of hydrides at the tips of cracks [40]. It's believed to work in a few steps [31,39]: first, hydrogen moves to areas of high hydrostatic stress at the crack tip. Then, a hydride phase forms and grows. Thirdly, when it reaches a certain size, the occurrence of a crack along a specific cleavage plane within the hydrides appears, and lastly, the hydride fractures or arrest of the crack at the interfaces between the matrix and hydrides, as shown in the figure below.

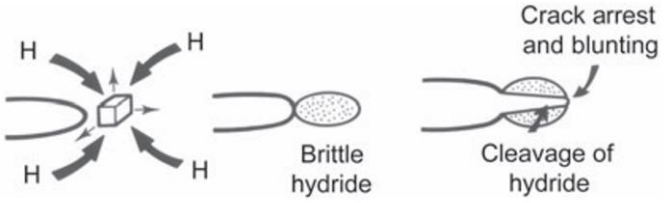

Figure 3-5 Hydride formation and fracture mechanism [25,40]

The hydride mechanism operates only within specific temperature and strain-rate ranges where hydrogen can diffuse to areas ahead of crack tips. Additionally, it's active only at temperatures where the hydride phase remains stable, typically resulting in brittle behaviour. The mechanism is summarised in Figure 3-5.

3.5.3 The hydrogen-enhance decohesion (HEDE) theory

This is sometimes referred to as hydrogen-induced decohesion (HID) [4]. It is hydrogen tends to diffuse to areas of high stress, similar to that found ahead of a crack tip, with the density of the hydrogen trapping sites increases along a crack path. This leads to a reduction in atomic cohesion as more hydrogen diffuses. The predominant experimental proof observed as a reduction in the crack-tip-opening angle with increasing hydrogen content is explained in Ref [67] and shown in Figure 3-6.

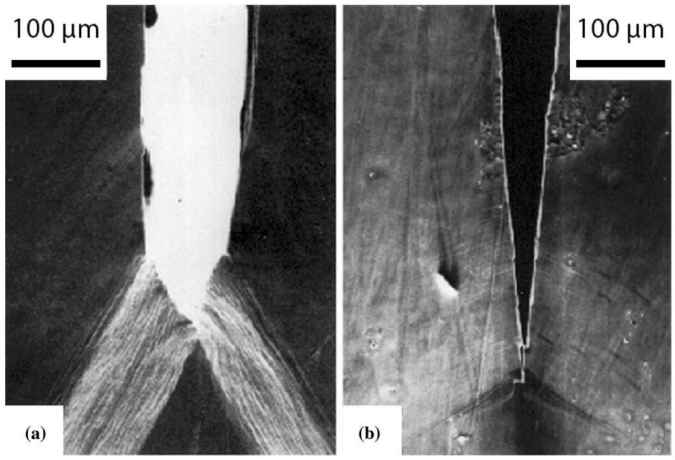

Figure 3-6 Effect of Hydrogen on the Crack Tip Opening Angle in: (a) Vacuum and (b) Hydrogen Atmosphere. [67]

In addition to reducing the atomic cohesion, ref [68] suggests using the Irwen–Orowan–Griffith theory that during the propagation of a brittle crack, the energy is expended not only for bond breaking but also for the emission of dislocations.

According to this concept, hydrogen weakens the cohesive bonds between metal atoms, making them more susceptible to separation even under low tensile stress [39,40]. As the concentration of hydrogen in a localized area increases, the weakening effect on the interatomic forces becomes more pronounced [31]. In intergranular fracture scenarios, hydrogen accumulates at the boundaries between metal grains, diminishing the cohesive forces among atoms within the metal structure [69]. This phenomenon leads to intergranular fracture or quasi-cleavage [70], similar to the effects of certain impurity elements such as sulphur, phosphorus, and bismuth, which also disrupt atomic cohesion along grain boundaries. This is shown in Figure 3-7 where the material can undergo plastic deformation and fracture under lower stress when hydrogen atoms accumulate in a region. Fracture typically occurs at the critical crack-tip opening displacement [71].

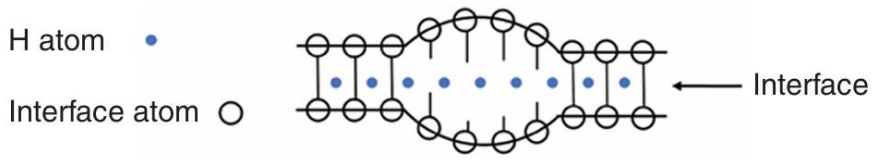

Figure 3-7 Illustration of HEDE mechanism [71]

Models have been used to quantify the HEDE under dynamic loading. One model uses two considerations to model the evolving equations for crack growth [72]: a) the growth rate in the absence of hydrogen and b) the growth rate in line with the plastic deformation and operating HE mechanism. Under similar conditions, ref [73] suggested a unified model that

resembles Paris law, while a model that uses a cohesive zone to describe the increment in the stress intensity factor has been formulated [74] where the Forman equation was used to predict the crack propagation rate. The crack growth rate is also modelled to be inversely proportional to the hydrogen concentration [75].

3.5.4 The hydrogen-enhanced localised plasticity (HELP) theory

The HELP theory suggests that hydrogen embrittlement occurs due to increased dislocation mobility in the presence of hydrogen [4,76]. According to this theory, hydrogen shields the elastic stress field around dislocations, which enhances their mobility and promotes slip localization. Substantial evidence supports the HELP mechanism in FCC metals [77]. For instance, experiments have demonstrated that hydrogen encourages slip planarity in FCC metals. The stacking fault energy (SFE) in FCC metals decreases with the presence of hydrogen, leading to greater dislocation mobility in areas of high stress concentration [4,78]. As SFE decreases, the work needed for partial dislocation constriction increases, limiting cross-slip. Hydrogen also reduces the repulsive forces between dislocations, facilitating their movement and allowing them to accumulate against barriers like grain boundaries and carbides. Additionally, hydrogen tends to migrate to the strain fields around dislocations, forming a Cottrell atmosphere that lowers yield strength, likely due to hydrogen screening the dislocations' elastic field.

Evidence supporting failure through hydrogen-enhanced localized plasticity in various steels has been obtained through macroscopic flow stress measurements, fractographic analysis, in situ TEM studies, observations of dislocation motion, and theoretical models [78]. This enhanced plasticity, leading to localised plastic failure, indicates that hydrogen promotes shear decohesion along slip planes, which differs from the traditional understanding of embrittlement.

In summary, this mechanism stipulates that hydrogen facilitates dislocation proliferation and motion, causing local dislocation pileups with premature failure of the material [39–41]. This mechanism has focused research attention on the interaction between the hydrogen atmosphere and dislocations and is primarily utilized to understand plastic traces on the fracture surfaces such as dimple fracture in hydrogenated alloys [31,44]. Unlike the HEDE mechanism, plasticity of the alloy plays a significant role in hydrogen-assisted fracture in the HELP mechanism [69,79].

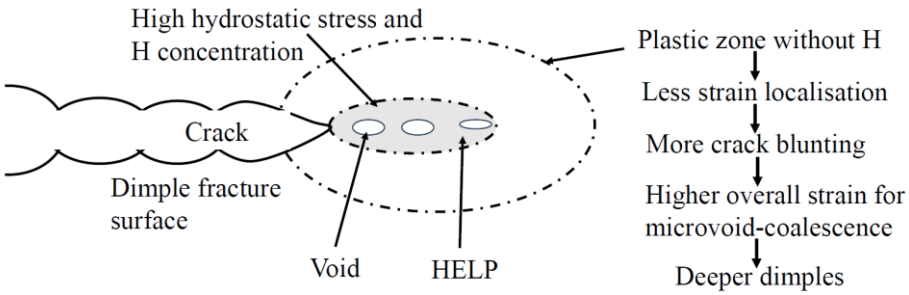

Figure 3-8 HELP mechanism, which involves a process of microvoid-coalescence.

3.5.5 The hydrogen-enhanced strain-induced vacancy (HESIV) mechanism

The hydrogen-enhanced strain-induced vacancy (HESIV) formation theory proposes that hydrogen increases the density and clustering of vacancies in metals [4]. These vacancies can coalesce into microvoids, which may further merge to form larger voids, ultimately reducing the material's resistance to ductile failure [80]. This effect was evident during tensile and fracture toughness testing of hydrogen-charged samples, where the fracture surface typically appears flat with some irregular ridges, exhibiting a quasi-cleavage fracture morphology. To verify hydrogen's impact on vacancy formation, ref [81] observed the hydrogen-induced increase in vacancy generation during deformation through positron lifetime measurements. Similarly, ref [82] found that the vacancy density in iron significantly increases compared to that at thermal equilibrium when exposed to a high-pressure, high-temperature hydrogen atmosphere. This suggests a reduction in the formation energy of vacancies due to iron–hydrogen interactions.

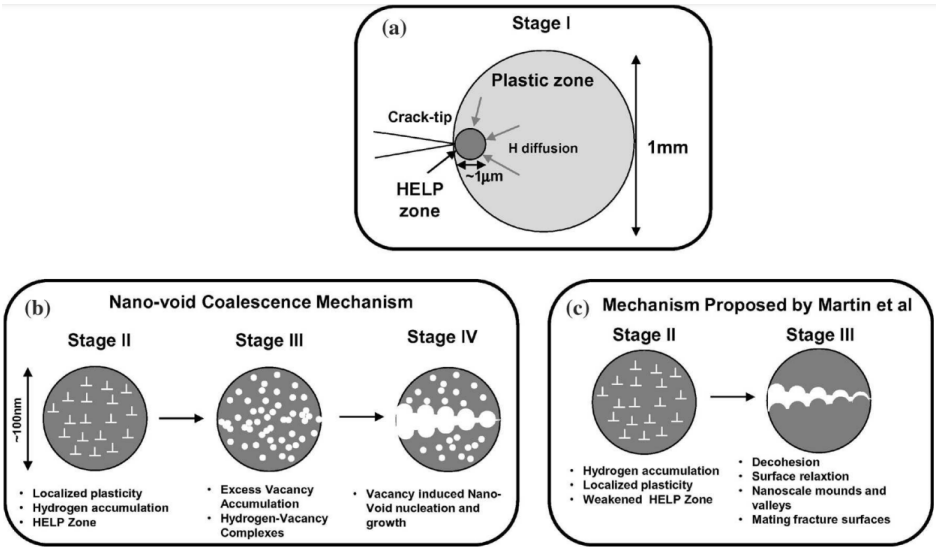

Figure 3-9 HESIV and HELP Schematic of macro- and micro-mechanism in Ref [4]

Although HESIV alone does not provide a definitive mechanism for embrittlement, ref [63] have proposed a combined mechanism involving HELP, HESIV and nanovoid coalescence to explain fracture failure by quasi-brittle fracture, as demonstrated in Figure 3-9. Thus HESIV mechanism suggests that hydrogen speeds up the creation of strain-induced vacancies and stabilizes vacancy clusters, as also supported by evidence from positron annihilation lifetime spectrum and molecular dynamics results [25,79]. Consequently, these vacancy clusters promote the initiation and growth of voids, leading to premature failure

3.5.6 The adsorption-induced dislocation emission (AIDE)

Hydrogen-assisted cracking is attributed to the adsorption of hydrogen at the crack tip otherwise known as adsorption-induced decohesion mechanism (AIDE) [4]. Embrittlement of metals in aqueous or hydrogen environments has been observed even at crack velocities too high for hydrogen to diffuse ahead of the cracks [40,83,84]. This observation further supports a mechanism involving hydrogen adsorption at crack tips. Metallographic and fractographic studies of crack growth reveal that environmentally assisted cracking occurs through more localized plastic flow and microvoid coalescence [85]. Specifically, adsorption facilitates the emission of dislocations from crack tips, which in turn promotes the coalescence of cracks with voids ahead of them. Thus AIDE mechanism operates by aiding the emission of dislocations through the presence of adsorbed hydrogen atoms [39,40,44]. In this process, hydrogen atoms adhering to the surface or residing just below it weaken the bonds between atoms, facilitating the initiation of dislocations at the crack tip. This, in turn, amplifies the local plastic deformation near the crack tip [84]. This is illustrated in the figure below.

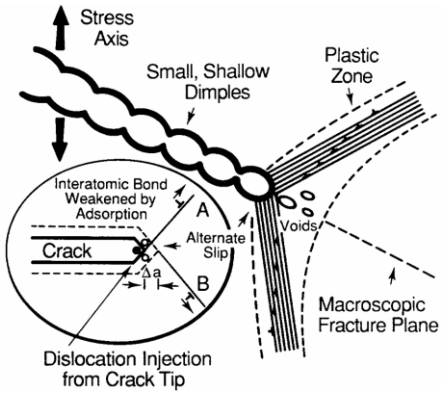

Figure 3-10 Schematic diagram illustrating the AIDE mechanism in hydrogen environment embrittlement, which involves crack growth by alternate-slip (for transgranular paths) from crack tips, facilitating coalescence of cracks with voids formed in the plastic zone ahead of cracks [40,84]

The concept of enhancing Fatigue Crack Growth (FCG) through AIDE shares similarities with the HELP mechanism [40]. However, a key distinction lies in the fact that AIDE involves hydrogen adsorption in the subsurface, while HELP's effect is attributed to the presence of solute hydrogen within the material.

3.5.7 The hydrogen pressure theory (HTP)

According to this theory, hydrogen atoms preferentially segregate at defect locations in the metal, such as micro-voids and inclusion sites [23]. Then, locally accumulated hydrogen atoms are combined into hydrogen molecules [17,86]. As time goes on, hydrogen atoms around these defects continuously diffuse toward the defect sites and produce a high hydrogen gas pressure which forms a load in the metal. As the pressure increases, the atomic bonds in the local region break, leading to crack initiation only when the local hydrogen gas pressure exceeds the critical strength of the material, hydrogen-induced cracking takes place. Hydrogen then diffuses into the initiated crack and this crack propagation then extends into a larger ladder-like crack [87], accelerating the overall fracture process [23,88]. HTP is often the reason why hydrogen-induced cracking and hydrogen bubbling occurs in metals without external loads.

3.6 Fatigue properties of pipeline metals in hydrogen environments

Having discussed the impact of hydrogen on metals and the various mechanisms by which hydrogen diffuses through them, this section will focus on assessing fatigue behaviour in a hydrogen environment. The goal is to understand how hydrogen influences the fatigue life of materials and to explore the factors contributing to hydrogen-assisted fatigue failure. Although most practical failures occur through fast fracture [89,90], hydrogen also impacts the fatigue properties of metals. This is unsurprising given the embrittlement mechanisms associated with fast fracture. Typically, hydrogen embrittlement has a significant influence on high-stress, low-cycle fatigue, but has minimal effect on high-cycle fatigue [12]. The HE effect will be discussed in this section by calculating the HE index, defined as [19,91]:

$$equalHEI\ (\%) = \frac{EL_0 - EL_H}{EL_0} \times 100\% \qquad (3\text{-}2)$$

Where EL_0 is the elongation charged for 0 hours and EL_H is the percentage elongation charged with hydrogen for a different length of time.

3.6.1 Effect of hydrogen pressure on fatigue properties of pipeline metals

For high-pressure hydrogen gas, hydrogen dissolution occurs in three steps [18]: First, physical absorption takes place on the solid surface due to van der Waals interactions between the hydrogen gas and the surface. The second step is chemical absorption, which occurs within a single atomic layer due to short-range chemical interactions. Lastly, in the third step, hydrogen atoms dissolve as they diffuse into the material's interior, driven by the hydrogen concentration gradient [92]. The dissolved hydrogen concentration is dependent on the hydrogen gas pressure and is described by Sieverts' law [18,88]:

$$C_H = S\sqrt{P_{H_2}} \tag{3-3}$$

In which C_H is dissolved hydrogen concentration, S is the solubility constant at a constant temperature [17] and P_{H_2} is the hydrogen partial pressure. Higher hydrogen pressure therefore increases a metal's susceptibility to HE [93] is in agreement with the equation above as well as Figure 3-11in ref [19]. This occurs because higher pressure results in a greater concentration of hydrogen atoms within the metal, allowing them to interact with defects and further weaken the material.

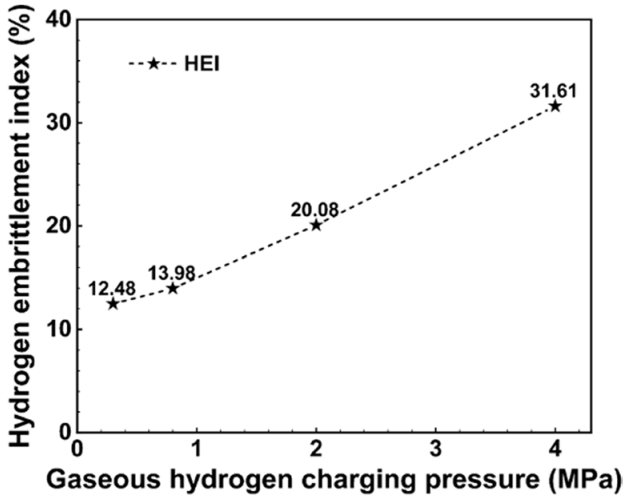

Figure 3-11 HE index as a function of hydrogen pressure [19]

For pipeline steels, the HE susceptibility of pipeline steel progressively increases with rising hydrogen partial pressure, leading to a significant acceleration of fatigue crack growth [18,19]. As hydrogen pressure increases, the irregular movement of hydrogen molecules intensifies, leading to more collisions with steel surfaces, which accelerates the dissociation and adsorption of hydrogen. This results in more hydrogen atoms diffusing

into the steel. The effect of hydrogen partial pressure on hydrogen diffusion is reflected in the fracture morphology as shown in Figure 3-12 [19].

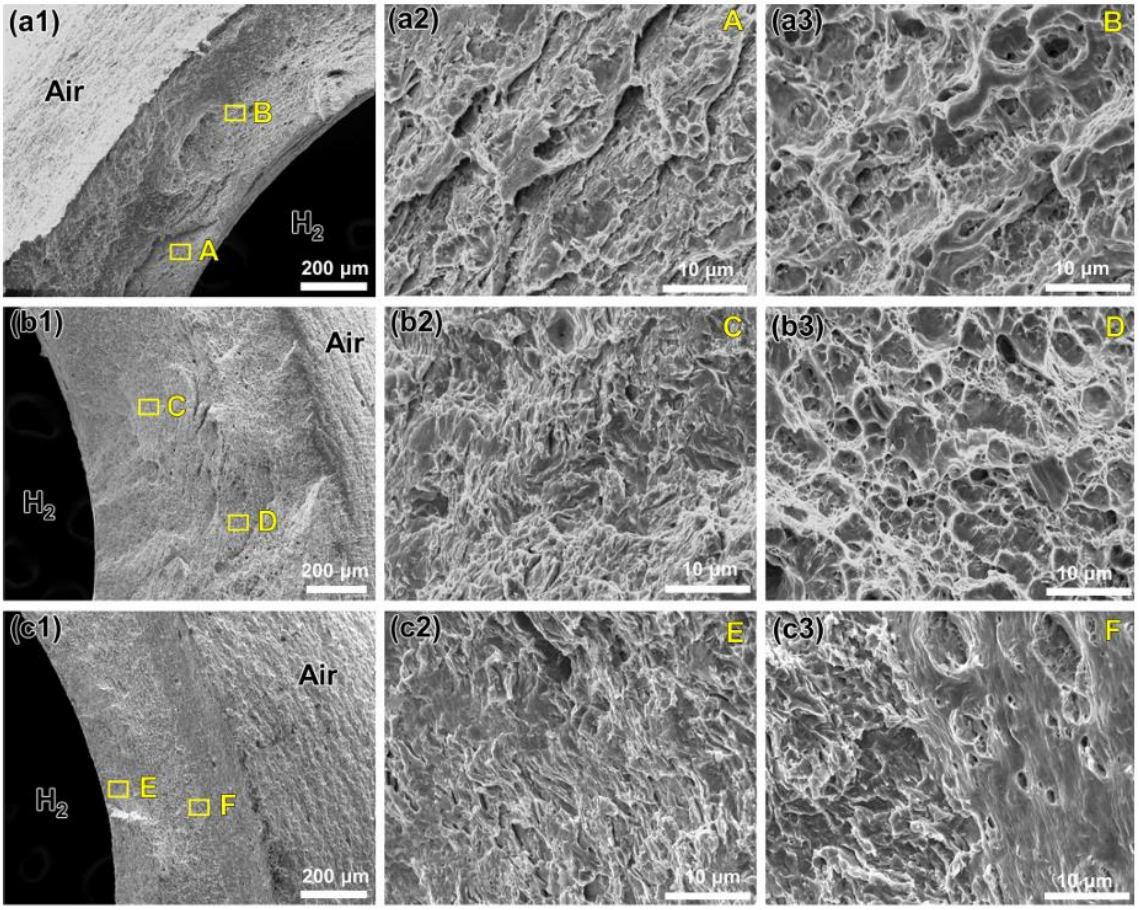

Figure 3-12 Fracture morphologies of X52 pipeline steel specimens exposed to hydrogen for 48 hours at varying pressures (a1-a3) at 0.3MPa, (b1-b3) at 0.8MPa and (c1-c3) at 2MPa [19]

At lower pressures (0.3 and 0.8 MPa), fractures show a mix of brittle, dimple, and ductile shear zones, with a small brittle fracture zone forming a ring inside the specimens. As hydrogen pressure rises to 2 and 4 MPa, the dimple zone disappears, and fractures consist only of brittle and ductile shear zones. The size of the brittle fracture zone increases with hydrogen pressure, and when it becomes large enough, the fracture shifts directly to a ductile shear mode, bypassing the dimple zone.

According to ref [94], high-strength hydrogen steel pipelines present a promising solution for reducing costs. The natural gas industry uses thin-walled, high-strength pipes to achieve similar cost savings, suggesting potential benefits for hydrogen infrastructure as well. Another question to address here is whether hydrogen gas at 0.8MPa pressures (8bars) can cause significant degradation. Figure 3-11 shows a change in the HEI of X52 steel at this

pressure compared to lower pressures, though this change is not as pronounced as at higher pressures. This aligns with Sieverts' equation, and the fractography summarized in Figure 3-12 highlights variations resulting from changes in hydrogen gas pressure including pressures of about 0.8MPa. therefore, the charging pressure of 8 bars (0.8MPa) used in this study is capable of producing significant degradation in pipeline materials.

3.6.2 Effect of hydrogen temperature on fatigue properties of pipeline metals

As seen earlier, the diffusion of hydrogen atoms into steel involves adsorption and desorption processes on the steel surface. Temperature changes influence these processes [95], and the atomic concentration which affects the fracture mode from ductile to brittle. However, according to ref [91], temperature is the most complicated factor that affects HE in pipeline metals. An increase in temperature can enhance HE by increasing hydrogen atom generation on the steel surface as well as facilitating its diffusion [96]. It also raises the number of transferred charges, resulting in higher hydrogen atom concentration on the surface [97,98]. In addition, the solubility of hydrogen in a metal is temperature dependent [4,10]. Consequently, the adsorption and desorption behaviours cause variations in the surface coverage of hydrogen atoms, making it challenging to quantify hydrogen concentration on the metal surface as temperatures fluctuate. However, the temperature-induced softening effect in metals like steel suggests that the fracture toughness of pipeline steel tends to increase as the temperature rises [91]. In Figure 3-13a strain-stress curves show that the elongation of X70 steel charged with a 20mA/cm^2 charging current at different temperatures can be used to assess the susceptibility of the material to HE.

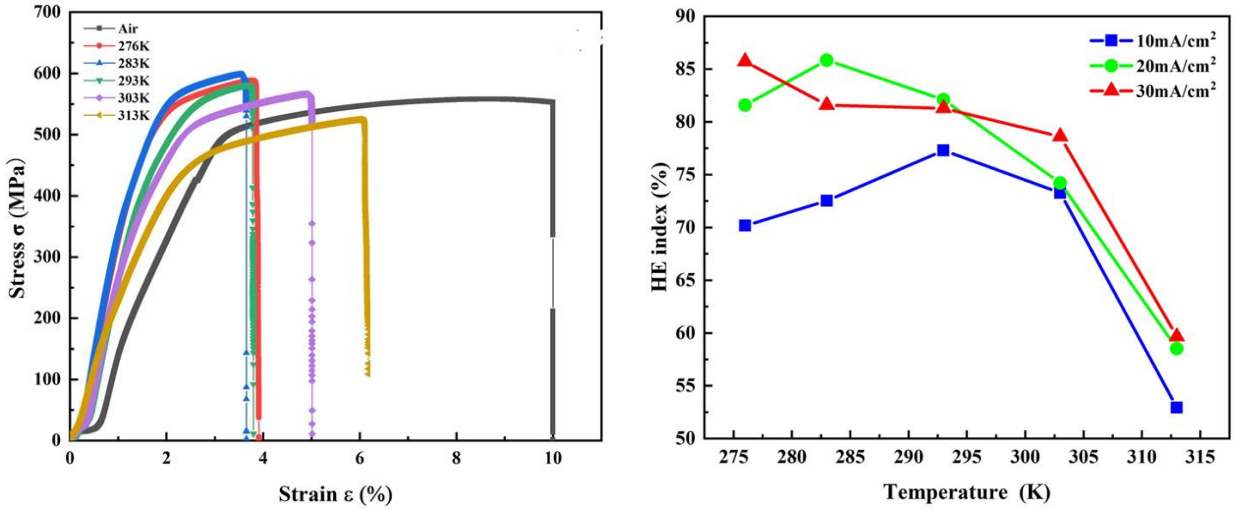

a) b)

Figure 3-13 a) The strain-stress curves of X70 steel at 20mA/cm^2 charging rate b) Hydrogen Embrittlement index different charging rates [91]

The yield strength is the point at which plastic deformation begins to dominate due to dislocation movement. An increase in yield strength indicates that plastic deformation is being restricted. When a material is exposed to hydrogen, the yield strength may show a slight increase, while elongation significantly decreases as seen in this figure. This phenomenon suggests hydrogen-induced inhibition of dislocation emission and a loss of toughness. Figure 3-13b shows the HEI at different charging rates and at different temperatures for X70 steel. This figure shows the different patterns in adsorption and desorption rates as temperature changes which confirms the complexity of this characteristic.

3.6.3 Effect of hydrogen charging time on fatigue properties of pipeline metals

When pipeline materials are exposed to a hydrogen environment, hydrogen molecules dissociate into atoms that enter them through adsorption and diffusion. These atoms become trapped at various sites such as vacancies, dislocations, precipitates, inclusions, and grain boundaries. As hydrogen charging time increases, more atoms are trapped. Once the hydrogen concentration surpasses a critical threshold, irreversible damage such as microcracks and hydrogen bubbles can form, reducing the steel's plasticity and leading to premature fracture. Prolonged hydrogen exposure increases the risk of cracks and accelerates failure.

The stress-strain curves summarised in Figure 3-14a show specimens of X52 exposed to varying hydrogen charging times at 4 MPa hydrogen pressure and a control specimen with

4 MPa nitrogen for 0 hours reveals how hydrogen charging affects the material's mechanical behaviour. These curves show differences in ductility and strength, with hydrogen exposure typically reducing the material's ability to withstand stress before failure.

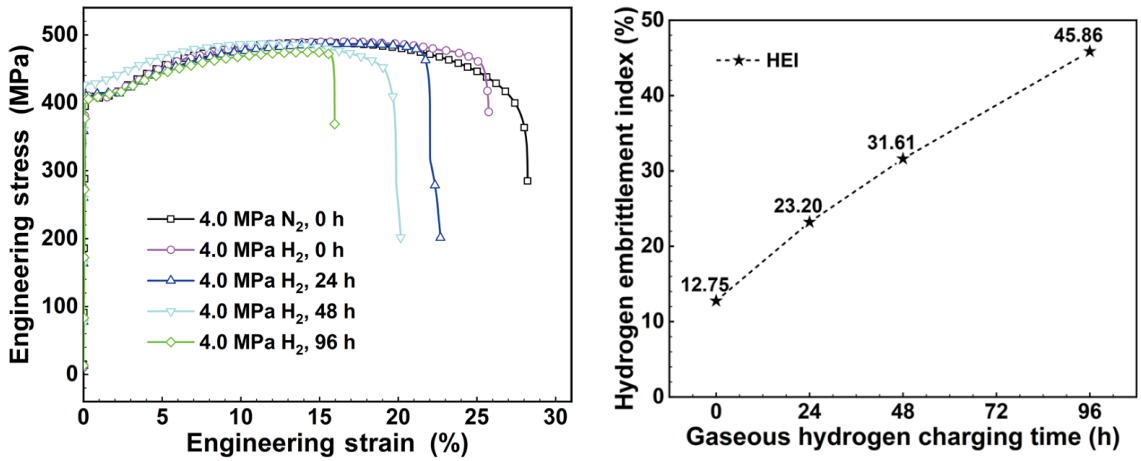

a) b)

Figure 3-14 a) stress–strain curves of X52 specimens under different gaseous hydrogen charging time b)HE index as a function of charging time [19]

From the figure above, the specimen charged with nitrogen showed the highest strain at fracture, indicating its superior plasticity. In contrast, the specimens charged with hydrogen exhibited lower strain at fracture, demonstrating that gaseous hydrogen charging reduces their plasticity. Furthermore, as the hydrogen charging time increased, the strain at fracture progressively decreased, highlighting the impact of extended hydrogen exposure on reducing material ductility.

As shown in Figure 3-14b, the HEI increased with longer hydrogen charging times, indicating that the susceptibility of X52 pipeline steel to hydrogen embrittlement rises as the duration of gaseous hydrogen exposure increases. Further analysis of the fracture surfaces revealed that the specimen with a 0-hour hydrogen charging time displayed a dimpled morphology, suggesting a ductile fracture mode in certain regions while no dimple morphology was present on specimens with hydrogen charging times greater than 0 hours [19]. As the hydrogen charging time increased, the brittle fracture area expanded, the ductile shear fracture zone became progressively narrower, and in some areas, the shear fracture zone vanished entirely leaving only the brittle fracture region.

3.6.4 Effect of material microstructure and hydrogen on fatigue properties of pipeline metals

Grain boundaries are generally regarded as the primary pathways for hydrogen diffusion in metallic alloys, and in addition, the microstructural characteristics significantly influence their hydrogen trapping behaviour [7,99]. Trapped hydrogen tends to remain longer in favourable locations, such as defects, rather than migrating through the lattice thereby lowering its solubility in the metal. Features that temporarily accumulate hydrogen atoms within the steel structure are considered reversible traps, while those that store hydrogen permanently are classified as irreversible traps. According to [99], hydrogen traps can be categorized into three types: a) Physical traps, such as voids, high-energy grain boundaries, and incoherent interfaces between particles and the steel matrix; b) Attractive traps, including coherent/semi-coherent interfaces, dislocations, and crack tips; c) Mixed traps, which combine characteristics of both physical and attractive traps. Reversible traps are more damaging to the metal because they allow hydrogen to migrate towards crack-prone zones. Therefore, hydrogen diffusion patterns in metals are influenced by the combined trapping effects of grain refinement and structural defects.

During steel processing, for example, various microstructural phase transformations take place, and these changes are often the result of phase evolution driven by the combined effects of deformation, recrystallization, and recovery [100]. However, heat treatment procedures reduced internal structural defects and indirectly minimized the number of hydrogen traps within the steel indirectly influencing the rate of HE.

3.7 Hydrogen embrittlement in gas pipeline materials

Hydrogen embrittlement (HE) poses a significant challenge to the integrity and safety of transmission pipes, particularly those used in natural gas pipelines. Hydrogen atoms permeate into the material of the pipes, leading to a degradation of mechanical properties and an increased susceptibility to cracking and failure. Understanding the effects of HE on pipeline materials is crucial for ensuring the reliability and longevity of these critical infrastructure components. This section explores the mechanisms of hydrogen embrittlement in pipeline materials, X52 steel, GCI and brass, considering factors such as operating conditions, material properties, and external influences. By examining the various manifestations of HE and its impact on transmission pipes, strategies to mitigate its detrimental effects and enhance the resilience of pipeline systems can be adopted.

3.7.1 HE in X52 carbon steel

X52 pipeline steel is recommended and has been used as a hydrogen pipeline material because, as a low-strength steel, it is considered more resistant to hydrogen embrittlement [19]. However, when hydrogen atoms diffuse into the steel, they can gather at microstructural features like grain boundaries, dislocations, and phase boundaries, and may lead to the formation of molecular hydrogen, generating high internal pressures that can result in cracks or blisters [101]. The microstructure of unused X52 carbon steel is shown in Figure 3-15 with a matrix structure characterised as ferrite and pearlite [102].

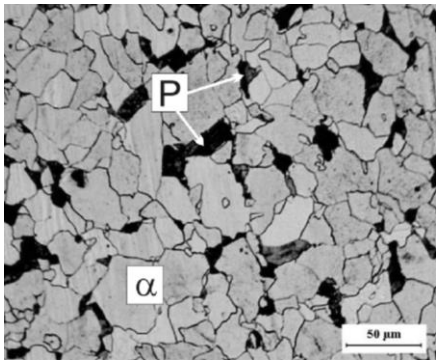

Figure 3-15 Light optical micrograph of the ferrite-pearlite microstructure of this steel

Hydrogen charging of steel increases the electrochemical activity of both phases with pearlite being more susceptible to hydrogen due to the differences in hydrogen diffusivity and trapping characteristics [103]. The engineering stress–strain curves of tubular specimens with varying hydrogen charging times at 40barrs of hydrogen pressure, along with the curve for 0 hours at 4 MPa nitrogen pressure, are shown in Figure 3-16 [19].

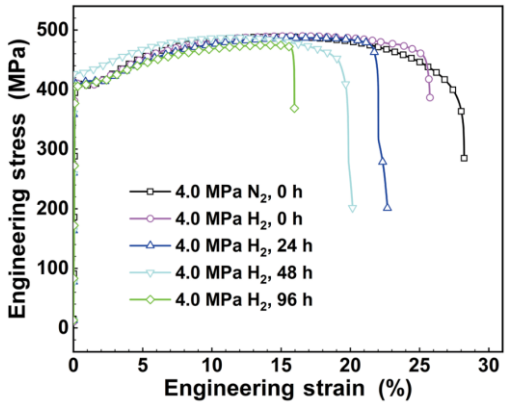

Figure 3-16 Stress–strain curves under varying gaseous hydrogen charging times [19]

The similarities in the curves before necking are coincidental. The nitrogen-charged specimen showed the highest strain at fracture, reflecting its high plasticity. In contrast, specimens charged with hydrogen had lower strain at fracture, indicating that gaseous

hydrogen reduces their plasticity. As the hydrogen charging time increased, the strain at fracture progressively decreased. The fracture surfaces of uncharged specimens are shown in Figure 3-17a where the yellow lines show the boundaries of 3 different fracture fracture regions, A shows brittle fracture, B shows some brittle and slip planes, and C is dimpled.

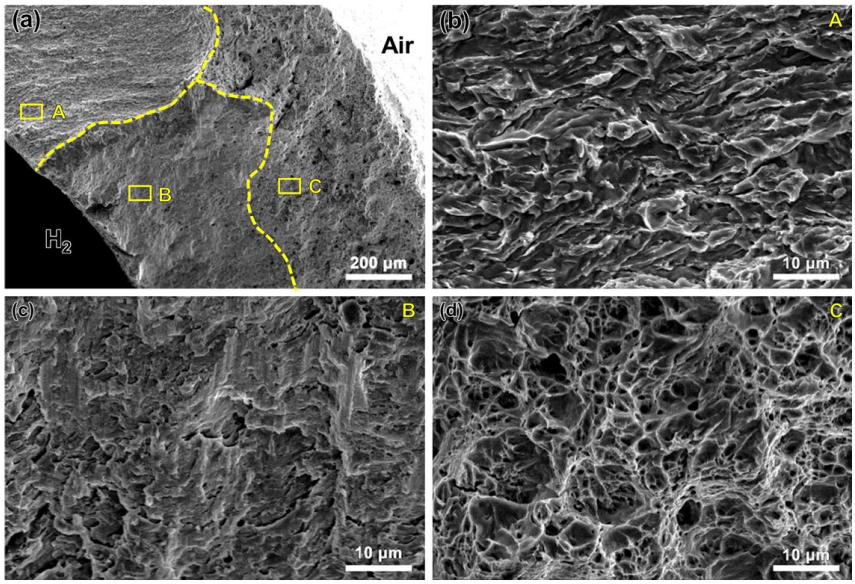

Figure 3-17 Fracture surface of the X52 pipeline steel specimen charged with 40barrs hydrogen for 0 hours: (a) overview of the fracture surface, (b) magnified view of the brittle fracture region, (c) close-up of region C, and (d) dimpled region D [19]

When charged for different lengths of time, the fracture surfaces consist of transgranular and ductile shear fractures with no dimples as shown in Figure 3-18 [19]

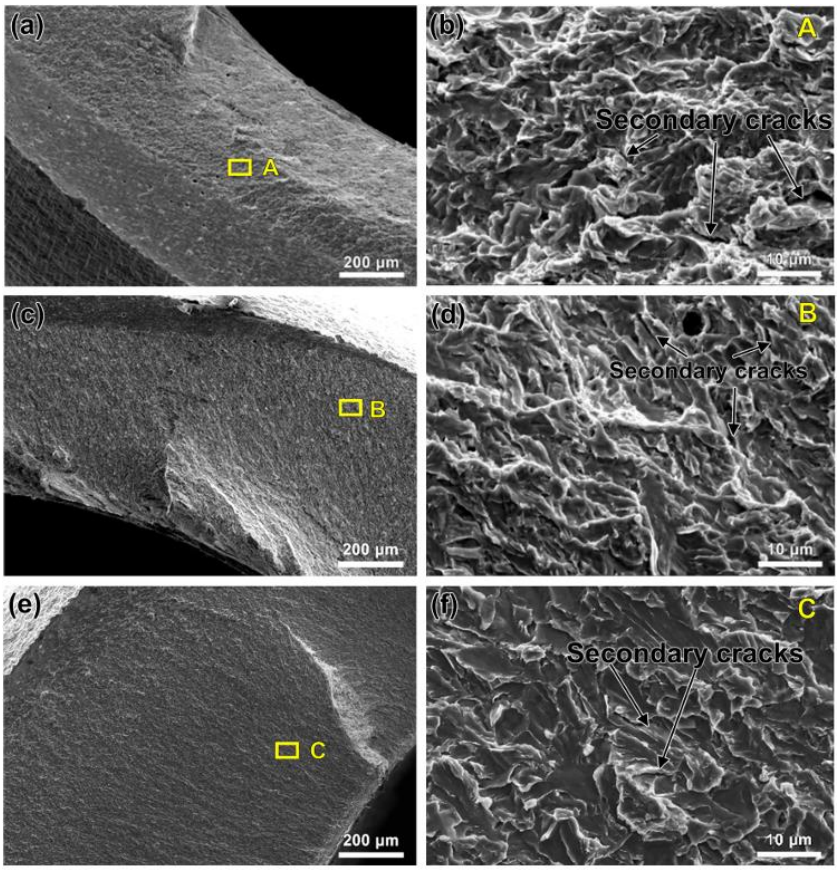

Figure 3-18 Fracture surface of the X52 pipeline steel specimen charged with 40barrs hydrogen for various durations: (a) 24 hours, (b) enlarged view of area A in (a), (c) 48 hours, (d) enlarged view of area B in (c), (e) 96 hours, and (f) enlarged view of area C in (e).[19]

Failure consists of ductile shear fracture in the transgranular fracture regions, to begin with, and the proportion of transgranular and ductile shear fractures varies with hydrogen charging time. It is observed that the area of brittle fracture gradually increases with hydrogen charging time.

X52 carbon steel is more prone to HE due to its larger grain size and higher content of impurity elements, which result in increased hydrogen solubility and a microstructure with lower resistance to HE. In hydrogen-blended natural gas steel pipelines, the interaction between hydrogen and pipeline steel is influenced by various operating conditions, particularly temperature and gas pressure [104]. Higher hydrogen pressure correlates with increased sensitivity to hydrogen embrittlement. Additionally, hydrogen diffusivity and temperature follow Arrhenius' law [105], where the thermal activation energy of hydrogen atoms rises with increasing temperature. In addition, a saturated hydrogen sulphide solution environment increases the saturation levels of the X52 pipeline with an increase in temperature [106,107]. According to Ref. [108] the sub-surface hydrogen concentration in

lattice increases with the hydrogen charging method, however, the hydrogen uptake from a hydrogen gas environment where naturally formed surface oxides are present remains to be explored.

3.7.2 HE in welded X52 carbon steel

Welding is a widely used method for producing complex structural parts, which often introduce local stress concentrations, inhomogeneities, and inclusions [109]. The integrity of welded joints is crucial for ensuring the quality of structural components, with resistance to hydrogen embrittlement being another aspect to consider. The complex thermal history, the non-equilibrium structure formed due to high heating and cooling rate in the weld thermal cycle and the pervasive presence of hydrogen in the processing environment heighten the susceptibility of pipeline welds to HE [110,111]. There may also be defects that complicate the effect of hydrogen in these welds. Hydrogen in weldments is either diffusible or non-diffusible. The hydrogen that is unable to migrate from the weld zone stays trapped while the diffusible hydrogen often causes damage to the weld [99]. The most HE susceptible area in a welded pipe is the heat-affected zone (HAZ) near the joint, where a significant amount of hydrogen from high-temperature processing and high hardness (high hardness creates multiple sites for crack initiation and propagation) in comparison to the base metal leads to a marked reduction in ductility [99,112]. This is due to the inhomogeneities presenting favourable sites for hydrogen diffusion and trapping in addition to the inherent stress concentration, chemical composition, microstructure and residual stresses.

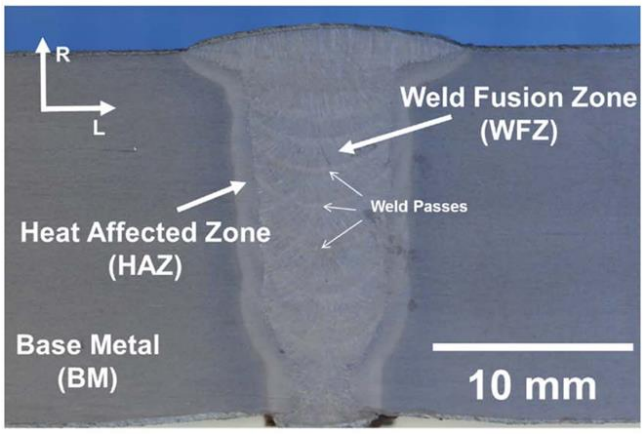

Figure 3-19 A macro-etched image of a gas metal arc weld reveals distinct sections of the weld, including the weld fusion zone (WFZ), the heat-affected zone (HAZ), and multiple weld passes, highlighting the different regions formed during the welding process [112]

3.7 Hydrogen embrittlement in gas pipeline materials

It remains challenging to assess the performance of a weld in terms of susceptibility to hydrogen embrittlement due to a lack of a well-established testing methodology and standards and high microstructural heterogeneity over a small volume of material around the dissimilar weld interface for example [113]. In addition, different welding techniques have varying levels of hydrogen exposure, with some processes being more susceptible to introducing hydrogen into the material [114]. Thus, the susceptibility of a weld to HE depends on various factors, ranging from material composition with high-strength steels more prone to HE due to their microstructure and chemical composition as well as the weld process and environment.

In pipeline transportation, welding is the primary fabrication process used for long-distance hydrogen transportation pipelines [113,115]. The interaction between the welding thermal cycle and the material's crystal structure can significantly affect the microstructural homogeneity in the sub-regions of a weld joint, influencing its susceptibility to HE. Amongst many weld processes [116], friction stir welding (FSW) has been widely used in the pipeline industry because it involves no melting of metal as compared to conventional arc welding [109,117], while post-weld heat treatment of welds has been widely used to promote the tempering of the martensitic microstructure, restore joint toughness and ductility, and reduce residual stress [113].

The tensile stress-strain curves of high-strength steel weldments after various hydrogen charging durations (shown in Figure Figure 3-20) reveal that as the hydrogen charging time of a welded joint increases, the elongation of the material gradually decreases, with minimal change before necking. Both tensile and yield strengths decline over time. In tensile tests, weldments typically show less pronounced yielding, and hydrogen embrittlement further reduces plasticity, eliminating a clear yield point and increasing brittleness. Welds exposed to hydrogen are more prone to sudden fractures instead of a defined yielding phase. It also shows that after 10 and 30 minutes of hydrogen charging, tensile strength remains similar, but elongation begins to decrease. However, elongation drops sharply after 1 hour of charging due to hydrogen molecules penetrating the material, disrupting crystallinity, increasing grain boundary margins, and thus reducing elongation. The elongation decreases from 19.2% to 13.2% at 1 hour of charging, and further to 9.8% after 4 hours. Figure 3-20b–d illustrate the fitted data plots of tensile strength, yield strength, and elongation across hydrogen charging times, showing a clear decreasing trend in these mechanical properties.

Consequently, hydrogen charging time significantly impacts the material's embrittlement and reduces its tensile strength, yield strength, and elongation.

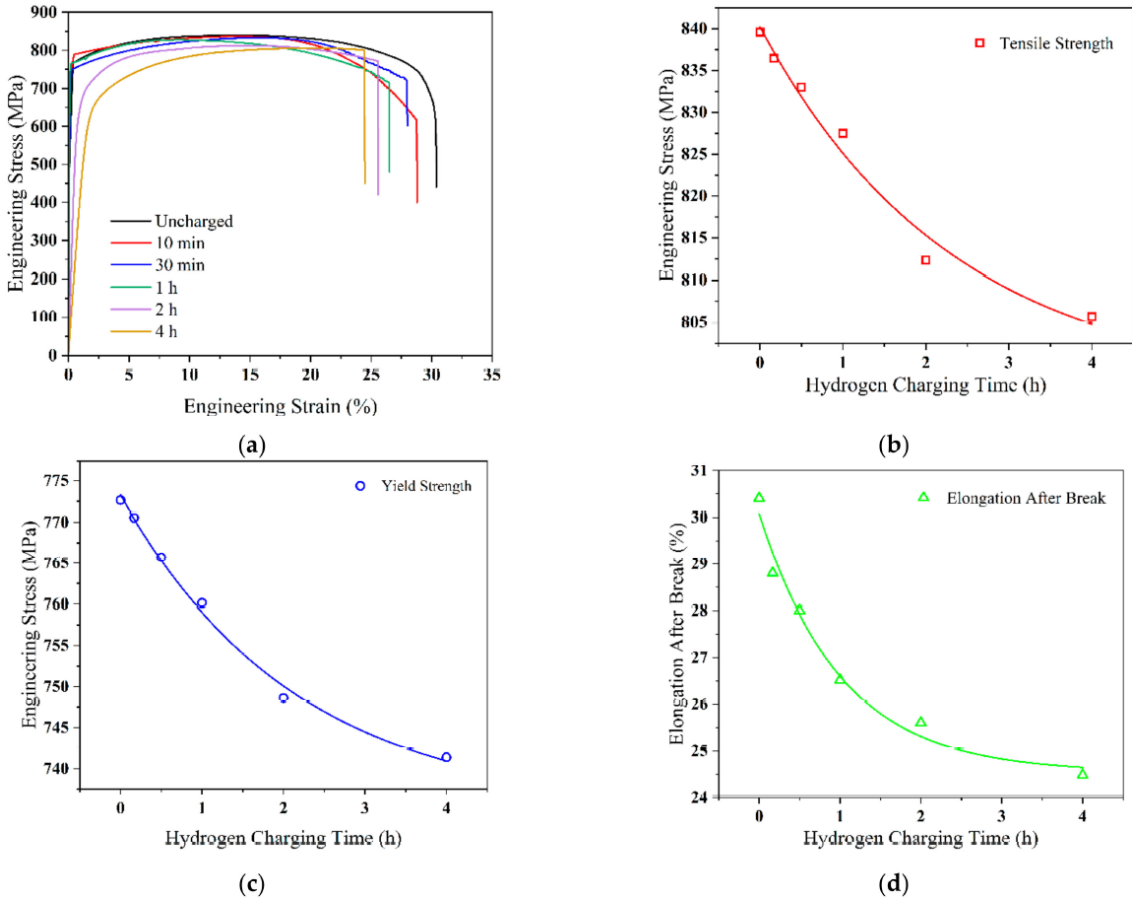

Figure 3-20 Tensile mechanical properties of Q690 high-strength steel weldments under different hydrogen charging current densities: (a) stress–strain curves; (b–d) relationships of tensile strength, yield strength, and elongation with hydrogen charging current densities, respectively [118]

3.7.3 HE in grey cast iron (GRI)

Cast iron is an alloy with a microstructure that includes graphite and thus a high amount of carbon. In the case of cast iron, unlike high-strength steels, grey cast irons have graphite that can accommodate diffused hydrogen, which delays the embrittlement effect [119,120]. This is because hydrogen atoms bind very strongly with vacancies, rather than other hydrogen atoms [121]. Figure 3-21 shows the displacement of hydrogen in iron materials at varying levels of vacancy concentrations.

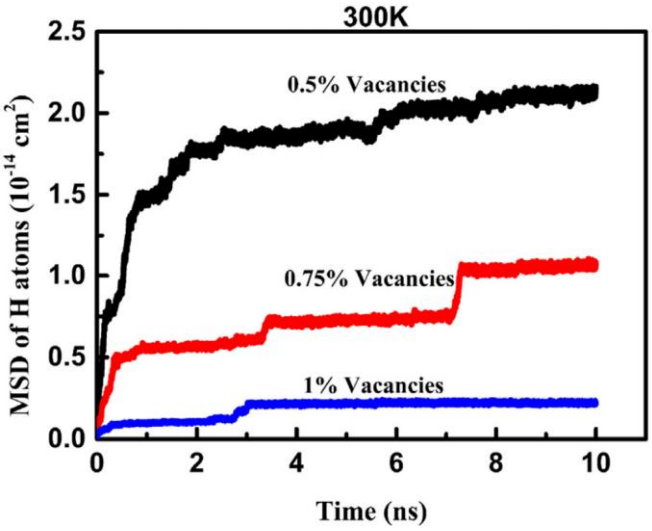

Figure 3-21 Mean square displacements of hydrogen atoms over time at three different vacancy concentrations in BCC Fe [121].

While cast iron may exhibit lower hydrogen diffusion rates (because graphite can accommodate diffused hydrogen [122]) and lower sensitivity to HE compared to steel, it can still experience embrittlement under certain conditions, especially if exposed to high hydrogen concentrations or severe service environments. In ductile cast irons, the presence of numerous spheroidal graphite particles not only serves as stress concentrator sites but also as hydrogen-trap sites [123,124]. This can lead to hydrogen-induced degradation in the material if present [125]. Therefore, while ductile cast irons may exhibit enhanced ductility and toughness compared to other cast iron types, the presence of graphite particles poses a unique challenge in managing the risk of hydrogen embrittlement.

In the crystal structure of cast iron, the presence of hydrogen leads to the initiation of multiple small cracks around graphite nodules, with both the number and severity of these cracks increasing as hydrogen content rises [126]. These cracks arise due to hydrogen diffusing freely through ferrite, but graphite nodules can absorb hydrogen and become saturated [122]. The accumulation of hydrogen and the resulting internal gas pressure can eventually cause the graphite nodules to detach from the ferrite matrix after reaching a critical minimum amount [6,122,123]. This detachment introduces cracks in the microstructure, leading to the initiation of brittle cleavage fractures. These hydrogen-induced cracks and defects at the graphite nodule interfaces are believed to contribute to the increased hydrogen uptake. With more tensile loading, the small cracks coalesce between the graphite nodules, resulting in larger cracks within the microstructure as summarised in Figure 3-22.

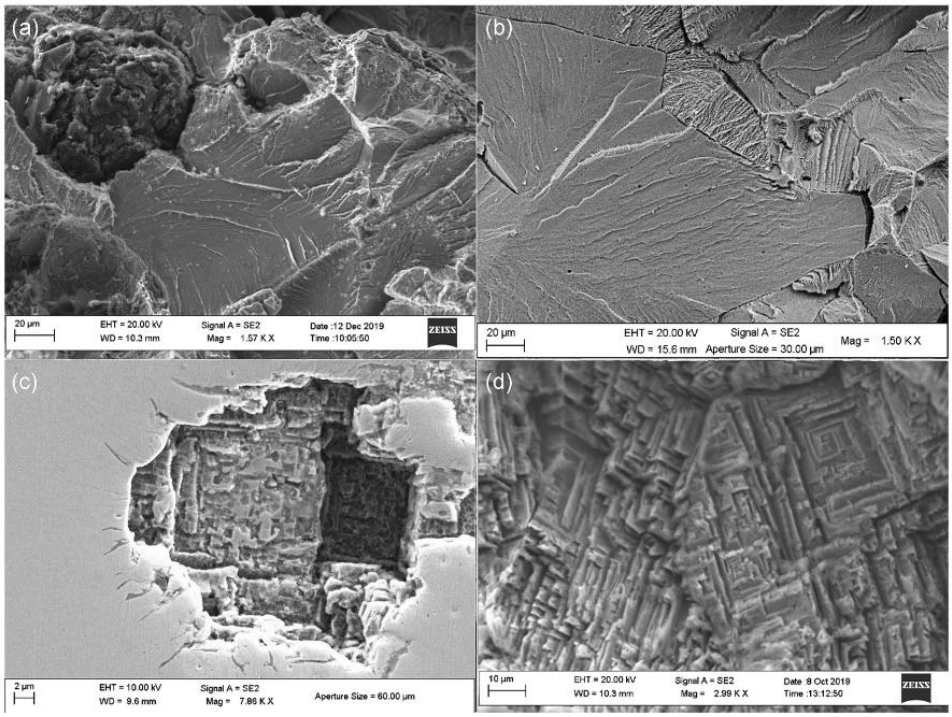

Figure 3-22 Hydrogen-charged nodular cast iron: (a) Overview of the fracture surface, (b) detailed view of brittle cleavage fracture facets in ferrite ligaments, (c) side view of a polished cross-section showing multiple small brittle cracks surrounding a cavity left by a detached graphite nodule, and (d) close-up of the cavity surface [126]

3.7.4 HE in brass and copper alloys

Electrolytic Tough Pitch copper is susceptible to hydrogen embrittlement at any temperature because it contains small copper oxide particles dispersed throughout the microstructure which react with hydrogen, producing water, leading to some form of HE [4]. Meanwhile, Copper and copper-rich alloys are generally resistant to hydrogen embrittlement unless they contain oxygen or copper oxide. When oxygen-bearing copper and copper alloys are annealed or exposed to a hydrogen environment, atomic hydrogen can diffuse into the metal and react with the copper oxide or oxygen to form water as shown in the equation [12]:

$$Cu_2O + 2H = 2Cu + H_2O \quad (3\text{-}4)$$

If the temperature exceeds 375°C, this water converts into high-pressure steam, potentially causing damage. However, brass does not contain these copper oxide particles, which makes it resistant to this form of HE [127]. Therefore, brass components are less likely to experience hydrogen embrittlement. In addition, the presence of copper influences the susceptibility of the metal to HE.

The materials mentioned above are integral components in the gas transmission network. This PhD research focuses on comprehending the impact of hydrogen embrittlement (HE) within these materials. Understanding the behaviour of HE in these materials is crucial, particularly in the context of projects like the HyDeploy, which involves blending natural gas with 20% hydrogen in the gas network. By understanding the behaviour of HE in these materials, it becomes possible to establish safe design principles for effective implementation.

3.7.5 Factors affecting hydrogen embrittlement in national gas network

Given hydrogen's ability to permeate metal surfaces readily, certain metal pipes utilized for natural gas transportation may undergo degradation upon exposure to hydrogen, particularly under high temperatures and pressures. This phenomenon can result in cracking or embrittlement of these pipelines. Some of these factors are explained below.

3.7.5.1 Presence of hydrogen in the network

One critical factor influencing hydrogen embrittlement (HE) within the gas network is the presence of hydrogen [128]. The presence of hydrogen in gas mixtures significantly affects embrittlement. Synthetic natural gas produced from coal gasification, as well as biogas and landfill gas, contains hydrogen by nature. While most of the hydrogen is unintentionally present in the distribution network system, this study focuses on situations where hydrogen is intentionally introduced into the network and mixed with natural gas to minimize the carbon footprint. Since these gases are blended with traditional natural gas for distribution to customers, it is crucial to assess the risk of hydrogen embrittlement in pipeline materials.

3.7.5.2 Pipeline material variables

The choice of steel alloy used in the pipelines is critical. Diverse steel alloys display differing degrees of susceptibility to hydrogen embrittlement. Therefore, assessing the mechanical properties of both base metals and weld metals is imperative [128,129]. Other material variables also play a critical role in influencing the susceptibility of metals to hydrogen embrittlement (HE) within hydrogen gas containment components [130]. Examples of such variables include the nickel content in austenitic stainless steels, material strength, and the presence of welds. Austenitic steels with higher nickel content, for instance, demonstrate greater resistance to HE and can endure a wider range of stress and temperature conditions. Conversely, materials with high strength are more prone to HE and exhibit resistance within a narrower range of stress and temperature levels. Additionally,

austenitic steels with lower nickel content are particularly vulnerable to HE within a narrower range of stress and temperature conditions. Understanding these material variables is essential for selecting suitable materials and designing structures to mitigate the risks associated with HE in engineering applications.

3.7.5.3 Environmental variables

Environmental factors exert a notable influence on hydrogen embrittlement (HE) in metals utilized within hydrogen gas containment components [130]. Temperature and hydrogen gas pressure are two pivotal environmental variables that can significantly affect the susceptibility of the pipeline materials to HE [128,129]. Generally, HE is more likely to occur at near-ambient temperatures, while its occurrence becomes less probable at cryogenic or elevated temperatures. Moreover, higher hydrogen gas pressure increases the likelihood of HE manifestation. In addition, corrosion weakens the material and enhances hydrogen penetration thereby leading to embrittlement.

3.7.5.4 Mechanical variables

The primary mechanical variables influencing hydrogen embrittlement (HE) in metals within hydrogen gas containment components include the nature of stress and its magnitude. Specifically, the distinction between constant stress and cyclic stress, along with the amplitude of these stresses, plays a crucial role. Higher levels of both constant stress and cyclic stress amplitudes typically heighten the likelihood of HE occurrence, whereas lower stress levels may reduce this susceptibility [129,130].

3.7.5.5 Exposure time and pipeline age

Exposure time to hydrogen is a critical factor influencing embrittlement. Prolonged exposure heightens the risk of hydrogen-induced damage. Moreover, the age of pipelines is also a significant consideration. Older pipelines may exhibit increased susceptibility due to material degradation over time [128].

3.8 Chapter summary and feedforward

This chapter has provided a comprehensive review of the fundamental aspects of HE. The mechanisms of hydrogen embrittlement were examined and the likely mechanical damage on the properties of these metals, highlighting the potential degradation of metal pipes when exposed to hydrogen. With a mastery of these concepts therefore, the focus of this PhD research will shift towards studying the changes occurring in the mechanical properties of metals when they are subjected to hydrogen environment. The subsequent chapter will

delve into the experimental setup devised to investigate the selected metals, and in particular the changes in their fatigue properties resulting from soaking them in a hydrogen environment. This will encompass the selection of materials, details of the experimental setup, and the results that were obtained by following the standard experimental protocols outlined.

3.9 References

[1] T. Graham, On the occlusion of hydrogen gas by metals, Proc. R. Soc. London. 16 (1868) 422–427. https://doi.org/10.1098/rspl.1867.0090.

[2] Y.I. Archakov, I.D. Grebeshkova, Nature of hydrogen embrittlement of steel, Met. Sci. Heat Treat. 27 (1985) 555–562. https://doi.org/10.1007/BF00699349.

[3] Y.S. Chen, C. Huang, P.Y. Liu, H.W. Yen, R. Niu, P. Burr, K.L. Moore, E. Martínez-Pañeda, A. Atrens, J.M. Cairney, Hydrogen trapping and embrittlement in metals – A review, Int. J. Hydrogen Energy. (2024). https://doi.org/10.1016/j.ijhydene.2024.04.076.

[4] O. Barrera, D. Bombac, Y. Chen, T.D. Daff, E. Galindo-Nava, P. Gong, D. Haley, R. Horton, I. Katzarov, J.R. Kermode, C. Liverani, M. Stopher, F. Sweeney, Understanding and mitigating hydrogen embrittlement of steels: a review of experimental, modelling and design progress from atomistic to continuum, J. Mater. Sci. 53 (2018) 6251–6290. https://doi.org/10.1007/s10853-017-1978-5.

[5] P.C. Okonkwo, E.M. Barhoumi, I. Ben Belgacem, I.B. Mansir, M. Aliyu, W. Emori, P.C. Uzoma, W.H. Beitelmal, E. Akyüz, A.B. Radwan, R.A. Shakoor, A focused review of the hydrogen storage tank embrittlement mechanism process, Int. J. Hydrogen Energy. 48 (2023) 12935–12948. https://doi.org/10.1016/j.ijhydene.2022.12.252.

[6] S.K. Dwivedi, M. Vishwakarma, Hydrogen embrittlement in different materials: A review, Int. J. Hydrogen Energy. 43 (2018) 21603–21616. https://doi.org/10.1016/j.ijhydene.2018.09.201.

[7] E. Ohaeri, U. Eduok, J. Szpunar, Hydrogen related degradation in pipeline steel: A review, Int. J. Hydrogen Energy. 43 (2018) 14584–14617. https://doi.org/10.1016/j.ijhydene.2018.06.064.

[8] D. Sobola, R. Dallaev, Exploring Hydrogen Embrittlement: Mechanisms, Consequences, and Advances in Metal Science, Energies. 17 (2024) 2972. https://doi.org/10.3390/en17122972.

[9] S.W. Ooi, T.I. Ramjaun, C. Hulme-Smith, R. Morana, M. Drakopoulos, H.K.D.H. Bhadeshia, Designing steel to resist hydrogen embrittlement Part 2–precipitate characterisation, Mater. Sci. Technol. (United Kingdom). 34 (2018) 1747–1758. https://doi.org/10.1080/02670836.2018.1496536.

[10] T.P. Perng, J.K. Wu, A brief review note on mechanisms of hydrogen entry into metals, Mater. Lett. 57 (2003) 3437–3438. https://doi.org/10.1016/S0167-577X(03)00095-8.

[11] H. Kasai, A.A.B. Padama, B. Chantaramolee, R.L. Arevalo, Behavior of Hydrogen and Hydrogen-Containing Molecules on Metal Surfaces, in: 2020: pp. 31–72. https://doi.org/10.1007/978-981-15-6994-4_2.

[12] J.A. Lee, Hydrogen Embrittlement, 2016. http://www.sti.nasa.gov.

[13] A. Pundt, R. Kirchheim, Hydrogen in metals: Microstructural aspects, Annu. Rev. Mater. Res. 36 (2006) 555–608. https://doi.org/10.1146/annurev.matsci.36.090804.094451.

[14] H. Grabert, H. Wipf, Tunneling of Hydrogen in Metals, 1990.

[15] J.M. Matxain, M.A. Huertos, Hydrogen Tunneling in Stoichiometric and Catalytic Reactions involving Transition Metals, ChemCatChem. 15 (2023). https://doi.org/10.1002/cctc.202300962.

[16] E. Fallahmohammadi, G. Fumagalli, P. Di Milano, F. Maria, B. Politecnico, D. Milano, E. Fallahmohammadi, G. Fumagalli, G. Re, F. Bolzoni, L. Lazzari, Study on hydrogen diffusion in pipeline steels, 2011. https://www.researchgate.net/publication/236325746.

[17] Q. Li, H. Ghadiani, V. Jalilvand, T. Alam, Z. Farhat, M.A. Islam, Hydrogen Impact: A Review on Diffusibility, Embrittlement Mechanisms, and Characterization, Materials (Basel). 17 (2024). https://doi.org/10.3390/ma17040965.

[18] X. Li, X. Ma, J. Zhang, E. Akiyama, Y. Wang, X. Song, Review of Hydrogen Embrittlement in Metals: Hydrogen Diffusion, Hydrogen Characterization, Hydrogen Embrittlement Mechanism and Prevention, Acta Metall. Sin. (English Lett. 33 (2020) 759–773. https://doi.org/10.1007/s40195-020-01039-7.

[19] H.J. Wan, X.Q. Wu, H.L. Ming, J.Q. Wang, E.H. Han, Effects of Hydrogen Charging Time and Pressure on the Hydrogen Embrittlement Susceptibility of X52 Pipeline Steel Material, Acta Metall. Sin. (English Lett. 37 (2024) 293–307. https://doi.org/10.1007/s40195-023-01625-5.

[20] F. Ustolin, N. Paltrinieri, F. Berto, Loss of integrity of hydrogen technologies: A critical review, Int. J. Hydrogen Energy. 45 (2020) 23809–23840. https://doi.org/10.1016/j.ijhydene.2020.06.021.

[21] E.B. Shone, 'Corrosion in the petrochemical industry';, Br. Corros. J. 30 (1995) 190–190. https://doi.org/10.1179/bcj.1995.30.3.190.

[22] J.P. Hirth, H.H. Johnson, Hydrogen Problems in Energy Related Technology, Corrosion. 32 (1976) 3–26. https://doi.org/10.5006/0010-9312-32.1.3.

[23] X. Wu, H. Zhang, M. Yang, W. Jia, Y. Qiu, L. Lan, From the perspective of new technology of blending hydrogen into natural gas pipelines transmission: Mechanism, experimental study, and suggestions for further work of hydrogen embrittlement in high-strength pipeline steels, Int. J. Hydrogen Energy. 47 (2022) 8071–8090. https://doi.org/10.1016/j.ijhydene.2021.12.108.

[24] V.A. Polyanskiy, B.K. Alexexander, Advances in Hydrogen Embrittlement Study, Springer, St Petersburb, 2020.

[25] X. Li, X. Ma, J. Zhang, E. Akiyama, Y. Wang, X. Song, Review of Hydrogen Embrittlement in Metals: Hydrogen Diffusion, Hydrogen Characterization, Hydrogen Embrittlement Mechanism and Prevention, Acta Metall. Sin. (English Lett. 33 (2020) 759–773. https://doi.org/10.1007/s40195-020-01039-7.

[26] J.R. Buckley, D. Hardie, Effect of low temperature on resistance of stable austenitic steel to embrittlement by hydrogen, Mater. Sci. Technol. (United Kingdom). 9 (1993) 259–263. https://doi.org/10.1179/mst.1993.9.3.259.

[27] D. Eliezer, The behaviour of 316L stainless steel in hydrogen, 1983.

[28] T. Kanezaki, C. Narazaki, Y. Mine, S. Matsuoka, Y. Murakami, Effects of hydrogen on fatigue crack growth behavior of austenitic stainless steels, Int. J. Hydrogen Energy. 33 (2008) 2604–2619. https://doi.org/10.1016/j.ijhydene.2008.02.067.

[29] G. Schuster, C. Altstetter, Fatigue of stainless steel in hydrogen, Metall. Trans. A. 14 (1983) 2085–2090. https://doi.org/10.1007/BF02662375.

[30] S. Papula, J. Talonen, H. Hänninen, Effect of residual stress and strain-induced α′-martensite on delayed cracking of metastable austenitic stainless steels, Metall. Mater. Trans. A Phys. Metall. Mater. Sci. 45 (2014) 1238–1246. https://doi.org/10.1007/s11661-013-2090-3.

[31] U.M. Gadade, P.D. Maskar, Study of Different Factors Affecting T Bolt Failure of Band Clamp, 10 (2021) 77–84.

[32] M. Devanathan, Z. Stachurski, The adsorption and diffusion of electrolytic hydrogen in palladium, Proc. R. Soc. London. Ser. A. Math. Phys. Sci. 270 (1962) 90–102. https://doi.org/10.1098/rspa.1962.0205.

[33] J.C. Meyer, C.O. Girit, M.F. Crommie, A. Zettl, Imaging and dynamics of light atoms and molecules on graphene, Nature. 454 (2008) 319–322. https://doi.org/10.1038/nature07094.

[34] M.P. Puls, Review of the thermodynamic basis for models of delayed hydride cracking rate in zirconium alloys, J. Nucl. Mater. 393 (2009) 350–367. https://doi.org/10.1016/j.jnucmat.2009.06.022.

[35] R. Ishikawa, E. Okunishi, H. Sawada, Y. Kondo, F. Hosokawa, E. Abe, Direct imaging of hydrogen-atom columns in a crystal by annular bright-field electron microscopy, Nat. Mater. 10 (2011) 278–281. https://doi.org/10.1038/nmat2957.

[36] B. Malard, B. Remy, C. Scott, A. Deschamps, J. Chêne, T. Dieudonné, M.H. Mathon, Hydrogen trapping by VC precipitates and structural defects in a high strength Fe–Mn–C steel studied by small-angle neutron scattering, Mater. Sci. Eng. A. 536 (2012) 110–116. https://doi.org/10.1016/j.msea.2011.12.080.

[37] M. Ohnuma, J. Suzuki, F.-G. Wei, K. Tsuzaki, Direct observation of hydrogen trapped by NbC in steel using small-angle neutron scattering, Scr. Mater. 58 (2008) 142–145. https://doi.org/10.1016/j.scriptamat.2007.09.026.

[38] I.M. Robertson, P. Sofronis, A. Nagao, M.L. Martin, S. Wang, D.W. Gross, K.E. Nygren, Hydrogen Embrittlement Understood, Metall. Mater. Trans. B Process Metall. Mater. Process. Sci. 46 (2015) 1085–1103. https://doi.org/10.1007/s11663-015-0325-y.

[39] A. Behvar, M. Haghshenas, M.B. Djukic, Hydrogen embrittlement and hydrogen-induced crack initiation in additively manufactured metals: A critical review on mechanical and cyclic loading, Int. J. Hydrogen Energy. 58 (2024) 1214–1239. https://doi.org/10.1016/j.ijhydene.2024.01.232.

[40] S. Lynch, Hydrogen embrittlement phenomena and mechanisms, Corros. Rev. 30 (2012) 105–123. https://doi.org/10.1515/corrrev-2012-0502.

[41] M.R. Louthan, Hydrogen embrittlement of metals: A primer for the failure analyst, J. Fail. Anal. Prev. 8 (2008) 289–307. https://doi.org/10.1007/s11668-008-9133-x.

[42] B.N. Popov, J.-W. Lee, M.B. Djukic, Hydrogen Permeation and Hydrogen-Induced Cracking, in Handb. Environ. Degrad. Mater., Elsevier, 2018: pp. 133–162. https://doi.org/10.1016/B978-0-323-52472-8.00007-1.

[43] M. Wasim, M.B. Djukic, External corrosion of oil and gas pipelines: A review of failure mechanisms and predictive preventions, J. Nat. Gas Sci. Eng. 100 (2022) 104467. https://doi.org/10.1016/j.jngse.2022.104467.

[44] T. Shinko, G. Hénaff, D. Halm, G. Benoit, G. Bilotta, M. Arzaghi, Hydrogen-affected fatigue crack propagation at various loading frequencies and gaseous hydrogen pressures in commercially pure iron, Int. J. Fatigue. 121 (2019) 197–207. https://doi.org/10.1016/j.ijfatigue.2018.12.009.

[45] T.S. Sudarshan, M.R. Louthan, T.A. Place, H.H. Mabie, Role of Hydrogen and Humidity in the Torsional Fatigue of Aluminum Alloy 2024-T351, 1985.

[46] T. An, S. Zhang, M. Feng, B. Luo, S. Zheng, L. Chen, L. Zhang, Synergistic action of hydrogen gas and weld defects on fracture toughness of X80 pipeline steel, Int. J. Fatigue. 120 (2019) 23–32. https://doi.org/10.1016/j.ijfatigue.2018.10.021.

[47] Y. Ogawa, H. Matsunaga, J. Yamabe, M. Yoshikawa, S. Matsuoka, Unified evaluation of hydrogen-induced crack growth in fatigue tests and fracture toughness tests of carbon steel, Int. J. Fatigue. 103 (2017) 223–233. https://doi.org/10.1016/j.ijfatigue.2017.06.006.

[48] T. Michler, J. Naumann, J. Wiebesiek, E. Sattler, Influence of frequency and wave form on S-N fatigue of commercial austenitic stainless steels with different nickel contents in inert gas and in high pressure gaseous hydrogen, Int. J. Fatigue. 96 (2017) 67–77. https://doi.org/10.1016/j.ijfatigue.2016.11.026.

[49] J.A. Ronevich, B.P. Somerday, C.W. San Marchi, Effects of microstructure banding on hydrogen assisted fatigue crack growth in X65 pipeline steels, Int. J. Fatigue. 82 (2016) 497–504. https://doi.org/10.1016/j.ijfatigue.2015.09.004.

[50] G. Pluvinage, J. Capelle, M.H. Meliani, Pipe networks transporting hydrogen pure or blended with natural gas, design and maintenance, Eng. Fail. Anal. 106 (2019). https://doi.org/10.1016/j.engfailanal.2019.104164.

[51] T. Michler, J. Naumann, E. Sattler, Influence of high pressure gaseous hydrogen on S-N fatigue in two austenitic stainless steels, Int. J. Fatigue. 51 (2013) 1–7. https://doi.org/10.1016/j.ijfatigue.2013.01.010.

[52] A. MacAdre, H. Yano, S. Matsuoka, J. Furtado, The effect of hydrogen on the fatigue life of Ni-Cr-Mo steel envisaged for use as a storage cylinder for a 70 MPa hydrogen station, Int. J. Fatigue. 33 (2011) 1608–1619. https://doi.org/10.1016/j.ijfatigue.2011.07.007.

[53] N. Nagaishi, M. Yoshikawa, S. Okazaki, J. Yamabe, F. Yoshida, H. Matsunaga, Evaluation of fatigue life and fatigue limit of circumferentially-notched Type 304 stainless steel in air and hydrogen gas based on crack-growth property and cyclic stress-strain response, Eng. Fract. Mech. 215 (2019) 164–177. https://doi.org/10.1016/j.engfracmech.2019.05.005.

[54] M. Kubota, M. Fukuda, R. Komoda, Effect of Hydrogen on Fatigue Limit of SCM435 Low-Alloy Steel, Procedia Struct. Integr. 19 (2019) 520–527.

https://doi.org/10.1016/j.prostr.2019.12.056.

[55] M. Kubota, N. Noyama, C. Sakae, Y. Kondo, Fretting fatigue in hydrogen gas, Tribol. Int. 39 (2006) 1241–1247. https://doi.org/10.1016/j.triboint.2006.02.014.

[56] R. Komoda, M. Kubota, Y. Kondo, J. Furtado, Effect of oxygen addition on fretting fatigue strength in hydrogen of JIS SUS304 stainless steel, Tribol. Int. 76 (2014) 92–99. https://doi.org/10.1016/j.triboint.2014.02.025.

[57] M. Kubota, K. Kuwada, Y. Tanaka, Y. Kondo, Mechanism of reduction of fretting fatigue limit caused by hydrogen gas in SUS304 austenitic stainless steel, in: Tribol. Int., 2011: pp. 1495–1502. https://doi.org/10.1016/j.triboint.2010.11.004.

[58] H. Matsunaga, M. Yoshikawa, R. Kondo, J. Yamabe, S. Matsuoka, Slow strain rate tensile and fatigue properties of Cr-Mo and carbon steels in a 115 MPa hydrogen gas atmosphere, Int. J. Hydrogen Energy. 40 (2015) 5739–5748. https://doi.org/10.1016/j.ijhydene.2015.02.098.

[59] J. Capelle, J. Gilgert, G. Pluvinage, A fatigue initiation parameter for gas pipe steel submitted to hydrogen absorption, Int. J. Hydrogen Energy. 35 (2010) 833–843. https://doi.org/10.1016/j.ijhydene.2009.10.063.

[60] G. Schauer, J. Roetting, M. Hahn, S. Schreijaeg, M. Bacher-Höchst, S. Weihe, Influence of Gaseous Hydrogen on Fatigue Behavior of Ferritic Stainless Steel - A Fatigue-life Estimation, in: Procedia Eng., Elsevier Ltd, 2015: pp. 362–378. https://doi.org/10.1016/j.proeng.2015.12.669.

[61] H. Uyama, M. Nakashima, K. Morishige, Y. Mine, Y. Murakami, Effects of hydrogen charge on microscopic fatigue behaviour of annealed carbon steels, Fatigue Fract. Eng. Mater. Struct. 29 (2006) 1066–1074. https://doi.org/10.1111/j.1460-2695.2006.01069.x.

[62] M. NAKATANI, K. MINOSHIMA, Influence of activation energy and sensitivity to hydrogen embrittlement on fatigue strength degradation by irreversible hydrogen in high-strength steels, Fatigue Fract. Eng. Mater. Struct. 34 (2011) 363–373. https://doi.org/10.1111/j.1460-2695.2010.01526.x.

[63] T. Neeraj, R. Srinivasan, J. Li, Hydrogen embrittlement of ferritic steels: Observations on deformation microstructure, nanoscale dimples and failure by nanovoiding, Acta Mater. 60 (2012) 5160–5171. https://doi.org/10.1016/j.actamat.2012.06.014.

[64] Y.J. Jia, W.Z. Han, Mechanisms of Hydride Nucleation, Growth, Reorientation, and Embrittlement in Zirconium: A Review, Materials (Basel). 16 (2023). https://doi.org/10.3390/ma16062419.

[65] D.S. Shih, I.M. Robertson, H.K. Birnbaum, Hydrogen embrittlement of α titanium: In situ tem studies, Acta Metall. 36 (1988) 111–124. https://doi.org/10.1016/0001-6160(88)90032-6.

[66] N. Narita, H.K. Birnbaum, ON THE ROLE OF PHASE TRANSITIONS IN THE HYDROGEN EMBRITTLEMENT OF STAINLESS STEELS, 1980.

[67] A. Barnoush, H. Vehoff, Recent developments in the study of hydrogen embrittlement: Hydrogen effect on dislocation nucleation, Acta Mater. 58 (2010) 5274–5285. https://doi.org/10.1016/j.actamat.2010.05.057.

[68] M.L. Jokl, V. Vxtek, C.J. Mcmahon, A MICROSCOPIC THEORY OF BRITTLE FRACTURE IN DEFORMABLE SOLIDS: A RELATION BETWEEN IDEAL WORK TO FRACTURE AND PLASTIC WORK, n.d.

[69] T. Neeraj, R. Srinivasan, J. Li, Hydrogen embrittlement of ferritic steels: Observations on deformation microstructure, nanoscale dimples and failure by nanovoiding, Acta Mater. 60 (2012) 5160–5171. https://doi.org/10.1016/j.actamat.2012.06.014.

[70] S. Shen, X. Song, Q. Li, X. Li, R. Zhu, G. Yang, Effect of CrxCy–NiCr coating on the hydrogen embrittlement of 17-4 PH stainless steel using the smooth bar tensile test, J. Mater. Sci. 54 (2019) 7356–7368. https://doi.org/10.1007/s10853-019-03356-4.

[71] J. Liu, M. Zhao, L. Rong, Overview of hydrogen-resistant alloys for high-pressure hydrogen environment: on the hydrogen energy structural materials, Clean Energy. 7 (2023) 99–115. https://doi.org/10.1093/ce/zkad009.

[72] A. Turnbull, MODELLING OF ENVIRONMENT ASSISTED CRACKING, 1993.

[73] X. Xing, W. Chen, H. Zhang, Prediction of crack propagation under cyclic loading based on hydrogen diffusion, Mater. Lett. 152 (2015) 86–89. https://doi.org/10.1016/j.matlet.2015.03.045.

[74] P. Hołobut, Fatigue crack growth model for a thin steel plate containing hydrogen, Int. J. Fatigue. 32 (2010) 1895–1903. https://doi.org/10.1016/j.ijfatigue.2010.06.005.

[75] B.T. Lu, Crack growth model for pipeline steels exposed to near-neutral pH groundwater, Fatigue Fract. Eng. Mater. Struct. 36 (2013) 660–669. https://doi.org/10.1111/ffe.12033.

[76] H.K. Birnbaum, P. Sofronis, Hydrogen-enhanced localized plasticity-a mechanism for hydrogen-related fracture, 1994.

[77] I.M. Robertson, The effect of hydrogen on dislocation dynamics, n.d. www.elsevier.com/locate/engfracmech.

[78] P.J. Ferreira, I.M. Robertson, H.K. Birnbaum, HYDROGEN EFFECTS ON THE INTERACTION BETWEEN DISLOCATIONS, n.d.

[79] S. Mitomi, H. Iwaoka, S. Hirosawa, Hydrogen Embrittlement Mechanism of Ultrafine-grained Iron with Different Grain Sizes, ISIJ Int. 63 (2023) ISIJINT-2022-562. https://doi.org/10.2355/isijinternational.ISIJINT-2022-562.

[80] M. Nagumo, Hydrogen related failure of steels - A new aspect, Mater. Sci. Technol. 20 (2004) 940–950. https://doi.org/10.1179/026708304225019687.

[81] K. Sakaki, T. Kawase, M. Hirato, M. Mizuno, H. Araki, Y. Shirai, M. Nagumo, The effect of hydrogen on vacancy generation in iron by plastic deformation, Scr. Mater. 55 (2006) 1031–1034. https://doi.org/10.1016/j.scriptamat.2006.08.030.

[82] R.B. Mclellan, Z.R. Xu, HYDROGEN-INDUCED VACANCIES IN THE IRON LATTICE, 1997.

[83] S.P. Lynch, A fractographic study of hydrogen-assisted cracking and liquid-metal

embrittlement in nickel, 1986.

[84] S.P. Lynch, Metallographic contributions to understanding mechanisms of environmentally assisted cracking, Metallography. 23 (1989) 147–171. https://doi.org/10.1016/0026-0800(89)90016-5.

[85] S.P. Lynch, ENVIRONMENTALLY ASSISTED CRACKING: OVERVIEW OF EVIDENCE FOR AN ADSORPTION-INDUCED LOCALISED-SLIP PROCESS, 1988.

[86] N. Eliaz, L. Banks-Sills, D. Ashkenazi, R. Eliasi, Modeling failure of metallic glasses due to hydrogen embrittlement in the absence of external loads, Acta Mater. 52 (2004) 93–105. https://doi.org/10.1016/j.actamat.2003.08.029.

[87] D.S. Bae, C.E. Sung, H.J. Bang, S.P. Lee, J.K. Lee, I.S. Son, Y.R. Cho, U.B. Baek, S.H. Nahm, Effect of highly pressurized hydrogen gas charging on the hydrogen embrittlement of API X70 steel, Met. Mater. Int. 20 (2014) 653–658. https://doi.org/10.1007/s12540-014-4010-5.

[88] J.G. Sezgin, C. Bosch, A. Montouchet, G. Perrin, K. Wolski, Modelling of hydrogen induced pressurization of internal cavities, Int. J. Hydrogen Energy. 42 (2017) 15403–15414. https://doi.org/10.1016/j.ijhydene.2017.04.106.

[89] R. Fernández-Sousa, C. Betegón, E. Martínez-Pañeda, Analysis of the influence of microstructural traps on hydrogen assisted fatigue, Acta Mater. 199 (2020) 253–263. https://doi.org/10.1016/j.actamat.2020.08.030.

[90] L. Vergani, C. Colombo, G. Gobbi, F.M. Bolzoni, G. Fumagalli, Hydrogen Effect on Fatigue Behavior of a Quenched&tempered Steel, Procedia Eng. 74 (2014) 468–471. https://doi.org/10.1016/j.proeng.2014.06.299.

[91] X. Xing, Z. Pang, H. Zhang, J. Liu, G. Cui, Study of temperature effect on hydrogen embrittlement in X70 pipeline steel, Corros. Sci. 230 (2024). https://doi.org/10.1016/j.corsci.2024.111939.

[92] Q. Liu, A. Atrens, A critical review of the influence of hydrogen on the mechanical properties of medium-strength steels, Corros. Rev. 31 (2013) 85–103. https://doi.org/10.1515/corrrev-2013-0023.

[93] H. Barthélémy, Effects of pressure and purity on the hydrogen embrittlement of steels, Int. J. Hydrogen Energy. 36 (2011) 2750–2758. https://doi.org/10.1016/j.ijhydene.2010.05.029.

[94] B.P. Somerday, J.A. Campbell, K.L. Lee, J.A. Ronevich, C. San Marchi, Enhancing safety of hydrogen containment components through materials testing under in-service conditions, Int. J. Hydrogen Energy. 42 (2017) 7314–7321. https://doi.org/10.1016/j.ijhydene.2016.04.189.

[95] L. Zhang, W. Cao, K. Lu, Z. Wang, Y. Xing, Y. Du, M. Lu, Effect of the cathodic current density on the sub-surface concentration of hydrogen in X80 pipeline steels under cathodic protection, Int. J. Hydrogen Energy. 42 (2017) 3389–3398. https://doi.org/10.1016/j.ijhydene.2016.09.214.

[96] I.M. Robertson, P. Sofronis, A. Nagao, M.L. Martin, S. Wang, D.W. Gross, K.E. Nygren, Hydrogen Embrittlement Understood, Metall. Mater. Trans. B Process Metall. Mater. Process. Sci. 46 (2015) 1085–1103. https://doi.org/10.1007/s11663-

015-0325-y.

[97] S. Wu, Z. Gao, D.-H. Xia, M. Wu, Y. Liu, W. Hu, Effect of temperature on process and kinetic parameters of the hydrogen evolution reaction of X80 under CP, Anti-Corrosion Methods Mater. 68 (2021) 219–228. https://doi.org/10.1108/ACMM-12-2020-2413.

[98] A.G. Oshchepkov, A. Bonnefont, V.N. Parmon, E.R. Savinova, On the effect of temperature and surface oxidation on the kinetics of hydrogen electrode reactions on nickel in alkaline media, Electrochim. Acta. 269 (2018) 111–118. https://doi.org/10.1016/j.electacta.2018.02.106.

[99] E.G. Ohaeri, W. Qin, J. Szpunar, A critical perspective on pipeline processing and failure risks in hydrogen service conditions, J. Alloys Compd. 857 (2021) 158240. https://doi.org/10.1016/j.jallcom.2020.158240.

[100] T. Ohmisawa, S. Uchiyama, M. Nagumo, Detection of hydrogen trap distribution in steel using a microprint technique, J. Alloys Compd. 356–357 (2003) 290–294. https://doi.org/10.1016/S0925-8388(03)00355-4.

[101] J. Gilberto Godinez Salcedo, J. Gibran Arenas Salcedo, I. Xicotencatl García Pérez, Hydrogen Permeation in Carbon Steels, in: Corros. Eng. - Recent Break. Innov. Solut., IntechOpen, 2024. https://doi.org/10.5772/intechopen.1005310.

[102] R. Zhang, C. Yuan, C. Liu, C. Wang, X. Xu, J. Zhang, Y. Li, Experimental and molecular dynamics study of the hydrogen embrittlement behavior of X52 steel: Analysis of abnormal hydrogen embrittlement susceptibility, Int. J. Hydrogen Energy. 83 (2024) 987–1002. https://doi.org/10.1016/j.ijhydene.2024.08.183.

[103] Q. Hu, Y. Li, Y.F. Cheng, Distribution of hydrogen atoms at metallurgical microphases of X52 pipeline steel studied by scanning Kelvin probe force microscopy and finite element modelling, Surf. Sci. Technol. 1 (2023) 1–14. https://doi.org/10.1007/s44251-023-00001-w.

[104] X. Xu, R. Zhang, C. Wang, C. Liu, J. Zhang, Y. Li, Experimental study on the temperature dependence of gaseous hydrogen permeation and hydrogen embrittlement susceptibility of X52 pipeline steel, Eng. Fail. Anal. 155 (2024) 107746. https://doi.org/10.1016/j.engfailanal.2023.107746.

[105] D. Rudomilova, T. Prošek, G. Luckeneder, Techniques for investigation of hydrogen embrittlement of advanced high strength steels, Corros. Rev. 36 (2018) 413–434. https://doi.org/10.1515/corrrev-2017-0106.

[106] Z. Zhang, C. Li, J. Zhang, D. Zeng, L. Zhang, T. Shi, Hydrogen permeation behaviors of X52 pipeline steel in NACE a solution with saturated H2S/CO2, J. Wuhan Univ. Technol. Sci. Ed. 27 (2012) 657–661. https://doi.org/10.1007/s11595-012-0523-2.

[107] C. Zhou, X. Chen, Z. Wang, S. Zheng, X. Li, L. Zhang, Effects of environmental conditions on hydrogen permeation of X52 pipeline steel exposed to high H2S-containing solutions, Corros. Sci. 89 (2014) 30–37. https://doi.org/10.1016/j.corsci.2014.07.061.

[108] E. Koren, C. M. H. Hagen, D. Wang, X. Lu, R. Johnsen, J. Yamabe, Experimental comparison of gaseous and electrochemical hydrogen charging in X65 pipeline

steel using the permeation technique, Corros. Sci. 215 (2023) 111025. https://doi.org/10.1016/j.corsci.2023.111025.

[109] X. Feng, Y. Shi, W. Zhang, K. Volodymyr, Hydrogen Embrittlement Failure Behavior of Fatigue-Damaged Welded TC4 Alloy Joints, Crystals. 13 (2023). https://doi.org/10.3390/cryst13030512.

[110] H. Li, R. Niu, W. Li, H. Lu, J. Cairney, Y.S. Chen, Hydrogen in pipeline steels: Recent advances in characterization and embrittlement mitigation, J. Nat. Gas Sci. Eng. 105 (2022) 104709. https://doi.org/10.1016/j.jngse.2022.104709.

[111] C. Pandey, M.M. Mahapatra, P. Kumar, N. Saini, Some studies on P91 steel and their weldments, J. Alloys Compd. 743 (2018) 332–364. https://doi.org/10.1016/j.jallcom.2018.01.120.

[112] J.A. Ronevich, C.R. D'Elia, M.R. Hill, Fatigue crack growth rates of X100 steel welds in high pressure hydrogen gas considering residual stress effects, Eng. Fract. Mech. 194 (2018) 42–51. https://doi.org/10.1016/j.engfracmech.2018.02.030.

[113] M.G.M. de Carvalho, M.A. Lage, D. de Figueiredo Cavalcante, K.S. de Assis, A.L. Pinto, C. Labre, F.P. Alves, O.R. Mattos, Hydrogen embrittlement in dissimilar welded joints interfaces – Influence of manufacturing parameters and evaluation of methodologies, Corros. Sci. 224 (2023). https://doi.org/10.1016/j.corsci.2023.111506.

[114] J.A. Ronevich, B.P. Somerday, Z. Feng, Hydrogen accelerated fatigue crack growth of friction stir welded X52 steel pipe, Int. J. Hydrogen Energy. 42 (2017) 4259–4268. https://doi.org/10.1016/j.ijhydene.2016.10.153.

[115] V. Beaugrand, L.. Smith, M.F. Gittos, Subsea Dissimilar Joints: Failure Mechanisms and Opportunities for Mitigation, Corros. 2008. (2009) 1–9.

[116] AMI, Natural Gas Pipeline Welding Procedures for Orbital Systems, Eng. Dep. Arc Mach. Inc. (2023).

[117] Z. Feng, Y.C. Lim, Final/Technical/Report:// Flexible/Friction/Stir/Joining/Technology, Houston, 2015. http://www.ntis.gov/help/ordermethods.aspx%25.

[118] W. Dan, C. Tang, H. Shi, X. Wang, Study on Mechanical Behaviours and Microstructure Features of Q690 Steel Weldments with Various Electrochemical Hydrogen Charging Conditions, (2024) 1–21.

[119] J. Turola, R.B. Obara, A. Ferrarese, A.F. Albaneze, C. de Souza Cabezas, Microstructure of cast iron resistant to hydrogen embrittlement, in: 2024. https://doi.org/10.4271/2023-36-0063.

[120] P. Sahiluoma, Y. Yagodzinskyy, A. Forsström, H. Hänninen, S. Bossuyt, Hydrogen embrittlement of nodular cast iron, Mater. Corros. 72 (2021) 245–254. https://doi.org/10.1002/maco.202011682.

[121] G. Lv, M. Zhang, H. Zhang, Y. Su, Hydrogen diffusion and vacancy clusterization in iron, Int. J. Hydrogen Energy. 43 (2018) 15378–15385. https://doi.org/10.1016/j.ijhydene.2018.06.075.

[122] J. Turola, R.B. Obara, A. Ferrarese, A.F. Albaneze, C. De Souza Cabezas,

Microstructure of cast iron resistant to hydrogen embrittlement, SAE Tech. Pap. (2024). https://doi.org/10.4271/2023-36-0063.

[123] T. Yoshimoto, T. Matsuo, T. Ikeda, The effect of graphite size on hydrogen absorption and tensile properties of ferritic ductile cast iron, Procedia Struct. Integr. 14 (2019) 18–25. https://doi.org/10.1016/j.prostr.2019.05.004.

[124] K. Okumura, K. Motoyama, H. Matsunaga, Fatigue crack-growth properties of ductile cast iron in hydrogen gas with oxygen impurity at various temperatures, Eng. Fail. Anal. 158 (2024). https://doi.org/10.1016/j.engfailanal.2024.108012.

[125] H. Matsunaga, T. Usuda, K. Yanase, M. Endo, Ductility loss in Hydrogen-charged Ductile Cast Iron, Beijin, 2013.

[126] P. Sahiluoma, Y. Yagodzinskyy, A. Forsström, H. Hänninen, S. Bossuyt, Hydrogen embrittlement of nodular cast iron, Mater. Corros. 72 (2021) 245–254. https://doi.org/10.1002/maco.202011682.

[127] Hardwick D.A, Thompson A.W., Bernstein I.M., THE EFFECT OF COPPER CONTENT AND HEAT, Corros. Sci. 28 (1988) 1127–1137.

[128] C.M. Kim, Y.P. Kim, W.S. Kim, Influence of gaseous components and pressures on hydrogen embrittlement of natural gas pipeline, J. Mech. Sci. Technol. 31 (2017) 3691–3695. https://doi.org/10.1007/s12206-017-0711-2.

[129] K. Yang, Z. Zhao, A. Zhang, W. Yang, Q. Li, S. Zeng, G. Peng, Risk modelling of hydrogen-enriched natural gas on pipelines and gas-electric coupled systems, IET Energy Syst. Integr. (2023). https://doi.org/10.1049/esi2.12124.

[130] S.C. Marchi, B.. Somerday, Technical Reference for Hydrogen Compatibility of Materials, California, 2012.

Chapter 4

Statistical Analysis of Fatigue Data

The information in this chapter was published in the Probabilistic Engineering Mechanics journal, and is found at the following:

- E. Kufoin, L. Susmel, Quantitative review of probabilistic approaches to fatigue design in the medium cycle fatigue regime, Probabilistic Eng. Mech. (2024) 103589. https://doi.org/10.1016/j.probengmech.2024.103589.
- E.N. Kufoin, L. Susmel, On the parametric assessment of fatigue disparities, Probabilistic Eng. Mech. 77 (2024) 103651. https://doi.org/10.1016/j.probengmech.2024.103651.

4.1 Introduction

This chapter aims to review crucial concepts essential for conducting fatigue assessment under constant amplitude loading. Initially, it will address the uniaxial fatigue problem by examining parameters influencing the overall fatigue strength of engineering materials. It's important to note that these basic concepts will be reviewed not only from the perspective of theories based on continuum mechanics but also those rooted in linear-elastic fracture

mechanics. These concepts will serve as the foundation for post-processing the fatigue data sets generated from both soaked and uncharged specimens discussed in the previous chapter.

The second part of this chapter delves into critically evaluating the significance of observed differences in any given pair of fatigue datasets. The objective extends beyond mere observation. It uses statistical indicators of fatigue resistance and its variation can be quantified by analysing various sets of fatigue data related to a particular material or test condition. Given the increasing availability of fatigue data sources, these methods aid designers in extracting fatigue properties by consolidating multiple data sets that might lack significant insights individually due to their limited scope. The process involves collecting fatigue data sets from similar populations (test programs) and assessing parameters such as variance, slope, and intercept.

Central to this PhD investigation lies the application of statistical parametric analysis, a robust methodology specifically employed for comparisons between two or more fatigue datasets as explained above. This analytical approach is designed to perceive whether observed differences in the fatigue data sets generated in this study are statistically significant or merely the result of random variation. The focal point here is to provide a comprehensive understanding of the significance or insignificance of disparities between fatigue data sets from charged and uncharged specimens used in this research. Through the use of statistical parametric analysis, therefore, this research not only ensures a rigorous examination of observed differences but also establishes a quantitative basis for evaluating the reliability of these disparities.

In addition to comparing disparities amongst fatigue data sets, and in alignment with the ongoing effort to advance the application of statistical significance tests, this chapter also seeks to address questions such as the accuracy of statistical methods in identifying the notch root radius from fatigue data (using statistics only) and, if so, how the variation in this radius influences the fatigue properties of the material. The primary focus of this inquiry centres on the development and application of statistical approaches to identify the notch root radius from fatigue data, with the ultimate goal of understanding the correlation between the identified variations in radius and their subsequent impact on fatigue properties.

It is worth mentioning also that merging fatigue data sets has consistently been a strategy to acquire more data to increase the reliability of fatigue assessment and design in the industry [1–3]. This also addresses the time and cost challenges associated with conducting numerous fatigue experiments [4,5]. This contribution adds depth to the dynamic field of fatigue data analysis, providing valuable insights for engineers and researchers as they endeavour to optimize designs and improve material reliability under cyclic loading conditions. By doing so, conclusions drawn from performed fatigue tests can be made with confidence based on a predetermined level of significance

4.2 Overview of the Wöhler diagram

Wöhler stands as a pioneering figure in the exploration of fatigue phenomena, beginning his investigation with a focus on train axles. He aimed to work out the causes behind axle failures occurring under cyclic loads, which were notably lower than the material's static strength. A few years later, experimental data from Wöhler's works were used on a linear scale to draw the relationship between his investigated quantities. This graph depicts the stress range on the y-axis and the number of cycles to failure on the x-axis. These diagrams, now recognized as Wöhler curves, have evolved and remain integral in predicting fatigue lifetime. The Wöhler curve serves as a potent tool, explaining the relationship between applied stress amplitude and the material's endurance over cycles. Constructing a Wöhler curve entails conducting a series of tests under identical load ratios for the same material but at varying stress amplitudes, resulting in a log-log graph where the curve appears as a straight line, governed by the renowned Wöhler equation which will be described later.

In conventional plain specimens subjected to a dynamic stress level S, for a load ratio, R, fatigue failure eventually occurs after a certain number of cycles N_f determined by the material's fatigue properties [6,7]. Decreasing the amplitude of the applied loading results in an increased number of cycles to failure. By subjecting numerous specimens to various stress levels ($S = \sigma_i,\ i = 1 \ldots n,$ with n being the total number of specimens), an experimental dataset ($\sigma_i, N_{f,i}$) is obtained, which in turn is used to construct the Wöhler curves otherwise known as the S-N curve for the material under examination [2,7]. This diagram is typically represented on a log-log scale and plots the number of cycles to failure (N_f) on the abscissa and the amplitude of the applied stress on the ordinate as shown in the Figure 4-1 below.

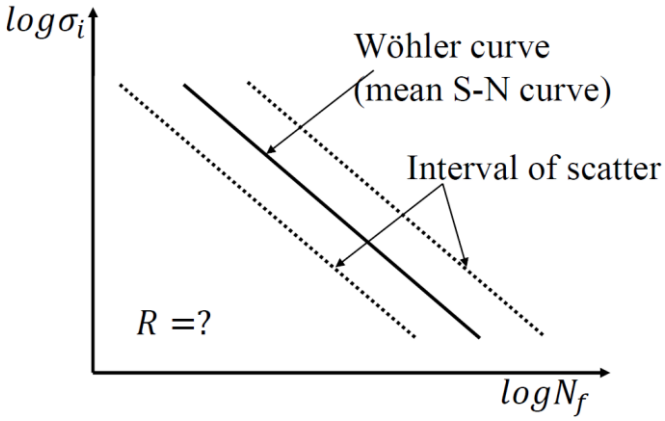

Figure 4-1 The Wöhler diagram

The Wöhler curve also demonstrates that fatigue results consistently exhibit a certain level of scatter, indicating variability in experimental data [6–9]. Therefore, it is crucial to post-process experimental data meticulously to establish a dependable reference fatigue curve. The range of scatter can be quantified using statistical concepts that define the probability of failure for each curve, a topic that will be addressed in the subsequent sections of this chapter. To quantify the fatigue behaviour of a material, therefore, a Wöhler diagram is required. While many approaches have been employed in the industry, the approach adopted by any industry is dependent on the industry, regulation, and application.

4.2.1 The Wöhler curve across different fatigue regimes

The shape of the Wöhler curve is dependent on the specific fatigue regime under which the investigation was carried out [10]. These regimes include the high-cycle fatigue (HCF) regime, characterized by a vast number of cycles usually considered to be greater than 10^3 cycles and threshold stress below which the material exhibits infinite life, the low-cycle fatigue (LCF) regime, typified by a finite number of cycles and a continual decline in fatigue life with increasing stress levels, often leading to plastic deformation and crack initiation [11,12]. Plastic deformation is dominant in the LCF regime where minor alterations in stress can induce significant changes in strain. The S-N curve in the LCF is either modelled by Coffin–Manson and Morrow model [11] or, under some stated considerations, the ASTM strain-energy approach [13]. A Weibull model can also be used as explained in Ref. [14].

There is also the medium cycle fatigue (MCF) regime which typically encompasses a range of load cycles from approximately 10^4 to 10^6 cycles. Stress levels experienced by materials in this regime are moderate, falling between those observed in the high cycle fatigue and

low cycle fatigue regimes. Unlike high cycle fatigue, MCF involves some degree of plastic deformation during each cycle. This plasticity contributes to the initiation and propagation of microscopic cracks within the material, eventually leading to failure. The behaviour observed in the MCF regime is crucial to understanding the endurance and fatigue life of materials subjected to cyclic loading conditions in various engineering applications. The behaviour in the MCF regime can be modelled using stress-based approaches like in linear regression analysis or by using the Basquin approach. Similar to the LCF, the Coffin–Manson strain–based–based approach can also be used in the MCF region. These approaches can be extended to the HCF regime where the plastic contribution to the fatigue properties is insignificant.

There is sometimes the very high cycle fatigue (VHCF) regime which encompasses an extensive range of load cycles beyond 10^6 cycles and extending up to 10^9 cycles [10,11,15] (see Figure 4-2). Materials subjected to VHCF experience ultra-high-stress amplitudes. Unlike other fatigue regimes, VHCF is characterized by cracks that initiate from inclusions or microstructural irregularities. Fatigue damage in VHCF occurs primarily due to microstructural changes, including the behaviour of grain boundaries [11,15–17]. This fatigue regime is particularly relevant in aerospace and engine components, where millions of load cycles are encountered during operational life. Understanding VHCF behaviour is critical for ensuring the reliability and longevity of materials in such demanding applications. Figure 4-2 is an example of a Wöhler curve of titanium [10,18]. In the VHCF region, the assumptions behind the application of models in the LCF to HCF may not hold due to the increase in experimental scatter for decreasing stress amplitudes. Weibull and extreme value statistics are approaches that can be used to model the S-N curve in this region [12,16,19]. In addition, Ref [20] defines the fatigue limit in the gigacycle can be modelled by first establishing a new S-N curve extending up to 10^{10} cycles, which typically exceeds the fatigue limit of most technological machinery. Secondly, the fatigue strength at 10^9 cycles must be predicted using conventional statistical methods. There are a few challenges in generating fatigue data in the VHCF regime, but it is not in the scope of this PhD.

For the sake of simplicity and practical application in design, this PhD research will focus primarily on exploring fatigue properties within the medium cycle fatigue regime. As such, the post-processing of fatigue data within this regime will involve generating the mean S-N curve, which serves as the basis for constructing the design curve and determining the

scatter band from experimental data sets. This constitutes the central theme of this research methodology. The approaches utilized include the linear regression method, as well as those recommended by the American Society for Testing and Materials (ASTM) and the International Institute of Welding (IIW). These methods will be employed to develop the Wöhler diagram which holds significant importance for design applications within the MCF.

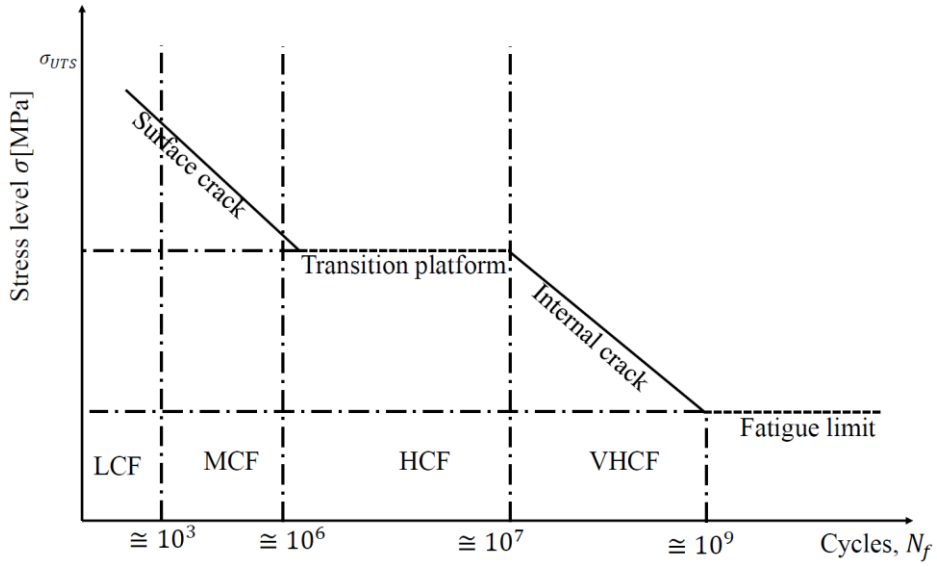

Figure 4-2 The Wöhler curve in LCF, MCF, HCF and VHCF regimes

4.2.2 The S-N curve and the design curve background in MCF

It has been highlighted that the shape of the S-N curve is dependent on the fatigue regimes, and in the MCF, it is linear (see Figure 4-2 and Figure 4-3a). It is also in this region that there is the observed scattering in the fatigue life of materials, where the variability arises from various sources. Some of these sources include material mechanical properties, discontinuities, environmental factors, and setup or equipment variations. Cutting-edge statistical approaches are commonly applied throughout the industry to post-process experimental fatigue data. For instance, in Ref. [21] a Weibull Probabilistic Technique is used to estimate parameters, followed by a Bootstrap method for critical design. Similarly, Ref.[22,23] uses neural networks (NN) machine language for fatigue design both of which do not assume a distribution in the fatigue data. Though this has been successful, the statistical analysis of fatigue data remains tricky because the stress vs. fatigue life relationship is fundamentally nonlinear and the fatigue life distribution is assumed [13,24]. Other challenges originate from the sample size, which is restricted by cost and time, as well as varied disproportionate scatter at stress levels which accounts for the complexity of

the re-analysis. More so, fatigue data can either be censored (runouts excluded) or uncensored, meanwhile the statistical distribution of fatigue life at a given stress level is assumed to be lognormal depending on the approach. Non-cutting-edge approaches are also known to be applied in the industry. For instance, the design-by-eye approach [25] is a very basic approach which is applied by drawing a line that follows the experimental data yet provides a "little white space" between these points and the design curve. Clearly, this design curve does not depend on a distribution, is subjective and lacks consistency across the board.

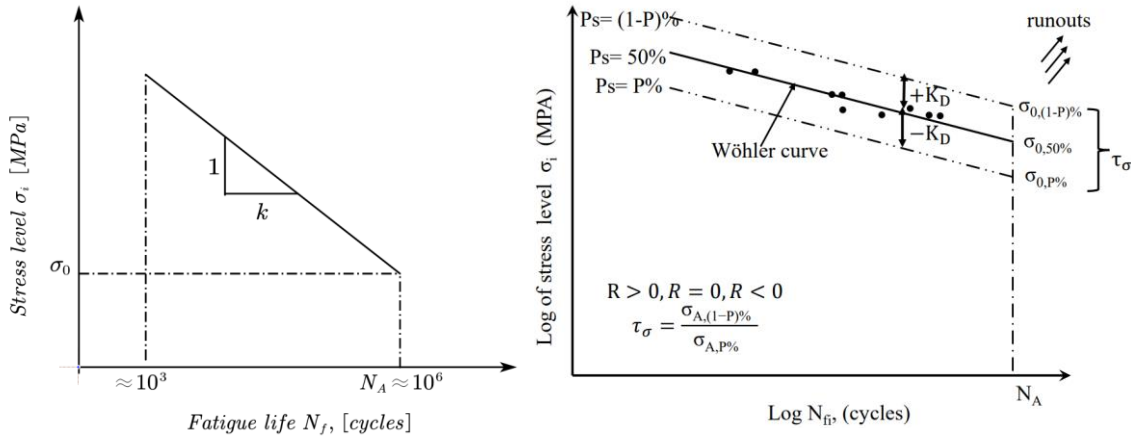

a) b)

Figure 4-3, a) Linearised S-N curve in the MCF regime b) Design curve in the MCF regime in log-log space

How is the design curve derived for the mean S-N curve? The design curve and corresponding design stress are determined by considering the variability in the fatigue data points. Through statistical analysis, the design stress ($\sigma_{0,P\%}$) based on the design curve at a given probability of survival Ps is obtained by shifting the mean curve by a scatter factor K_D as illustrated in Figure 4-3b). Therefore, the design stress/curve depends on the size of the scatter factor, which in turn is dependent on the approach and the recommended probability of survival. This will constitute the key focus of this chapter. For example, Eurocode 3 (EN1993-1-9) suggests a probability of survival of 97.7% for design purposes [9,13,26] of welded joints.

4.2.3 Linear characterization of the S-N curve in the MCF regime and the endurance limit

Considering the linear schematization of the S-N curve in the MCF (see Figure 4-3); one of the linear functions that is commonly used in a log-log representation is [8,9,27]:

$$LogN_f = C_o + C_1 Log\sigma \quad (4\text{-}1)$$

where N_f is the fatigue life and σ is the stress level. C_o and C_1 are the intercept and inverse slope constant respectively which are dependent on the fatigue data. The inverse slope determines the sensitivity of the material to fatigue, and a lower value indicates that the material is more sensitive to changes in stress or strain. At any point on the curve, equation (4-1) is similar to Basquin's equation. Basquin's equation assumes a power-law relationship between the stress level and the number of cycles to failure. Consider, for example, two reference points in the HCF regime, one defined as (σ_0, N_A) at the endurance limit and any other point, the corresponding equation (often referred to as the Wöhler equation) can be written as [27–29]:

$$\sigma^k N_f = {\sigma_0}^k N_A = constant \quad (4\text{-}2)$$

where k is the negative inverse slope ($k = -C_1$) as defined in Figure 4-3a.

Based on this linear characterization, the curve generated from experimental data while using this schematization will be referred to as the mean S-N curve with a probability of survival Ps equal to 50%. From this mean curve, the fatigue limit σ_0, (if it exists) or the endurance limit is determined. The fatigue limit is the theoretical stress level below which failure does not occur. For materials that do not have a fatigue limit, an endurance limit is estimated at a referenced number of cycles, typically in the region of 10^6 and 10^8 cycles, and the curve continues with the same gradient beyond this point.

Materials with a fatigue limit often exhibit the formation of non-propagating cracks, halted either by the initial grain boundary or by the first microstructural obstacle. Conversely, non-ferrous metals such as aluminium alloys lack a fatigue limit, so they are required to be designed for a finite lifespan. In such cases, it's customary to establish an endurance limit, σ_A, a stress level extrapolated in the high-cycle fatigue range at a specified number of cycles to failure N_A, typically ranging between 10^6 to 10^8 cycles [27,28,30]. Additionally, it's noteworthy that the experimental behaviour of materials without a fatigue limit may not always conform to a single linear trend line in the high-cycle fatigue range. Instead, experimental points tend to scatter along a line with a shallower slope compared to the one describing the medium-cycle fatigue behaviour of the same material. A typical S-N curve depicting such a behaviour has been reported in the literature review chapter: The Fundamentals to Fatigue Assessment (see Figure 2-14).

4.2.4 The S-N curve and its associated scatter band: theoretical schematization

A critical aspect to consider is the failure criterion used in gathering data for S-N curves [7,30,31]. Fatigue life typically involves three stages: initiation, propagation, and ultimate failure. While theoretically any of these stages could serve as a suitable failure criterion, the choice significantly impacts the distribution of points on the S-N curves, thereby producing distinct fatigue curves. Consequently, S-N curves are typically experimentally generated with crack initiation as the chosen failure criterion. In this context, crack initiation is commonly defined as the number of cycles needed to initiate a technical crack of a few millimetres in length. Alternatively, another approach is to define crack initiation based on the lifetime leading to a specified reduction in specimen stiffness. The selected criterion is always determined prior to the investigation and creation of fatigue datasets. With this crucial aspect clarified, this research specifically uses complete breakage as the failure criterion.

The mean S-N curve plotted from the experimental data sets consisting of a stress level and the number of cycles to failure, has a probability of survival Ps = 50%, from which the fatigue limit is determined as well as the design curve. In cases where the fatigue tests are runouts (the test is stopped after a certain reference number of cycles), different methods handle this data differently. Some methods include runouts as failures [9], while others ignore (censor) them completely [29,32,33]. However, both approaches tend to underestimate the variation around the fitted line, as indicated by the standard deviation. In research, censored data sets will be used to generate the mean curve [13,27] and the endurance limit.

A confidence interval represents the range of stress levels for which the estimated endurance limit is likely to lie, based on the sample data. The confidence interval depends on the chosen confidence level, which indicates the probability that the estimated range will contain the true endurance limit [13,26]. Suppose the endurance limit is calculated at a probability of survival P%, (i.e $\sigma_{0,P\%}$). The maximum value of the endurance limit at this probability is the value estimated at 1-P%. (i.e. $\sigma_{0,(1-P)\%}$). The interval between these stress levels is known as the confidence interval, and its size is referred to as the scatter band, τ_{σ}. This scatter band is extrapolated for the mean curve and serves as a visualisation tool to indicate the accuracy of estimation from experimental data sets. It further makes use of statistical analysis to represent the uncertainty in the estimate of the S-N curve and is calculated as the ratio between the endurance limit in the HCF regime for (1-P) % and P%

probabilities of survival (see Figure 4-3b). The size of the scatter band is, therefore, dependent on the chosen approach as well.

Returning to the previously summarised challenges, the first of which is the generation of the S-N curve from a set of experimental results, and the second challenge is the determination of the associated scatter band with a probability of survival, what follows is a description of how these challenges can be addressed using some standardised approaches. The S-N curve problem will be addressed using the approach suggested by ASTM and its confidence interval [8,9,13,26]. The scatter bands problem will be determined using approaches suggested by the IIW [26,34], the ASTM and the LRM [9,27,35,36]. In the considered fatigue lifetime region, it is assumed that the distribution of the logarithm of the fatigue life is normal at each stress level. However, this is not always the case since different materials show different behaviours in the medium-cycle fatigue regime. Accordingly, the validity of this initial hypothesis must be checked before determining the associated scatter band. This will be discussed below.

4.3 Generating the mean S-N curve according to the ASTM

To determine a mean S-N curve from a set of experimental data, there are some essential assumptions that need to be considered before progressing [8,13,26,37–41]. In addition to these assumptions, Refs. [34,35] further emphasise the requirement to test several identical specimens at different stress levels such that the stress-life approach can be accurately utilised. Ref. [13] further emphasises the necessity of replication and suggests that the design curve with a probability greater than 50% is as good as its level of replication. According to Refs. [8,26,42], the suggested replication levels are summarised in Table 4-1.

Table 4-1 Minimum number of specimens and replication requirements for testing

Type of test	Minimum Number of specimens	Replication percentage (%)
Preliminary and exploratory	6 – 12	17 - 33
Research and Development testing of components	6 – 12	33 - 50
Design data	12 – 24	50 - 75
Reliability data	12 – 24	75 - 88

Generally, the replication level is estimated as [9,42]:

$$Rep\% = 100\left[1 - \frac{n_\sigma}{n}\right] \tag{4-3}$$

In which n_σ is the number of stress levels and n is the total number of specimens. Based on the replication percentage, the quantity of available specimens, and the chosen approach, one can pre-determine the number of stress levels. However, while ISO 12107 suggests that to statistically verify the adequacy of the linear model, at least two specimens should be tested at each stress level for accurate regression analysis, the ASTM only suggests that the stress levels should be greater than or equal to 3. So, the number of stress levels is dependent on the approach used in investigating fatigue. Examining both standards collectively and considering the recommended minimum specimen numbers in each, it is inappropriate to use the minimum number of specimens suggested for preliminary tests in a test program that combines ISO12107 (6) and the minimum ASTM replication level (17%). This combination results in a program encompassing four stress levels with only two repeat tests, which does not align with the stipulations of ISO12107. Instead, to adhere to ISO12107, when testing six specimens, a replication rate of 50% is necessary (i.e., two tested at each of three stress ranges). This corresponds to the highest replication rate suggested for R&D tests in ASTM379-10.

For the statistical methods mentioned above to be consistent and accurate for S-N curves in the MCF region, the following arguments are required to be true. These arguments are essential in designing the S-N field around the mean curve.

4.3.1 Linearity

The relationship linking fatigue life and the stress level in a log-log representation must be linear [13,26,42]. There are a few possible linear relations used in fatigue [34] and the most common linear relationship in the log-log schematization is as defined in equation (4-1). This equation holds only within set limits of the lifecycle of a specimen, for which the lower limit corresponds to the endurance/fatigue limit and the upper limit the transition region into low cycle fatigue which varies depending on the material, into the static strength of the material specimen. Each stress level produces a unique impact on the fatigue life, and if this is not the case, then the assumption of linearity is invalid, and the Analysis of Variance (ANOVA) statistical model calculations are executed. In this case, the variance procedure uses an F-test to compare variances amongst duplicates in the data with the variance of the estimated population. If the variance within the replicates is far less than the variance in the estimated line, then the linearity assumption is rejected.

4.3 Generating the mean S-N curve according to the ASTM

To verify the condition of linearity, the test statistic is employed in the null hypothesis. This involves using the F-distribution, which is effective in comparing the variances of two or more sample sets derived from continuous data sets with continuous distributions [9,13]. The critical values of the F-distribution are determined based on the desired level of confidence, which can be obtained from the F-tables in Refs. [13,26,31,43]. The degrees of freedom, denoted as n_1 and n_2 are derived from the two respective sample sets.

To determine if a fatigue dataset is linear, the sample data set can be grouped into two subsets. The first subset consists of the stress levels used to generate the data and the second subset considers all individual specimens independently. Suppose there are l number of stress levels with m replicates in the first subset with weighted averages $(\log N)_{fi,j}$ representing the average life at each stress level. $(i = 1 \ldots l, j = 1 \ldots m)$. This weighted fatigue life has a degree of freedom defined as $n_1 = l - 2$. The second subset of the data is treated as the complete set of experimental data without any replications, has degrees of freedom $n_2 = n - l$, where n is the overall sample set. To determine the critical value F_p, the two entries n_1 and $n_2$is used as:

$$F_p cal = \frac{n_1}{n_2} = \frac{l-2}{n-l} \tag{4-4}$$

Similarly, the F_p calculated is compared to the $F_p crit$ value calculated using the equation:

$$F_p crit = \frac{\sum_{i=1}^{l} \frac{m_i \left(log\left(N_{fi}\right) - \overline{logN}_{fi}\right)^2}{(l-2)}}{\sum_{i=1}^{n} \sum_{j=1}^{m_i} \frac{(log(N_{fij}) - \overline{logN}_{fij})^2}{n-l}} \tag{4-5}$$

in which $\log N_{fij}$ $(i = 1..l$ and $j = 1..m)$ is the logarithm of life at the replication level. The stress levels are carefully chosen to fall within the medium cycle fatigue region [13,38]. The null hypothesis is then used to determine the linearity of the data set as follows:

Null Hypothesis:

- $F_p$cal $\leq F_p crit$; Null hypothesis confirmed, linearity model consideration can be adopted.
- $F_p$cal $> F_p crit$; The null hypothesis is rejected and a Non-linear model of some form: $logN_f = C_0 + C_1 log\sigma_i + C_2 log\sigma_i{}^2$, where C_0, C_1 and C_2 are polynomial constants that describe the envelope of the curve.

Where the null hypothesis cannot be confirmed, Ref. [13,26] suggests that the non-linear consideration is adopted. Under this approach, the estimated mean curve is approximated as:

$$LogN_f = C_0 + C_1 log(\sigma_i - C_2) \tag{4-6}$$

In this case, C_0 and C_1 are as defined previously while C_2 is a fatigue limit term. Other examples of non–linear considerations are defined by [9,27,44,45]:

$$LogN_f = C_0(log\sigma_i)^{n_1} + C_1(log\sigma_i)^{n_2} \tag{4-7}$$

Generally, a simple non-linear approach is defined as:

$$LogN_f = C_0 + C_1(log\sigma_i) + C_2(log\sigma_i)^2 \tag{4-8}$$

where C_0, C_1 and C_2 are empirical constants that define the fatigue life [24,46]. Non-linear schematisation will not be the focus of this research. However, it is worth acknowledging the effects that the constants in equation (4-8) for example, will have on the shape of a fatigue curve. Specifically, C_0 defines a position on the ordinate axis, resulting in a parabola that either opens upwards or opens downward. The shape of the parabola is determined by the sign of C_2. A positive C_2 causes the parabola to open upwards, with C_0 determining the minimum point on the estimated curve. Conversely, a negative C_2, positions C_0 as the maximum point on the estimated mean curve. For very small values of $log\sigma_i$, the second term does not significantly impact the shape of the curve. However, C_1 translates the turning point of the parabolic mean curve depending on its magnitude and direction. The translation is diagonal while ensuring that the curve includes the point C_0. A positive C_1 translates the turning point onto the third quadrant, while a negative C_1 will translate the turning point onto the fourth quadrant.

It is also important to acknowledge the significance of the bilinear and hyperbolic models proposed in Ref. [16,19] for ultra-high-cycle regimes, particularly when dealing with large data sets. These models provide valuable insights and are based on non-linear considerations. However, a comprehensive discussion of these non-linear aspects is beyond the scope of this research.

4.3.2 Other essential statistical assumptions in addition to linearity

Log normally distributed: the fatigue life is normally distributed or log-normally distributed in the log-log space for any stress levels. This is achieved by assessing whether

the probability plot in the log-log space departs from the mean S-N curve and follows a linear trend. In this paper, it is assumed that, at each stress level, the fatigue life has a normal distribution around the mean life.

Statistical Independence: The fatigue life of any single sample is considered independent of the fatigue lives of other samples or data points. This independence can be verified by examining the residuals of $logN_f$ in the datasets to ensure there are no recurrent patterns. If any noticeable patterns emerge, the data is grouped accordingly, and an analysis of variance (ANOVA) is conducted on the data.

Homogeneity and standard deviation: It is assumed that, at each stress level, the variance and standard deviation of fatigue life are constant. This assumption is verified by examining the plots of residuals from the mean curve with $log\sigma$. To assess statistical homogeneity, Bartlett's test is applied if the fatigue life is normally distributed at each stress level; otherwise, Levene's test is used. It's important to note that while these tests are relevant, they are not the primary focus of this research and will not be used in the subsequent analysis of the results.

4.4 Fitting the S-N mean curve and confidence interval

Having asserted the above essential assumptions, the first challenge in this chapter, namely the method of fitting a mean S-N curve onto an experimental fatigue data set, can be addressed. The statistical approaches chosen for this study use the same process for the mean curve, i.e., the regression analysis. The regression analysis uses the least squares approximation [27,28,46] to determine the parameters of the mean curve by minimising the sum of the squares of the differences between the observed dependent variable (fatigue life) and the output of the linear function of the independent variable (stress levels). Consequently, estimates of the slope and intercept are generated. This is possible by applying a $\log - \log$ plot of the data assuming a log-normal distribution of fatigue life at each stress level. The estimated mean curve has a 50% probability of survival, (i.e. $P_s = 50\%$) and the function that defines the equation of the regression curve defined in equation (4-1) has an error band is defined as [28,46]:

$$log\ N_f\ =\ C_o + \ C_1 log\ \sigma_i + \xi \tag{4-9}$$

where ξ is the unknown random measurement error connected with the estimation of fatigue life. The maximum likelihood method can also be used to determine the parameters C_o and C_1 because of its good statistical properties [29,47]. However, the main disadvantage is that the likelihood equations need to be derived for each specific distribution, which can be cumbersome. To simplifier this process, the least squares approach will be used to estimate the parameters in the mean curve [9,27,48–50]. Thus C_o and C_1 are estimated at the mean points of the dataset as:

$$C_1 = \frac{\sum_{i=1}^{n}[log\ (\sigma_i) - \overline{log\sigma_\iota}][log\ (N_i) - \overline{logN_\iota}]}{\sum_{i=1}^{n}[log\ (\sigma_i) - \overline{log\sigma_\iota}]^2} \tag{4-10}$$

$$C_0 = \overline{logN_\iota} - C_1\overline{log\sigma_\iota} \tag{4-11}$$

in which n is the sample set and $i = 1,2..n$. $\overline{log\sigma_\iota}$ is the mean of log stress levels and $\overline{logN_{f\iota}}$ is the mean of the log of fatigue life. The inverse slope k, whose value is of great significance in fatigue analysis and design, and in the least squares estimation is defined as:

$$k = -C_1 \tag{4-12}$$

According to this schematisation, the endurance limit $\sigma_{0,50\%}$, at the corresponding reference number of cycles N_A, can be determined as,

$$\sigma_{0,50\%} = \left[\frac{10^{C_0}}{N_A}\right]^{\frac{1}{k}} \tag{4-13}$$

Having estimated the parameters in the mean S-N curve, what follows is an estimate of the amount of uncertainty associated with the mean curve otherwise known as the confidence interval.

4.4.1 Confidence level of the estimators C_0 and C_1 of the mean S-N curve

The parameters defining the mean S-N curve C_0 and C_1 are estimates and have associated confidence intervals. This confidence level defines the probability that each parameter will fall within a specified range of values. With a 95% confidence level, it is expected that 95% of the time the suggested parameter will exist within this limit.

Assuming that all the arguments described in section 4.3 are true, and the estimators of C_0 and C_1 are normally distributed irrespective of the sample size, a t-distribution is used to determine the confidence interval for these parameters [9,13,38]. The confidence interval for C_0 is defined as:

$$C_0 - t_p s\sqrt{\frac{1}{n} + \frac{\overline{log\sigma_\iota}^{\,2}}{\sum_{i=1}^{n}\left(log\sigma_i - \overline{log\sigma_\iota}\right)^2}} \leq C_0 \leq C_0 + t_p s\sqrt{\frac{1}{n} + \frac{\overline{log\sigma_\iota}^{\,2}}{\sum_{i=1}^{n}\left(log\sigma_i - \overline{log\sigma_\iota}\right)^2}} \tag{4-14}$$

where t_p is the critical value of the t-distribution patterning to a probability of survival P_S, and s is the unbiased estimator of the standard deviation of fatigue life defined by equation (4-15) [26,31,34,43,51] where $logN_i$ is the log of observed live at the stress level.

$$s^2 = \frac{\sum_{i=1}^{n}\left(logN_{fi} - logN_f\right)^2}{n-2} \tag{4-15}$$

Similarly, C_1 will lie within the limits defined by,

$$C_1 - \frac{t_p s}{\sum_{i=1}^{n}\sqrt{log\sigma_i - \overline{log\sigma_\iota}}} \leq C_1 \leq C_1 + \frac{t_p s}{\sum_{i=1}^{n}\sqrt{log\sigma_i - \overline{log\sigma_\iota}}} \tag{4-16}$$

These estimations remain valid under the condition that the life estimation of a random sample is independent, and all the previously defined assumptions hold true, with the additional requirement that there are no runouts in the fatigue data set.

4.4.2 Confidence level of the mean S-N curve (ASTM)

Based on the assumptions defined in section 3.1, the confidence interval for the mean curve is defined by:

$$\mathrm{Log}N_f = C_0 + C_1\, log\sigma_i \pm \sqrt{2F_p}\, s\sqrt{\frac{1}{n} + \frac{\left(log\sigma_i - \overline{log\sigma_\iota}\right)^2}{\sum_{i=1}^{n}\left(log\sigma_i - \overline{log\sigma_\iota}\right)^2}} \tag{4-17}$$

The confidence interval uses a constant F_p, known as the critical value of the F – distribution (otherwise called the Snedecor distribution) which is read from statistical tables found in Refs. [9,13,27,35]. In addition, the actual mean S-N curve is only an approximation of the best straight line representing the dataset in the interval of the stress levels used during testing, with estimators defined with a confidence level of 95%.

Consequently, confidence levels for the entire mean S-N curve with a confidence greater than 95% is not recommended for this mean curve and this method should not be recommended to extrapolate the S-N curve beyond the test interval.

The curves generated using equation (4-17) produces hyperbolas which are closest to the mean curve at the mean points as illustrated in Figure 4-4. These hyperbolic curves are of little interest to design engineers and will be transformed to parallel lines that provide the confidence interval along any stress level [13,24,46] and is used to generate the scatter band. The length of the perpendicular bisector at the mean point to the mean S-N curve determines the position of the parallel curves and this is half the size of the confidence interval. The endurance limit $\sigma_{0,P\%}$ at N_A cycles to failure of the mean curve characterised by a probability of survival $P_s = P\%$ is estimated as:

$$\sigma_{0,P\%} = \left[\frac{10^{(C_0 - K_{D(ASTM)}S)}}{N_A}\right]^{1/k} \tag{4-18}$$

In which $K_{D(ASTM)}$ is the scatter factor and is defined as:

$$K_{D(ASTM)} = \sqrt{\frac{2F_p}{n}} \tag{4-19}$$

The critical value F_p, of the F – distribution is dependent on the probability of survival. In a similar way, the endurance limit $\sigma_{0,(1-P)\%}$, at N_A cycles to failure of the line delimiting the calculated scatter band, with a probability of survival $P_s = (1 - P)\%$ is defined as:

$$\sigma_{0,(1-P)\%} = \left[\frac{10^{(C_0 + K_{D(ASTM)}S)}}{N_A}\right]^{1/k} \tag{4-20}$$

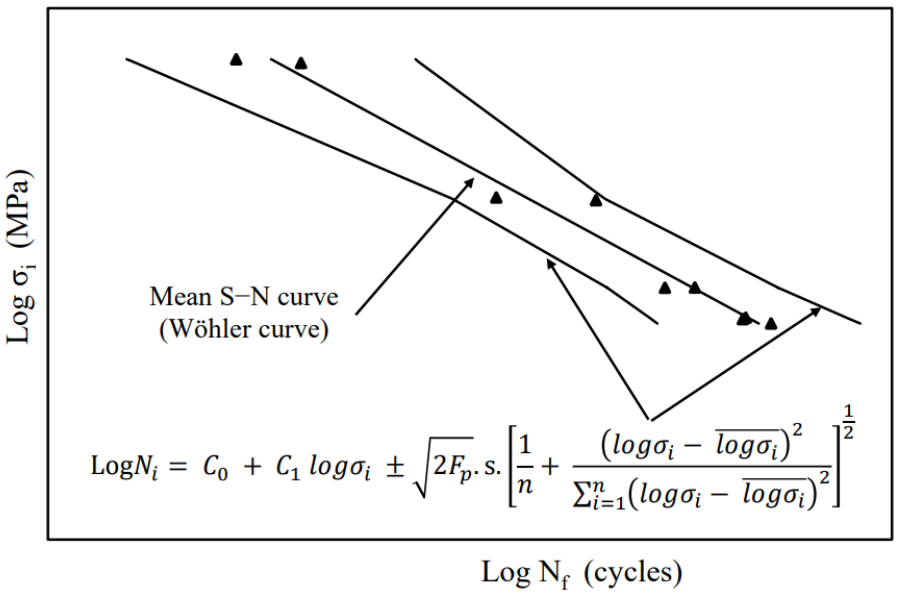

Figure 4-4 Hyperbolic curves showing the confidence interval of a mean curve and the associated data points

These are parallel lines which are equidistant from the mean S-N curve define the region for the confidence interval of the mean S-N curve. By determining these two reference stress levels, the scatter band to this confidence interval can calculated as:

$$\tau_{\sigma(IIW)} = \frac{\sigma_{0,(1-P)\%}}{\sigma_{0,P\%}} \tag{4-21}$$

Before proceeding to address the second challenge of generating fatigue design curves and their associated scatter bands, it is necessary to explore the wide range of available approaches that are applicable in the industry.

4.5 The design curves (scatter factors) based on ASTM, IIW and Linear Regression Method

Having determined the mean curve that is common to all the approaches and also explored some of the approaches that are used in the industry, this section will explain how the standardised methods suggested by the ASTM, the IIW and the Linear Regression Method are used to construct the design curve based on a probability of survival, and the associated scatter bands using their respective scatter factors. The ASTM approach that uses prediction limits to determine a design curve and scatter band will be considered in this case.

4.5.1 ASTM

According to Ref. [8,9,13], the ASTM assumes the considerations described in section 4.3 on censored data. In this standard, the S-N relationships are approximated by $log - log$

plots in the MCF where it is considered linear. ASTM standard reiterates the variance be defined as:

$$s^2 = \frac{\sum_{i=1}^{n}\left(LogN_f - LogN_i\right)^2}{n-2} \tag{4-22}$$

wherein the term $(n-2)$ in the denominator is the adjusted degrees of freedom patterning to C_0 and C_1 and enables the variance to be unbiased. In cases where the data is fitted to standard curves with predetermined parameters, for instances in approaches where $C_1 = 3,5,..$, the degree of freedom in this case is adjusted to $n-1$. The prediction limits for which the lower limit is the design curve is defined as [38,43]:

$$\mathrm{Log}N_{f,D} = C_0 + C_1\, log\sigma_i \pm \sqrt{2F_p}s\sqrt{1+\frac{1}{n}+\frac{\left(log\sigma_i - \overline{log\sigma_\iota}\right)^2}{\sum_{i=1}^{n}\left(log\sigma_i - \overline{log\sigma_\iota}\right)^2}} \tag{4-23}$$

$$K_{D(ASTM)} = \sqrt{2F_p\left(1+\frac{1}{n}\right)} \tag{4-24}$$

Following on from equation (4-23)(4-24) and (4-24), the reference stress at the reference cycle is as defined in equation (4-13). The prediction limit at this point based on a probability of survival is established. Subsequently, the endurance limit $\sigma_{0,P\%}$, with a probability of survival $P\%$, is determined using the equation:

$$\sigma_{0,P\%(ASTM)} = \left[\frac{10^{(C_0 - K_{D(ASTM)}s)}}{N_A}\right]^{\frac{1}{k}} \tag{4-25}$$

Similarly, the endurance limit in error at $(1-P)$ delimiting the interval generated by the design curve can be calculated using the equation:

$$\sigma_{0,(1-P)\%(ASTM)} = \left[\frac{10^{(C_0 + K_{D(ASTM)}s)}}{N_A}\right]^{\frac{1}{k}} \tag{4-26}$$

The scatter band τ_σ, according to the ASTM is calculated as:

$$\tau_{\sigma(ASTM)} = \frac{\sigma_{0,(1-P)\%(ASTM)}}{\sigma_{0,P\%(ASTM)}} \tag{4-27}$$

4.5.2 IIW

The IIW also takes into consideration the assumptions explained in section 4.2.34.3 The mean curve is generated using the same procedure as defined using estimates detailed in section 4.4 [9,34]. Accordingly, the scatter factor used to calculate the scatter band with a 95% confidence level uses a student t – distribution and is defined as:

$$\mathrm{Log}N_{f,D} = C_0 + C_1 log\sigma_i \pm t\, s \sqrt{1 + \frac{1}{n} + \frac{\left(log\sigma_i - \overline{log\sigma_\iota}\right)^2}{\sum_{i=1}^{n}\left(log\sigma_i - \overline{log\sigma_\iota}\right)^2}} \tag{4-28}$$

C_0 and C_1 are constants as described in section 4.4.1. t is the corresponding percentage point of the Student's t distribution with of degrees of freedom equal to $n-2$ and s^2 the best guess of the variance around the mean curve.

For a large sample sizes, the IIW approximates the term $1/n$ in equation (4-28) to zero, in accordance with Gurney and Maddox as reported in Ref. [26,34]. Consequently, this term in the prediction equation is ignored for a sample size of 20 or more, which only accounts for a 2% error in the estimation of the width of the scatter band. For a sample set less than 10, the term under the square root sign assumes the value of one as well as the degrees of freedom is adjusted to $f = n-1$ as summarised in a Table 2. For $n \leq 10$, consider the extreme case under this condition where $n = 1$. This means that $\frac{1}{n} = 1$ and the point variance of each of the data is always less than one. Therefore, the term under the square root sign in equation (4-28) can be approximated to 1 without great loss in the size of the scatter band. Similarly, for $n \geq 20$, the extreme case corresponds to $n = \infty$, for which $1/n \approx 0$. The degree of freedom is adjusted which reduces the size of the corresponding scatter band by a very negligible amount. The scatter factor $K_{D(IIW)}$, according to the IIW is calculated as:

$$K_{D(IIW)} = \mathrm{t}\sqrt{1 + \frac{1}{n}} \tag{4-29}$$

Similar to the other approaches under review, the endurance level $\sigma_{0,P\%(IIW)}$, for a probability of survival P is defined as in equation (4-30), while the endurance limit in error at the reference cycle $\sigma_{0,(1-P)\%(IIW)}$ is defined in equation (4-31).

4.6 Application of the ASTM, IIW and LRM on theoretical data set

$$\sigma_{0,P\%(IIW)} = \left[\frac{10^{(C_0 - K_{D(IIW)}S)}}{N_A}\right]^{\frac{1}{k}} \tag{4-30}$$

and

$$\sigma_{0,(1-P)\%(IIW)} = \left[\frac{10^{(C_0 + K_{D(IIW)}S)}}{N_A}\right]^{\frac{1}{k}} \tag{4-31}$$

Therefore, the scatter band generated according to the IIW is defined as,

$$\tau_{\sigma(IIW)} = \frac{\sigma_{0,(1-P)\%(IIW)}}{\sigma_{0,P\%(IIW)}} \tag{4-32}$$

Table 4-2 Calculating the size of scatter band which is dependent on sample size as recommended by the IIW

Calculating estimate in error with small sample set	Calculating estimate in error with large sample set
$n \leq 10$	$n \geq 2o$
$\sqrt{1 + \frac{1}{n} + \frac{(X - X_m)^2}{\sum_{i=1}^{n}[X_i - X_m]^2}} = 1$	$\frac{1}{n} = 0 \Rightarrow \sqrt{1 + \frac{(X - X_m)^2}{\sum_{i=1}^{n}[X_i - X_m]^2}}$
$\mathrm{Y(x)} = \hat{Y}(X) - t * s$	$\mathrm{Y(x)} = \hat{Y}(X) - t * s * \sqrt{1 + \frac{(X - X_m)^2}{\sum_{i=1}^{n}[X_i - X_m]^2}}$
$Y(x) = C_0 + C_1.X_m \pm t\,.s.$	$Y(x) = C_0 + C_1.X_m \pm t\,.s.\sqrt{1 + \frac{(X - X_m)^2}{\sum_{i=1}^{n}[X_i - X_m]^2}}$
$s = \sqrt{\frac{\sum_{i=1}^{n}[Y_i - Y(x_i)]^2}{n-2}}$	$s = \sqrt{\frac{\sum_{i=1}^{n}[Y_i - Y(x_i)]^2}{n-1}}$

4.5.3 Linear Regression

According to the linear regression schematisation, the predicted mean curve follows through the assumptions defined in section 4.3 [14,43,52,53]. The estimated constants C_0 and C_1 are also estimated using the method described in section 4.4. The endurance limit

can be gotten by computing σ_0 using equation (4-13). However, the variance is calculated as:

$$s^2 = \frac{\sum_{i=1}^{n}\left(LogN_f - LogN_i\right)^2}{n-1} \tag{4-33}$$

The unbiased condition is attained by reducing the degrees of freedom by 1. i.e., $f = n - 1$ [28,53]. Consequently, the reference stress level at N_A cycles to failure for various probabilities can be computed using the standard deviation, the reference stress level at $P50\%$, and other empirical constant q, which is read of standard statistical tables for normal or log-normal distributions found in Refs. [13,36,43,53]. These values are dependent on the desired probability of survival, confidence level and sample set. In this context the endurance limit is defined using the scatter factor $K_{D(LM)}$ and the empirical constants q as:

$$\sigma_{0,P\%(LM)} = \sigma_0 \left[\frac{N_A}{10^{log\,(N_A)+qs}}\right]^{\frac{1}{k}} \tag{4-34}$$

This has been established by using the well-known Wöhler relationship which considers that for a material with a fatigue limit and a known value of the inverse slope k, this equation is always true. Alternatively, materials without a defined fatigue limit, the endurance limit is determined, and equation (4-36) holds true whenever $N_f \leq N_{KP}$, where N_{KP} is the fatigue life at the knee point.

$$\sigma^k N_f = {\sigma_0}^k N_0 = {\sigma_A}^k N_A = constant \tag{4-35}$$

$$\sigma^{k_1} N_f = {\sigma_{KP}}^{k_1} N_{KP} \tag{4-36}$$

σ_i is the stress level corresponding with the fatigue life N_f at that point. Thus, the delimiting endurance limit is defined as:

$$\sigma_{0,(1-P)\%(LM)} = \sigma_0 \left[\frac{N_A}{10^{log\,(N_A)-qs}}\right]^{\frac{1}{k}} \tag{4-37}$$

Similarly, the scatter band according to this approach can be written as:

$$\tau_{\sigma(LM)} = \frac{\sigma_{0,(1-P)\%(LM)}}{\sigma_{0,P\%(LM)}} \tag{4-38}$$

4.6 Application of the ASTM, IIW and LRM on theoretical data sets

Setting out to explore the various approaches, will be achieved by applying them to both theoretical data sets and experimental fatigue data sets sourced from literature. By analysing these diverse data sources, valuable insights will uncover patterns that will justify the application of each approach. This section, therefore, is intended to explore the impacts of the variation in fatigue data due to the aforementioned approaches. Particularly, the effects of varied statistical characteristics that define the scatter band. To achieve this, some theoretical data sets have been generated with defined parameters, by continuous correction and improvement until the desired statistical properties were achieved. The complexity and cost of generating experimental data sets with desired statistical characteristics, and the time involved have been the motivation for applying this approach. Moreover, it cannot be determined a priory if a set of specimens will generate data sets with predetermined statistical characteristics. The inverse slopes chosen range from 30 – 3, which are common with plain and notched metals, and the spreads will vary from a base standard deviation to about three times the base standard deviations. In addition, the impact of the level of percentage replication and degrees of freedom will also be investigated.

4.6.1 Impact of slope in fatigue data on scatter bands

Consider fatigue data generated such that the inverse slope increases as summarised in Table 4-3 such that each data set has approximately the same level of spread in the direction of fatigue life. The replication level of 75% is constant throughout which is a requirement for experimental data to be used for design [24,35,46]. The mean curves produced by applying the various approaches are summarized in Figure 4-5, as well as the design curves for a 95% probability of survival in the scatter factors described in the approaches previously.

The data sets for the various slopes are randomly generated such that the resulting curve always lies within the same critical stress range, and each data set produced a required value of the slope. Since these curves have not been systematically generated using reference points, hence the analysis will be limited only to how the scatter band changes with the various approaches, with no reference to the respective endurance limits.

According to the data summarised in Figure 4-6, as the inverse slope increases, the size of the scatter bands for each of the approaches reduces. Additionally, for very large values of inverse slope, it is observed that the sizes of the scatter bands converge to similar sizes. Hence it can be concluded that for fatigue data with equal variances in the direction of

fatigue life, the design curves described by ASTM, IIW, and LRM approaches all agree for high values of inverse slopes.

Table 4-3 Randomly generated theoretical data sets such that the inverse slope increases.

k =3		k =10		k =15		k =25	
σ (MPa)	N_f [cycles]	σ (MPa)	N_f [cycles]	σ (MPa)	N_f [cycles]	σ (MPa)	N_f [cycles]
300	7301	300	1547	300	2991	300	1547
300	1245	300	2001	300	3045	300	586
300	1685	295	5400	300	5701	295	2585
300	4505	295	5487	300	3905	295	4587
250	6498	290	8575	275	4498	290	2598
250	12560	290	14587	275	2454	290	6587
250	4510	290	9588	275	2584	290	7542
250	6500	290	12458	275	3542	290	12458
200	8250	280	15785	250	6998	280	19546
200	16040	280	16040	250	9854	280	25489
200	14456	280	14456	250	16258	280	32544
200	11000	280	11000	250	24887	280	52458
150	88001	270	88001	225	140945	270	100001
150	94000	270	94000	225	239825	270	73942
150	95254	270	95254	225	255856	270	99658
150	89580	270	89580	225	669524	270	101254
100	128100	260	128100	200	435456	260	128100
100	121023	260	121023	200	875687	260	151023
100	128600	240	128600	200	648754	240	158001
100	127210	190	127210	200	1258214	230	1394825

4.6 Application of the ASTM, IIW and LRM on theoretical data set

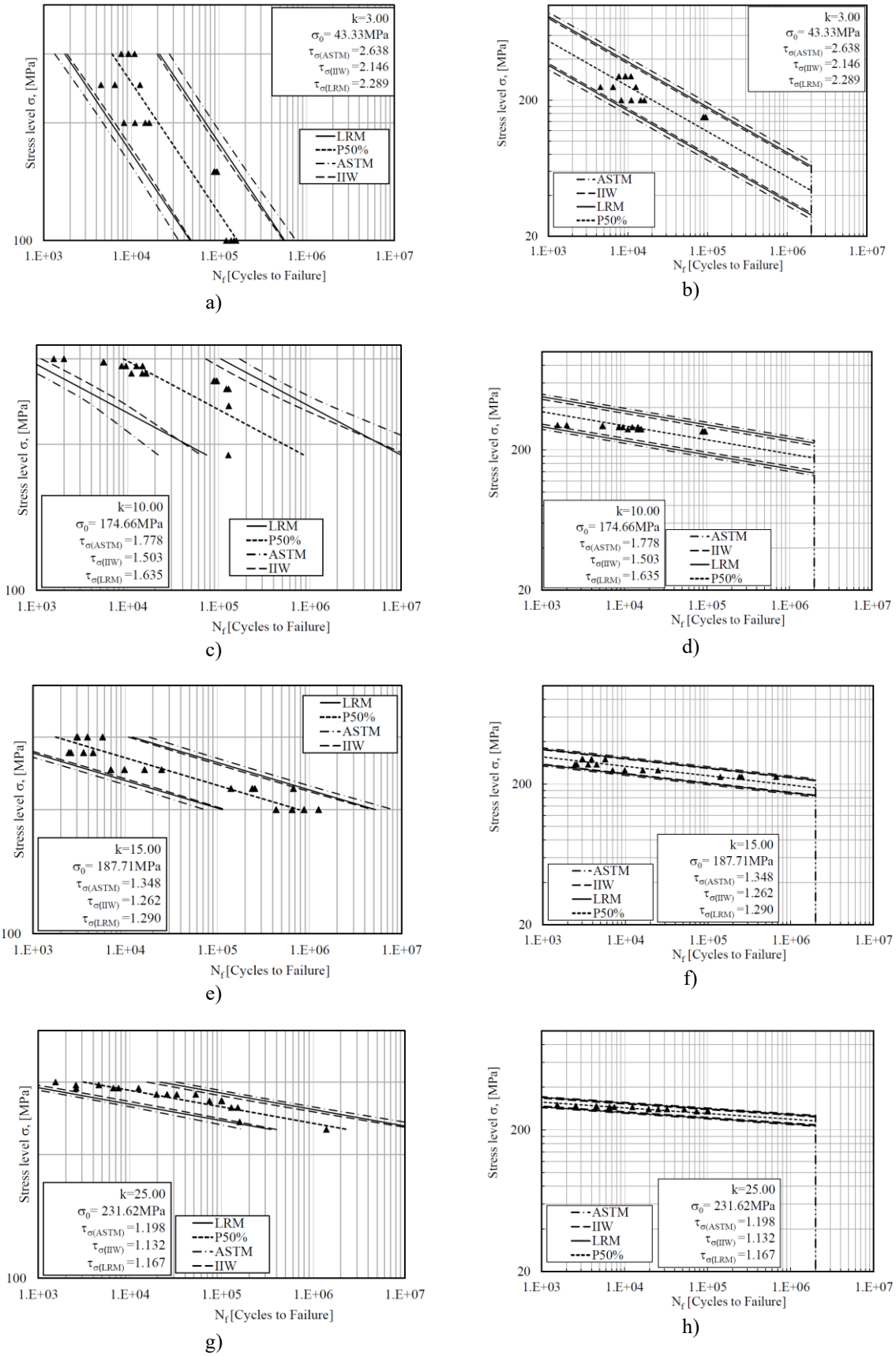

Figure 4-5 Scatter bands and 95% design curves with increasing inverse slopes for the data in Table 4-3. a) k=3.00 scatter band, b) k=3.00 design curve, c) k=10 scatter band, d) k=10 design curve e) k=15 scatter band f) k=10 design curve, g) k=25 scatter band h) k=25 design curve

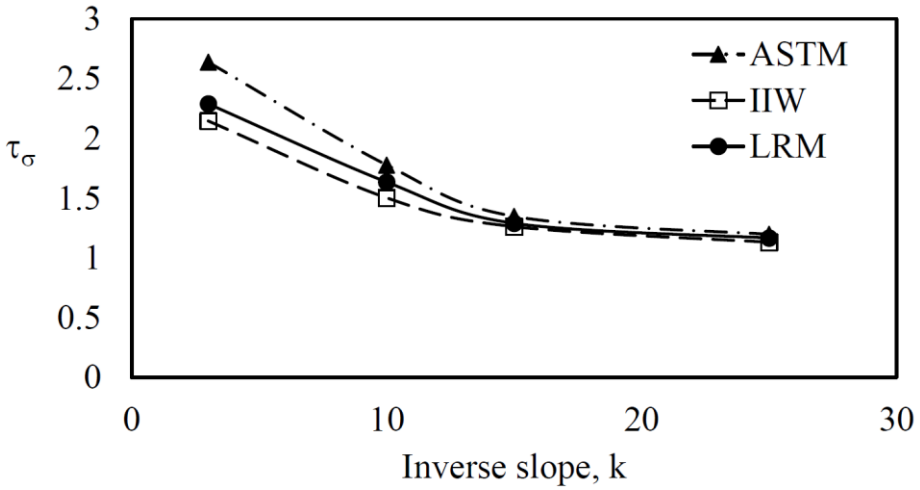

Figure 4-6 The change in scatter bands with increasing inverse slope

4.6.2 Impact of variability in fatigue data on scatter bands

The spread of statistical data shows how extreme the values in the data set occur. The spread can be variated by either altering the range in stress level, determining the variance or standard deviation, and/or determining the absolute deviations or the interquartile range. Table 4-4, shows data with increasing spread from one base standard deviation to three times the base standard deviations at each of the stress levels. This is the weighted spread with a replication level of 75%. Each graph is generated by considering the data in the first column, with each of the data series columns. The mean curves along with the design curves are illustrated in Figure 4-7.

The relationship between the weighted spread and the variance of the entire data set is not always straightforward. Increasing the weighted spread from one standard deviation to multiple standard deviations does not necessarily affect the overall variance. However, it does have an impact on the endurance stresses of the design curves, causing them to decrease. This is reflected in the drop height of the design curves compared to the mean curve. It is noteworthy that the approach recommended by ASTM is particularly influenced by an increase in the spread of fatigue data.

An increase in the design curve will generate a similar size in the error of probability of survival, in this case 95%. This is because the prediction limits are always symmetrical about the mean curve. Consequently, as the spread of fatigue data increases, the prediction limits also increase, as depicted in Figure 4-8. The size of the scatter bands also increases, and notably, the ASTM approach exhibits a more conservative stance compared to other approaches.

4.6 Application of the ASTM, IIW and LRM on theoretical data set

Table 4-4 Theoretical data generated such that the variance is increasing, while percentage replication, sample set, and inverse slope kept constant. The stress level is paired with each data column in N_f (cycles)

σ (MPa)	N_f (cycles)			
	Data 1	Data 2	Data 3	Data 4
300	3650	1450	1650	1020
300	3345	3345	3145	7145
300	3685	11295	19995	24869
300	10505	16505	20985	29985
250	5498	3599	5599	3599
250	11560	16750	22750	29120
250	3510	3510	2310	2310
250	5500	14500	20990	17990
200	9250	6002	7002	3992
200	17040	21004	32704	37804
200	15456	20391	19654	18004
200	12000	17014	18914	29914
150	28060	31860	25860	22860
150	20600	20851	20151	21171
150	23754	23754	34954	45954
150	27580	35892	44102	47292
100	108100	118100	125700	129901
100	101123	101123	100923	99923
100	108600	108200	115801	129801
100	107210	108980	108980	112780

It would be expected that within the same stress range, if the spread in the fatigue data increases in multiples of the variance, the endurance limit tends to reduce and hence the design stress level also reduces. Thus, the scatter bands should increase also. However, due to the limitations associated with generating this virtual data, the changes in the endurance limit will not be discussed here due to its inherence in fatigue data, a characteristic of each material.

When considering a range of two standard deviations, the scatter bands produced by the ASTM, IIW, and LRM approaches exhibit similarity. However, as the spread of data increases beyond this range, the approaches start to diverge, showing differences of up to 50%. In such cases, the ASTM approach tends to be more conservative in its predictions compared to the other approaches.

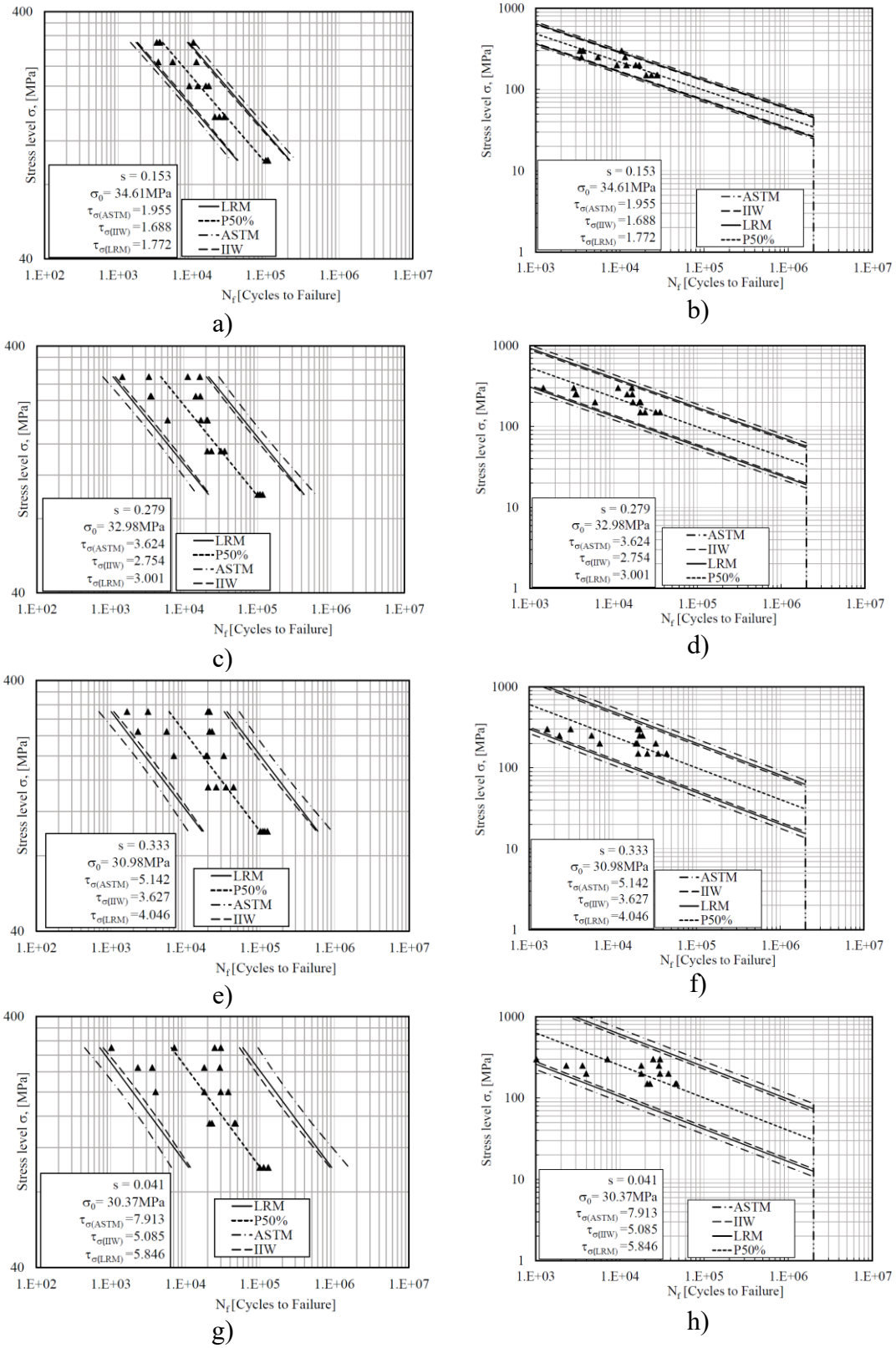

Figure 4-7 Increasing spread and scatter band for 95% probability of survival from Table 4-4. a&b data series 1, c&d data series 2, e&f data series 3 and g&h data series 4 scatter bands and design curves respectively

4.6 Application of the ASTM, IIW and LRM on theoretical data set

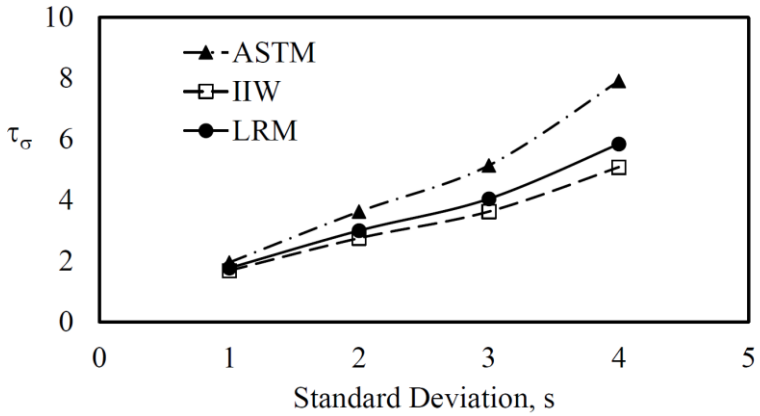

Figure 4-8 Change of scatter band with increasing standard deviation

4.6.3 Impact of replication percentage on scatter bands

Consider for example the data summarised in Table 4-5. The levels of replication and application have been summarised in Table 4-1. The replication levels have been carefully selected such that the various replications levels are analysed. The stress levels range has been kept constant as well as the overall spread of fatigue life at $s \cong 0.18$. The only varied parameter in this case is the stress level and the number of specimens at each stress level. The various scatter bands generated using the approaches in this study have been summarised in Figure 4-9 along with the design curves with a 95% probability of survival. The scatter bands remain constant as the percentage replication increases as illustrated by the graph in Figure 4-10.

Table 4-5 Variated replication level of theoretical fatigue data with constant variance, sample set and inverse slope

R = 20%		R=35%		R = 55%		R = 75%	
σ (MPa)	N_f (cycles)	σ (MPa)	N_f (cycles)	σ (MPa)	N_f (cycles)	σ (MPa)	N_f (cycles)
300	3650	300	3650	300	3650	300	3650
290	3345	290	3345	300	3345	300	3345
280	3685	280	3685	280	3685	300	3685
270	10505	275	10505	280	10505	300	10505
260	5498	265	5498	250	5498	250	5498
250	11560	255	11560	250	11560	250	11560
240	3510	240	3510	230	3510	250	3510
230	5500	240	5500	230	5500	250	5500
220	9250	235	9250	200	9250	220	9250
210	17040	235	17040	200	17040	220	17040
200	15456	180	15456	175	15456	220	15456
190	12000	180	12000	175	12000	220	12000
160	28060	160	28060	165	28060	150	28060
160	20600	160	20600	165	20600	150	20600
130	23754	140	23754	150	23754	150	23754
130	27580	140	27580	150	27580	150	27580
115	108100	115	108100	100	108100	110	108100
115	101123	115	101123	100	101123	110	101123
100	108600	100	108600	100	108600	110	108600
100	107210	100	107210	100	107210	110	107210

4.6 Application of the ASTM, IIW and LRM on theoretical data set

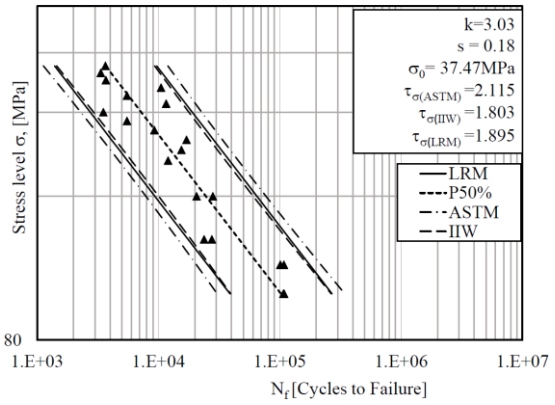

a) R = 20%

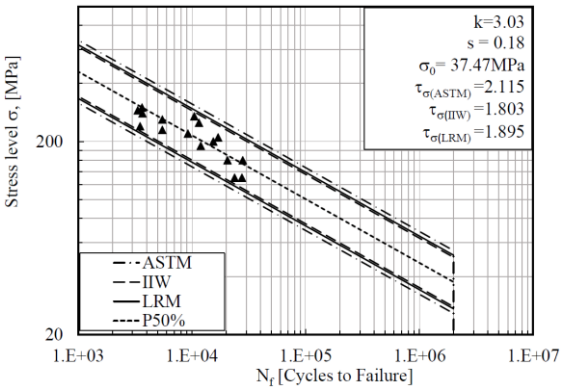

b) R = 20%

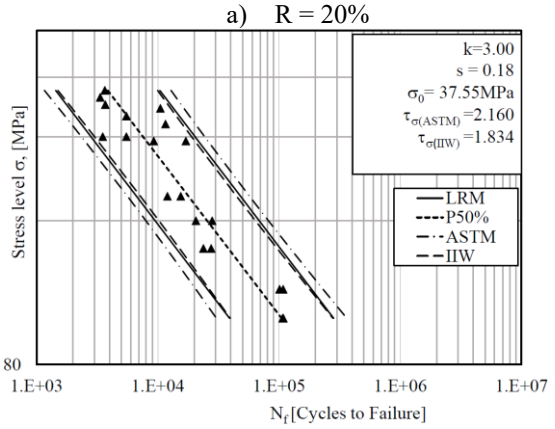

c) R = 35%

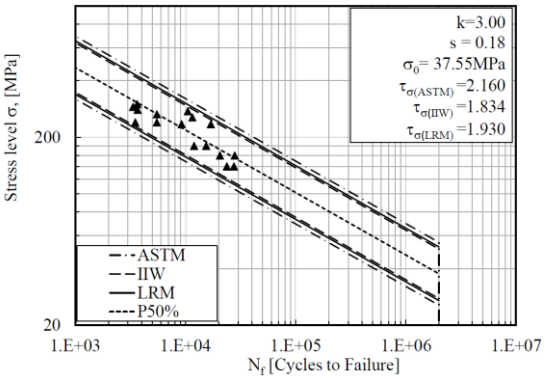

d) R = 35%

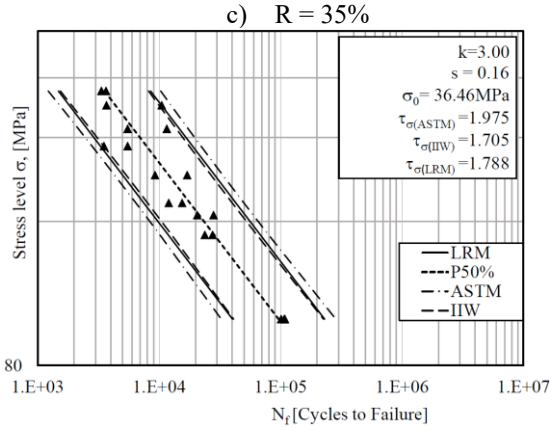

e) R = 55%

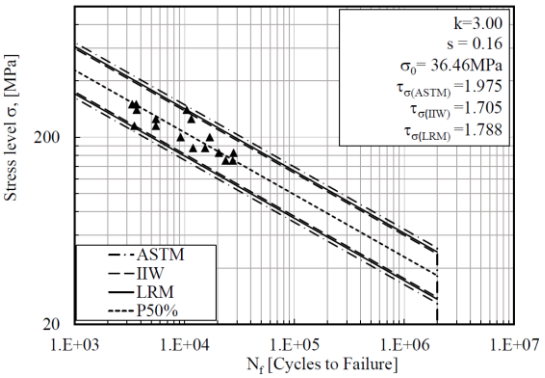

f) R = 55%

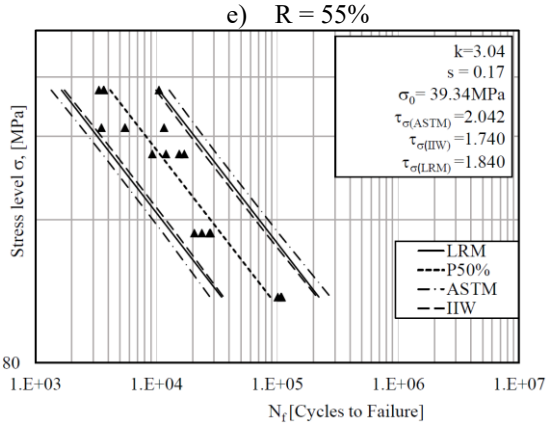

g) R = 75%

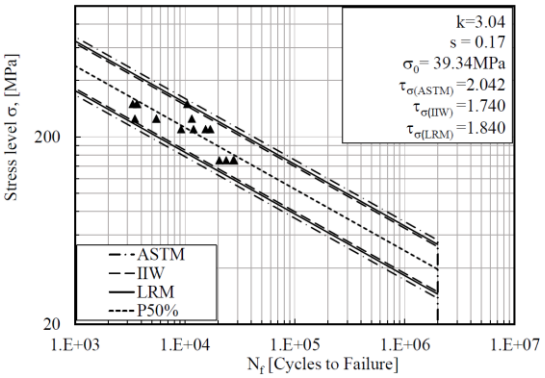

h) R = 75%

Figure 4-9 Variated replication showing parabolic scatter bands and 95% design curves respectively of theoretical fatigue data with constant variance, sample set and inverse slope and spread. a&b) 20%, c&d) 35%, e&f) 55% and g&h) 75%

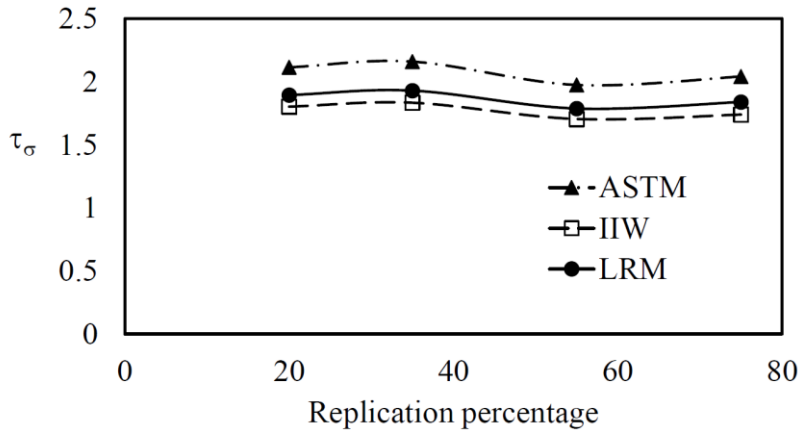

Figure 4-10 Change in the size of scatter band with percentage replication

4.6.4 Impact of sample size on scatter bands

Table 4-1 details the various sample sizes in fatigue experiments about the purpose for which the data is intended. Accordingly, this sets a minimum sample set of six specimens with at least four stress levels such that there is always the presence of replicate data. Attention will be limited in this case to data for preliminary studies requiring just about 6 to 12 data points. Consider the data in Table 4-6 in which each set of data has the same sample standard deviation of about 0.9 and with just at least one pair of replicate data in the sample sets. The stress level range is also constant, and the only varying parameter is the degrees of freedom.

Table 4-6 Theoretical fatigue data with a varied sample set with constant percentage replication and variance

n = 6		n = 8		n = 12	
σ (MPa)	N_f(cycles)	σ (MPa)	N_f(cycles)	σ (MPa)	N_f(cycles)
290	4682	290	2912	290	1956
270	56245	280	45258	280	17256
250	123254	270	60254	270	36124
230	358222	250	135246	260	49123
210	1235452	230	452132	255	65123
210	1352658	220	985254	250	85568
		210	1113256	240	92624
		210	1292583	230	109253
				220	852358
				215	1052581
				210	1088653
				210	1366875

4.6 Application of the ASTM, IIW and LRM on theoretical data set

The graphs summarised in Figure 4-11 illustrates how the scatter band changes as the degrees of freedom increase. Generally, a large sample size leads to more statistically significant results, a better estimation of population parameters and a reduction in the impacts caused by random variability. However, this does not have a noticeable impact on the changes in the proportion of the scatter bands considered in this case. Hence, the size of the scatter band considering each of the approaches change to the same extent, is constant as long as the stress range and standard deviation are kept constant. This is illustrated by the graph in Figure 4-12

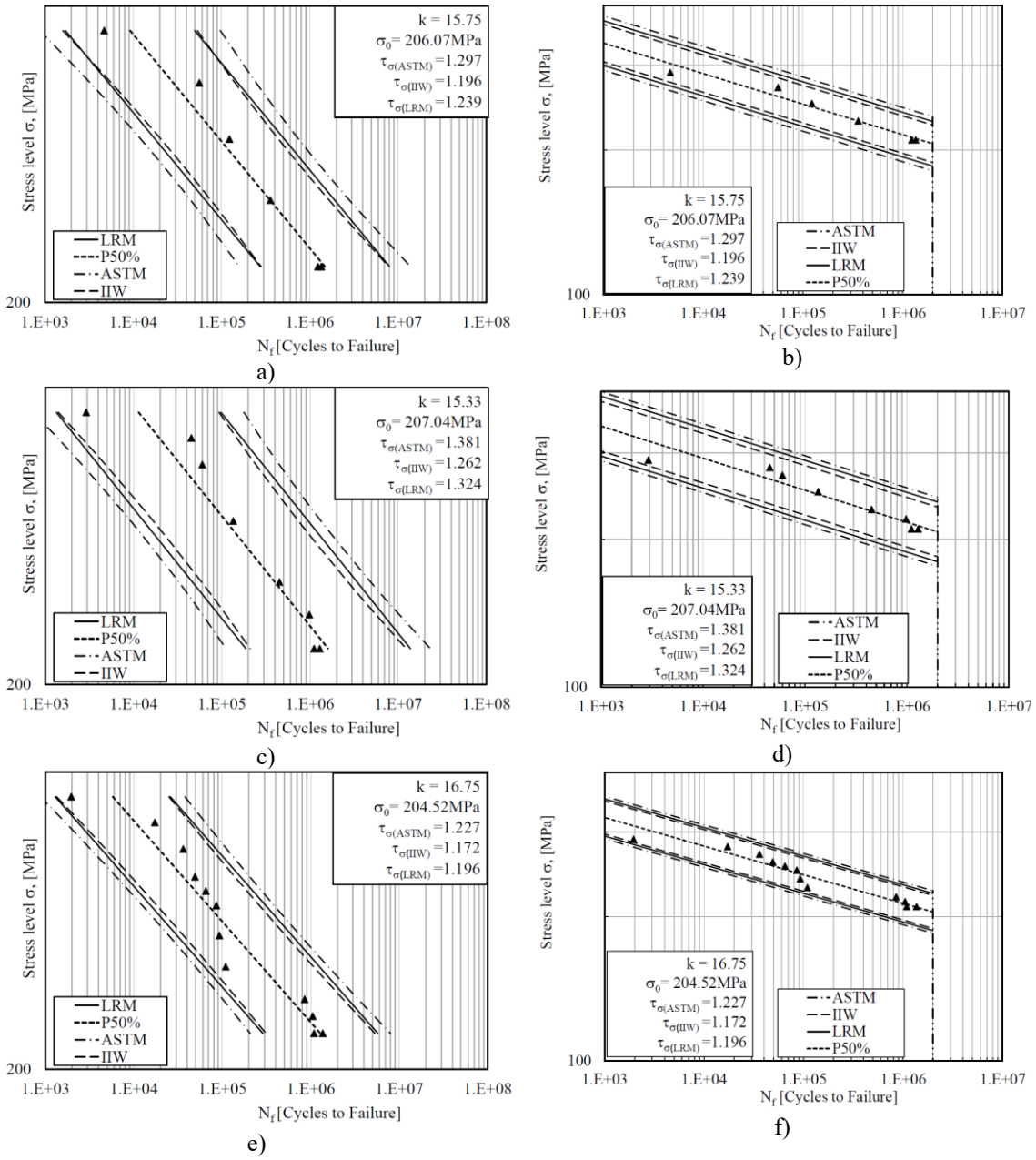

Figure 4-11 Scatter bands and design curves for 95% probability of survival of varied magnitude of sample set a&b) $n = 6$, c&d) $n = 8$, and e&f) $n = 12$.

It should be noted that the analysis considered in this section has been adjusted as summarised in Table 4-2. Because, even when the adjustment is omitted, the impact on the size of the scatter band generated by IIW is not more than 2% [26,34,51], and therefore will have a negligible effect on the size of the scatter band in comparison with the other approaches.

4.6 Application of the ASTM, IIW and LRM on theoretical data set

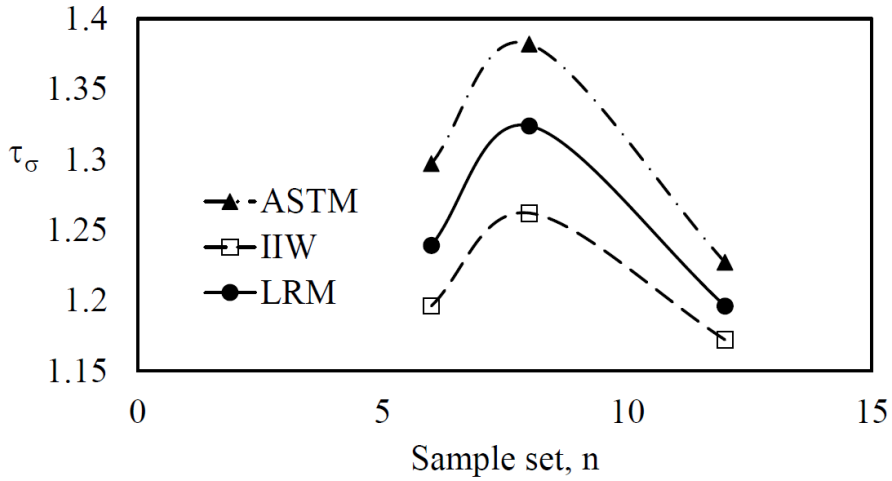

Figure 4-12 Change in scatter bands as the sample set increases in the virtual data in Table 4-6

Table 4-7 summarises the impacts of the statistical characteristics of fatigue data sets on the sizes of the scatter bands generated using the aforementioned approaches. The spread and the inverse slope are the deterministic parameters that greatly impact the fatigue design curve using the standardised approaches described in this study.

Table 4-7 Summary of the changes in the size of the scatter band with the characteristics of fatigue data.

Parameter	Impact on scatter bands
1) Inverse slope	➢ Scatter bands decrease with an increase in inverse slope ➢ Scatter bands converge for inverse slopes ≥20.
2) Spread (variance)	➢ Scatter bands increase ➢ For spread ≤ 2s, scatter bands are similar
3) Replication	➢ No change in the size of scatter bands ➢ Depending on the spread at each stress amplitude
4) Sample size	➢ No change in the size of scatter bands. ➢ Depends on the overall spread of the data.

4.7 Application of ASTM, IIW and LRM on fatigue data sets from literature

The approaches were also tested on real fatigue data sets from the literature. Though it is a challenge to find fatigue data sets that have statistical characteristics that change in defined patterns, it is essential to see how these approaches are impacted by the varied statistical properties of experimental fatigue data. Table 4-8 summarises some of the fatigue data sets obtained from the literature that were used to compare these approaches.

Table 4-8 Summary of fatigue data sets from literature with sample set, variances and inverse slope parameters determined.

Source	Description (fig/table)	Sample set, n	Inverse slope, k	Variance, s^2	$\tau_{\sigma(ASTM)}$	$\tau_{\sigma(IIW)}$	$\tau_{\sigma(LM)}$
[54]	Fig. 1	5	22.01	0.26	1.30	1.19	1.22
[54]	Fig. 2	4	41.49	0.29	1.24	1.143	1.14
[54]	Fig. 3	5	24.87	0.42	1.46	1.28	1.33
[54]	Fig. 4	4	33.88	0.23	1.24	1.145	1.14
[54]	Fig.9, Dry	6	17.82	0.09	1.09	1.06	1.07
[54]	Fig. 9, Aged	8	16.48	0.29	1.31	1.22	1.27
[55]	Fig. 11	16	16.22	0.16	1.14	1.10	1.12
[56]	Fig. 5	11	6.97	0.14	1.32	1.24	1.27
[27]	Tab 4.2	12	26.5	0.49	1.29	1.21	1.25
[57]	Fig. 5, Plain specimens	7	7.71	0.13	1.31	1.21	1.26
[57]	Fig. 5, Blunt U-notch	8	3.50	0.08	1.43	1.29	1.36
[57]	Fig. 5, Sharp U-notch	7	3.40	0.12	1.78	1.50	1.64
[57]	Fig. 5, Sharp V-notch	9	2.65	0.21	3.2	2.33	2.76
[58]	Fig. 2a), R=0	6	7.25	0.31	2.22	1.73	1.92
[58]	Fig. 2b)	6	18.45	0.13	1.14	1.10	1.11
[58]	Fig. 3a), R = -1	6	9.85	0.34	1.89	1.55	1.69
[59]	Fig. 5, TMM	4	11.51	0.26	2.06	1.57	1.55
[59]	Fig. 5, Exp.	4	17.32	0.25	1.58	1.33	1.32
[59]	Fig. 6, Exp.	5	17.83	0.37	1.59	1.36	1.42
[59]	Fig. 6, TMM	5	3.69	0.003	1.02	1.01	1.01
[53]	Fig. 6c), R = 0.1	8	4.38	0.24	2.34	1.84	2.09
[53]	Fig. 6c), R = -1	6	6.45	0.24	2.00	1.61	1.77
[53]	Fig. 6e), R=-1	11	10.77	0.40	1.68	1.50	1.58

4.7.1 Impact of increasing inverse slope

In as much as the variance and sample set are not constant, the sizes of the scatter band reduce and tend to arrive at a common size for high values of inverse slopes. At low values of the inverse slope, the impact on the scatter band is rigorous, though this could be dependent on the other statistical properties that characterise the data set. The scatter band from the ASTM approach is always bigger while those from the IIW and LRM approaches are similar as illustrated in Figure 4-13.

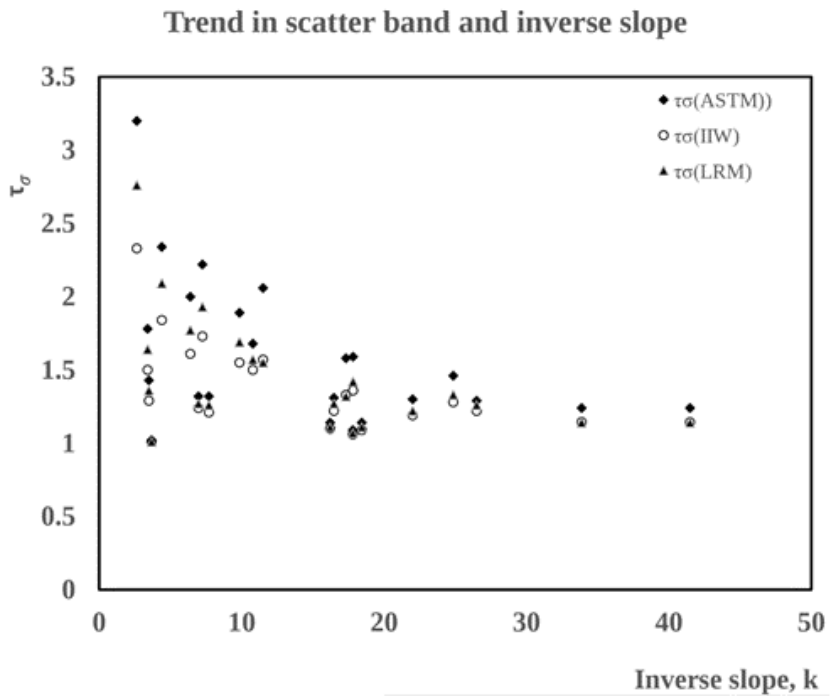

Figure 4-13 Trends in scatter band with an increasing inverse slope of selected fatigue datasets from the literature.

4.7.2 Impact of variance

As summarised in Table 4-8, the sizes of the scatter band for all data sets from the literature fall in the range between 1 and 3. As the variance increases, the sizes of the scatter bands increase and the ratio of each scatter band to the other remains fairly constant. The ASTM remains the approach that produces the largest scatter band. Figure 4-13 further illustrates the scatter bands of the data summarized in Table 4-8.

4.7.3 Impact of the sample set and replication percentage

No noticeable effect was observed when the data set was increased. However, the sizes of the scatter bands were dependent on the slope and variance of the fatigue data sets. This same effect was observed with the percentage replication as both properties of fatigue data only increase the accuracy and reliability of the estimated statistical properties of the data set.

The graphs in Figure 4-14 compares the S-N curves in Ref. [59,60]. As the variance increases from 0.21 to about 0.42, the sizes of the scatter bands reduce. However, the inverse slope increases from 2.65 to 24.87, as well the endurance limits increase for these sets of fatigue data. It is difficult to attribute the change in the scatter bands to a change in any of the statistical properties because of their interdependence. This illustrates one of the

challenges of using experimental data sets without defined patterns in the statistical properties to compare the impacts of the approaches reviewed in this chapter

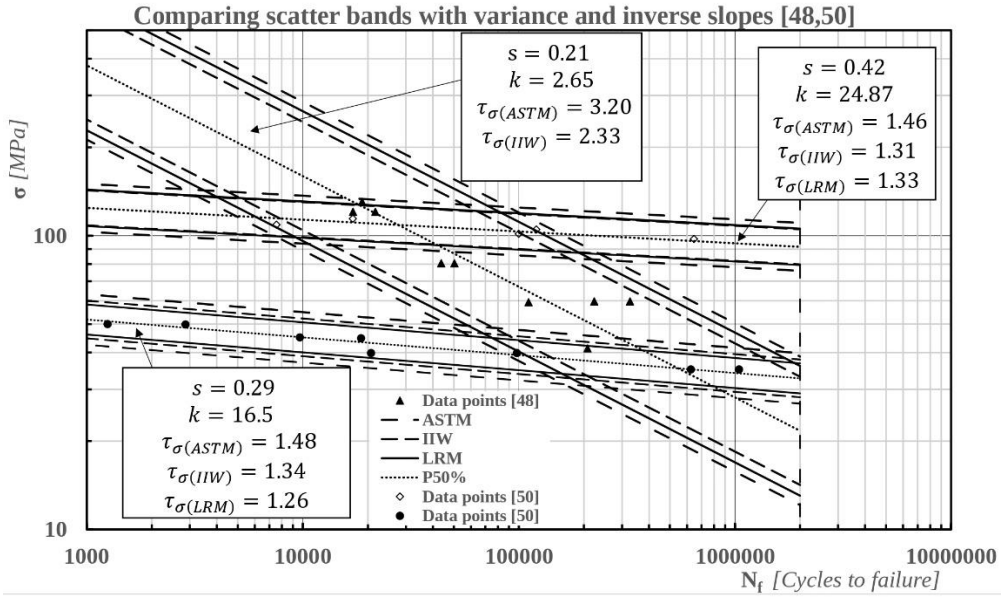

Figure 4-14 Comparing scatter bands of ASTM, IIW and LRM of fatigue data sets from literature with changing variance, inverse slope, and sample set.

4.8 Remarks and conclusions on post-processing of fatigue data sets

A sound understanding of the statistical behaviour of fatigue properties is essential for the design industry. To estimate the probability of survivals of materials, a suitable probability distribution function that is well suited for the data set is essential. While Weibull two and three parameter, log normal, extreme maximum value, smallest extreme value are well established distributions extensively used on fatigue data sets, priory knowledge on these distributions on the data is prerequisite. This might be tricky for use on new data sets on new materials and approaches described in this chapter provide an alternative approach to design with less knowledge on which distribution fits well on the data. However, some of the cutting-edge models for example the 9 parameters Weibull regression model [52] that can be estimated by maximum likelihood and also by non-linear regression analyses uses a regression model that includes the consideration of mean stress effects.

Evidently, whenever a fatigue limit exists [61], the plots of fatigue life versus stress often exhibit curvature at lower stress levels. In addition to this, the variance of the fatigue life decreases as the stress levels increase. Ideally, the standard deviation should be modelled as a function of the stress levels for which an endurance limit can be estimated at that stress levels [47]. This is the model behind the fatigue limit approach of constructing the design

curves. This is quite straight forward as compared to the approaches described herein where the fatigue limit may not be known in advance, and particularly useful when considering endurance limits rather than the fatigue limits. However, the variability in design curves could be expected because of the fatigue limit dependent on the material structural properties which may vary from specimen to specimen. This limits the accuracy of the design curves generated using this approach to the factors that determine the fatigue limit of the material in question.

In as much as the Maximum Likelihood Estimate methodology is the preferred method of analysis of censored and uncensored data using the staircase method to generate experimental results [29], this still attain some limitations and consequently, there does not exist a more preferred method to post process experimental fatigue censored data and the approach used by any organisation is a decision of choice. While some make use of safety factors, others choose a probabilistic approach for which this study owes its relevance. There are other cutting-edge approaches that use statistical considerations, some of which are the one-sided approximate Owen lower limit as well as the Weibull approaches which all agree to the approaches described in this chapter. Other organisations use software packages behind which the concepts are similar. This buttresses the fact that no method is more accurate than the other, however when cost, sustainability and critical application is put into perspective, some methods tend to be more favourable than others.

Also, the approaches have been assumed to have a linear relationship from the fatigue data and there exist quite a few linear models [9,27] which differ in approach to estimate the parameters in the mean S-N curve. Linearity is not usually the case; fatigue test is expected to be carried out around stress levels where the S-N will be linear. This priory knowledge is dependent on the researcher and may not be assessable for new materials. However, the linear relation consideration has enabled the impacts of distributions that are symmetrical or tend to approximate to symmetric distributions under considerations.

Furthermore, fatigue data has been censored by ignoring runouts or suspended tests. This is the simplified approach to runouts and results in the mean curve being biased slightly in the long-life regime [9]. While the ASTM advises against censoring fatigue data for good practice, however, there isn’t much difference on design curves with censored data. Though this is insignificant with low spreads, it becomes quite observant in situations with very low stress levels where the spread in fatigue life is very significant. Had it been the runouts

been treated as a failure as mentioned in Ref. [9], the biasness would increase further. In such a case, this will tilt the mean curve towards more conservativeness. Other methods consider runouts as failures for those that occur at stress levels above the reference stress. Maximum likelihood procedures consider runouts as part of the data to be analysed while the iterative least squares procedures are another option even though these approaches have proven to be quite rigorous.

The use of prediction limits as the fatigue design curve in the ASTM approach has shown that it is very conservative. The approach detailed by the IIW is less conservative and differs from the LRM approach by not more than 5%. The adjustment in the scatter bands as described by the IIW approach makes great use of the statistical characteristics of the data set when compared with the LRM approach. However, the LRM is straightforward to use even though it is less sensitive to outliers and applies to all data. The LRM is not restricted by the sample sets when compared with the other models, especially the ASTM approach.

More so, the LRM approaches assume data to be independent of each other. The fatigue life at high stress levels does not change at the same rate as at low stress levels. The fatigue life resulting from a stress level determines the next stress level during testing up to the vicinity of the endurance limit, yet the variance of this fatigue life increases along the S-N curve in reality.

To conclude, considering the assumptions outlined in section 4.3, this chapter has undertaken a thorough comparison and evaluation of the fatigue assessment procedures recommended by ASTM, IIW, and LRM. The results clearly indicate that all three approaches lead to the attainment of a safe design methodology. Building upon the detailed analysis conducted in this study, which covers uniaxial S-N curves derived from both virtual fatigue data sets and some existing fatigue data sets from literature, the following conclusions can be drawn:

- The IIW approach is the most non-conservative approach and would reduce any chance of overdesign when compared to the other approaches. This would be very applicable for sustainable components. The design curve in this case is dependent on the characteristics of the data, in particular the sample size and its spread. The use of a student t-distribution makes case for application due to the inherent null hypothesis with future population. The critical values for each probability can easily be calculated or read from statistical tables which are readily available in the literature.

4.8 Remarks and conclusions on post-processing of fatigue data sets

- Sensitivity of the design approach to the spread of the fatigue data was observed more in the ASTM approach. This method is therefore very conservative and would substitute approaches with very large factors of safety or in designing critical parts of components.
- Fatigue data with very little spread will not be affected greatly by the approach for the design curve. However, with very large probability of survivals used for design, care should be taken on which approach is recommended.
- The simplest to use approach is the linear regression method and the empirical constants corresponding to sample sizes are defined in the ASTM standards for fatigue distributions with assumed shapes. This approach is not limited by the sample size of the data set.

This section has provided a detailed description of post-processing fatigue data approaches. The following subsequent sections in this chapter will explain how to compare two S-N curves for statistical significance for any observed changes in the fatigue behaviour from experiments.

4.9 Introduction to statistical significance of fatigue data sets

Assessing fatigue data is crucial for designing resilient structures, but experimental fatigue datasets can vary significantly. Statistical analysis is a valuable tool for addressing this issue. Additionally, fatigue experiments are often time-consuming and expensive, making it essential to have a large amount of data for reliable design. To tackle these challenges, data sets from different sources can be used and apply standard methods for integration and validation, such as parametric analysis. This method helps identify differences in fatigue properties, revealing the underlying mechanical characteristics of materials and establishing significance across various experimental conditions. By consolidating fatigue data sets, reliability and reduction in time and cost of conducting numerous fatigue experiments can be improved. Consequently, confident conclusions from fatigue test data based on a predetermined level of significance can be established.

4.10 Statistical test of significance between two S-N curves

The question that this section is setting out to answer is that given two sample data sets, how can statistical approaches be employed to determine whether the difference in the data sets is statistically significant (different and are from different populations) or insignificant (similar and are from the same population)? In the context of this research, the section will illustrate how statistical approaches can be used to ascertain if the fatigue properties observed in uncharged specimens are significantly different from those obtained from hydrogen-charged specimens or insignificant. This is achieved using hypothesis testing

summarised by the flowchart in Figure 4-15 below [46,62]. By doing so, conclusions drawn from performed fatigue tests were made with confidence, relying on a predetermined level of significance. To accomplish this objective, additional fatigue data sets are needed to explain, test and validate the approach. For this reason, data will be generated from specimens with different notch geometries.

Notches were particularly selected as the basis for generating fatigue data because they are well-known for reducing the endurance limit of engineering materials [63,64] and the inverse slope [65], effectively shifting the mean S-N curve downward. They also change the level of scattering depending on the notch root radius and the material type [66]. By using notches, therefore, it was then anticipated that the fatigue data sets generated were statistically significant.

By using specimens with different notch geometry, allowed distinct fatigue data sets to be generated that were subsequently used to illustrate the statistical significance testing. Moreover, notch geometry was a parameter that could be conveniently controlled and accurately measured. For this PhD research, three different materials – steel, cast iron, and brass were used to produce the notched specimens, with three different notch diameters: 1mm, 2mm, and 3mm. The results generated from notched specimens have been reported in Appendix B of this thesis. To begin with, what follows is a brief description of parametric and nonparametric statistical analyses.

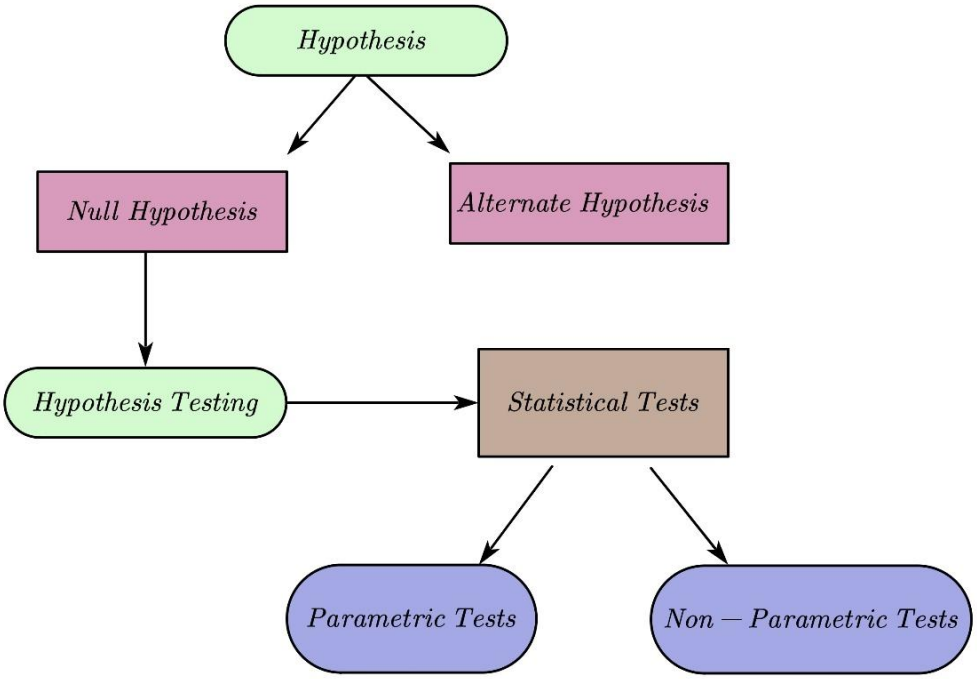

Figure 4-15 Flow chart illustrating the use of test statistics in the null hypothesis testing [67]

4.10.1 Brief overview of parametric and non-parametric analysis

Parametric and non-parametric analyses are two types of statistical procedures through which disparities can be probed on fatigue data sets [68]. In parametric analysis, a fixed number of parameters are considered for statistical tests[69,70]. Here, statistical tests are carried out based on some assumptions about the data sets [71]. It requires less data as compared to non-parametric methods [72]. More so, the parametric analysis assumes that the data has a normal distribution and this approach works best when the spread in the data set of each data set is different [73]. The parameters analysed in this approach include the variance, slope, and intercepts. Meanwhile, non-parametric analysis tends to test medians. It is utilised based on fewer assumptions about data sets [74,75], and usually requires a large data set than parametric methods and has no assumed distribution to the data. Non-parametric methods can perform well in many situations but its performance is at peak when the spread of data in each group is the same. Nonparametric analysis uses the rank test for two or more groups to compare the medians[9]. Here ranks for two groups are totalled separately and the total for the smallest group should fall within the critical chi-squared lower and upper rank totals depending on the levels of significance. This is summarised in Table 4-9.

In this research, only the parametric significance test procedures will be used. The procedure is used on portions of the S-N curve that are linear. The data sets are assumed to have a normal distribution and will generate S-N curves with near parallel or parallel characteristics. This ensures that comparisons are valid solely for stress level ranges pertinent to a given design or application. Having identified the types of analyses to be used in this research, it is important to explain the fundamental concept of statistical hypothesis testing in parametric tests, the null hypothesis, which is crucial when comparing two or more fatigue data sets.

4.10.2 The t-test and null hypothesis meaning and application

A t-test is an inferential statistic used to determine if there is a significant difference between two measured observables. It compares the values of the measured quantities from two data sets and determines if they came from the same population. This comparison helps to determine the effect of chance on the difference, and whether the difference is outside that chance's range. T-tests are used when the data sets follow a normal distribution and

have unknown variances. The t-test value is calculated as the ration of the difference between the measured quantities to the variation that exists in the sample data sets as shown below [9,26,34,46].

$$t = \frac{x_1 - x_2}{\sqrt{{s_{x_1}}^2 - {s_{x_2}}^2}} \tag{4-39}$$

Having determined the type of analyses that will be used in this chapter, it is therefore essential to proceed to explain the fundamental concept in statistical hypothesis testing of Where x_1 and x_2 are any two observed quantities (such as mean, slope, etc.) with variances ${s_{x_1}}^2$ and ${s_{x_2}}^2$ respectively. Higher values of the t-score calculated using equation (4-39) indicate that a large difference exists between the two sample data sets.

The smaller the t-value, the more similarity exists between the two sample sets. The value of the calculated test statistic is compared with a critical value t_β obtained from the critical value table known as the t-distribution table. This value is depended on the level of significance β, and the degrees of freedom f.

The t-distribution table can be formatted for either one-tail or two-tail analyses. One-tail values are employed to assess changes in data sets with a fixed direction of change, whereas two-tail values represent variations in more than one direction, encompassing both increases and decreases. In the analysis conducted in this research, the two-tail distribution table will be used, allowing for the monitoring of both positive and negative effects on the measured observables.

Comparing the t-statistic value from equation (4-39) with the critical value t_β obtained from a two-tail t-distribution table, the null hypothesis is used to conclude as follows.

For:

$t \leq t_\beta$, Null hypothesis accepted (no statistical significance from the two observables)

$t > t_\beta$, Alternate hypothesis or null hypothesis rejected.

What follows is a description of how parametric analysis is used in conjunction with the null hypothesis to establish statistical significance between fatigue data sets.

Table 4-9 Summary of the differences between parametric and non-parametric analyses. [67]

Differences between parametric and non-parametric analyses		
Comparison basis	**Parametric**	**Non-parametric**
Definition	Makes assumptions about fixed parameters (defining properties) of population distribution from which sample is drawn	No knowledge or limited information known.
Assumptions	Normal distribution Homogeneity Linearity Independence	No assumptions considered. Distribution is non-normal or arbitrary
Applications	Compares means of sample with population means	Compares medians of data sets when • Sample is not normally distributed. • Sample size is small • the variables are measured on nominal or ordinal scale
Test involved	• t-test (either a single sample t-test, independent sample t-test or 2 sample t-test, paired sample t-test) • z-test (for sample set > 30) • F-test (used with variances)	• uses the rank test for two or more groups to compare the medians
Sample set	fewer data required, small sample set	Large sample set
Peak performance	Data sets with different spreads	Homogenous spread
Parameters used in this study	Variance Inverse slope Intercept (C_0)	Not applicable

4.10.3 Statistical test on sample fatigue life data sets ($N_{f,i}$) generated at the same stress level

Parametric analysis can be used on fatigue life data sets to ascertain whether sample sets exhibit statistical significance compared to the parent population for the fatigue lives that are generated at the same stress level. To use this approach, the fatigue lives are assumed to follow a normal distribution at this stress level. In this case, the parameters to be tested for significance are the variance and the mean. The test on variance is otherwise known as the test for homogeneity of variance and is assessed and described as below.

4.10.4 Statistical test on homogeneity of variances of two fatigue life data sets.

Consider two normally distributed fatigue datasets at the same stress level with variances ${s_1}^2$ and ${s_2}^2$ with corresponding sample sets n_1 and n_2, respectively. The test statistic F_{cal}, for the homogeneity of the fatigue data sets is calculated as [8,9,24,35,46];

$$F_{cal} = \frac{{s_1}^2}{{s_2}^2} \tag{4-40}$$

In order to ascertain the presence of a significant difference at a designated level of significance (β), the critical value of the F_p distribution associated with $n_1 - 1$ degrees of freedom for s_1 and $n_2 - 1$ degrees of freedom for s_2, derived from statistical tables found in Refs. [8,13,26,34] is compared with the F-distribution value F_{cal}, calculated using equation (4-40). Should $F_{cal} \leq F_p$ the sample variances are deemed not significantly different (homogeneous) in accordance with the null hypothesis. Conversely, if $F_{cal} > F_p$, the two datasets are considered significant.

4.10.5 Statistical test on two means when the standard deviations are not significantly different.

Suppose two homogenous fatigue life data sets belong to the same population; in this scenario, the common estimate of the population variance ${s_e}^2$, is calculated as follows [46,76]:

$${s_e}^2 = \frac{(n_1 - 1){s_1}^2 + (n_2 - 1){s_2}^2}{n_1 + n_2 - 2} \tag{4-41}$$

in which n_1 and n_2 represent the sample sizes of the two fatigue life datasets, and s_1 and s_2 are their respective standard deviations. The test statistic for comparing their means t_μ, is calculated as [9,46]:

$$t_{\mu} = \frac{\overline{\log N_{f1}} - \overline{\log N_{f2}}}{s\sqrt{\frac{1}{n_1} + \frac{1}{n_2}}} \tag{4-42}$$

where $\overline{\log N_{f1}}$ and $\overline{\log N_{f2}}$ represent the mean values of the logarithm of fatigue life for the two fatigue life sample sets. Given a predetermined significance level β, the corresponding critical value t_{β} associated with degrees of freedom $f = n_1 + n_2 - 2$ is obtained from statistical tables as in Refs. [13,35,43,55]. If $/t_{\mu}/> t_{\beta}$, it can be concluded that the populations from which the sample datasets are derived are distinct; otherwise, there is no statistically significant difference in the means of the sample sets.

4.10.6 Statistical test on two means when the standard deviations are significantly different.

If the sample standard deviations can be verified to be significantly different, then the hypothesis that the populations means are significant or not can be tested by calculating a test statistic t'_{μ} as [9,34]:

$$t'_{\mu} = \frac{\overline{\log N_{f1}} - \overline{\log N_{f2}}}{\sqrt{\frac{{s_1}^2}{n_1} + \frac{{s_2}^2}{n_2}}} \tag{4-43}$$

Similarly, for a predefined significance level β, the associated characteristic value t_{β} is determined based on a defined value of the degree of freedom defined as:

$$f = \left[\frac{c^2}{n_1 - 1} + \frac{(1-c)^2}{n_2 - 1}\right]^{-1} \tag{4-44}$$

where c is a dimensionless quantity defined as [9]:

$$c = \frac{\frac{{s_1}^2}{n_1}}{\frac{{s_1}^2}{n_1} + \frac{{s_2}^2}{n_2}} \tag{4-45}$$

If the value for the calculated degree of freedom f is not an integer, then its value is approximated to the nearest smaller integer. The value of f is then used to extract the associated characteristic value t_{β} based on the predefined level of significance. In the same way, if $/t'_{\mu}/< t_{\beta}$, then there is no significance in the means of fatigue lives of the two data sets and for $/t'_{\mu}/> t_{\beta}$, the means are judged to be different.

The analysis outlined above is carried out on fatigue life datasets under the assumption that they have been collected at uniform stress levels and follow a normal distribution. When dealing with datasets acquired from a variety of stress levels, the parametric analysis is extended by considering the parameters within the mean curves generated from these datasets, as elaborated below.

4.11 Parametric Statistical analysis on fatigue data sets $(\boldsymbol{\sigma_i, N_{f,i}})$

To statistically compare the significance of two fatigue data sets, particularly the mean S-N curves using the null hypothesis, three steps are employed [24,46]. The initial step entails testing whether the standard deviations around the distinct lines can be assumed to be drawn from the same population, thus demonstrating homogeneity. Secondly, the examination involves assessing whether the two mean curves can be viewed as parallel. Lastly, the investigation centres on determining if the two parallel regression lines can be considered collinear, meaning they lie on the same line [43].

4.11.1 Test that the variance of the data set is homogenous

Homogeneity of variance is used to describe a data set that has the same variance as another [26,34]. This equivalence can be visually identified through consistent scatter on a scatter plot or by observing equivalent standard deviations in the derived parameters summarized in Table 4-10 [46,77]. If, upon inspection, the data exhibits heteroscedasticity, a statistical hypothesis test is carried out by constructing a test for the homogeneity of variances between the fatigue data sets.

Consider for example the data summarized in Table 4-10, with two data sets 1&2 having sample sizes n_1 and n_2 respectively, with corresponding degrees of freedom $(n_1 - 2)$, and $(n_2 - 2)$.

Table 4-10; Summary of regression quantities associated with two sample data sets

i	n	Mean Log stress	Mean life	Corrected sum of squares	Corrected sum of squares	Corrected sum of cross products	Slope	Common error stand.Dev	Stand. dev.
1	n_1	$\overline{X}_1$	$\overline{Y}_1$	$\sum(X_1 - \overline{X}_1)^2$	$\sum(Y_1 - \overline{Y}_1)^2$	$\sum(X_1 - \overline{X}_1)(Y_1 - \overline{Y}_1)$	$C_{1,1}$	$s_{y1.x1}$	s_1
2	n_2	$\overline{X}_2$	$\overline{Y}_2$	$\sum(X_2 - \overline{X}_2)^2$	$\sum(Y_2 - \overline{Y}_2)^2$	$\sum(X_2 - \overline{X}_2)(Y_2 - \overline{Y}_2)$	$C_{1,2}$	$s_{y2,x2}$	s_2

Additionally, assume that ${s_1}^2$ and ${s_2}^2$ represent the variances of the respective data sets 1 and 2, with $s_1 > s_2$. The test statistic F_{cal} is calculated according to equation (4-40) [9,13,34,46]. By referring to standard F-distribution tables, the critical value entry (F_{crit}) corresponding to the degrees of freedom $f_1 = (n_1 - 2)$ and $f_2 = (n_2 - 2)$ is extracted and subsequently compared with the calculated value.

If it turns out that $F_{cal} \leq F_{crit}$, it can be concluded that both variance estimates are homogeneous and can be considered as independent estimators of the population. Consequently, the null hypothesis is validated, signifying that the variances of the two mean curves are not significant. In this situation, the variance estimate ${s_e}^2$ defining both data sets is defined as:

$${s_e}^2 = \frac{(n_1 - 1){s_1}^2 + (n_2 - 1){s_2}^2}{(n_1 - 2) + (n_2 - 2)} \tag{4-46}$$

To summarize, the two sample variances are considered significant if the equation below is validated.

$$\frac{{s_n}^2}{{s_d}^2} - F_{crit}(1 - \beta, f_n, f_d) < 0 \tag{4-47}$$

In this equation, ${s_n}^2$ and ${s_d}^2$ represent the variances of the numerator and denominator of equation (4-40) respectively. Additionally, f_n and f_d correspond to the degrees of freedom of the numerator and the denominator, respectively. And $F_{crit}(1 - \beta, f_n, f_d)$ denotes the critical value obtained from entries corresponding to the significance level β, and the respective degrees of freedom.

4.11.2 Test that the lines are parallel

From Table 4-10, let $C_{1,1}$ and $C_{1,2}$ represent the slopes of two data sets 1 & 2 respectively. The t-test statistic for the significance of the slopes t_{C_1} is calculated as [34,46]:

$$t_{C_1} = \frac{\left|C_{1,1} - C_{1,2}\right|}{\sqrt{\left(\frac{1}{\sum_{i=1}^{n_1}\left(\log\sigma_{i,1} - \overline{\log\sigma_{1,1}}\right)^2} + \frac{1}{\sum_{i=1}^{n_2}\left(\log\sigma_{i,2} - \overline{\log\sigma_{1,2}}\right)^2}\right)}\, s_e} \tag{4-48}$$

This value of t_{C_1} is compared with the student's distribution value t_β obtained from statistical tables aligning with degrees of freedom $f_1 + f_2 = (n_1 - 2) + (n_2 - 2)$ and the chosen significance level. Should the value of t_{C_1} be lower than this critical value, the

slopes are deemed not statistically significant. Conversely, if t_{C_1} is more than the critical value, there is no bases to accept the null hypothesis.

In the case of statistical insignificance, the mean curves are considered to be parallel. Hence, a common estimate for the slopes C_1 is determined. This estimation takes the form of the weighted average of both slopes $C_{1,1}$ and $C_{1,2}$ it can be calculated as [46]:

$$C_1 = \frac{\sum_{i=1}^{n_1}\left(\log\sigma_{i,1} - \overline{\log\sigma_{1,1}}\right)^2 \times C_{1,1} + \sum_{i=1}^{n_2}\left(\log\sigma_{i,2} - \overline{\log\sigma_{1,2}}\right)^2 \times C_{1,2}}{\sum_{i=1}^{n_1}\left(\log\sigma_{i,1} - \overline{\log\sigma_{1,1}}\right)^2 + \sum_{i=1}^{n_2}\left(\log\sigma_{i,2} - \overline{\log\sigma_{1,2}}\right)^2} \qquad (4\text{-}49)$$

The resulting estimate of the variance of C_1 denoted as ${s_{C_1}}^2$ is such that the combined estimate of both variances and the error in the estimation of C_1 has one degree of freedom is calculated as:

$${s_{C_1}}^2 = \frac{\left(C_{1,1} - C_{1,2}\right)^2}{\frac{1}{\sum_{i=1}^{n_1}\left(\log\sigma_{i,1} - \overline{\log\sigma_{1,1}}\right)^2} + \frac{1}{\sum_{i=1}^{n_2}\left(\log\sigma_{i,2} - \overline{\log\sigma_{1,2}}\right)^2}} \qquad (4\text{-}50)$$

However, ${s_{C_1}}^2$ is always small [46] when the two lines are considered parallel. Alternatively, the estimated common variance ${s_e}^2$ is defined as in equation (4-46) and according to the null hypothesis, the individual slopes are significant if $t_{C_1} > t_\beta$ in equation (4-48).

4.11.3 Test that the parallel lines are collinear

The two mean curves from the fatigue data sets are collinear if both have similar intercept and slope. Suppose the expected values for both curves are defined as $\mu_{N_{f,1}/\sigma_1} = C_0 + C_1\log\sigma_1$ and $\mu_{N_{f,2}/\sigma_2} = C_0 + C_1\log\sigma_2$ for any stress level σ, with both intercept and slope constant. Then at the mean point, there is a random variable δ defined as:

$$\left(\overline{\log N_{1,i}} - \overline{\log N_{2,i}}\right) - C_1\left(\overline{\log\sigma_{1,i}} - \overline{\log\sigma_{2,i}}\right) = \delta \qquad (4\text{-}51)$$

δ is normally distributed with mean equal to zero and variance $\mathrm{Var}(\delta)$ defined by [24,26].

$$\mathrm{Var}(\delta) = s^2\left[\frac{1}{n_1} + \frac{1}{n_2} + \frac{\left(\overline{\log\sigma_{1,i}} - \overline{\log\sigma_{2,i}}\right)^2}{\sum_{i=1}^{n_1}\left(\log\sigma_{i,1} - \overline{\log\sigma_{1,1}}\right)^2 + \sum_{i=1}^{n_2}\left(\log\sigma_{i,2} - \overline{\log\sigma_{1,2}}\right)^2}\right] \qquad (4\text{-}52)$$

Then a test statistic $t(\delta)$ for the random variable δ can be calculated as shown in equation (4-53) where s_e is the new pooled estimate of the combined variance corresponding to $[(n_1 - 2) + (n_2 - 2) + 1]$ degrees of freedom.

$$t(\delta) = \frac{\left|\left(\overline{\log N_{1,1}} - \overline{\log N_{2,1}}\right) - C_1\left(\overline{\log\sigma_{1,1}} - \overline{\log\sigma_{2,1}}\right)\right|}{\sqrt{\left[\frac{1}{n_1} + \frac{1}{n_2} + \frac{\left(\overline{\log\sigma_{1,1}} - \overline{\log\sigma_{2,1}}\right)^2}{\sum_{i=1}^{n_1}\left(\log\sigma_{i,1} - \overline{\log\sigma_{1,1}}\right)^2 + \sum_{i=1}^{n_2}\left(\log\sigma_{i,2} - \overline{\log\sigma_{1,2}}\right)^2}\right]} s_e} \quad (4\text{-}53)$$

Hence, the two mean curves are considered not to be collinear if the test statistic $t(\delta)$ is significant. i.e. $/t(\delta)/> t_\beta$ where $t_\beta$is the characteristic value associated with the predefined significance level and degrees of freedom. If $/t(\delta)/\leq t_\beta$, then the null hypothesis confirms that the two curves are collinear [46].

In conclusion, when considering the null hypothesis, two mean curves from two fatigue data sets are considered insignificant if the variances, gradients, and intercepts are found to be statistically insignificant. If there is no substantial evidence to support the acceptance of significance for any of these parameters, then, in accordance with the criteria of the null hypothesis, there is no foundation to assert that the data sets are insignificant.

4.11.4 Composite hypotheses and its significance level

It is important to highlight that in composite hypothesis testing, the null hypothesis is evaluated separately for each parameter of variance, intercept, and slope, all at a specified significance level. The cumulative level of significance is obtained by summing all the individual significance levels when each parameter is tested as illustrated in the flow chart in Figure 4-16. This can potentially lead to a high chance of rejecting these hypotheses even if all three parameters are accurate. As a result, it is advisable to employ a lower significance level for each individual parameter test when conducting composite hypothesis testing [9,26,46]. For instance, a significance level of 1.7% could be used, resulting in an approximate combined level of significance of about 5%. Under a similar condition, when testing for the consistency in sample variance and means, a significance level of 2.5% would be appropriate. This approach helps reduce the increased risk of erroneous rejections associated with composite hypothesis testing. In general, the significance level for each tested parameter is calculated by dividing the significance level for the null hypothesis by the total number of parameters being evaluated [8,9,34].

The composite hypothesis is deemed acceptable only when all the test statistics pertaining to the parameters of variance, intercept, and slope are insignificant. If any of these parameters lacks sufficient evidence to support the acceptance of the null hypothesis, it follows that there is no valid ground to accept the significance of two S-N curves from the data sets.

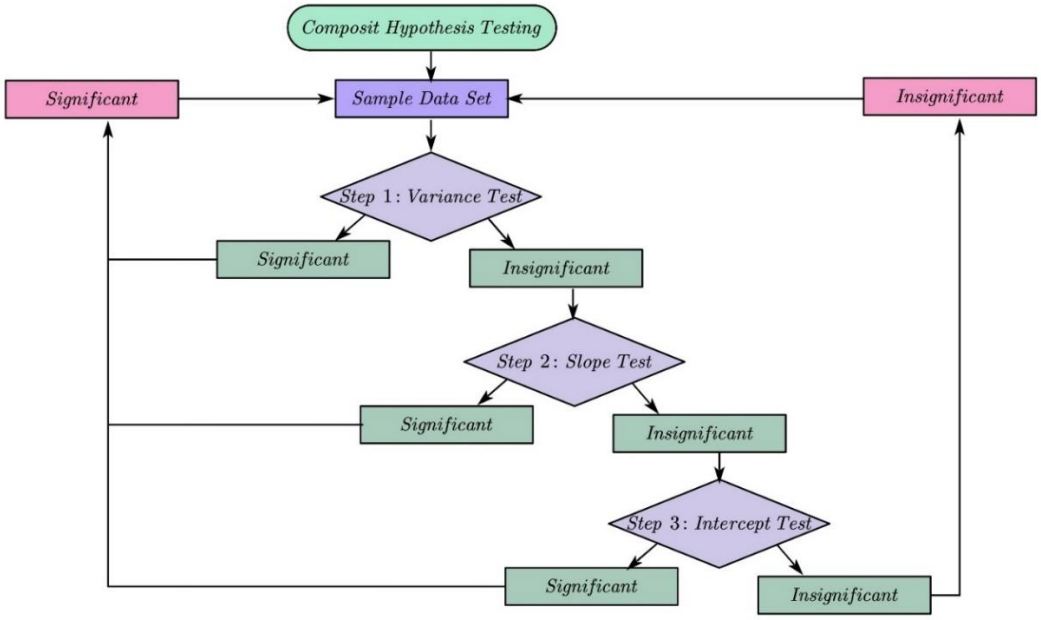

Figure 4-16 The flow chart illustrating how to test the statistical significance of two S-N curves [67]

4.12 Validation of parametric fatigue data analysis using notched fatigue data sets

The notched fatigue data sets were produced using the protocols described in Chapter 5. In the analysis of the fatigue results, only the gross stresses were taken into consideration. The gross stress is the nominal stress experienced by the specimen, assuming it is smooth and free of any geometric discontinuities that could affect the stress distribution. By using gross stresses, all specimens are therefore assumed to have the same geometry and it is hoped that only the statistical approach is able to identify the difference in notch geometry by analysing the experimental results. By so doing, this approach focused only on utilizing statistical methods to determine whether the discrepancies in the generated fatigue data sets were statistically significant, based on a predetermined threshold. Before delving into the details of this statistical analysis procedure, it is essential to provide a brief overview of the types of analyses that can be applied to these data sets.

4.12 Validation of parametric fatigue data analysis using notched data

4.12.1 Application of parametric test analysis on mean curves from notched specimens

For any two data sets considered for each of the material, only the scatter bands and data points will be represented on each graph to visualize the significance in these data. The goal is to establish confidence in the execution of this procedure and validate its applicability. As mentioned in the introduction, upon validation, this approach will be used to evaluate the statistical significance of datasets exclusively derived from plain specimens charged with hydrogen compared with data sets from specimens that did not undergo any hydrogen charging.

To achieve this, the approaches were used by considering the gross stress amplitudes with the corresponding fatigue life. The use of gross stress amplitudes served to hide the presence and influence of notch geometry in the data sets compared. The primary goal was to investigate whether these statistical approaches can effectively identify the presence of different notch geometry in the datasets. Table 4-11 summarises the fatigue properties of the materials steel, brass and cast iron, which were used to generate the data sets required for this statistical analysis in this chapter. The fatigue and fracture properties were generated using the post-processing techniques suggested by the ASTM, LRM and the IIW, described in this research.

As gathered from the literature, alterations in the scatter of fatigue data sets usually indicate shifts in material variability, surface finishes, notch sensitivity, environmental factors, or testing conditions [5,9,42]. Examining Table 4-11 reveals minimal change in the data scatter from the steel specimens, with a variance of approximately 0.2. This implies reduced variability in the steel material properties, geometry, and test conditions. However, a visible decrease in the estimated endurance limits after 2 million cycles suggests an underlying characteristic contributing to this change. Likewise, there is a noticeable shift in the scatter of fatigue data generated from brass specimens, revealing a reduction in their endurance limits. Conversely, cast iron specimens display an increase in data scatter, indicating a rise in conditions influencing this change. By analysing the data in this table, it is conceivable that certain factors impact the fatigue properties of these materials used in this research. The next step involves the application of parametric test analysis on these data sets to determine the statistical significance of the observed variations, thereby illustrating the use of statistical approaches to set apart data sets.

Table 4-11 Summary of fatigue properties at a probability of 95%, of notch specimens under uniaxial loading in tension at a frequency of 10Hz

Specimen type	Fatigue test results							
	Sample set, n	R	Inverse slope, k	Variance s^2	σ_0 [MPa]	$\sigma_{0,95\%}$ [MPa]	$\sigma_{0,5\%}$ [MPa]	τ_σ
S_1mm	10	0.1	9.35	0.024	119.10	108.56	130.66	1.20
S_2mm	10	0.1	8.38	0.023	96.06	86.86	106.21	1.22
S_3mm	10	0.1	8.10	0.015	79.87	73.32	87.01	1.19
Br_1mm	10	0.1	8.56	0.012	72.58	67.56	77.98	1.15
Br_2mm	10	0.1	7.00	0.011	56.33	51.72	61.36	1.19
Br_3mm	10	0.1	6.14	0.015	46.75	41.91	52.15	1.24
CI_1mm	10	0.1	11.06	0.257	33.04	25.60	42.66	1.67
CI_2mm	10	0.1	13.00	0.071	27.76	24.68	31.23	1.27
CI_3mm	10	0.1	10.69	0.031	21.07	19.23	23.08	1.20

4.12.1.1 Parametric analyses of data sets generated from steel specimens.

The raw data from steel specimens have been reported in the experiments and raw data chapter. Considering steel specimens with 1mm notches, the specimens that survived the fatigue test at the tested stress level, such as specimen S_1mm_1 and S_2mm_8, ware retested at a higher stress amplitude of 2.43.83MPa and 243.24MPa respectively. Similarly, for steel specimens with a 2mm diameter notches, specimens S_2mm_3, S_2mm_9 and S_2mm_10 survived the tests and were retested at stress amplitudes of 182.72MPa, 183.01MPa and 175.53MPa respectively. And the results from testing 3mm diameter notched steel specimens, only specimen S_3mm_6 survived the test and was retested at a stress amplitude of 154.65MPa. For some sample failed specimens and fracture surfaces, see chapter on experiments and raw data.

At a confidence level of 95% and significance level of 5%, the S-N curves and scatter bands, for steel are summarised in Figure 4-17. The curves have been determined using the post-processing techniques described in this research. These curves also show the endurance limits estimated after 2×10^6cycles and values of their inverse slopes.

Building upon the statistical test analysis explained, the analyses summarised in Table 4-12, is generated using the fatigue data sets for steel by considering the gross stress amplitude. From this table and considering S_1mm and S_2mm data sets, their variances show that they were drawn from the same population as well as their inverse slopes. However, the mean curves representing these data sets do not lie on the same plane and are not collinear.

Thus, both data sets cannot be represented by the same line with a 95% confidence level. It is then concluded that these data sets are statistically significant.

Similarly, S_1mm and S_3mm data sets are statistically insignificant in variance and inverse slope, yet they are not collinear and thus these two data sets are also statistically significant. S_2mm and S_3mm follow the same pattern as the previous data sets and are statistically significant.

In summary, these data sets show that the curves representing the data sets are not collinear, and hence do not lie on the same plane. These data sets are statistically significant (are different) and does not come from the same population. Because these fatigue data sets were generated by testing specimens with different notch radii, (1mm, 2mm and 3mm circular notches), it can be concluded that the t-test statistical analyses are capable of detecting a change in the geometry of these notches for steel specimens.

Table 4-12 Summary of statistical analysis using the null hypothesis for the fatigue data sets generated by testing steel specimens with 1mm, 2mm and 3mm notches

Source of data sets compared	**Variance test ($\boldsymbol{\beta = 1.7\%}$)**	**Slope test ($\boldsymbol{\beta = 1.7\%}$)**	**Intercept test ($\boldsymbol{\beta = 1.7\%}$)**	**Conclusion ($\boldsymbol{\sum \beta \cong 5\%}$)**
S_1mm and S_2mm	-4.01	-1.47	0.48	Significant
S_1mm and S_3mm	-3.50	-0.88	1.09	Significant
S_2mm and S_3mm	-3.58	-1.87	0.41	Significant

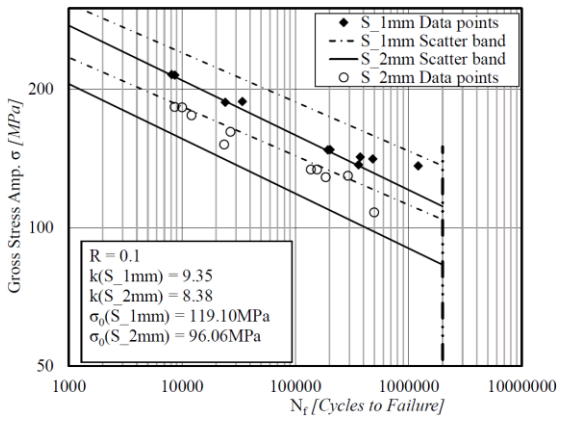

a)

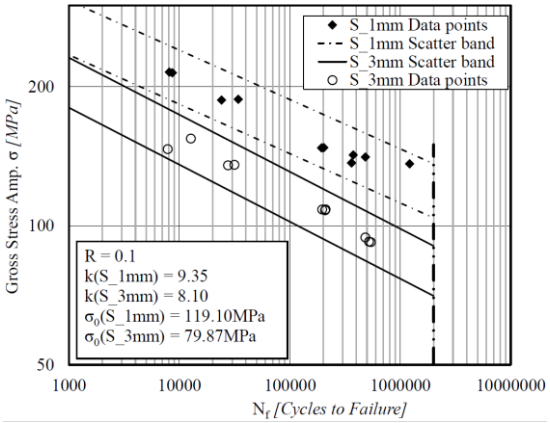

b)

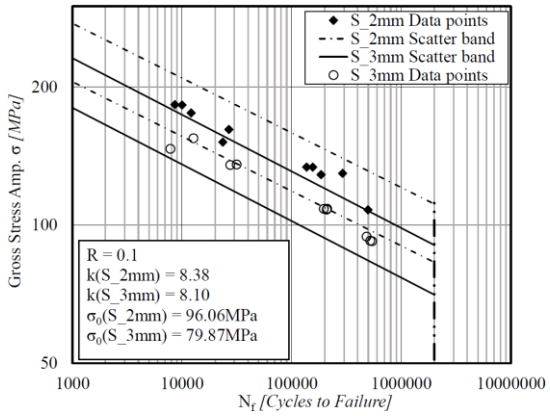

c)

Figure 4-17 a) Scatter bands at 95% level of confidence and 5% level of significance for: a) S_1mm and S_2mm curves, b) S_1mm and S_3mm curves and c) S_2mm and S_3mm curves [67].

4.12.1.2 Parametric analyses on data sets generated by testing brass specimens.

The data sets produce from brass specimens are reported in the experiment and raw data chapter, as well as some selected failed specimens from the three different lots. For any two data sets, the scatter bands of the mean curves at a confidence level of 95% and 95% probability of survival representing the data sets, using gross stresses, are summarized in Figure 4-18. There were no runouts in the stress levels for brass.

The test statistic values generated by comparing these graphs for statistical significance are summarized in Table 4-13. Similar to the case of steel, the data sets in this table are found to be statistically significant because each of the pair of data are not collinear. This is shown by the positive characteristic test values, which show that the difference in the intercepts of each of the curves is far greater than the characteristic value at the chosen probability. Hence, statistical test analysis is capable of detecting changes in geometry from brass fatigue data sets as seen in this example.

4.12 Validation of parametric fatigue data analysis using notched data

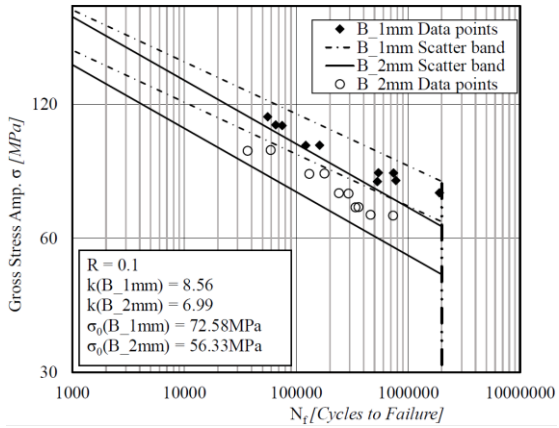

a)

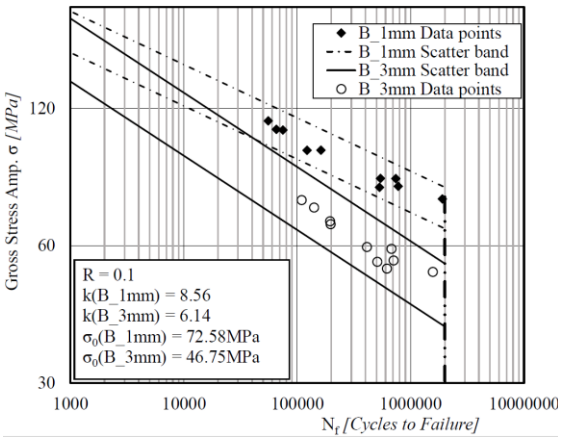

b)

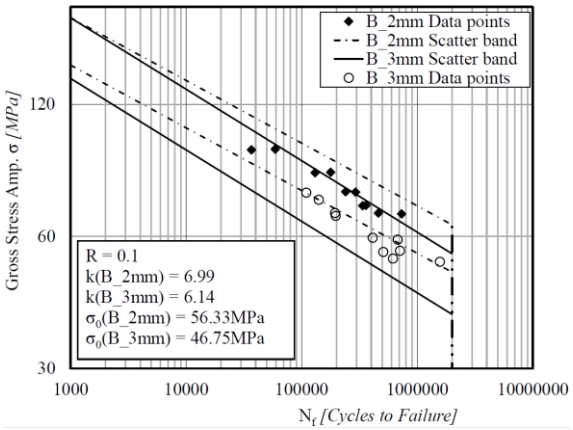

c)

Figure 4-18 Scatter bands at 95% level of confidence and 5% level of significance for: a) B_1mm and B_2mm curves, b) B_1mm and B_3mm curves and c) B_2mm and B_3mm curves [67].

Table 4-13 Summary of statistical analysis using the null hypothesis for the fatigue data sets generated by testing brass specimens with 1mm, 2mm and 3mm notches

Source of data sets compared	**Variance test ($\beta = 1.7\%$)**	**Slope test ($\beta = 1.7\%$)**	**Intercept test ($\beta = 1.7\%$)**	**Conclusion ($\sum \beta \cong 5\%$)**
B_1mm and B_2mm	-4.01	-0.77	0.52	Significant
B_1mm and B_3mm	-3.86	-0.03	0.90	Significant
B_2mm and B_3mm	-3.80	-1.69	0.23	Significant

4.12.1.3 Parametric analyses from data sets generated by testing cast iron specimens.

The data sets produced from cast iron specimens are reported in the experiment and raw data chapter, as well as some selected failed specimens. The scatter bands for any two data sets for cast iron are presented in Figure 4-19 at a confidence level of 95% and 95%

probability of survival using gross stresses. Similarly, the results of the statistical test analyses for significance are also summarised in Table 4-14.

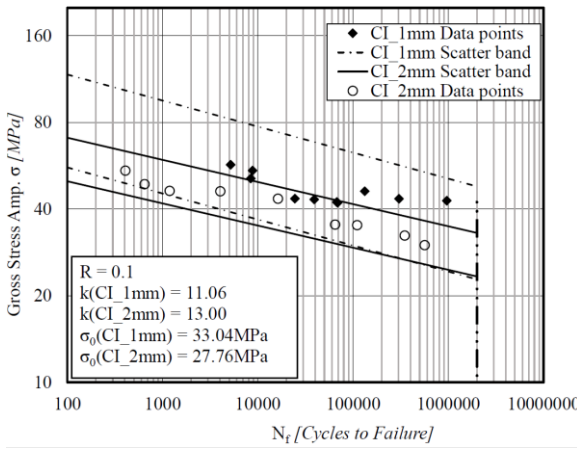

a)

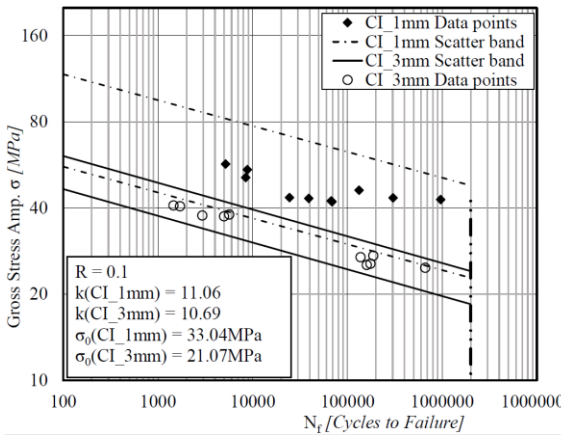

b)

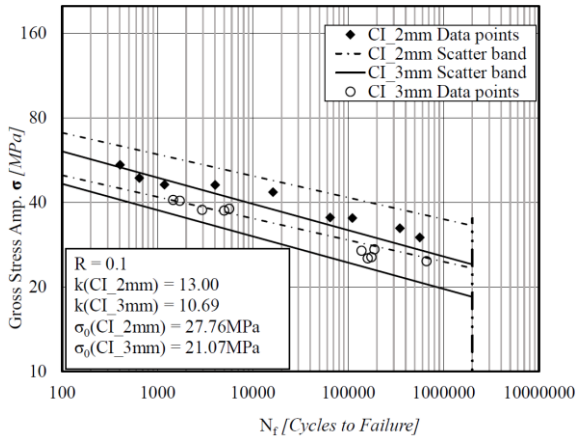

c)

Figure 4-19 Scatter bands at 95% level of confidence and 5% level of significance for: a) CI_1mm and CI_2mm curves, b) CI_1mm and CI_3mm curves and c) CI_2mm and CI_3mm curves [67].

Table 4-14 Summary of statistical analysis using the null hypothesis for the fatigue data sets generated by testing cast iron specimens with 1mm, 2mm and 3mm notches

Source of data sets compared	**Variance test ($\beta = 1.7\%$)**	**Slope test ($\beta = 1.7\%$)**	**Intercept test ($\beta = 1.7\%$)**	**Conclusion ($\sum \beta \cong 5\%$)**
CI_1mm and CI_2mm	-2.04	-6.75	0.68	Significant
CI_1mm and CI_3mm	3.30	-7.36	1.36	Significant
CI_2mm and CI_3mm	-2.87	-0.86	0.69	Significant

As observed from the test statistic values for cast iron in Table 4-14, the data obtained by testing the various batches of cast iron specimens are all statistically significant. For the data sets from cast iron specimens with 1mm and 2mm notches, and using gross stresses,

the spread in these data sets suggests that they are drawn from the same population. The inverse slopes of these sets are not statistically significant. However, the mean curves representing these datasets are not collinear, indicating statistical significance.

Also considering data sets from specimens with 1mm and 3mm notches, the spread in these datasets shows that they do not belong to the same population, even though the inverse slopes from these datasets are not statistically significant. In addition, the mean curves representing the data sets are not collinear. Therefore, it is reasonable to conclude that these datasets are indeed significant.

Similar to the data sets from specimens with 2mm and 3mm notches are also statistically significant because the mean curves representing both sets are not collinear.

Thus, it has been possible to show that, by using gross stresses and statistical approaches, the data sets from the different batches of cast iron are all significant. This approach has been able to verify that notches with varied geometry will have an impact on the fatigue property of cast iron even when some types of cast iron show less responsivity to small notch radii [78].

4.12.2 Application of parametric test analysis for data sets that are statistically insignificant

The question of how the parametric analyses work for data sets that are statistically insignificant remains to be visualised. The section above has been able to show that the data sets generated by testing notched specimens of different geometry are statistically significant. It is also important to illustrate how this approach will work for data sets that are statistically insignificant. To achieve this, data from the literature was used, particularly the data in Ref. [57], in which the data sets were generated by testing plain specimens with two types of surface finishes; a smooth-polished surface finish and a hot-forged surface finish with different levels of hardness, used to evaluate and quantify forged surface finish effect at several hardness levels. It should be noted that this project is only interested in using the data sets produced in this reference rather than reviewing the research reported therein.

Table 4-15 Fatigue data from fig 10a of Ref. [57]

As-forged cantilever		As-forged bending	
σ (MPa)	N(cycles)	σ (MPa)	N(cycles)
892	5951	546	43586
607	23826	398	94495
596	39661	396	110938
551	43176	273	698654
396	144489	274	820228
396	195427	227	851781
324	328393	227	981303
324	367768		
274	753441		
248	623852		
249	760585		
229	1327244		

The data set considered in this case is the data shown in Fig 10a of this reference for as-forged in bending and as-forged in cantilever testing. This data is summarised in Table 4-15, while the overlapping scatter bands from the S-N curves plotted at a confidence level of 95% with a probability of survival of 95%, derived from this data set is as shown in Figure 4-20.

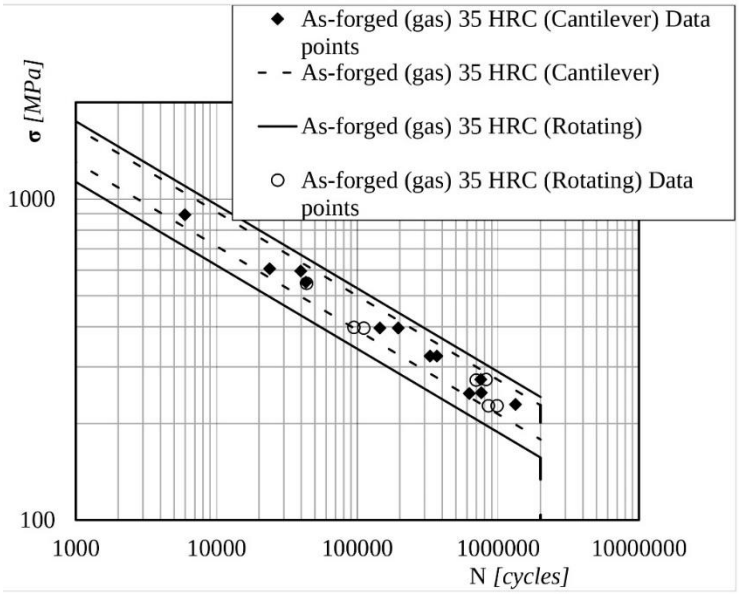

Figure 4-20 Scatter band at 95% level of confidence and 5% level of significance for a significant data set of as-forged (cantilever) and as-forged (bending) in Ref. [57]

4.12 Validation of parametric fatigue data analysis using notched data

The analysis for this pair of data is summarised in Table 4-16 and it clearly shows that the difference in the data set is statistically insignificant at a level of 5%. These two data sets can be seen as drawn from the same population, despite the difference in the endurance limits extrapolated after 2 million cycles. In this example, the endurance limits differ by about 3%. Because the data sets are insignificant, it can be concluded that there is a difference in the fatigue behaviours for forged surface finish in rotating bending and cantilever bending.

Table 4-16 Summary of parametric statistical analysis of fatigue data set from Ref.[57]

Source of data sets compared	**Variance test ($\boldsymbol{\beta = 1.7\%}$)**	**Slope test ($\boldsymbol{\beta = 1.7\%}$)**	**Intercept test ($\boldsymbol{\beta = 1.7\%}$)**	**Conclusion ($\boldsymbol{\sum \beta \cong 5\%}$)**
Forged bending-cantilever	-5.66	-0.89	-0.07	Insignificant

The analysis was conducted by examining the mean curves derived from the compared data sets. If the stress levels, considered in generating fatigue data during testing, are statistically insignificant, their mean stress levels should also be statistically insignificant. Ref. [34] recommends performing a check for statistical significance only for stress levels around the mean stress levels during testing. In this scenario, the variance and slope test statistics are calculated using equations (4-47) and (4-48) respectively, while the equation for checking collinearity is defined as follows [9,24,46]:

$$t(\delta) = \frac{\left|C_{0,1} - C_{0,2}\right|}{\sqrt{\left[\frac{1}{n_1} + \frac{1}{n_2} + \frac{\left(\overline{\log\sigma_{1,ı}}\right)^2}{\sum_{i=1}^{n_1}\left(\log\sigma_{i,1} - \overline{\log\sigma_{ı,1}}\right)^2} + \frac{\left(\overline{\log\sigma_{2,ı}}\right)^2}{\sum_{i=1}^{n_2}\left(\log\sigma_{i,2} - \overline{\log\sigma_{ı,2}}\right)^2}\right]} s_e} \quad (4\text{-}54)$$

In which $C_{0,1}$ and $C_{0,2}$are the estimated intercepts of the regression lines through the two data sets, s_e the estimate of the common variance of the two data sets defined by equation (4-46). By applying this to the experimental data, Table 4-17 summarises the significant conclusions arrived at. The results in this table show that by restricting the stress range to a narrow region around the mean stress for the statistical significance tests, only changes of approximately 36% in the endurance limit are necessary to indicate a potential statistical significance within the fatigue data sets. Therefore, restricting the statistical significance analysis to only sections of fatigue data sets will result in different conclusions about

significance and may not accurately represent the fatigue properties revealed by the entire data set.

Table 4-17 Summary of statistical analysis for the fatigue data sets generated by testing all specimens around their mean stresses

	Source of data sets compared	Variance test ($\beta = 1.7\%$)	Slope test ($\beta = 1.7\%$)	Intercept test ($\beta = 1.7\%$)	Conclusion ($\sum \beta \cong 5\%$)
Steel	S_1mm and S_2mm	-4.00	-1.47	**-2.55**	Insignificant
	S_1mm and S_3mm	-3.50	-0.88	**-0.56**	Insignificant
	S_2mm and S_3mm	-3.58	-1.87	**-3.35**	Insignificant
Brass	B_1mm and B_2mm	-4.01	-0.77	**-0.82**	Insignificant
	B_1mm and B_3mm	-3.87	-0.03	**1.09**	Significant
	B_2mm and B_3mm	-3.80	-1.69	**-2.69**	Insignificant
Cast Iron	CI_1mm and CI_2mm	-2.04	-6.75	**-12.40**	Insignificant
	CI_1mm and CI_3mm	**3.30**	-7.36	**-9.97**	Significant
	CI_2mm and CI_3mm	-2.87	-0.86	**-0.34**	Insignificant

By applying this approach to the statistically insignificant data from the literature, it should be noted that the test statistics calculated from the datasets are expected to be considerably smaller in this case. Specifically, the test-statistical value for the intercept decreases from -0.07 to -2.29.

4.13 Remark on statistical significance analyses and application to this research

In this section, it has been confirmed that statistical tests can effectively compare various fatigue data sets by evaluating the statistical significance testing hypotheses using t-tests. The use of gross stresses permitted the assumption that the geometry of all specimens used to generate the test data were the same. The outcomes indicated that the fatigue datasets are statistically significant, indicating that they originate from specimens with distinct geometries. This was true because the data sets were derived from specimens with varying notch dimensions and root radii.

4.12 Validation of parametric fatigue data analysis using notched data

Thus, parametric analysis employs a well-established statistical method that provides robust conclusions based on the level of significance. This greatly helps in making informed decisions between fatigue data sets for design purposes. It offers an objective way to assess the significance of differences in fatigue properties, by reducing subjective biases in interpretation of results. It is data-driven, consistent and efficiently handles all the parameters that define the mean curve and further offers a more comprehensive assessment of the fatigue behaviour as opposed to visual assessments. When utilised accurately, parametric analysis helps minimize errors that might arise from misinterpreting data or drawing conclusions solely based on visual observations.

Furthermore, this analysis has demonstrated a comprehensive approach that can be employed to determine the feasibility of merging fatigue datasets from various sources for enhanced reliability. This approach aims to minimize the time and cost associated with conducting fatigue experiments, as well as compare the impact of specific characteristics on the mechanical properties of a material. Some of these characteristics may include and not limited to, surface finish, environmental impacts, or curing conditions, Machining, etc. This is important because more data increases the level of reliability and fatigue experiments are costly and time-consuming. Using data sets from a variety of sources will reduce the cost of time and money. More so, in the case of fatigue data sets used in the very high cycle fatigue regime, where a substantial amount of data is needed to establish distributions at each stress level, this process becomes especially valuable.

This concept will be used in this research to compare the fatigue behaviour of specimens pre-charged with hydrogen and specimens without any pre-charging of selected metals. Therefore, the design stress from these selected pipeline metal specimens that have been charged with hydrogen will be compared to specimens that have not been charged with hydrogen (existing pipeline network) can be conveniently established based on a desired level of significance.

4.14 Chapter conclusion

In conclusion, this chapter has provided a detailed description of post-processing approaches for fatigue data, aimed at illustrating how the fatigue data sets generated in this research will be used to determine the fatigue properties of ex-service pipeline metals. While the statistical significance test method proves adept at detecting very small changes in fatigue data sets, a challenge arises in determining the significance of such changes,

especially when monitoring the percentage change in the endurance limit. Nevertheless, this approach remains valuable, provided a well-defined level of significance is employed, allowing for a better understanding of the impact of hydrogen exposure on the metals' fatigue properties.

Therefore, to determine the fatigue properties of materials, a fatigue data set is required. In the next chapter, a detailed description of the experimental procedures used to generate the fatigue data sets for this research will be provided, so that the methodology described in this chapter can be used to estimate the change in the fatigue properties. The experiments will aim to determine the corresponding fatigue life for each specimen under specific stress levels and defined loading conditions. The fatigue data sets will be generated under constant amplitude loading to assess the fatigue properties of various ex-service pipeline materials exposed to a hydrogen environment for varying durations.

4.15 References

[1] Y. Feng, C. Gao, Y. He, T. An, C. Fan, H. Zhang, Investigation on tension-tension fatigue performances and reliability fatigue life of T700/MTM46 composite laminates, Compos. Struct. 136 (2016) 64–74. https://doi.org/10.1016/j.compstruct.2015.09.057.

[2] F. Campbell, Fatigue and Fracture, Understanding The Basics, ASM International, Materials Park, Ohio, 2012.

[3] Y. Feng, B. Ma, T. Zhang, T. Zhang, Y. He, S. Jiao, Reliability Fatigue Life and A New S–N Curve Model of Composite Laminates Under Tensile-Tensile Fatigue Load, Appl. Compos. Mater. 28 (2021) 129–148. https://doi.org/10.1007/s10443-020-09847-x.

[4] W. Feng, F. Xu, W. Xie, M. Zhang, Fatigue performances and reliability analysis of fatigue life for scarf-repaired composite laminates, J. Adhes. 98 (2022) 367–389. https://doi.org/10.1080/00218464.2020.1834389.

[5] J. Schijve, Fatigue of Structures and Materials, , second, Springer, Netherlands, 2009.

[6] L. Susmel, Multiaxial Notch Fatigue, From nominal to local stress/strain quantities, Woodhead Publishing Limited and CRC Press LLC, Cambridge, 2009.

[7] Suresh S., Fatigue of Materials, Second, Cambridge University Press, New York, 2004.

[8] R.C. Rice, Statistical Aspects of Design, Mater. Sel. Des. 20 (1997) 72–86. https://doi.org/10.31399/asm.hb.v20.a0002431.

[9] R.C. Rice, B.C. Laboratories, Fatigue Data Analysis, ASM Handb. Comm. (2015).

[10] R. He, H. Peng, F. Liu, M.K. Khan, Y. Chen, C. He, C. Wang, Q. Wang, Y. Liu, Crack Initiation Mechanism and Life Prediction of Ti60 Titanium Alloy Considering Stress Ratios Effect in Very High Cycle Fatigue Regime, Materials (Basel). 15 (2022). https://doi.org/10.3390/ma15082800.

[11] A. Tridello, D.S. Paolino, LCF-HCF strain–life model: Statistical distribution and design curves based on the maximum likelihood principle, Fatigue Fract. Eng. Mater. Struct. 46 (2023) 2168–2179. https://doi.org/10.1111/ffe.13990.

[12] A. Tridello, C. Boursier Niutta, F. Berto, M.M. Tedesco, S. Plano, D. Gabellone, D.S. Paolino, Design against fatigue failures: Lower bound P-S-N curves estimation and influence of runout data, Int. J. Fatigue. 162 (2022) 106934. https://doi.org/10.1016/j.ijfatigue.2022.106934.

[13] ASTM E739-10, Standard practise for statistical analysis of linear or linearized stress-life (S-N) and strain-life (ε-N) fatigue data, ASTM. (2010) 1–7. https://doi.org/10.1520/E0739-23.2.

[14] E. Castillo, A. Fernández-Canteli, H. Pinto, López-Aenlle M., A general regression model for statistical analysis of strain-life fatigue data, Mater. Lett. 62 (2008) 3639–3642. https://doi.org/10.1016/j.matlet.2008.04.015.

[15] A. Tridello, C.B. Niutta, F. Berto, D.S. Paolino, Size-effect in Very High Cycle Fatigue: A review, Int. J. Fatigue. 153 (2021) 106462.

https://doi.org/10.1016/j.ijfatigue.2021.106462.

[16] D.S. Paolino, A. Tridello, G. Chiandussi, M. Rossetto, S-N curves in the very-high-cycle fatigue regime: statistical modeling based on the hydrogen embrittlement consideration, Fatigue Fract. Eng. Mater. Struct. 39 (2016) 1319–1336. https://doi.org/10.1111/ffe.12431.

[17] A. Tridello, C. Boursier Niutta, M. Rossetto, F. Berto, D.S. Paolino, Statistical models for estimating the fatigue life, the stress–life relation, and the P-S–N curves of metallic materials in Very High Cycle Fatigue: A review, Fatigue Fract. Eng. Mater. Struct. 45 (2022) 332–370. https://doi.org/10.1111/ffe.13610.

[18] A. Behvar, M. Haghshenas, A critical review on very high cycle corrosion fatigue: Mechanisms, methods, materials, and models, J. Sp. Saf. Eng. 10 (2023) 284–323. https://doi.org/10.1016/j.jsse.2023.05.002.

[19] A. Arcari, N. Apetre, N. Dowling, M. Meischel, S. Stanzl-Tschegg, N. Iyyer, N. Phan, Variable Amplitude Fatigue Life in VHCF and Probabilistic Life Predictions, Procedia Eng. 114 (2015) 574–582. https://doi.org/10.1016/j.proeng.2015.08.107.

[20] C. Bathias, Introduction on Very High Cycle Fatigue, in: G. Pijaudier-Cabot (Ed.), Fatigue Limit Met., 1st ed., John Wiley & Sons, Incorporated, Hokoken, 2013: pp. 11–26.

[21] J.P. Park, S. Mohanty, C.B. Bahn, S. Majumdar, K. Natesan, Weibull and Bootstrap-Based Data-Analytics Framework for Fatigue Life Prognosis of the Pressurized Water Nuclear Reactor Component Under Harsh Reactor Coolant Environment, J. Nondestruct. Eval. Diagnostics Progn. Eng. Syst. 3 (2020) 332–370. https://doi.org/10.1115/1.4045162.

[22] J. Chen, Y. Liu, Fatigue modelling using neural networks: A comprehensive review, Fatigue Fract. Eng. Mater. Struct. 45 (2022) 945–979. https://doi.org/10.1111/ffe.13640.

[23] M.S. Nashed, M.S. Mohamed, O.T. Shady, J. Renno, Using probabilistic neural networks for modelling metal fatigue and random vibration in process pipework, Fatigue Fract. Eng. Mater. Struct. 45 (2022) 1227–1242. https://doi.org/10.1111/ffe.13660.

[24] R.E. Little, J.C. Ekvall, Statistical Analysis Of Fatigue Data, ASTM STP 744, American Society for Testing and Materials, 1981.

[25] C.L. Shen, P.H. Wirsching, G. T. Cashman, Design curve to characterize fatigue strength, J. Eng. Mater. Technol. Trans. ASME. 118 (1996) 535–541. https://doi.org/10.1115/1.2805953.

[26] C.R Schneider, S.J Maddox, BEST PRACTICE GUIDE ON STATISTICAL ANALYSIS OF FATIGUE DATA, 2003.

[27] Y.-L. Lee, J. Pan, R.B. Hathaway, M.E. Barkey, Fatigue testing and analysis : theory and practice, Elsevier Butterworth-Heinemann., Amsterdam ; Boston: , 2005.

[28] R.I Stephens, A. Fatemi, R.R Stepens, H.O Fuchs, Metal Fatigue in Engineering, 2nd Edition, Second, John Wiley & Sons, New York, 2001.

[29] C.C. Engler-Pinto, J.. Lasecki, S.R.. Frisch, A.D. Michael, E.A. John, Statistical Approaches Applied to Fatigue Test Data Analysis, SAE Int. 114 (2005) 422–431.

[30] T.. Anderson, Fracture Mechanics, Fundamentals and Applications, Third, Taylor & Francis Group, CRC Press, New York, 2005.

[31] M. V. Gerov, Y.Y. Vladislavskaya, V.F. Terentyev, D. V. Prosvirnin, O.S. Antonova, A.G. Kolmakov, Fatigue Strength of an AlSi10Mg Alloy Fabricated by Selective Laser Melting, Deform. Fract. Mater. (2018) 11–16. https://doi.org/10.31044/1814-4632-2018-10-11-16.

[32] N.E. Dowling, Estimating Fatigue Life, in: Fatigue Fract., ASM International, 1996: pp. 250–262. https://doi.org/10.31399/asm.hb.v19.a0002365.

[33] E.N. Downing, Mechanical Behavior of Materials: Engineering Methods for Deformation, Fracture, and Fatigue, 4th ed., Pearson Education, London, 2012.

[34] F. Lefebvre, I Huther, G. Parmentier, M. Huther, Document XIII-2807-19 BEST PRACTICE GUIDELINE FOR STATISTICAL ANALYSES OF FATIGUE RESULTS, (2019).

[35] S. M. Marco, H. E. Frankel, M. N. Torrey, C. A. Moyer, A Guide for Fatigue Testing and the Statistical Analysis of Fatigue Data, Am. J. Orthod. 51 (1963) 318. https://doi.org/10.1016/0002-9416(65)90116-8.

[36] ASTM E3080, Standard Practice for Regression Analysis with a Single Predictor Variable 1, ASTM. (2019) 1–20. https://doi.org/10.1520/E3080-19.2.

[37] G.J. Hahn, Statistical methods for creep, fatigue and fracture data analysis, J. Eng. Mater. Technol. Trans. ASME. 101 (1979) 344–348. https://doi.org/10.1115/1.3443700.

[38] J.. Barbosa, J.. Correia, R. Freire Junior, S.. Zhu, A.. De Jesus, Probabilistic S-N fields based on statistical distributions applied to metallic and composite materials: State of the art, Adv. Mech. Eng. 11 (2019) 168781401987039. https://doi.org/10.1177/1687814019870395.

[39] D. Leonetti, J. Maljaars, H.H. (Bert) Snijder, Fitting fatigue test data with a novel S-N curve using frequentist and Bayesian inference, Int. J. Fatigue. 105 (2017) 128–143. https://doi.org/10.1016/j.ijfatigue.2017.08.024.

[40] P.H. Wirsching, Statistical Summaries of Fatigue Data for Design Purposes., NASA Contract. Reports. (1983).

[41] R. Khelif, A. Chateauneuf, K. Chaoui, Statistical analysis of HDPE fatigue lifetime, Meccanica. 43 (2008) 567–576. https://doi.org/10.1007/s11012-008-9133-7.

[42] C. Johnston, STATISTICAL ANALYSIS OF FATIGUE TEST DATA, Trondheim, Norway, 2017.

[43] L. Tanner, S. Collier, H.F. Dodge, R.J. Hader, G.J. Lieberman, W.. Youden, ASTM MANUAL ON FITTING STRAIGHT LINES, Prentice Hall Inc. Englewood Cliffs, N.J, 1959.

[44] A. Kurek, Using Fatigue Characteristics to Analyse Test Results for 16Mo3 Steel

under Tension-Compression and Oscillatory Bending Conditions, Materials (Basel). 13 (2020) 1197. https://doi.org/10.3390/ma13051197.

[45] A. Kurek, for 16Mo3 Steel under Tension-Compression and, (2020).

[46] R.E. Little, E.H. Jebe, Statistical design of fatigue experiments, Applied Science Publishers., London, 1975.

[47] R.D. Pollak, A.N. Palazotto, A comparison of maximum likelihood models for fatigue strength characterization in materials exhibiting a fatigue limit, Probabilistic Eng. Mech. 24 (2009) 236–241. https://doi.org/10.1016/j.probengmech.2008.06.006.

[48] K. Störzel, J. Baumgartner, Statistical evaluation of fatigue tests using maximum likelihood, Mater. Test. 63 (2021) 714–720. https://doi.org/10.1515/mt-2020-0116.

[49] M. Braun, J. Baumgartner, G. Hofmann, K. Drebenstedt, N.M. Bauer, H. Bakhschi, U. Kuhlmann, A statistical assessment of the fatigue strength improvement of butt-welded joints by flush grinding, Weld. World. 67 (2023) 2345–2359. https://doi.org/10.1007/s40194-023-01569-5.

[50] Y. Peng, J. Chen, J. Dong, Experimental Data Assessment and Fatigue Design Recommendation for Stainless-Steel Welded Joints, Metals (Basel). 9 (2019) 723. https://doi.org/10.3390/met9070723.

[51] S.. Maddox, FATIGUE DESIGN RULES FOR WELDED STRUCTURES, Prog. Struct. Eng. Mater. TWI. 2 (2000) 102–109.

[52] E. Castillo, A. Fernández-Canteli, R. Koller, M.L. Ruiz-Ripoll, A. García, A statistical fatigue model covering the tension and compression Wöhler fields, Probabilistic Eng. Mech. 24 (2009) 199–209. https://doi.org/10.1016/j.probengmech.2008.06.003.

[53] L. Susmel, D.G. Hattingh, M.N. James, R. Tovo, Multiaxial fatigue assessment of friction stir welded tubular joints of Al 6082-T6, Int. J. Fatigue. 101 (2017) 282–296. https://doi.org/10.1016/j.ijfatigue.2016.08.010.

[54] Q.C.P. Bourgogne, V. Bouchart, P. Chevrier, Prediction of the Wöhler curves of short fibre reinforced composites considering temperature and water absorption, Mater. Today Commun. 33 (2022) 104655. https://doi.org/10.1016/j.mtcomm.2022.104655.

[55] L. Jegou, Y. Marco, V. Le Saux, S. Calloch, Fast prediction of the Wöhler curve from heat build-up measurements on Short Fiber Reinforced Plastic, Int. J. Fatigue. 47 (2013) 259–267. https://doi.org/10.1016/j.ijfatigue.2012.09.007.

[56] O. Kaleva, H. Orelma, D. Petukhov, Parameter estimation of a high-cycle fatigue model combining the Ottosen-Stenström-Ristinmaa approach and Lemaitre-Chaboche damage rule, Int. J. Fatigue. 147 (2021). https://doi.org/10.1016/j.ijfatigue.2021.106153.

[57] R. Louks, L. Susmel, The linear-elastic Theory of Critical Distances to estimate high-cycle fatigue strength of notched metallic materials at elevated temperatures, Fatigue Fract. Eng. Mater. Struct. 38 (2015) 629–640. https://doi.org/10.1111/ffe.12273.

[58] A. Niesłony, M. Böhm, Fatigue Life of S355JR Steel under Uniaxial Constant Amplitude and Random Loading Conditions, Mater. Sci. 55 (2020) 514–521. https://doi.org/10.1007/s11003-020-00333-0.

[59] M.R.A. Rahim, S. Schmauder, Y.H.P. Manurung, P. Binkele, M.I.M. Ahmad, K. Dogahe, Cycle Number Estimation Method on Fatigue Crack Initiation using Voronoi Tessellation and the Tanaka Mura Model, J. Fail. Anal. Prev. 23 (2023) 548–555. https://doi.org/10.1007/s11668-023-01603-0.

[60] L. D'Angelo, A. Nussbaumer, Estimation of fatigue S-N curves of welded joints using advanced probabilistic approach, Int. J. Fatigue. 97 (2017) 98–113. https://doi.org/10.1016/j.ijfatigue.2016.12.032.

[61] O. Kaleva, H. Orelma, Statistical properties of the model parameters in the continuum approach to high-cycle fatigue, Probabilistic Eng. Mech. 63 (2021). https://doi.org/10.1016/j.probengmech.2021.103117.

[62] M.T. Yu, F.J. Lu, T.H. Topper, P. Irving, Fatigue Data Pooling and Probabilistic Design, American Society for Testing and Materials, Philadelphia, 1991. www.astm.org.

[63] Y. Murakami, T. Takagi, K. Wada, H. Matsunaga, Essential structure of S-N curve: Prediction of fatigue life and fatigue limit of defective materials and nature of scatter, Int. J. Fatigue. 146 (2021) 106138. https://doi.org/10.1016/j.ijfatigue.2020.106138.

[64] J. Mei, S. Xing, A. Vasu, J. Chung, R. Desai, P. Dong, The fatigue limit prediction of notched components – A critical review and modified stress gradient-based approach, Int. J. Fatigue. 135 (2020) 105531. https://doi.org/10.1016/j.ijfatigue.2020.105531.

[65] J.R. Duran, On fatigue life predictions for notched members by the nominal stress-based and the local strain-based methods, Appl. Comput. Mech. 16 (2022). https://doi.org/10.24132/acm.2022.678.

[66] B.J. Tian, J.J. Xiong, J.Z. Liu, A new approach for evaluating fatigue lives of multi-fastener mechanical joints based on a nominal stress concept and minimal datasets, Int. J. Fatigue. 80 (2015) 257–265. https://doi.org/10.1016/j.ijfatigue.2015.06.013.

[67] E.N. Kufoin, L. Susmel, On the parametric assessment of fatigue disparities, Probabilistic Eng. Mech. 77 (2024) 103651. https://doi.org/10.1016/j.probengmech.2024.103651.

[68] G. Rugg, Using Statistics [electronic resource] : A Gentle Introduction, McGraw-Hill Education, Maidenhead, 2007.

[69] P. Strzelecki, T. Tomaszewski, Analytical models of the S-N curve based on the hardness of the material, Procedia Struct. Integr. 5 (2017) 832–839. https://doi.org/10.1016/j.prostr.2017.07.065.

[70] S.F. Masri, A hybrid parametric/nonparametric approach for the identification of nonlinear systems, 1994.

[71] A.J. Vickers, Parametric versus non-parametric statistics in the analysis of randomized trials with non-normally distributed data, BMC Med. Res. Methodol. 5

(2005) 35. https://doi.org/10.1186/1471-2288-5-35.

[72] S. Pajevic, P.J. Basser, Parametric and non-parametric statistical analysis of DT-MRI data, J. Magn. Reson. 161 (2003) 1–14. https://doi.org/10.1016/S1090-7807(02)00178-7.

[73] V. Bagdonavičius, Non-parametric tests for censored data (electronic resource), ISTE ; Hoboken, N.J. : Wiley, London, 2011.

[74] L. Shi, L. Khalij, H. Bai, C. Gautrelet, A non-parametric evaluation method in staircase test for improving fatigue limit assessment, Probabilistic Eng. Mech. 70 (2022). https://doi.org/10.1016/j.probengmech.2022.103373.

[75] C. Soize, A nonparametric model of random uncertainties for reduced matrix models in structural dynamics, France, 2000. www.elsevier.com/locate/probengmech.

[76] C.C. Engler-Pinto Jr, J. V Lasecki, R.J. Frisch Sr, M.A. DeJack, J.E. Allison, R.J. Frisch Michael A DeJack, Statistical Approaches Applied to Fatigue Test Data Analysis Statistical Approaches Applied to Fatigue Test Data An, 2005.

[77] STP46393S, ASTM Manual on Fitting Straight Lines, ASTM Man. Fitting Straight Lines. (2009) 1-1–28. https://doi.org/10.1520/stp46393s.

[78] A. Durmuş, H. Aydın, M. Tutar, A. Bayram, K. Yiğit, Effect of the microstructure on the notched tensile strength of as-cast and austempered ductile cast irons, Proc. Inst. Mech. Eng. Part C J. Mech. Eng. Sci. 226 (2012) 2214–2229. https://doi.org/10.1177/0954406211433248.

Chapter 5

Experimental Setup and Fatigue Data

5.1 Introduction

The previous chapter outlined some of the standardised approaches found in the literature that are used to post-process fatigue data sets, thereby setting the stage to justify the experimental quantities and procedures needed to measure them to generate fatigue data sets that will be used to determine the fatigue properties of pipeline materials in this research. In this chapter, a description of the experimental setups and protocols that were employed to produce the measure fatigue quantities are detailed, as well as the procedure used to generate the raw data from notched specimens that have been used to test and validate the procedure to statistically determine any significant changes in fatigue properties. Therefore, two distinct experiments (plain specimens and notched specimens) will be described in this chapter because they were conducted under identical load and environmental conditions and using the same fatigue machine.

The first experiment entails the testing conditions and protocols for uncharged plain specimens and those exposed to a hydrogen environment. The second experiment describes

testing specimens with different notch geometries. The primary goal of the experiment with soaked specimens is to assess the impact of hydrogen exposure on the fatigue characteristics of materials. In contrast, the second experiment aims to generate data sets for testing and validating the statistical significance of fatigue curves. As mentioned earlier, this approach to test for significance will be useful to determine whether the exposure of the pipeline metals to a hydrogen environment had a significant effect on the fatigue properties when compared with data from uncharged specimens.

Focusing on the experimental setup for the hydrogen-soaked specimens will provide a comprehensive account of the soaking process. It will also detail the protocols for transporting and storing the specimens before subjecting them to fatigue testing in the Civil and Structural Laboratory at the University of Sheffield. The chapter will then delve into the specified loading conditions and the criteria used to identify failure, and a summary of the results in tables, emerging from these experiments.

It is important to note that the researcher intended to be involved in preparing the specimens at the Department of Materials at the University of Manchester. However, due to the national lockdown imposed as a result of Covid-19 and the ensuing protocols, this was not feasible because of limited accessibility to the laboratory. Nevertheless, in coordination with the team at the Manchester University department, they were able to prepare these specimens and send them to the researcher using specialist courier services.

5.2 Experimental design for hydrogen-soaked specimens

This section provides a comprehensive explanation of the materials selected for this investigation, including their respective characteristics. It also outlines the machinery and protocols employed to generate the fatigue data sets.

5.2.1 Material specification

The materials considered for this research were cast iron, brass, X52 pipeline steel and X52 welded pipeline steel. These specimens underwent surface preparation within the laboratory facilities of The School of Natural Sciences, Department of Materials at the University of Manchester. The surfaces were manually ground to achieve a 600-grit finish [1–3], thus eliminating any pre-existing scale or contamination originating from the manufacturing process or reducing the impact of any surface stress concentrators from the surface of these specimens [4]. Characterization and analysis of microstructures were performed on polished cross-sections using optical microscopy and scanning electron

microscopy (SEM). Additionally, optical images at higher magnification and 3D laser surface profiles were obtained using a Keyence VK-X200 laser confocal microscope.

The hardness test for X52 steel, cast iron and brass was conducted using a Buehler Micromet micro-hardness tester with an applied load of HV0.2 (2N) and a Struers Durascan 80 tester with a load of HV0.5 (4.8N). Five indents were made with the Buehler tester, and an additional 10 measurements were taken using the Durascan. The indentation hold time for the test was 10 seconds [3,5,6].

5.2.1.1 Ex-service X52 carbon steel

SEM images of the X52 steel microstructure were obtained after etching in 2-5% nital (a solution of nitric acid and methanol). The resulting images revealed a ferritic-pearlitic microstructure, with pearlite, interphase regions, and grain boundaries being highlighted by the nital etch [7]. The presence of a banded microstructure indicated process orientations linked to the manufacturing process of the pipeline material. The steel, extracted from an ex-service pipe provided by HSE, exhibited larger grains interspersed with regions of smaller grains, forming parallel bands. This suggests a steel microstructure produced through warm-forming processes, characterized by flattened ferrite grains and planar pearlite colonies [8].

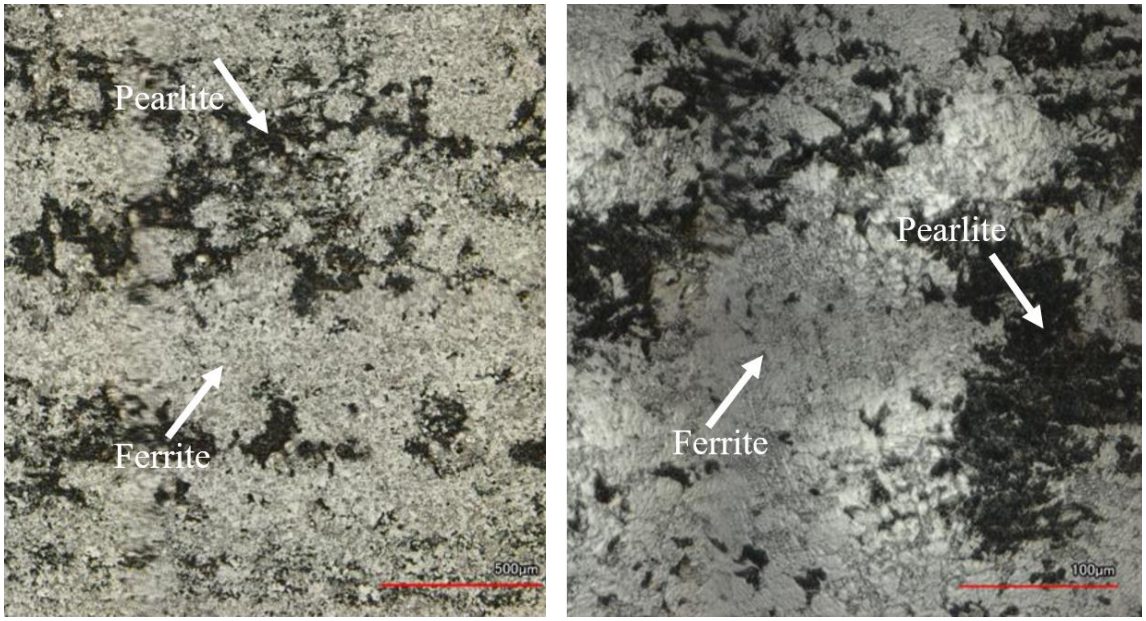

a) b)

Figure 5-1 a) Low magnification (500µm), b) high magnification (100µm), of an optical image of X52 microstructure [3]

The hardness for X52 carbon steel was $184HV_{0.2}$, where $HV_{0.2}$ denotes the Vickers Hardness using an applied load of 2N [3,9].

5.2.1.2 Ex-service X52 welded steel

In the national transmission system, mostly high-pressure steel pipes are used consisting of over 5000 miles of pipeline [10,11]. These steel pipelines are welded to cover distribution within the network and are subjected to cyclic pressure loading, making them susceptible to a subcritical cracking mode known as hydrogen-accelerated fatigue crack growth over their time in use [12]. The focus on welded X52 steel in this research stems primarily from the widespread use of welded joints in the steel pipeline network in the distribution of natural gas in the UK. The weld specimens were obtained from pipeline welds ensuring that the gauge length of the specimen entirely contained the weld as illustrated in Figure 5-2a, with a rectangular sample weld region highlighted in b)

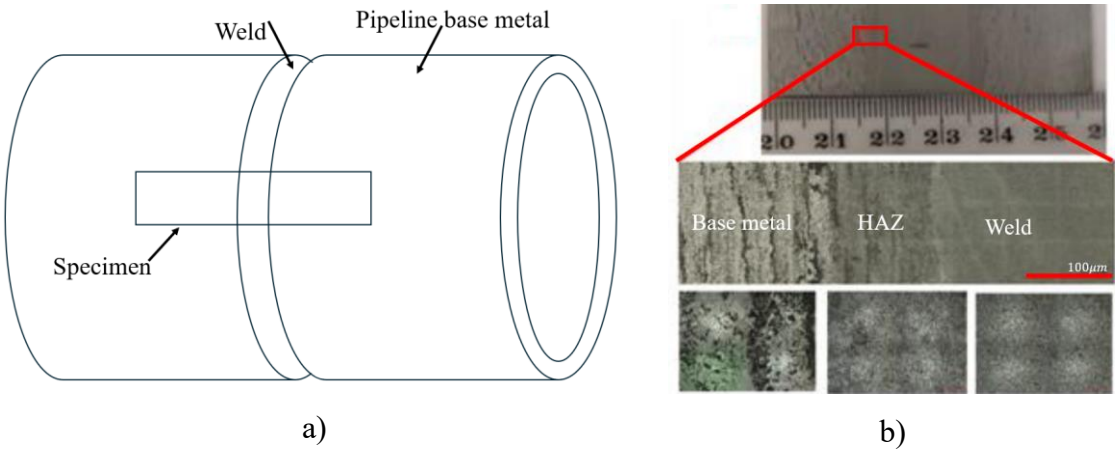

Figure 5-2 a) Schematic of specimen orientations relative to the pipe b) Natal etched rectangular sample images of the different regions of the welded carbon steel

Vickers hardness tests were conducted using an applied load of 9.8 N (HV1). Measurements were taken along a straight line perpendicular to the weld, with the distance between each indentation set to 1 mm. No visible difference in hardness between the base and weld regions was observed, with a mean hardness value of 175 HV1, with one value for the hardness of a heat-affected zone (HAZ) reaching a maximum of approximately 200 HV1[3]. SEM images of the ex-service X52 welded steel were generated after etching with 2-5% nital and revealed a pearlitic and ferritic matrix microstructure. The higher magnification optical images revealed the X52 matrix microstructure with banded regions of pearlite and ferrite, a HAZ located between the weld and base metal, and the surrounding region as shown in Figure 5-3 below, with the distribution of ferrite and pearlite fairly uniform.

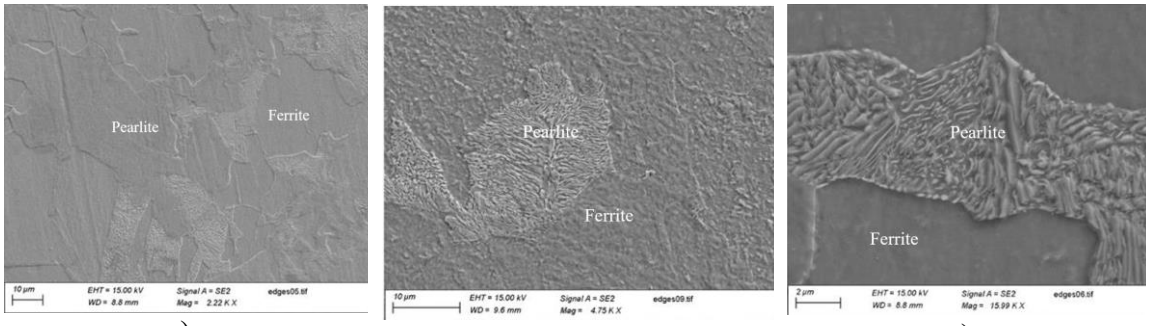

a) b) c)

Figure 5-3 SEM images of the base region in a welded steel sample at different magnifications a) $100\mu m$ b) $10\mu m$ c) $2\mu m$ [3]

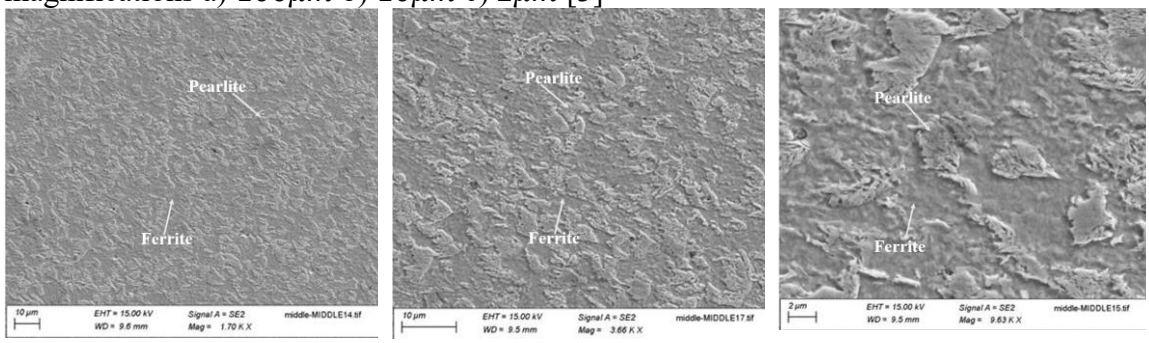

d) e) f)

Figure 5-4 High-resolution images of HAZ d) $100\mu m$ e) $10\mu m$ f) $2\mu m$ [3]

Further analysis of the welded steel specimens reveals some inclusions of MnS. These inclusions typically impact hydrogen-induced cracking in the specimens, with size and shape being significant factors in the metal's susceptibility to hydrogen cracking.

5.2.1.3 Ex-service cast iron

Optical images of the cast iron microstructure were obtained after etching with 5% Nital. The microstructure, when unetched, revealed elongated and convoluted graphite flakes embedded in the matrix. The size and shape of these flakes indicated a grey cast iron type. Images of SEM microstructure revealed different compositions of a heterogenous matrix with constituents, including Fe, P, Mn, S, C, and Si, revealing regions with different phase compositions. These regions included ferrite, pearlite (Fe; Fe3C), graphite, and Steadite (phosphor-containing eutectic) as shown in Figure 5-5 below[3]. Additionally, small particles with high Mn and S content were present as bright discrete spots, indicating the presence of MnS.

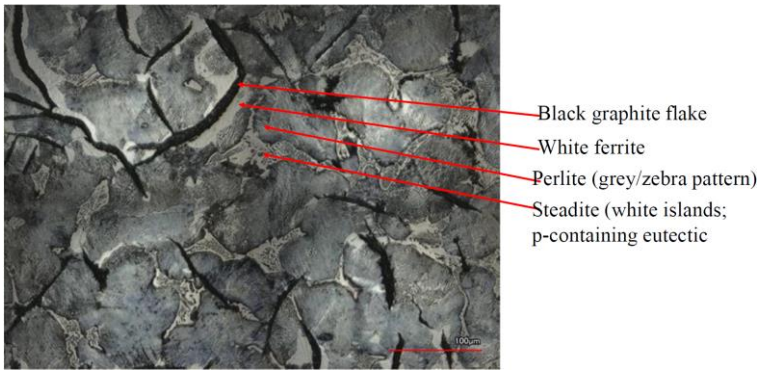

Figure 5-5 Nital etched cast iron microstructure [3] with individual phases at high magnification

The hardness of cast iron was $348HV_{0.2}$, using an applied load of 2N for the Vickers hardness [3,9].

5.2.1.4 Brass

Optical images of the brass microstructure were obtained after etching with 5% Nital. The brass exhibited a two-phase α-/β-microstructure, indicating a more zinc-rich alloy composition. Energy dispersive X-ray (EDX) analysis was conducted to determine the chemical composition of all constituents, with five data points of each phase recorded and the mean composition calculated. The darker grains, rich in Cu (>58%) and Zn (>35.5%), indicated α-phase composition, while the lighter grains showed lower Cu content (>51%) and higher Zn content (42%), suggesting β-phase composition. Additionally, small amounts of Fe, Sn, and Pb were present in the microstructure. This shown in Figure 5-6 below.

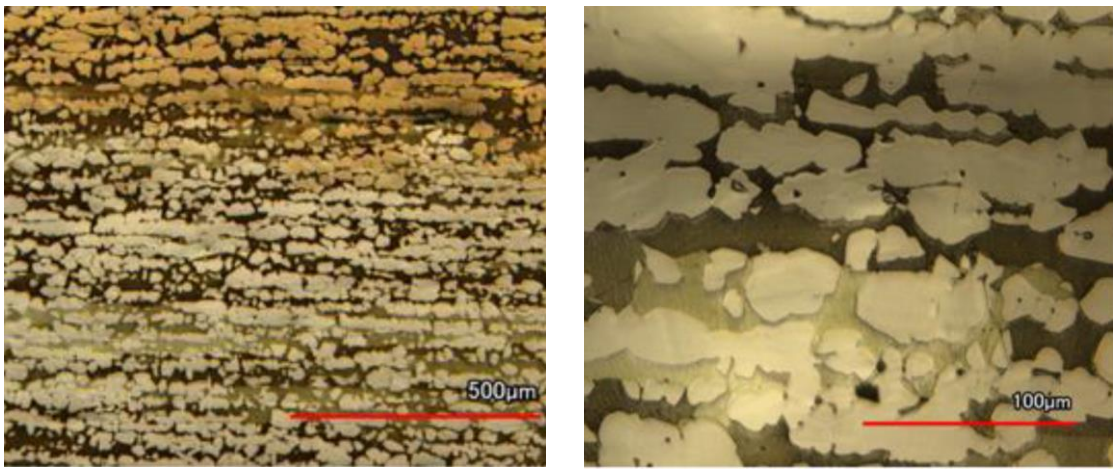

a) b)

Figure 5-6 Optical images of brass microstructure at a) Low magnification (500µm), b) high magnification (100µm) [3]

The hardness for brass was $111HV_{0.2}$, using an applied load of 2N for the Vickers hardness [3,9]

5.2.2 Specimen geometry

For constant amplitude axial fatigue tests, the design of the specimen should be such that failure occurs in the tested section [13]. The specimen geometry chosen was the dog-bone design [14,15] as illustrated in Figure 5-7 And with the use of a Vernier calliper, the dimensions consisted of a length of 65mm, a thickness of 2mm, and a width of 5mm. (If rectangular specimens were used instead, this would lead to stress concentrations around the grip area where failure would occur or any other weak link in the material. It would be challenging to establish a unifying failure criterion for all other specimens.) The thickness measurement was taken at different points along the length of each specimen and the results averaged out. The net width was measured three times in the middle of the gauge length of the specimen. By using this configuration, the stress involved in these tests was net stress, expected at the gauge length of the critical section of this specimen design.

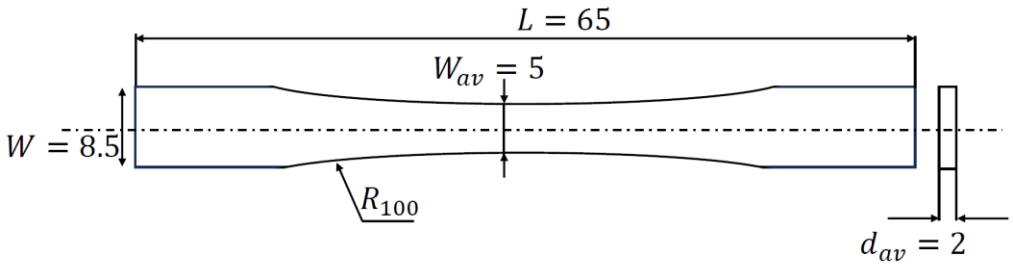

Figure 5-7 Hydrogen-soaked specimen dimension in mm

5.2.3 Hydrogen charging Equipment and hydrogen charging procedure

Because of the national lockdown imposed on the country at the time, the researcher could not travel to Manchester to prepare the specimens. The specimen preparation was done at the University of Manchester according to Ref. [1]. The equipment used to expose the specimens to a hydrogen environment consisted of flanged circular pressure tubes. These tubes were specifically designed to conduct exposure tests in a gaseous environment containing hydrogen at known pressure levels. Each pressure tube was constructed from type 316L stainless steel pipe, with a wall thickness of approximately 3.5mm and welded end flanges at both ends.

Figure 5-8 Tubes used for exposing specimens to a hydrogen environment, courtesy of the Department of Materials at the University of Manchester [1]

These tubes measured 1000 mm in length with an internal diameter of 52 mm, resulting in a total volume of approximately 2.17 litres. The end flanges were subsequently sealed using bolted end plates. One of these end plates featured a single ¼" NPT threaded female penetration to facilitate a gas inlet, while the other end plate had two ¼" NPT threaded female penetrations to enable a gas outlet and a pressure sensor connector. These pressure tubes are shown in Figure 5-8.

Each tube had an information label that showed details of its pressure rating and specifications. The test specimens were packed in bundles of 3 to 5 and secured with stainless steel bolts on both sides as shown in Figure 5-9a). Nuts were used as spacers between each sample to allow unrestricted exposure to hydrogen gas. The specimens were then placed inside the tube by a specimen holder specifically designed for retrieving samples from the pressure tubes easily using a copper wire as shown in Figure 5-9b). Once positioned inside the pressure tube, the end flange was then securely closed and sealed by tightening the bolts.

This setup of specimens on their holders enabled the safe access and storage of samples in extremely cold liquid nitrogen, and it enabled easy access to specimens for further tests. If there were samples left, they could be put back into the cold nitrogen to help keep the hydrogen gas from getting out.

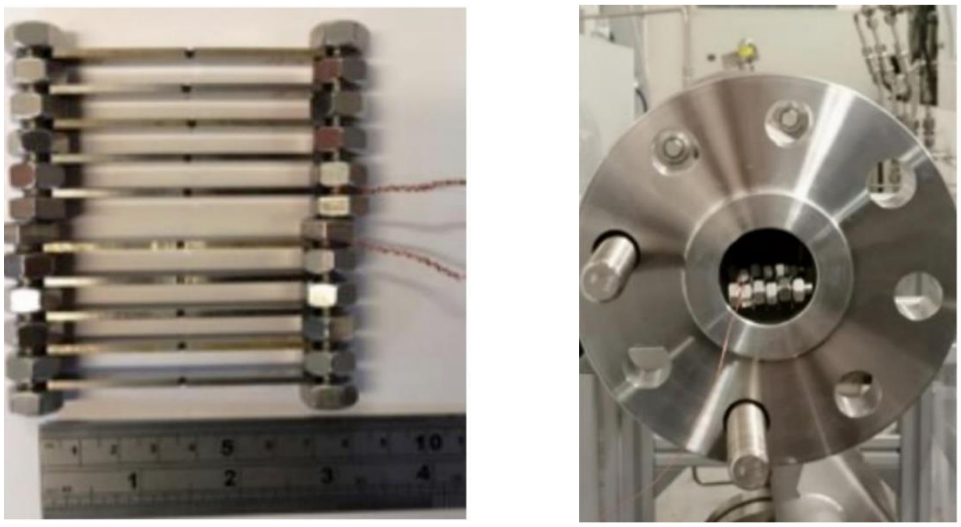

a) b)

Figure 5-9 a) specimens mounted on a first-generation sample holder and b) specimens placed inside a hydrogen environment in a pressure tube [1]

5.2.4 The charging process of the specimens in the hydrogen environment

The hydrogen exposure procedure while specimens are placed in the pressure tube is outlined in the flowchart presented in Figure 5-10. To initiate the test, once the samples were positioned inside the tubes, the end flange was securely closed and sealed by tightening the bolts. The system was initially pressurized with nitrogen gas (using BOC Oxygen Free Nitrogen, product code UN1066) to approximately 8 bars, with the assistance of valves 1 and 3. The vessel and associated pipework underwent thorough leak checks, including pressure testing and gas tightness tests, typically conducted over a minimum duration of 24 hours. Subsequently, the system was depressurized using a vacuum pump connected through valve V6 to eliminate any remaining moisture or impurities. The hydrogen test gas (100% hydrogen, product code UN1049) was then introduced through valve V2, pressurizing the tube to approximately 8 or 10 bars, after which it was isolated using valves V3 and V4. This was the static exposure of these specimens to hydrogen and lasted a few hours.

The specimens were exposed to hydrogen soaking for various durations ranging from three to five months. This duration was intended to allow reasonable amounts of hydrogen to be absorbed into the specimens. Specialized equipment, accessible only to the researcher from the University of Manchester, was used to monitor any alterations in the soaking conditions. It should be noted that the rate at which these specimens absorbed hydrogen was not studied due to lockdown protocols. However, this diffusion rate could be examined in future

research on this subject. At the end of the hydrogen exposure process, the hydrogen atmosphere within the tube was released by opening valve V4, followed by the flow of nitrogen gas through the tube for approximately 30 seconds to ensure the complete removal of hydrogen from the system. The transfer of samples from the hydrogen exposure environment to liquid nitrogen typically took between 5 and 10 minutes, starting from the moment the hydrogen gas exposure was halted.

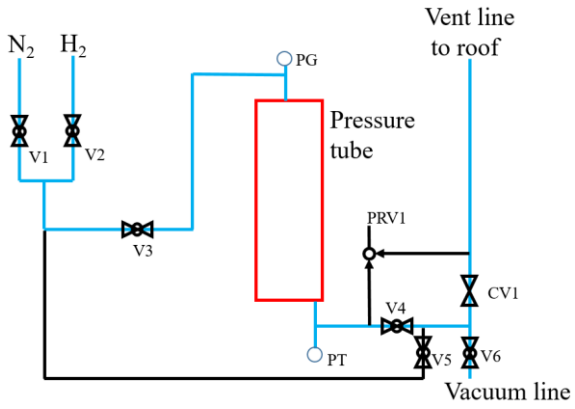

V-valve PT – pressure transducer PRV – Pressure relief valve

CV – check valve PG – Pressure gauge

Figure 5-10 Diagram illustrating the gas flow and pressure tube with operational specifics of gaseous hydrogen exposure[1]

5.2.5 Estimating hydrogen diffusion and hydrogen concentration in the pipeline material

The theoretical hydrogen concentration, as described in the previous chapter using Sievert's law, depends on the hydrogen partial pressure and solubility, both of which are influenced by temperature and defined as [16,17]:

$$C_H = S\sqrt{P_{H_2}} \tag{5-1}$$

The diffusion of hydrogen through the investigated pipeline materials can be estimated using Fick's law of diffusion [18,19]. The one-dimensional solution used to define a time-dependent diffusion of hydrogen in metals is estimated as:

$$\frac{\partial C}{\partial t} = D\frac{\partial^2 C}{\partial x^2} \tag{5-2}$$

Where C is the concentration of hydrogen, x is a spatial coordinate, t is the charging time and D is the lattice diffusion coefficient defined by the Arrhenius equation [19]:

$$D = D_0 e^{(-E/RT)} \quad (5\text{-}3)$$

in which E is the activation energy (J/mol) and R is the gas constant (8.314 J/molK), D_0 is the pre-exponential factor and T the temperature in Kelvin.

By following the above schematization, the amount of hydrogen adsorbed and diffused through each specimen can be quantified as:

$$C = \int_0^{t(months)} D \frac{\partial^2 C}{\partial x^2} \partial t \quad (5\text{-}4)$$

However, the focus of this research was not on modelling hydrogen adsorption in these metals, but rather on determining whether there is any change in the fatigue properties when specimens are exposed to such a hydrogen environment. The quantitative analysis will be the core of future work. Consequently, this analysis to estimate the amount of hydrogen diffused through each specimen was not included in the current research.

5.2.6 Specimen retrieval and transportation for fatigue testing

Following hydrogen exposure, the samples were taken out of the exposure tubes and placed in liquid nitrogen to preserve as much hydrogen as possible within them (by minimising the diffusion rate). These samples were then transferred from liquid nitrogen to a container with dry ice and transported in a foam box, using specialist courier services under a low-temperature storage environment of about -78.5°C (194K). The samples were received at the Department of Civil and Structural Engineering at the University of Sheffield where they were stored in a freezer at similar low temperatures and used sequentially for fatigue testing.

To minimize the duration during which the specimens were exposed to room temperature where hydrogen could potentially escape, two approaches were adopted. Firstly, the specimens were transferred from liquid nitrogen to a dry ice container at the preparation site before being transported by a specialized courier service capable of maintaining very low temperatures. This was to reduce any possibility of hydrogen escaping from the soaked specimens in transit from the University of Manchester to the testing site at the University of Sheffield. Secondly, to minimize the time each specimen spent outside of cryogenic conditions when loading onto the fatigue machine, a systematic approach was employed. The testing machine was set up first, and then the specimen was retrieved and loaded onto the machine for testing, reducing the time it was exposed to room temperature. This process

was carefully monitored and optimized to minimize the time spent at room temperature before the test.

It should be noted that the rate at which hydrogen diffused into these specimens can be estimated using equation (5-1) to (5-3) which is time-dependent, however, this was beyond the scope of this research and will be assessed in future work. Allowing the specimens to remain in a high-pressured hydrogen environment for various durations of charging times enabled us to investigate only the fatigue properties with different amounts of hydrogen diffusion in these specimens. Storing at cryogenic conditions allowed testing of other specimens while preserving the hydrogen content in the remaining specimens.

5.3 Fatigue machine used and test configuration

The fatigue machine used to run the fatigue tests from these hydrogen-charged specimens was the Multipurpose Servo Hydraulic Testing machine, the LFV-L series in the structure's lab at the University of Sheffield. This machine has a static load test capacity of up to 25 KN, and a recommended fatigue testing capacity of 20 KN. According to the manufacturing notes, this series is well suited to perform static tension, compression, flexure, shear tests, LCF (low cycle fatigue), fatigue crack growth testing, fracture toughness testing, and further applications including the testing of biomechanical products and implants. Figure 5-11 shows an overview of the multipurpose servohydraulic universal testing machine series LFV-25KN as used in this research.

a)

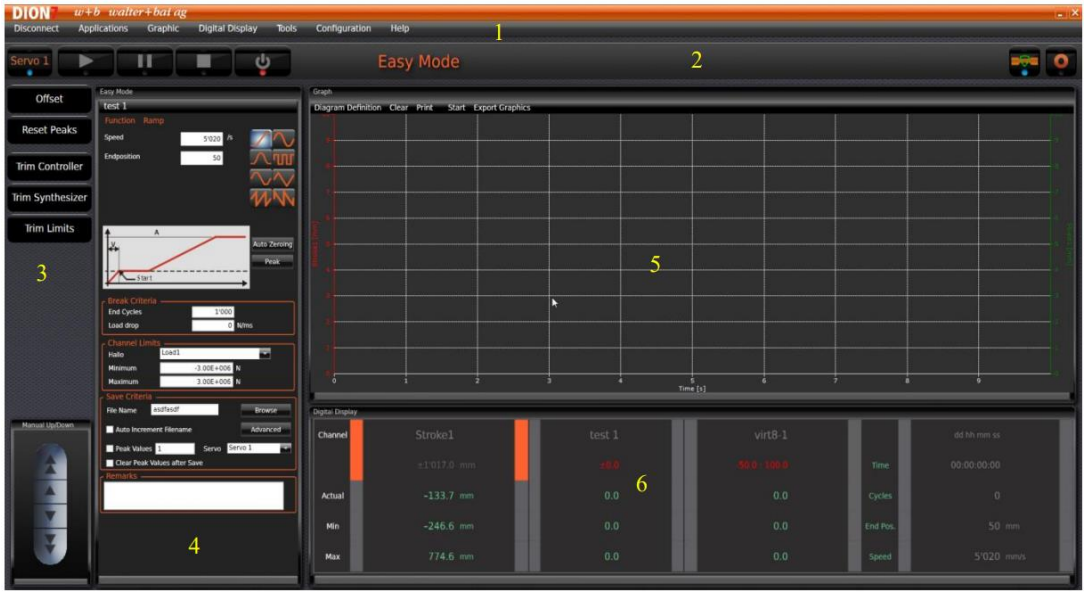

b)

Figure 5-11 a) the system overview of the multipurpose servohydraulic universal testing machine series LFV-25KN b) the user interface on the easy mode setup.

This fatigue machine uses the Type DION7 software, and for this investigation, the machine was used in the DION7 EASYMODE set-up. Test on this machine can either be load-controlled or displacement-controlled.

5.3.1 Specimen retrieval, Loading specimen and test configuration

To prepare for the fatigue test with the hydrogen-charged specimen, the loading setup (which will be explained shortly) was imputed using the machine interface in advance of retrieving the soaked specimens from the freezer. The cold-resistant gloves were used to extract each specimen from the freezer and rinsed them under running tap water to take the temperature up to a room temperature level and ensure safe handling during the loading onto the fatigue machine.

Running the specimen under tap water did not impact the results because, according to a pilot test conducted in ref. [3] the effects of bringing charged samples from cryogenic temperatures to room temperature were quantified and compared by two methods: allowing specimens to warm in air and running the specimens under tap water. To achieve this, three samples were tested: Sample 1 was exposed to air, and the temperature gap from below -30℃ to 10℃ was bridged only after about 330 seconds, while Samples 2 and 3 were immersed in water. The result is shown in Figure 5-12.

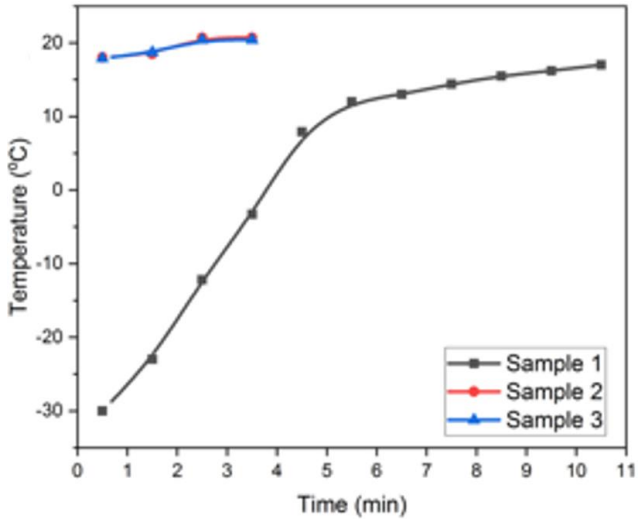

Figure 5-12 surface temperature of specimens allowed to cool in the air (sample 1) compared with specimens cooled by immersing in tap water (samples 2 & 3) [3]

After immersing samples 2 and 3 were immersed in water, resulting in a rapid temperature increase to a stabilized value of 20℃ within about the first 30-60 seconds of immersion. This highlights the effectiveness of water immersion in quickly bringing the specimen to room temperature compared to air exposure without a significant loss in the amount of hydrogen.

The time in minutes it took from removing the specimen from the freezer to the start of the fatigue test was also noted as Δt^*, to minimize this duration. Using Vernier callipers, the dimensions of each specimen were measured and recorded. When dealing with uncharged specimens, the procedure for loading them onto the fatigue machine was much more straightforward. With the measurements taken, each specimen was loaded onto the fatigue machine and the loading configuration was set using the machine interface, before initiating the test.

To input the loading configuration, the load ratio of $R = 0.1$, representing a loading condition in tension-tension [15,20–22], was chosen for each test. This load ratio was

selected to: (i) investigate the mean stress effect [23–25] and (ii) avoid buckling during testing [14]. Using the interface, setting the load configuration for each test entailed defining and inputting the mean load value, and the load amplitude, setting the frequency to 10Hz, and selecting the sinusoidal load wave function. The break limit or failure criterion (described in the next section) was inputted, and the save criteria to include the total number of cycles at the end of the test was enabled. This test could then be initiated by selecting the "run test" option on the user interface.

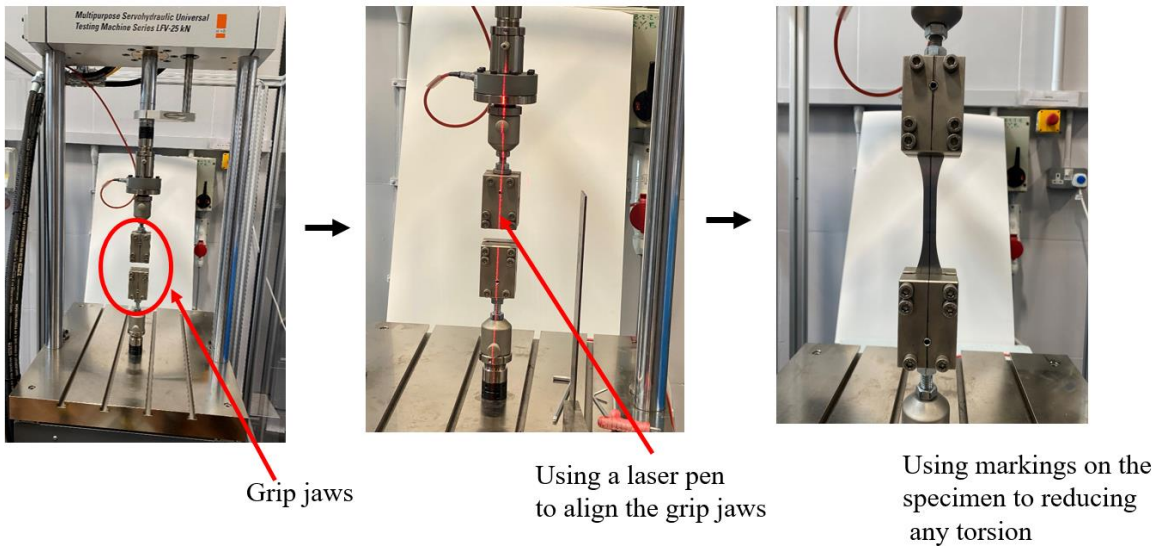

Figure 5-13 Specimen loading precaution to reduce any forms of torsional loading

When loading the specimens onto the machine's grip jaws, special care was taken to minimize any torsional load. This was especially critical because certain materials and geometry (cast iron for example) are notably sensitive to small torsional loadings originating from specimen twisting, and only the uniaxial load condition was being investigated in this research. To achieve this, a digital laser spirit level was used to guide the precise alignment of the grip jaws and, consequently, the specimen during the fatigue test. Furthermore, a bold marker was used to mark the vertical load axis on the specimen. This served as a visual guide during the loading process to maintain the desired alignment. This is illustrated in Figure 5-13.

5.3.2 Failure criterion

The failure criterion employed in this research was the complete breakage of each test specimen during testing. This was because the net area of the gauge length was small, thereby enabling the crack propagation part of the total fatigue life considered to be negligible. In a pilot test, it was observed that most of the time during each test was spent

on crack initiation following expectations [26,27], and once the crack was initiated, failure occurred rapidly. In addition, the difference number of cycles from when the crack initiates to complete failure is not significant compared to the overall fatigue life of the specimen. This is illustrated by the graph in Figure 5-14, which shows the stroke profile (displacement of the load around the mean stress level) as fatigue loading progresses over time. The time taken to change from minimum displacement to maximum displacement was minimal, illustrating that the time needed to propagate the crack around the gauge region was critical.

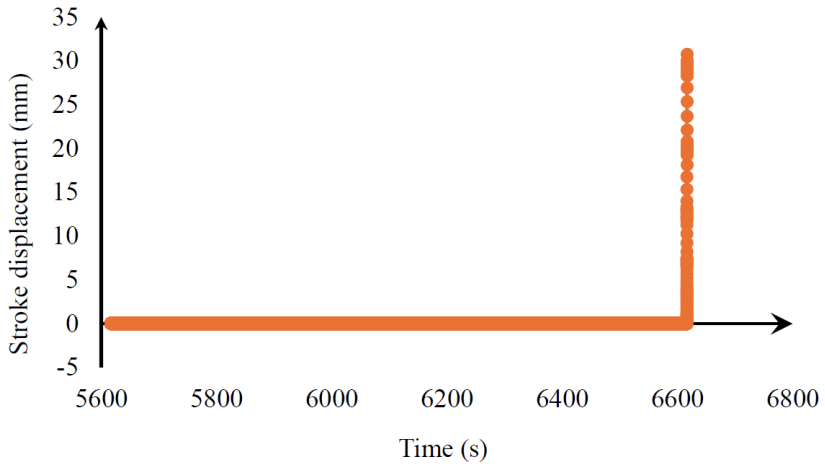

Figure 5-14 Displacement profile during a fatigue test

To achieve this, the tests were carried out using displacement (stroke) control, with a predetermined stroke length of 35mm on the fatigue machine. Given the materials utilized in this investigation, none were anticipated to undergo plastic deformation sufficiently large to reach this stroke level without experiencing total breakage. Figure 5-15 shows a failed specimen still attached to the machine's grip jaws, along with the end-of-test message displayed on the user interface upon reaching the stroke limit. The total number of cycles was recorded as the cycle count. Thereafter, the specimen was removed from the grip jaws, and the machine was ready for setting up the next test.

In situations where the specimen did not experience failure, the endpoint was initially set at 2 million cycles for all tests. This meant that the test terminated when the cycle count reached 2 million cycles, at which point the specimen was considered to have successfully survived the test, often referred to as a runout. If the specimen that survived the test was uncharged, it is retested at a higher stress amplitude. For hydrogen-charged specimens, specimens that survived a test were not retested at a higher stress level, based on the assumption that the hydrogen quantity in them must have changed considerably during the initial test. Since this aspect was not part of the initial research scope of this research, it

remains unexplored and could constitute the focus of future research by investigating the effects on fatigue properties when quantifiable amounts of hydrogen diffuse into and out of pipeline materials.

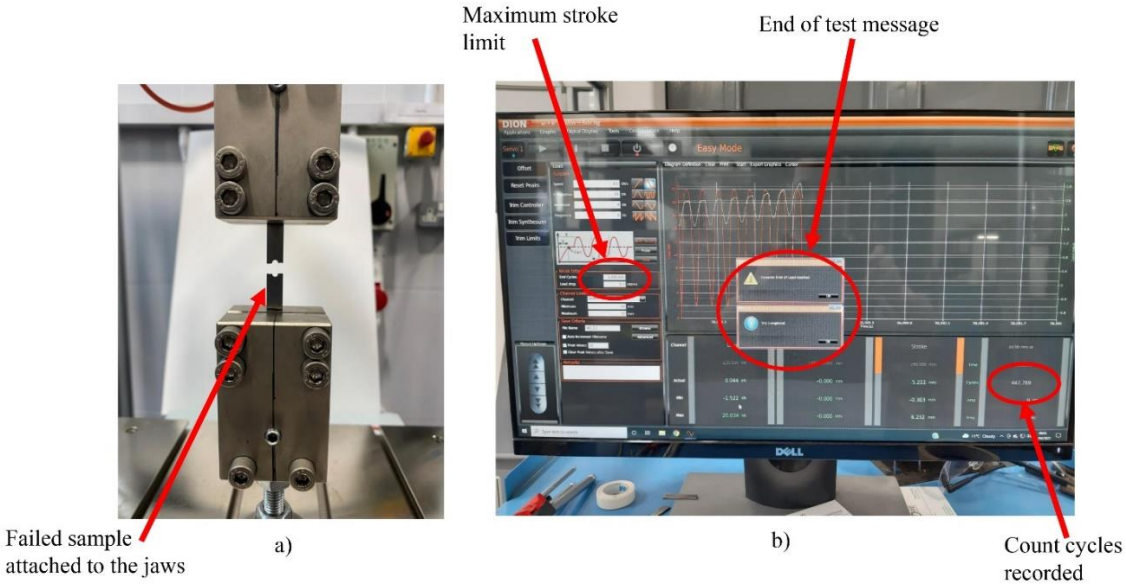

Figure 5-15 Failure criterion a) complete failure of specimen still attached to the grip jaws b) end test message displayed on the user interface

Therefore, considering that the stress at the minimum section (W_{ad} in Figure 5-7) of the specimen is the conventional nominal stress [28], which occurs at the gauge length of the specimen, is the maximum stress experienced by the specimen during loading. If there are no stress raisers in the microstructure of the material, then it is expected that the specimen will fail along this gauge plane.

Utilizing this failure criterion, Figure 1 in the appendix displays several randomly selected specimen fracture surfaces. The images were captured using a Zeiss Stemi 2000-C Stereo Microscope with a zoom range of 0.65x - 5.0x, to take pictures of the failure surfaces at the Department of Civil and Structural Engineering at the University of Sheffield.

5.4 Mechanical test – Izod/Charpy Impact test

The Izod and Charpy Impact Test evaluates the energy absorbed by a material during fracture [29]. In these tests, a standard-sized specimen is struck by a hammer dropped from a specific height and position and the energy absorbed by the specimen during an impact test is determined by measuring the difference in the height of the hammer's swing before and after impact. This test was carried out for uncharged specimens and specimens charged for about 42 weeks.

5.4.1 Impact test on X52

The impact energy of X52 steel samples after exposure to hydrogen gas for durations of 1, 5, 18, 24, 42, and 45 weeks is summarised in Figure 5-16. Overall, significant variability in fracture energies was observed across all exposure periods, including the uncharged samples and this is likely because of the heterogeneities in the microstructures.

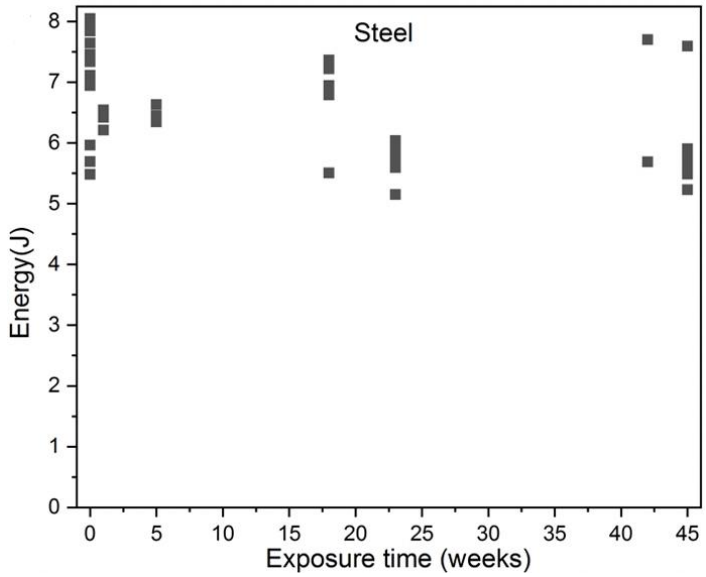

Figure 5-16 Izod fracture energy of X52 steel hydrogen-charged for 1, 5, 18, 24, 42, and 45 weeks, compared to uncharged specimens [3]

5.4.2 Impact test on welded X52 steel

The impact energy of the as-received welded steel samples ranged from 3.15 to 3.8 J. After 18 weeks of exposure, the impact energy was similar, ranging from 3.1 to 3.75 J, and remained consistent after 45 weeks, ranging from 3.15 to 3.5 J. The measured impact energy of the welded steel is shown in Figure 5-17 and was found to measure up to only half the energy for the X52 steel shown in Figure 5-16.

By comparing the fracture energy results after hydrogen exposure to the lowest energy value measured in the as-received reference condition, no significant effect of hydrogen gas exposure on Izod fracture energy was observed for the welded steel material, even after exposure to 10 bar hydrogen gas.

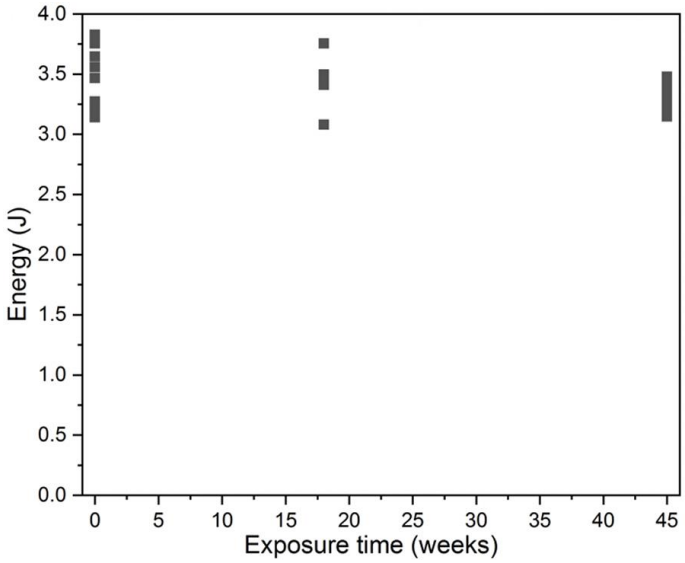

Figure 5-17 Fracture energy of all Izod-tested welded steel samples [3]

5.4.3 Impact test on cast iron

The impact test result for cast iron after exposing it to an 8-bar hydrogen environment for 1,5,18,24,42 weeks is shown in XXX. An 11 J hammer was initially used for all tests involving the reference sample and the samples exposed for 1 and 5 weeks. However, a 1 J hammer was later employed for all subsequent tests. This change in hammer impact energy was necessary for cast iron specimens, as their measured fracture energy was typically below 0.085 J which is comparable to the air resistance of the 11 J hammer (0.038 J) and the 1 J hammer (0.016 J).

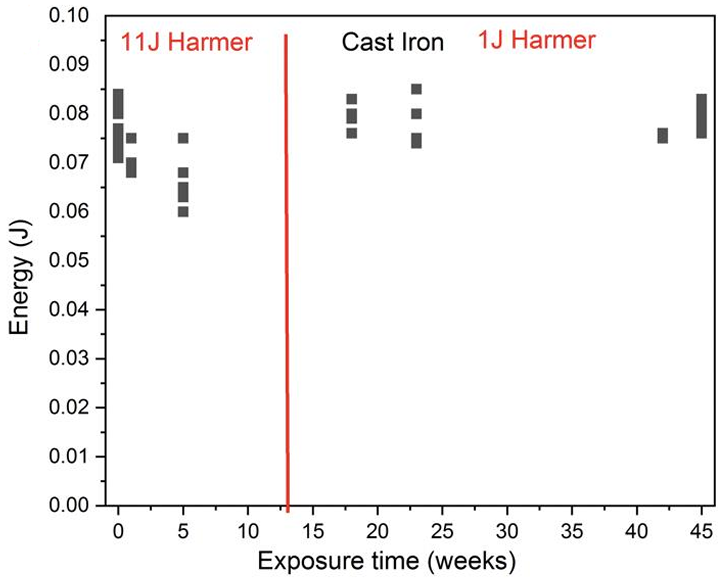

Figure 5-18 Fracture energy of all Izod-tested cast iron samples obtained with the 1J and 11J Izod hammer [3]

Results from the 1J indicate no significant change in impact energy after hydrogen gas exposures of up to 45 weeks. However, some variations were observed in the data spread for the longer-term exposure samples, with energy values ranging from 0.075J to just below 0.085J after the longest exposure. For data obtained using the 11J hammer, a slight reduction in average impact energy was noted with increasing hydrogen exposure time, decreasing from 0.077J in the as-received condition to 0.066J after 5 weeks of hydrogen exposure. Only the samples exposed for 5 weeks appeared to show slightly lower fracture energies, with no significant effect of long-term hydrogen exposure on impact fracture energies observed.

5.4.4 Impact test on brass

For brass specimens, samples were exposed to a hydrogen environment for 1- and 5- weeks of 8-bar hydrogen pressures. This is illustrated in Figure 5-19.

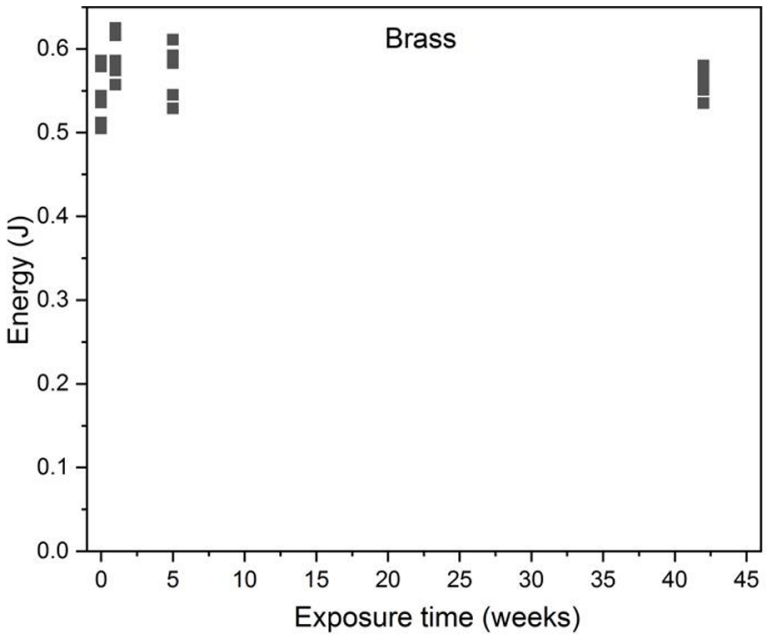

Figure 5-19 Fracture energy of all Izod-tested brass samples [3]

The mean impact energy showed a slight increase from 0.52J in the reference condition to 0.56J after 42 weeks of hydrogen exposure. This indicates that there was no significant difference in impact energy between the as-received samples and those exposed for up to 42 weeks to 8-10 bar of hydrogen gas atmosphere.

5.5 Fractography of Impact Tested Specimens

To determine the impact toughness of pipeline materials used in this research, which is a measure of a material's ability to absorb energy and resist fracture when subjected to sudden impact, the Izod/Charpy impact tests were used [3]. This section summarises the fracture surfaces at different hydrogen charging times.

5.5.1 Brass

Figure 5-20 shows the fracture surface of the as-received brass samples, which predominantly exhibit a ductile fracture mode. At higher magnification (b-d), small void-like features are visible, possibly corresponding to deep dimples. Macroscopic banding is visible in the macrograph (Figure 5-20a). No necking was observed in either the as-received or hydrogen-exposed samples.

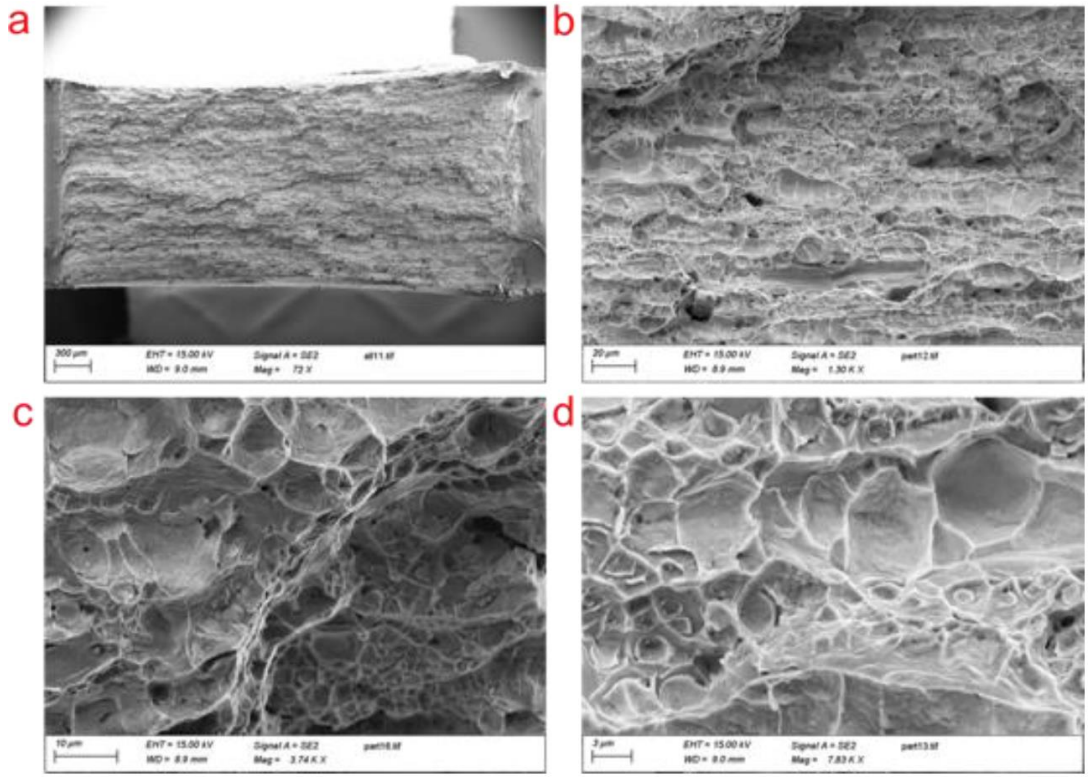

Figure 5-20 Fracture surface of uncharged brass specimen [3]

Figure 5-21 illustrates the fracture surface after 42 weeks of hydrogen exposure. No significant differences were observed between the as-received brass specimen and the fracture surface after 42 weeks of exposure. At higher magnification, the small voids or dimples appeared slightly larger (10 μm).

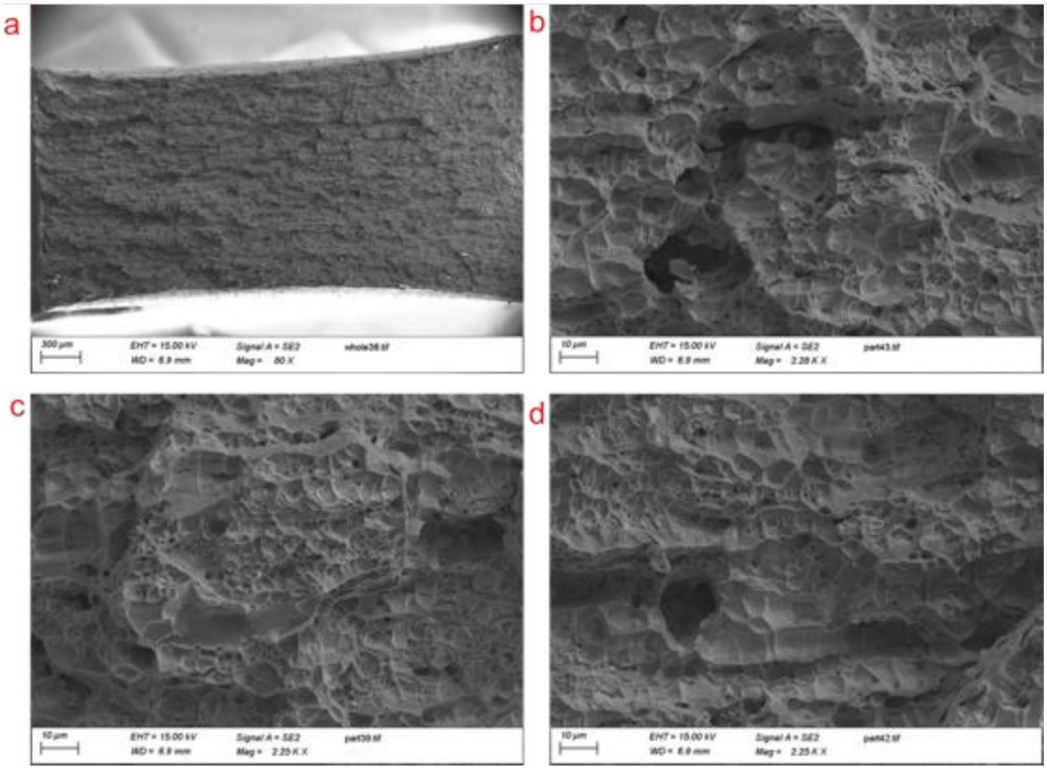

Figure 5-21 Fracture surfaces of the hydrogen-charged brass sample for 42 weeks [3]

5.5.2 Cast iron

Similarly, Figure 5-22 and Figure 5-23 illustrate the fracture surfaces of cast iron samples in the as-received condition and after 42 weeks of hydrogen exposure, respectively. Even in the as-received state, cast iron exhibited a predominantly brittle fracture surface, characterized by numerous cleaved facets. These were interspersed with regions and bands that appeared somewhat less cleaved. After 42 weeks of hydrogen exposure, similar features were observed, with the fracture surface still dominated by cleaved facets and bands with a less pronounced cleaved appearance. There were no visible differences between the samples with and without hydrogen charging, and no necking was observed in either case.

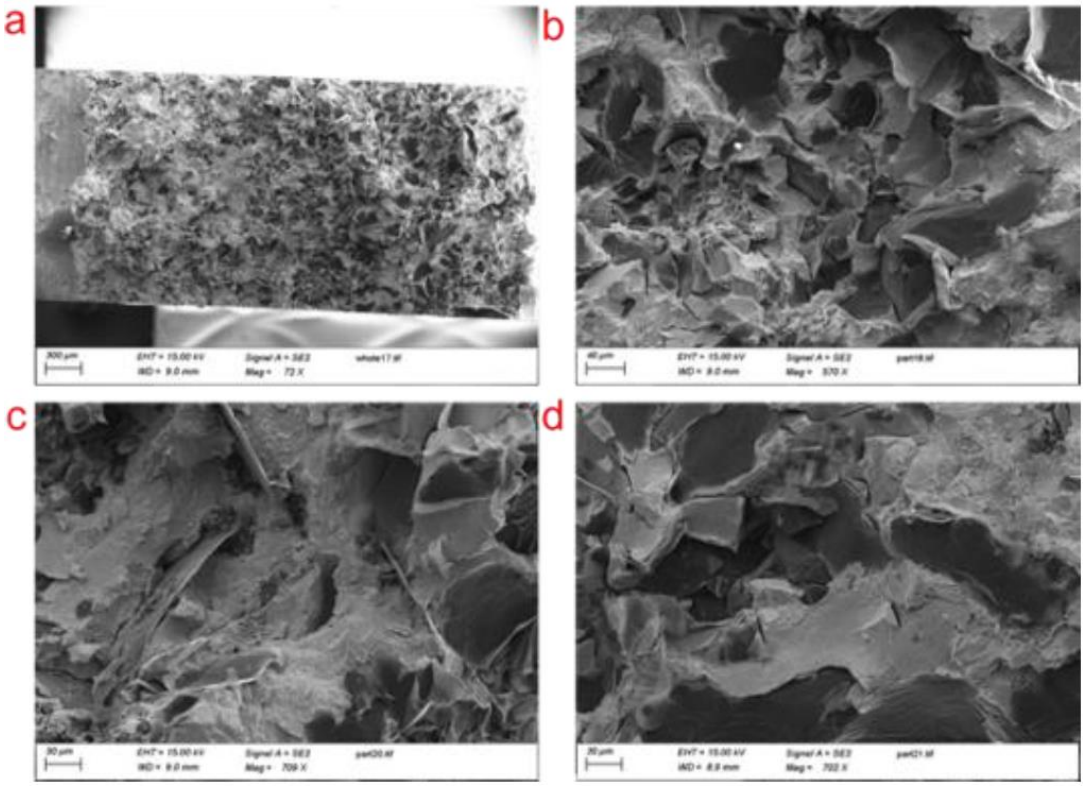

Figure 5-22 Facture surfaces of the uncharged cast iron [3]

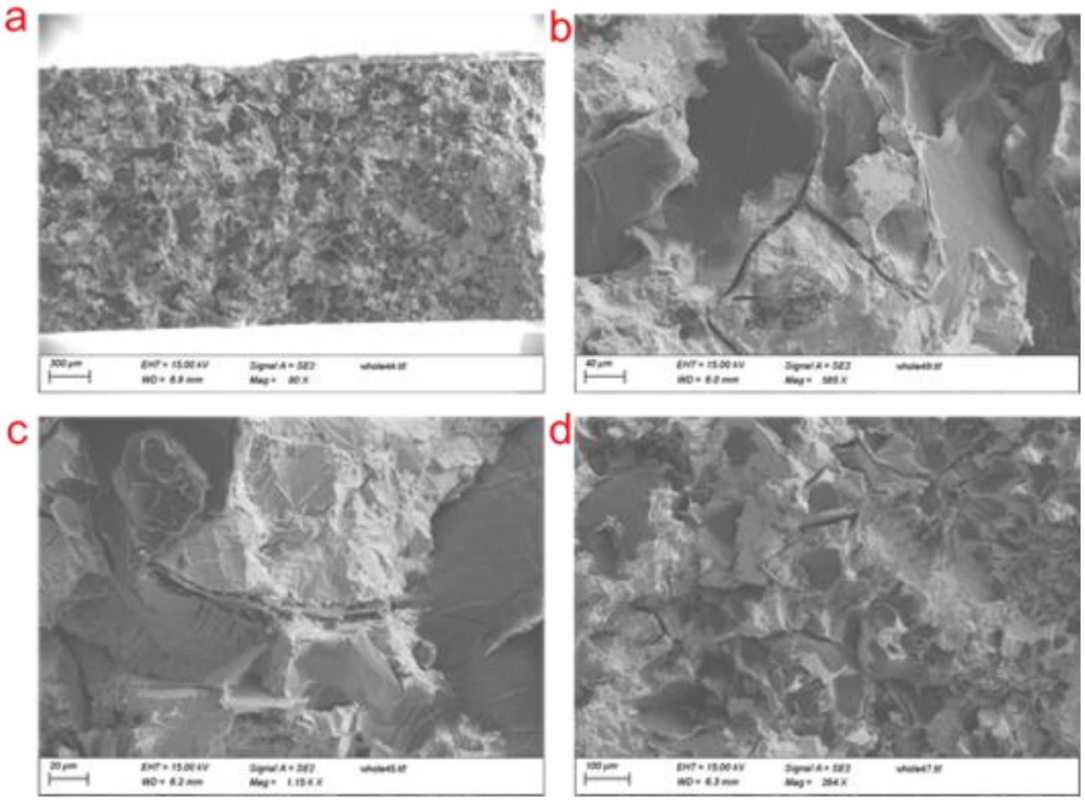

Figure 5-23 Fracture surfaces hydrogen charged cast iron specimens for 42 weeks [3]

5.5.3 X52 carbon steel

For X52 carbon steel surfaces shown in Figure 5-24, necking of the specimen indicates a predominantly ductile failure. A prominent secondary crack, over 100µm in length, is visible on the fracture surface, along with smaller cracks of approximately 30µm, which may contribute to the reduced fracture resistance of the sample. The fracture exhibits a mixed mode, with brittle regions and cracks surrounded by ductile bands containing micro-voids. Similarly, in Figure 5-25, necking is also observed, with a primarily ductile fracture mode. The reason for these differences in fracture behaviour could be attributed to microstructural inhomogeneities in the larger pipe sections, as the material tested was sourced from an ex-service pipe [3].

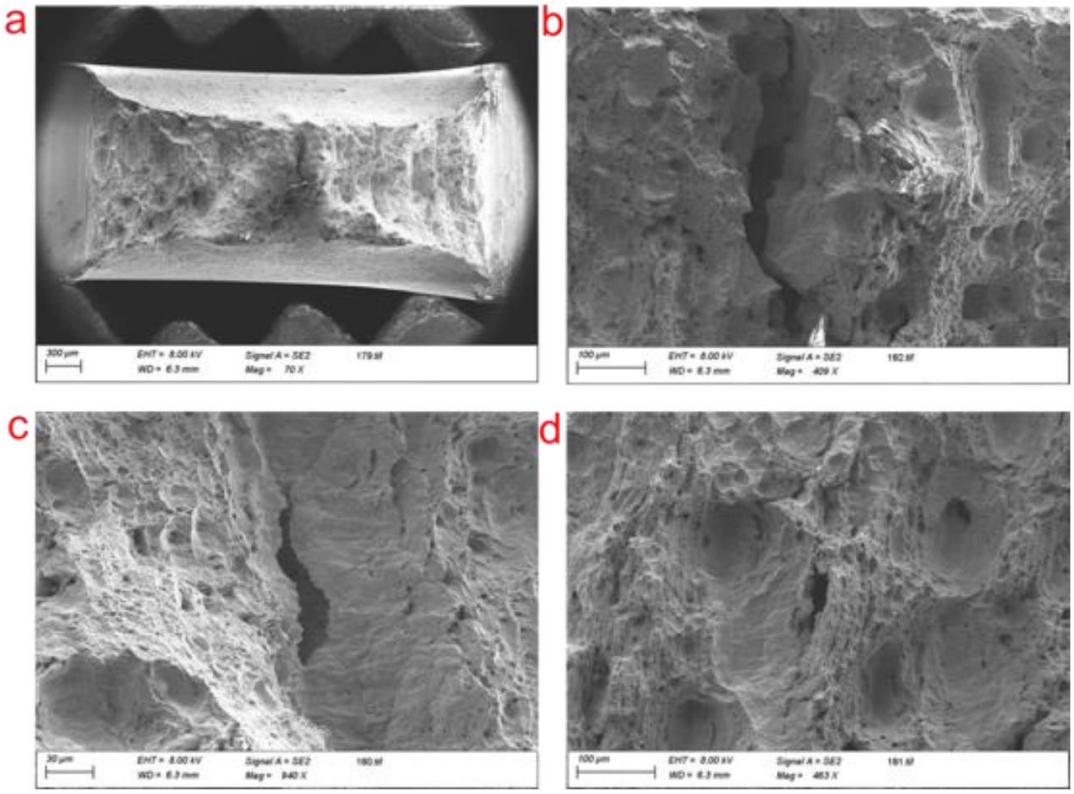

Figure 5-24 Fracture surface of uncharged X52 steel [3]

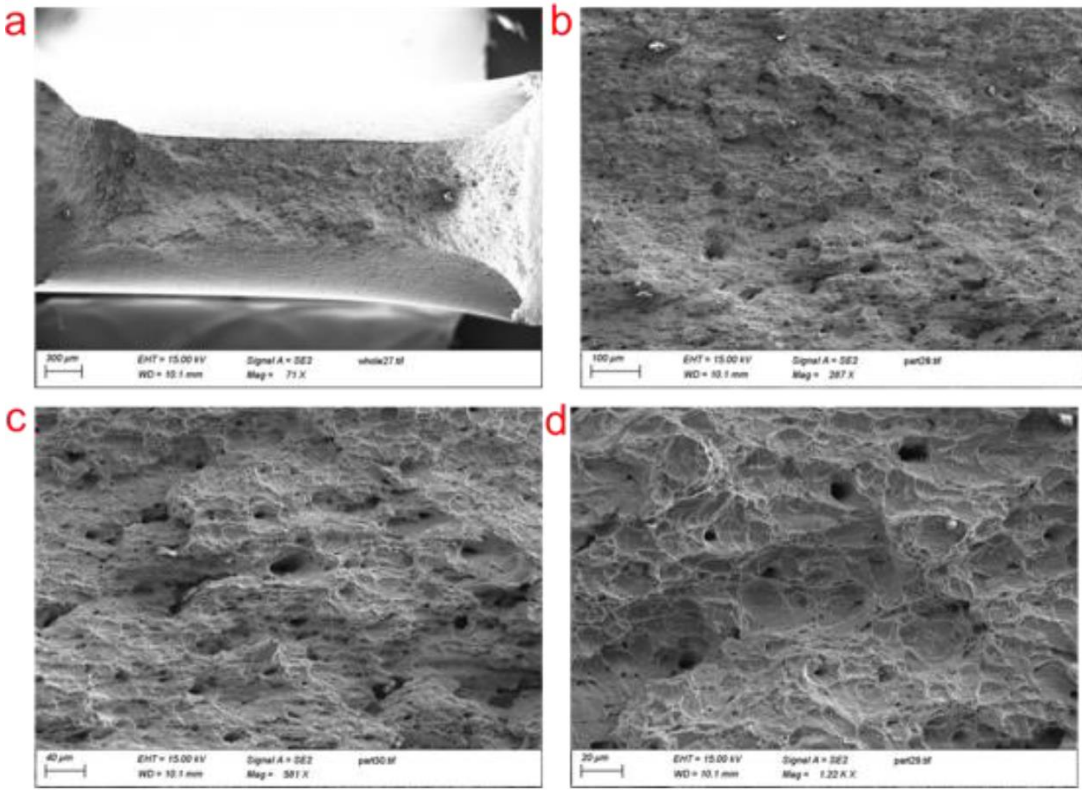

Figure 5-25 Fracture surfaces of the 42 weeks hydrogen exposed X52 steel [3]

5.5.4 Welded X52 steel

As shown in Figure 5-26, the SEM fracture morphology of a welded steel specimen in its uncharged state reveals both brittle and ductile areas with large cracks or voids. The most prominent crack on this surface measures over 100μm in length. Meanwhile, Figure 5-27 presents the fracture morphology after 42 weeks of hydrogen exposure, showing no significant differences compared to the as-received surface. The degree of necking observed in the hydrogen-exposed sample is similar to that seen in the as-received specimen.

5.5 Fractography of Impact Tested Specimens

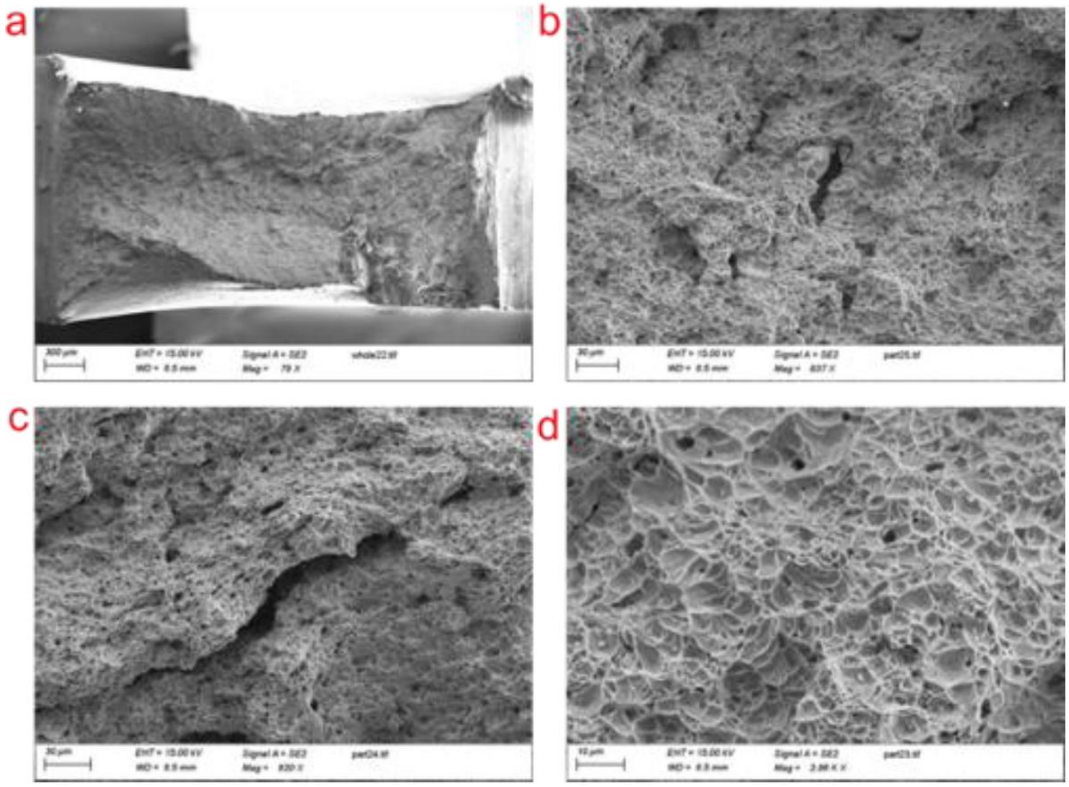

Figure 5-26 Fracture surfaces of uncharged welded steel [3]

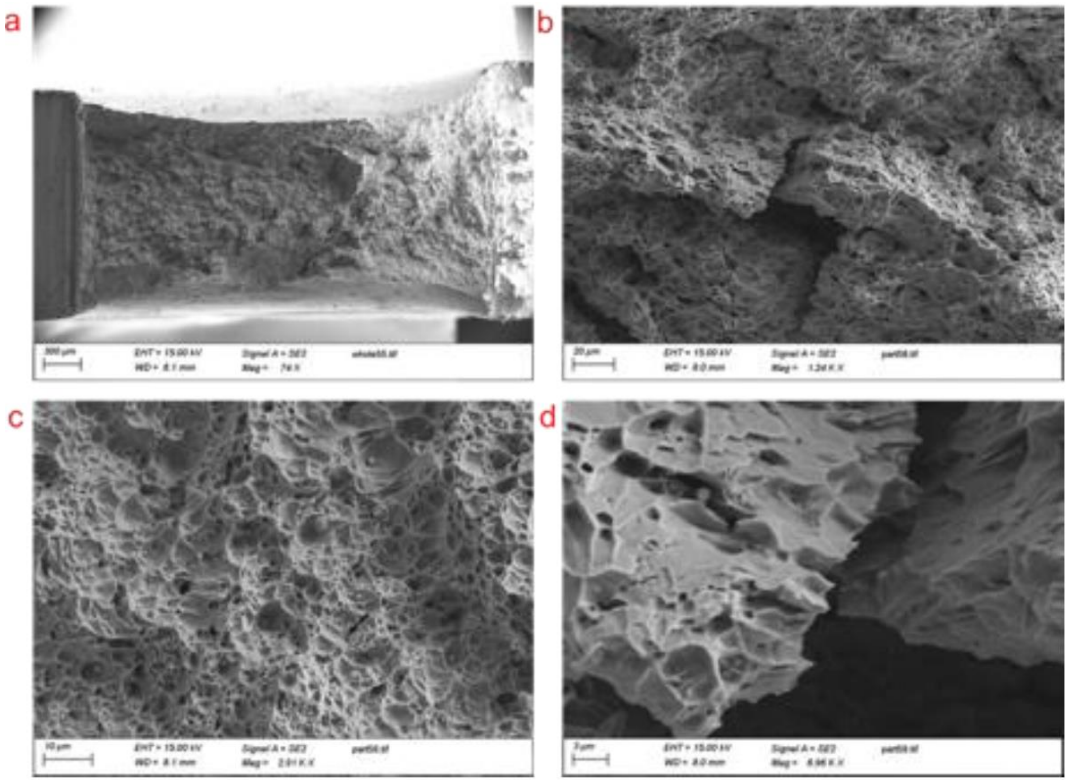

Figure 5-27 Fracture surfaces of hydrogen-charged welded steel for 42 weeks [3]

5.6 Analysing fatigue failure surface

There are three main types of fractures in metals and alloys [27,30]. The first type occurs in ductile materials, which usually fail as a result of the nucleation, growth, and coalescence of voids, typically initiated at inclusions and second-phase particles. The second type is cleavage, where the fracture involves separation along specific crystallographic planes. In this case, the fracture path is transgranular. Although cleavage is often referred to as brittle fracture, it can be preceded by large-scale plasticity and ductile crack growth. The third type is intergranular fracture, which occurs when grain boundaries become the preferred fracture path for crack propagation in the material [26].

Fatigue failure initiates on a microscopic scale as a tiny crack at a point of high-stress concentration, often referred to as a "stress-sensitive spot," and gradually extends due to stress fluctuations, leading to rupture [31]. Rupture typically occurs under conditions of severe restraint at the crack apex, where plastic deformation is largely inhibited, resulting in a crystalline appearance on the surface (dark region).

In ductile materials experiencing simple fatigue failure in air, the fracture surface typically displays two distinct zones [31,32]: one with a smooth appearance and conchoidal markings (beach marks), representing the fatigue crack development, and another with a crystalline or occasionally fibrous appearance, indicating sudden rupture. Despite the astonishing extent of crack development before complete failure, the final rupture zone may be as small as 10% of the original cross-sectional area, especially if the part is relieved of load as the crack progresses [31–34]. Figure 5-28 taken using an optical camera shows the fatigue fracture surface of steel specimens with the beach mark regions labelled A and the possible final fracture regions labelled as B. More of these fatigue failure surfaces all also found in Appendix B and more will be observed with notched specimens in the later sections.

The conchoidal markings serve as valuable indicators of the crack origin location, with abrupt changes in contour or crack front direction suggesting modifications in the stress system driving crack development. In addition, if there are ridges oriented perpendicular to the crack propagation direction, provide evidence of multiple cracks. These ridges result from level differences in individual crack planes, typically more pronounced near the crack origin surface and occasionally associated with machining marks, where cracks originate in parallel marks nearby.

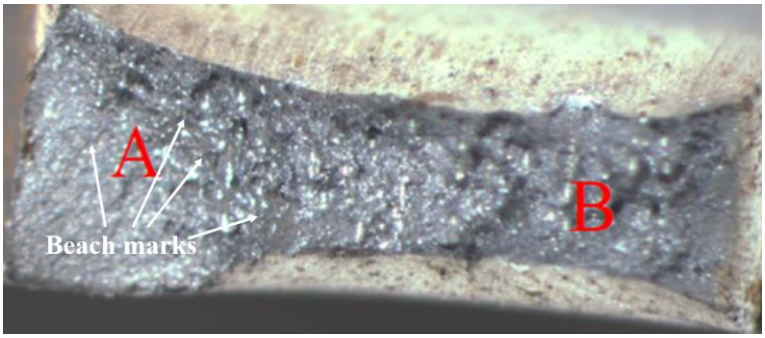

Figure 5-28 Fatigue fracture surface showing the possible region of conchoidal markings (A) and regions of sudden fracture (B)

In materials such as cast iron and certain cast aluminium alloys, most of the fracture occurs along the graphite flakes [35]. Distinguishing whether a fracture was preceded by a slow-developing crack can be challenging. Unless there has been artificial scratching of the crack surfaces or staining by some fluid medium, determining the presence of a fatigue crack in these materials is generally difficult as seen with the fatigue failure surfaces in cast iron in Appendix B.

5.7 Results of fatigue tests from hydrogen-charged specimens

The results involved in this research have been reported in the appendix section of this thesis, for both hydrogen-charged and uncharged specimens, and these results will be used to analyse the effects hydrogen charging has on the fatigue properties of the researched materials involved according to ref [36]. The hydrogenation was achieved by exposing the materials to hydrogen gas by leaving them in a hydrogen-pressurised tube of between 8 – 10 bars, the results of which are synonymous with exposing pipeline material used for natural gas to a more hydrogen environment. The relevance of this is to investigate if the present natural gas network can safely distribute blended natural gas, which is the motivation of this research.

5.7.1 Experimental fatigue data from steel specimens

The data presented in Table 1 in Appendix A summarizes the uniaxial fatigue results generated by testing uncharged steel specimens in tension at a frequency of 10Hz. There were three batches of steel specimens in this case with a combined total of twenty-one specimens. Specimens that did not fail during the fatigue test were not retested at higher stress amplitudes.

Figure 5-29 represents a selection of randomly chosen steel specimens from the various hydrogen-charged lots after the fatigue test. The specimen that survived the test after 2 million cycles is clearly labelled in this figure and showed noticeably less visible plastic deformation compared to the other failed specimens.

Figure 5-29 Runout steel specimen and failed steel specimens from fatigue test

Table 2 in Appendix A summarizes all the raw fatigue data that was generated from hydrogen-charged steel specimens and stored for different lengths of time in the freezer at -80^0C temperatures. Every effort was made to minimise the time between the specimens taken out of the freezer and the time the test started running. Like with the uncharged steel specimens, those that did not fail during the fatigue test were not retested at higher stress amplitudes.

5.7.2 Experimental fatigue data from hydrogen-charged welded steel specimens

The data presented in Table 3 in Appendix A also summarises the uniaxial fatigue results generated by testing welded steel plain specimens in tension at a frequency of 10Hz. There were two batches of uncharged welded steel specimens with a combined total of 20 specimens, of which 4 were runouts. The runout specimens were not retested at a higher stress amplitude. Meanwhile, 21 specimens were hydrogen-charged, 11 of which were cured for 3 months, and 10 specimens cured for 9 months. Some randomly selected failed specimens of welded steel and shown in Figure 5-30. These specimens were tested under the same conditions as the steel specimens.

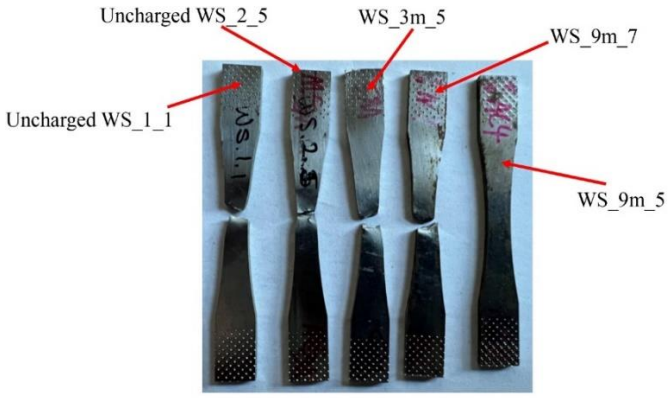

Figure 5-30 Randomly selected failed and survived welded steel specimens

5.7.3 Experimental fatigue data from hydrogen-charged brass specimens

The data presented in Table 4 of Appendix A summarizes the uniaxial fatigue results generated from plain brass specimens. Only 5 specimens were unchanged, and 10 specimens were hydrogen-charged and cured for 9 months. There were no runout tests witnessed in this case. Figure 5-31 shows some randomly selected failed hydrogen-charged and uncharged specimens of brass.

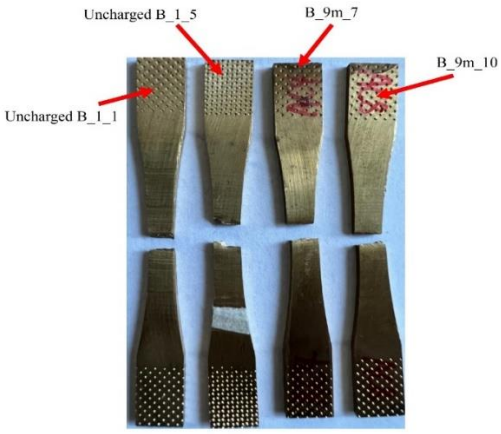

Figure 5-31 Failed uncharged and hydrogen-charged brass specimens.

5.7.4 Experimental fatigue data from hydrogen-charged cast iron specimens

For cast iron specimens, there were 21 uncharged plain specimens, 10 and 11 hydrogen-charged plain specimens cured for 3 and 9 months respectively. Table 5 of Appendix A presents the data generated by running uniaxial fatigue tests on these plain cast iron samples. Some of the randomly selected failed specimens for cast iron are shown in Figure 5-32.

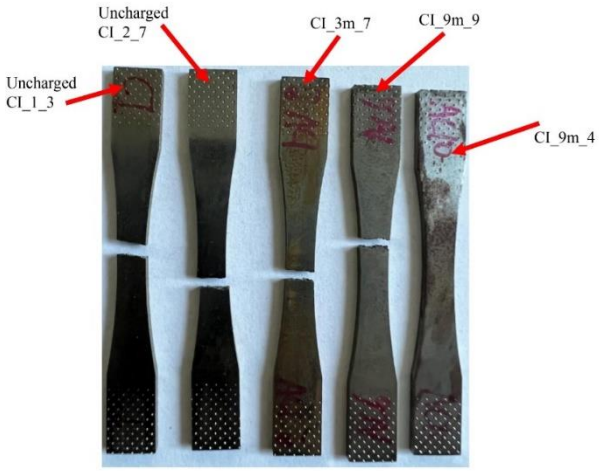

Figure 5-32 Failed uncharged and hydrogen-charged cast iron specimens.

These failed samples of cast iron do not show considerable plastic deformation. There were also about 9 runouts in total and these specimens were not retested at higher amplitudes.

Fatigue data sets were also generated from notched specimens using the experimental protocols described in the section. The following section elucidates its relevance to the overarching research objectives

5.8 Experimental fatigue tests with notched specimens

One of the objectives of this PhD research was to employ statistical analysis to elucidate and examine the significance displayed by fatigue data sets. To accomplish this goal, experimental data was generated from notched specimens. The data obtained from these notched specimens were used in subsequent chapters to validate the tests for statistical significance. This statistical significance test aspect is crucial in this research because it will be applied to the fatigue data sets derived from uncharged and hydrogen-charged data sets to ascertain whether there exists a statistically significant difference between them. Before delving into these analyses, it is imperative to describe the methods used to generate this data from notched specimens in the experimental chapter of this research, hence its relevance here.

5.8.1 Why were notches used to generate data sets used to describe statistical significance test

To produce fatigue data with the prior knowledge that each dataset will differ from another, such data can be generated using specimens with measured geometric discontinuities. A good geometric configuration that can be easily measured and varied is a notch. The notch

root radius determines the fracture toughness of a material [26,27,37]. In this research, notches were particularly selected as the basis for generating fatigue data for use in describing statistical significance because they are well-known for reducing fracture toughness [38,39] and endurance limits of engineering materials, effectively shifting the mean S-N curve downward. They also change the slope of S-N curves and scattering. By introducing a notch, therefore, it is then anticipated that the fatigue data sets will be statistically significant. Altering the notch geometry, allowed distinct fatigue data sets to be generated that can subsequently be employed in the statistical significance testing. Moreover, notch geometry is a parameter that can be conveniently controlled and accurately measured. For this reason, different materials were used to produce the notched specimens, with three different notch diameters: 1mm, 2mm, and 3mm.

5.8.2 Material specification and specimen/notch geometry

The materials chosen for this section were cast iron, brass, and X52 pipeline steel. The specimens were rectangular in shape and underwent surface preparation to make them smooth by manual machining. This surface preparation was carried out at the School of Natural Sciences, Department of Materials at the University of Manchester. Subsequently, these prepared specimens were transported to the Department of Civil and Structural Engineering at the University of Sheffield for testing.

To introduce notches onto the specimens, this was done in the Workshop for Civil and Mechanical Engineering at the University of Sheffield. The notches were created using drills with varying diameters to produce circular holes at the centre of the specimens. The dimensions of the specimens measured a length of 65mm, 8.5mmm in width and had a cross-sectional thickness of 2mm. These measurements were obtained with a Vanier calliper by taking readings at three different points on the surface of each specimen and then averaging the results. Figure 5-33 illustrates the geometry of the specimen used in this case.

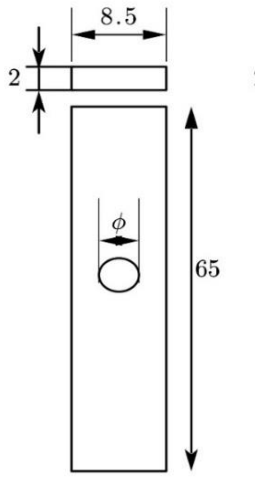

Figure 5-33 Specimen geometry in mm having a circular notch of diameter ∅.

5.8.3 Test procedure and protocols with notched specimen

The test machine and the testing load settings applied to these notched specimens followed the same configuration used in the fatigue test with plain hydrogen-charged and uncharged specimens, as described in Section 5.3 and the failure criterion was complete breakage as described in this section. Some fatigue failure surfaces from these specimens are shown in the figure below.

Notched steel specimens

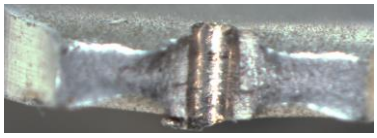

Specimen ID: **S_1mm_1**
$\sigma_i = 243.8$MPa
$N_f = 8{,}103$ Cycles

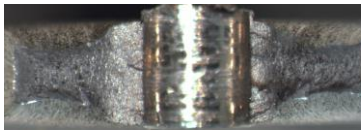

Specimen ID: **S_2mm_10**
$\sigma_i = 229.8$MPa
$N_f = 12{,}105$ Cycles

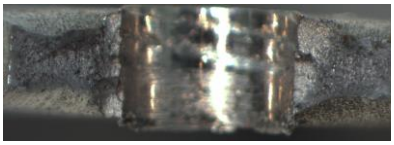

Specimen ID: **S_3mm_6**
$\sigma_i = 239.4$MPa
$N_f = 12{,}684$ Cycles

Notched cast iron specimens

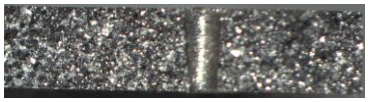

Specimen ID: **CI_1mm_1**
$\sigma_i = 61.7$MPa
$N_f = 8{,}798$ Cycles

Specimen ID: **CI_2mm_9**
$\sigma_i = 46.0$MPa
$N_f = 110{,}298$ Cycles

Specimen ID: **CI_3mm_9**
$\sigma_i = 57.7$MPa
$N_f = 4{,}988$ Cycles

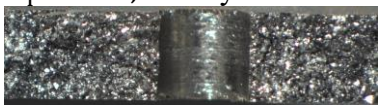

Specimen ID: **CI_2mm_2**

Specimen ID: **CI_3mm_2**

Specimen ID: **CI_1mm_2**
$\sigma_i = 52.2$MPa
$N_f = 132{,}604$ Cycles

$\sigma_i = 56.9$MPa
$N_f = 16{,}266$ Cycles

$\sigma_i = 41.6$MPa
$N_f = 137{,}409$ Cycles

Notched brass specimens

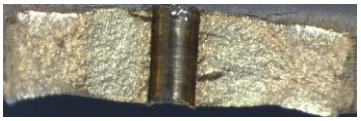

Specimen ID: **Br_1mm_1**
$\sigma_i = 95.4$MPa
$N_f = 541{,}945$ Cycles

Specimen ID: **Br_2mm_5**
$\sigma_i = 88.3$MPa
$N_f = 732{,}233$ Cycles

Specimen ID: **Br_3mm_10**
$\sigma_i = 116.5$MPa
$N_f = 109{,}362$ cycles

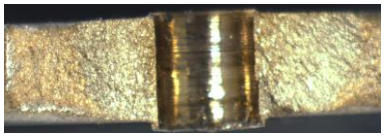

Specimen ID: **Br_2mm_6**
$\sigma_i = 88.6$MPa
$N_f = 460{,}968$ Cycles

Specimen ID: **Br_3mm_9**
$\sigma_i = 82.5$MPa
$N_f = 109{,}362$ Cycles

Figure 5-34 Randomly selected fatigue fracture surfaces of notched specimens

The analysis of some of the fatigue fracture surfaces from notched specimens showing possible regions of conchoidal markings (A) and regions of sudden fracture (B) is shown in Figure 5-35. More pictures to show fracture surfaces are reported in Appendix B of this thesis.

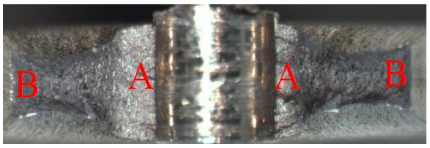

Figure 5-35 Randomly selected fatigue surfaces of notched steel specimens showing possible regions of conchoidal markings (A) and regions of sudden fracture (B)

5.9 Results of fatigue test on notched specimens

This section summarizes the fatigue results generated through the testing of notched specimens of the materials selected in question, with different notch geometries. These results will be presented in terms of gross stress amplitude with the corresponding cycles to failure.

The data presented in Table 6 in Appendix A summarizes all the raw data generated from fatigue testing of steel specimens with three different notch sizes. Ten specimens were

allocated for each notch geometry. Specimens that survived the fatigue test after 2 million cycles were subsequently subjected to retesting at a higher stress amplitude, as indicated in the table. Out of the specimens with a 1mm notch, only two specimens (S_1mm_1 and S_1mm_8) resulted in runouts and were retested at 243.83MPa and 243.24MPa respectively. Meanwhile, three survived with a 2mm notch (S_2mm_3, S_2mm_9 and S_2mm_10) were runouts and were retested at stress amplitudes of 182.72, 183.01 and 175.53MPa respectively. For specimens with a 3mm notch only specimen S_3mm_6 survived and was retested at 154.65MPa. Figure 5-36 shows a selection of randomly chosen failed steel specimens from each of the notch geometries.

a) b) c)

Figure 5-36 Failed steel specimens after fatigue test: a) specimen S_1mm_1 and S_1mm_2, b) specimens S_2mm_3 and S_2mm_4 and c) specimens S_3mm_5 and S_3mm_6

5.9.1 Experimental fatigue data from brass notched specimens

Similarly, the data presented in Table 7 of Appendix A summarizes all the raw data generated from testing brass specimens with different notch geometries. There were ten specimens allocated for each notch geometry. There were no runouts from the specimens with 1mm and 3mm notch sizes. Specimen B_2mm_3 survived the test and was retested at a higher stress amplitude of 94.43MPa. Figure 5-37 shows a selection of randomly chosen failed brass specimens from each of the notch geometries.

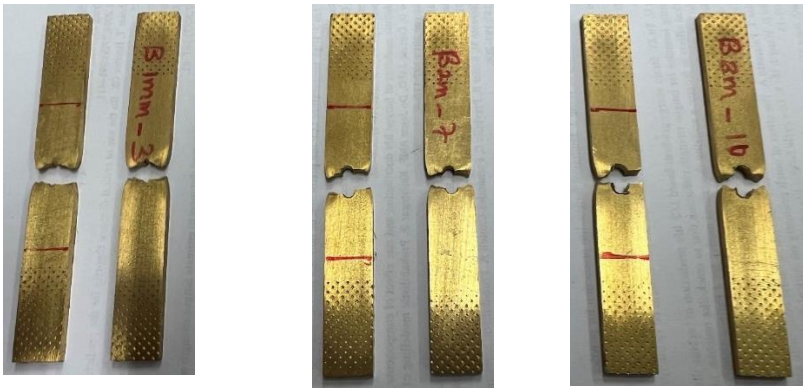

a) b) c)

Figure 5-37 Failed brass specimens after fatigue test: a) specimen B_1mm_1 and B_1mm_3, b) specimens B_2mm_5 and B_2mm_7 and c) specimens B_3mm_9 and B_3mm_10

5.9.2 Experimental fatigue data from cast iron notched specimens

The data presented in Table 8 of Appendix A summarizes the raw fatigue data that was generated by testing cast iron specimens with three different notch sizes. Also, ten specimens were allocated for each notch geometry for cast iron. There were a good number of specimens that survived the fatigue test after 2 million cycles as illustrated in the table. Figure 5-38 also shows a selection of randomly chosen failed specimens of cast iron from each notch geometry.

a) b) c)

Figure 5-38 a) failed specimen of CI_1mm_1 and CI_1mm_2 b) failed specimen CI-2mm_1 and CI_2mm_2 and c) CI_3mm_1 and CI_3mm_2 after failure.

5.10 Chapter Feedforward

After detailing the experimental equipment and procedures used to generate the raw data for this PhD research in this chapter, the focus in the next chapter shifts to post-processing

these raw data sets using the methodology described in the previous chapter, to draw meaningful and applicable conclusions for fatigue design. These methodologies will be applied to the data obtained from both hydrogen-charged and uncharged specimens, (data sets summarized in Appendix A of this thesis). The next part will also use the validated statistical significance tests, also described in the previous chapter, to determine whether the differences observed from the fatigue data sets from both hydrogen-charged and uncharged specimens are statistically significant or not. The data generated from notched specimens, which were used to validate the statistical significance tests, are also summarized in Appendix B.

5.11 References

[1] O. Obiukwu, L.U. Grema, The Effect of Surface Finish on the Low Cycle Fatigue of Low and Medium Carbon Steel, n.d. https://www.researchgate.net/publication/335240807.

[2] M.R. Bayoumi, A.K. Abdellatif, Effect of surface finish on fatigue strength, Eng. Fract. Mech. 51 (1995) 861–870. https://doi.org/10.1016/0013-7944(94)00297-U.

[3] D. Engelberg, F. Scenini, Y. Zhou, J. Duff, HyDeploy2 –Materials Analysis & Testing, 2023.

[4] G.H. Farrahi, H. Ghadbeigi, An investigation into the effect of various surface treatments on fatigue life of a tool steel, J. Mater. Process. Technol. 174 (2006) 318–324. https://doi.org/10.1016/j.jmatprotec.2006.01.014.

[5] HyDeploy, HyDeploy Project, Project Close Down Report, Revision 03 (Final), 2021.

[6] ASTM E384, Standard Test Method for Microindentation Hardness of Materials, ASTM Int. (2022). https://doi.org/10.1520/E0384-22.

[7] B.P. Somerday, P. Sofronis, K.A. Nibur, C. San Marchi, R. Kirchheim, Elucidating the variables affecting accelerated fatigue crack growth of steels in hydrogen gas with low oxygen concentrations, Acta Mater. 61 (2013) 6153–6170. https://doi.org/10.1016/j.actamat.2013.07.001.

[8] J. Capelle, J. Gilgert, I. Dmytrakh, G. Pluvinage, The effect of hydrogen concentration on fracture of pipeline steels in the presence of a notch, Eng. Fract. Mech. 78 (2011) 364–373. https://doi.org/10.1016/j.engfracmech.2010.10.007.

[9] E.N. Kufoin, L. Susmel, On the parametric assessment of fatigue disparities, Probabilistic Eng. Mech. 77 (2024) 103651. https://doi.org/10.1016/j.probengmech.2024.103651.

[10] National Gas, National Gas Transmission: Our network and assets, (2024). https://www.nationalgas.com/our-businesses/our-network-and-assets#:~:text=The National Transmission System consists of 500 above-ground installations. (accessed September 13, 2024).

[11] S.K. Sharma, S. Maheshwari, A review on welding of high strength oil and gas pipeline steels, J. Nat. Gas Sci. Eng. 38 (2017) 203–217. https://doi.org/10.1016/j.jngse.2016.12.039.

[12] J.A. Ronevich, B.P. Somerday, Z. Feng, Hydrogen accelerated fatigue crack growth of friction stir welded X52 steel pipe, Int. J. Hydrogen Energy. 42 (2017) 4259–4268. https://doi.org/10.1016/j.ijhydene.2016.10.153.

[13] ASTM E466 - 21, Standard Practice for Conducting Force Controlled Constant Amplitude Axial Fatigue Tests of Metallic Materials, (2021). https://doi.org/10.1520/E0466-21.

[14] H. Su, Y. Gao, X. Liang, Y. Lu, C. Lin, Z. Cao, The Effect of Buckling Restraint on Axial Strain Life Fatigue Data, J. Test. Eval. 52 (2024). https://doi.org/10.1520/JTE20230366.

[15] ASTM E467, Standard Practice for Verification of Constant Amplitude Dynamic Forces in an Axial Fatigue Testing System 1, ASTM Stand. . (2021). https://doi.org/10.1520/E0467-21.

[16] O. Barrera, D. Bombac, Y. Chen, T.D. Daff, E. Galindo-Nava, P. Gong, D. Haley, R. Horton, I. Katzarov, J.R. Kermode, C. Liverani, M. Stopher, F. Sweeney, Understanding and mitigating hydrogen embrittlement of steels: a review of experimental, modelling and design progress from atomistic to continuum, J. Mater. Sci. 53 (2018) 6251–6290. https://doi.org/10.1007/s10853-017-1978-5.

[17] S. Lynch, Hydrogen embrittlement phenomena and mechanisms, Corros. Rev. 30 (2012) 105–123. https://doi.org/10.1515/corrrev-2012-0502.

[18] M. Brilz, J. Biehler, H. Hoche, M. Oechsner, Development of a hydrogen absorption model to determine absorption kinetics and diffusion coefficients by means of carrier gas hot extraction, Int. J. Hydrogen Energy. 43 (2018) 10496–10501. https://doi.org/10.1016/j.ijhydene.2018.04.101.

[19] V. Olden, C. Thaulow, R. Johnsen, Modelling of hydrogen diffusion and hydrogen induced cracking in supermartensitic and duplex stainless steels, Mater. Des. 29 (2008) 1934–1948. https://doi.org/10.1016/j.matdes.2008.04.026.

[20] ASTM C1361, Standard Practice for Constant-Amplitude, Axial, Tension-Tension Cyclic Fatigue of Advanced Ceramics at Ambient Temperatures 1, ASTM Stand. Reapproved 2019. (2010). https://doi.org/10.1520/C1361-10R19.

[21] ASTM D3479/D3479M, Standard Test Method for Tension-Tension Fatigue of Polymer Matrix Composite Materials 1, ASTM Stand. Reapproved 2023. (2019). https://doi.org/10.1520/D3479_D3479M-19R23.

[22] ASTM F2118, Standard Test Method for Constant Amplitude of Force Controlled Fatigue Testing of Acrylic Bone Cement Materials 1, ASTM Stand. Reapproved 2020. (2014). https://doi.org/10.1520/F2118-14R20.

[23] L. Pallarés-Santasmartas, J. Albizuri, A. Avilés, R. Avilés, Mean Stress Effect on the Axial Fatigue Strength of DIN 34CrNiMo6 Quenched and Tempered Steel, Metals (Basel). 8 (2018) 213. https://doi.org/10.3390/met8040213.

[24] A. Niesłony, M. Böhm, Fatigue Life of S355JR Steel under Uniaxial Constant Amplitude and Random Loading Conditions, Mater. Sci. 55 (2020) 514–521. https://doi.org/10.1007/s11003-020-00333-0.

[25] L. Susmel, D.G. Hattingh, M.N. James, R. Tovo, Multiaxial fatigue assessment of friction stir welded tubular joints of Al 6082-T6, Int. J. Fatigue. 101 (2017) 282–296. https://doi.org/10.1016/j.ijfatigue.2016.08.010.

[26] Suresh S., Fatigue of Materials, Second, Cambridge University Press, New York, 2004.

[27] T.. Anderson, Fracture Mechanics, Fundamentals and Applications, Third, Taylor & Francis Group, CRC Press, New York, 2005.

[28] STP46393S, ASTM Manual on Fitting Straight Lines, ASTM Man. Fitting Straight Lines. (2009) 1-1–28. https://doi.org/10.1520/stp46393s.

[29] ASTM D256, Standard Test Methods for Determining the Izod Pendulum Impact

Resistance of Plastics 1, ASTM Int. (2023). https://doi.org/10.1520/D0256-23E01.

[30] R.A. Martínez, Fracture surfaces and the associated failure mechanisms in ductile iron with different matrices and load bearing, Eng. Fract. Mech. 77 (2010) 2749–2762. https://doi.org/10.1016/j.engfracmech.2010.07.013.

[31] G.A. Cottell, Fatigue Failures, With Special Reference to Fracture Characteristics, in ASM Fail. Anal. Case Hist. Fail. Modes Mech., ASM International, 2019. https://doi.org/10.31399/asm.fach.modes.c9001459.

[32] A. Pineau, A.A. Benzerga, T. Pardoen, Failure of metals I: Brittle and ductile fracture, Acta Mater. 107 (2016) 424–483. https://doi.org/10.1016/j.actamat.2015.12.034.

[33] R. Biswal, X. Zhang, M. Shamir, A. Al Mamun, M. Awd, F. Walther, A. Khadar Syed, Interrupted fatigue testing with periodic tomography to monitor porosity defects in wire + arc additive manufactured Ti-6Al-4V, Addit. Manuf. 28 (2019) 517–527. https://doi.org/10.1016/j.addma.2019.04.026.

[34] P. Zhang, J. Li, Y. Zhao, J. Li, Crack propagation analysis and fatigue life assessment of high-strength bolts based on fracture mechanics, Sci. Rep. 13 (2023). https://doi.org/10.1038/s41598-023-41804-z.

[35] W.L. Bradley, M.N. Srinivasan, Fracture and fracture toughness of cast irons, Int. Mater. Rev. 35 (1990) 129–161. https://doi.org/10.1179/095066090790324028.

[36] ASTM E468/E468M, Designation: E468/E468M − 23a Standard Practice for Presentation of Constant Amplitude Fatigue Test Results for Metallic Materials 1, ASTM Stand. (2023). https://doi.org/10.1520/E0468_E0468M-23A.

[37] K. Chandra Shekar, B. Anjaneya Prasad, N. Eswara Prasad, Effect of Notch Root Radius on the Fracture Toughness of Epoxy and 0.5 wt% Amino MWCNTs-Reinforced Nanocomposite, Trans. Indian Inst. Met. 69 (2016) 1069–1075. https://doi.org/10.1007/s12666-015-0623-8.

[38] J.S. Kim, N.O. Larrosa, A.J. Horn, Y.J. Kim, R.A. Ainsworth, Notch bluntness effects on fracture toughness of a modified S690 steel at 150 °C, Eng. Fract. Mech. 188 (2018) 250–267. https://doi.org/10.1016/j.engfracmech.2017.05.047.

[39] N.O. Larrosa, A dislocation-based method using generative algorithms to model notch geometries: Determination of Mode I SIFs, Eng. Fract. Mech. 127 (2014) 327–335. https://doi.org/10.1016/j.engfracmech.2014.06.001.

Chapter 6

Fatigue Results and Statistical Significance

6.1 Introduction

Fatigue data were generated in this PhD research, and methods recommended by ASTM, IIW, and LRM to post-process and analyse the fatigue data were discussed. By applying these established methodologies to theoretical data and data from the literature, confidence was developed in the analysis and interpretation of the resulting data sets. Post-processing, in this context, refers to analysing and interpreting fatigue data sets to determine properties such as the endurance limit (high-cycle fatigue strength), the inverse slope in the medium-cycle fatigue regime, and the associated scattering. This methodology involves using S-N curves to estimate the endurance limit at 2 million cycles for analytical purposes and applying statistical approaches to establish the design curve based on a probability of

survival and level of scatter. This process also enables the estimation of scatter bands and their sizes, contributing to the ability to design confidently.

This chapter will therefore focus on post-processing the fatigue results generated by testing plain specimens pre-charged with hydrogen and made of ex-service X52 steel, ex-service X52 welded steel, grey cast iron (GCI), and brass under uniaxial loading conditions, as reported in the previous chapter. These specimens were pre-charged with hydrogen by soaking them in pressure tubes filled with hydrogen for varying durations, ranging from three to nine months. After exposure, the specimens were stored at -80°C to minimise the diffusion of the absorbed hydrogen before testing. Subsequently, uniaxial fatigue tests under tension-tension ($R = 0.1$) were conducted on these specimens, and the resulting data sets were post-processed. The primary objective was to assess the impact of hydrogen exposure on fatigue properties, with the interpretation of scatter bands being crucial for understanding reliability and consistency in fatigue performance. This understanding provides valuable insights into the material's response to fatigue loading under the defined conditions, aiding in the formulation of effective strategies for material design and practical applications, like in the HeDeploy project of which this PhD project is part.

Furthermore, the procedure to test and establish statistical significance has been explained and validated using data from notched specimens and the literature. This chapter leverages the knowledge gained in illustrating this statistical analysis to ascertain the significance of observed differences in fatigue properties. The approaches used to test for statistical significance were explained using data sets from notched specimens and literature data. The objective was to use this knowledge of statistical significance to justify, with a level of confidence, whether significant changes indeed exist in the fatigue and fracture properties of the metals of interest due to hydrogen charging. The chosen significance level for this analysis was 5%. This is because 5% significance strikes a balance between the risk of making a Type I error (false positive) and a Type II error (false negative). This research minimized the likelihood of drawing incorrect conclusions without overly increasing the risk of missing the impacts of hydrogen on the selected pipeline materials. Also, the 5% significance level is often widely accepted as a conventional threshold, allowing results to be compared across the field and ensuring that conclusions drawn from fatigue analysis are consistent with accepted practices in the industry [1,2]. It corresponds to a 95% confidence level, meaning there is a high degree of certainty that the observed results are not due to random chance. In metal fatigue analysis, where safety and reliability are paramount, this

level of confidence is appropriate for making critical decisions. Other standardised approaches use different levels of significance like the Euro code and BS standards, but this research is considered a broad scope in its application.

6.1.1 Fatigue Characterisation Analysis Considered

To begin with, what does it mean by the fatigue characterisation of a metal? Fatigue characterization of a metal involves studying its response to repeated or cyclic loading, which is crucial for understanding how materials withstand fluctuating stresses over time. This process includes determining fatigue strength, representing the maximum stress a material can endure before failure, and assessing the fatigue life, indicating the number of loading cycles until failure. The concept of an endurance limit, where a material can survive a referenced number of cycles without failure, is also considered. In this PhD research, these fatigue properties will be explained using the Wöhler equation defined as [2,3]:

$$\sigma^k N_f = {\sigma_0}^k N_A = \ constant \tag{6-1}$$

Where σ is the stress amplitude, σ_0 the stress amplitude at the endurance limit, N_A the reference number of cycles at the endurance limit and k the value of the inverse slope. This equation shows that the fatigue strength at any cycle is mainly determined by two parameters, the fatigue strength coefficient and the fatigue strength exponent [4] (see chapter 5). The fatigue strength exponent b represents the degree of the fatigue damage [5], which must be associated with the damage mechanisms. It must always be less than zero for the endurance limit must always be less than the fatigue strength coefficient due to damage accumulation during every load cycle. It has been shown that the fatigue strength exponent is the negative inverse slope of the mean S-N curve. For analytic purposes, the endurance limit is estimated at 2 million cycles. The size of the scatter band generated using the ASTM, IIW and LRM approaches, is quantified using a specified level of confidence and percentage probability of survival. This scatter band is estimated in the high cycle fatigue regime at the reference point (endurance limit), and it represents the interval between the maximum and minimum stress amplitudes at this point.

6.1.2 Choosing a statistical distribution of fatigue data

To assess the suitability of the adopted distribution in describing fatigue life data, the correlation coefficient r is determined. The analyses used in this investigation assumed

that the fatigue life distribution is log-normal. The correlation coefficient r is then defined as [6,7]:

$$r = \frac{\sum_{i=1}^{n}(\sigma_i - \bar{\sigma})\left(N_{f,i} - \bar{N}_f\right)}{\sqrt{\sum_{i=1}^{n}(\sigma_i - \bar{\sigma})^2 \sum_{i=1}^{n}\left(N_{f,i} - \bar{N}_f\right)^2}} \quad (6\text{-}2)$$

in which σ_i and $\bar{\sigma}$ are the stress and mean stress amplitude respectively. $N_{f,i}$ the fatigue life and $\bar{N}_{f,i}$ is the mean fatigue. It is worth noting that, |r|≤1 and when |r| is close to one, it indicates a strong correlation between σ and N_f in the selected distribution field. Consequently, the better fitting of distribution can be determined by comparing the r values. Usually, the larger the sample sizes are, the more precise the fitting results are in this distribution.

6.2 Fatigue characterization of steel

Recall that there is always a decline in both the mechanical and electrochemical properties of steel following operational use [8–10]. This deterioration extends to their resistance to environmentally assisted cracking, leading to diminished plasticity, strength, toughness, fracture resistance, and fatigue. Refs [11–13] identified that crack propagation notably decreases the resistance to corrosion fatigue and hydrogen-induced cracking. While Ref [14] also show that the fatigue lifetime of a ferrite-pearlite microstructure is more affected by microstructural degradation due to the long-term service of the steel. These factors are commonly associated with the failure mode observed in steel pipes used for transporting natural gas, particularly in moist environments.

In this research, ex-service X52 low-carbon steel, which had been in use for over 30 years, was employed as the steel specimens [15]. Although this research doesn't specifically investigate the degradation process in the ex-service X52 pipeline steel, it does examine the influence of exposure to certain levels of hydrogen, comparing its impact to data available in the literature.

This section will post-process the data generated from ex-service X52 plain steel specimens used in this research. Seventeen plain specimens were uncharged, while fifteen specimens each were hydrogen charged by soaking them for three and five months. The fatigue data generated by testing these steel specimens have been reported in the previous chapter (see experiments and raw data chapter).

6.2.1 The mean S-N curve and parabolic scatter bands from fatigue data sets for steel

By utilizing the post-processing techniques described in the methodology chapter, the graphs summarized in Figure 6-1 depict the mean S-N curve, the endurance limit, and the parabolic scatter bands of the fatigue data sets generated using approaches suggested by the ASTM, IIW and LRM. These scatter bands were constructed at a 95% probability of survival.

The mean points ($\overline{log\sigma_i}, \overline{logN_{f,i}}$) of these curves do not align, despite a minimal percentage difference in the direction of life. As a result, this mean point cannot be regarded as a fixed reference for observing changes in these S-N curves due to hydrogen charging. These graphs will be analysed by comparing each of the fatigue properties represented by these curves, spread, slope, intercept, endurance limit and size of scatter bands.

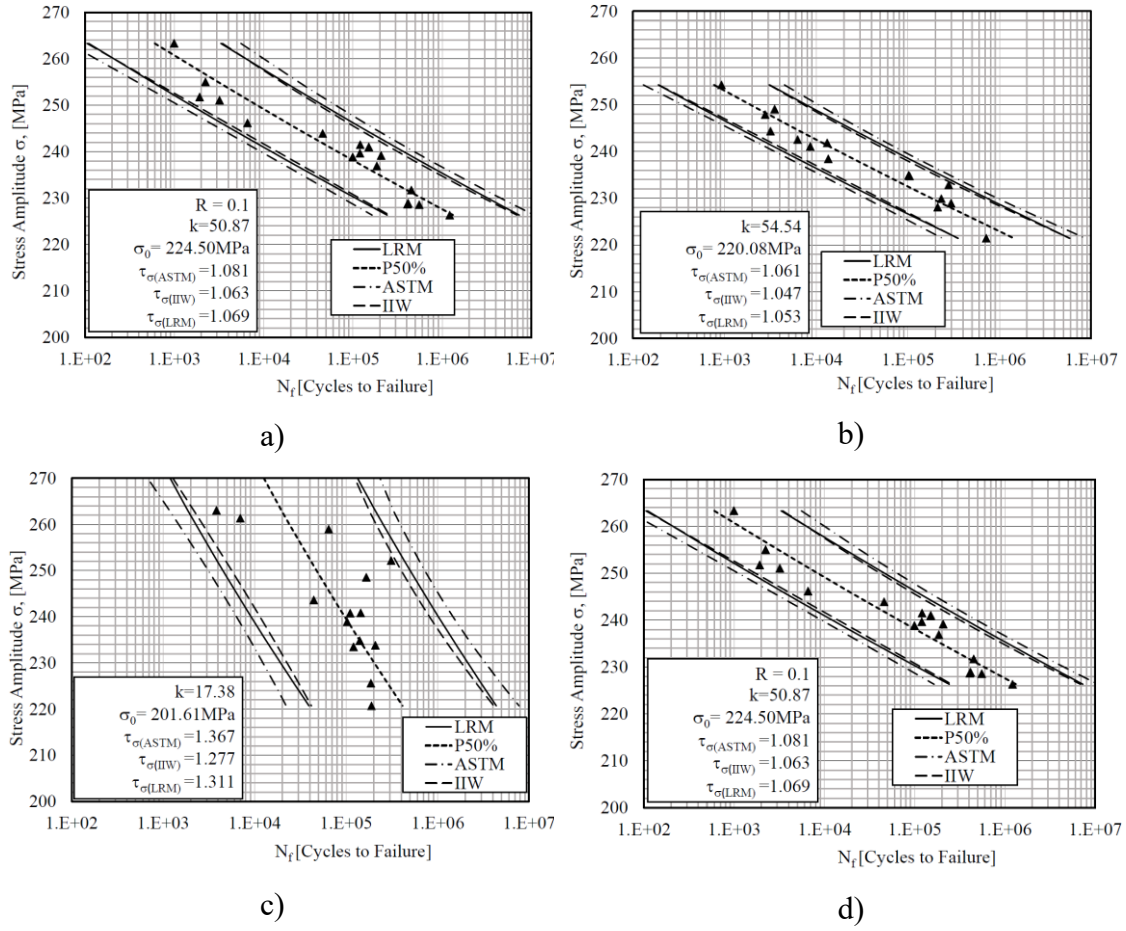

Figure 6-1 Mean S-N curves and parabolic scatter bands of steel fatigue data sets a) plain uncharged, b) plain hydrogen-charged for 3 months c) plain hydrogen charged for 5 months and d) plain hydrogen-charged for 9 months.

Table 6-1 summarises all the fatigue properties for steel generated from testing steel plain specimens under various hydrogen-charging and curing conditions. This table shows the various values for the sample set, the standard deviation as well as values of the inverse slope from steel data sets.

Table 6-1 Summary of fatigue properties of steel in tension (R = 0.1), at a frequency of 10Hz for hydrogen-charged specimens and cured in months, and uncharged plain specimens, (N_A = 2 x10^6)

Specimen ID	Fatigue results									
	n	s	k	R	C_o	r	σ_0 [MPa)]	τ_σ (ASTM)	τ_σ (IIW)	τ_σ (LRM)
S_uncharged	17	0.09	50.87	0.1	125.91	0.95	224.5	1.08	1.06	1.07
S_3m	15	0.06	54.54	0.1	134.07	0.97	220.1	1.06	1.05	1.05
S_5m	15	0.41	17.38	0.1	46.36	0.78	201.6	1.37	1.28	1.31
S_9m	9	0.07	45.80	0.1	113.59	0.96	219.5	1.09	1.07	1.08

The endurance limits determined using linear regression are also summarized and the sizes of the scatter bands calculated from the standardized approaches (ASTM, IIW, LRM) used in this research are shown. These scatter bands approximate to unity across the different data sets for steel.

Based on the correlation coefficient factors presented in the table above, it is apparent that the log-normal distribution employed for the fatigue data sets for steel in this study exhibited correlations close to unity, indicating a strong correlation in the fatigue life distribution. However, the steel specimens soaked for five months displayed the lowest correlation among them, suggesting potential variations in the fatigue properties revealed by this particular data set, which will be further investigated.

It is also possible that the results obtained after charging the specimens for 9 months do not align with the trends observed in other charging durations. During the extended charging period, the material may have become saturated with hydrogen, leading to minimal net migration of hydrogen atoms leading to a reduction in the decohesion mechanism of HE. Once hydrogen migration ceases, the risk of further embrittlement is minimized, as no more hydrogen atoms move to critical stress regions to influence the stress distribution and cause cracks can initiate. Furthermore, for hydrogen that has already diffused into specific regions (e.g., grain boundaries or dislocations), further movement is halted, which may prevent additional degradation, depending on the initial amount of hydrogen absorbed.

6.2.2 The size of the scatter bands of steel data sets at a 95% probability of survival

Parabolic scatter bands in the life field are not employed in practical design, as detailed in the post-processing chapter [2,3,16–18]. These parabolic scatter bands are transformed into parallel scatter bands (τ_σ) in the stress field by considering the perpendicular bisectors at the mean point of the curves. By so doing the scatter factors (K_D) are generated for all the approaches considered in this research. Figure 6-2 illustrates the parallel scatter bands constructed using this approach for steel, which is highly applicable in design. The sizes of these scatter bands are calculated using these scatter factors from the various approaches, based on a 95% probability of survival at 95% confidence.

The next question to address is the proportional change in the scatter bands for the various steel data sets. This change is contingent on the considered probability of survival. The main deterministic factor influencing this change in the scatter band is the spread in the

fatigue data sets. The spread changes as a result of variations in the material properties, even within the same alloy or grade, which can lead to differences in fatigue behaviour. Inconsistencies in manufacturing processes, composition, or microstructure also contribute to increased spreads. The condition of the specimen's surface, including imperfections, roughness, or irregularities, can affect fatigue life and can be manifested in the spread of the data. Other factors like geometry, environmental factors, testing conditions and microstructural variations could also show up in the spread of fatigue data.

Figure 6-3 illustrates the alterations in each of the scatter bands employed for different groups of the steel specimens. These scatter bands either maintain the same size or change in the same proportion for all the fatigue data generated from steel specimens. The scatter band generated using the ASTM approach is always more conservative, while the IIW approach is the least conservative of the approaches considered in this PhD research.

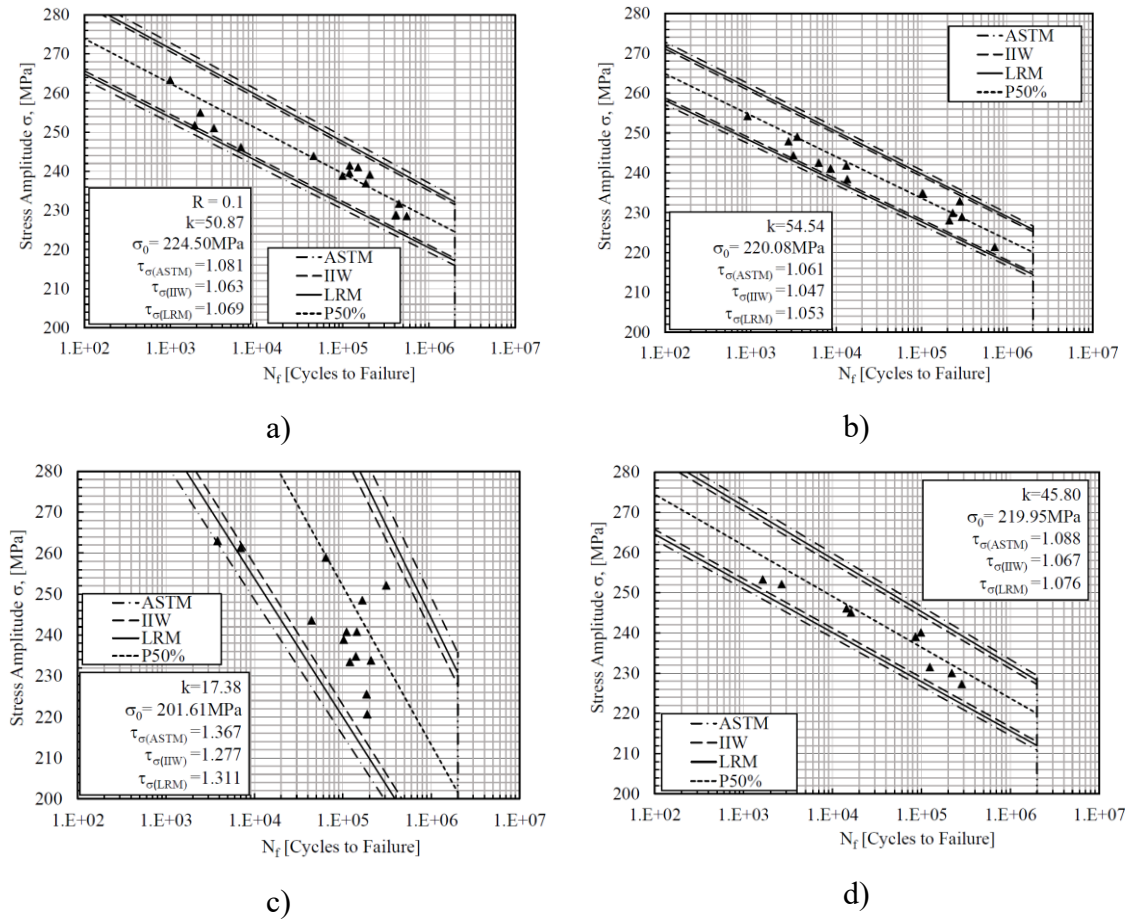

Figure 6-2 Parallel scatter bands (τ_σ) used for design purposes at a 95% probability of survival for steel a) plain uncharged, b) plain hydrogen-charged for 3 months c) plain hydrogen-charged for 5 months and d) plain hydrogen-charged for 9 months

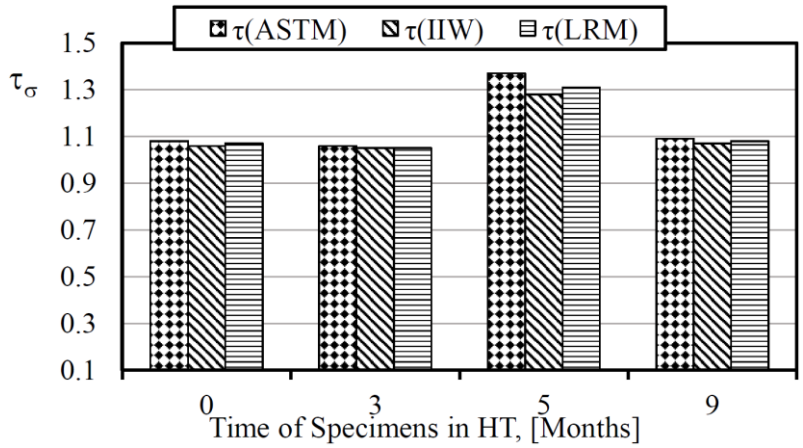

Figure 6-3 Change in the size of scatter bands using the ASTM, IIW and LRM approaches at a 95% confidence and 95% probability of survival

Specifically, there is a noticeable increase in the sizes of the scatter bands for the charged steel specimen left for five months in the pressured hydrogen tubes (HT) as compared to the scatters for the other groups of specimens. This suggests that there is a substantial impact on the fatigue properties. However, the size of the scatter band for these specimens still does not exceed the size of 3 for example, a case of unreasonable spread in the fatigue data. An obvious question is what has contributed to the increased scatter band of the data set from five months of hydrogen soaking. Before delving into this, it will be necessary to examine the other fatigue properties of steel as shown by all the data.

6.2.3 The change in the inverse slope of specimens from steel

The inverse slope for most metals falls in the range of 20 to 8 [7,19], although these values can vary depending on the specific steel alloy, heat treatment, and other factors. From Table 6-1, the data set from specimens cured for five months is observed to have the smallest inverse slope ($k = 17.38$). It falls within the range of the inverse slope in the literature. The mean curve produced by these specimens is steeper compared to the other datasets, indicating a significant reduction in the fatigue resistance of the material specimens [20]. The reduction in the fatigue strength is because of an increase in the defecting size [21,22] or discontinuities in the material, presumed to enhance hydrogen embrittlement. However, the inverse slopes generated by the other data sets are observed to be notably higher than expected. This is summarised in Figure 6-4.

The specimens used in this investigation are ex-service steel specimens and it remains to be confirmed the mechanical properties of these specimens compared with other conventional materials. The extent of degradation over its use is a contributory factor, in particular the environment where the material was used. Moreover, the size effect, often

observed in smaller specimens where the stress distribution and other factors may differ from larger counterparts [23], could be a factor influencing these values.

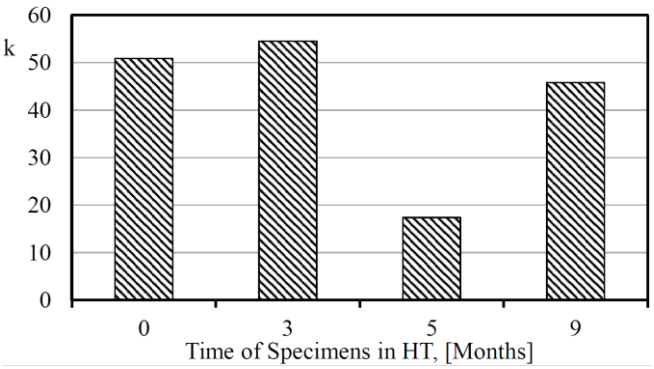

Figure 6-4 The trend in the inverse slope of steel specimens with time in HT

6.2.4 Change in the spread of steel specimens

The spread in fatigue data denotes the variability observed in a set of fatigue test results for a specific material subjected to cyclic loading. As has been mentioned, this variability can stem from factors such as material composition, manufacturing processes, heat treatment, and other variables, leading to differences in fatigue properties among specimens. Additionally, the spread in fatigue data may also highlight the influence of factors like surface finish, notch sensitivity, material defects, and environmental conditions on a material's fatigue behaviour. As seen from Table 6-1 the fatigue life spread lies in the range 0.06 – 0.14 as shown also in Figure 6-5. The specific value of the spread always depends on the material properties, and it is calculated based on the differences between individual data points and the mean of the data set. The properties influencing this spread vary from specimen to specimen and cannot be determined a priori. Subsequently, the values shown in the figure below will be compared with values from the literature, in the hope that they are similar. However, from the results, the spread from specimens soaked for five months is the largest as compared to the other data sets. This can be attributed to the inherent properties of the material, changes due to degradation during use, and the influence of hydrogen introduced during the research. This increased spread could have arisen due to unaccounted differences in material inhomogeneity, testing conditions including specimen preparation, loading conditions, and environmental factors which further contribute to this variability [1,24,25]. As fatigue analysis is a statistical phenomenon, even minor fluctuations in material properties or testing conditions can result in substantial differences in fatigue life.

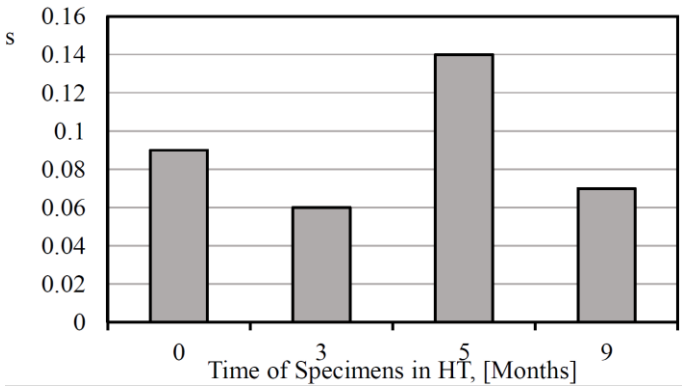

Figure 6-5 The trend in the scatter of steel specimens

6.2.5 Change in the intercept of data sets from steel

Similarly, the vertical intercept C_0 shows the fatigue strength of steel. This value is often about one-quarter of the first fatigue life in the stress-life curve of a material [7,19]. According to Table 6-1, the values of the intercept increase as the specimen's time in hydrogen increases. Accordingly, the fatigue strength demonstrated by these data sets also shows that the fatigue strength for steel was reduced as the specimens stayed longer in the pressured hydrogen tubes. This change in the intercept is summarised in the Figure 6-6 below.

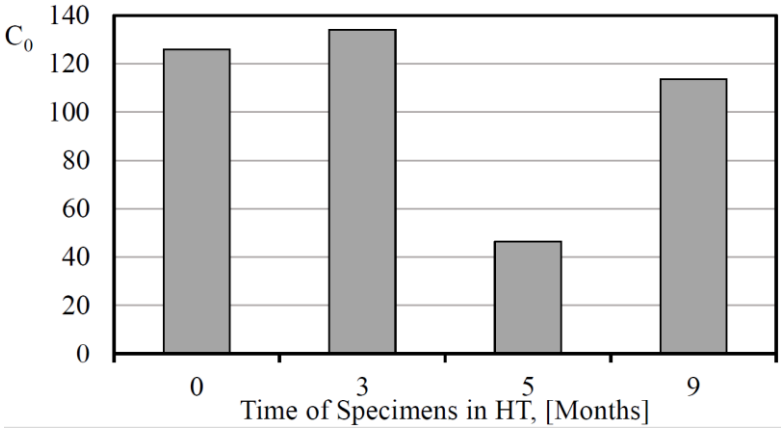

Figure 6-6 Change in the intercept for steel specimens with time in the HT

The results show that the S-N curve was flexing about an arbitrary mean point for all the data sets as the charging time in hydrogen increased. The greatest change in these quantities was noticed with specimens charged for five months. Again, the characteristics of the specimens charged for five moments are continuously different from the other data sets.

6.2.6 Change the endurance limit for steel

Recall also that the endurance limits of most steels are between 35% to 50% of the tensile strength of the material [7,19]. In this PhD research, the endurance limit was estimated at

2 million cycles for analysis purposes. For steel specimens, the endurance limit was seen to reduce as the specimens were soaked in hydrogen for prolonged periods. This is illustrated in Figure 6-7 below.

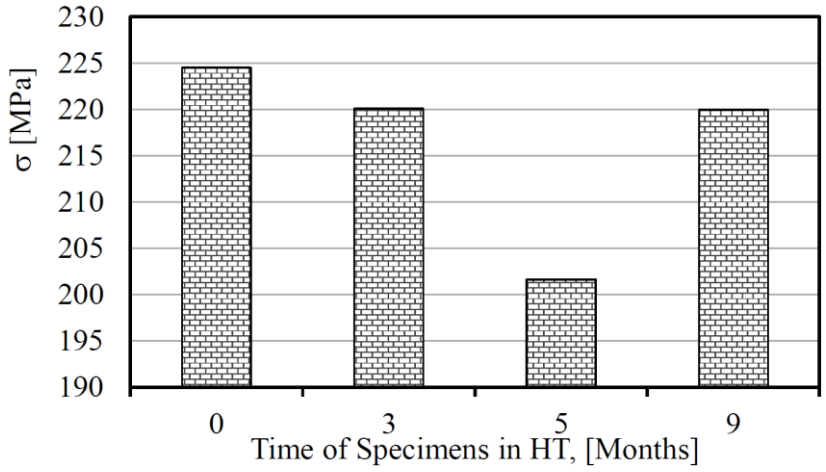

Figure 6-7 The trends in the endurance limit as time in HT increases

The values of the endurance limit only differ by 2%, except for specimens that were soaked in HT for five months. Even after this period, the difference in the endurance limit from unsoaked specimens was only 10%. This discrepancy still falls within the range considered reasonable for changes in the endurance limits of metals. Similar to other fatigue properties of metals, the endurance limit is influenced by a multitude of factors related to the material's composition, processing, and testing conditions. The composition and heat treatment processes also affect the endurance limit, along with the microstructure of the metal. Surface conditions, environmental factors, and size effects all contribute to the variability in the endurance limit. In this case, in particular, the degradation of steel after use was the most considerable factor.

Figures 6-1 to 6-7 clearly illustrate the impact of hydrogen on the fatigue properties, such as the endurance limit, which decreases as the charging time increases. Prolonged charging allows more hydrogen atoms to diffuse into the metal as shown using Sievert's equation. As hydrogen penetrates the steel material, it accumulates at locations like grain boundaries, dislocations, and microstructural defects. This increased hydrogen concentration aggravates embrittlement effects, making the pipeline steel material more brittle and prone to cracking under stress. The formation of hydrogen-induced cracks is facilitated as hydrogen accumulates at stress concentrators (discontinuities), which promotes crack initiation. With increased charging time, these cracks propagate more easily, leading to hydrogen-induced cracking. From zero to five months, the reduction in the endurance limit is highly noticeable. By nine months, however, the decrease is less pronounced, possibly

due to hydrogen saturation in the metal or slower material degradation in comparison to other specimens. Despite this, the endurance limit is still lower than that of uncharged specimens. This may also be influenced by increased variability in the fatigue data due to the heterogeneity of discontinuities in each material specimen. However, the variability in the endurance limit remains within the same scatter band when compared to uncharged specimens. Overall, a decreasing trend in the endurance limit is observed, with greater variability in the data as charging time increases.

6.2.7 Fatigue properties of ex-service steel from literature

To assess how these properties compare with literature data, Table 6-2 present selected fatigue properties of ex-service X52 steel obtained from various sources. The table includes the approximate number of years the steel pipe was in use, after which the specimens were produced. Specifically, the endurance limits have been normalized using the ultimate tensile stress (fatigue ratio) for each specimen and reported in the last column of the table. The fatigue properties of these materials also depend on other factors such as material properties, application, time in use, and testing conditions. These factors could not be easily quantified for verification and comparison purposes.

The differences in the summarized fatigue properties presented in Table 6-2 can be attributed to a variety of factors influencing the S-N curves. These variations may stem from inherent material heterogeneity, including differences in chemical composition, microstructure, and grain size. Additionally, surface finish irregularities and variations in heat treatment processes also contribute to this variation in fatigue properties. Notch sensitivity, as seen in the example in Ref [10] (though nominal stresses were used), along with the impact of surface defects, environmental conditions, and the frequency of testing further accounts for the variability in the summarised data. The methodology employed in testing, such as specimen geometry size factors and loading conditions, as well as statistical fluctuations, may also have contributed to the observed differences. The level of degradation in the various specimens could also account for this variability as steel pipelines degrade in the course of usage over the years. The rate at which degradation takes effect is also dependent on many other factors. Thus, it was not expected to observe fatigue properties that would be the same, although it is expected that they should all agree to some extent.

Table 6-2 Normalised endurance limit and fatigue properties of ex-service X52 pipeline steel literature in comparison to measured fatigue properties in this research

Source	Material type	Years in use	Net area (mm^2)	σ_{UTS} [MPa]	k	R	σ_0 [MPa]	$\sigma_{0,50\%}/\sigma_{UTS}$
[14]	X52-S1	14	625	534	13.50	0.10	299.9	0.56
[14]	X52-S2	21	625	544	12.23	0.10	252.5	0.46
[26]	X52 pipe (surface finish)	New	412	540	8.11	0.10	367.4	0.68
[26]	X52 pipe (W. surface finish)	-	412	540	5.49	0.10	262.4	0.49
[27]	X52 Pipeline	Ex-service	200	616	43.80	0.50	249.2	0.40
[10]	API X52 (notched)	Ex-service (air)	-	528	43.75	0.50	249.1	0.47
[10]	API X52 (notched)	Ex-service (hydrogen)	-	570	78.50	0.50	252.1	0.44
S_0m	Uncharged X52	Ex-service	9.51	501	50.87	0.10	224.5	0.45

The inverse slope in particular was high as compared to fatigue data sets from the literature. However, the value obtained is not too significant compared to the values from Refs. [27] and [10]. From the normalized endurance limits, it can be inferred that the specimens used in this research align well with those reported in the literature. The values obtained are closely comparable, focusing only on the properties of the uncharged steel specimens and comparing them with those in the references cited.

6.2.8 Statistical significance of fatigue properties in steel

Using the data sets detailed in experiments and the raw data chapter for steel, the characteristic significance test values calculated using the approach described in the chapter for significance tests, are summarised in Table 6-3. Each data set, obtained from the soaking time, underwent statistical significance testing with uncharged specimens. The parameters considered for determining statistical significance at a 95% confidence level included variance, inverse slope, and vertical intercept. This was accomplished through the application of a composite hypothesis test. From the results summarised in this table, it is

Table 6-3 Summary of significance steel specimens for the various soaking times for a confidence level of 95%

Compared data sets	$\sigma_{0,unch.}$ $\sigma_{0,xm}$ [MPa]	% $\Delta\sigma_0$	Variance test ($\beta = 1.7\%$)	Slope test ($\beta = 1.7\%$)	Intercept test ($\beta = 1.7\%$)	Conclusion ($\sum \beta \cong 5\%$)
S_uncharged and S_3m	224.5 220.1	-2	-1.80	-11.34	0.32	**Significant**
S_uncharged and S_5m	224.5 201.6	-10	-1.55	18.54	-0.05	**Significant**
S_uncharged and S_9m	224.5 219.9	-2	-3.83	-13.55	-0.05	**Insignificant**

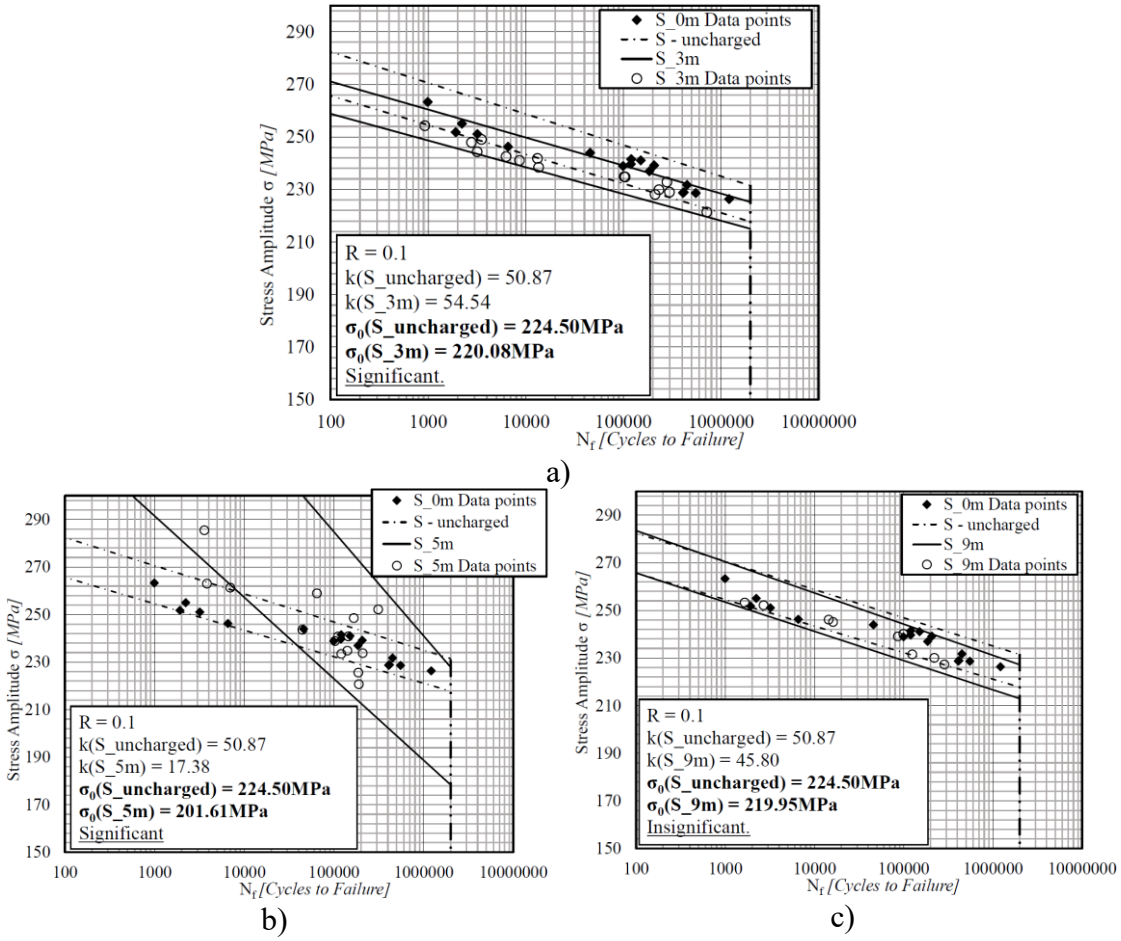

Figure 6-8 Significance S-N curves for steel, a) scatter bands and significance for uncharged and charged for 3 months, b) scatter bands and significance for uncharged and 5 months charged and c) scatter bands and significance for uncharged and 9 months charged

observed that the steel specimens soaked for three months fall the null hypothesis for the intercept and are therefore significant with the uncharged specimens. Similarly, specimens soaked for five months fail the null hypothesis for inverse slope and are statistically significant from the uncharged specimens. It is then concluded that the two data sets (three

and five months soaked) do not have the same characteristics as the uncharged specimens at a 95% level of significance. However, the specimens soaked for nine months produce mean curves with parameters that are statistically insignificant from uncharged specimens at a 95% level of significance.

The graph in Figure 6-8 illustrates the overlapping scatter bands obtained from the datasets used in the significance test for steel specimens. The comparison between uncharged specimens and specimens soaked for three months reveals a significant alteration in fatigue properties resulting from hydrogen soaking. This conclusion is drawn based on the non-collinearity of the intercepts of the mean curves estimated from these data sets. Specifically, the test statistic for the fatigue strength coefficient (the intercept) is found to be statistically significant across the entirety of the stress-life region. However, when focusing the analysis in and around the mean stress amplitude considered during testing, without extrapolating to stress levels significantly different from this point, the retained test statistic is less than the critical value (by -27.54). Consequently, the test fails to reject the null hypothesis, indicating an insignificant difference in this case. It can then be concluded that under this consideration, charging steel specimens for 3 months is statistically insignificant if they are tested around the mean stress amplitude, and the endurance limit is reduced by just 2%.

When considering steel specimens subjected to a hydrogen environment for 5 months, a dataset was generated with an inverse slope value of 17.38 (indicating a fatigue strength exponent within the expected range for metals), a statistically significant contrast to the value of 50.87 is observed for uncharged specimens. The observed change in the endurance limit is approximately 10%. While a 10% shift in the endurance limit remains within the acceptable range for metals (35% to 50% of the tensile strength), the variance and inverse slope of this data set show statistical significance when compared to uncharged steel specimens. This implies that, at a 95% significance level, there is evidence suggesting a notable difference in variance and inverse slopes between the two fatigue curves. A more in-depth discussion of these results will be explored in the next chapter.

Additionally, when examining specimens soaked in hydrogen for approximately nine months, the resulting curves exhibit high values of the inverse slope, comparable to the inverse slope observed in unsoaked specimens. However, the test statistic values for both variances and inverse slopes reveal that there is not enough evidence at the 95% significance level to claim a significant difference between the two datasets.

Putting together all these data sets from steel into a unified graph is presented in Figure 6-9. This figure was generated using a very conservative probability of survival of 99.9%. It is noted that only a few data points align close to the boundary of the scatter band, all of which belong to the batch of specimens soaked for 5 months. The data points from this soaking period did not exhibit a clear pattern and did not offer any meaningful insights into the fatigue properties from an engineering perspective. This data set can be cleaned by ignoring all anomalies from the data set. To determine the anomalies, this is achieved by excluding all the data points that exceed about 3 standard deviations from the mean point, it becomes evident that these points fall entirely within the scatter band generated with such a high probability of survival (99.9%).

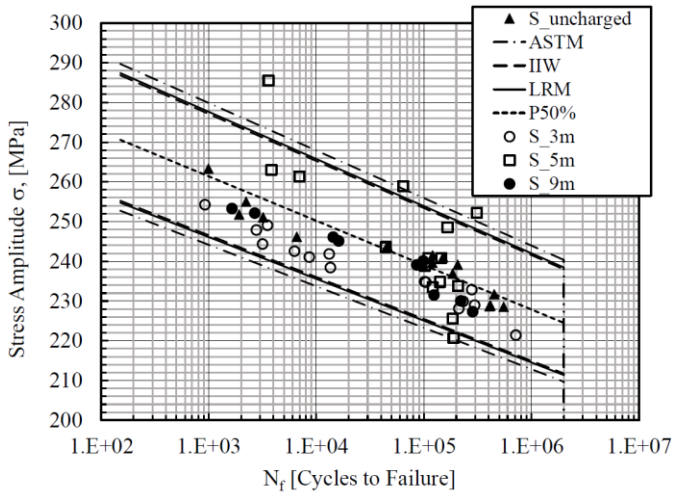

Figure 6-9 Superposed steel data sets into 99.9% probability scatter band of survival of uncharged specimens.

If the design curve for these steel datasets considers other correcting factors for surface finish, loading, environment, size, temperature, and surface treatments, it would effectively encompass all data points. Consequently, a single design curve, incorporating a safety factor, becomes suitable for designing with this data. Thus, it can be concluded that with an existing design probability of survival of 99.9% and an appropriate safety factor, such a design would be capable of safely handling natural gas blended with hydrogen as considered in this study. Although there is a noticeable change in the fatigue properties of X52 steel used in the distribution network, the new fatigue properties of this material used in transporting the blended natural gas would still fall within the current design curves of the pipeline in the existing network.

.

6.3 Fatigue characterization of welded steel

Existing literature has also demonstrated a decrease in both the mechanical and electrochemical properties of steel pipes after they have been in use [1,2]. In line with this degradation, as outlined in Ref.[26], fatigue performance for X52 welded joint specimens, with or without surface finish, showed that both the pipe bodies and the welded joints of the high-frequency electric resistance welding (X52 HF-ERW) pipes maintained an excellent balance of strength and impact toughness. Notably, the cyclic strength of the welded joints experienced a more significant reduction compared to the pipe bodies, and the fatigue resistance was notably influenced by the presence of surface defects. The welded steel specimen used in this research was obtained from ex-service X52 low carbon steel [15] and it would be expected that this material would behave like those reported in the literature, albeit to what extent.

For this research, the specimens available for welded steel consisted of sixteen uncharged plain specimens. For the hydrogen-charged specimens, ten were cured for three months, while nine were cured for nine months. Similarly, the raw data generated from testing these welded steel specimens is reported in the experimental setup and raw data chapter of this research. All tests were performed under the same conditions as the steel specimens.

6.3.1 The mean curve and parabolic scatter bands for welded steel

Using the post-processing approaches described in the methodology chapter produced mean S-N curves at a confidence level of 95% and 95% probability of survival. The diagram in Figure 6-10 summarizes the mean curves and parabolic scatter bands generated by testing welded steel hydrogen-soaked specimens for three and nine months, and uncharged specimens. The procedure to extract welded specimens from welded pipes has been described in the experimental chapter (see Figure 4-2). These scatter bands were also constructed using the standardized approaches with the ASTM approach being the most conservative. Similar to the steel specimens, the mean points ($\overline{log\sigma_i}, \overline{logN_{f,i}}$) of the S-N curves for welded steel do not align, despite a minimal percentage difference in the direction of life, and hence will also not be considered as a reference point for comparing the curves.

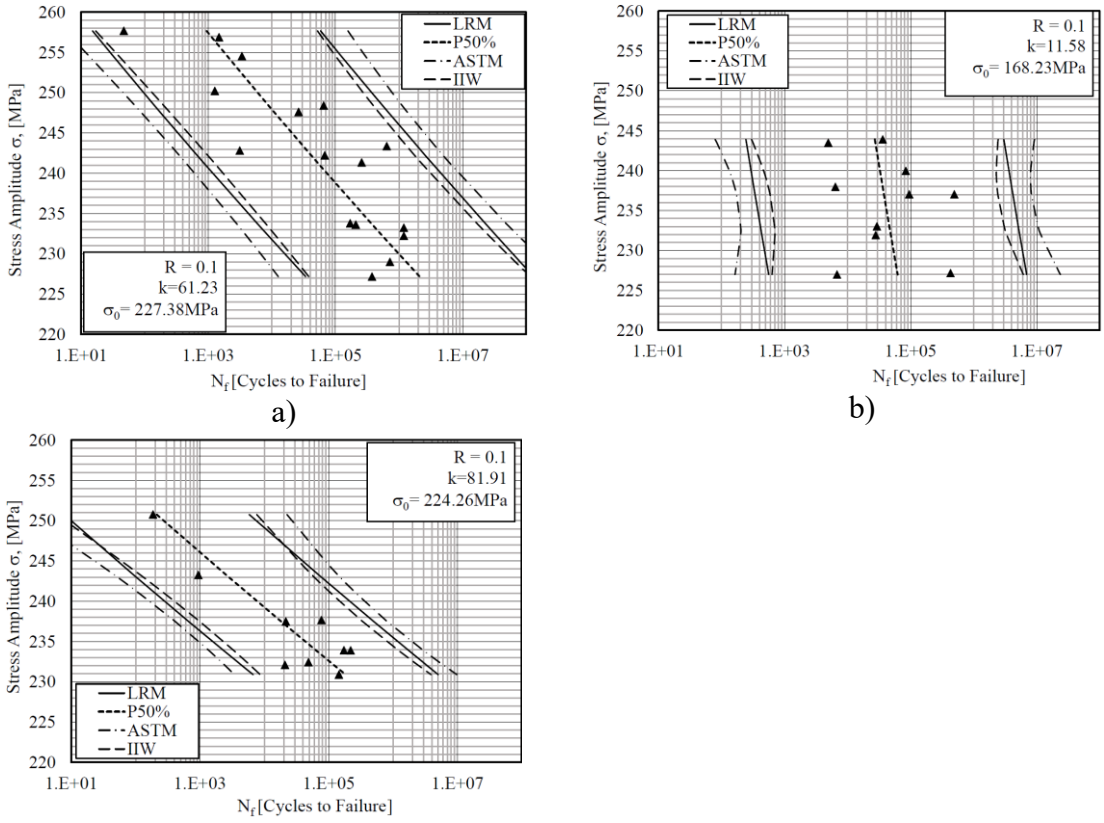

Figure 6-10 Mean S-N curves and parabolic scatter bands of welded steel fatigue data sets a) plain uncharged, b) plain hydrogen-charged for 3 months and c) plain hydrogen charged for 9 months.

The fatigue properties generated from testing welded steel specimens are summarized in Table 6-4. This includes the values for the number of specimens and the stress ratio at which the fatigue tests were carried out. The values of the vertical intercept C_0 are also included, the endurance limit, spread, inverse slope, and the various sizes of the scatter bands generated using the standardised approaches considered in this research. The correlation coefficients have also been generated from these data sets. The scatter bands from specimens soaked for 3 months are observed to be the largest revealing a higher variability in the conditions accountable for the fatigue properties of welded steel. Moreover, the correlation coefficients for the data sets obtained from welded steel specimens were generally high, indicating strong correlations, except for the data set from specimens soaked for three months. Interestingly, the data points from this soaking period did not exhibit a clear pattern and did not offer any meaningful insights into the fatigue properties from an engineering perspective.

Table 6-4 Summary of fatigue properties of welded steel ($R = 0.1$) frequency of 10Hz

Specimen ID	Fatigue results									
	n	s	k	R	C_o	r	σ_0 [MPa)]	τ_σ (ASTM)	τ_σ (IIW)	τ_σ (LRM)
WS_uncharged	16	0.74	61.23	0.1	150.61	0.84	227.4	1.17	1.13	1.14
WS_3m	10	0.75	11.58	0.1	32.09	0.18	168.2	2.53	2.05	2.26
WS_9m	9	0.51	81.91	0.1	198.86	0.89	224.3	1.10	1.07	1.08

6.3.2 Size of the scatter band for welded steel

Using the same approach adopted for the steel specimens above, the parallel design curves generated from the parabolic curves above are summarized in Figure 6-11. These scatter bands were generated with a 95% probability of survival and are affected similarly as the data traverses through the soaking durations. The largest scatter band is observed after the hydrogen-charged specimens have been soaked in hydrogen for three months, and it is the smallest when they have been soaked in hydrogen for nine months. This variation could be attributed to factors such as the heterogeneity of material properties, different levels of hydrogen absorption, or varying degrees of microstructural changes during the manufacture and curing process. However, assuming that none of these factors contributed to the fatigue properties besides hydrogen charging, it can be concluded that the specimens most impacted in terms of the fatigue properties in this investigation were those soaked in hydrogen for three months. The trend in the scatter band is illustrated in Figure 6-12.

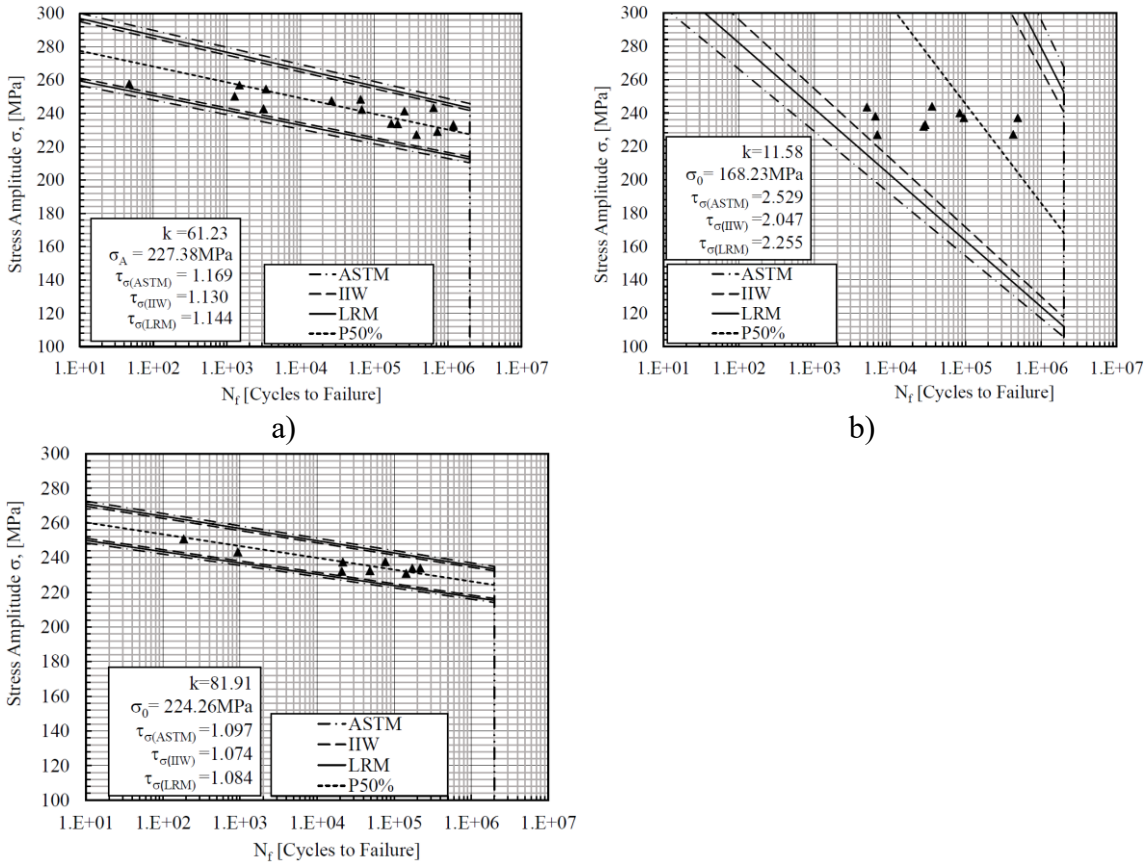

Figure 6-11 Parallel scatter bands (τ_σ) used for design purposes at a 95% probability of survival for welded steel a) plain uncharged, b) plain hydrogen-charged for 3 months c) plain hydrogen-charged for 9 months

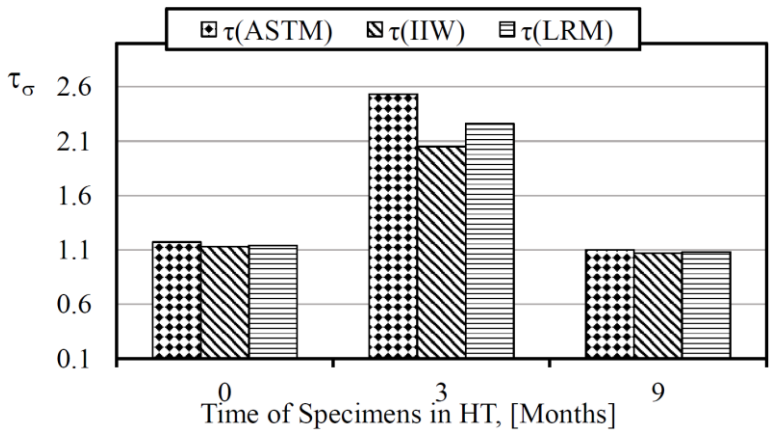

Figure 6-12 The trends in scatter bands of welded steel at 95% probability of survival

While the scatter bands for specimens soaked for three months exhibited the largest dispersion, these scatter bands did not change in the same order of magnitude. Upon closer examination of the results obtained during the testing of specimens WS_3m_4 and WS_3m_6, flawed crack surfaces were observed, visible to the naked eye. These are

discontinuities (see Figure 6-13) in the specimens that cannot be ignored due to their easily traceable nature.

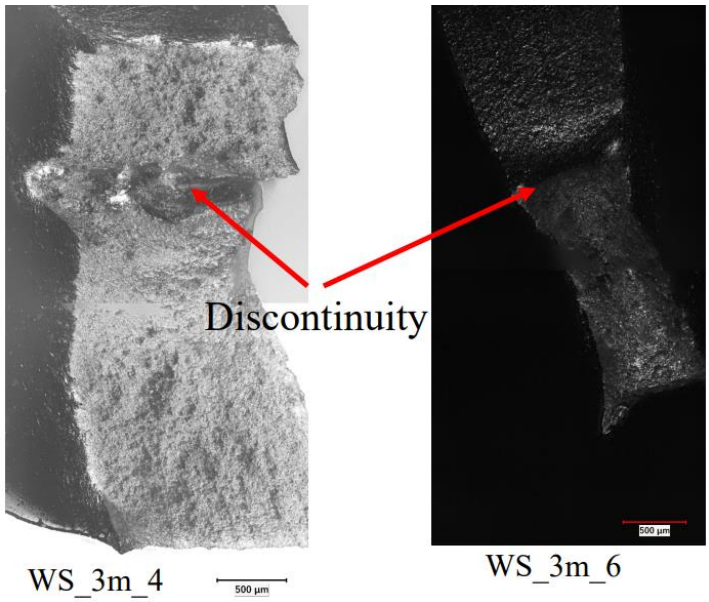

Figure 6-13 Discontinuity at the crack surfaces of welded steel specimens

Disregarding the contribution of this pair of data from the dataset results in new estimates for the parameters of the mean curve: the variance reduces to 0.65, the intercept to 54.50, and the endurance limit adjusts to 200.33 MPa. The scatter bands adjust accordingly and converge to similar values, as seen in the other datasets from both charged and uncharged welded steel specimens. The new trend in the data set is shown in Figure 6-14

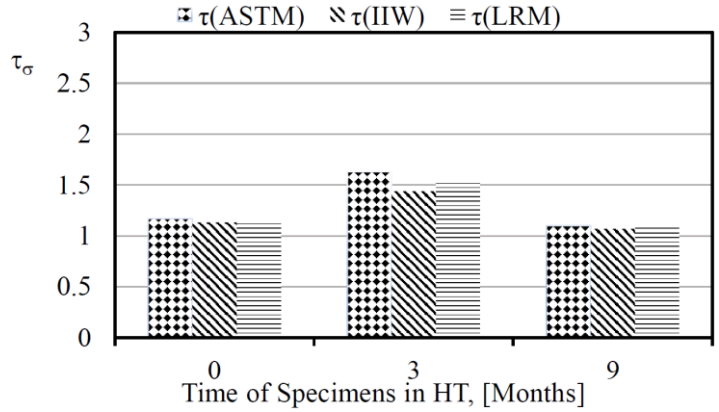

Figure 6-14 The trends in scatter bands of welded steel at 95% probability of survival with edited data

Nevertheless, the specimens soaked for three months still exhibit the most adversely affected fatigue properties due to hydrogen charging.

6.3.3 Change in the inverse slope of welded steel

Similar to the case of steel and Eurocode recommendation, the inverse slope for welded steel falls in the range of 20 to 3 [28,29]. These values also depend on a priori knowledge, application and the other factors that determine the fatigue property of the material. A value of 3 is recommended by the IIW and Eurocode 3 [29–34] for analysis and design purposes. The values of the inverse slopes generated from welded steel in this PhD research were 61.23 when uncharged to about 11.58 when soaked for three months but increased to 81.91 when cured for nine months. These are high values as compared to the recommendations cited herein. The recommended values for the inverse slope are typically intended for design purposes, prioritizing safe design practices by over-conservatively evaluating experimental results [22]. However, the values generated in this context are specifically for research and development. It's essential to note that the material under investigation was X52 ex-service welded steel, which introduces various material, environmental, and loading factors that the researcher might not have initially identified or accounted for. The slopes of all the curves were observed to be greater than m = 3, and if the data set were analysed with a fixed slope of 3, it would result in fatigue strength values at two million cycles that are relatively lower and in line with Ref. [34].

In particular, it was observed that there was a significant reduction in fatigue resistance when welded steel specimens were soaked for three months compared to nine months. The inverse slopes of 61.23 and 81.91 depict a gradual decrease in the fatigue resistance of these specimens, resulting in a longer fatigue life. This suggests that the rate at which this fatigue resistance changes impacts the fatigue properties. The inverse slope for specimens soaked for three months was consistent with the values recommended for welded joints. Considering that the fatigue strength of welded joints is typically influenced by local and global stress concentrators, welding residual stresses, weld defects, and flaws, this study also highlighted that these factors provided pathways for hydrogen embrittlement due to hydrogen charging. The trend in the change of the inverse slope with hydrogen soaking time is illustrated in the Figure 6-15 below.

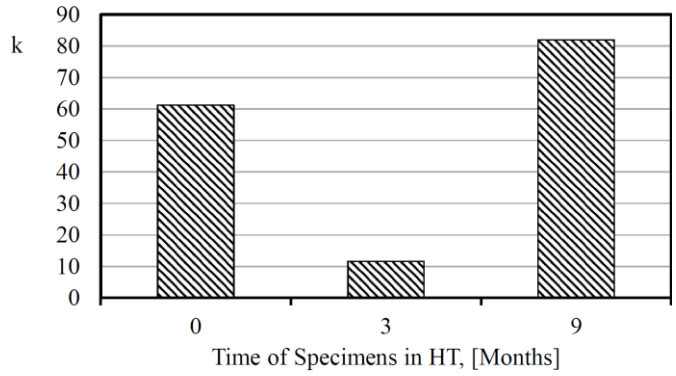

Figure 6-15 The trends in inverse slope for welded steel specimens

6.3.4 Change in spread welded steel data

The spread in fatigue date of welded joints is typically influenced by local and global stress concentrators, welding residual stresses, weld defects and flaws [28,29,31–33]. The change in the spread of fatigue data for welded steel was large as compared to the data cited herein. While this also depends on the welding process, the larger the scatter the more the variation in magnitude of these deterministic factors. Figure 6-16 shows the trend in the data for welded steel that was generated in the PhD research.

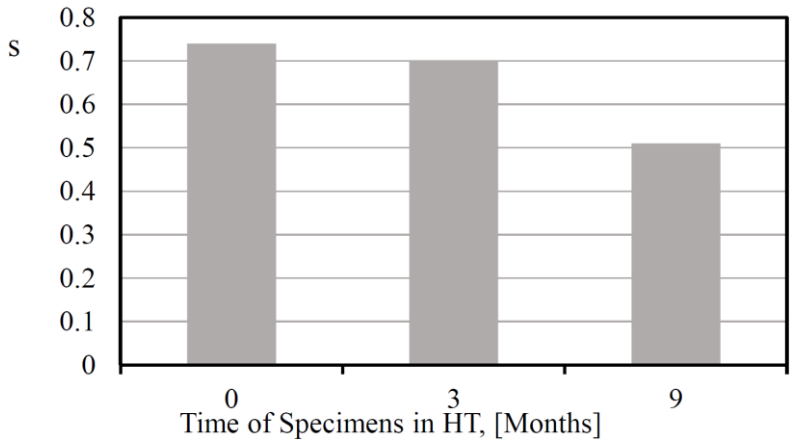

Figure 6-16 The trend in the spread of welded steel

6.3.5 Change in the intercept of welded steel

According to the fatigue properties summarised in Table 6-4 for welded steel, the approximate fatigue strength coefficient after about a quarter of a cycle changes as the soaking time of the specimens increase [7,19]. If a fixed inverse slope of 3 was fixed to these data sets, a different value of the intercept constant will be observed [35]. Using the properties as revealed by the fatigue data in this research produced intercepts as summarised in Figure below for the different lengths the specimens were soaked in hydrogen.

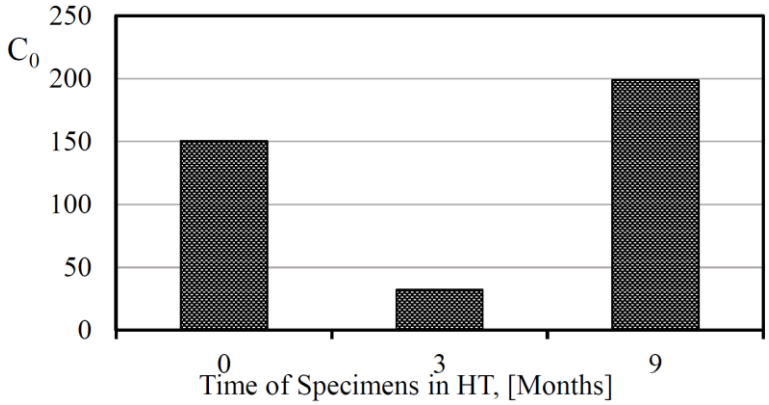

Figure 6-17 The trend in fatigue strength coefficient of welded steel

6.3.6 Endurance limit of welded steel

The endurance limit of a welded joint is dependent on the intrusion size and other factors that prevent crack propagation within the applied stress range. If the intrusion size is not appropriately considered, it may result in underestimating or overestimating the fatigue strength of the welded joint. Therefore, it is crucial to carefully account for intrusion size variations in fatigue data analysis to ensure more accurate and reliable predictions of the joint's fatigue performance. The recommendations by the IIW to use an inverse slope of 3 seem to cater for these uncertainties, by predicting much lower values for the endurance limit.

This research used the inverse slope generated from the fatigue data sets of welded steel for analysis purposes and the endurance limit was estimated after 2 million cycles. Figure 6-18 shows how the endurance limit varied for ex-service X52 welded steel specimens that were used in this research.

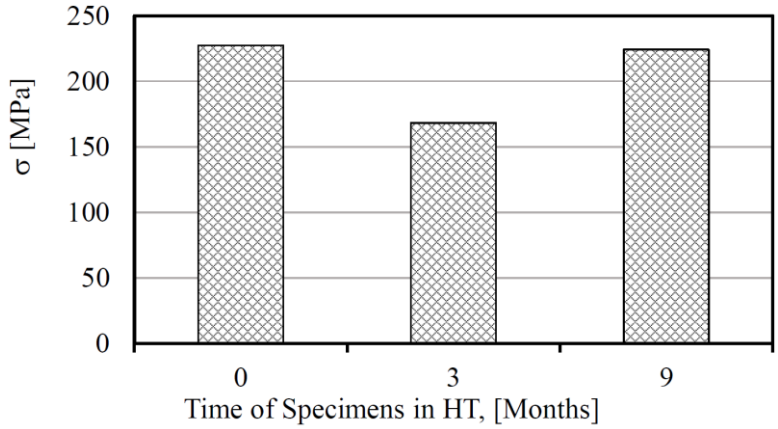

Figure 6-18 The trend in the endurance of welded steel with soaking time

The endurance limits of the unsoaked specimens and those soaked for nine months were similar, differing by just 1%. However, they differed from the specimens soaked for three

months by up to 33%. Nevertheless, upon removing the specimens with obvious discontinuities (WS_3m_4 and WS_3m_6), the difference was reduced to about 11%.

6.3.7 Fatigue Properties of ex-service welded steel from the Literature

The fatigue properties of welded steel are influenced by the alterations in the microstructure of the steel joint during welding [36]. The hardenability or susceptibility to cracking in steel welds is assessed through the carbon equivalent, offering an estimate of the combined influence of essential alloying elements on the microstructure. Furthermore, the thermal cycles and cooling rates during welding play a crucial role in inducing modifications in the microstructure. Some equivalent high-strength steel materials commonly employed in the pipeline industry and similar to X52, are ISO 3183, EN 10208, and DIN 17172, under ICS NO. 75200. Post-weld heat treatment can influence the fatigue properties by modifying the microstructure

Table 6-5 Fatigue properties of X52 welded steel pipeline from the literature in comparison to measured fatigue properties in this research

Source	Weld type	Material type	Years in use	Net area (mm^2)	σ_{UTS} [MPa]	k	R	σ_0 [MPa]	$\sigma_{0,50\%}/\sigma_{UTS}$
[37]		JIS SPV50	-	1000	648	5.08	0.5	186.5	0.29
[26]	Frict. stir	X52 surface fin	New	412	542	6.69	0.1	335.9	0.61
[26]	Frict. stir	X52 no surface fin	New	412	542	5.22	0.1	231.9	0.43
[38]	STT	API 5L X52 (A) (110Hz)	In-service	127.5	580	4.25	0.5	135.5	0.23
[38]	STT	API 5L X52 (A) (1Hz)	In-service	127.5	580	3.43	0.5	118.2	0.20
[39]	-	S355J2G3 (X52)	New	-	460	3.7		108.6	0.23
Present research		X52	Ex-service	9.25	542	61.23	0.1	227.4	0.41

Table 6-5 illustrates certain fatigue properties of X52 welded steel extracted from the literature. Notably, the inverse slope of the uncharged welded steel specimens employed in this study surpasses the values reported in the literature. This discrepancy suggests a more pronounced reduction in fatigue life with increasing stress for the specimens in comparison to the literature data. Several factors could contribute to this variance, including the possible

introduction of hydrogen in this research, the extraction of specimens from ex-service pipes that have experienced variable degradation over years of use, variations in loading conditions, and the impact of size effects. Furthermore, direct comparison of fatigue life at equivalent stress levels like in low, medium, and high-stress regimes is a challenge due to the fatigue life dependent on stress level in materials. This complicates the sensitivity analysis of the dataset when compared to literature data. The presence of specimens with stress concentration features introduces variations in the observed data from the literature, influenced by the notch sensitivity. The influence of mean stress on fatigue properties is noteworthy, and the consideration of frequency during testing (as highlighted in Ref [38]) is crucial in understanding the material's fatigue behaviour. In summary, the normalized fatigue ratio (endurance limit to ultimate tensile strength) in this PhD research aligns reasonably well with literature-generated values, indicating a similarity in the fatigue properties of X52 welded steel between this study and literature data.

6.3.8 Statistical significance of fatigue properties in welded steel

The data summarised in Table 6-6 illustrates the characteristic values of the hypothesis test for welded steel. The results indicate that the fatigue properties of welded steel are not statistically significant when pre-charged with 20% hydrogen by soaking in a hydrogen environment for three months. However, when the specimens are soaked for nine months, the alterations in the fatigue properties become statistically significant even when the change in the endurance limit is just about 1%.

Likewise, by validating the lack of significance in mean stress levels considered during testing, the curves derived from welded steel can be examined for statistical relevance around the mean stress. Initially, specimens charged and cured for 9 months were deemed statistically significant due to the influence of the intercept. However, upon confirming statistical insignificance in the means of the tested stress levels and concentrating solely on the mean stresses, it is observed that the test statistic returns a negative value, indicating that the two data sets are statistically insignificant. Therefore, it is concluded that the data sets from uncharged welded steel specimens and specimens soaked in a hydrogen environment for 9 months lack statistical significance.

Table 6-6 Summary of statistical analysis for the fatigue data sets from uncharged and charged specimens of welded steel cured for 3 months and 9 months, at a confidence level of 95%

Source of data sets compared	$\sigma_{0,unch.}$ $\sigma_{0,xm}$ [MPa]	**%** $\Delta\boldsymbol{\sigma_0}$	**Variance test** ($\boldsymbol{\beta} = \mathbf{1.7\%}$)	**Slope test** ($\boldsymbol{\beta} = \mathbf{1.7\%}$)	**Intercept test** ($\boldsymbol{\beta} = \mathbf{1.7\%}$)	**Conclusion** ($\sum \boldsymbol{\beta} \cong \mathbf{5\%}$)
WS_uncharged and S_3m	227.38 168.23	-26	-3.67	-14.05	-0.19	Insignificant
WS_uncharged and S_9m	227.38 224.26	-1	-3.18	-37.77	0.14	Significant

$\sigma_{0,unch}$* the endurance limit of uncharged specimens

$\sigma_{0,xm}$** the endurance limit of charged specimens cured for x months

To bolster this conclusion, the drop in the endurance limit in this case is only 1%. Figure 6-19 summarises the scatter band generated from the data sets obtained from welded steel specimens. A detailed discussion of these results will be provided in the next chapter.

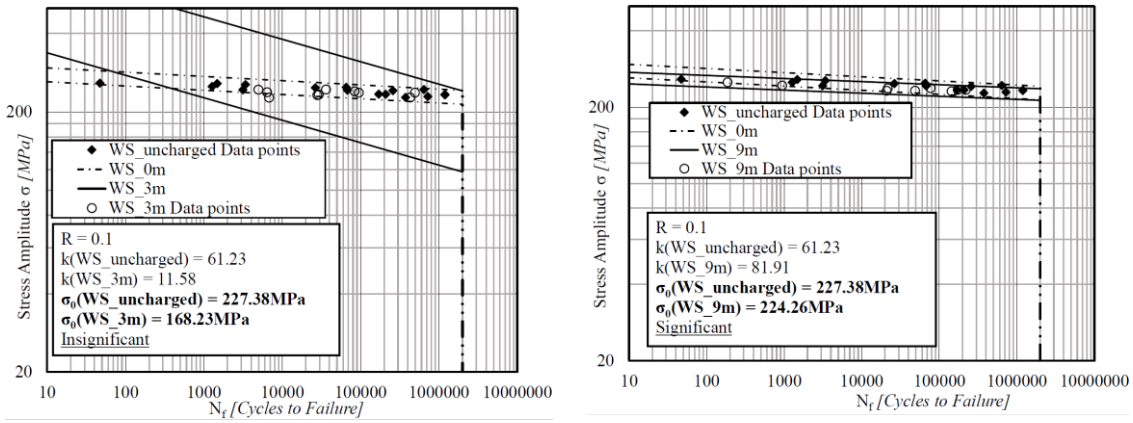

Figure 6-19 Significance S-N curves for welded steel. a) scatter bands and significance for uncharged and charged for 3 months and b) scatter bands and significance for uncharged and charged for 9 months

Having established that certain data sets from welded steel specimens exhibit statistical significance in particular specimens soaked for three months, while specimens charged for nine months show statistical insignificance, the next inquiry is whether these datasets can neatly align within a very conservative scatter band generated at a 99.9% probability and a 95% confidence interval. To address this, a scatter band at a 99.9% probability of survival is created for uncharged specimens, and the data sets from soaked specimens are visually

fitted into this scatter band. If the data points from charged specimens seamlessly integrate into this scatter band, it can be inferred that, from an engineering standpoint, there is no apparent alteration in the fatigue datasets due to hydrogen charging from welded steel. This conclusion should be valid because, when using these data sets for design, as appropriate design factor considerations for surface finish, surface treatment, loading conditions, environment, and temperature are applied to the design curve, along with a further safety factor. The design under such considerations would be safe. The superimposed datasets for welded steel are depicted in Figure 6-20.

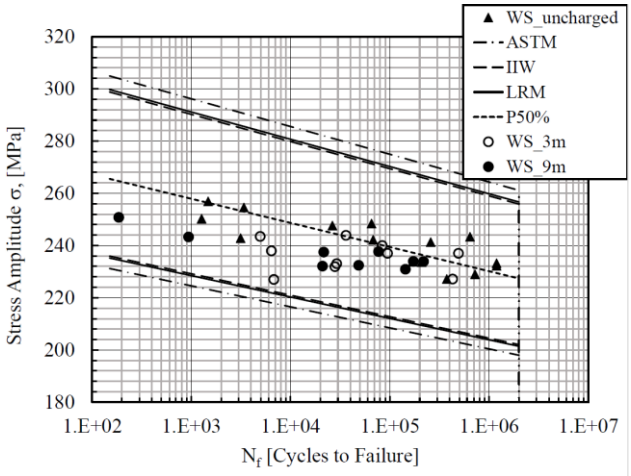

Figure 6-20 Superposed welded steel data sets into 99.9% probability of survival of uncharged specimens.

Based on the graph above, it is evident that all the datasets from welded steel, subjected to hydrogen soaking for various durations, seamlessly align within a single, conservative scatter band derived from unsoaked specimens, generated at a 99.9% probability of survival.

6.4 Fatigue Characterization of GCI

The GCI specimens included in this investigation followed the same protocols as the previous specimens, undergoing hydrogen soaking for both three months and nine months. Overall, fifteen plain specimens were left uncharged and tested, while nine specimens each were hydrogen-charged for three months and nine months. The raw data from these specimens has been reported alongside the other results in the experiments and raw data chapter.

According to Ref [13], GCI pipelines are prone to corrosion and other damaging factors leading to pipe degradation. The degradation of pipes reflects common external damage

experienced by both cast and ductile iron pipelines. In the context of GCI pipelines, this damage might be less apparent due to a phenomenon known as "graphitization." This term describes the network of graphite flakes that remain within an iron pipe after corrosion-induced leaching [40]. The GCI used in this research was ex-service GCI (spun cast) [15] which would have experienced similar degrees of degradation. Similarly, this research was setting off to examine the fatigue properties of the ex-service GCI due to hydrogen exposure in natural gas. Cast iron is a brittle material and is known to fracture without significant deformation (strain) when subjected to stress. Due to this brittleness of the material, there was no observable narrowing (necking) of the fatigue-failed specimens. The observations of the fracture surface accurately reflected the dimensions of the specimens before testing as seen with pictures of the fracture surfaces (see experiment and results chapter).

6.4.1 The mean curve and parabolic scatter band for GCI

The fatigue strength of GCI is observed to be influenced by various factors and properties, predominantly associated with its microstructure. These factors encompass the shape, size, and distribution of graphite, along with the microstructural properties of the matrix, whether it is ferritic or ferritic perlite. Additionally, the distribution of defects such as cavities, porosities, and inclusions play a significant role in the fatigue strength of GCI [15,41–43]. This was characteristic of the GCI used in this research. The fatigue properties summarised in Table 6-7 show the fatigue properties of GCI that were used in this PhD research by plain testing GCI specimens, some of which are hydrogen-charged at a pressure of 8-10 bars for three and nine months. It also contains the design scatter bands generated at a 95% probability of survival using the standardized approaches considered in this research. There were fifteen uncharged plain specimens, while nine specimens were each hydrogen soaked for three and nine months.

Table 6-7 Summary of fatigue properties of welded steel ($R = 0.1$) frequency of 10Hz

Specimen ID	Fatigue results									
	n	s	k	R	C_o	r	σ_0 [MPa)]	τ_σ (ASTM)	τ_σ (IIW)	τ_σ (LRM)
CI_uncharged	15	0.36	8.9	0.1	19.81	0.85	32.7	1.76	1.56	1.64
CI_3m	9	0.35	9.56	0.1	21.18	0.84	36.0	1.73	1.49	1.61
CI_9m	9	0.26	17.19	0.1	34.32	0.96	42.7	1.25	1.18	1.22

The correlation coefficients obtained from the data sets of cast iron specimens were above 0.84, close to unity and indicate a strong correlation between the assumed distribution of fatigue life and the stress levels tested for this material. The graphical representation of scatter band and fatigue properties generated using the various approaches in this research are summarized in Figure 6-21. The graphs were plotted in a semi-log scale to illustrate all the stress amplitudes. What follows is a description of how these fatigue properties changed as the soaking time in hydrogen increased.

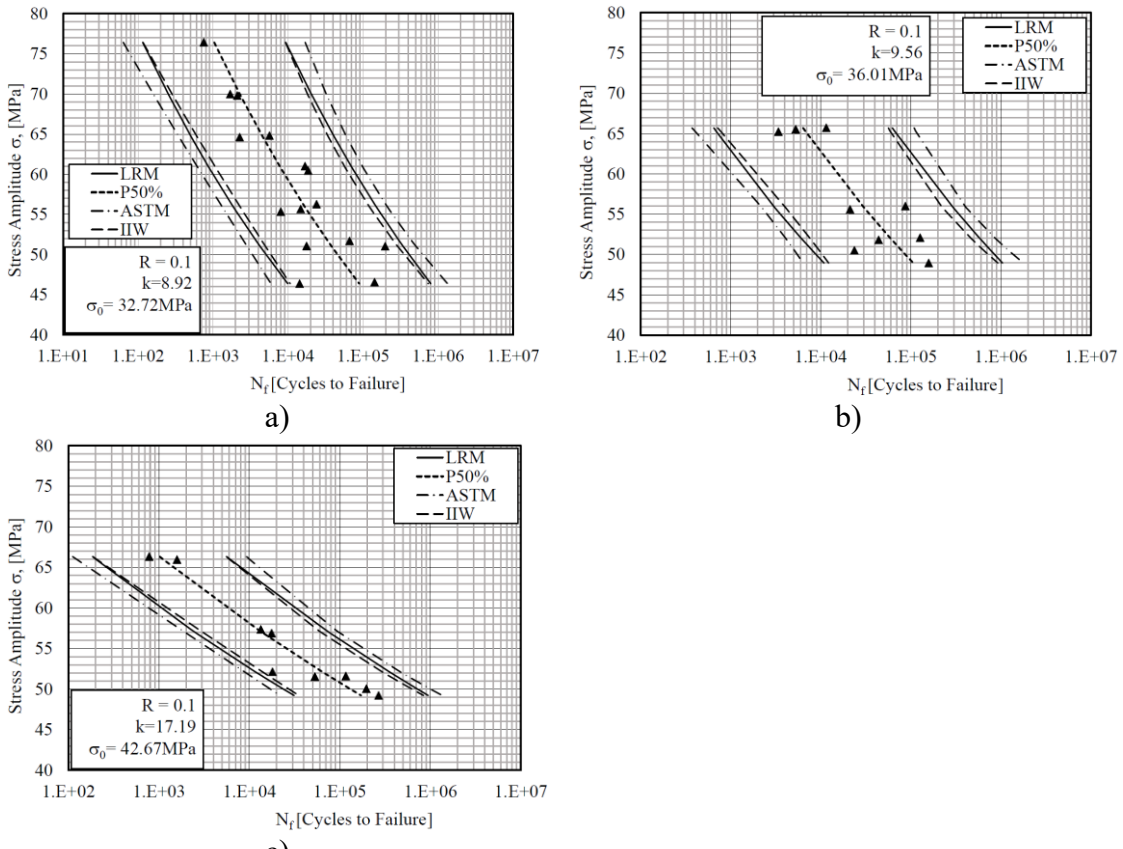

Figure 6-21 Mean S-N curves and parabolic scatter bands of GCI fatigue data sets a) plain uncharged, b) plain hydrogen-charged for 3 months and c) plain hydrogen charged for 9 months.

6.4.2 Size of scatter bands of GCI

As the soaking increased to nine months the trend in the scatter bands generated by the various approaches decreased. The approach suggested by the ASTM decreased by 29%, while the IIW and LRM reduced by 24% and 26% respectively. The trend in the change in scatter bands as the soaking time increased is summarised in Figure 6-23. As has been confirmed in the methodology chapter, the size of the scatter band generated from the ASTM approach is always more conservative while the approach is tied to its distinctive microstructure. The randomness of graphite flakes distribution within a ferritic or pearlitic

matrix plays a crucial role, with variations in the size, shape, and distribution of these graphite flakes impacting the fatigue strength. More so, casting variables, such as cooling rates, solidification conditions, and the overall casting process, introduce variability in microstructural features, thereby influencing its fatigue properties. Casting quality, including the presence of inclusions and surface irregularities, contributes to scatter. Alloy composition, although generally limited in GCI, may still influence mechanical properties and fatigue behaviour. The loading conditions adopted during fatigue testing, coupled with the influence of surface conditions and potential defects, potentially contribute to the observed scatter in fatigue data for GCI. Careful consideration of these factors in experimental design is essential for accurate interpretation and reliable fatigue assessments for GCI.by the IIW is the least. In analysing fatigue behaviour in GCI, key factors influencing scatter in fatigue data are

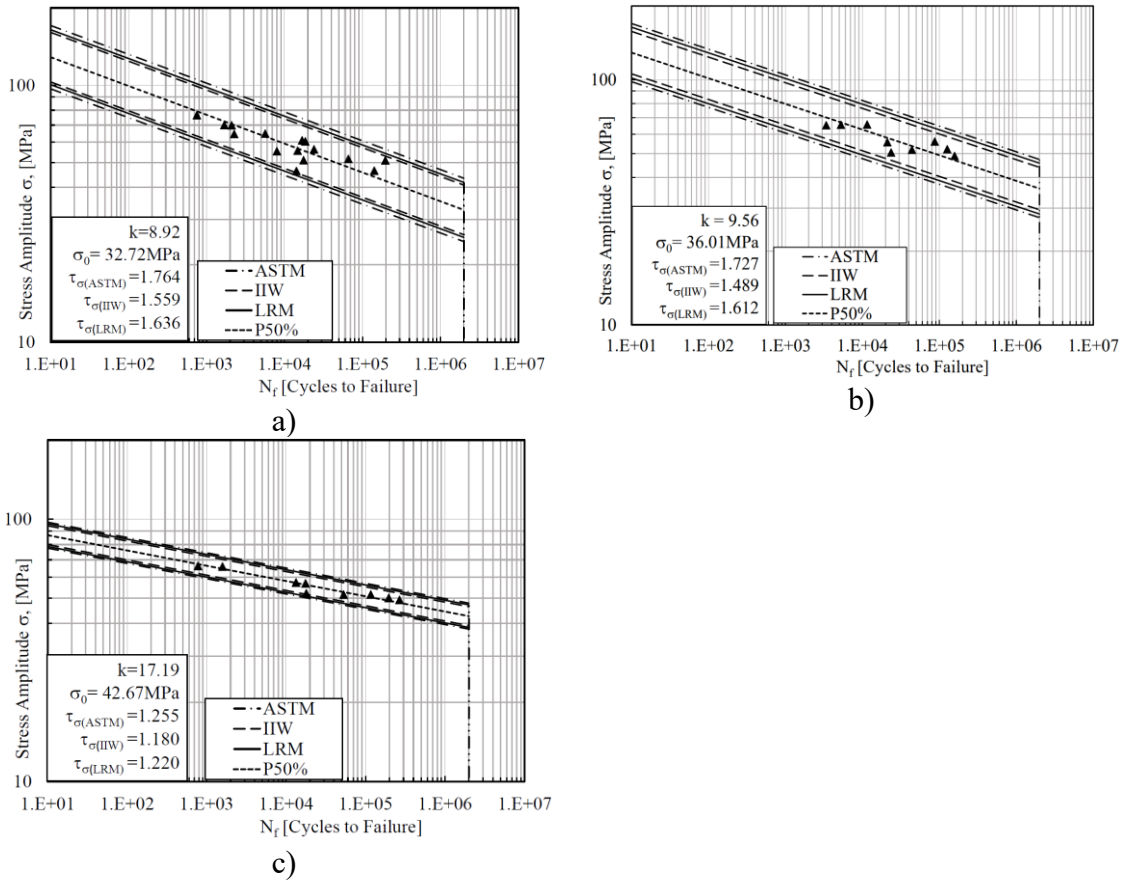

Figure 6-22 Parallel scatter bands (τ_σ) used for design purposes at a 95% probability of survival for GCI a) plain uncharged, b) plain hydrogen-charged for 3 months and c) plain hydrogen-charged for 9 months

Similar to the steel materials, the parallel scatter bands τ_σ constructed from the parabolic scatter bands by considering the perpendicular bisectors at the mean point of the curves is summarized in Figure 6-22. The scatter bands were generated using the standardised approaches at a 95% probability of survival. These scatter bands are observed to be fairly consistent and reduce in size as the curing duration increases. This change in scatter bands is illustrated in Figure 6-23. The narrowing of the scatter band may imply that the influence of hydrogen charging on fatigue behaviour becomes less pronounced with longer curing times.

Table 6-7 summarizes the fatigue properties from data sets obtained by plain testing GCI specimens, some of which are hydrogen-charged at a pressure of 8-10 bars. It also contains the design scatter bands generated at a 95% probability of survival using the standardized approaches considered in this research, and these scatter bands almost approximate to unity.

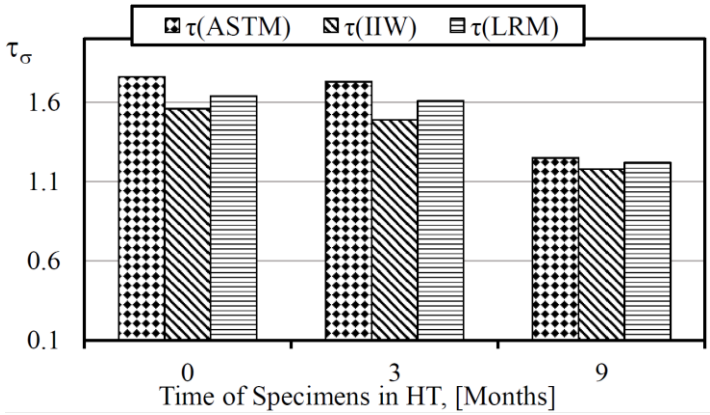

Figure 6-23 The trend of decreasing scatter band with increasing soaking time

6.4.3 Change in inverse slope of GCI.

Unlike the other specimens examined in this research, the inverse slope of the data from GCI specimens was observed to increase as the curing time extended from three to nine months. The values of k changed through 8.9, 9.56 to 17.19 respectively. This implied that the fatigue resistance of this material will also increase slightly as a result of hydrogen charging. The trend in the inverse slope for GCI is summarised in Figure 6-24.

According to Ref. [44] the fatigue strength exponent of these metals ranges from -0.05 to 0.1, corresponding to inverse slope ranges of 20 to 10. The values of the inverse slope generated from the ex-service GCI used in this research were within the expected range.

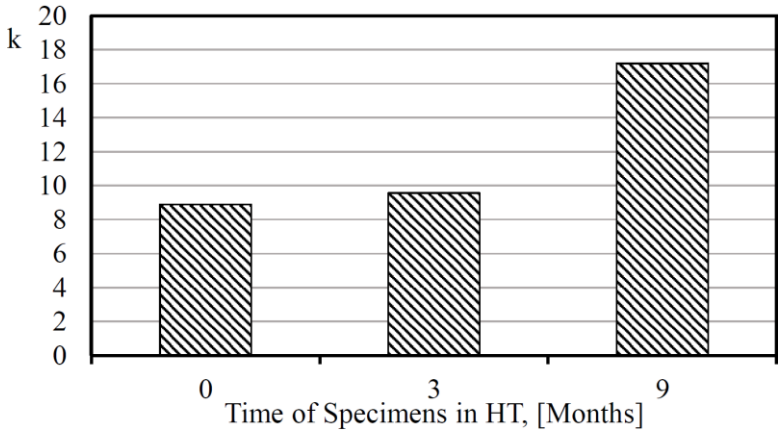

Figure 6-24 The trend of the inverse slope with increasing soaking time of GCI

6.4.4 Change in the spread of GCI specimen

The spread in the fatigue data for GCI depends on external factors, as well as the stress amplitude considered during testing and internal microstructural parameters. The microstructural parameters include the graphite content and length, as well as the stress concentration factors at its tip [45]. In addition, the fatigue life is usually dominated either by crack growth along shear planes or along tensile planes [46,47]. Then the crack is shear or tensile dominant. The fatigue growth observed in the GCI specimens was seen to be shear-resistant mode 1 cracks [48]. GCI momentarily become resistant to mode 1 crack initiation when exposed to hydrogen. However, they become very brittle with no significant plastic deformation before failure, leading to a substantial reduction in the crack propagation regime. Because of this shear resistance, the material tends to show an increase in its fracture toughness. Some of the failed specimen's fracture surfaces have already been reported in the experimental set-up and raw data chapter. The trend in the spread of fatigue data is represented in Figure 6-25 below.

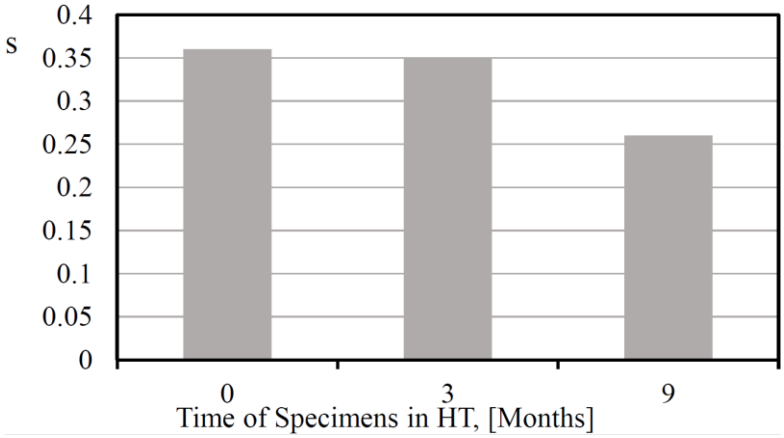

Figure 6-25 The trend of spread with increasing soaking time of GCI

The spread reduces as the soaking time increases to nine months. This indicates that the fatigue property of the GCI was more highly dispersive when uncharged than when charged. This could be as a result of a reduction in fatigue strength as soaking increases, or simply down to material discontinuity. However, the percentage change in the spread of the fatigue data sets was small suggesting that the fatigue properties were impacted to the same extent by the determining factors of scatter.

6.4.5 Change in the intercept of GCI fatigue data

The fatigue strength coefficient can be assumed to be equal to the true fracture strength of GCI [44], although this can be influenced by discontinuities at the free carbon flakes. In this research, the fatigue strength coefficient was observed to increase with the soaking time of the specimens. This is possibly a result of an increase in the fatigue ductility coefficient or cyclic hardening [49]. Figure 6-26 shows the trend in the fatigue strength coefficient as the soaking time increased for GCI specimens.

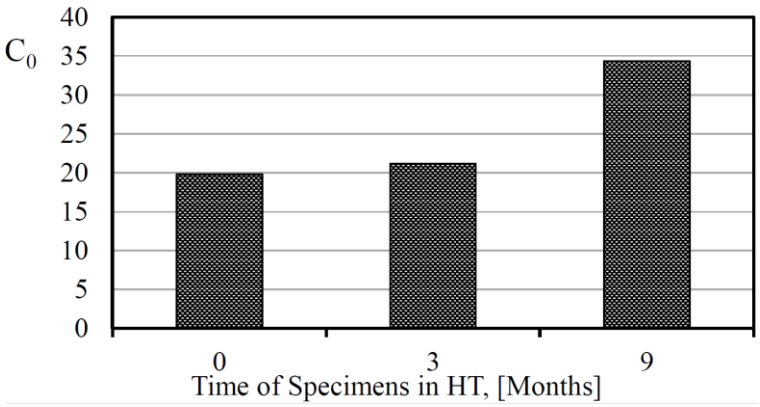

Figure 6-26 The trend in the fatigue strength component with increasing soaking time of GCI

6.4.6 Change in the endurance limit of GCI

As observed in the data sets generated from GCI, the fatigue strength coefficient increased which has also been reflected in an increase in the values of the endurance limit estimated after two million cycles. The fatigue limit of GCI lies in the range of 25-35% UTS [50]. This is dependent on the chemical composition and metallurgical processing and testing. The change in the endurance limit estimated after 2 million cycles is summarised in Figure 6-27. Its value increases by 30% which is out of the estimated range.

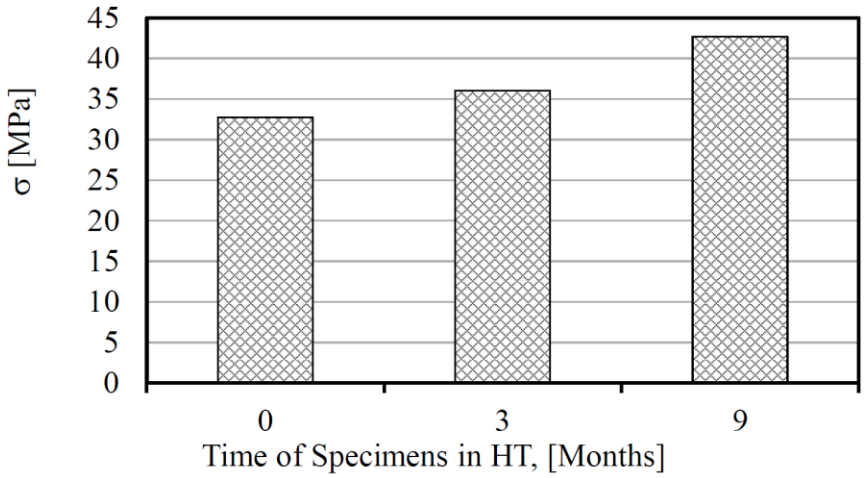

Figure 6-27 The trend in the endurance limit of GCI with increasing soaking time

To assess how the endurance limit compares to values in the literature, this research compared the endurance limits of various GCIs with those documented in existing literature. Given the diverse nature of defects in GCI, particularly in specimens retired from use, a normalization process was also employed for the comparison. The summary of this normalization is presented in the Table 6-8 below.

6.4.7 Fatigue properties of GCI from the literature.

It has been observed that the chemistry, hardness, and overall strength attributes of grey cast iron exhibit considerable variation based on factors such as cupola charge, foundry practice, and cooling rate. Specifically, the stress versus life properties may differ across various sections within a single casting of the same specimen [44]. In used cast iron pipes, significant deterioration due to corrosion is observed while in pipes from some types of cast iron with strength below 200MPa, the effects of reducing fatigue resistance by the discontinuities in them are limited [47]. Table 6-8 summarizes some datasets from the literature for GCI. The inverse slopes of these datasets all fall below 20, as suggested by the literature. The specimens tested under fully reversed loads are observed to have a higher fatigue strength compared to those in tension. The mean effect has an impact on the fatigue properties. In all, the fatigue ratios generated from this investigation fall within the range of those reported in the literature. The observed discrepancies are primarily attributed to the level of degradation in the ex-service pipe samples used in this research and the material variability in chemistry and physical properties. This deterministic approach aligns with references [44,47], which suggests that no two GCI datasets will have identical fatigue properties due to the explained factors.

Table 6-8 Normalised endurance limit and fatigue properties of GCI from literature in comparison to measured fatigue properties of GCI in this research

Source	Material type GCI	Years in use	σ_{UTS} [MPa]	k	R	σ_0 [MPa]	$\sigma_{0,50\%}/\sigma_{UTS}$
[48]	Spun cast	-	203	10.5	0.1	53.9	0.26
[51]	As cast	Industrial	225	4.29	-1	60.00	0.26
[48]	Spun cast	-	203	11.5	-1	85.8	0.44
[44]	Sample 1	-	262	9.6	-1	95.3	0.36
[44]	Sample 2	-	145	8.3	-1	78.7	0.54
[47]pipe1	Pit-cast	In-service	104	12.9	0.1	24.2	0.23
[47]pipe3	Spun cast	In-service	173	17.5	0.1	47.6	0.28
[47]pipe5	Spun cast	In-service	214	16.0	0.1	55.1	0.26
Present research	Spun cast	Ex-service	268	8.92	0.1	32.7	0.12

6.4.8 Statistical significance of fatigue properties in GCI

After investigating the fatigue properties of GCI and comparing the results to results from the literature, this section aims to determine whether the fatigue properties exhibited in specimens soaked in hydrogen are significant or simply as a result of randomness in the material characteristics. The data summarised in Table 6-9 presents the results of the significance tests generated from GCI data sets. It indicates that the charged specimens cured for three months are statistically insignificant, whereas significance is observed when the specimens are cured for nine months. Unlike the other materials, it's noteworthy that the endurance limit in GCI specimens tends to increase with the introduction of hydrogen.

Table 6-9 Statistical analysis for the fatigue data sets from uncharged and charged GCI specimens, cured for 3 and 9 months, at a confidence level of 95%

Source of data sets compared.	$\sigma_{0,unch.}$ $\sigma_{0,xm}$ [MPa]	**% $\Delta\sigma_0$**	**Variance test ($\beta =$ 1.7%)**	**Slope test ($\beta =$ 1.7%)**	**Intercept test ($\beta =$ 1.7%)**	**Conclusion ($\sum \beta \cong$ 5%)**
CI_ uncharged and CI_3m	32.72 36.01	+10	-4.11	-7.08	-0.17	Insignificant
CI_ uncharged and CI_9m	32.72 42.67	+30	-3.15	0.82	-0.34	Significant

There is no apparent change in the fatigue property with an increase of up to 10% in the endurance limit, as revealed by this result. For GCI specimens that were charged and cured for 9 months, the endurance limit changed by up to 30%, and statistical analyses indicate

that the data sets are significant when compared with those from uncharged specimens. Figure 6-28 shows the graphical representation of this analysis at a significance level of 5%. This result will also be reviewed in detail in the next chapter.

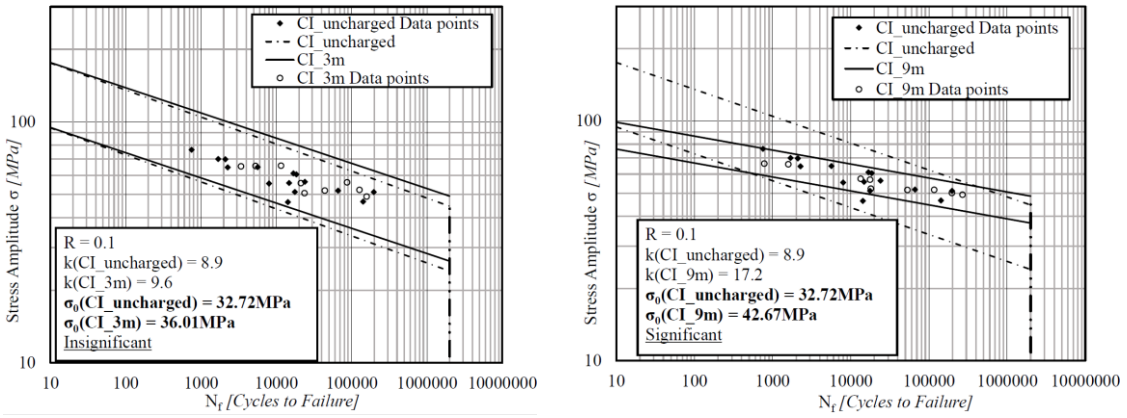

a) b)

Figure 6-28 Significance curves of; a) uncharged specimens of GCI and charged specimens for 3 months and b) uncharged specimens of GCI and charged specimens for 9 months

Likewise, the datasets from soaked GCI can be visually examined to determine if they can seamlessly integrate into a conservative scatter band of the uncharged specimens. This is depicted in Figure 6-29 below.

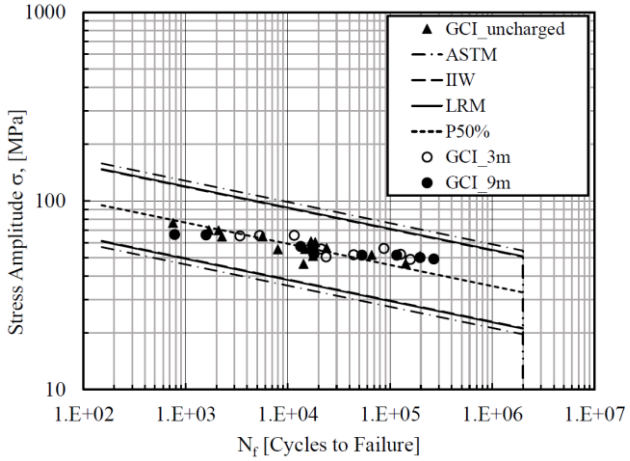

Figure 6-29 Superposed GCI data sets into 99.9% probability of survival of uncharged specimens

The datasets derived from hydrogen-soaked specimens of cast iron are observed to align smoothly within a 99.9% conservative scatter band of uncharged specimens. From a visual engineering perspective, it can be inferred that the datasets exhibit no discernible difference in fatigue properties due to hydrogen charging.

While there has been a noted change in some of the fatigue properties of GCI, it is reported in the literature that the fatigue properties of this material tend to vary due to a variety of reasons. It has been observed that the datasets from all charged specimens can be designed using a design curve from uncharged specimens. Thus, to some degree, it can be stated that there is no significant change in the fatigue properties of cast iron when exposed to a hydrogen environment at 8 – 10 bars of hydrogen.

6.5 Fatigue characterisation of brass

Copper-based alloys possess somewhat lower mechanical properties due to their relatively larger grain size and elastic anisotropy. Brass is a generic term for copper-zinc alloys and in addition also exhibits diverse mechanical, corrosion, and thermal properties depending on the specific proportions in which it is alloyed with zinc [52]. In this PhD research investigation, the brass used was a zinc rich alloy [15]. A total of fifteen brass specimens were used in this investigation, amongst which five plain specimens were uncharged and ten specimens were hydrogen-charged for nine months. The raw data generated from these specimens has been reported previously in the experimental set-up and raw data chapter.

6.5.1 The mean curve, parabolic and parallel design curves for brass

The failure of the brass specimens was purely brittle in nature, without the formation of lateral deformation which is in conformity with the literature [53]. Table 6-10 summarizes the fatigue properties of brass generated in this PhD investigation, which contains the various sample sets, standard deviations, inverse slopes, and endurance limits. It also contains the sizes of the scatter bands generated at a 95% probability of survival using the standardized approaches described in this PhD research. Figure 6-30 a & c show the associated parabolic scatter bands as suggested by these approaches. In a similar way, the mean points ($\overline{log\sigma_i}, \overline{logN_{f,i}}$) of these curves do not align, despite a minimal percentage difference in the direction of life. Consequently, this point cannot be regarded as a fixed reference for observing changes in the S-N curves due to hydrogen charging. These graphs will be analysed by comparing each of the fatigue properties of spread, slope, intercept, endurance limit and size of scatter bands represented by these curves.

The correlation coefficients for brass, measuring 0.88 and 0.91, respectively, denote a robust correlation between the distribution of fatigue life and the stress levels examined during testing in this investigation. There is a clear pattern evident from the data points of these specimens.

Table 6-10 Summary of fatigue properties of brass in tension (R=0.1), at a frequency of 10Hz for hydrogen charged over 9 months and uncharged plain specimens

Specimen ID	Fatigue results									
	n	s	K	R	C_o	r	σ_0 [MPa]	τ_σ (ASTM)	τ_σ (IIW)	τ_σ (LRM)
Br_uncharged	5	1.37	40.10	0.1	92.44	0.88	140.6	1.91	1.54	1.63
Br_9m	10	0.51	29.80	0.1	69.57	0.91	132.7	1.41	1.29	1.35

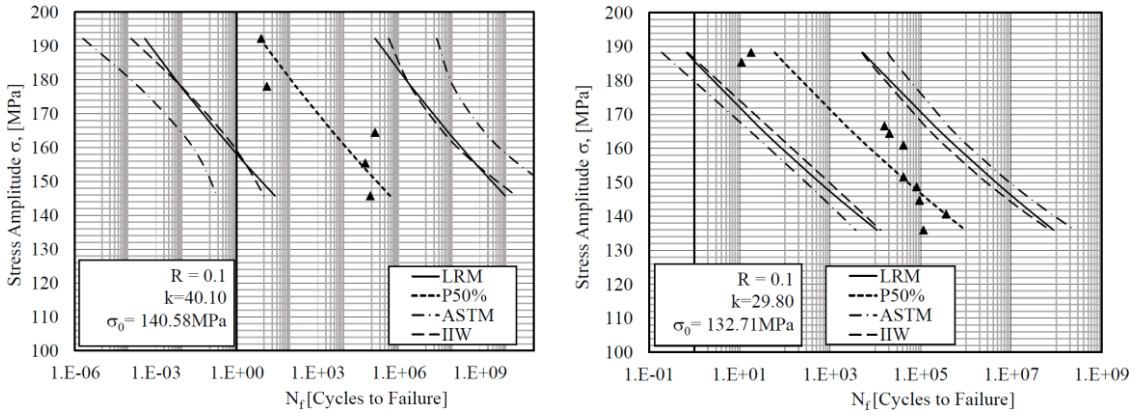

a) b)

Figure 6-30 Mean S-N curve and parabolic scatter band for a) uncharged brass and b) 9 months charged brass

6.5.2 The size of the scatter band of brass

The scatter band of brass diminished in size as specimens underwent a nine-month soaking in hydrogen. The reliability of the data was enhanced by using ten specimens for the extended soaking period compared to only five uncharged specimens. The data obtained from the nine-month soaking provides a more representative and reliable representation compared to the limited data points from the uncharged specimens. The approach suggested by the ASTM was more conservative as compared with the IIW and LRM approaches as observed. The sizes were all less than 2 in both cases as illustrated in Figure 6-31 and these scatter bands tend to unity stipulating that the design curves agree.

From the notes that were written after running the first two tests with uncharged specimens, it was observed that the stress amplitude used in these tests was high. This high stress amplitude induced significant microstructural changes which included the formation of dislocations and grain boundary deformation resulting in a shortened fatigue life due to accelerated damage accumulation [54]. A brittle fracture was observed characterised by minimal plastic deformation before failure. The issue with this therefore is that it becomes erroneous to estimate the endurance limit from such data, strain-controlled tests illustrate

the fatigue behaviour much better. However, not considering these values in the analysis also impacts the estimation of the fatigue properties. This research will include these data points in the analysis of the fatigue properties of brass in this PhD research.

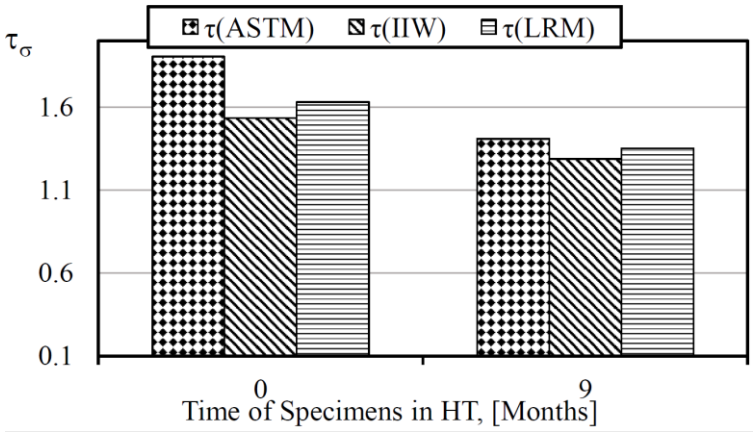

Figure 6-31 The trend in the scatter band for brass with hydrogen soaking time

6.5.3 The change in the inverse slope of brass

The inverse slopes derived from brass were 40.10 for uncharged specimens and 29.80 for specimens soaked for nine months. Consequently, the mean curve becomes steeper, indicating a rapid reduction in fatigue strength. However, these values are notably higher when compared with the literature data summarized in Table 6-11. The trend in the change of the inverse slope is depicted in Figure 6-32

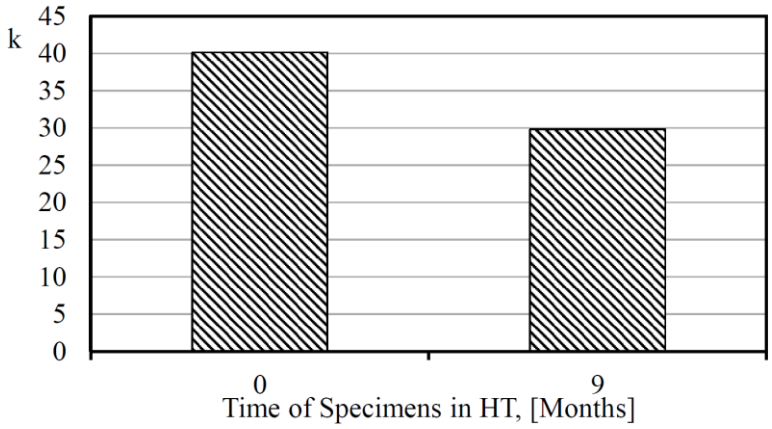

Figure 6-32 The trend in the inverse slope of brass specimens

The elevated value of the inverse slope can be attributed to various factors, one of which is the size effect stemming from the smaller dimensions of the specimens used in this research compared to those reported in the literature [55,56]. The considerable discrepancy in specimen size offers a plausible explanation for the notably high inverse slope observed. Moreover, the grain size plays a role in influencing the fatigue strength exponent for copper

alloys [5,57,58]. Stress levels associated with fatigue lives less than 10^3 are assigned to low cycle fatigue tests. For ultra-fine grain copper and copper-zinc (brass) alloys, this contributes to the rapid softening due to grain coarsening, leading to localized shear bands and eventual instant fracture [5,59]. This sudden fracture was observed during the testing of some of the specimens at higher stress amplitudes.

6.5.4 Change in the spread of brass data

Similar to the fatigue property described above the spread of the fatigue data was particularly higher for uncharged specimens recording a very high standard deviation of 1.37. This suggests that the individual fatigue strength measurements deviate widely from the average or mean fatigue strength. This variability suggests that there were considerable differences among the fatigue properties of individual specimens. The effect of rapid softening must have contributed to the variability of this data set. After nine months of soaking in a hydrogen environment, the spread of the data converges to a value similar to those observed in the literature. The change in the spread is also summarised in Figure 6-33.

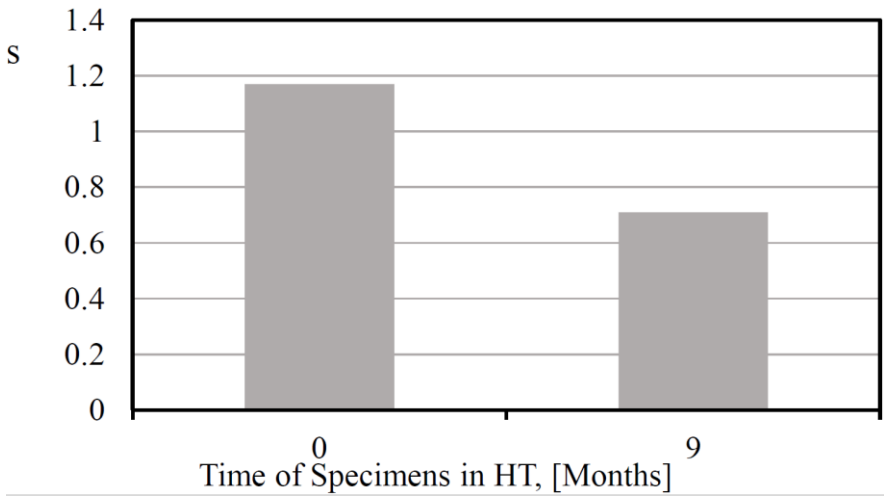

Figure 6-33 The trend in the spread for brass data sets with hydrogen soaking time

6.5.5 Change in the intercept of brass data sets

As noted earlier, the fatigue strength coefficient for brass can vary depending on the specific alloy composition, heat treatment, and other material factors. In addition, the fatigue strength coefficient indicates the resistance to variations in applied tension and is identified as the vertical intercept of the mean S-N curve. The vertical intercept of the datasets for brass reduced when the specimens were subjected to nine months of charging and was observed to be lower compared to uncharged specimens. Clearly, a lower fatigue strength coefficient of the Cu-Zn alloy signifies a reduced fatigue strength [4,5]. This

indicates that the fatigue strength of brass diminished when the brass specimens underwent nine months of charging. The change in the intercept is summarized in Figure 6-34.

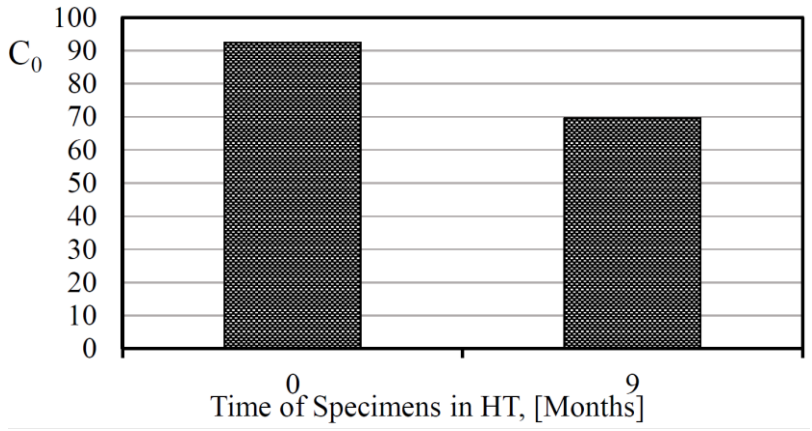

Figure 6-34 The trend in the fatigue strength coefficient for brass data sets with hydrogen soaking time

6.5.6 Change in the endurance limit of brass

The fatigue properties summarised in Table 6-11 show that the endurance limit of brass at 2 million cycles was 140.58MPa when uncharged as compared to 132.70MPa when soaked in a hydrogen environment for nine months. This is a slight reduction in the endurance limit, but it is left to be seen what typical values of the endurance limit are in the literature. Its endurance limit is estimated to around 40% of the ultimate tensile strength.

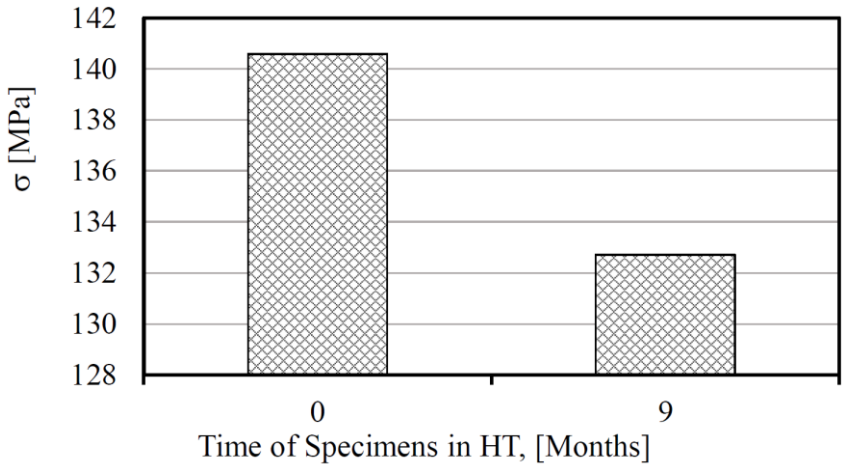

Figure 6-35 The trend in the endurance limit for brass data sets with hydrogen soaking time

Because only two different conditions of brass specimens were used in this investigation, it is difficult to say if the change in the endurance limit characteristics shown by the analyses is due to chance or as a result of the conditions tested.

6.5.7 Fatigue properties of brass from the literature

Table 6-11 summarizes selected fatigue properties of brass gathered from the literature. It is noted that the normalized endurance limit of uncharged brass, as considered in this research, aligns closely with some of the values reported in other studies. The observed slight differences can be attributed once more to variations in geometry and size, introducing a scale factor that influences the fatigue properties of brass.

Table 6-11 The fatigue properties of brass from literature

Source	Material type	Area [mm^2]	Temper	σ_{UTS} [MPa]	k	R	σ_0 [MPa]	$\sigma_{0,50\%}/\sigma_{UTS}$
[60]	CuZn37			366	24.37	-1	197	0.53
[5]	Cu-5 %Zn	12	800^0C	229	10.41		75	0.32
[5]	Cu-5 %Zn	12	800^0C	350	8.26		90	0.26
[5]	Cu-5 %Zn	12	800^0C	433	7.52		140	0.32
[5]	Cu-11 %Zn	20	800^0C	245	14.01		120	0.49
[5]	Cu-11 %Zn	20	800^0C	545	8.20		160	0.29
[5]	Cu-11 %Zn	20	800^0C	614	8.13		180	0.29
[61]	C26000, brass		HO1	421	-	-1	120	0.29
[61]	C26000, brass		HO2	476	-	-1	155	0.32
[61]	C26000, brass		HO4	572	-	-1	170	0.30
[61]	C26000, brass		HO8	676	-	-1	190	0.28
[62]	Used alloy		-	297	8.48	-1	124	0.42
[63]	Brass alloy		-	594	23.64	+	321	0.54
Br_uncharged	Cu-Zn	9.31	-	252	40.10	0.10	141	0.56

6.5.8 Statistical significance of fatigue properties in brass data

Table 6-12 displays the results of the statistical significance analysis for brass specimens. These results indicate that the impact of 20% hydrogen embrittlement on brass specimens, even when cured for nine months, is not statistically significant at a 5% significance level, even when there is an endurance limit reduced by 6%. The scatter band is also visualized in Figure *6-36*. Thus, it can be concluded that there was no noticeable change in the fatigue

properties of brass when soaked in hydrogen for nine months as compared to uncharged specimens.

Table 6-12 Statistical analysis for the fatigue data sets from uncharged and charged specimens of brass cured 9 months, at a confidence level of 95%

Source of data sets compared.	$\sigma_{0,unch.}$ $\sigma_{0,xm}$ [MPa]	**%** $\Delta\boldsymbol{\sigma_0}$	**Variance test** ($\boldsymbol{\beta} = \mathbf{1.7\%}$)	**Slope test** ($\boldsymbol{\beta} = \mathbf{1.7\%}$)	**Intercept test** ($\boldsymbol{\beta} = \mathbf{1.7\%}$)	**Conclusion** ($\sum \boldsymbol{\beta} \cong \mathbf{5\%}$)
Br_ uncharged and CI_9m	140.58 132.71	-6	-3.55	-20.20	-1.30	Insignificant

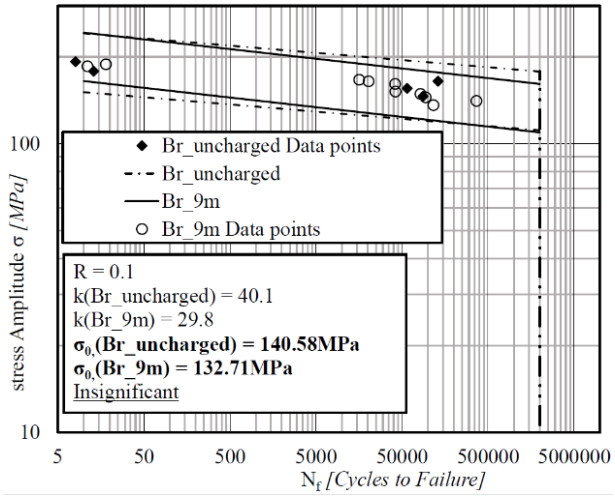

Figure 6-36 Significance curve for charged and uncharged specimens of brass

Similarly, in the case of brass, the data set from specimens charged for nine months seamlessly fits into the conservative scatter band with a 99.9% probability of survival for uncharged brass specimens. Therefore, using visual judgment of overlapping scatter bands, it is evident that a single design curve can effectively be employed to design for these data sets from brass. Furthermore, the datasets have been determined to be statistically insignificant. The superposed datasets are summarized in Figure 6-37.

One noticeable effect is the discrepancy in the sizes of the scatter bands generated from these datasets. They do not seem to agree and differ significantly. This discrepancy is likely a result of the specimens that were tested at very high stress amplitudes which demonstrated a high level of variability in the data.

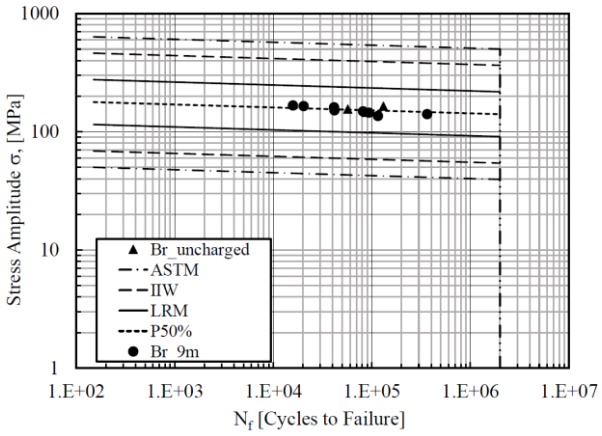

Figure 6-37 Superposed brass data sets into 99.9% probability of survival of uncharged specimens

6.6 Comment and Conclusion

Given the limited number of specimens used in the fatigue experiments at each stress level due to cost constraints, it becomes essential to establish a threshold value for the correlation coefficient (r) across various sample sizes and confidence levels. This involves determining a threshold value (r_a) for correlation, which is computed using a statistical test defined as follows:

$$t_{(n-2)} = r\sqrt{(n-2)} \Big/ \sqrt{1-r^2} \tag{6-3}$$

In which $t_{(n-2)}$ is the student distribution with $n-2$ degrees of freedom. The threshold value r_a, is then determined at a given confidence level β. The test will pass if the calculated value of r is bigger than the threshold value r_a.

$$r_a = \frac{t_{\beta(n-2)}}{\sqrt{(n-2)+t^2{}_{\beta(n-2)}}} \tag{6-4}$$

Given also the variability in the number of specimens for each metal available in this investigation, establishing a threshold correlation coefficient posed a challenging task. Therefore, data sets were not rejected based solely on their correlation coefficients. Nonetheless, it is essential to consider this aspect when utilizing the data sets for design purposes in subsequent works, as it provides valuable insight into the reliability and consistency of the results.

In conclusion, this chapter presented aa exploration of the fatigue properties of uncharged and charged specimens. By utilizing standard post-processing methodologies, it estimated the sizes of the scatter bands, data spread, inverse slope (fatigue strength exponent), vertical intercept (or the fatigue strength coefficient), and the endurance limits extracted from experimental data sets for each metal considered in this research. The fatigue properties of these materials were then compared with data from the literature. While some disparities existed in the literature data sets, these were suggested to arise from a variety of factors which include size and scale effects, as well as the length of time in service for ex-service specimens. Some would have arisen because of the loading condition which the experimenter failed to spot at the time of testing. Like in the welded steel specimens, the unique microstructure of each weld influences its fatigue properties in addition to whether the specimens were extracted from larger or smaller ex-service pipelines.

Following the results of the fatigue properties of the pipeline materials, statistical significance approaches were employed to determine whether the differences observed in the fatigue properties between uncharged samples and those soaked in hydrogen for varying durations were significant or insignificant. In cases of significance, it was concluded that there was a notable change in the fatigue properties of the metal because of HE, and not associated with some form of randomness. In instances where the statistical tests indicated preserved statistical insignificance, the conclusion that the soaking of the specimens in hydrogen had little or no effect on the fatigue properties was made.

While the statistical significance test method proved effective in detecting subtle changes in the experimental data sets, a challenge emerged in determining the meaningful level of significance for these changes, especially when monitoring the percentage change in the considered fatigue properties. Nevertheless, this approach consistently adhered to a well-defined level of significance, ensuring effective and consistent analyses of the potential impacts of hydrogen embrittlement on the researched materials.

In the next chapter, a detailed discussion on the implications of the observed changes from the gathered data will be compared with data from the literature to bring out the similarities and differences. This analysis will be conducted in alignment with some industry practices, drawing insights from established methodologies. Theoretical perspectives on fatigue will also be employed to provide a comprehensive understanding of the implications of the identified alterations in fatigue properties. Through this synthesis of practical industry

approaches and theoretical insights, a more comprehensive interpretation of the observed changes will be achieved, contributing to the broader understanding of the impact of hydrogen charging or other factors on the fatigue properties of these ex-service metals.

6.7 References

[1] C.R Schneider, S.J Maddox, BEST PRACTICE GUIDE ON STATISTICAL ANALYSIS OF FATIGUE DATA, 2003.

[2] R.E. Little, J.C. Ekvall, Statistical Analysis Of Fatigue Data, ASTM STP 744, American Society for Testing and Materials, 1981.

[3] R.C. Rice, B.C. Laboratories, Fatigue Data Analysis, ASM Handb. Comm. (2015).

[4] X. An, Q. Lin, S. Wu, Z. Zhang, Improved Fatigue Strengths of Nanocrystalline Cu and Cu–Al Alloys, Mater. Res. Lett. 3 (2015) 135–141. https://doi.org/10.1080/21663831.2015.1029645.

[5] Z.J. Zhang, J.C. Pang, Z.F. Zhang, Optimizing the fatigue strength of ultrafine-grained Cu-Zn alloys, Mater. Sci. Eng. A. 666 (2016) 305–313. https://doi.org/10.1016/j.msea.2016.04.076.

[6] Y. Feng, C. Gao, Y. He, T. An, C. Fan, H. Zhang, Investigation on tension-tension fatigue performances and reliability fatigue life of T700/MTM46 composite laminates, Compos. Struct. 136 (2016) 64–74. https://doi.org/10.1016/j.compstruct.2015.09.057.

[7] F. Campbell, Fatigue and Fracture, Understanding The Basics, ASM International, Materials Park, Ohio, 2012.

[8] H. Nykyforchyn, O. Zvirko, I. Dzioba, H. Krechkovska, M. Hredil, O. Tsyrulnyk, O. Student, S. Lipiec, R. Pala, Assessment of Operational Degradation of Pipeline Steels, Materials (Basel). 14 (2021) 3247. https://doi.org/10.3390/ma14123247.

[9] G. Bolzon, G. Gabetta, H. Nykyforchyn, Lecture Notes in Civil Engineering Degradation Assessment and Failure Prevention of Pipeline Systems, Cham, Switzerland, n.d. http://www.springer.com/series/15087.

[10] J. Capelle, J. Gilgert, G. Pluvinage, A fatigue initiation parameter for gas pipe steel submitted to hydrogen absorption, Int. J. Hydrogen Energy. 35 (2010) 833–843. https://doi.org/10.1016/j.ijhydene.2009.10.063.

[11] H. Nykyforchyn, H. Krechkovska, O. Student, O. Zvirko, Feature of stress corrosion cracking of degraded gas pipeline steels, in: Procedia Struct. Integr., Elsevier B.V., 2019: pp. 153–160. https://doi.org/10.1016/j.prostr.2019.07.035.

[12] A. Zagórski, H. Matysiak, O. Tsyrulnyk, O. Zvirko, H. Nykyforchyn, K. Kurzydłowski, CORROSION AND STRESS-CORROSION CRACKING OF EXPLOITED STORAGE TANK STEEL, 2004.

[13] A. Agala, M. Khan, A. Starr, Degradation mechanisms associated with metal pipes and the effective impact of LDMs and LLMs in water transport and distribution, Proc. Inst. Mech. Eng. Part C J. Mech. Eng. Sci. 237 (2023) 1855–1876.

https://doi.org/10.1177/09544062221133948.

[14] M.A. Beltrán-Zúñiga, D.I. Rivas-López, H.J. Dorantes-Rosales, W. González-Zapatero, C. Ferreira-Palma, V.M. López-Hirata, F. Hernández-Santiago, Fatigue life assessment of low carbon API 5L X52 pipeline steels retired from long-term service, Eng. Fail. Anal. 143 (2023). https://doi.org/10.1016/j.engfailanal.2022.106769.

[15] D. Engelberg, F. Scenini, Y. Zhou, J. Duff, HyDeploy2 –Materials Analysis & Testing, 2023.

[16] R.C. Rice, Statistical Aspects of Design, Mater. Sel. Des. 20 (1997) 72–86. https://doi.org/10.31399/asm.hb.v20.a0002431.

[17] ASTM E3080, Standard Practice for Regression Analysis with a Single Predictor Variable 1, ASTM. (2019) 1–20. https://doi.org/10.1520/E3080-19.2.

[18] ASTM E739-10, Standard practise for statistical analysis of linear or linearized stress-life (S-N) and strain-life (ε-N) fatigue data, ASTM. (2010) 1–7. https://doi.org/10.1520/E0739-23.2.

[19] Suresh S., Fatigue of Materials, Second, Cambridge University Press, New York, 2004.

[20] Y.B. Liu, Y.D. Li, S.X. Li, Z.G. Yang, S.M. Chen, W.J. Hui, Y.Q. Weng, Prediction of the S–N curves of high-strength steels in the very high cycle fatigue regime, Int. J. Fatigue. 32 (2010) 1351–1357. https://doi.org/10.1016/j.ijfatigue.2010.02.006.

[21] R.E. Little, E.H. Jebe, Statistical design of fatigue experiments, Applied Science Publishers., London, 1975.

[22] Y. Peng, J. Chen, J. Dong, Experimental Data Assessment and Fatigue Design Recommendation for Stainless-Steel Welded Joints, Metals (Basel). 9 (2019) 723. https://doi.org/10.3390/met9070723.

[23] T. Tomaszewski, P. Strzelecki, Study of the size effect for non-alloy steels S235JR, S355J2+C and acid-resistant steel 1.4301, AIP Conf. Proc. 1780 (2016). https://doi.org/10.1063/1.4965940.

[24] S. M. Marco, H. E. Frankel, M. N. Torrey, C. A. Moyer, A Guide for Fatigue Testing and the Statistical Analysis of Fatigue Data, Am. J. Orthod. 51 (1963) 318. https://doi.org/10.1016/0002-9416(65)90116-8.

[25] J. Schijve, Fatigue and Scatter. In Fatigue of Structures and Materials, in: Fatigue Struct. Mater., First, Kluwer Academic Publishers, Dordrecht, 2004: pp. 310–328. https://doi.org/10.1007/0-306-48396-3_12.

[26] P. Tian, K. Xu, G. Ping Lu, G. Ying Qiao, B. Liao, F. Ren Xiao, Evaluation of the mechanical properties of the X52 high-frequency electric resistance welding pipes, Int. J. Press. Vessel. Pip. 165 (2018) 59–67. https://doi.org/10.1016/j.ijpvp.2018.06.006.

[27] J. Capelle, J. Gilgert, G. Pluvinage, HYDROGEN EFFECT ON FATIGUE AND FRACTURE OF PIPE STEELS, France, 2006.

[28] S.. Maddox, FATIGUE DESIGN RULES FOR WELDED STRUCTURES, Prog. Struct. Eng. Mater. TWI. 2 (2000) 102–109.

[29] C. Johnston, STATISTICAL ANALYSIS OF FATIGUE TEST DATA, Trondheim, Norway, 2017.

[30] S. Cicero, T. García, J.A. Álvarez, A. Bannister, A. Klimpel, A. Martín-Meizoso, J. Aldazabal, Fatigue behaviour of structural steels with oxyfuel, plasma and laser cut straight edges. Definition of Eurocode 3 FAT classes, Eng. Struct. 111 (2016) 152–161. https://doi.org/10.1016/j.engstruct.2015.12.004.

[31] P. Foti, S. Filippi, F. Berto, Fatigue assessment of welded joints by means of the strain energy density method: Numerical predictions and comparison with Eurocode 3, Frat. Ed Integrita Strutt. 13 (2019) 104–125. https://doi.org/10.3221/IGF-ESIS.47.09.

[32] G. Kang, H. Luo, Review on fatigue life prediction models of welded joint, Acta Mech. Sin. Xuebao. 36 (2020) 701–726. https://doi.org/10.1007/s10409-020-00957-0.

[33] M.D. Chapetti, L.F. Jaureguizahar, Estimating the fatigue behaviour of welded joints, in: Procedia Eng., Elsevier Ltd, 2011: pp. 959–964. https://doi.org/10.1016/j.proeng.2011.04.158.

[34] A.-C. Hesse, J. Hensel, T. Nitschke-Pagel, K. Dilger, Investigations on the fatigue strength of beam-welded butt joints taking the weld quality into account, Weld. World. 63 (2019) 1303–1313. https://doi.org/10.1007/s40194-019-00774-5.

[35] M. Braun, J. Baumgartner, G. Hofmann, K. Drebenstedt, N.M. Bauer, H. Bakhschi, U. Kuhlmann, A statistical assessment of the fatigue strength improvement of butt-welded joints by flush grinding, Weld. World. 67 (2023) 2345–2359. https://doi.org/10.1007/s40194-023-01569-5.

[36] S.K. Sharma, S. Maheshwari, A review on welding of high strength oil and gas pipeline steels, J. Nat. Gas Sci. Eng. 38 (2017) 203–217. https://doi.org/10.1016/j.jngse.2016.12.039.

[37] Ohta A., Maeda Y, Mawari T., Nishijima S, Nakamura H, Fatigue strength evaluation of welded joints containing high tensile residual stresses , Int. J. Fatigue. (1986) 147–150.

[38] Z. Gao, B. Gong, Q. Xu, D. Wang, C. Deng, Y. Yu, High cycle fatigue behaviours of API X65 pipeline steel welded joints in air and H2S solution environment, Int. J. Hydrogen Energy. 46 (2021) 10423–10437. https://doi.org/10.1016/j.ijhydene.2020.12.140.

[39] P. Žlábek, T. Košco, M. Semeš, Fatigue properties of weld joint of gas pipelines, Procedia Struct. Integr. 33 (2021) 1007–1012. https://doi.org/10.1016/j.prostr.2021.10.111.

[40] R. Yakut, Investigation of Mechanical Properties of Grey Cast Irons Reinforced with Carbon Titanium Nitride (TiNC), Lubricants. 11 (2023). https://doi.org/10.3390/lubricants11100454.

[41] R. Tovo, P. Lazzarin, F. Berto, M. Cova, E. Maggiolini, Experimental investigation of the multiaxial fatigue strength of ductile cast iron, Theor. Appl.

Fract. Mech. 73 (2014) 60–67. https://doi.org/10.1016/j.tafmec.2014.07.003.

[42] J.W. Fash, Fatigue Crack Initiation And Growth in Gray Cast Iron, Illinois Urbana, 1980.

[43] D. WEINACHT, D. SOCIE, Fatigue damage accumulation in grey cast iron, Int. J. Fatigue. 9 (1987) 79–86. https://doi.org/10.1016/0142-1123(87)90048-X.

[44] L.E. Tucker, D.R. Olberts, Fatigue Properties of Gray Cast Iron, 1969. https://www.jstor.org/stable/44580239.

[45] X. Teng, J. Pang, F. Liu, C. Zou, X. Bai, S. Li, Z. Zhang, Fatigue Life Prediction of Gray Cast Iron for Cylinder Head Based on Microstructure and Machine Learning, Acta Metall. Sin. (English Lett. 36 (2023) 1536–1548. https://doi.org/10.1007/s40195-023-01566-z.

[46] D.F. Socie, G.B. Marquis, MULTIAXIAL FATIGUE, Warrendale, U.S.A., 2000.

[47] R. Jiang, S. Rathnayaka, B. Shannon, X.-L. Zhao, J. Ji, J. Kodikara, Analysis of failure initiation in corroded cast iron pipes under cyclic loading due to formation of through-wall cracks, Eng. Fail. Anal. 103 (2019) 238–248. https://doi.org/10.1016/j.engfailanal.2019.04.031.

[48] E. John, J. Boxall, R. Collins, E. Bowman, L. Susmel, Multiaxial fatigue of water pipe grey cast iron, Int. J. Fatigue. 178 (2024) 108002. https://doi.org/10.1016/j.ijfatigue.2023.108002.

[49] J.L. Dossett, C.V. White, Heat Treating of Gray Irons, in: Heat Treat. Irons Steels, ASM International, 2018: pp. 493–507. https://doi.org/10.31399/asm.hb.v04d.a0005942.

[50] T. Willidal, W. Bauer, P. Schumacher, Stress/strain behaviour and fatigue limit of grey cast iron, Mater. Sci. Eng. A. 413–414 (2005) 578–582. https://doi.org/10.1016/j.msea.2005.08.200.

[51] X.Y. Teng, J.C. Pang, F. Liu, C.L. Zou, C. Gao, S.X. Li, Z.F. Zhang, Fatigue strength optimization of grey cast iron processed by different austempering temperatures, Int. J. Fatigue. 175 (2023). https://doi.org/10.1016/j.ijfatigue.2023.107831.

[52] M. Engineering, Enhancing the mechanical fatigue resistance of the Cu-Zn-Al alloy Enhancing the mechanical fatigue resistance of the Cu-Zn-Al alloy, (2018).

[53] P. Sangeetha, M. Shanmugapriya, Modeling and prediction of fatigue life of brass and EN24 steel using soft computing tool, in Mater. Today Proc., Elsevier Ltd, 2020: pp. 2912–2918. https://doi.org/10.1016/j.matpr.2020.09.241.

[54] K. Tahmasbi, F. Alharthi, G. Webster, M. Haghshenas, Dynamic frequency-dependent fatigue damage in metals: A state-of-the-art review, Forces Mech. 10 (2023) 100167. https://doi.org/10.1016/j.finmec.2023.100167.

[55] A. Tridello, C.B. Niutta, F. Berto, D.S. Paolino, Size-effect in Very High Cycle Fatigue: A review, Int. J. Fatigue. 153 (2021) 106462. https://doi.org/10.1016/j.ijfatigue.2021.106462.

[56] S.P. Zhu, Y. Ai, D. Liao, J.A.F.O. Correia, A.M.P. De Jesus, Q. Wang, Recent

advances on size effect in metal fatigue under defects: a review, Int. J. Fract. 234 (2022) 21–43. https://doi.org/10.1007/s10704-021-00526-x.

[57] P. Lukáš, L. Kunz, J. Krejčí, Fatigue behaviour of single crystals of a Cu-22%Zn alloy, Mater. Sci. Eng. A. 158 (1992) 177–183. https://doi.org/10.1016/0921-5093(92)90006-M.

[58] X.X. Wu, X.Y. San, Y.L. Gong, L.P. Chen, C.J. Li, X.K. Zhu, Studies on strength and ductility of Cu–Zn alloys by stress relaxation, Mater. Des. 47 (2013) 295–299. https://doi.org/10.1016/j.matdes.2012.12.020.

[59] Z.J. Zhang, P. Zhang, Z.F. Zhang, Cyclic softening behaviours of ultra-fine-grained Cu-Zn alloys, Acta Mater. 121 (2016) 331–342. https://doi.org/10.1016/j.actamat.2016.09.020.

[60] D. Skibicki, Ł. Pejkowski, Low-cycle multiaxial fatigue behaviour and fatigue life prediction for CuZn37 brass using the stress-strain models, Int. J. Fatigue. 102 (2017) 18–36. https://doi.org/10.1016/j.ijfatigue.2017.04.011.

[61] J. Crane, J.O. Ratka, J.F. Breedis, Fatigue Properties of Copper Alloys, Fatigue Fract. 19 (2018) 869–873. https://doi.org/10.31399/asm.hb.v19.a0002411.

[62] H. Aziz Ameen, A. Hassan Ismail, Study of the short and long fatigue cracks for brass alloy, J. Mech. Eng. Res. 3 (2011) 181–185. http://www.academicjournals.org/jmer.

[63] M. Baklouti, R. Mnif, R. Elleuch, Impact of surface hardening treatment generated by shot peening on the fatigue life of brass alloy, J. Mech. Sci. Technol. 26 (2012) 2711–2717. https://doi.org/10.1007/s12206-012-0738-3.

Chapter 7

Discussion of Fatigue Results

7.1 Introduction

To understand the effects of hydrogen embrittlement on fatigue properties, this chapter delves into a comprehensive discussion of the results obtained in this research by testing specimens soaked in natural gas blended with 20% hydrogen compared to the existing knowledge in this domain. In this project, fatigue test data have been diligently generated, providing valuable insights into the behaviour of materials under the influence of hydrogen embrittlement. However, understanding the significance of these results requires meticulous further analysis. Statistical significance tests have been employed to systematically analyze, using significance levels, and ascertain whether the observed changes in the fatigue properties, particularly the endurance limits, carry statistical significance. Statistical rigour is essential for drawing meaningful conclusions in this research.

This chapter does not merely stop at presenting empirical results. It takes a step further by integrating the findings with established theories from existing literature. It is a synthesis of practical results and theoretical underpinnings. Observations from industry practices will also be included, providing a real-world context to this research. Therefore, the core of this chapter revolves around an analytical exploration of the experimental observations and theories, as well as a judicious assessment of the data in conjunction with well-established principles, supplemented by personal judgment.

To ensure clarity and organization, this chapter is structured in a way that addresses each material separately. For each principle and practice being considered, it will be applied to each of the materials involved in this research.

7.2 Fatigue properties of pipeline materials in a hydrogen environment

In this section, the existing knowledge explored in the literature will be reviewed, including a comparative analysis of the fatigue properties of each of the pipeline materials used in this research in hydrogen environments. The similarities, differences, and possible reasons for observed trends will be highlighted.

7.2.1 Hydrogen embrittlement as observed in X52 pipeline steel

The intricate microstructures within steel play a pivotal role in dictating its hydrogen permeation characteristics. By subjecting the steel to diverse heat treatments, a variety of microstructures emerge which influence the amount of hydrogen and the HE effects on the material. Hydrogen atoms are introduced into pipeline steel material by two principal methods, electrochemical cathodic hydrogen charging [1,2] or gaseous hydrogen charging [3]. High-strength materials are more susceptible to hydrogen embrittlement due to their fine-grained structure. The smaller grain size increases the number of grain boundaries and defects, providing more sites for hydrogen atoms to be trapped within the material's structure [4]. Among these grains are hydrogen traps: physical sites like defects and structural inhomogeneities such as dislocations, particles, inclusions, and grain boundaries, where hydrogen localizes and prevents further movement to cause destruction in the material [5,6]. These traps enhance the likelihood of hydrogen accumulation, which can greatly influence embrittlement under stress.

It has been shown that the susceptibility of X52 pipeline steel material to HE increases with longer hydrogen charging times [3]. This explains the observed reduction in the fatigue properties of X52 steel when exposed to prolonged periods in a hydrogen environment. In

this research, as the duration of exposure to the hydrogen environment increased, it is hypothesized that the amount of hydrogen absorbed also increased (using Sievert's law), making the specimens more susceptible to HE. According to previous research, the microstructure of X52 pipeline steel is illustrated in Figure 7-1 consisting of ferrite and pearlite phases.

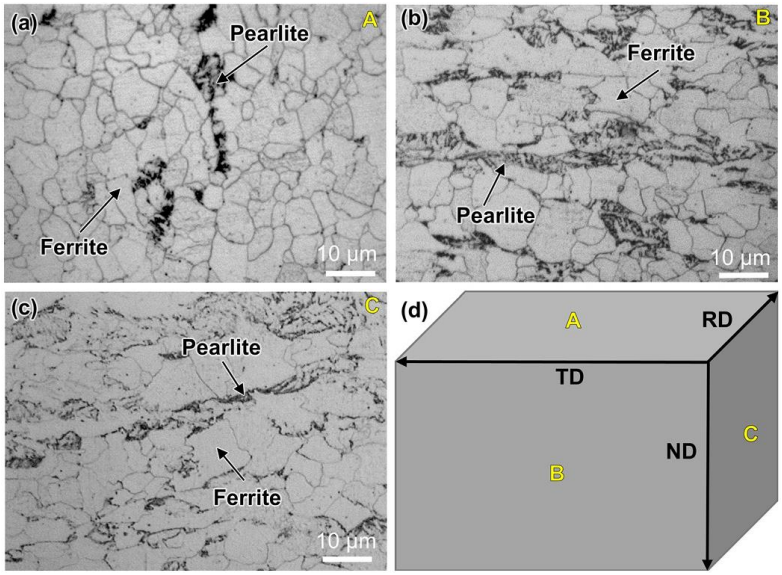

Figure 7-1 Metallography images of X52 pipeline steel in the a) transverse direction. B) transverse-normal direction planes, c) rolling-normal direction planes, and d) image position diagram [3]

Meanwhile, the distinct transitions in crack growth rate for X52 steel in high-purity hydrogen gas have been linked to changes in fracture surface characteristics [3]. As accelerated crack growth begins, this leads to a hydrogen-induced ductility loss in the ferritic or ferritic–pearlitic steels [7–9], for which the fracture surfaces show facets indicative of intergranular crack growth as shown in Figure 7-2. The proportion of intergranular facets increased with accelerating crack growth rate regimes. The initially predominant intergranular crack growth then transitioned into a trans-granular mode, with fracture surfaces showing exclusively trans-granular features representative of hydrogen-assisted crack growth. This contrasts with the trans-granular features typically seen in crack growth occurring in air.

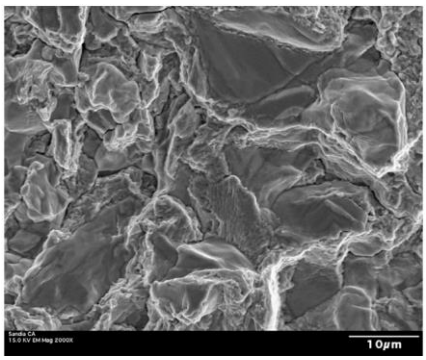

a)

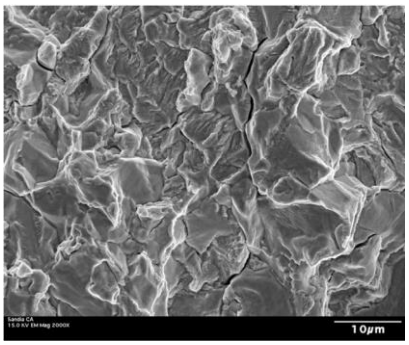

b)

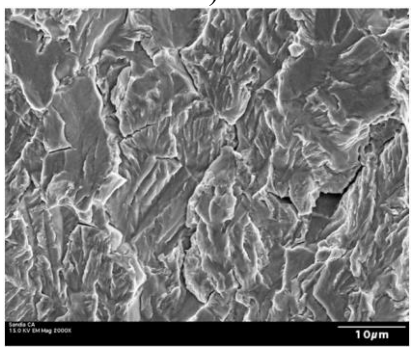

c)

Figure 7-2 Scanning electron microscope fracture surfaces from X52 pipeline steel tested at R=0.1and a frequency of 10Hz in high purity hydrogen gas. (a) Intergranular facets (b)Mixed intergranular and trans-granular facets at a later stage of hydrogen-assisted crack growth (c) Predominantly trans-granular facets during hydrogen-assisted crack growth near test termination [3]

The decohesion concept used to describe fatigue failure under hydrogen and applies to hydrogen-assisted intergranular crack growth in both low-strength and high-strength materials is the model that assumes that the local stress is the driving force behind crack growth in the hydrogen environment. This is dependent on the intensity of the stress and the volume of the microstructure over the microstructure-related distance involved in this failure, a procedure that is likely the predominant embrittlement mechanism in this research.

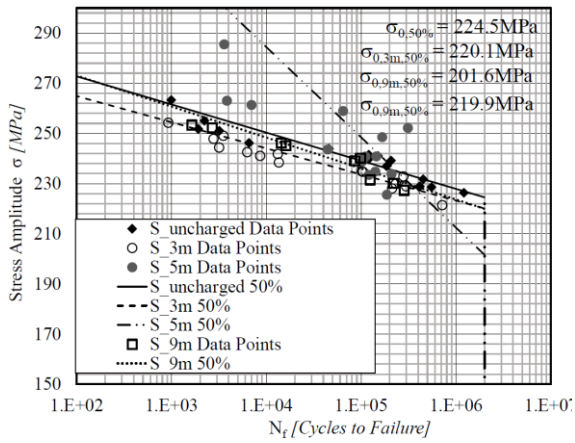

a)

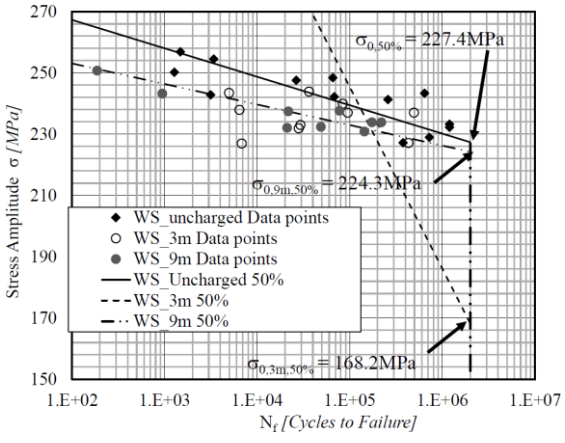

b)

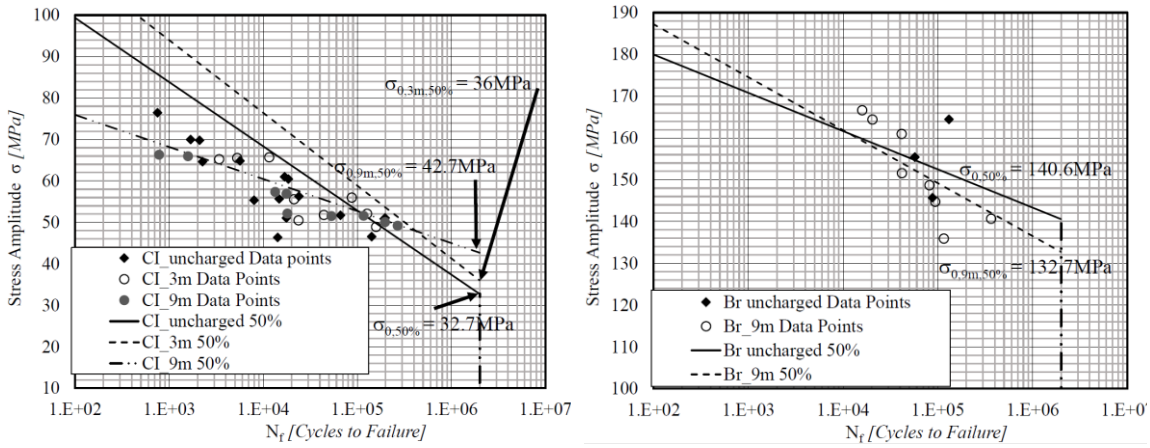

c) d)

Figure 7-3 Endurance limits and mean curves (solid curve) for each material compared with charging times a) steel b) welded steel c) cast iron and d) brass

With the failed samples, the necking of the specimen was seen which was due to ductile failure. Brittle regions were also found on the crack surface and some cracks were surrounded by regions containing microvoids as ductile bands. As the charging time increased, these features became more noticeable and thus led to an increased susceptibility of the materials to HE. These effects were observed in the reduction of the endurance limit as the charging time increased, as illustrated in Figure 7-3a. As explained in the results chapter, the reduction in the endurance limit did not follow a consistent trend. This could be attributed to the inherent variability in the specimens' microstructure which plays a major impact on the HE susceptibility as shown in the fatigue data. There is also the possibility of the specimens degassing the hydrogen content as the charging time increases as was observed in the specimens charged for over 9 months, which is also dependent on the microstructure of the steel that plays a crucial role, for which the hydrogen trapping behaviours might be different. These all dependent on whether the hydrogen trapping sites were weakly trapped hydrogen, which is thought to be in local equilibrium with lattice sites whereas hydrogen in strong traps requires a significant amount of energy to be able to overcome the energy barrier and diffuse in interstitial sites [10,11]. However, the endurance limit for uncharged steel was seen to be reasonable in comparison with steel metals from the literature. Therefore, increasing the charging time of these specimens in the hydrogen environment decreases the fatigue properties as seen in Refs [3,12,13].

7.2.2 Hydrogen embrittlement of X52 welded steel

There have been extensive studies on hydrogen-induced degradation in steel pipeline welds, with significant achievements in areas such as metallurgical microstructure, stress

distribution, hydrogen diffusion and trapping, and their interactions at the welds [14,15]. The hydrogen-induced damage mechanism in the welds of hydrogen-blended natural gas pipelines resembles that in the base material. The mechanical properties vary among different parts of the circumferential weld (base material, weld, and heat-affected zone), and material non-uniformity can impact the stability of the welded structure [16]. As a result, welds are particularly vulnerable to hydrogen-induced damage in hydrogen-blended natural gas pipelines. Figure 7-4 illustrates the mechanisms of hydrogen-induced damage in hydrogen-blended natural gas pipeline welds, including single hydrogen-induced damage, damage combined with mechanical stress, damage combined with brittle fracture, and damage combined with corrosion.

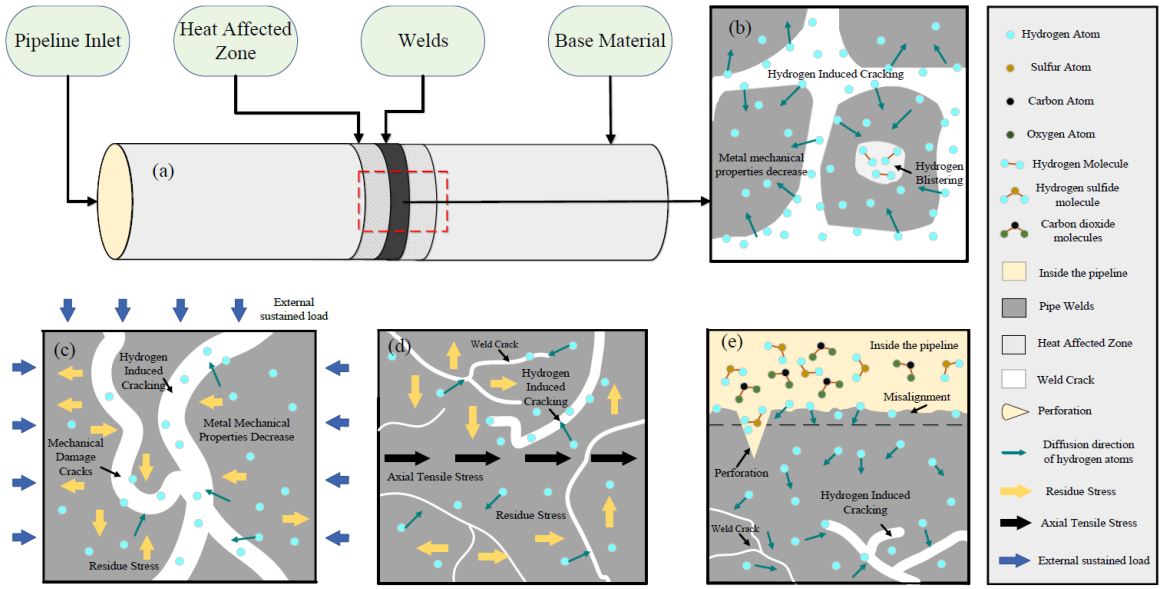

Figure 7-4 a) welded and HAZ b) single hydrogen damage mechanism c) hydrogen damage in addition to mechanical damage d) brittle fracture and hydrogen damage and e) mechanism of HE combined with corrosion [16]

However, the topic of degradation in this field remains highly contested due to the microstructural heterogeneity at welds, resulting from complex welding, manufacturing, and application processes, that leads to variations in mechanical properties from the weld centre to the heat-affected zone (HAZ) and the base metal. Acicular ferrite enhances the toughness of high-strength steels due to its fine grains and increased resistance to crack propagation. However, coarse grains near the welding pool, which undergo extensive heating and become more than five times larger than the grains in the base steel, exhibit the lowest toughness due to the grain coarsening effect. Hydrogen is more soluble in austenite, making it less susceptible to hydrogen embrittlement. In contrast, microstructures with high hardness, such as martensite, have lower solubility for hydrogen but are more prone to

hydrogen-induced cracking [4]. The distribution of micro-hardness in the welds is mainly determined by the microstructures present. Typically, the fine acicular ferrite in the weld metal and bainitic ferrite in high-strength base steels contribute to higher hardness. Conversely, the coarse grain structure and soft allotriomorphic ferrite phase in the HAZ are responsible for the lower hardness [14,15]. The lowest hardness in the HAZ is located near the fusion line.

The microstructure of the welds primarily consists of ferrite [17], which tends to form a crystalline structure where the energy barrier for hydrogen absorption is significantly lower than that of high-strength base steels [14,18]. Non-metallic inclusions within the welds act as irreversible hydrogen traps, effectively capturing mobile hydrogen within the crystalline lattice [11,19]. These inclusions, being harder than the base steel, cause lattice distortion, creating stress concentrations that further promote hydrogen permeation. Therefore, the unique microstructure, metallurgical defects, and stress distribution for high-strength steel pipeline welds result in hydrogen permeation behaviour that differs from that of base steel. Due to their small size, hydrogen molecules cannot easily diffuse through bulk metal and instead accumulate locally increasing internal pressure. When this internal pressure causes local stress to exceed a critical threshold, cracks can initiate. Additionally, hydrogen reduces the cohesive force between iron atoms.

The weld metal exhibits the highest hydrogen permeation rate and sub-surface hydrogen concentration, attributed to the extensive presence of fine acicular ferrite [14]. This microstructure forms a network of grain boundaries that act as pathways for hydrogen permeation [20]. If the welding temperature is too high, the grains of the weld metal will grow and become coarse leading to reduced hydrogen permeation. The X52 base steel consists of polygonal ferrite and some pearlite, while the X52 steel weld contains polygonal ferrite, carbide particles, and acicular ferrite [4,14,15]. As mentioned earlier, the randomly distributed carbide particles reduce hydrogen diffusion, resulting in lower hydrogen diffusivity in both low- and high-strength steel welds compared to the base steels. This suggests that the welded steel in this study would be stronger than the base metal. As demonstrated in the results chapter, this is supported by the fatigue data, as the endurance limit for welded X52 steel was slightly greater than that of the X52 base steel.

For welded steel in this research, necking is seen, and the fracture surface shows both brittle and ductile regions with large cracks. Some cracks were quite visible even with normal eye

inspection which accounts for the increased spread in the fatigue data. One of the possible reasons for this observation is dependent on the unique microstructure of welds which allows for higher hydrogen trapping thereby making them more susceptible to hydrogen damage. There is also the possibility that if the welded specimens were extracted from smaller pipes, the distribution of these unique microstructures would differ from specimens obtained from a larger pipe. Thus, the HE of a weld depends on some key factors like the microstructure of the base metal and the heat-affected zone, the welding process and parameters like welding temperature, speed and shielding gas quality [21–23]. The metallurgical heterogeneity at pipeline welds therefore significantly influences the behaviour of hydrogen permeation and diffusion. The factors that affect the microstructure and hydrogen permeation were not the focus of this research. However, charging the welded specimen over long periods, ensured that a uniform hydrogen distribution of hydrogen is achieved in the weld of each specimen.

It is observed that the endurance limits of hydrogen-charged welded steel were slightly higher than that of X52 steel as expected as shown in Figure 7-3b. The HE is taking place in the weld would be by HELP and the HEDE mechanisms as stated in the literature due to the effect of hydrogen trapping in the various regions of the weld zone.

While there is still some misunderstanding regarding the impact of the hydrogen source on the degradation behaviour of pipeline steels, the reality is that hydrogen atoms from gaseous environments, such as high-pressure hydrogen gas pipelines, have different effects on the mechanical properties and degradation of pipeline steels. For instance, gaseous hydrogen charging does not produce a significant hardening effect on steels compared to electrochemical hydrogen charging which drastically hardens the material [14,24]. Furthermore, the timing of hydrogen introduction into pipeline welds significantly influences hydrogen permeation and the resulting degradation. Quantitative data on the effects of metallurgical microstructures in welds on hydrogen permeation is currently unavailable. Although the finite element method can simulate hydrogen distribution at welds, the input parameters are mostly derived from hydrogen permeation tests under controlled conditions. The synergistic effects of microstructure, stress, and hydrogen entry are not yet fully understood. These gaps highlight the challenges in understanding and controlling hydrogen degradation in X52 pipeline welds. In addition, conventional testing techniques struggle to produce convincing results for understanding the mechanisms of hydrogen degradation, especially at the atomic scale in welded X52 steel. Due to the

complex microstructure of high-strength pipeline steel welds, hydrogen adsorption, absorption, diffusion, and trapping at various weld zones have not been fully studied individually. However, a complete understanding of the overall hydrogen degradation behaviour at the welds remains unclear.

7.2.3 Hydrogen embrittlement of GCI

What distinguishes cast irons from steel is their high carbon content. This higher carbon level, combined with other alloying elements and solidification conditions, dictates the specific form that graphite assumes within grey-cast irons and therefore determines its mechanical properties [25,26]. The graphite can accommodate diffused hydrogen thereby delaying the embrittlement effect. Figure 7-5 shows a graphite nodule from a nodular cast iron sample and the stress-strain curve [26]. Thus, the process of hydrogen-induced degradation in cast iron could be more complex than in carbon steels due to the presence of graphite which acts as stress concentrator sites as well as hydrogen trap sites.

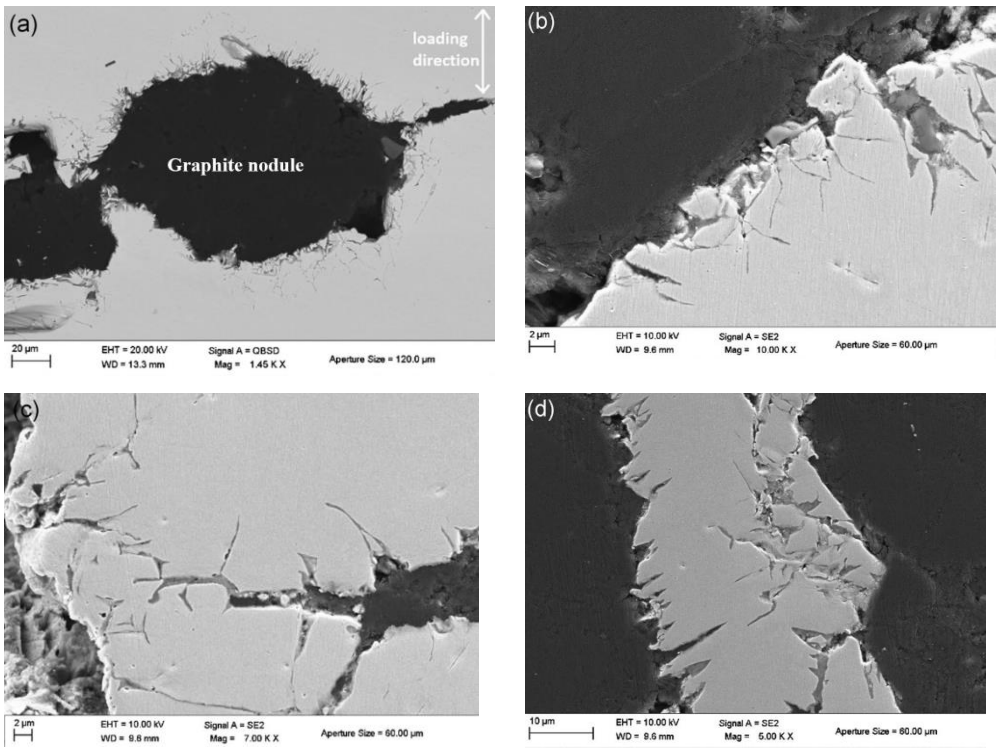

Figure 7-5 Graphite nodules a) The general appearance of cracking around a nodule, (b) close-up of cracking at nodule/matrix interface, and (c and d) linking between adjacent graphite nodules by brittle cleavage cracking [26]

The graphite is mostly nodular with an uneven distribution of nodules most likely due to the segregation of alloying elements during solidification. As shown in Figure 7-5a, the graphite nodules are affected by hydrogen charging, and especially, the graphite

nodule/ferrite matrix interfaces exhibit multiple small cracks in the ferrite matrix formed under hydrogen charging as seen in Figure 7-5b–d. Due to hydrogen charging and with increasing charging time, microcracking at graphite nodule/ferrite matrix interfaces becomes dominant and the cracks grow and interconnect forming a series of larger step-wise brittle cracks in the cast iron.

It is expected that the fracture surface of cast iron in air displays typical ductile fracture features, characterized by large cavities surrounding the graphite nodules and small dimples in the ligaments [26]. However, when exposed to hydrogen under constant load, the ligaments between these large cavities exhibit brittle cleavage fracture facets and become less ductile [7,27]. This cleavage fracture occurs within the ferrite that lies between the graphite nodules, leaving significant cavities in the ferrite matrix where the interface between the graphite nodules and the ferrite becomes apparent, displaying a faceted surface structure. The average number of graphite nodules on a fracture surface of hydrogen-charged specimens when compared with uncharged specimens is summarized in Figure 7-6.

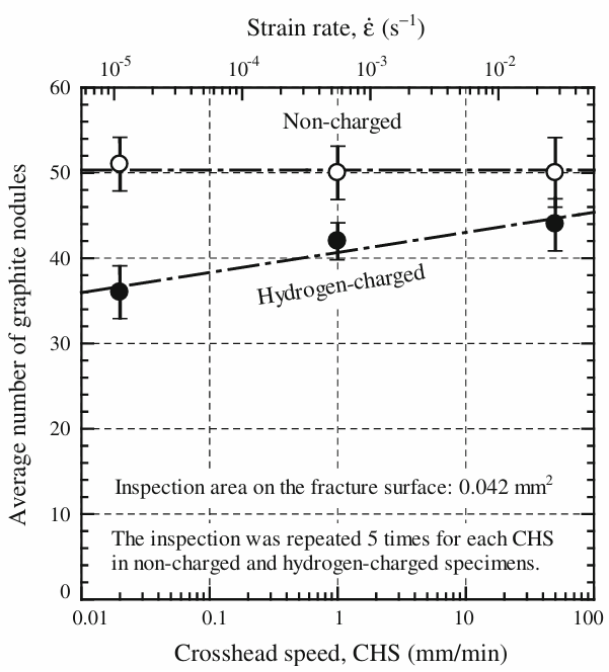

Figure 7-6 Numbers of graphite nodules that appeared in an inspection area on the fracture surface in the uncharged and the hydrogen-charged specimens [7,27]

In non-charged specimens, most of the graphite particles merged, resulting in typical ductile fracture behaviour. However, in hydrogen-charged specimens, the fracture process

included interconnected cracks forming between neighbouring graphite sites as shown in Figure 7-7.

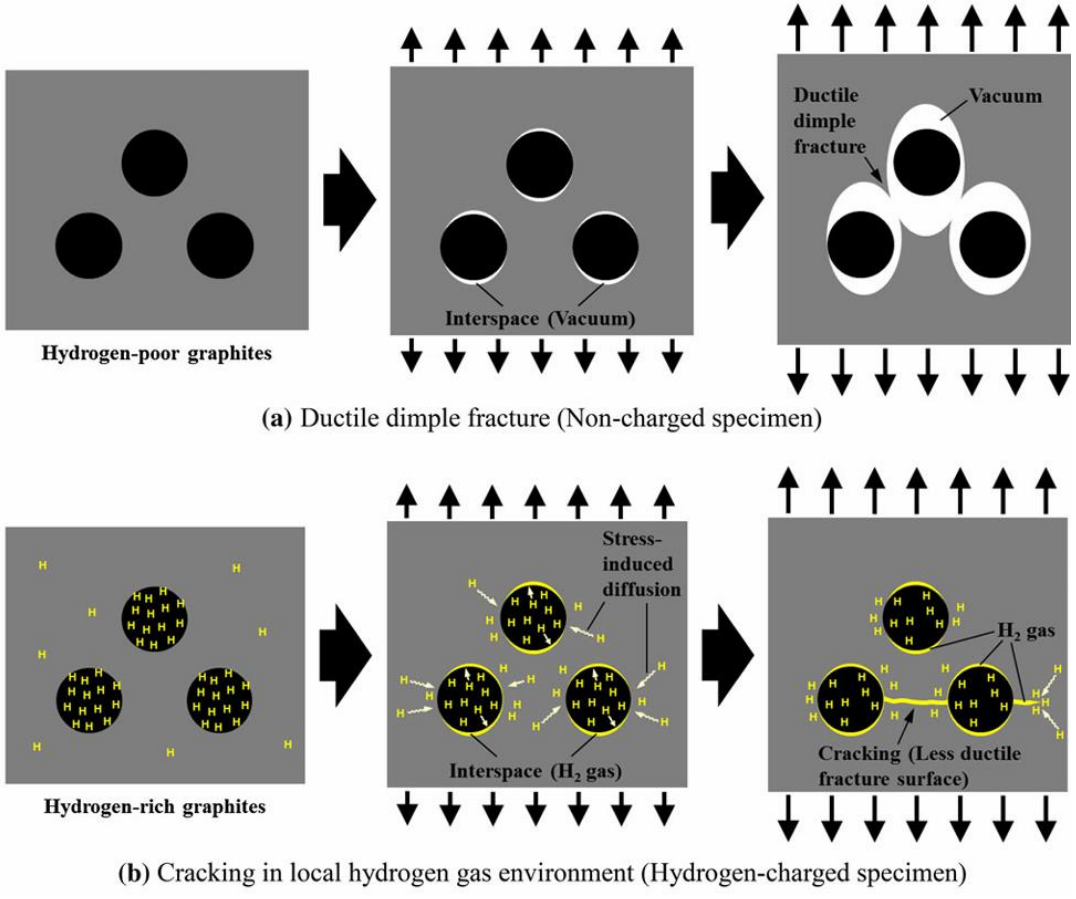

Figure 7-7 Two typical fracture processes in the non-charged and the hydrogen-charged cast iron specimens [7,27]

However, for cast iron specimens used in this research and summarized in Figure 7-3c, an increasing trend in the endurance limit was noted in the data. One possible explanation for this occurrence is the fact that graphite strongly traps hydrogen when held for prolonged periods at lower temperatures [28,29], thereby reducing the desorption process. This is also dependent on the size, shape, and distribution of the graphite flakes in the cast iron [30] in the degraded specimen. A uniform trend was observed in the fatigue properties of cast iron and these properties were consistent with the results found in the literature. It would have been better if a qualitative analysis of the fracture surfaces was done for fatigue failure surfaces. However, this will constitute part of the future works.

7.2.4 Hydrogen embrittlement of brass

It has been shown that the brass used in this research had a two-phase α/β-microstructure, pointing towards a more Zn-rich alloy composition [31]. Further analysis revealed darker

grains which were rich in copper ($> 58\%$) with zinc only about 35%. The lighter grains had a copper content of $> 51\%$ and more zinc of about $> 42\%$. This is a copper rich alloy, and the results will be compared with those of copper pipeline material.

Copper and its alloys generally resist hydrogen attack, but they can become vulnerable if they contain copper oxide [32]. The presence of copper oxide provides sites that facilitate hydrogen absorption, potentially leading to hydrogen embrittlement or other degradation processes. When oxygen-containing copper is heated in the presence of hydrogen or hydrogen-rich gases, hydrogen diffuses into the metal and reacts with the copper oxide. This reaction forms water, which turns to high-pressure steam at temperatures above 375°C (705°F). The steam molecules formed inside copper cannot diffuse through the solid metal and consequently force their way outward along the grain boundaries, causing a phenomenon known as hydrogen embrittlement [33–35]. The steam generates fissures within the metal, reducing its ductility and making it more prone to brittleness. Without these oxides, pure copper and its alloys maintain stability and are unaffected by hydrogen exposure, even in environments where other metals might suffer from hydrogen-related issues.

It is well known that hydrogen can be stored in a copper material at defects and structural inhomogeneities with the binding energies between the traps and hydrogen controlling if they contribute to degassing. For instance, the binding energy of an H atom in the copper lattice to a vacancy is calculated to be about 0.24eV and the type of trap is quite shallow but can bind many hydrogen atoms since 6 hydrogen atoms can be associated with each vacancy [6]. In copper, oxygen impurities create vacancies that act as deep traps, which can bind hydrogen atoms. This forms a stable trap for dissolved hydrogen, with a binding energy of approximately 1.23 eV. Since each hydrogen atom is bound to one oxygen atom, the number of these deep traps is directly related to the oxygen content in the copper. This binding mechanism involves atomic hydrogen specifically, where the vacancy-oxygen combination effectively captures and retains hydrogen, reducing its mobility within the copper lattice.

Electrochemical hydrogen charging of copper leads to a surface layer with increased hydrogen content. This layer is often around 50 µm thick, affecting only the outermost surface, leaving the bulk of the copper shell's mechanical properties intact [6]. Even with extensive charging, the hydrogen penetration depth is limited. In cases with large grain

sizes, the layer might extend to around 200 µm, which remains too shallow to compromise the structural integrity of the copper shell [36].

7.3 Fatigue results in conjunction with theories considered for application in the industry or described in the literature

For practical fatigue design purposes, this involves a systematic approach beginning with a clear definition of functional requirements and an understanding of the material properties. Critical areas and features that may influence the fatigue performance of the design product are identified, and the relevant design codes and standards are selected based on the industry and regulations. The potential load spectra over time of application are determined and the stress-life analysis is performed. Then appropriate safety factors are chosen to ensure a conservative approach to the potential unknowns during the lifespan in use. Fracture mechanics and probabilistic methods may be integrated for critical components. This process is iterative, with adjustments made based on results. Documentation and validation are crucial, and a regular inspection and maintenance program is implemented for ongoing monitoring and prevention of critical failures. This comprehensive approach ensures that fatigue design accounts for uncertainties and variations, leading to reliable and durable structures or components. In this section, some industry-used approaches are discussed in relation to the results obtained in the PhD research.

7.3.1 Fatigue properties of soaked specimens compared with lower 2-sigma or 3-sigma design curves of the uncharged scatter band.

According to the lower 2-sigma or 3-sigma design approach, as described in Refs. [37–40], a design curve is created by shifting the mean S-N curve within the stress range downwards by 2 or 3 times its standard deviation. The key question here is whether the data generated from the hydrogen-soaked specimens falls within or outside of the scatter band generated using the 2-sigma or 3-sigma approach. If the data falls within this scatter band, it suggests that the design approach is conservative when considering design applications for 20% hydrogen-blended natural gas. This, in turn, implies that there is no substantial impact on the fatigue properties due to hydrogen embrittlement (HE).

Consider the design equation defined as [37,38]:

$$\log N_{f,D} = C_0 + C_1 log\sigma_i - p.s \tag{7-1}$$

In this equation, $\log N_{f,D}$ is the log of the design life at a stress level σ_i. Here C_0 denotes the fatigue strength coefficient, and C_1 represents the inverse slope derived from test data. The standard deviation of the fatigue data set is denoted by s, and p takes values of either 1, 2 or 3 depending on the number of standard deviations the mean curve is shifted for design considerations. By using the uncharged specimens for each material in this research, the lower bound and the design curve with different values of p (1, 2, 3) can be generated.

Consider for instance the data set obtained from uncharged steel specimens, as illustrated in Figure 7-8. The Lower design curves have been plotted for different values of p (1, 2, 3). The data sets derived from charged steel specimens are superimposed on this graph to visually assess if these data points fall within the scatter band of the uncharged specimens. It is observed that the data set from specimens charged for five months exhibits inconsistencies compared to the rest of the data sets. The variance for this data set is significantly larger than for the other steel data sets. The researcher did not observe any changes in the display load profile during the testing of these specimens, nor a discernible trend in the results of this batch. This implies that the most plausible explanation is in the difference in the mechanical and physical properties of the specimens used during the five month soaking duration. Possible factors include varying degradation levels in the parent pipe from which the specimens were initially made, the presence of microstructural discontinuities, or the influence of environmental conditions on the parent material.

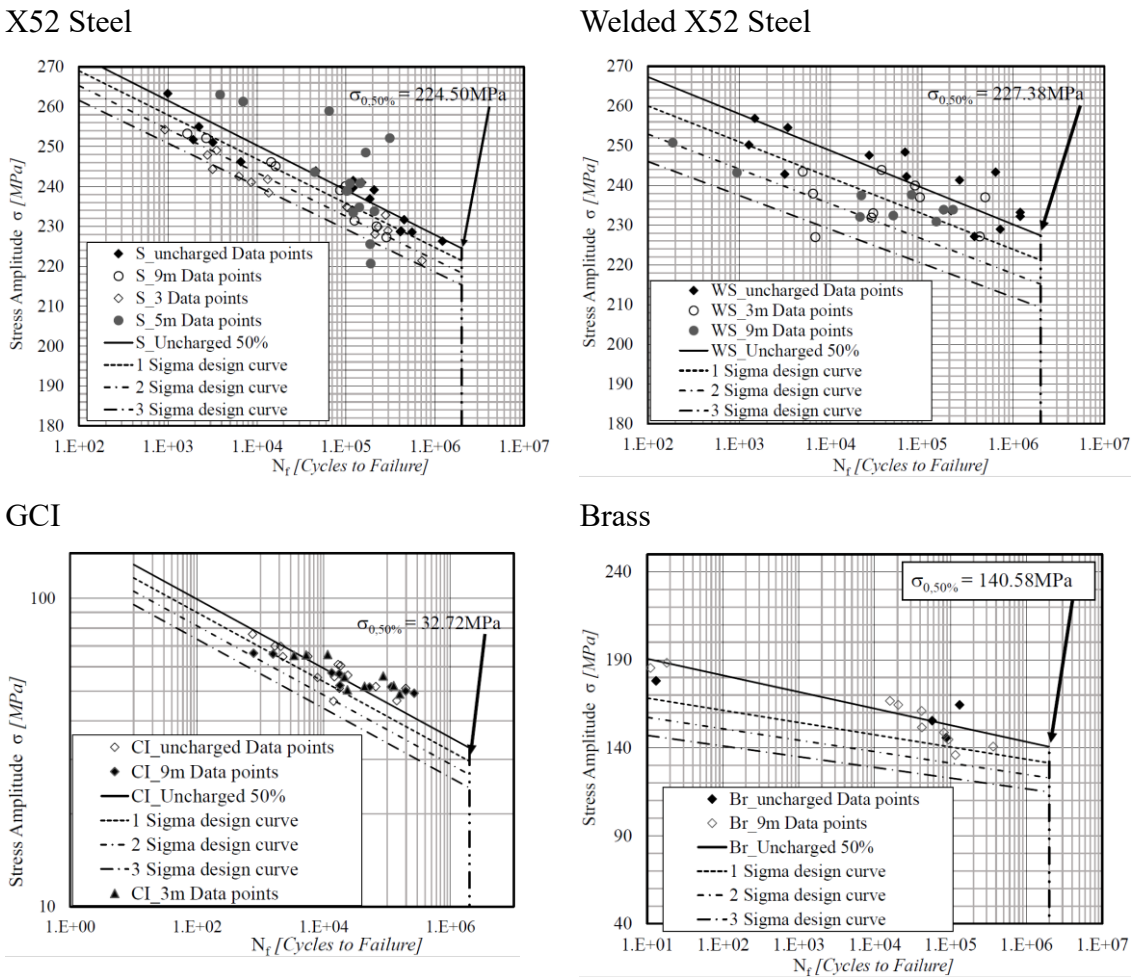

Figure 7-8 Lower 2-sigma or 3-sigma design curves for steel, welded X52 steel, GCI, and brass

It is seen from this graph for steel that not all the rest of the data points even lie in the conservative scatter band for p=3. If other factors for loading, surface finish, environment, and reliability factor of safety are applied to this design curve, all the points.

Considering the welded steel specimens, the data set from specimens soaked for three months exhibits distinct characteristics compared to the other data sets. Some specimens displayed visual discontinuities, as previously explained and when these individual specimens were excluded from the data from the cracked specimens in the analysis, it was observed that the highly conservative scatter band, approximating a 3-sigma design curve, contains all data points from the other specimens, with only a very few data points falling below the S-N design curves. Based on visual inspection, it can be inferred that if the data points from charged welded specimens fall within the scatter band of the uncharged specimens, there are no significant changes in the fatigue properties of welded steel

specimens. This aligns with the conclusion drawn using statistical significance in the previous chapter.

In the context of cast iron, all data points consistently surpass the design curves for 2 and 3 sigma, with the endurance limit exhibiting an upward trend as the soaking time extends. Designing based on uncharged cast iron specimens appears to be a secure approach for accommodating data from different soaking durations. Visual assessments therefore affirm that there is no noticeable alteration in the fatigue properties of the cast iron used in this research.

For the brass specimens, it's important to note the limitation of only having two data sets, which may render the analysis less reliable. The available data, however, show that both data sets fall within the design curves for 2 and 3 sigma. The endurance limit tends to decrease with prolonged soaking time. While the limited data set introduces some uncertainty, however, the visual inspection suggests that there was no significant change in the fatigue properties of brass in this research. This also aligns with the conclusion using statistical approaches.

7.3.2 Considering the fully corrected endurance limit

The examination of the plots of charged specimens with uncharged specimens reveals that the data points from the soaked specimens predominantly fall within the scatter band of the uncharged specimens. Introducing additional safety factors would effectively shift the design curve farther away from the mean S-N curve for uncharged specimens, resulting in highly conservative scatter bands that account for the observed variations in the scattering of the tested specimens. According to Marin's equation, some of the correction factors are estimated based on the conditions of the specimen or component [41,42]. These are estimated as:

$$S_e = k_a k_b k_c k_d k_e k_f \grave{s_e} s_e \tag{7-2}$$

where

k_a = surface condition modification factor

k_b= size modification factor

k_c = load modification factor

k_d = temperature modification factor

k_e = reliability factor

k_f = miscellaneous-effects modification factor

$s_e^{`}$ = rotary-beam test specimen endurance limit

s_e = endurance limit at the critical location of a machine part in the geometry and condition of use

In the realm of fatigue design, modifications to the endurance limit can be implemented through both subtractive and multiplicative corrections. These adjustments serve to accommodate diverse factors influencing the fatigue performance of a material in varied conditions. The outcome of these corrections manifests as scatter bands with a notably conservative nature, encompassing all the data points derived from the materials analysed in this research.

7.3.3 Do the endurance limits from soaked specimens fall in the 95% confidence interval of the uncharged specimens?

Assume that the endurance limit from the uncharged specimens is the mean endurance limit for each material. Defining the confidence interval as

$$Confidence\ interval\ (\sigma_0) = \bar{\sigma}_0 \pm (Z \times \frac{s_\sigma}{\sqrt{n}}) \tag{7-3}$$

In which $\bar{\sigma}_0$ is the endurance limit of the uncharged specimen, Z is the Z-score associated with the desired confidence level (e.g., for a 95% confidence interval, Z≈1.96), s_σ is the standard deviation observed in the endurance limits and n the number of fatigue data sets considered. This approach allows for an assessment to determine whether the endurance limits derived from the soaked specimens align with the scatter band of the uncharged specimens. If this alignment occurs, it provides a basis to conclude, with a 95% confidence level, that there has been no significant alteration in the fatigue properties under the specific conditions investigated in this research.

By example the graphs illustrated in Figure 7-9 for steel, it becomes evident that, except for the specimens charged for 5 months, the endurance limits of the other specimens align within the scatter band of the uncharged specimens. As previously discussed in the results analysis chapter, it is suggested that this particular batch of specimens may possess distinct properties compared to the others utilized in this research. The scatter band theory further validates the differences observed in the properties of these specimens in relation to the others investigated.

For cast iron specimens, all the endurance limits of the hydrogen charged specimens fall

within the 95% scatter band of uncharged specimens. According to this schematisation, it suggests that there is no apparent change in the fatigue properties of cast iron. Although the endurance limit for specimens charged for nine months exhibited a 30% increase, this further suggests that designing with a lower consideration of endurance limit results in a very conservative and therefore safer design approach.

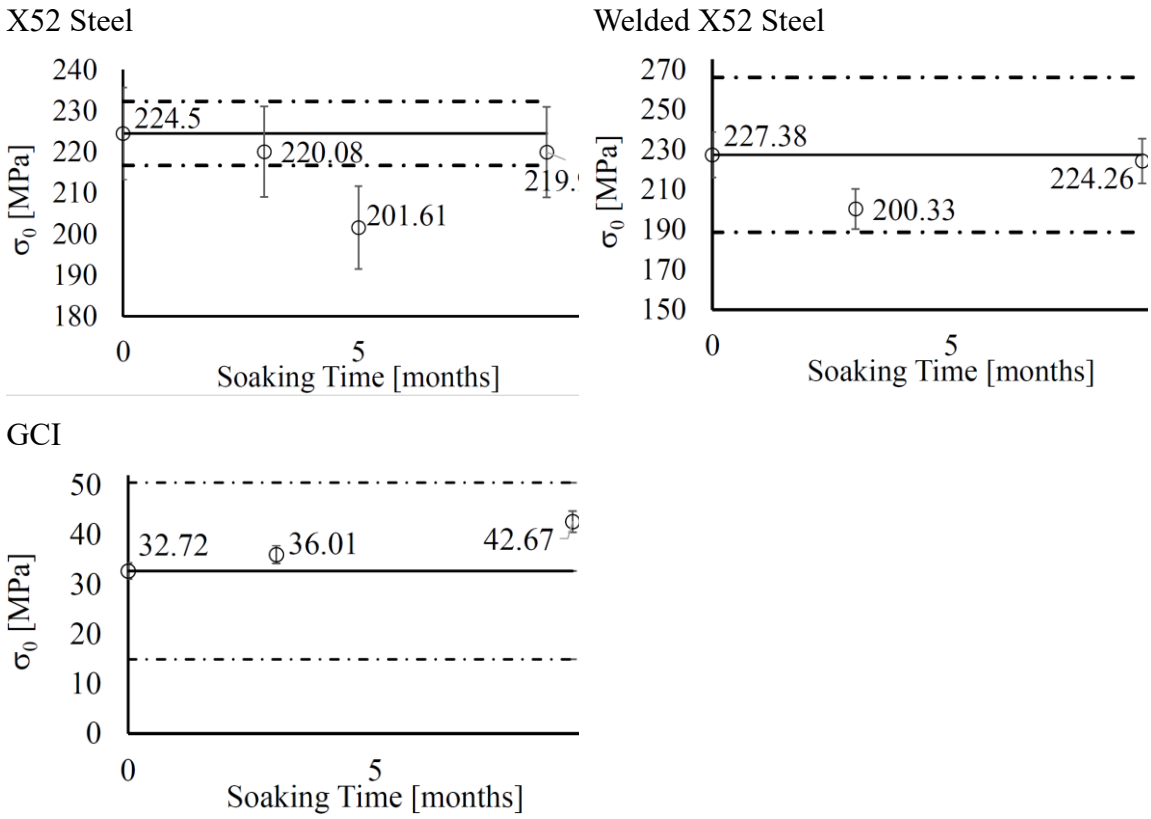

Figure 7-9 Endurance limit with 5% vertical error bands and 95% confidence interval of uncharged specimens

This analysis was not conducted for brass specimens due to the limitations in the number of data sets available in this research. Brass specimens were only charged for nine months, and statistical significance tests indicated insignificance in the data and its data set fell in the scatter band of the uncharged specimens. Furthermore, the fatigue properties of the tested specimens aligned with some of the grade cast iron data found in the literature.

7.3.4 What is the basis of choosing a design curve (compare with the target curve as recommended by TWI for welded joints

While the IIW recommends validating a particular design with limited fatigue data sets by comparing the design curve to existing design classes, provided the standard deviation of

the log of fatigue life is known, this approach has its limitations. For instance, when designing welded joints using an inverse slope of 3, this value must fall within the confidence interval of the slope generated from the test data. Additionally, the standard deviation of the fatigue life should align with that of the target design class. However, while this method yields conservative design approaches for welded joints due to the influences of weld characteristics and processes on its fatigue properties, its applicability to other materials remains unproven. Adopting a fixed inverse slope introduces the challenge of assuming uniform fatigue behaviour across all materials, which may not reflect reality. Consequently, using a fixed slope value may not accurately capture the fatigue response of different materials or loading conditions, potentially leading to inaccurate predictions and unsafe designs in engineering applications.

7.3.5 Choosing a statistical distribution of fatigue data

To estimate whether a distribution can describe the fatigue life data better, the correlation coefficient r is applied. The correlation coefficient r is defined as [43,44]

$$r = \frac{\sum_{i=1}^{n}(\sigma_i - \bar{\sigma})\,(N_i - \bar{N})}{\sqrt{\sum_{i=1}^{n}(\sigma_i - \bar{\sigma})^2 \sum_{i=1}^{n}(N_i - \bar{N})^2}} \tag{7-4}$$

Notably, $|r| \leq 1$ and a good correlation can be affirmed between variable σ and N_f if |r| is close to one. Consequently, the better fitting of distribution can be determined by comparing the r values. Usually, the larger the sample sizes are, the more precise the fitting results are.

Only a few specimens were used in the fatigue experiments at each given stress level because of the high cost. Consequently, it would have been necessary to determine a threshold value for r under different sample sizes and confidence levels. This correlation coefficient has been defined in the previous chapter and should be predefined a priori. The values derived from the materials analyzed in this study have consistently approached a value of 1. This indicates a strong association and suggests that the assumptions regarding the lognormal distribution of fatigue data in real-world operating conditions are accurately represented by the findings of this research.

7.3.6 Comparing industry design factor of safety and the probabilistic design curve

The factor of safety f_s in safe design against fatigue is a critical parameter that ensures the reliability and durability of a structure or component. It is calculated to provide a margin of safety between the expected loading conditions and the endurance limit in fatigue design. According to Ref [45], designing for fatigue safety involves incorporating a safety margin either on the stress field or the anticipated number of cycles until failure. Certain engineering standards dictate a safety factor of 10 for the number of cycles until failure and a safety factor of 2 for the stress field. The factor of safety f_s is calculated as:

$$f_s = \frac{\sigma_{50\%}}{\sigma_{(1-P)\%}} \tag{7-5}$$

In which $\sigma_{(1-P)\%}$ is the design stress level at a probability of survival. In this doctoral research, the calculated factor of safety equals half the scatter band applied to each of the materials. Across all materials investigated in this study, this figure notably falls below 2, which is the standard factor of safety employed in industry practices. This observation underscores the conservative nature of the industry approach, as the design curves derived from specimens subjected to hydrogen charging remain within the industry's designated factor of safety. Based on this design methodology, it can be inferred that using ex-service materials for transporting blended gas is deemed safe. This conclusion stems from the fact that the design curves generated from the research fall comfortably within the conservative band established by employing a design safety factor of 2.

7.4 Technical Research Challenges

This section examines the possible hurdles and complexities encountered while undertaking the collection of the fatigue data within this research. These obstacles stemming from various sources if not planned to mitigate against had the potential of significantly influencing the integrity of the results of the investigation. Some of the challenges that were observed by the researcher included:

7.4.1 Specimen hydrogen content

These specimens were placed within high-pressure tubes filled with hydrogen for varying durations. The hydrogen was allowed to diffuse into these specimens naturally. However, this setup did not accurately replicate the environment that gas pipeline materials typically encounter during normal operation. In reality, blended natural gas flows steadily through pipelines at a designated gas pressure and velocity, with only the inner portion of the pipe

coming into contact with the blended gas. Consequently, it's plausible that the rate of hydrogen diffusion into the pipeline material, which is partly dependent on these factors could lead to the amount of hydrogen embrittlement. However, the adopted hydrogen soaking approach used in this research is far worse than the real-life approach and therefore should produce results that are very conservative to real life experiences. To maintain gas pressure along transmission networks, substations are typically positioned at intervals. These substations serve to re-pressurize the system in the event of pressure drops from the initial source. This variation in gas pressure during real-life transportation processes highlights the significant influence of pressure on hydrogen embrittlement rates.

Similarly, quantifying the amount of hydrogen absorbed in each specimen proved challenging. This difficulty stemmed from the unknown rate at which hydrogen diffused into the specimens, which was not apparent to the researcher and varied depending on the degree of degradation of the pipeline material. To address this uncertainty, all specimens were exposed to the hydrogen environment for an identical duration. Furthermore, the specimens were sourced from ex-service pipelines and it is well-established that pipeline materials degrade over time due to usage, with the extent of degradation influenced by numerous factors, including environmental conditions. Given these circumstances, it was impossible to ascertain beforehand whether all specimens had undergone an equivalent level of degradation. However, the specimens were extracted from sections of the pipeline material located in close proximity to each other approximately the same level of degradation in the specimens.

The specimens were retrieved from the testing environment and stored in cryonic conditions to prevent the diffusion of absorbed hydrogen during the fatigue tests. Upon retrieval, each specimen underwent a rinsing process under tap water to return to room temperature for safe handling. Efforts were made to minimize the time taken for measurements and loading onto the fatigue machine. An unanswered question remains regarding whether this process impacted the amount of hydrogen remaining in the specimen before testing. Nevertheless, every specimen treated with hydrogen followed this procedure, ensuring uniformity of treatment. A potential solution to this uncertainty would be to conduct future fatigue tests within a hydrogen environment.

7.4.2 The grip jaws of the fatigue machine

The jaws of the multipurpose servo-hydraulic universal testing machine series LFV-25KN were secured by multiple fastening nuts and grip screws. Consequently, the grip jaws exhibited a degree of looseness, potentially resulting in minor misalignments. Such misalignments could significantly impact the stress distribution on the test sample. Furthermore, it was observed that tightening each of the nut and grip screws resulted in slight preloads being applied to the test specimen. Special attention was dedicated to this aspect during each loading condition to minimize these preloads. The figure below illustrates this grip jaw configuration alongside an example of a misaligned specimen.

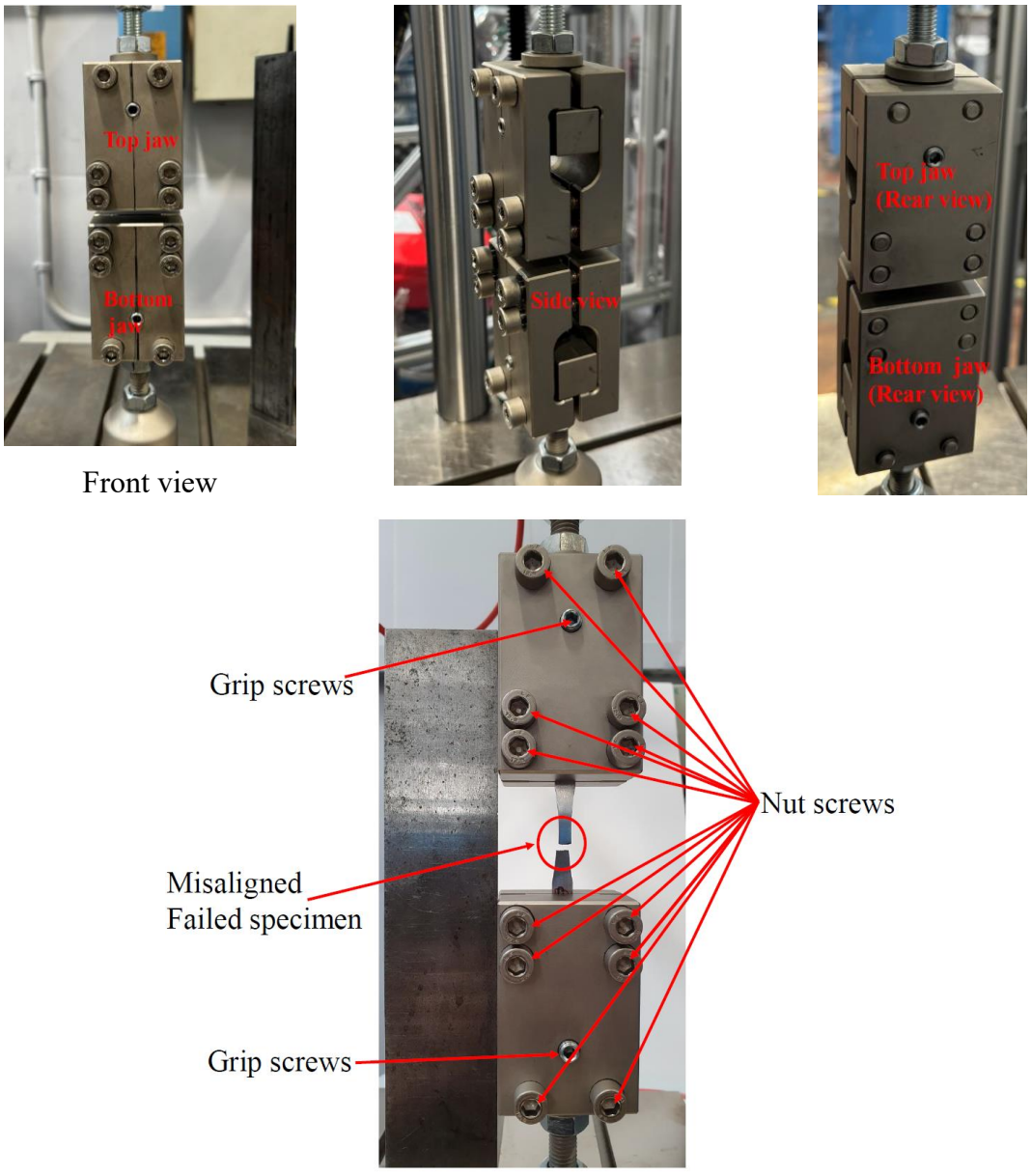

Figure 7-10 Physiology of grip jaws and misaligned specimen after failure

To address the issue of misalignment during loading, a spirit level laser was employed to detect and rectify potential misalignments in a loaded specimen prior to initiating the fatigue test as described in Chapter 4.

7.4.3 Sample and Data Collection

The quantity of specimens used in this research potentially influenced the quality and reliability of the results obtained. While the sample size for certain specimens was deemed adequate, others fell short of this standard. Nonetheless, for research and development (R&D), the findings presented serve as a foundational platform for future investigations with a larger sample size. Expanding the sample set in subsequent studies could provide deeper insights and enhance the robustness of the results. This approach would allow for a more comprehensive examination of the fatigue properties of repurposing pipeline material, thereby facilitating a clearer understanding of the observed trends and phenomena. Thus, while acknowledging the limitations imposed by the sample size in this study, the results offer valuable groundwork for further exploration and refinement.

7.4.4 Size and scale factor by specimen configuration

This pertains to the dimensions and proportions of the test specimens employed in the experimentation process. The physical dimensions of the specimen could significantly influence the outcomes of fatigue tests, as larger specimens may manifest different mechanical behaviours compared to smaller ones. The scale factor is linked to the ratio between the dimensions of the specimen and those of the actual pipelines used in the industry. This discrepancy became apparent in the results obtained from this research when compared to data from the literature. The choice of specimen geometry was based on the available machinery for testing while adhering to standardized procedures. Unfortunately, these aspects were beyond the control of the researcher. However, the application of confidence intervals in handling the fatigue results accommodated these challenges stemming from the size and scale factor issue.

7.4.5 Scope of the HyDeploy Steering Committee

The steering committee led by Cadent [46–48] and with the various representatives from the project partners (Northern Gas Network, Progressive Energy, Bespoke Research and Consultancy HSE, Keele University, and ITM Power Energy Storage Clean Fuel) comprised of industry specialists and consultants whose invaluable insights profoundly shaped the direction of this research [47]. Their guidance played an indispensable role in

steering the realisation of this PhD research work and the overall success of the HyDeploy project towards fruition. However, their significant influence also meant that the scope and trajectory of this research were confined to the committee's specifications. While this focus aimed to yield results directly applicable to industrial needs, it concurrently posed the risk of narrowing the research's broader perspective and potential impact.

7.5 Conclusion

Following an overview of various challenges encountered during this PhD research and a thorough examination of the strategies employed to overcome them and yield results, the subsequent chapter will present a summary of the conclusions reached.

7.6 References

[1] C. Zhou, X. Chen, Z. Wang, S. Zheng, X. Li, L. Zhang, Effects of environmental conditions on hydrogen permeation of X52 pipeline steel exposed to high H2S-containing solutions, Corros. Sci. 89 (2014) 30–37. https://doi.org/10.1016/j.corsci.2014.07.061.

[2] Q. Li, H. Ghadiani, V. Jalilvand, T. Alam, Z. Farhat, M.A. Islam, Hydrogen Impact: A Review on Diffusibility, Embrittlement Mechanisms, and Characterization, Materials (Basel). 17 (2024). https://doi.org/10.3390/ma17040965.

[3] H.J. Wan, X.Q. Wu, H.L. Ming, J.Q. Wang, E.H. Han, Effects of Hydrogen Charging Time and Pressure on the Hydrogen Embrittlement Susceptibility of X52 Pipeline Steel Material, Acta Metall. Sin. (English Lett. 37 (2024) 293–307. https://doi.org/10.1007/s40195-023-01625-5.

[4] S.K. Sharma, S. Maheshwari, A review on welding of high strength oil and gas pipeline steels, J. Nat. Gas Sci. Eng. 38 (2017) 203–217. https://doi.org/10.1016/j.jngse.2016.12.039.

[5] D. Sobola, R. Dallaev, Exploring Hydrogen Embrittlement: Mechanisms, Consequences, and Advances in Metal Science, Energies. 17 (2024) 2972. https://doi.org/10.3390/en17122972.

[6] R. Sandström, The role of hydrogen in copper, Memo 2014-01-27 Contain. Doc. to Be Used in Response to Issues Brought up by SSM. (2014) 1–16.

[7] H. Matsunaga, T. Usuda, K. Yanase, M. Endo, Ductility loss in ductile cast iron with internal hydrogen, Metall. Mater. Trans. A Phys. Metall. Mater. Sci. 45 (2014) 1315–1326. https://doi.org/10.1007/s11661-013-2109-9.

[8] Y. Ogawa, H. Matsunaga, J. Yamabe, M. Yoshikawa, S. Matsuoka, Unified evaluation of hydrogen-induced crack growth in fatigue tests and fracture toughness tests of carbon steel, Int. J. Fatigue. 103 (2017) 223–233. https://doi.org/10.1016/j.ijfatigue.2017.06.006.

[9] Y. Ogawa, H. Matsunaga, J. Yamabe, M. Yoshikawa, S. Matsuoka, the Fatigue limit of carbon and Cr–Mo steels as a small fatigue crack threshold in high-pressure hydrogen gas, Int. J. Hydrogen Energy. 43 (2018) 20133–20142. https://doi.org/10.1016/j.ijhydene.2018.09.026.

[10] A. Turnbull, Perspectives on hydrogen uptake, diffusion and trapping, Int. J. Hydrogen Energy. 40 (2015) 16961–16970. https://doi.org/10.1016/j.ijhydene.2015.06.147.

[11] A. Turnbull, Hydrogen diffusion and trapping in metals, in Gaseous Hydrog. Embrittlement Mater. Energy Technol., Elsevier, 2012: pp. 89–128. https://doi.org/10.1533/9780857095374.1.89.

[12] B.P. Somerday, P. Sofronis, K.A. Nibur, C. San Marchi, R. Kirchheim, Elucidating the variables affecting accelerated fatigue crack growth of steels in hydrogen gas with low oxygen concentrations, Acta Mater. 61 (2013) 6153–6170. https://doi.org/10.1016/j.actamat.2013.07.001.

[13] J.A. Ronevich, B.P. Somerday, C.W. San Marchi, Effects of microstructure banding on hydrogen assisted fatigue crack growth in X65 pipeline steels, Int. J. Fatigue. 82 (2016) 497–504. https://doi.org/10.1016/j.ijfatigue.2015.09.004.

[14] Y. Sun, Y. Frank Cheng, Hydrogen-induced degradation of high-strength steel pipeline welds: A critical review, Eng. Fail. Anal. 133 (2022). https://doi.org/10.1016/j.engfailanal.2021.105985.

[15] Y. Sun, Y.F. Cheng, Hydrogen permeation and distribution at a high-strength X80 steel weld under stressing conditions and the implication on pipeline failure, Int. J. Hydrogen Energy. 46 (2021) 23100–23112. https://doi.org/10.1016/j.ijhydene.2021.04.115.

[16] J. Ban, X. Yan, B. Song, S. Deng, H. Wu, Y. Tang, W. Yin, Research Progress and Prospects on Hydrogen Damage in Welds of Hydrogen-Blended Natural Gas Pipelines, Processes. 11 (2023). https://doi.org/10.3390/pr11113180.

[17] D.E. Jiang, E.A. Carter, Diffusion of interstitial hydrogen into and through bcc Fe from first principles, Phys. Rev. B - Condens. Matter Mater. Phys. 70 (2004). https://doi.org/10.1103/PhysRevB.70.064102.

[18] T. Hickel, R. Nazarov, E.J. McEniry, G. Leyson, B. Grabowski, J. Neugebauer, Ab initio based understanding of the segregation and diffusion mechanisms of hydrogen in steels, Jom. 66 (2014) 1399–1405. https://doi.org/10.1007/s11837-014-1055-3.

[19] G.M. Pressouyre, A classification of hydrogen traps in steel, Metall. Trans. A. 10 (1979) 1571–1573. https://doi.org/10.1007/BF02812023.

[20] N. Boes, H. Züchner, Electrochemical methods for studying diffusion, permeation and solubility of hydrogen in metals, J. Less-Common Met. 49 (1976) 223–240. https://doi.org/10.1016/0022-5088(76)90037-0.

[21] T.T. Nguyen, N. Tak, J. Park, S.H. Nahm, U.B. Beak, Hydrogen embrittlement susceptibility of X70 pipeline steel weld under a low partial hydrogen environment, Int. J. Hydrogen Energy. 45 (2020) 23739–23753. https://doi.org/10.1016/j.ijhydene.2020.06.199.

[22] L.A. Hughes, B.P. Somerday, D.K. Balch, C. San Marchi, Hydrogen compatibility of austenitic stainless steel tubing and orbital tube welds, in Int. J. Hydrogen Energy, Elsevier Ltd, 2014: pp. 20585–20590. https://doi.org/10.1016/j.ijhydene.2014.03.229.

[23] Y. Yang, L. Shi, Z. Xu, H. Lu, X. Chen, X. Wang, Fracture toughness of the materials in the welded joint of X80 pipeline steel, Eng. Fract. Mech. 148 (2015) 337–349. https://doi.org/10.1016/j.engfracmech.2015.07.061.

[24] A. Díaz, I.I. Cuesta, E. Martinez-Pañeda, J.M. Alegre, Analysis of hydrogen permeation tests considering two different modelling approaches for grain boundary trapping in iron, Int. J. Fract. 223 (2020) 17–35. https://doi.org/10.1007/s10704-019-00411-8.

[25] T. Yoshimoto, T. Matsuo, T. Ikeda, The effect of graphite size on hydrogen absorption and tensile properties of ferritic ductile cast iron, Procedia Struct. Integr. 14 (2019) 18–25. https://doi.org/10.1016/j.prostr.2019.05.004.

[26] P. Sahiluoma, Y. Yagodzinskyy, A. Forsström, H. Hänninen, S. Bossuyt, Hydrogen embrittlement of nodular cast iron, Mater. Corros. 72 (2021) 245–254. https://doi.org/10.1002/maco.202011682.

[27] H. Matsunaga, T. Usuda, K. Yanase, M. Endo, Ductility loss in Hydrogen-charged Ductile Cast Iron, Beijing, 2013.

[28] K. Takai, Y. Chiba, K. Noguchi, A. Nozue, Visualization of the hydrogen desorption process from ferrite, pearlite, and graphite by secondary ion mass spectrometry, Metall. Mater. Trans. A Phys. Metall. Mater. Sci. 33 (2002) 2659–2665. https://doi.org/10.1007/s11661-002-0387-8.

[29] V. Alander, Fatigue and fracture aspects of spherical cast iron in hydrogenous environment: Tampere, 2024.

[30] N. Meyer, A. Fatemi, S. McCutcheon, B. Havard, W. Fairchilds, Fatigue Behavior of Cast Iron Including Mean Stress Effects, SAE Int. J. Mater. Manuf. 8 (2015) 2015-01–0544. https://doi.org/10.4271/2015-01-0544.

[31] D. Engelberg, F. Scenini, Y. Zhou, J. Duff, HyDeploy2 –Materials Analysis & Testing, 2023.

[32] A. Cohen, Corrosion of Copper and Copper Alloys, in: S.D. Cramer, B.S. Covino Jr (Eds.), Corros. Mater., ASM International, 2005: pp. 125–163. https://doi.org/10.31399/asm.hb.v13b.a0003816.

[33] T.W. Pelletiers, W.K. Daye, Production of Copper and Copper Alloy Powders, in Powder Metall., ASM International, 2015: pp. 544–554. https://doi.org/10.31399/asm.hb.v07.a0006139.

[34] W.T. Becker, R.J. Shipley, Hydrogen Damage and Embrittlement, in Fail. Anal. Prev., ASM International, Tennessee, 2002: pp. 809–822. https://doi.org/10.31399/asm.hb.v11.a0003552.

[35] B. Craig, Hydrogen Damage, in: S.D. Cramer, B.S. Covino Jr (Eds.), Corros. Fundam. Testing, Prot., ASM International, 2003: pp. 367–380. https://doi.org/10.31399/asm.hb.v13a.a0003634.

[36] Å. Martinsson, R. Sandström, C. Lilja, Hydrogen in oxygen-free, phosphorus-doped copper: charging techniques, hydrogen contents and modelling of hydrogen diffusion and depth profile, (2013).

[37] C.L. Shen, P.H. Wirsching, G. T. Cashman, Design curve to characterize fatigue strength, J. Eng. Mater. Technol. Trans. ASME. 118 (1996) 535–541. https://doi.org/10.1115/1.2805953.

[38] Y.-L. Lee, J. Pan, R.B. Hathaway, M.E. Barkey, Fatigue testing and analysis : theory and practice, Elsevier Butterworth-Heinemann., Amsterdam ; Boston: 2005.

[39] L. Tanner, S. Collier, H.F. Dodge, R.J. Hader, G.J. Lieberman, W.. Youden, ASTM MANUAL ON FITTING STRAIGHT LINES, Prentice Hall Inc. Englewood Cliffs, N.J, 1959.

[40] STP46393S, ASTM Manual on Fitting Straight Lines, ASTM Man. Fitting Straight Lines. (2009) 1-1–28. https://doi.org/10.1520/stp46393s.

[41] R.G. Budynas, N.K. J, Shigley's Mechanical Engineering Design, Ninth, The McGraw-Hill Companies, New York, 2011.

[42] G.H. Farrahi, H. Ghadbeigi, An investigation into the effect of various surface treatments on fatigue life of tool steel, J. Mater. Process. Technol. 174 (2006) 318–324. https://doi.org/10.1016/j.jmatprotec.2006.01.014.

[43] Y. Feng, C. Gao, Y. He, T. An, C. Fan, H. Zhang, Investigation on tension-tension fatigue performances and reliability fatigue life of T700/MTM46 composite laminates, Compos. Struct. 136 (2016) 64–74. https://doi.org/10.1016/j.compstruct.2015.09.057.

[44] F. Campbell, Fatigue and Fracture, Understanding The Basics, ASM International, Materials Park, Ohio, 2012.

[45] C. Tsiklios, M. Hermesmann, T.E. Müller, Hydrogen transport in large-scale transmission pipeline networks: Thermodynamic and environmental assessment of repurposed and new pipeline configurations, Appl. Energy. 327 (2022). https://doi.org/10.1016/j.apenergy.2022.120097.

[46] HyDeploy FAQs, About HyDeploy, Who Is Involv. HyDeploy? (n.d.). https://hydeploy.co.uk/faqs/who-is-involved-in-hydeploy/ (accessed January 19, 2024).

[47] HyDeploy 2024, Pioneering the safe use of blended hydrogen in gas networks to reduce carbon emissions, (2017). https://hydeploy.co.uk (accessed April 5, 2023).

[48] HyDeploy, Pioneering the safe use of blended hydrogen in gas networks to reduce carbon emissions., Online. (n.d.). https://hydeploy.co.uk/ (accessed December 19, 2023).

Chapter 8

Conclusions and Recommendations for Future Work

8.1 Introduction

The primary objective of this research was to quantify the alterations in the fatigue properties of ex-service X52 steel, ex-service X52 welded steel, ex-service grey cast iron, and ex-service brass resulting from both their degradation over time in use and exposure to a hydrogen environment. To achieve this goal, specimens sourced from ex-service pipeline materials were obtained from the industry and subjected to a hydrogen environment before undergoing fatigue testing. Following testing, standardized approaches were employed to post-process the fatigue data sets, enabling the determination of their fatigue properties. Subsequently, these fatigue properties were compared with those documented in the

literature. Notably, a statistical significance test was introduced and validated using fatigue data sets from notched specimens and cross-validated with fatigue data from previous studies. This validated significance test was then applied to the fatigue data obtained from hydrogen-soaked plain specimens and compared with data from unsoaked plain specimens. This comparison aimed to ascertain whether the observed changes in the fatigue data sets were merely due to random errors or were primarily attributed to exposure to a hydrogen environment.

The driving motive of this research has been to contribute to the safe implementation of the delivery of hydrogen blended natural gas in the HyDeploy project in the UK. This concluding chapter will therefore make a comprehensive analysis and synthesis of the fatigue results obtained from this research centered on the fatigue properties of ex-service pipeline materials. The suggested hydrogen environment consisted of a pressurized hydrogen gas of about 8 bars and the researched materials were tested for fatigue life of up to 2 million cycles under uniaxial cyclic loading conditions in tension. These investigations have provided critical insights essential for enhancing the integrity and longevity of pipeline infrastructures that are intended to transport hydrogen-blended natural gas as explained in the HyDeploy project. Building upon the foundations laid in preceding chapters, this section consolidates the key observations and defines pathways for future research endeavours aimed at advancing the understanding of fatigue mechanisms in ex-service pipeline materials. This chapter also aims to continue to contribute significantly to the ongoing discourse surrounding pipeline integrity management and structural resilience in the face of hydrogen embrittlement in green energy projects.

8.2 Conclusions

After this project, all objectives were achieved, and the primary aims of this thesis were realized. The main conclusions drawn from this project are summarized below:

1) The fatigue properties, particularly the endurance limit of ex-service pipeline material charged with hydrogen gas under 8 bar pressure after 2 million cycles when tested in tension, differ from uncharged materials. However, the change in the endurance limit falls within the scatter band of the design paradigm of the existing network. This indicates that the present natural gas distribution network in the UK can operate safely if hydrogen gas at 8 bar pressure is introduced into the system. Current engineering standards dictate a safety factor of 10 for the number of cycles

until failure and a safety factor of 2 for the stress field. The calculated factor of safety equals half the scatter band of the approaches applied to each of the materials in this research. The safety factor extracted from the design curves suggested in this study is less than 2, which is the standard factor of safety employed in industry practices. This observation underscores the conservative nature of the industry approach, as the design curves derived from specimens subjected to hydrogen charging remain within the industry's designated factor of safety. Based on this design methodology, it can be inferred that repurposing ex-service materials for transporting blended gas is deemed safe. This conclusion stems from the fact that the design curves generated from the research fall comfortably within the conservative band established by employing a design safety factor of 2.

2) Parametric statistical analysis can detect very small changes in fatigue data sets based on a predefined level of significance. When consistently applied, this approach is capable of identifying variations in fatigue data from different geometries without considering its root radius. It successfully identified differences in the fatigue properties of notched specimen geometries that differed by only 1 mm in root radius. This procedure was validated and therefore provides an alternative method to monitor the effect of geometry on structures without directly measuring the root radius of the geometry involved.
3) While the statistical significance test method proves adept at detecting even subtle changes in the data sets used, a challenge arises in determining the significance of such changes, especially when monitoring the percentage change in the endurance limit. Nevertheless, this approach remains valuable, provided a well-defined level of significance is employed, allowing for a better understanding of the impact of hydrogen exposure on the metals' fatigue properties.
4) In estimating design curves in MCF, the IIW approach is the most non-conservative approach and would reduce any chance of overdesign when compared to the other approaches. It is very applicable for sustainable components and the design curve in this case is dependent on the characteristics of the data, in particular the sample size and its spread.
5) The ASTM standardized method to post-process fatigue data sets is the most sensitive to the spread of the fatigue data sets. This approach is very conservative and would be very useful for critical design.

6) The simplest-to-use approach to construct a design curve in MCF is the linear regression method and the empirical constants corresponding to sample sizes are also defined in the ASTM standards for fatigue distributions with assumed shapes. In particular, this approach is not limited by the sample size of the data set, the assumptions under which the approach is applicable have to be meticulously examined to produce practical design curves.

Currently pipeline materials undergo degradation over use depending on a list of factors and are currently inspected and replaced over time. Surprisingly the level of degradation of these pipeline materials is not quantified over time. To date, replacement or maintenance schedules for pipelines in a hydrogen gas network vary depending on several factors, including regulatory requirements, industry standards, the specific type of pipeline material used, environmental conditions, and the overall condition of the pipeline infrastructure. Continuous inspection and end-of-life design recommendations are the sole driving factors.

7) It is essential to consider the correlation coefficient threshold aspect when utilizing the data sets for design purposes, as it provides valuable insight into the reliability and consistency across the industry.

8.3 Recommendation for future work

With the popularity of hydrogen as an alternative energy source growing, the construction and planning of hydrogen pipelines for transporting gas are underway, and the study of pipeline fault diagnosis, maintenance, and fatigue issues is becoming particularly important and prominent. The UK has an extensive network of natural gas pipelines; however, there remain significant engineering challenges in safely transporting blended natural gas using the existing UK gas transmission pipelines. The results from this research will help address some of the challenges involved in using the existing network to transport blended natural gas due to hydrogen embrittlement. Based on the work carried out in this thesis, recommendations for future work are provided below.

8.3.1 Investigate the fatigue limit of notches

Most fatigue failures in mechanical components and structures typically originate from stress concentrators, including macroscopic notches, rough surfaces, scratches, cavities, inclusions, and welded joints. Despite substantial knowledge gained through experiments, mechanics, material science, and statistical analysis, fully addressing this issue remains a

complex and ongoing challenge. This is because Fatigue cracks often initiate from persistent slip bands and micro-scale weak points such as grain boundaries [1–3], secondary phases, inclusions, and phase interfaces, and in many engineering applications, a distinct crack initiation stage may not even occur, as pre-existing defects introduced during manufacturing or machining processes act as initial cracks [4,5]. Notches are a good example in this case and how hydrogen damage under the conditions defined in this research will impact the stress distribution in ex-service pipeline materials remains to be studied. In this case, classical fatigue limit prediction models and material-dependent characteristic length parameters for notched components will be used, along with a modified stress gradient-based approach [3] to account for the non-propagation behaviour of microstructurally small cracks in ex-service pipeline materials.

8.3.2 Characterization of the degraded microstructure of ex-service pipeline metals with age

It has been observed that the degree of embrittlement is influenced by the microstructure of the material [6–8]. Microstructures that confer high strength, often monitored by hardness level, or those with specific distributions of grain boundary particles or inclusions can increase susceptibility to embrittlement. In materials science, the relationship between the structure and properties of materials is recognized as critical. Structural analysis of materials can be conducted at various levels: atomic, microstructural, or macrostructural. Therefore, understanding the HE susceptibility of degraded pipeline materials requires (i) knowledge of the different microstructural features present in these degraded materials and (ii) insight into how these structures influence HE susceptibility. However, to the author's knowledge, there is very little research that quantifies the relationship between the degradation coefficient and age in the use of pipeline materials in the UK; discussions often address only material degradation over time without defining a clear relationship between usage and age.

8.3.3 Investigate the amount of hydrogen absorbed by a degraded pipeline over time

Another factor influencing the hydrogen embrittlement of pipeline material is the amount of hydrogen the material is exposed to. It is essential to investigate the amount of hydrogen absorbed by degraded pipeline materials under various conditions over time and the hydrogen diffusion rates. While Sievert's Law and the one-dimensional solution of Fick's Law have been used to describe hydrogen concentration and diffusion rates in metals, these

models have not yet been validated for the materials used in the UK distribution network. Hydrogen's diffusion behaviour significantly impacts steel's susceptibility to hydrogen embrittlement, and its high diffusivity in steel presents a challenge for designing and developing hydrogen-resistant pipeline materials as suggested in ref. [9]. This implies that further studies on the diffusion characteristics of hydrogen in metallic materials are crucial for understanding and preventing HE, ultimately improving the performance and reliability of hydrogen-based equipment.

Improved quantification of hydrogen absorption rates based on pipeline age in service will enhance the understanding and safe use of the existing network for supplying blended natural gas. One approach to achieve this is through Gas Chromatography and Mass Spectrometry. Gas chromatography (GC) or gas chromatography-mass spectrometry (GC-MS) can be used to analyze the presence and quantity of hydrogen in pipeline samples [10]. In this process, samples are heated in a controlled environment to release any trapped hydrogen, which is then measured to quantify absorbed hydrogen levels. Alternatively, Thermal Desorption Spectroscopy (TDS) offers a sensitive and accurate technique for studying hydrogen diffusion and trapping in crystalline and non-crystalline materials [11]. TDS involves gradually heating a sample to release absorbed gases and measuring the desorption rate of gas atoms that are either dissolved or trapped in the material. TDS can identify the amount of hydrogen desorbed at various temperatures, helping to distinguish between hydrogen loosely adsorbed by the pipeline material and hydrogen embedded in microstructural defects or trapped in voids within the pipeline metal.

8.3.4 Investigate the mechanical properties of pipeline materials in a hydrogen environment

The degree of embrittlement is influenced both by the amount of hydrogen absorbed and the microstructure of the material. Pipeline materials are susceptible to hydrogen embrittlement in high-pressure hydrogen environments [12,13]. Various impurity gases such as oxygen and carbon dioxide can either exacerbate or mitigate sensitivity to the hydrogen embrittlement [14] and due to the high hydrogen diffusion, testing for HE in a hydrogen environment typically requires specialized and expensive equipment designed for pressurized environments, which also entails stringent safety measures due to the explosive risks involved. More so, load and strain measurements are often conducted using electrical resistance strain gauges, which are prone to drift in a high-pressure hydrogen gas environment [14]. Mini-flat tensile specimens are widely used to characterize the

mechanical properties of materials. In this study, sub-sized specimens will be employed to rigorously assess factors that may impact result quality and accuracy, particularly for smooth tensile specimen geometries. These factors include machining and surface preparation, metrology, and the ratio of microstructural grain size to specimen size. Using these specimens will allow for monitoring both the material's degradation in a hydrogen environment and the evolution of its mechanical properties because of HE. In a hydrogen environment, the technique used for local mechanical properties is the Edge Tracing (ET) technique which uses an optical extensometer [14,15]. This ensures accurate measurements without the need for internal mechanical devices, and it remains unaffected by time-dependent drift during exposure to hydrogen gas.

The engineering stress-strain curves of pipeline materials at varying hydrogen charging times need to be studied to compare changes in material plasticity over time. With longer hydrogen charging durations, the strain at fracture gradually decreases. To achieve this, the elongation after fracture (EL) and reduction in area (RA) of the material specimens can be analyzed. Additionally, examining the yield strength (YS) and tensile strength (TS) over these charging periods will help assess the effects of hydrogen charging on the yield and tensile strength of pipeline materials under a constant pressure environment.

Similarly, tensile tests on specimens with varying hydrogen charging times showed that charging duration can impact the mechanical properties of pipeline materials. Given that gas pressure influences the rate of hydrogen embrittlement in metals, it is also essential to examine the effect of hydrogen charging pressure on these properties. While a hydrogen pressure of 8 bars was used to charge the specimens in this research, this pressure does not represent the full range of operating pressures within the UK gas network. Gas pressure in transmission lines varies between sub-stations, and these fluctuations are likely to affect the mechanical properties of the transmission lines impact the rate of hydrogen diffusion in the pipeline material as well as exert some form of loading.

8.3.5 Investigate the very high-cycle fatigue behaviour of steel in a hydrogen environment

In a hydrogen environment, hydrogen atoms penetrate the material's interior, adding complexity to the behaviour of very high cycle fatigue (VHCF) [16]. For the long-life design with very high reliability, which is essential in the gas distribution network, accurately evaluating their VHCF characteristics in a hydrogen environment is the key to the future advancement of the hydrogen energy industry. Applications will include terminals of hydrogen energy applications as in the engineering equipment in marine vessels, aerospace, and civil transportation where structures subjected to high-frequency and low-stress amplitude loads for design life that exceed 10^7 load cycles.

8.3.6 Investigate fatigue crack growth law in degraded pipeline material

The Paris equation is useful for estimating the fatigue crack growth rate about the cyclic stress intensity factor range. For materials exhibiting varying behaviours, such as brittleness or ductility, linear elastic fracture mechanics is primarily applicable to brittle materials, where the crack growth criterion is defined by the stress intensity factor K. However, a limitation of this approach is that it does not account for the effect of the stress ratio. Theoretically, the stress intensity factor range remains unchanged for different R-ratios under constant amplitude loading. To address this, modifications to Paris's law have been developed that incorporate the influence of stress ratios.

Similarly, the impact of the stress-strain field around a notch on crack growth rate warrants further investigation. This is particularly relevant for transmission pipelines, which contain numerous girth welds made in field conditions. Both the construction process and prolonged operation can introduce additional stresses beyond internal pressure in these welds. The history of observed damage and the need for safe operation call for full-scale testing to accurately model and analyze these effects.

8.4 References

[1] Suresh S., Fatigue of Materials, Second, Cambridge University Press, New York, 2004.

[2] T.. Anderson, Fracture Mechanics, Fundamentals and Applications, Third, Taylor & Francis Group, CRC Press, New York, 2005.

[3] J. Mei, S. Xing, A. Vasu, J. Chung, R. Desai, P. Dong, The fatigue limit prediction of notched components – A critical review and modified stress gradient based

approach, Int. J. Fatigue. 135 (2020) 105531. https://doi.org/10.1016/j.ijfatigue.2020.105531.

[4] W. Schäf, M. Marx, A.F. Knorr, Influence of microstructural barriers on small fatigue crack growth in mild steel, Int. J. Fatigue. 57 (2013) 86–92. https://doi.org/10.1016/j.ijfatigue.2012.11.006.

[5] W. Schaef, M. Marx, H. Vehoff, A. Heckl, P. Randelzhofer, A 3-D view on the mechanisms of short fatigue cracks interacting with grain boundaries, Acta Mater. 59 (2011) 1849–1861. https://doi.org/10.1016/j.actamat.2010.11.051.

[6] Y.S. Chen, C. Huang, P.Y. Liu, H.W. Yen, R. Niu, P. Burr, K.L. Moore, E. Martínez-Pañeda, A. Atrens, J.M. Cairney, Hydrogen trapping and embrittlement in metals – A review, Int. J. Hydrogen Energy. (2024). https://doi.org/10.1016/j.ijhydene.2024.04.076.

[7] H. Li, R. Niu, W. Li, H. Lu, J. Cairney, Y.S. Chen, Hydrogen in pipeline steels: Recent advances in characterization and embrittlement mitigation, J. Nat. Gas Sci. Eng. 105 (2022) 104709. https://doi.org/10.1016/j.jngse.2022.104709.

[8] J. Venezuela, Q. Zhou, Q. Liu, H. Li, M. Zhang, M.S. Dargusch, A. Atrens, The influence of microstructure on the hydrogen embrittlement susceptibility of martensitic advanced high strength steels, Mater. Today Commun. 17 (2018) 1–14. https://doi.org/10.1016/j.mtcomm.2018.07.011.

[9] C. Yin, Y. Wu, Z. Xu, D. Ye, J. Yao, J. Chen, Q. Liu, X. Ge, M. Ding, A novel strategy for estimating the diffusion behaviour of hydrogen in metallic materials with the combined effect of stress corrosion and hydrogenation: Case study of 2.25Cr-1Mo-0.25V high-strength steel, Vacuum. 219 (2024) 112751. https://doi.org/10.1016/j.vacuum.2023.112751.

[10] H. Addach, P. Berçot, M. Wery, M. Rezrazi, Quantitative determination of hydrogen in solids by gas chromatography, J. Chromatogr. A. 1057 (2004) 219–223. https://doi.org/10.1016/j.chroma.2004.09.067.

[11] E. Tal-Gutelmacher, D. Eliezer, E. Abramov, Thermal desorption spectroscopy (TDS)-Application in the quantitative study of hydrogen evolution and trapping in crystalline and non-crystalline materials, Mater. Sci. Eng. A. 445–446 (2007) 625–631. https://doi.org/10.1016/j.msea.2006.09.089.

[12] C. Zhou, X. Chen, Z. Wang, S. Zheng, X. Li, L. Zhang, Effects of environmental conditions on hydrogen permeation of X52 pipeline steel exposed to high H2S-containing solutions, Corros. Sci. 89 (2014) 30–37. https://doi.org/10.1016/j.corsci.2014.07.061.

[13] C. Zhou, H. Zhou, L. Zhang, The Impact of Impurity Gases on the Hydrogen Embrittlement Behavior of Pipeline Steel in High-Pressure H2 Environments, Materials (Basel). 17 (2024). https://doi.org/10.3390/ma17092157.

[14] Y. Madi, L.M. Santana, S. Belkacemi, V. Farrugia, A. Meddour, P.J. Marchais, M. Bertin, J. Furtado, Mechanical characterization of hydrogen embrittlement in a gaseous environment: An innovative test setup using sub-size specimens, Eng. Fail. Anal. 162 (2024) 108362. https://doi.org/10.1016/j.engfailanal.2024.108362.

[15] Z. Shokeir, J. Besson, C. Belhadj, T. Petit, Y. Madi, Edge tracing technique to

study post-necking behaviour and failure in Al alloys and anisotropic plasticity in line pipe steels, Fatigue Fract. Eng. Mater. Struct. 45 (2022) 2427–2442. https://doi.org/10.1111/ffe.13754.

[16] S. Yang, A.M.P. De Jesus, D. Meng, P. Nie, R. Darabi, E. Azinpour, S.P. Zhu, Q. Wang, Very high-cycle fatigue behaviour of steel in hydrogen environment: State of the art review and challenges, Eng. Fail. Anal. 166 (2024). https://doi.org/10.1016/j.engfailanal.2024.108898.

Appendix A – Fatigue Results

Table 1 Summary of the uniaxial fatigue results generated from plain steel specimens

Specimen ID		Fatigue results							
		W_{av} [mm]	d_{av} [mm]	A [mm^2]	Load amp. [KN]	Stress ratio R	Freq. [Hz]	σ_i [MPa]	N_f [cycles]
Uncharged specimens	S_1_1	4.98	1.88	9.38	1.80	0.10	10.00	191.9	2000000
	S_1_2	4.99	1.89	9.41	2.25	0.10	10.00	239.2	206621
	S_1_3	4.97	1.89	9.40	2.48	0.10	10.00	263.3	992
	S_1_4	4.98	1.87	9.34	2.25	0.10	10.00	241.0	150677
	S_1_5	4.97	1.88	9.33	2.03	0.10	10.00	217.0	2000000
	S_2_1	5.02	1.90	9.54	2.16	0.10	10.00	226.3	1214072
	S_2_2	4.98	1.90	9.45	2.16	0.10	10.00	228.7	408035
	S_2_3	4.98	1.89	9.40	2.16	0.10	10.00	229.7	2000000
	S_2_4	4.99	1.90	9.50	2.25	0.10	10.00	236.9	185381
	S_2_5	4.99	1.90	9.50	2.30	0.10	10.00	241.5	120477
	S_2_6	5.00	1.88	9.41	2.36	0.10	10.00	251.1	3196
	S_2_7	5.01	1.90	9.53	2.43	0.10	10.00	255.0	2223
	S_2_8	5.00	1.90	9.52	2.21	0.10	10.00	231.7	450485
	S_2_9	5.01	1.92	9.61	2.30	0.10	10.00	238.8	99367
	S_2_10	5.01	1.93	9.69	2.36	0.10	10.00	243.9	45777
	S_2_11	5.01	1.93	9.65	2.43	0.10	10.00	251.8	1917
	S_2_12	5.03	1.92	9.63	2.21	0.10	10.00	228.9	416095
	S_2_13	5.00	1.92	9.58	2.30	0.10	10.00	239.6	119636
	S_2_14	5.01	1.92	9.60	2.36	0.10	10.00	246.2	6576
	S_2_15	5.03	1.92	9.65	2.21	0.10	10.00	228.6	552564
	S_3_1	4.97	1.93	9.57	2.43	0.10	10.00	253.9	831

Table 2 Summary of the uniaxial fatigue results generated from plain hydrogen-charged steel specimens and cured for a range of time in months

Specimen ID		Fatigue results								
		W_{av} [mm]	d_{av} [mm]	A [mm^2]	Load amp. [KN]	Stress ratio, R	Freq. [Hz]	Δt^* [Mins]	σ_i [MPa]	N_f [cycles]
Charged + cured 3 months	S_3m_1	5.01	1.95	9.77	2.36	0.10	10.00	11.00	241.8	13187
	S_3m_2	5.04	1.94	9.78	2.30	0.10	10.00	12.00	234.7	104268
	S_3m_3	5.00	1.95	9.76	2.43	0.10	10.00	12.00	249.1	3516
	S_3m_4	5.03	1.96	9.87	2.25	0.10	10.00	10.00	228.1	211179
	S_3m_5	5.00	1.93	9.63	2.21	0.10	10.00	8.00	228.9	296724
	S_3m_6	5.03	1.90	9.56	2.16	0.10	10.00	10.00	226.0	2,000,000
	S_3m_7	5.03	1.96	9.83	2.39	0.10	10.00	9.00	242.5	6273
	S_3m_8	5.00	1.94	9.67	2.36	0.10	10.00	10.00	244.4	3170
	S_3m_9	5.05	1.94	9.77	2.30	0.10	10.00	9.00	234.9	101709
	S_3m_10	4.93	1.94	9.56	2.43	0.10	10.00	10.00	254.2	923
	S_3m_11	5.01	1.93	9.66	2.25	0.10	10.00	11.00	232.9	278971
	S_3m_12	4.96	1.94	9.59	2.21	0.10	10.00	12.00	229.9	231417
	S_3m_13	5.02	1.90	9.54	2.16	0.10	10.00	10.00	226.3	2,000,000
	S_3m_14	4.95	1.95	9.62	2.39	0.10	10.00	9.00	247.9	2770
	S_3m_15	5.02	1.94	9.71	2.34	0.10	10.00	10.00	241.1	8604
	S_3m_16	5.03	1.95	9.82	2.34	0.10	10.00	9.00	238.4	13534
	S_3m_17	4.99	1.96	9.76	2.16	0.10	10.00	12.00	221.4	715762
Charged + cured 5 months	S_5m_1	4.76	1.92	9.12	2.36	0.10	10.00	26.00	258.9	64,490
	S_5m_2	5.12	1.92	9.83	2.30	0.10	10.00	9.00	233.5	120,626
	S_5m_3	4.82	1.92	9.24	2.43	0.10	10.00	14.00	263.0	3,833
	S_5m_4	4.97	1.93	9.58	2.25	0.10	10.00	10.00	234.8	140,970
	S_5m_5	5.07	1.93	9.78	2.21	0.10	10.00	12.00	225.6	186,453
	S_5m_6	5.03	1.93	9.70	2.36	0.10	10.00	20.00	243.6	44,393
	S_5m_7	4.93	1.93	9.53	2.30	0.10	10.00	9.00	240.8	110,699
	S_5m_8	4.86	1.91	9.30	2.43	0.10	10.00	9.00	261.3	6,974
	S_5m_9	4.90	1.91	9.34	2.25	0.10	10.00	8.00	240.8	144,385
	S_5m_10	4.90	1.93	9.43	2.21	0.10	10.00	9.00	233.8	208,574
	S_5m_11	4.88	1.92	9.37	2.36	0.10	10.00	8.00	252.2	310,422
	S_5m_12	4.81	1.92	9.24	2.30	0.10	10.00	14.00	248.5	166,398
	S_5m_13	4.48	1.90	8.51	2.43	0.10	10.00	10.00	285.5	3,589
	S_5m_14	4.88	1.93	9.42	2.25	0.10	10.00	11.00	238.9	102,534
	S_5m_15	5.08	1.93	9.79	2.16	0.10	10.00	10.00	220.7	189,283
Charged + 9 months	S_9m_1	5.02	1.92	9.64	2.36	0.10	10.00	11.00	245.1	16,133
	S_9m_2	4.94	1.94	9.56	2.30	0.10	10.00	10.00	240.1	98,744
	S_9m_3	5.01	1.92	9.59	2.43	0.10	10.00	9.00	253.3	1,644
	S_9m_4	5.01	1.94	9.72	2.25	0.10	10.00	11.00	231.5	124,372
	S_9m_5	5.01	1.94	9.70	2.21	0.10	10.00	11.00	227.3	284,899
	S_9m_6	5.00	1.92	9.60	2.36	0.10	10.00	14.00	246.1	14,382
	S_9m_7	4.99	1.93	9.60	2.30	0.10	10.00	11.00	239.1	85,856
	S_9m_8	5.01	1.93	9.64	2.43	0.10	10.00	20.00	252.1	2,680
	S_9m_9	5.00	1.96	9.78	2.25	0.10	10.00	17.00	230.0	219,910

Δt^* is the time elapsed between removing the specimen from the freezer and initiating the test

Table 3 Summary of the uniaxial fatigue results generated from plain hydrogen-charged and uncharged welded steel specimens in tension (R=0.1) and cured for a range of time in months

	Specimen ID	Fatigue results									
		W_{av} [mm]	d_{av} [mm]	A [mm^2]	Load amp. [KN]	Stress ratio, R	Freq. [Hz]	Δt^* [Mins]	σ_i [MPa]	N_f [cycles]	Run out
Uncharged	WS_1_1	5.06	1.90	9.62	2.25	0.10	10.00	-	233.8	170697	
	WS_1_2	5.05	1.87	9.43	2.16	0.10	10.00	-	228.9	721722	
	WS_1_3	5.07	1.91	9.66	2.34	0.10	10.00	-	242.2	67901	
	WS_1_4	5.06	1.90	9.63	2.25	0.10	10.00	-	233.6	209135	
	WS_1_5	5.05	1.91	9.64	2.48	0.10	10.00	-	256.9	1478	
	WS_2_1	5.03	1.92	9.65	2.12	0.10	10.00	-	219.1	2,000,000	X
	WS_2_2	5.06	1.92	9.69	2.41	0.10	10.00	-	248.4	65449	
	WS_2_3	5.05	1.93	9.72	2.41	0.10	10.00	-	247.6	26409	
	WS_2_4	5.01	1.94	9.70	2.34	0.10	10.00	-	241.3	258298	
	WS_2_5	5.05	1.93	9.72	2.48	0.10	10.00	-	254.5	3392	
	WS_2_6	5.02	1.94	9.72	2.16	0.10	10.00	-	222.3	2,000,000	X
	WS_2_7	5.02	1.91	9.60	2.48	0.10	10.00	-	257.7	47	
	WS_2_8	5.02	1.92	9.62	2.41	0.10	10.00	-	250.2	1272	
	WS_2_9	5.02	1.92	9.62	2.34	0.10	10.00	-	243.4	641747	
	WS_2_10	5.04	1.92	9.69	2.25	0.10	10.00	-	232.2	1192184	
	WS_2_11	5.05	1.90	9.61	2.18	0.10	10.00	-	227.2	375513	
	WS_2_12	5.03	1.93	9.72	2.14	0.10	10.00	-	219.9	2,000,000	X
	WS_2_13	5.04	1.91	9.64	2.34	0.10	10.00	-	242.8	3141	
	WS_2_14	5.03	1.92	9.65	2.25	0.10	10.00	-	233.2	49409	
	WS_2_15	5.02	1.93	9.69	2.18	0.10	10.00	-	225.3	2,000,000	X
Charged + 3 months	WS_3m_1	5.05	1.94	9.78	2.39	0.10	10.00	11.00	243.9	36,126	
	WS_3m_2	5.03	1.94	9.75	2.34	0.10	10.00	12.00	239.9	83,914	
	WS_3m_3	5.03	1.93	9.70	2.25	0.10	10.00	9.00	231.9	27,987	
	WS_3m_4	5.03	1.93	9.71	2.21	0.10	10.00	9.00	226.9	6,793	
	WS_3m_5	5.02	1.93	9.68	2.30	0.10	10.00	9.00	237.0	492,367	
	WS_3m_6	5.02	1.95	9.80	2.39	0.10	10.00	10.00	243.5	4,943	
	WS_3m_7	5.03	1.96	9.83	2.34	0.10	10.00	10.00	237.9	6,411	
	WS_3m_8	5.03	1.90	9.55	2.25	0.10	10.00	13.00	235.6	2,000,000	X
	WS_3m_9	5.02	1.94	9.71	2.21	0.10	10.00	11.00	227.2	429,447	
	WS_3m_10	5.02	1.93	9.68	2.30	0.10	10.00	11.00	237.0	94,884	
	WS_3m_11	5.01	1.89	9.46	2.21	0.10	10.00	11.00	233.0	29,217	
Charged + 9 months	WS_9m_1	5.01	1.92	9.60	2.41	0.10	10.00	9.00	250.8	186	
	WS_9m_2	5.01	1.92	9.62	2.34	0.10	10.00	10.00	243.3	941	
	WS_9m_3	5.02	1.92	9.62	2.25	0.10	10.00	11.00	233.9	218997	
	WS_9m_4	5.00	1.91	9.55	2.21	0.10	10.00	10.00	230.9	143660	
	WS_9m_5	5.03	1.90	9.55	2.25	0.10	10.00	15.00	235.6	2,000,000	X
	WS_9m_6	5.00	1.93	9.66	2.30	0.10	10.00	9.00	237.7	76994	
	WS_9m_7	4.99	1.90	9.49	2.21	0.10	10.00	11.00	232.2	48563	
	WS_9m_8	5.02	1.93	9.66	2.30	0.10	10.00	9.00	237.5	21633	
	WS_9m_9	5.01	1.90	9.50	2.21	0.10	10.00	12.00	232.1	20962	
	WS_9m_10	5.01	1.92	9.62	2.25	0.10	10.00	11.00	233.9	172687	

Δt^* is the time elapsed between removing the specimen from the freezer and initiating the test

Table 4 Summary of uniaxial fatigue test results generated from plain uncharged and hydrogen-charged brass specimens in tension (R=0.1) and cured for 9 months

Specimen ID		Fatigue results									
		W_{av} [mm]	d_{av} [mm]	A [mm^2]	Load amp. [KN]	Stress ratio, R	Freq. [Hz]	Δt^* [Mins]	σ_i [MPa]	N_f cycles	Run out
uncharged	B_2_1	5.02	1.87	9.36	1.80	0.10	10.00	-	192.2	8	
	B_2_2	5.00	1.87	9.35	1.67	0.10	10.00	-	178.1	13	
	B_2_3	4.99	1.86	9.30	1.53	0.10	10.00	-	164.4	131,262	
	B_2_4	5.00	1.85	9.27	1.44	0.10	10.00	-	155.4	57,180	
	B_2_5	4.99	1.86	9.26	1.35	0.10	10.00	-	145.7	87,888	
Charged + 9 months	B_9m_1	5.03	1.84	9.22	1.71	0.10	10.00	15.00	185.4	11	
	B_9m_2	5.00	1.86	9.31	1.53	0.10	10.00	20.00	164.4	20,368	
	B_9m_3	5.01	1.77	8.84	1.67	0.10	10.00	16.00	188.3	18	
	B_9m_4	5.00	1.85	9.23	1.49	0.10	10.00	11.00	160.9	41,482	
	B_9m_5	4.99	1.84	9.18	1.53	0.10	10.00	18.00	166.6	15,876	
	B_9m_6	4.99	1.88	9.38	1.40	0.10	10.00	9.00	148.7	81,667	
	B_9m_7	5.00	1.90	9.50	1.44	0.10	10.00	10.00	151.6	41,787	
	B_9m_8	4.99	1.86	9.28	1.31	0.10	10.00	10.00	140.7	364,987	
	B_9m_9	5.02	1.80	9.02	1.31	0.10	10.00	22.00	144.7	93,848	
	B_9m_10	4.98	1.86	9.27	1.26	0.10	10.00	12.00	135.9	115,739	

Δt^* is the time elapsed between removing the specimen from the freezer and initiating the test

Gg

Table 5 Uniaxial fatigue test results from plain uncharged and hydrogen-charged cast iron

	Specimen ID	Fatigue results									
		W_{av} [mm]	d_{av} [mm]	A [mm^2]	Load amp. [KN]	Stress ratio, R	Freq. [Hz]	Δt^* [Mins]	σ_i [MPa]	N_f [cycles]	Run out
Uncharged	AA4	5.03	1.93	9.71	0.74	0.10	10.00	-	76.4	751	
	AA5	5.01	1.93	9.65	0.68	0.10	10.00	-	69.9	1,690	
	AA6	5.04	1.92	9.70	0.54	0.10	10.00	-	55.7	14,74	
	AA7	5.02	1.93	9.67	0.45	0.10	10.00	-	46.6	142,029	
	AA8	5.05	1.92	9.69	0.36	0.10	10.00	-	37.2	2,000,000	X
	AA9	5.02	1.93	9.70	0.50	0.10	10.00	-	51.0	197,025	
	CI_1_1	5.04	1.94	9.76	0.41	0.10	10.00	-	41.5	2,000,000	X
	CI_1_2	5.01	1.91	9.58	0.50	0.10	10.00	-	51.7	66,103	
	CI_1_3	5.02	1.91	9.59	0.54	0.10	10.00	-	56.3	23,930	
	CI_1_4	5.02	1.91	9.59	0.59	0.10	10.00	-	61.0	16,839	
	CI_2_1	5.05	1.93	9.73	0.41	0.10	10.00	-	41.6	2,000,000	X
	CI_2_2	5.04	1.92	9.67	0.68	0.10	10.00	-	69.8	2,101	
	C1_2_3	5.04	1.92	9.68	0.59	0.10	10.00	-	60.5	18,501	
	C1_2_4	5.04	1.93	9.72	0.63	0.10	10.00	-	64.8	5,651	
	C1_2_5	5.06	1.93	9.78	0.43	0.10	10.00	-	43.7	2,000,000	X
	C1_2_6	5.06	1.93	9.75	0.63	0.10	10.00	-	64.6	2,264	
	C1_2_7	5.06	1.93	9.76	0.54	0.10	10.00	-	55.4	7,987	
	C1_2_8	5.02	1.93	9.70	0.50	0.10	10.00	-	51.1	17,621	
	CI_2_9	5.03	1.93	9.70	0.45	0.10	10.00	-	46.4	14,235	
	C1_2_10	5.04	1.93	9.74	0.43	0.10	10.00	-	43.9	2,000,000	X
	C1_2_11	5.03	1.94	9.75	0.41	0.10	10.00	-	41.6	2,000,000	X
Charged + 3months	CI_3m_1	5.01	1.92	9.59	0.63	0.10	10.00	10.00	65.7	11,533	
	CI_3m_2	5.02	1.94	9.71	0.54	0.10	10.00	10.00	55.6	21,186	
	CI_3m_3	5.03	1.95	9.80	0.50	0.10	10.00	12.00	50.5	23,660	
	CI_3m_4	4.98	1.90	9.47	0.47	0.10	10.00	9.00	49.9	2000000	X
	CI_3m_5	5.02	1.93	9.66	0.63	0.10	10.00	11.00	65.2	3,396	
	CI_3m_6	5.02	1.92	9.64	0.54	0.10	10.00	9.00	55.9	87,109	
	CI_3m_7	4.98	1.91	9.51	0.50	0.10	10.00	9.00	52.1	127,020	
	CI_3m_8	5.02	1.93	9.66	0.47	0.10	10.00	11.00	48.9	158,005	
	CI_3m_9	4.96	1.93	9.55	0.50	0.10	10.00	10.00	51.8	44,033	
	CI_3m_10	4.99	1.93	9.61	0.63	0.10	10.00	10.00	65.5	5,280	
Charged + 9 months	CI_9m_1	5.00	1.91	9.55	0.63	0.10	10.00	8.00	65.9	1,583	
	CI_9m_2	4.96	1.92	9.49	0.54	0.10	10.00	8.00	56.9	17,599	
	CI_9m_3	4.97	1.91	9.49	0.50	0.10	10.00	9.00	52.2	18,006	
	CI_9m_4	4.96	1.93	9.55	0.45	0.10	10.00	13.00	47.1	2000000	X
	CI_9m_5	4.93	1.93	9.50	0.63	0.10	10.00	10.00	66.3	780	
	CI_9m_6	4.98	1.93	9.59	0.50	0.10	10.00	9.00	51.6	116,397	
	CI_9m_7	5.00	1.92	9.61	0.45	0.10	10.00	9.00	46.8	2000000	X
	CI_9m_8	4.92	1.92	9.42	0.54	0.10	10.00	13.00	57.4	13,348	
	CI_9m_9	4.99	1.93	9.61	0.50	0.10	10.00	10.00	51.5	52,975	
	CI_9m_10	4.92	1.92	9.44	0.47	0.10	10.00	11.00	50.1	196,388	
	CI_9m_11	4.99	1.93	9.60	0.47	0.10	10.00	9.00	49.2	267,794	

Δt^* is the time elapsed between removing the specimen from the freezer and initiating the test

Table 6 Summary of the uniaxial fatigue tests generated by testing notched brass specimens in tension (R=0.10) and at a frequency of 10Hz

	Specimen Reference	Fatigue test results								
		W_{av} [mm]	d_{av} [mm]	A_{gross} [mm^2]	Load max [KN]	Load min [KN]	Load Amp. [KN]	σ_i [MPa]	N_f [cycles]	Run out
1mm notches	S_1mm_1	8.52	1.96	16.73	4.80	0.48	2.16	129.1	2,000,000	X
	S_1mm_1.1	8.52	1.96	16.73	8.00	0.80	3.60	215.2	8,103	
	S_1mm_2	8.50	1.97	16.75	5.50	0.55	2.48	147.8	203,115	
	S_1mm_3	8.51	1.98	16.85	5.10	0.51	2.30	136.2	1,215,396	
	S_1mm_4	8.51	1.97	16.76	5.10	0.51	2.30	136.9	362,177	
	S_1mm_5	8.49	1.98	16.78	5.50	0.55	2.48	147.5	193,751	
	S_1mm_6	8.48	1.98	16.76	7.00	0.70	3.15	188.0	34,155	
	S_1mm_7	8.50	1.98	16.82	7.00	0.70	3.15	187.2	24,110	
	S_1mm_8	8.50	1.97	16.77	4.95	0.50	2.23	132.8	2,000,000	X
	S_1mm_8.1	8.50	1.97	16.77	8.00	0.80	3.60	214.6	8,643	
	S_1mm_9	8.52	1.99	16.92	5.30	0.53	2.39	140.9	483,252	
	S_1mm_10	8.49	1.97	16.75	5.30	0.53	2.39	142.4	374,787	
2mm notches	S_2mm_1	8.49	1.96	16.68	4.00	0.40	1.80	107.9	496,775	
	S_2mm_2	8.5	1.93	16.66	4.80	0.48	2.16	129.7	291,168	
	S_2mm_3	8.49	1.97	16.75	4.00	0.40	1.80	107.5	2,000,000	X
	S_2mm_3.1	8.49	1.97	16.75	6.80	0.68	3.06	182.7	10,000	
	S_2mm_4	8.49	1.97	16.78	4.80	0.48	2.16	128.8	185,460	
	S_2mm_5	8.48	1.98	16.82	5.00	0.50	2.25	133.8	136,806	
	S_2mm_6	8.49	1.98	16.82	5.00	0.50	2.25	133.8	155,536	
	S_2mm_7	8.48	1.96	16.71	6.00	0.60	2.70	161.6	26,734	
	S_2mm_8	8.49	2.19	17.80	6.00	0.60	2.70	151.7	23,547	
	S_2mm_9	8.47	1.96	16.72	4.00	0.40	1.80	107.7	2,000,000	X
	S_2mm_9.1	8.47	1.96	16.72	6.80	0.68	3.06	183.0	8,606	
	S_2mm_10	8.47	1.97	16.66	4.10	0.41	1.85	110.7	2,000,000	X
	S_2mm_10.1	8.47	1.97	16.66	6.50	0.65	2.93	175.5	12,105	
3mm notches	S_3mm_1	8.50	1.96	16.63	5.00	0.50	2.25	135.3	27529	
	S_3mm_2	8.51	1.95	16.59	5.00	0.50	2.25	135.6	31457	
	S_3mm_3	8.48	1.96	16.65	4.00	0.40	1.80	108.1	208275	
	S_3mm_4	8.46	1.96	16.58	4.00	0.40	1.80	108.6	210278	
	S_3mm_5	8.49	1.99	16.87	5.50	0.55	2.48	146.7	7826	
	S_3mm_6	8.48	1.96	16.59	3.30	0.33	1.49	89.5	2,000,000	X
	S_3mm_6.1	8.48	1.96	16.59	5.70	0.57	2.57	154.7	12684	
	S_3mm_7	8.48	1.97	16.68	3.50	0.35	1.58	94.4	481826	
	S_3mm_8	8.46	1.96	16.58	4.00	0.40	1.80	108.6	196032	
	S_3mm_9	8.49	1.95	16.55	3.40	0.34	1.53	92.5	519988	
	S_3mm_10	8.46	1.96	16.59	3.40	0.34	1.53	92.2	540895	

Table 7 Summary of the uniaxial fatigue tests generated by testing notched brass specimens in tension (R=0.10) and at a frequency of 10Hz

	Specimen Reference	Fatigue test results								
		W_{av} [mm]	d_{av} [mm]	A_{gross} [mm^2]	Load max [KN]	Load min [KN]	Load Amp. [KN]	σ_i [MPa]	N_f [cycles]	Runout
1mm notches	B_1mm_1	8.52	1.94	16.56	3.10	0.31	1.40	84.2	541,945.00	
	B_1mm_2	8.50	1.96	16.68	3.60	0.36	1.62	97.1	161,869.00	
	B_1mm_3	8.53	1.96	16.68	4.00	0.40	1.80	107.9	65,518.00	
	B_1mm_4	8.54	1.96	16.77	3.00	0.30	1.35	80.5	530,996.00	
	B_1mm_5	8.54	1.97	16.79	4.20	0.42	1.89	112.6	55,514.00	
	B_1mm_6	8.53	1.95	16.60	2.80	0.28	1.26	75.9	1,903,387.00	
	B_1mm_7	8.52	1.95	16.58	3.10	0.31	1.40	84.1	739,815.00	
	B_1mm_8	8.52	1.96	16.69	3.60	0.36	1.62	97.1	121,909.00	
	B_1mm_9	8.53	1.96	16.74	4.00	0.40	1.80	107.5	74,827.00	
	B_1mm_10	8.53	1.96	16.68	3.00	0.30	1.35	80.9	776,713.00	
2mm notches	B_2mm_1	8.53	1.95	16.66	2.80	0.28	1.26	75.7	292,589.00	
	B_2mm_2	8.51	1.95	16.62	3.10	0.31	1.40	83.9	178,161.00	
	B_2mm_3	8.51	1.96	16.68	2.40	0.24	1.08	64.8	2000000.00	X
	B_2mm_3.1	8.51	1.96	16.68	3.50	0.35	1.58	94.4	36,739.00	
	B_2mm_4	8.53	1.95	16.61	2.60	0.26	1.17	70.5	337,359.00	
	B_2mm_5	8.50	1.96	16.66	2.50	0.25	1.13	67.5	732,233.00	
	B_2mm_6	8.51	1.95	16.59	2.50	0.25	1.13	67.8	460,968.00	
	B_2mm_7	8.52	1.95	16.59	2.60	0.26	1.17	70.5	359,750.00	
	B_2mm_8	8.51	1.95	16.62	2.80	0.28	1.26	75.8	240,122.00	
	B_2mm_9	8.49	1.96	16.65	3.10	0.31	1.40	83.8	130,672.00	
	B_2mm_10	8.51	1.95	16.62	3.50	0.35	1.58	94.8	59,018.00	
3mm notches	B_3mm_1	8.53	1.97	16.83	2.50	0.25	1.13	66.9	196,858.00	
	B_3mm_2	8.53	1.94	16.58	2.50	0.25	1.13	67.8	194,403.00	
	B_3mm_3	8.53	1.97	16.78	2.20	0.22	0.99	59.0	676,739.00	
	B_3mm_4	8.52	1.96	16.71	2.70	0.27	1.22	72.7	140,561.00	
	B_3mm_5	8.52	1.95	16.61	2.20	0.22	0.99	59.6	410,938.00	
	B_3mm_6	8.51	1.96	16.68	2.05	0.21	0.92	55.3	507,491.00	
	B_3mm_7	8.51	1.95	16.57	2.05	0.21	0.92	55.7	706,821.00	
	B_3mm_8	8.52	1.96	16.71	1.95	0.20	0.88	52.5	1,568,334.00	
	B_3mm_9	8.52	1.93	16.42	1.95	0.20	0.88	53.4	616,481.00	
	B_3mm_10	8.52	1.96	16.69	2.80	0.28	1.26	75.5	109,362.00	

Table 8 Summary of the uniaxial fatigue tests generated by testing circular notched cast iron specimens in tension (R=0.10) and at a frequency of 10Hz

	Specimen Reference	Fatigue test results								
		W_{av} [mm]	d_{av} [mm]	A_{gross} [mm^2]	Load max [KN]	Load min [KN]	Load Amp. [KN]	σ_i [MPa]	N_f [cycles]	Runout
1mm notches	CI_1mm_1	8.48	1.95	16.54	1.30	0.13	0.59	35.4	2000000	X
	CI_1mm_1.1	8.48	1.95	16.54	2.00	0.20	0.90	54.4	8,798	
	CI_1mm_2	8.50	1.95	16.60	1.70	0.17	0.77	46.1	132,604	
	CI_1mm_3	8.51	1.97	16.74	1.90	0.19	0.86	51.1	8,442	
	CI_1mm_4	8.51	1.95	16.60	1.50	0.15	0.68	40.7	2000000	X
	CI_1mm_4.1	8.51	1.95	16.60	2.10	0.21	0.95	56.9	5,176	
	CI_1mm_5	8.50	1.95	16.58	1.60	0.16	0.72	43.4	24,487	
	CI_1mm_6	8.49	1.98	16.84	1.60	0.16	0.72	42.8	963,511	
	CI_1mm_7	8.51	1.95	16.59	1.60	0.16	0.72	43.4	303,117	
	CI_1mm_8	8.49	1.95	16.58	1.55	0.16	0.70	42.1	68,918	
	CI_1mm_9	8.49	1.94	16.50	1.55	0.16	0.70	42.3	67,485	
	CI_1mm_10	8.51	1.96	16.67	1.60	0.16	0.72	43.2	39,080	
2mm notches	CI_2mm_1	8.50	1.95	16.55	0.70	0.07	0.32	19.0	2000000	X
	CI_2mm_1.1	8.50	1.95	16.55	2.00	0.20	0.90	54.3	406	
	CI_2mm_2	8.49	1.95	16.56	1.60	0.16	0.72	43.5	16,266	
	CI_2mm_3	8.49	1.97	16.70	1.20	0.12	0.54	32.3	347,842	
	CI_2mm_4	8.50	1.95	16.60	1.00	0.10	0.45	27.1	2000000	X
	CI_2mm_4.1	8.50	1.95	16.60	1.80	0.18	0.81	48.8	645	
	CI_2mm_5	8.50	1.94	16.51	1.10	0.11	0.50	29.9	563,403	
	CI_2mm_6	8.51	1.95	16.59	1.10	0.11	0.50	29.8	2000000	X
	CI_2mm_6.1	8.51	1.95	16.59	1.70	0.17	0.77	46.1	4,025	
	CI_2mm_7	8.48	1.96	16.62	1.20	0.12	0.54	32.5	2000000	
	CI_2mm_8	8.50	1.95	16.55	1.20	0.12	0.54	32.6	2000000	X
	CI_2mm_8.1	8.50	1.95	16.55	1.70	0.17	0.77	46.2	1,183	
	CI_2mm_9	8.50	1.96	16.63	1.30	0.13	0.59	35.2	110,298	
	CI_2mm_10	8.51	1.95	16.57	1.30	0.13	0.59	35.3	64,586	
3mm notches	CI_3mm_1	8.48	1.96	16.65	1.50	0.15	0.68	40.5	1,708	
	CI_3mm_2	8.50	1.97	16.71	1.00	0.10	0.45	26.9	137,409	
	CI_3mm_3	8.50	1.95	16.54	0.80	0.08	0.36	21.8	2000000	X
	CI_3mm_3.2	8.50	1.95	16.54	1.50	0.15	0.68	40.8	1,455	
	CI_3mm_4	8.50	1.95	16.60	0.90	0.09	0.41	24.4	2000000	X
	CI_3mm_4.1	8.50	1.95	16.60	1.40	0.14	0.63	37.9	5,641	
	CI_3mm_5	8.52	1.96	16.73	0.95	0.10	0.43	25.6	174,677	
	CI_3mm_6	8.52	1.97	16.75	0.92	0.09	0.41	24.7	660,480	
	CI_3mm_7	8.53	1.96	16.74	0.95	0.10	0.43	25.5	2000000	X
	CI_3mm_7.1	8.53	1.96	16.74	1.40	0.14	0.63	37.6	2,933	
	CI_3mm_8	8.50	1.93	16.37	0.92	0.09	0.41	25.3	159,794	
	CI_3mm_9	8.53	1.97	16.84	1.00	0.10	0.45	26.7	2000000	X
	CI_3mm_9.1	8.53	1.97	16.84	1.40	0.14	0.63	37.4	4,988	
	CI_3mm_10	8.52	1.94	16.52	1.00	0.10	0.45	27.2	187,383	

Appendix B – Statistics of Fatigue data

Calculate the mean S-N curve by using equation 4-13

$$\sigma_{0,50\%} = \left[\frac{10^{C_0}}{N_A}\right]^{\frac{1}{k}}$$

The constants in the above equation are calculated as:

$$C_0 = \overline{logN_i} - C_1\overline{log\sigma_i}$$

And

$$C_1 = \frac{\sum_{i=1}^{n}[log\,(\sigma_i) - \overline{log\sigma_i}][log\,(N_i) - \overline{logN_i}]}{\sum_{i=1}^{n}[log\,(\sigma_i) - \overline{log\sigma_i}]^2}$$

$$k = -C_1$$

Then choose any arbitrary number of cycles and estimate the corresponding stress. The line linking these two points estimates the mean S-N curve in accordance with equation 4-2.

Calculate the scatter factors according to each of the approaches:

ASTM:

$$K_{D(ASTM)} = \sqrt{2F_p\left(1 + \frac{1}{n}\right)}$$

IIW:

$$K_{D(IIW)} = t\sqrt{1 + \frac{1}{n}}$$

LRM:

$$K_{D(LRM)} = q.s$$

$s^2 = \frac{\sum_{i=1}^{n}(LogN_f - LogN_i)^2}{n-1}$ or

$s^2 = \frac{\sum_{i=1}^{n}(LogN_f - LogN_i)^2}{n-2}$ depending on the approach used.

The scatter band estimated for the various approaches by using the equation:

$$\tau_{\sigma(LM)} = \frac{\sigma_{0,(1-P)\%(LM)}}{\sigma_{0,P\%(LM)}}$$

Values for the characteristic values of the distributions are either read off statistical tables (like in the LRM approach) of estimated numerically using the statistical function in excel.

Estimation of the characteristic values of the t-distribution using statistical function in excel:

$$t_s = T.INV.2T(probability, Deg\ of\ freedom)$$

Estimation of the characteristic value for the F-distribution using the statistical function in excel:

$$F_p = F.INV.RT(probability, Deg\ of\ freedom1, Deg\ of\ freedom2)$$

Calculating the characteristic value of F-distribution manually

$$F_p crit = \frac{\sum_{i=1}^{l} \frac{m_i\left(log\left(N_{fi}\right) - \overline{logN}_{fi}\right)^2}{(l-2)}}{\sum_{i=1}^{n}\sum_{j=1}^{m_i} \frac{(log(N_{fij}) - \overline{logN}_{fij})^2}{n-l}}$$

where $\log N_{fij}$ ($i = 1..l$ and $j = 1..m$) is the logarithm of life at the replication level

Mean S-N curve and scatter bands from the various approaches

1) ASTM

$$\sigma_{0,P\%(ASTM)} = \left[\frac{10^{(C_0 - K_{D(ASTM)}S)}}{N_A}\right]^{\frac{1}{k}}$$

$$\sigma_{0,(1-P)\%(ASTM)} = \left[\frac{10^{(C_0 + K_{D(ASTM)}S)}}{N_A}\right]^{\frac{1}{k}}$$

$$\tau_{\sigma(ASTM)} = \frac{\sigma_{0,(1-P)\%(ASTM)}}{\sigma_{0,P\%(ASTM)}}$$

2) IIW

$$\sigma_{0,P\%(IIW)} = \left[\frac{10^{(C_0 - K_{D(IIW)}S)}}{N_A}\right]^{\frac{1}{k}}$$

$$\sigma_{0,(1-P)\%(IIW)} = \left[\frac{10^{(C_0 + K_{D(IIW)}S)}}{N_A}\right]^{\frac{1}{k}}$$

$$\tau_{\sigma(IIW)} = \frac{\sigma_{0,(1-P)\%(IIW)}}{\sigma_{0,P\%(IIW)}}$$

3) LRM

$$\sigma_{0,P\%(LM)} = \sigma_0 \left[\frac{N_A}{10^{log\,(N_A)+qs}}\right]^{\frac{1}{k}}$$

$$\sigma_{0,(1-P)\%(LM)} = \sigma_0 \left[\frac{N_A}{10^{log\,(N_A)-qs}}\right]^{\frac{1}{k}}$$

$$\tau_{\sigma(LM)} = \frac{\sigma_{0,(1-P)\%(LM)}}{\sigma_{0,P\%(LM)}}$$

Statistical Parametric tests

Test for homogenous fatigue data sets

$$\frac{{s_n}^2}{{s_d}^2} - F_{crit}(1-\beta, f_n, f_d) < 0$$

Test for parallel lines

$$t_{C_1} = \frac{\left|C_{1,1} - C_{1,2}\right|}{\sqrt{\left(\frac{1}{\sum_{i=1}^{n_1}\left(\log\sigma_{i,1} - \overline{\log\sigma_{1,1}}\right)^2} + \frac{1}{\sum_{i=1}^{n_2}\left(\log\sigma_{i,2} - \overline{\log\sigma_{1,2}}\right)^2}\right)}\, s_e}$$

$$t_{C_1} - t_\beta) < 0$$

Test for collinear lines

$$t(\delta) = \frac{\left|\left(\overline{\log N_{1,1}} - \overline{\log N_{2,1}}\right) - C_1\left(\overline{\log\sigma_{1,1}} - \overline{\log\sigma_{2,1}}\right)\right|}{\sqrt{\left[\frac{1}{n_1} + \frac{1}{n_2} + \frac{\left(\overline{\log\sigma_{1,1}} - \overline{\log\sigma_{2,1}}\right)^2}{\sum_{i=1}^{n_1}\left(\log\sigma_{i,1} - \overline{\log\sigma_{1,1}}\right)^2 + \sum_{i=1}^{n_2}\left(\log\sigma_{i,2} - \overline{\log\sigma_{1,2}}\right)^2}\right]}\, s_e}$$

$$/t(\delta) - t_\beta/ \leq 0$$

Appendix C – Fracture Surfaces plain specimen

Plan ex-service X52 steel

Specimen ID: **S_3m_2**
$\sigma_i = 234.7$MPa
$N_f = 104{,}268$ Cycles

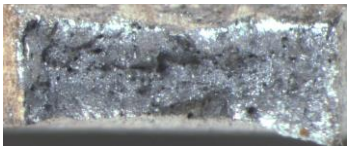

Specimen ID: **S_5m_8**
$\sigma_i = 261.3$MPa
$N_f = 6{,}974$ Cycles

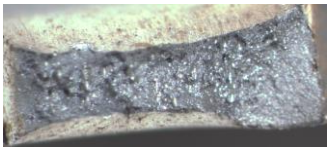

Specimen ID: **S_9m_5**
$\sigma_i = 227.3$MPa
$N_f = 284{,}899$ Cycles

Plan ex-service X52 welded steel

Specimen ID: **WS_1_5**
$\sigma_i = 256.9$MPa
$N_f = 1{,}478$ Cycles

Specimen ID: **WS_1_4**
$\sigma_i = 233.6$MPa
$N_f = 209{,}135$ Cycles

Specimen ID: **WS_9m_3**
$\sigma_i = 233.9$MPa
$N_f = 218{,}997$ Cycles

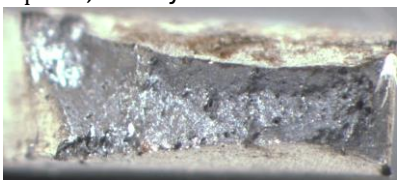

Specimen ID: **WS_1_3**
$\sigma_i = 242.2$MPa
$N_f = 67{,}901$ Cycles

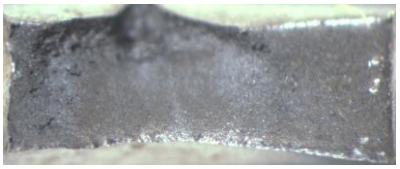

Specimen ID: **WS_2_5**
$\sigma_i = 254.5$MPa
$N_f = 3{,}392$ Cycles

Plan ex-service cast iron

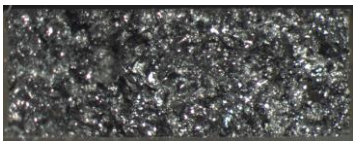

Specimen ID: **CI_9m_6**
$\sigma_i = 51.6$MPa
$N_f = 116{,}392$ Cycles

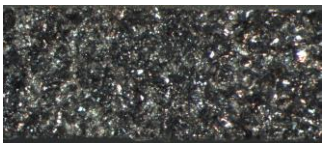

Specimen ID: **CI_3m_6**
$\sigma_i = 55.9$MPa
$N_f = 87{,}109$ Cycles

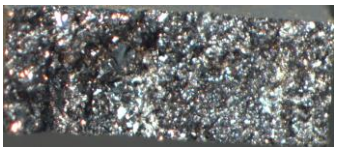

Specimen ID: **CI_9m_1**
$\sigma_i = 65.9$MPa
$N_f = 1{,}583$ Cycles

Plan brass

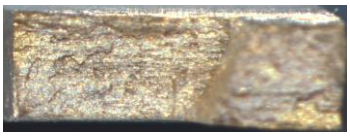

Specimen ID: **Br_2_2**
$\sigma_i = 178.1$MPa
$N_f = 13$ Cycles

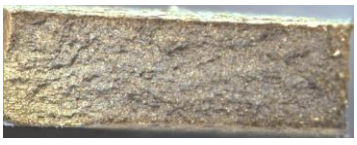

Specimen ID: **Br_9m_8**
$\sigma_i = 140.7$MPa
$N_f = 364{,}987$ Cycles

Figure 1 Randomly selected failure surfaces of some plain specimens after fatigue tests from an optical camera with a 2x magnification

Appendix A1 Failed hydrogen charged and uncharged specimens

Welded Steel

WS_1_1
σ[MPa]=233.78
N_f[Cycles] =170697

WS_1_2
σ[MPa]=228.99
N_f[Cycles] =721722

WS_1_3
σ[MPa]=242.22
N_f[Cycles]=67901

WS_1_4
σ[MPa]=233.62
N_f[Cycles]=209135

WS_1_5
σ[MPa]=256.88
N_f[Cycles]=1478

WS_2_2
σ[MPa]=248.40
N_f[Cycles]=65449

WS_2_3
σ[MPa]=247.60
N_f[Cycles]=26409

WS_2_4
σ[MPa]=241.33
N_f[Cycles]=258298

WS_2_5
σ[MPa]=254.54
N_f[Cycles]=3392

WS_2_7
σ[MPa]=257.68
N_f[Cycles]=47

WS_2_8
σ[MPa]=250.22
N_f[Cycles]=1272

WS_2_9
σ[MPa]=243.36
N_f[Cycles]=641747

WS_2_10
σ[MPa]=232.23
N_f[Cycles]=1192184

WS_2_11
σ[MPa]=227.17
N_f[Cycles]=375513

WS_2_13
σ[MPa]=242.82
N_f[Cycles]=3141

WS_2_14
σ[MPa]=233.23
N_f[Cycles]=49409


WS_3m_1
σ[MPa]=243.91
N_f[Cycles]=36126


WS_3m_2
σ[MPa]=3239.96
N_f[Cycles]=83914


WS_3m_3
σ[MPa]=231.92
N_f[Cycles]=27987


WS_3m_4
σ[MPa]=226.98
N_f[Cycles]=6793


WS_3m_5
σ[MPa]=237.03
N_f[Cycles]=492367


WS_3m_6
σ[MPa]=243.48
N_f[Cycles]=4943


WS_3m_7
σ[MPa]=237.96
N_f[Cycles]=6411


WS_3m_11
σ[MPa]=233.02
N_f[Cycles]=29217


WS_3m_9
σ[MPa]=227.15
N_f[Cycles]=429447


WS_3m_10
σ[MPa]=237.03
N_f[Cycles]=94888


WS_9m_1
σ[MPa]=250.77
N_f[Cycles]=186


WS_9m_2
σ[MPa]=243.26
N_f[Cycles]=941


WS_9m_3
σ[MPa]=233.90
N_f[Cycles]=218997


WS_9m_4
σ[MPa]=230.89
N_f[Cycles]=143660


WS_9m_6
σ[MPa]=237.67
N_f[Cycles]=76994


WS_9m_7
σ[MPa]=232.42
N_f[Cycles]=48563


WS_9m_8
σ[MPa]=237.49
N_f[Cycles]=21633


WS_9m_9
σ[MPa]=232.10
N_f[Cycles]=20962

WS_9m_10
σ[MPa]=233.91
N_f[Cycles]=172687

Steel

S_1_2
σ[MPa]=239.15
N_f[Cycles]=206621

S_1_3
σ[MPa]=263.31
N_f[Cycles]=992

S_1_4
σ[MPa]=241.02
N_f[Cycles]=150677

S_2_1
σ[MPa]=226.31
N_f[Cycles]=1214072

S_2_2
σ[MPa]=228.68
N_f[Cycles]=408035

S_2_4
σ[MPa]=236.90
N_f[Cycles]=185381

S_2_5
σ[MPa]=241.48
N_f[Cycles]=120477

S_2_6
σ[MPa]=251.05
N_f[Cycles]=3196

S_2_7
σ[MPa]=255
N_f[Cycles]=2223

S_2_8
σ[MPa]=231.70
N_f[Cycles]=450485

S_2_9
σ[MPa]= 238.84
N_f[Cycles]=99367

S_2_10
σ[MPa]=243.91
N_f[Cycles]=45777

S_2_11

S_2_13

σ[MPa]= 251.75
N_f[Cycles]=1917

S_2_15
σ[MPa]=228.56
N_f[Cycles]=552564

S_2_12
σ[MPa]=228.87
N_f[Cycles]=416095

S_5m_1
σ[MPa]=258.95
N_f[Cycles]=64490

σ[MPa]=239.64
N_f[Cycles]=119636

S_5m_2
σ[MPa]=233.46
N_f[Cycles]=120626

S_2_14
σ[MPa]=246.19
N_f[Cycles]=6576

S_5m_3
σ[MPa]=263.03
N_f[Cycles]=3833

S_m_4
σ[MPa]=234.80
N_f[Cycles]=140970

S_5m_5
σ[MPa]=225.57
N_f[Cycles]=186453

S_5m_6
σ[MPa]=243.60
N_f[Cycles]=44393

S_5m_7
σ[MPa]=240.78
N_f[Cycles]=110699

S_5m_8
σ[MPa]=261.32
N_f[Cycles]=6974

S_5m_9
σ[MPa]=240.83
N_f[Cycles]=144385

S_5m_10
σ[MPa]=233.80
N_f[Cycles]=208574

S_5m_11
σ[MPa]=252.15
N_f[Cycles]=310422

S_5m_12
σ[MPa]=248.51
N_f[Cycles]=166398

S_5m_13
σ[MPa]=285.48
N_f[Cycles]=3589

S_5m_14
σ[MPa]=238.89
N_f[Cycles]=102534

S_5m_15
σ[MPa]=220.69
N_f[Cycles]=189283

S_3m_1
σ[MPa]=241.82
N_f[Cycles]=

S_3m_2
σ[MPa]=234.72
N_f[Cycles]=104682

S_3m_3
σ[MPa]=249.06
N_f[Cycles]=3516

S_3m_4
σ[MPa]=228.07
N_f[Cycles]=211179

S_3m_5
σ[MPa]=228.94
N_f[Cycles]=296724

S_3m_7
σ[MPa]=242.53
N_f[Cycles]=6273

S_3m_8
σ[MPa]=244.35
N_f[Cycles]=3170

S_3m_9
σ[MPa]=234.86
N_f[Cycles]=101709

S_3m_10
σ[MPa]=254.24
N_f[Cycles]=923

S_3m_11
σ[MPa]=232.85
N_f[Cycles]=278971

S_3m_12
σ[MPa]=229.90
N_f[Cycles]=231417

S_3m_14
σ[MPa]=247.89
N_f[Cycles]=2770

S_3m_15
σ[MPa]=241.06
N_f[Cycles]=8604

S_3m_16
σ[MPa]=238.41
N_f[Cycles]=13534

S_3m_17
σ[MPa]=221.41
N_f[Cycles]=715762

S_9m_1
σ[MPa]=245.11
N_f[Cycles]=16133

S_9m_2
σ[MPa]=240.09
N_f[Cycles]=98744

S_9m_3
σ[MPa]=253.28
N_f[Cycles]=1644

S_9m_4
σ[MPa]=231.50
N_f[Cycles]=124372

S_9m_5
σ[MPa]=227.30
N_f[Cycles]=284899

S_9m_6
σ[MPa]=246.09
N_f[Cycles]=14382

S_9m_7
σ[MPa]=239.08
N_f[Cycles]=85856

S_9m8
σ[MPa]=252.13
N_f[Cycles]=2680

S_9m_9
σ[MPa]=230.03
N_f[Cycles]=219910

Cast Iron

AA4
σ[MPa]=76.43
N_f[Cycles]=751

AA5
σ[MPa]=69.98
N_f[Cycles]=1690

AA6
σ[MPa]=55.67
N_f[Cycles]=14745

AA7
σ[MPa]=46.56
N_f[Cycles]=142029

AA9
σ[MPa]=51.04
N_f[Cycles]=197025

CI_1_2
σ[MPa]=51.69
N_f[Cycles]=66103

CI_1_3
σ[MPa]=56.28
N_f[Cycles]=23930

CI_1_4
σ[MPa]=61.01
N_f[Cycles]=16839

CI_2_2
σ[MPa]=69.80
N_f[Cycles]=2101

CI_2_3
σ[MPa]=60.45
N_f[Cycles]=18501

CI_2_4
σ[MPa]=64.81
N_f[Cycles]=5651

CI_2_6
σ[MPa]=64.62
N_f[Cycles]=2264

CI_2_7
σ[MPa]=55.35
N_f[Cycles]=7987

CI_2_8
σ[MPa]=51.06
N_f[Cycles]=17621

CI_2_9
σ[MPa]=46.38
N_f[Cycles]=14235

CI_3m_1
σ[MPa]=65.71
N_f[Cycles]=11533

CI_3m_2
σ[MPa]=55.59
N_f[Cycles]=21186

CI_3m_3
σ[MPa]=50.50
N_f[Cycles]=23660

CI_3m_5
σ[MPa]=65.24
N_f[Cycles]=3396

CI_3m_6
σ[MPa]=55.99
N_f[Cycles]=87109

CI_3m_7
σ[MPa]=52.08
N_f[Cycles]=127020

CI_3m_8
σ[MPa]=48.93
N_f[Cycles]=158005

CI_3m_9
σ[MPa]=51.80
N_f[Cycles]=44033

CI_3m_10
σ[MPa]=65.54
N_f[Cycles]=5280

Brass

Br_2_1
σ[MPa]=192.22
N_f[Cycles]=8

Br_2_2
σ[MPa]=178.07
N_f[Cycles]=13

Br_2_3
σ[MPa]=164.44
N_f[Cycles]=131262

Br_2_4
σ[MPa]=145.71
N_f[Cycles]=87888

Br_2_1
σ[MPa]=192.22
N_f[Cycles]=8

Br_9m_1
σ[MPa]=
N_f[Cycles]=

Br_9m_2
σ[MPa]=
N_f[Cycles]=

Br_9m_3
σ[MPa]=
N_f[Cycles]=

Br_9m_4
σ[MPa]=
N_f[Cycles]=

Br_9m_5
σ[MPa]=
N_f[Cycles]=

Br_9m_6
σ[MPa]=
N_f[Cycles]=

Br_9m_7
σ[MPa]=
N_f[Cycles]=

Br_9m_8
σ[MPa]=
N_f[Cycles]=

Br_9m_9
σ[MPa]=
N_f[Cycles]=

Br_9m_10
σ[MPa]=
N_f[Cycles]=

Appendix A2 Failed notched specimens

Br_1mm

B_1mm_1
σ[MPa]=84.2
N_f[Cycles] =541945

B_1mm_3
σ[MPa]=107.9
N_f[Cycles] =65518

B_1mm_4
σ[MPa]=80.5
N_f[Cycles]=530996

B_1mm_5
σ[MPa]=112.6
N_f[Cycles]=55514

B_1mm_6
σ[MPa]=75.9
N_f[Cycles]=1903387

B_1mm_7
σ[MPa]=84.1
N_f[Cycles]=739815

B_1mm_8
σ[MPa]=97.1
N_f[Cycles]=121909

B_1mm_9
σ[MPa]=107.5
N_f[Cycles]=74827

B_1mm_10
σ[MPa]=80.9
N_f[Cycles]=776713

Br_2mm

B_2mm_1
σ[MPa]=75.7
N_f[Cycles]=292589

B_2mm_2
σ[MPa]=83.9
N_f[Cycles]=178161

B_2mm_3
σ[MPa]=94.4
N_f[Cycles]=36739

B_2mm_4
σ[MPa]=70.5
N_f[Cycles]=337359

B_2mm_5
σ[MPa]=67.5
N_f[Cycles]=732233

B_2mm_7
σ[MPa]=70.5
N_f[Cycles]=359750

B_2mm_8
σ[MPa]=75.8
N_f[Cycles]=240122

B_2mm_9
σ[MPa]=83.8
N_f[Cycles]=130672

B_2mm_10
σ[MPa]=94.8
N_f[Cycles]=59018

Br_3mm

B_3mm_1
σ[MPa]=66.9
N_f[Cycles]=196858

B_3mm_2
σ[MPa]=67.8
N_f[Cycles]=194403

B_3mm_3
σ[MPa]=59.0
N_f[Cycles]=676739

B_3mm_4
σ[MPa]=72.7
N_f[Cycles]=140561

B_3mm_5
σ[MPa]=59.6
N_f[Cycles]=410938

B_3mm_6
σ[MPa]=55.3
N_f[Cycles]=507491

B_3mm_7
σ[MPa]=55.7
N_f[Cycles]=706821

B_3mm_8
σ[MPa]=52.5
N_f[Cycles]=1568334

B_3mm_9
σ[MPa]=53.4
N_f[Cycles]=616481

CI_1mm

CI_1mm_2
σ[MPa]=46.1
N_f[Cycles]=132604

CI_1mm_3
σ[MPa]=51.1
N_f[Cycles]=8442

CI_1mm_4
σ[MPa]=56.9
N_f[Cycles]=5176

CI_1mm_5
σ[MPa]=43.4
N_f[Cycles]=24487

CI_1mm_6
σ[MPa]=42.8
N_f[Cycles]=963511

CI_1mm_7
σ[MPa]=43.4
N_f[Cycles]=303117

CI_1mm_8
σ[MPa]=42.1
N_f[Cycles]=68918

CI_1mm_9
σ[MPa]=42.3
N_f[Cycles]=39080

CI_2mm

CI_2mm_1
σ[MPa]=54.4
N_f[Cycles]=406

CI_2mm_2
σ[MPa]=43.5
N_f[Cycles]=16266

CI_2mm_3
σ[MPa]=32.3
N_f[Cycles]=347842

CI_2mm_4
σ[MPa]=48.8
N_f[Cycles]=647

CI_2mm_5
σ[MPa]=29.9
N_f[Cycles]=563403

CI_2mm_6
σ[MPa]=46.1
N_f[Cycles]=4025

CI_2mm_7
σ[MPa]=44.7
N_f[Cycles]=15354

CI_2mm_8
σ[MPa]=46.2
N_f[Cycles]=1183

CI_2mm_10
σ[MPa]=35.31
N_f[Cycles]=64586

CI_3mm

CI_3mm_1
σ[MPa]=40.5
N_f[Cycles]=1708

CI_3mm_10
σ[MPa]=27.2
N_f[Cycles]=187383

CI_3mm_3
σ[MPa]=40.8
N_f[Cycles]=1455

CI_3mm_4
σ[MPa]=37.9
N_f[Cycles]=5641

CI_3mm_5
σ[MPa]=25.6
N_f[Cycles]=174677

CI_3mm_6
σ[MPa]=24.7
N_f[Cycles]=660480

CI_3mm_7
σ[MPa]=37.6
N_f[Cycles]=2933

CI_3mm_8
σ[MPa]=25.3
N_f[Cycles]=159794

CI_3mm_9
σ[MPa]=37.4
N_f[Cycles]=4988

S_1mm

S_1mm_1
σ[MPa]=215.2
N_f[Cycles]=8103

S_1mm_2
σ[MPa]=147.8
N_f[Cycles]=203115

S_1mm_3
σ[MPa]=136.2
N_f[Cycles]=1215396

S_1mm_4
σ[MPa]=136.9
N_f[Cycles]=362177

S_1mm_5
σ[MPa]=147.5
N_f[Cycles]=193751

S_1mm_6
σ[MPa]=188
N_f[Cycles]=34155

S_1mm_7
σ[MPa]=187.2
N_f[Cycles]=24110

S_1mm_8
σ[MPa]=214.6
N_f[Cycles]=8643

S_1mm_9
σ[MPa]=140.9
N_f[Cycles]=483252

S_1mm_10
σ[MPa]=142.4
N_f[Cycles]=374787

S_2mm

S_2mm_1
σ[MPa]=107.9
N_f[Cycles]=496775

S_2mm_2
σ[MPa]=129.7
N_f[Cycles]=291168

S_2mm_3
σ[MPa]=182.7
N_f[Cycles]=10000

S_2mm_4
σ[MPa]=128.8
N_f[Cycles]=185460

S_2mm_5
σ[MPa]=133.8
N_f[Cycles]=136806

S_2mm_6
σ[MPa]=133.8
N_f[Cycles]=155536

S_2mm_7
σ[MPa]=161.6
N_f[Cycles]=26734

S_2mm_8
σ[MPa]=151.7
N_f[Cycles]=23547

S_2mm_9
σ[MPa]=183.0
N_f[Cycles]=8606

S_2mm_10
σ[MPa]=175.5
N_f[Cycles]=12105

S_3mm

S_3mm_1
σ[MPa]=135.3
N_f[Cycles]=27529

S_3mm_2
σ[MPa]=135.6
N_f[Cycles]=31457

S_3mm_3
σ[MPa]=108.1
N_f[Cycles]=208275

S_3mm_4
σ[MPa]=108.6
N_f[Cycles]=210278

S_3mm_5
σ[MPa]=146.7
N_f[Cycles]=7826

S_3mm_6
σ[MPa]=154.7
N_f[Cycles]=12684

S_3mm_7
σ[MPa]=94.4
N_f[Cycles]=481826

S_3mm_8
σ[MPa]=108.6
N_f[Cycles]=196032

S_3mm_9
σ[MPa]=92.5
N_f[Cycles]=519988

S_3mm_10
σ[MPa]=92.2
N_f[Cycles]=540895

Appendix A3

1) Matlab code to generate virtual S-N curves with different standard deviations

```
clear; clc; close all;
prompt = 'filename';

% Input Data
str = input(prompt,'s');
a = insertAfter(str,strlength(str),".xlsx");
raw = readtable(a,'Sheet','Raw data');
convert_data = table2array(raw(:,4:5));

count = 1;
for i = 1:length(convert_data)
    if convert_data(count,1) >= 0
        count = count + 1;
    end
end

input_data = convert_data(1:count-1,1:2);

% Post-processing
log_sigma = log10(input_data(:,1));
log_N = log10(input_data(:,2));
Mean_sigma = mean(log_sigma);
Mean_N = mean(log_N);
Xminus_mean = log_sigma - Mean_sigma;
Xminus_mean_square = Xminus_mean.^2;
Yminus_mean = log_N - Mean_N;
Yminus_mean_square = Yminus_mean.^2;
prod_XY = Xminus_mean.*Yminus_mean;
Sum_XminusXmean_square = sum(Xminus_mean_square);
Sum_prodXY = sum(prod_XY);
C1 =  Sum_prodXY/Sum_XminusXmean_square;
C0 = Mean_N - C1 * Mean_sigma;
k = -C1;
Y_hat = C0 + C1 * log_sigma;
Yminus_Y_hat_square = (log_N - Y_hat).^2;
Sum_Yminus_Y_hat_square = sum(Yminus_Y_hat_square);
s1 = sqrt(Sum_Yminus_Y_hat_square/(length(input_data)-1));
s2 = sqrt(Sum_Yminus_Y_hat_square/(length(input_data)-2));

P_50 = 10.^Y_hat;

alpha = input('Please input alpha: ');
Fp = finv(1-alpha,2,length(input_data)-2);
t_distribution = tinv(1-alpha/2,length(input_data)-2); %one-tailed by default for
matlab hence need divide alpha by 2

raw_2 = readtable(a,'Sheet','q_table');
q_table = table2array(raw_2);

% interpolate q value, column 2 = 90%, column 3 = 95%, column 4 = 99%
if alpha == 0.01
```

```
    column = 4;

elseif alpha == 0.05
    column = 3;

elseif alpha == 0.10
    column = 2;

else
    column = 5;
end

row = find(q_table(:,1)==length(input_data));
q_value = q_table(row,column);

scatterband_ini = 150;
scatterband_final = 2000000;

sig_ini_mean = (10^(C0)/scatterband_ini)^(1/k);
sig_final_mean = (10^(C0)/scatterband_final)^(1/k);

loglog([scatterband_ini scatterband_final],[sig_ini_mean sig_final_mean],"-- k")

% loglog(P_50,input_data(:,1),"-- k")
% xlim([10 10^7])
% ylim([200 300])
grid on
hold on

scatter(input_data(:,2),input_data(:,1),'k','filled','^')

% Plot linear model
sig_ini_1P = (10^(C0 + q_value*s1)/scatterband_ini)^(1/k);
sig_final_1P = (10^(C0 + q_value*s1)/scatterband_final)^(1/k);
sig_ini_99P = (10^(C0 - q_value*s1)/scatterband_ini)^(1/k);
sig_final_99P = (10^(C0 - q_value*s1)/scatterband_final)^(1/k);


loglog([scatterband_ini scatterband_final],[sig_ini_1P sig_final_1P])
loglog([scatterband_ini scatterband_final],[sig_ini_99P sig_final_99P])
```